The copyright of this thesis vests in the author. No quotation from it or information derived from it is to be published without full acknowledgement of the source. The thesis is to be used for private study or non-commercial research purposes only.

Published by the University of Cape Town (UCT) in terms of the non-exclusive license granted to UCT by the author.

University of Cape Town

46

THE GEOCHEMISTRY OF SELECTED MID-OCEAN RIDGE BASALTS FROM THE SOUTHERN MID-ATLANTIC RIDGE (40°-55°S)

University of Cape Town

Petrus Jacobus le Roux

Thesis Presented for the Degree of

DOCTOR OF PHILOSOPHY

in the Department of Geological Sciences

UNIVERSITY OF CAPE TOWN

March 2000

DECLARATION

I hereby declare that all the work presented in this thesis is my own, except where otherwise stated.

Petrus Jacobus le Roux

University of Cape Town

ACKNOWLEDGEMENTS

I owe a huge debt of gratitude to numerous people, and I am certain these words will not sufficiently convey my heartfelt appreciation.

Anton le Roex gave me excellent supervision and always his true opinions. It wasn't always what I wanted to hear, but on reflection, invariably what I needed to be told. The late Dick Rickard's assistance with the electron microprobe was invaluable. He will be sorely missed. Andreas Späth not only assisted in LA-ICP-MS analyses, but with a recent Ph.D. thesis behind him always encouraged me. Dave Reid, whom I blame partially for getting me into geology and totally for me being at UCT, always had an open door and advice for numerous enquiries, usually concerning computer catastrophes. The many discussion I had with Phil Janney, the banjo-playing geochemist, assisted greatly in developing my theories and ideas when these were in early stages of formulation. Other friends and fellow students, at UCT and elsewhere, who gave me advice and assistance are, in no particular order: Lewis McCaffrey, Paul Macey, Russell Maytham, Clare Appleyard, Jefferson Chaumba, Andrew Menzies, Kalle Westerlund, Bernadette Azzie, Lisa Cavé, Stewart Whyte, Peter Foelling, Martin Wieneke, Mark Schmitz and Ingrid Chinn.

Jean-Guy Schilling provided the bulk of the samples, and Jill Douglass and Denis Fontignie provided the isotope data before publication. Bill Perkins and Nick Pearce allowed me free-reign on the LA-ICP-MS at Aberystwyth. Nobu Shimizu, gave his time, ion probe, and general scientific advice during my time at Woods Hole. Yaoling Niu, Tim Grove and Peter Michael endured request for advice and/or software, and always gave me some of their time.

My parents, sisters and brother always gave support and encouragement, although at times they had difficulty understanding why I would choose to put myself through this! Finally, without Pippa being there every step of the way, the good times and the bad, I am absolutely certain I would never have reached the end. For her love and support I will be eternally grateful.

The financial assistance of the National Research Foundation towards this research is hereby acknowledged. Opinions expressed in this work, or conclusions arrived at, are those of the author and are not necessarily to be attributed to the National Research Foundation.

University of Cape Town

TABLE OF CONTENTS

ACKNOWLEDGEMENTS

ABSTRACT i

CHAPTER 1: INTRODUCTION 1.1

1.1 General Background 1.1

1.2 Present Study 1.5

CHAPTER 2: PREVIOUS WORK 2.1

2.1 Previous Work on MORB From 40-55°S on the Southern Mid-Atlantic Ridge 2.1

2.2 Previous Work on Basalts From the Greater South Atlantic Region 2.3

2.3 Final Comments 2.5

CHAPTER 3: SAMPLING & ANALYTICAL TECHNIQUES 3.1

3.1 Sampling 3.1

3.2 Analytical Techniques 3.1

3.2.1 Electron microprobe (EMP) analysis 3.1

3.2.2 X-ray fluorescence (XRF) spectrometry 3.3

3.2.3 Laser ablation-inductively coupled plasma-mass spectrometry (LA-ICP-MS) 3.3

CHAPTER 4: REGIONAL VARIATIONS 4.1

4.1 Petrography 4.2

4.2 Mineralogy 4.13

4.3 Bulk-Rock Compositions 4.28

4.4 Quenched Igneous-Glass Compositions 4.33

4.4.1 Classification 4.33

4.4.2 Major-element variations 4.40

4.4.3 Trace-element variations 4.52

4.4.4 Major-element systematics of quenched igneous glass-~~bulk-rock sample pairs~~ 4.59

4.5 Regional Summary 4.67

University of Cape Town

CHAPTER 5: GEOCHEMICAL CHARACTERISTICS OF MANTLE SOURCE REGIONS 5.1
5.1 Incompatible Trace-Element Characteristics of Mantle Source-Regions 5.2
5.2 Possible Origins of Observed Incompatible Trace-Element Anomalies in Mantle Source-Regions 5.16
5.3 Discussion 5.32

CHAPTER 6: MELTING PROCESSES BENEATH THE SOUTHERN MID-ATLANTIC RIDGE (40°-55°S) 6.1
6.1 Fractionation-Corrected Major-Element Compositions 6.2
6.1.1 Details and discussion of data recalculation 6.2
6.1.2 The global trend 6.6
6.1.3 The local trend 6.18
6.2 Variations in Calculated Melting Parameters 6.28
6.3 Residual Garnet During Melting Beneath Discovery-Influenced Ridge Segments . 6.36
6.4 Discussion 6.58
6.4.1 Major-Element systematics as indicators of melting parameters - the global trend. 6.58
6.4.2 Major-element systematics orthogonal to the global trend - the local trend. 6.64
6.4.3 The possible role for compositionally distinct pyroxenitic material, derived from small degree melts formed in the garnet-lherzolite stability-field, during melting beneath Discovery-influenced ridge segments. 6.65

CHAPTER 7: CRYSTALLISATION PROCESSES BENEATH THE SOUTHERN MID-ATLANTIC RIDGE (40°-55°S) 7.1
7.1 Observed Compositional Variations in MORB From the SMAR Due to Crystallisation 7.1
7.2 Forward-Modelling of Crystallisation 7.6
7.3 Pressures of Crystallisation 7.36
7.4 Discussion 7.44

CHAPTER 8: CONCLUSIONS 8.1

University of Cape Town

REFERENCES R.1

APPENDIX A: DREDGE STATION DETAILS A.1

Table A.1: Dredge station details for R/V Maurice Ewing samples. A.2

Table A.2: Dredge station details for Agulhas 32 samples. A.6

APPENDIX B: ANALYTICAL DATA B.1

Table B.1: Olivine phenocryst compositions (EMP) B.2

Table B.2: Plagioclase phenocryst compositions (EMP) B.8

Table B.3: Clinopyroxene phenocryst compositions (EMP) B.14

Table B.4: Spinel microphenocryst compositions (EMP) B.14

Table B.5: Major- (EMP) and trace-element (LA-ICP-MS) compositional data for quenched igneous glasses. B.15

Table B.6: Major- and trace-element (XRF) compositional data for bulk-rock samples. B.34

APPENDIX C: DETAILED PETROGRAPHY C.1

Table C.1: Petrographic thin section descriptions C.2

University of Cape Town

ABSTRACT

In 1993, dredge-sampling from 40.6°S to 52.5°S, during cruise 9309 of the R/V Maurice Ewing, greatly increased the number of basalts recovered from this section of the southern Mid-Atlantic Ridge (SMAR), and significantly expanded the global suite of samples from slow-spreading ridges. Radiogenic isotope (Douglass *et al.*, 1999) and noble gas (Moreira *et al.*, 1995) studies of these samples have been concluded, and the work in this thesis focusses on the major- and trace-element compositions of bulk-rock and quenched igneous-glass samples, as well as the petrography and mineralogy of constituent phenocryst phases. These data are used to classify and describe general variations in MORB compositions, investigate the major- and trace-element characteristics of MORB mantle source-regions beneath the SMAR, and define the melting and crystallisation processes active beneath these ridge segments.

The basalts investigated in this study are aphyric to sparsely phyric (<10-20% total phenocrysts) and dominated by large, resorbed or rounded and optically zoned plagioclase phenocrysts (≤20%, few samples ≤40%; $An_{\sim 80-90}$) frequently containing inclusions of quenched igneous glass. Less-abundant plagioclase microphenocrysts are frequently skeletal with compositions of $An_{\geq 60}$ and occur in basalts with low Mg#'s. Olivine is the second-most abundant phenocryst (≤3%) and occurs mainly as microphenocrysts (Fo_{82-87}, with Fo_{70-73} in low Mg# basalts). Large olivine phenocrysts (Fo_{88-89}) are less-abundant and frequently rounded or resorbed. Clinopyroxene and spinel occur as rare microphenocryst phases, and occasional sulphide blebs are also present.

The major-element compositions of bulk-rock samples and quenched igneous glasses of MORB recovered from the SMAR, classify these samples as predominantly olivine-normative tholeiitic basalts with a few exceptions classified as quartz-normative basaltic andesites. Their trace-element compositions range from incompatible trace-element depleted (Nb/Zr ≤0.03, Zr/Y ≤2.91, $(La/Sm)_N$ ≤0.79, K/Ti ≤0.14) to incompatible trace-element enriched (Nb/Zr ≤0.17, Zr/Y ≤6.88, $(La/Sm)_N$ ≤2.94, K/Ti ≤1.15). The basalts with enriched incompatible trace-element compositions are also enriched in radiogenic isotopes (Douglass *et al.*, 1999) and were recovered from ridge segments with anomalously shallow bathymetry associated with the influence of two proximal mantle plumes, Discovery and Shona. Compositional trajectories defined by incompatible trace-element ratios support mixing between ambient depleted MORB mantle and

University of Cape Town

enriched material derived from these two, isotopically distinct mantle plumes.

The incompatible trace-element compositions of Discovery- and Shona-influenced MORB substantiate the classification of these mantle plumes as EM- and HIMU-type, respectively (Douglass *et al.*, 1999). Furthermore, Douglass *et al.* (1999) found unusually low $^{206}Pb/^{204}Pb$, $^{143}Nd/^{144}Nd$ and high $^{87}Sr/^{86}Sr$ background ratios in some Discovery-influenced MORB and proposed the presence of a so-called LOMU component representing delaminated subcontinental lithosphere in the mantle source-regions of these basalts. These basalts, and in addition also most N-MORB, were found to have anomalously high Ba, and low Nb and Ta abundances, relative to other elements with similar compatibility, compared to compositions of "typical" N-MORB or incompatible trace-element enriched MORB.

Modelling of trace-element abundance variations in these low $^{206}Pb/^{204}Pb$, low Nb basalts necessitate the presence of <2.5% of subcontinental lithosphere in their mantle source-regions, and in addition are indicative of a subduction-zone compositional "imprint" on this subcontinental material, consistent with the proposed composition of the subcontinental lithosphere beneath southern Africa. This variously termed background contamination or "pollution" of the ambient upper-oceanic mantle, as defined by radiogenic isotope and Ba/Nb data for MORB, beneath the South Atlantic seems to correspond broadly with the latitudinal extent of the Dupal anomaly in the South Atlantic, from approximately 15°-50°S. This supports the possible division of the Dupal anomaly into two distinct entities: one shallow in origin and composed of delaminated "rafts" of subcontinental lithosphere, sampled predominantly by shallow MORB mantle melting and early mantle plume-related oceanic volcanism; the other deep in origin and sampled mostly by present mantle plume magmatism, i.e. the Tristan/Gough mantle plume.

Broad co-variations in fractionation-corrected major-element data (Na_8-Fe_8) for basalts from the SMAR correspond to the orientation of the global trend. However, data for Discovery-influenced MORB range towards lower initial pressures of melting (13-20kbar) relative to data for N-MORB (~18±3kbar), whereas data for Shona-influenced MORB conform to the accepted model for the origin of the global trend. Melting beneath these ridge segments initiated at greater pressures (≤23kbar) relative to N-MORB. The Discovery-influenced mantle source-regions are proposed to contain significant proportions of pyroxenite veins and the derivation of substantial

University of Cape Town

fractions of the final magmas from these veins could account for the observed anomalous major-element compositions. Additionally, local trends observed in finer-scale Na_8-Fe_8 co-variations in data of all MORB from the SMAR are best-accounted for by variable extents of crystallisation at pressures of 1atm to at least 6kbar.

Some Discovery-influenced basalts, recovered from near ends of ridge segments terminated by the Falkland-Agulhas Fracture Zone (at ~47.5°S) and another, unnamed, significant off-set transform (at ~48.4°S), have particularly high $^{87}Sr/^{86}Sr$ ratios (0.705093-0.705878) and low $^{143}Nd/^{144}Nd$ ratios (0.512365-0.512567), and were viewed by Douglass *et al.* (1999) as carrying the strongest signal of the compositional influence of the Discovery mantle plume. These samples also have anomalous trace-element compositions (low Sc concentrations, ≥22.2ppm, and low Yb concentrations, ≥1.37ppm, resulting in high $(Sm/Yb)_N$ of 1.73-2.83, at Mg# of 63-65) and fractionation-corrected major-element compositions (yielding initial pressures of melting of 5-7kbar).

It is proposed that these anomalous basalts were primarily derived by melting of pyroxenite veins reflecting frozen small-degree melts (2-3%), associated with the upwelling Discovery mantle plume, formed within the garnet-lherzolite stability-field. These pyroxenite veins therefore carried the radiogenic-isotope values of the Discovery mantle plume, and trace-element compositions reflecting the presence of residual garnet during melting. Mantle flow delivered the pyroxenite-veined mantle to proximal ridge segments where they became entrained in the general sub-ridge axis upwelling. Due to subdued upwelling and the suppressed thermal regime beneath the sections of ridge segments in the vicinity of this substantial fracture zone and off-set transform, mantle melting occurred at shallow-levels over restricted pressure intervals, and preferentially consumed the pyroxenite veins, due to their low-temperature solidus relative to ambient spinel-lherzolitic mantle. The tectonic setting also favoured ineffective melt-focussing towards the central eruptive zone of the ridge segments and little homogenisation with melts derived from the ambient spinel-lherzolitic mantle occurred, resulting in the eruption of magmas with exceptionally undiluted pyroxenite compositions. These magmas then contain major-element compositions indicative of low initial pressures of melting, but anomalous radiogenic-isotope and trace-element characteristics inherited from the mantle plume.

The semi-quantitative modelling of observed variations of major- and selected trace-

University of Cape Town

element abundances for MORB from the SMAR indicate significant crystallisation involving olivine, plagioclase and clinopyroxene at variable pressures. Theoretical primary melt compositions (Kinzler, 1997) require 30-40% crystallisation, of initially only olivine and later three-phase crystallisation of olivine, plagioclase and clinopyroxene, at pressures of 6-8kbar to attain compositions similar to basalts with high-MgO concentrations recovered from the SMAR.

General decreasing trends in CaO concentrations and CaO/Al_2O_3 ratios with decreasing MgO concentrations and Mg#'s, and the relatively constant Sc concentrations with decreasing Mg#'s of basalts from the SMAR necessitate the presence of clinopyroxene on the liquidus during crystallisation beneath the SMAR, although clinopyroxene is rarely observed as a phenocryst phase. In excess of 50% crystallisation of basalts with high-MgO concentrations is required to account for some Shona- and Discovery-influenced MORB with Mg#'s of 0.40-0.48. Pressures of crystallisation obtained from qualitative comparisons between modelled crystallisation trends and observed variations in basalt compositions, and quantitative methods (Grove *et al.*, 1992; Michael & Cornell, 1998) all agree, and indicate crystallisation occurred at relatively high pressures beneath the SMAR. Basalts recovered from ridge segments unaffected by mantle plumes experienced crystallisation predominantly at pressures of 3-6kbar. Beneath ridge segments affected by the Discovery mantle plume north of the Falkland-Agulhas Fracture Zone (at ~47.5°S), crystallisation occurred mainly at 4-6kbar, whereas south of this fracture zone crystallisation occurred at 1atm-4kbar beneath Discovery-influenced ridge segments. Basalts recovered from the northern-most Shona-influenced ridge segments experienced crystallisation at 2-8kbar, while further south Shona-influenced MORB underwent crystallisation at 1atm-3kbar.

University of Cape Town

CHAPTER 1: INTRODUCTION

The global mid-ocean ridge system consists of some of the most active volcanic and tectonic areas on the planet. The formation of new ocean crust at mid-ocean ridges is probably the largest exchange of material and heat between the Earth's interior and exterior. The study of mid-ocean ridge basalts (MORB), the eruptive products of this process, aims to define and explain the petrogenetic mechanisms active beneath the different ridges spread around the globe and to investigate the upper-oceanic mantle from which MORB were extracted.

At present, the study of MORB is significantly skewed towards basalts erupted along fast- and superfast-spreading ridges. These ridges are predominantly located in the northern oceans, closer to the home-ports of the majority of research vessels capable of dredging cruises. The slower spreading ridges, predominantly located in the southern oceans as well as the Arctic Ocean, are relatively under-represented in the global data-set due to logistical and financial constraints, as well as unfavourable sea and weather conditions in these regions. This imbalance in the geographical coverage of the global MORB data-set has led to uncertainty regarding the diversity of mantle source-region compositions present and/or processes active beneath mid-ocean ridges. The need therefore exists to address the neglected status of the slow-spreading end-member of the mid-ocean ridge spectrum which have not been explored, defined and explained to the same degree as fast-spreading ridge environments (Michael & Cornell, 1998; Niu & Batiza, 1993, and references therein; Niu & Hékinian, 1997). The compositions of MORB mantle source-regions and the processes at work beneath these ridges are most-probably significantly different in nature from those beneath fast-spreading ridges (Langmuir *et al.*, 1992).

University of Cape Town

1.1 GENERAL BACKGROUND

The chemical and mineralogical composition of MORB mantle source-regions (Douglass *et al.*, 1999; Fontignie & Schilling, 1996; Hirschmann & Stolper, 1996; le Roex, 1987; Michael, 1995), the details of mantle flow and upwelling (Lin & Phipps Morgan, 1992), the melting processes (Kinzler, 1997; Kinzler & Grove, 1992a; Kinzler & Grove, 1992b; Kinzler & Grove, 1993; Klein & Langmuir, 1987; Niu, 1997; Niu & Batiza, 1991; Walter *et al.*, 1995), the details of melt migration (Asimow & Stolper, 1999; Kelemen *et al.*, 1997; Korenaga & Kelemen, 1998; Niu, 1997; Suhr, 1999) and melt focussing (Magde *et al.*, 1996; Magde *et al.*, 1997), the interaction or lack thereof between melt and ambient mantle (Asimow & Stolper, 1999; Niu &

Batiza, 1994; Reiners, 1998), crystallization, collection and homogenization of magma (Langmuir *et al.*, 1992; Michael & Cornell, 1998), and the presence of shallow, ridge-centred magma chambers (Batiza *et al.*, 1996; Detrick *et al.*, 1990; Singh *et al.*, 1998; Sinton & Detrick, 1992) beneath various mid-ocean ridges, are some of the questions which have been the focus of MORB studies in recent years.

This thesis addresses three fundamental issues relating to the geochemical and petrogenetic study of MORB from the SMAR. The chemical and mineralogical compositions of the underlying mantle source-regions, the nature and parameters of the melting processes which yielded the parental magmas, and the nature and parameters of processes which might have modified the compositions of these magmas following their removal from the melting regime and prior to their final eruption on the sea-floor.

Mantle source-regions. The study of differences in radiogenic isotope data for MORB and ocean-island basalts (OIB) has resulted in the identification of at least four mantle end-member compositions: depleted MORB mantle (DMM); high U/Pb mantle (HIMU); and two enriched mantle end-members (EMI & EMII) (Hart, 1988; Zindler & Hart, 1986). Radiogenic isotope characteristics of these end-members are their defining criteria, which have been combined with incompatible trace-element characteristics to further refine distinction between end-members and attempt to define origins for these mantle components (Hofmann, 1997; Hofmann *et al.*, 1986; Weaver, 1991).

The origins of these mantle end-member components are still a matter of ongoing research and debate. A major point of contention is the role of recycled subcontinental lithosphere versus subducted oceanic lithosphere in the origin of the enriched mantle end-members, sampled by ocean island volcanism (Cohen & O'Nions, 1982; Hofmann, 1997; McKenzie & O'Nions, 1983; McKenzie & O'Nions, 1995). The origin and nature of the so-called Dupal anomaly (the almost restricted occurrence of EMI & EMII end-members to the Southern Hemisphere, in a belt between the equator and 50°S) (Hart, 1988; Zindler & Hart, 1986) have received substantial attention, but again no conclusive explanation have been resolved. Postulated origins of the Dupal mantle anomaly range from deep-seated accumulation of subducted oceanic material, to shallow-level "rafters" of delaminated subcontinental lithosphere embedded in the upper oceanic mantle during the breakup of Gondwana and opening of the

University of Cape Town

South Atlantic (Castillo, 1988; Hawkesworth *et al.*, 1986; Peate *et al.*, 1999; Sun & McDonough, 1989).

Mantle upwelling and melting. Mantle upwelling beneath slow-spreading ridges is generally viewed as three-dimensional "plumes", but beneath fast-spreading ridges the upwelling is believed to be more "sheet"-like and two-dimensional (Lin & Phipps Morgan, 1992). The basis for the contrast in mantle-upwelling style being an increase in the relative importance of passive upwelling over buoyant upwelling with increasing spreading rate (Lin & Phipps Morgan, 1992).

The melting process which produces MORB is widely accepted to occur in adiabatically rising mantle material and to be polybaric and near-fractional in nature (Johnson *et al.*, 1990; Kinzler, 1997; Kinzler & Grove, 1992b; Klein & Langmuir, 1987; Langmuir *et al.*, 1992; McKenzie & Bickle, 1988). The parameters of the melting processes beneath mid-ocean ridges, e.g. mantle mode, melting mode, mantle compositions, pressure range of melting, degree of melting, and rate of production, have been the subject of considerable debate. Isobaric experimental studies which aimed to simulate, or approximate, the MORB melting process are numerous (Baker *et al.*, 1995; Baker & Stolper, 1994; Fujii, 1989; Kinzler, 1997; Kinzler & Grove, 1992a; Kinzler & Grove, 1992b; Kinzler & Grove, 1993; Niu & Batiza, 1991; Takahashi *et al.*, 1993; Walter & Presnall, 1994; Walter *et al.*, 1995). These studies have become more controlled and inclusive, i.e. involving more components and less assumptions or simplifications (Kinzler, 1997; Walter & Presnall, 1994; Walter *et al.*, 1995). Nevertheless, the applicability of isobaric experiments to a fundamentally polybaric and dynamic, in terms of e.g. chemical composition, mantle mode and melting mode, process remains a contentious point (Niu, 1999; Walter, 1999). Notwithstanding understandable reservations, experimental studies have aided considerably in the understanding of this unobservable natural process.

The experimental studies are augmented by theoretical thermodynamic models of the melting system which have become more refined and inclusive, tested against results from experimental studies, and have been applied with success to study actual MORB data (Asimow, 1999; Asimow *et al.*, 1995; Ghiorso *et al.*, 1994; Ghiorso & Sack, 1995; Hirschmann *et al.*, 1999a; Hirschmann *et al.*, 1999b; Hirschmann *et al.*, 1998; Iwamori *et al.*, 1995; Sack & Ghiorso, 1994a; Sack & Ghiorso, 1994b; Sack & Ghiorso, 1994c).

University of Cape Town

Magma transport and crystallisation. Two modes of melt migration which have received considerable attention are diffuse, reactive porous flow (Kelemen *et al.*, 1997; Niu, 1997; Reiners, 1998; Scott & Stevenson, 1989) and chemically isolated melt transport by focussed flow of melt in spatially restricted conduits such as the dunites observed in ophiolite sections (Asimow & Stolper, 1999; Kelemen *et al.*, 1997; Korenaga & Kelemen, 1997; Korenaga & Kelemen, 1998; Suhr, 1999). These seemingly opposing processes can be reconciled in a model where melt migration occurs predominantly in highly permeable and chemically isolated conduits, such as replacive dunites, while a smaller, but significant, fraction of the melt migrates by diffuse porous flow in the volumes of mantle between the major conduits (Aharonov *et al.*, 1995; Kelemen *et al.*, 1997). Models of decoupling between mantle and melt flow regimes beneath mid-ocean ridges, and effective focussing of melts towards ridge segment centres have been constructed and successfully applied to account for observed characteristics of certain ridges (Magde *et al.*, 1996; Magde *et al.*, 1997).

MORB are commonly assumed to retain the geochemical signatures of the mantle depth at which they were formed (Klein & Langmuir, 1987; Salters & Hart, 1989). This necessitates that melts which are formed at various depths in the mantle must be extracted rapidly without subsequent chemical equilibrating or other compositional interaction with the surrounding mantle at lower pressures (Langmuir *et al.*, 1992; Niu, 1997). Although some evidence for melt-mantle chemical interaction does seem to exist (Kamenetsky *et al.*, 1998; Seyler & Bonatti, 1997), the scale of the impact on the compositions of erupted MORB remains unresolved.

The most dominant process modifying the compositions of melts subsequent to removal from the melting region is thought to be crystallization of mineral phases, induced by cooler mantle surroundings, followed by subsequent fractionation of these solid phases from the remaining liquid (Grove *et al.*, 1992). Crystallization occurs predominantly at shallow levels, probably in ridge-centred magma-chambers (Sinton & Detrick, 1992), and the most common crystallisation sequence at low pressures is olivine, followed by olivine-plagioclase and then olivine-plagioclase-clinopyroxene (Grove *et al.*, 1992; Yang *et al.*, 1996). However, there is growing evidence that beneath some slower-spreading ridges crystallization occurs at elevated pressures (Grove *et al.*, 1992; le Roex *et al.*, 1996; Michael & Cornell, 1998), and while geophysical studies support the presence beneath fast-spreading ridges of relatively long-lived, steady-state axial magma chambers, these features are yet to be detected beneath slow-spreading

University of Cape Town

ridges, (Batiza *et al.*, 1988; Batiza & Niu, 1992; Detrick *et al.*, 1990; Michael & Cornell, 1998; Michael *et al.*, 1994; Reynolds *et al.*, 1992; Singh *et al.*, 1998; Sinton & Detrick, 1992).

Experimental and theoretical studies have attempted to simulated and quantify the process of fractional crystallization of MORB. The role of paired assimilation and fractionation, periodic recharge and "tapping" of the evolving system and the behaviour of trace elements during fractionation have also received attention (Ariskin *et al.*, 1993; Danyushevsky *et al.*, 1996; Ghiorso & Sack, 1995; Grove *et al.*, 1992; Langmuir *et al.*, 1992; Nielsen, 1988a; Nielsen, 1988b; Nielsen, 1989; Nielsen, 1990; Shi, 1992; Shi, 1993; Shi & Libourel, 1991; Yang *et al.*, 1998). The predicted changes in melt composition, sequence and pressure of appearance of phases, and the compositions of the phases yielded by some of the resulting algorithms and software have been compared to results from experimental work, with variable success (Yang *et al.*, 1998). At present, empirical models, based largely on experimental work, are more successful than theoretical and/or thermodynamic models at forward modelling changes observed in experimental work, and yield more realistic major element trends for an evolving basaltic magma (Yang *et al.*, 1998).

1.2 PRESENT STUDY

The section of the slow-spreading (2cm/year half-spreading rate over last 80My; Silver, 1998), southern Mid-Atlantic Ridge (SMAR), between 40°S to 55°S, just north of the Bouvet Triple Junction, has been sampled to limited degrees in the northern and southern extremities during previous dredging cruises (Fontignie & Schilling, 1996; Humphris *et al.*, 1985; le Roex *et al.*, 1987). In 1993, the section from 40.6°-52.6°S was extensively dredge-sampled during cruise 9309 of the R/V Maurice Ewing (Douglass *et al.*, 1995). In all, 44 dredge-stations at approximately 25km spacing have greatly increased the number of samples from this section of the SMAR, and also the global sample suite from slow-spreading ridges.

This thesis will deal primarily with the major- and trace-element compositions of these whole-rock and quenched igneous glass samples, as well as the major-element compositions and petrographic characteristics of constituent phenocrysts. The radiogenic-isotope and noble-gas characteristics of these MORB samples have recently received attention by other researchers (Douglass *et al.*, 1999; Moreira *et al.*, 1995). Two hotspots, Discovery and Shona, occur in the vicinity of this section of the SMAR (Douglass *et al.*, 1999; Hartnady & le Roex, 1985; Small,

University of Cape Town

1995), but the trace-element compositional characters of neither have been well-documented (Kempe & Schilling, 1974; le Roex *et al.*, 1987) with most of the information coming from studies of MORB from mantle plume-influenced ridge segments (Douglass *et al.*, 1999; Douglass *et al.*, 1995; le Roex *et al.*, 1987); one sample is available from the Discovery seamount (Kempe & Schilling, 1974). These recent studies have used MORB from proximal ridge-segments to define the radiogenic-isotope and noble-gas characteristics of these hotspots. The tectonic structure of the mid-ocean ridge in this area is diverse, having both long and short ridge segments, the large Falkland-Agulhas Fracture Zone bisecting the area, a range of large and small offset- and non-offset transforms, and ridge bathymetry spanning a significant range in depth below sea-level. The slow-spreading character of this ridge might also limit the existence of significant shallow, ridge-centred magma chambers, which could serve to collect and homogenize magma fractions derived from heterogeneous mantle source-regions and/or a range of different physical melting conditions (Detrick *et al.*, 1990). Slow-spreading could probably also affect the efficiency of melt migration and focussing towards ridge centres (Magde *et al.*, 1997). The probable absence of long-lived shallow-level magma chambers (Batiza *et al.*, 1988; Detrick *et al.*, 1990; Michael & Cornell, 1998; Michael *et al.*, 1994; Reynolds *et al.*, 1992; Sinton & Detrick, 1992) could preclude extensive low-pressure fractionation of magmas, which might obscure evidence of possible high-pressure processes. It is likely that some MORB erupted along this slow-spreading ridge might retain geochemical signatures of diverse and distinct melting environments and/or processes, or high-pressure fractionation processes (Michael & Cornell, 1998).

University of Cape Town

The aims of this study are to use a coherent data-set, combining major- and trace-element compositions of bulk-samples and quenched igneous glasses, as well as major-element compositions and petrographic characteristics of phenocryst phases, to:

- describe the general variations in MORB compositions and phenocryst characteristics observed along this section of the slow-spreading SMAR;
- investigate the major- and trace-element characteristics of mantle source-regions beneath this section of the SMAR;
- define the parameters of the melting processes along this slow-spreading ridge, i.e. pressure, extent of melting, and rate of melting, and to address variations and correlations with tectonic setting observed;
- probe the affect of crystallization processes on MORB compositions, especially

evidence of high-pressure crystallization preserved due to magmas having experienced little or no residency in long-lived, shallow-level, ridge-centred magma chambers.

University of Cape Town

CHAPTER 2: PREVIOUS WORK

This chapter will deal primarily with previous work on mid-ocean ridge basalts recovered from ridge segments between 40-55°S on the southern Mid-Atlantic Ridge. Studies of MORB from the greater South Atlantic will be discussed in less detail and, where deemed appropriate, basalts from ocean-islands located in the South Atlantic.

2.1 PREVIOUS WORK ON MORB FROM 40-55°S ON THE SOUTHERN MID-ATLANTIC RIDGE

Results of studies from previous sampling. The southern Mid-Atlantic Ridge between 40-55°S has not been sampled and studied as a coherent entity, prior to the initiative of which the current project forms part. A limited number of basalts were recovered by le Roex *et al.* (1987) from the southernmost section (51-54.5°S) of the MAR. The bulk-rock samples reported (le Roex *et al.*, 1987; van Heerden, 1987) spanned a range of incompatible trace-element compositions from normal depleted MORB to moderately enriched MORB, which combined with radiogenic isotope data defined and confirmed the compositional influence of the then postulated Shona mantle plume (Hartnady & le Roex, 1985). The noble gas data for selected samples of le Roex *et al.* (1987) presented by Kurz *et al.* (1998) supported the influence of the Shona mantle plume on basalts erupted between 51°-54.5°S.

Bulk-rock trace-element compositions of basalts recovered by Humphris *et al.* (1985) from limited dredge-stations to the north of ~46-47°S were used to define the compositional influence of the Tristan da Cunha/Gough mantle plume on MORB erupted at proximal ridge segments. Later radiogenic isotope studies of the same samples (Fontignie & Schilling, 1996; Hanan *et al.*, 1986; Humphris *et al.*, 1985; Schilling *et al.*, 1985) confirmed and further defined the influence of the mantle plume on basalts from proximal ridge segments.

Results of studies which form part of current initiative. Thus far, the basalts recovered from 40°-55°S on the SMAR by the cruise of the R/V Maurice Ewing in 1993 have only been investigated for the influences of the Discovery and Shona mantle plumes, respectively, on the mantle source-regions of MORB from the SMAR. Douglass *et al.* (1995) used chondrite-normalised La/Sm ratios of 66 basalt glasses to delineate the latitudinal extent of the influence of the Discovery and Shona mantle plumes on the compositions of these samples, placing the

University of Cape Town

Discovery mantle plume at present at 44.45°S, 6.45°E, i.e. ~425km to the northeast of the MAR, whereas the Shona mantle plume may be located on or very close to the MAR at 51.5°S. The location of the Shona mantle plume was later confirmed by Small (1995) using gravity, bathymetric and magnetic data. Douglass *et al.* (1999) reported Sr, Nd and Pb isotope data for the same 66 basalt glasses previous studied by Douglass *et al.* (1995) and defined Discovery to be derived from the enriched mantle component, while Shona is derived from the HIMU mantle end-member. General broad isotopic "pollution" of the depleted MORB mantle beneath the SMAR, previously defined by Hanan *et al.* (1986) and Fontignie & Schilling (1996) at 2°-47°S, have also been detected in MORB from the ridge section of interest (40-55°S) (Douglass *et al.*, 1999).

Douglass *et al.* (1999) presented radiogenic isotope evidence, especially low $^{206}Pb/^{204}Pb$ values in selected basalts from the SMAR, for the presence of a so-called LOMU end-member beneath the South Atlantic. This component, combined with the ambient MORB mantle and Discovery and Shona derived mantle plume material, is argued to partake in so-called pseudo-binary mixing, resulting in mantle plume-compositional influences superimposed on variably "polluted" depleted MORB mantle (Douglass *et al.*, 1999). The origin of this so-called LOMU end-member material is proposed to be thermally eroded, delaminated subcontinental lithosphere, rafted into the ambient upper mantle as large, competent and relatively cold and refractory domains (Douglass *et al.*, 1999). The quantitative details of this radiogenic isotope-based model are not available at present (Douglass & Schilling, submitted manuscript, 1998), and since the term "LOMU" as defined by Douglass *et al.* (1999) indicates specific radiogenic isotope characteristics, which do not form a part of the data-set for this study, the term LOMU will not be explicitly used in the subsequent discussions. However the LOMU samples of Douglass *et al.* (1999) as best can be determined fall within the Southern Discovery-influenced group recognised in this study (see later discussion).

The He and Ne data presented by Moreira *et al.* (1995) for a subset of basalts from 8 dredge stations located between 51°-52°S reported the noble gas characteristics of the Shona mantle plume, later expanded by Kurz *et al.* (1998). The results of investigations of geophysical data collected during cruise 9309 of the R/V Maurice Ewing (Small, 1995; Small *et al.*, 1994; Small *et al.*, 1995) confirmed and further refined earlier models of a migrating mantle plume for the formation of the Meteor Rise and Shona Ridge (Hartnady & le Roex, 1985).

University of Cape Town

2.2 PREVIOUS WORK ON BASALTS FROM THE GREATER SOUTH ATLANTIC REGION

Identification, classification and origins of mantle end-members. The study of basalts recovered from ocean islands (Kempe & Schilling, 1974; le Roex, 1985; le Roex *et al.*, 1990; le Roex *et al.*, 1995; Weaver *et al.*, 1987) and mantle-plume tracks (Humphris & Thompson, 1983; Richardson *et al.*, 1982) within the greater South Atlantic region, and continental margins flanking the South Atlantic (Hawkesworth *et al.*, 1986; Milner & le Roex, 1996; Peate *et al.*, 1999) aided in the identification and classification of global mantle compositional end-members, e.g. EM & HIMU (Hart, 1988; Hofmann, 1997; Weaver, 1991; Zindler & Hart, 1986) and regional mantle compositional anomalies, e.g. the Dupal mantle anomaly (Hart, 1984; Hart, 1988; Milner & le Roex, 1996; Peate *et al.*, 1999.

Compositional influences on the mantle upwelling beneath the SMAR. Studies of basalts recovered from mid-ocean ridges in the greater South Atlantic region have successfully focussed on defining the compositional influences of identified or postulated proximal mantle plumes on the upper-oceanic MORB mantle source-regions beneath ridge segments (Douglass *et al.*, 1999; Douglass *et al.*, 1995; Fontignie & Schilling, 1996; Hanan *et al.*, 1986; Hartnady & le Roex, 1985; Humphris *et al.*, 1985; Kurz *et al.*, 1998; le Roex *et al.*, 1987; Moreira *et al.*, 1995; Schilling *et al.*, 1985). Clearly defined latitudinal correlations between distinctive values of radiogenic isotope compositions of recovered MORB, elevations in bathymetry of ridge segments and the geographical proximity of the ridge segments to identified or postulated mantle plumes have been identified along significant lengths of the SMAR. The influence of the Ascension-Circe, St. Helena, Tristan da Cunha-Gough, Discovery, Shona, and possibly Bouvet, at the southernmost extreme of the MAR, mantle plumes have been delineated (Douglass *et al.*, 1999; Fontignie & Schilling, 1996; Hanan *et al.*, 1986; Humphris *et al.*, 1985; le Roex *et al.*, 1987; Schilling *et al.*, 1985).

Radiogenic isotope ratios, e.g. $^{206}Pb/^{204}Pb$, indicate the possible broad isotopic "pollution" of the ambient MORB mantle beneath the SMAR, progressively increasing southwards (Douglass *et al.*, 1999; Hanan *et al.*, 1986), and which might be due to the presence of dispersed and stranded "rafters" of delaminated subcontinental lithosphere in the MORB source-regions (Douglass *et al.*, 1999; Fontignie & Schilling, 1996; Hanan *et al.*, 1986). MORB recovered from a ridge segment at 33°S were found to be enriched in terms of incompatible trace-element and

University of Cape Town

radiogenic isotope compositions, but this geochemical "signature" is unrelated to any know mantle plume, and might be due to interaction of mantle upwelling beneath this ridge segment with a passively embedded chemical heterogeneity in the underlying mantle (Michael *et al.*, 1994).

Mantle melting and magma crystallisation beneath the SMAR. Studies of MORB from the SMAR which did not focus on the influences of mantle plumes on compositions of erupted basalts are few. When major-element data were obtained for basalts from the SMAR, the inferred melting parameters indicated lower degrees of melting in the proximity of fracture zones, relative to the centre of ridge segments (le Roex *et al.*, 1987; Niu & Batiza, 1994). For MORB from the ridge segment at 26°S, the range in degree of melting was quantified as approximately 15% at the ridge segment ends, to 18% in the ridge segment centre, attributed to deeper cessation of melting due to the cooling effect of the fracture zones on the underlying mantle, resulting in local suppression of mantle upwelling(Langmuir & Bender, 1984; Niu & Batiza, 1994). Also at 26°S, Niu & Batiza (1994) presented MORB compositional evidence to stress the probably importance of interaction of migrating melts with surrounding mantle, with the proposed reaction of melt A + pyroxene ⇒ melt B + olivine, especially at slow-spreading ridges.

Major-element variations in the compositions of MORB recovered from the SMAR beyond 40-55°S are mostly consistent with crystallization of olivine, plagioclase and lesser clinopyroxene. At 26°S, two sequences of crystallization were proposed: plagioclase → plagioclase + olivine → plagioclase + olivine + clinopyroxene beneath the centre of the segment; with olivine → olivine + plagioclase → olivine + plagioclase + clinopyroxene for MORB from near the fracture zones (Niu & Batiza, 1994). CaO and CaO/Al_2O_3 variations in compositions of MORB from 31°-34°S on the SMAR favour a role for clinopyroxene during early stages of crystallization and these basalts probably experienced crystallization at high pressures, from where they were erupted with little or no equilibration at shallow crustal levels (Michael *et al.*, 1994).

Trace-element heterogeneities in compositions of MORB from 31°-34°S on the SMAR preclude the presence of long-lived, shallow-level axial magma chambers (Michael *et al.*, 1994), consistent with the high pressures of crystallisation of these basalts. Lack of significant shallow-

University of Cape Town

level, axial magma chambers beneath the slow-spreading SMAR is supported by compositional characteristics of MORB from ridge segments at ~26°S, bound by the Rio Grande and Moore fracture zones which necessitate a model of deep, central magma supply beneath these ridge segments (Batiza *et al.*, 1988).

2.3 FINAL COMMENTS

The aims of this thesis, as expressed in Chapter 1, are well-formulated to address specific topics which are in need of further attention in terms of the geochemistry and petrogenesis of mid-ocean ridge basalts from the southern Mid-Atlantic Ridge. The geochemical characteristics of MORB mantle source-regions beneath the SMAR have not previously been studied with an extensive compositional data-set, ranging from major elements to highly-incompatible and low-abundance trace elements supported by radiogenic-isotope data all for the same samples. The quantitative details of melting and crystallization processes beneath the ridge segments at 40°-55°S specifically, and slow-spreading ridges in general, have not received significant attention. The tectonic and geochemical diversity of this section of the SMAR are ideal for yielding MORB with a wide range of characteristics which can further the understanding of a range of geochemical mantle domains and petrogenetic processes.

University of Cape Town

CHAPTER 3: SAMPLING & ANALYTICAL TECHNIQUES

In this chapter, the initial discussion will deal with the details of the dredging cruises which collected the MORB samples used in this study, as well as the location of the dredging stations and the section of the SMAR sampled. The second section of the chapter contains descriptions of the analytical techniques employed to obtain chemical compositional data for bulk-rock, and quenched igneous-glass samples, as well as the constituent mineral phases present in these basalts.

3.1 SAMPLING

The majority of the MORB samples used in this study were collected from the southern Mid-Atlantic Ridge (40°S to 52°30'S) during November/December 1993 by the scientific party, led by Jean-Guy Schilling from the Graduate School of Oceanography, University of Rhode Island, onboard the R/V Maurice Ewing (EW9309) (Douglass *et al.*, 1999; Douglass *et al.*, 1995). A much smaller number of samples from the southernmost extreme of the area of interest were collected by Anton le Roex and the scientific party onboard the S.A. Agulhas (le Roex *et al.*, 1987). The samples were collected by dredging the central valleys of segments of the mid-ocean ridge, the station locations are shown in relation to the tectonics of the region in fig. 3.1 and described in Appendix A. The differently coloured ridge segments indicate the recovery of MORB with incompatible trace-element compositions variably influenced by the proximal mantle plumes, as will be discussed in detail in later chapters. The regional location of this sampled section of the SMAR, relative to the greater South Atlantic, is illustrated by the inset of the regional bathymetry (Smith & Sandwell, 1997) in fig. 3.1.

University of Cape Town

3.2 ANALYTICAL TECHNIQUES

3.2.1 Electron Microprobe (EMP) Analysis

The major element compositions of quenched igneous glasses and minerals presented in this study were obtained by EMP analysis. The data for quenched igneous glasses were determined on hand-picked shards mounted in epoxy resin discs (1" diameter) and the mineral compositions were determined on standard 30μm thick, polished thin-sections. The instrument used was the Cameca Camebax four spectrometer electron microprobe of the Department of Geological Sciences, University of Cape Town. For routine analysis, the instrument was set to an accelerating voltage of 15kV, a beam current of approximately 40nA, and a focussed beam

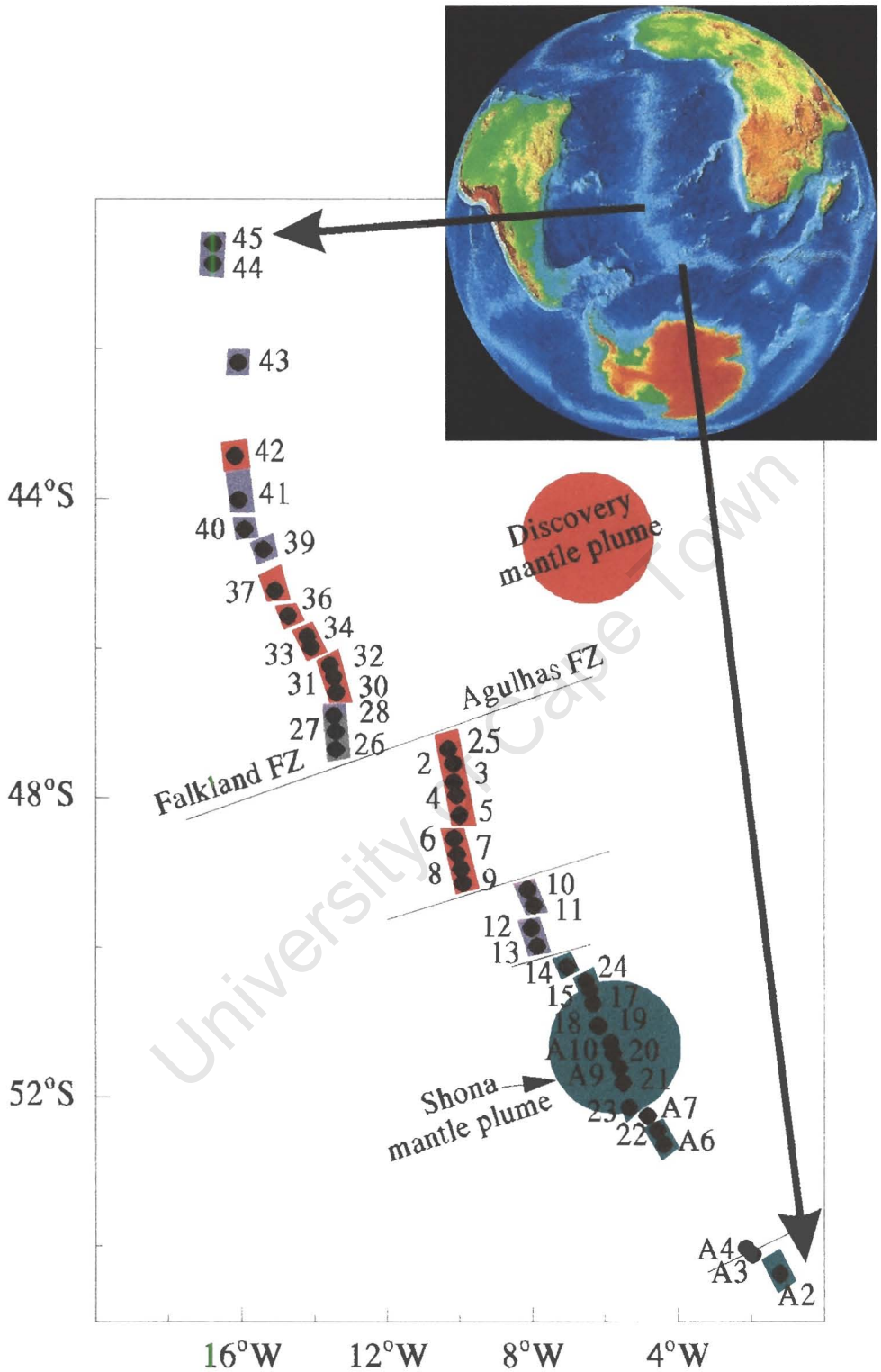

University of Cape Town

Figure 3.1: Geographical location of dredge-stations, solid black markers, along the southern Mid-Atlantic Ridge and the approximate locations of the Discovery and Shona mantle plumes (Douglass *et al.*, 1995; Douglass *et al.*, 1999; Small, 1995). Labels indicate dredge station numbers, with Agulhas 32 dredge stations indicated by labels with initial "A". Filled areas represent individual ridge segments, blue ridge segments unaffected by mantle plumes; red ridge segments affected by Discovery mantle plume; and green ridge segments affected by Shona mantle plume. Insert shows the bathymetry of the greater South Atlantic (Smith & Sandwell, 1997), with arrows indicating the section of the SMAR sampled.

for mineral analyses (spot-size: 4-5μm) or a defocussed beam for glass analyses (spot-size: 20-30μm). The following analysing crystals were used to detect the X-ray emissions of the specified analyte elements: TLAP - Na, Mg, Si, Al; LiF(200) - Fe, Mn, Ni; and PET - Ca, K, Ti, Cr, P. Ten second counting times at peak and combined background positions were used for all analytes, except Ni in olivine and Na & P in glasses, for which 30 second counting times were used. The on-line data reduction was done according to the method of Bence & Albee (1968), using factors from Albee & Ray (1970), as well as using the Cameca PAP routine. The typical lower limits of detection (LLD) and 2σ errors for EMP analyses of the quenched igneous glass and individual mineral phases are given in table 3.1. The majority of the mounted quenched igneous-glass shards were analysed for their major element compositions by Anton le Roex, prior to the initiation of the current study.

3.2.2 X-Ray Fluorescence (XRF) Spectrometry

The major, minor and selected trace element concentrations of bulk-rock samples were obtained using a Philips PW1400 and X'Unique or Siemens SRS303AS XRF spectrometer in the Department of Geological Sciences at UCT. The analyses were conducted at operating conditions adopted for routine analysis in the department and sample preparation and analytical procedures followed were those described by Duncan *et al.* (1984). The lithium tetraborate fusion method of Norrish & Hutton (1969) was used to determine all major and minor elements, except Na. Pressed powder briquettes were used for the determination of the trace elements and Na concentrations. A loss-on-ignition (LOI) value was obtained for each sample by heating in a furnace for at least 12 hours at 950°C. The analytical errors and detection limits are similar to those quoted by le Roex & Dick (1981) and Duncan *et al.* (1984), reproduced in table 3.2. The XRF major and trace-element analyses of the bulk-rock samples were conducted by Anton le Roex, again prior to the initiation of the current study.

3.2.3 Laser Ablation-Inductively Coupled Plasma-Mass Spectrometry (LA-ICP-MS)

Instrument and methodology used for final data acquisition. The trace element concentrations of the quenched igneous glass shards, analysed by EMP for major element compositions, were determined by LA-ICP-MS, using the Perkin-Elmer ELAN6000 ICP-MS and CETAC LSX-200 laser ablation system in the Department of Geological Sciences at UCT. The NdYAG laser used was frequency quadrupled to operate at 266nm and the repetition rate was set at 5Hz. The diameter of the beam was set by selecting an aperture resulting in ablation

University of Cape Town

Table 3.1: Representative EMP lower limits of detection (wt%) and 2σ errors (wt%) for quenched igneous-glass and mineral analyses. FeO^*: all iron expressed as Fe^{2+}.

	Glass		**Oliv.**		**Plag.**		**Cpx**		**Spl.**	
	LLD	2σ	LLD	2σ	LLD	2σ	LLD	2σ	LLD	2σ
SiO_2	0.045	0.260	0.510	0.266	0.055	0.298	0.052	0.294	0.038	0.028
TiO_2	0.040	0.060	0.039	0.027			0.041	0.042	0.041	0.043
Al_2O_3	0.030	0.130	0.038	0.027	0.043	0.214	0.037	0.063	0.036	0.196
Cr_2O_3			0.044	0.030			0.047	0.042	0.051	0.219
FeO^*	0.075	0.250	0.070	0.323	0.072	0.071	0.074	0.199	0.079	0.362
MnO	0.065	0.055	0.065	0.059			0.060	0.054	0.078	0.063
MgO	0.030	0.100	0.037	0.230	0.026	0.024	0.030	0.151	0.033	0.148
CaO	0.025	0.130	0.027	0.027	0.028	0.151	0.030	0.172	0.027	0.018
NiO			0.052	0.038						
Na_2O	0.020	0.050			0.028	0.068	0.028	0.029		
K_2O	0.020	0.030			0.024	0.019	0.023	0.015		
P_2O_5	0.030	0.030								

glass: quenched igneous glass; oliv.: olivine; plag.: plagioclase; cpx: clinopyroxene; spl.: spinel.

Table 3.2: Lower limits of detection (wt% for major-element oxides, and ppm for trace elements) and 2σ errors (wt% for major-element oxides, and ppm for trace elements) for XRF analysis of bulk-rock samples.

	Duncan *et al.* (1984)		le Roex & Dick (1981)	
	2σ errors	LLD	2σ errors	LLD
SiO_2	0.140	0.040		
TiO_2	0.008	0.005		
Al_2O_3	0.080	0.020		
Fe_2O_3	0.038	0.014		
MnO	0.008	0.008		
MgO	0.148	0.070		
CaO	0.028	0.008		
Na_2O	0.032	0.080		
K_2O	0.002	0.002		
P_2O_5	0.012	0.011		
Sc	1.0-1.2	1.2	1.2	1.2
V	2.4-3.7	5.5	3.7	5.0
Cr	1.5-2.1	2.2	2.0	3.4
Co	1.9-2.5	4.5	2.0	3.4
Ni	0.7-1.0	1.2	3.7	5.0
Cu	1.8-2.1	2.9	1.9	2.2
Zn	0.9-1.7	1.4	1.9	2.2
Rb	0.8-1.1	1.5	0.9	1.4
Sr	1.0-1.7	1.5	0.9	1.4
Y	0.8-1.0	1.3	0.9	1.4
Zr	0.9-1.4	1.4	0.9	1.4
Nb	1.0-1.2	1.8	1.0	2.5
Ba	2.1-6.0	3.7	2.0	3.7

University of Cape Town

pits measuring approximately 100μm in diameter. A 45 second read-delay (ablation of sample without data being collected) was employed before every analysis. The ICP-MS was set with the main gas flow at 15*l*/min, the auxiliary gas flow at 0.75*l*/min and the nebuliser gas flow at 1.06-1.08*l*/min; and the RF (radio-frequency) generator was set at 1075W. The ion beam was manipulated with the instrument's auto-lens (Ti: 4.6V; La: 5.2V; Yb: 5.8V); and the gas flow was optimized to minimise oxides such that ThO/Th < 0.5%. Isobaric corrections (where an analyte isotope mass is equal to an isotope of another element, e.g. Nd^{144}[analyte] = Sm^{144}), based on known natural abundance ratios of isotopes, were automatically made by the software as data were collected.

The preferred average values of the NIST 610 & 612 reference glass standards (Pearce *et al.*, 1997) were used for calibration. In order to avoid any possibly significant instrumental drift, over and above that corrected for through the use of ^{44}Ca as internal standard, standardization was done at approximately hourly intervals. Table 3.3 lists the standard values used; the isotope measured; the lower limit of detection (LLD); and 2σ error for each analyte element. The LLD reported in table 3.3 are based on three standard deviations of the gas blank and using the net peak intensities from the analysis of quenched igneous glass shards and eq. 3.1 given below (Perkins & Pearce, 1995). The 2σ errors were obtained from 31 repeat analyses, done after each standardization, of MORB quenched igneous glass shards from a single sample, Vulcan 40-56 from the America-Antarctic Ridge, and eq. 3.2 given below (Long, 1995).

$$LLD_{element\ x} = 3 \times \sqrt{2 \times average\ gas\ blank\ cps_{element\ x}} \times \frac{sample\ concentration_{element\ x}}{sample\ cps_{element\ x}}$$

where cps = counts per second

equation 3.1

$$2\sigma\ errors_{element\ x} = 2 \times \sum_{i=1}^{n} \frac{(x_i - \bar{x})^2}{n-1}$$

equation 3.2

where n = number of repeat analyses

The calculated lower limits of detection listed in table 3.3 are <0.5 ppm for all elements except Ni (1.06 ppm). The concentrations of Ni are significantly higher than the calculated value for the LLD, by at least a factor of 10, in all the quenched igneous-glass shards analysed and

University of Cape Town

Table 3.3: Standard values (ppm) for NIST 610 & 612 (Pearce *et al.*, 1997) used; isotope measured; lower limits of detection (LLD) (ppm) at 3 standard deviations of the background, using eq. 3.1; 2σ errors (ppm), using eq. 3.2 and 31 repeat analyses of the Vulcan 40-56 sample; and 1σ relative standard deviations (RSD) for each element analysed by LA-ICP-MS.

	NIST 610	NIST 612	Isotope	LLD	2σ errors	RSD (%)
Sc	443.9	41.05	Sc^{45}	0.36	2.10	2.74
Ni		38.44	Ni^{60}	1.06	7.29	3.73
Rb	497.4	31.63	Rb^{85}	0.12	0.32	6.53
Sr		76.15	Sr^{88}	0.08	3.67	1.07
Y	439.9	38.25	Y^{89}	0.07	3.56	4.70
Zr		35.99	Zr^{90}	0.19	10.2	3.02
Nb	424.1	38.61	Nb^{93}	0.11	0.41	2.77
Ba	457.4	37.74	Ba^{137}	0.41	1.37	2.63
La	447.8	35.77	La^{139}	0.08	0.42	2.70
Ce	430.8	38.35	Ce^{140}	0.06	0.67	1.71
Nd	450.5	35.24	Nd^{144}	0.23	0.84	2.62
Sm	461.1	36.72	Sm^{152}	0.19	0.37	3.88
Eu		34.44	Eu^{153}	0.08	0.19	5.65
Gd	426.5	36.95	Gd^{160}	0.21	0.73	5.99
Dy	426.0	35.97	Dy^{163}	0.19	0.66	5.15
Er	461.5	37.43	Er^{166}	0.14	0.35	4.64
Yb		39.95	Yb^{174}	0.13	0.37	4.93
Ta		39.77	Ta^{181}	0.06	0.07	6.73
Pb		38.96	Pb^{208}	0.18	0.57	32.4
Th		37.23	Th^{232}	0.03	0.06	6.20
U		37.15	U^{238}	0.02	0.04	11.0

therefore the higher calculated LLD need not be considered when working with the data. The 2σ errors and 1σ relative standard deviations listed in table 3.3 are low for all the element except Pb, which is probably due to high background counts per second values for Pb (490-418, in contrast with 13-8 for Ta and 11-10 for Th).

Evaluation of data quality against secondary-ion mass spectrometry (SIMS) analyses and previous LA-ICP-MS analyses. The Cameca IMS 3f ion microprobe at the Woods Hole Oceanographic Institution (WHOI) was used to obtain limited trace element compositional data for a subset of the quenched igneous glass shards which were also analysed by LA-ICP-MS at the University of Cape Town. The routine techniques and methodology used have been described previously (Johnson *et al.*, 1990; Shimizu & Hart, 1982; Shimizu & le Roex, 1986). Empirical relationships between secondary ion intensities and concentrations, i.e. working curves, (Johnson *et al.*, 1990) were used to determine the trace element concentrations in the quenched igneous glass shards.

Earlier in the current study, trace-element data for the MORB quenched igneous glass

University of Cape Town

shards were also obtained using the LA-ICP-MS facility at the Institute of Earth Studies, University of Wales, Aberystwyth. This facility comprised a VG Elemental LaserLab laser ablation system (based on a Nd:YAG infra-red laser) coupled to a VG PlasmaQuad II+ ICP MS (Jeffries *et al.*, 1995; Pearce *et al.*, 1996; Perkins & Pearce, 1995). The NIST 610 & 612 reference glass standards were used for calibration and MORB quenched igneous glass shards from the same single sample as used later at UCT, Vulcan 40-56 from the America-Antarctic Ridge, were analysed at regular, approximately hourly, intervals. The instrument settings and data-reduction methodology for these analyses were as for previous analyses of quenched igneous glass conducted at this facility (Jeffries *et al.*, 1995; Pearce *et al.*, 1996, and references therein).

The trace-element data for quenched igneous glass shards obtained using the LA-ICP-MS facility at UCT, as described above, are in good agreement with the data obtained using the more established SIMS facility at WHOI, as is illustrated in fig. 3.2. The trace elements presented in fig. 3.2 span a range in concentrations from ~50-200ppm for Zr to ~2-15ppm for La, and the data from the two techniques agree over this extensive range of concentrations despite different methods of data reduction and standards used for quantitative calibration. This agreement is further underscored by the concordant chondrite-normalised rare-earth element (REE) patterns of representative quenched igneous glass shards presented in fig. 3.3 resulting from these two techniques. A significant advantage of using the LA-ICP-MS to obtained the trace-element compositional data for the quenched igneous glasses in this study was the rapid acquisition of compositional data, relative to the SIMS technique. To obtain concentration data for eight REE (La, Ce, Nd, Sm, Eu, Dy, Er, Yb) and six minor and trace elements (Ti, V, Cr, Sr, Y, Zr) using the SIMS facility at WHOI took 45 and 35 minutes respectively. In contrast, obtaining the concentrations of 21 trace elements, listed in table 3.3, using the LA-ICP-MS facility at UCT was done in a single analysis which took <3 minutes.

Although the trace element compositional data for the quenched igneous glass shards obtained using the LA-ICP-MS facility at Aberystwyth were invaluable at the time, it is clear from fig. 3.2 & 3.3 that these data were not of the same quality as the SIMS data and the data obtained using the LA-ICP-MS facility at UCT. The Aberystwyth data are significantly off-set to higher values from the SIMS and UCT data in fig. 3.2, especially at higher concentrations. The REE patterns plotted in fig. 3.3 using the Aberystwyth data are also significantly more

University of Cape Town

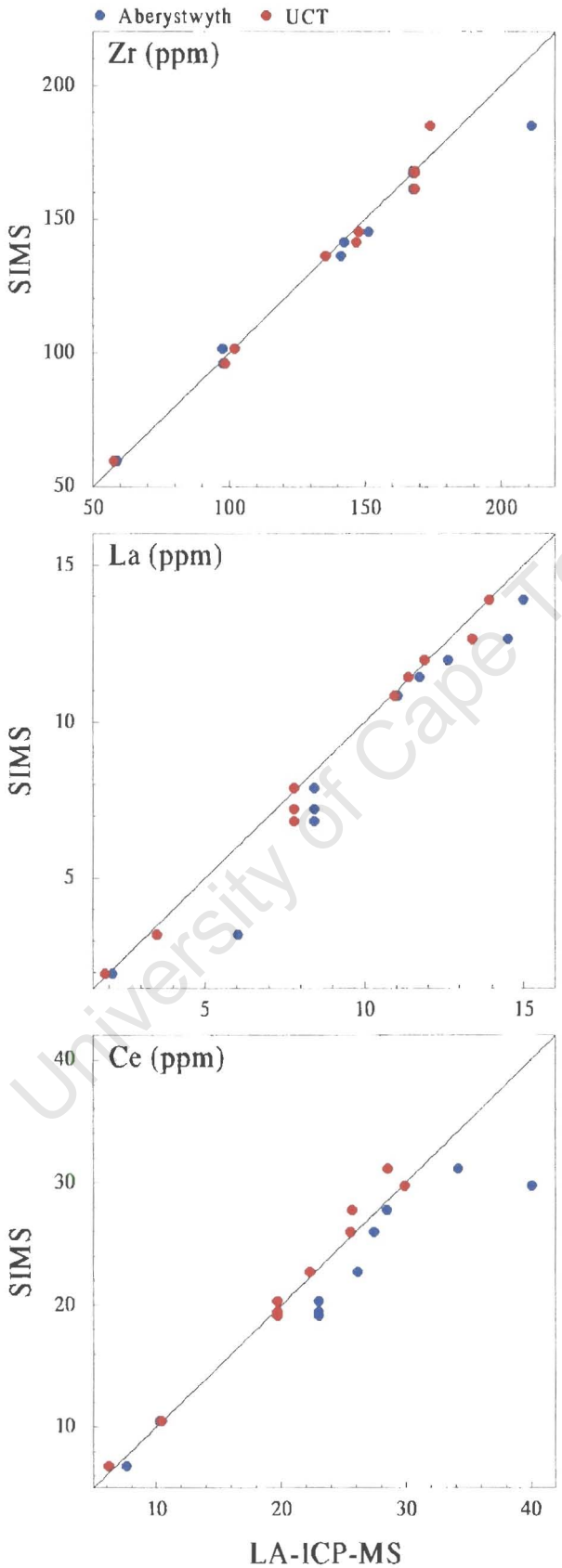

University of Cape Town

Figure 3.2: Representative trace-element data for quenched igneous glass shards obtained by SIMS (Woods Hole Oceanographic Institution) versus data obtained by LA-ICP-MS at the University of Wales at Aberystwyth and at UCT. All values in ppm, with solid line indicating perfect agreement between the SIMS and LA-ICP-MS data.

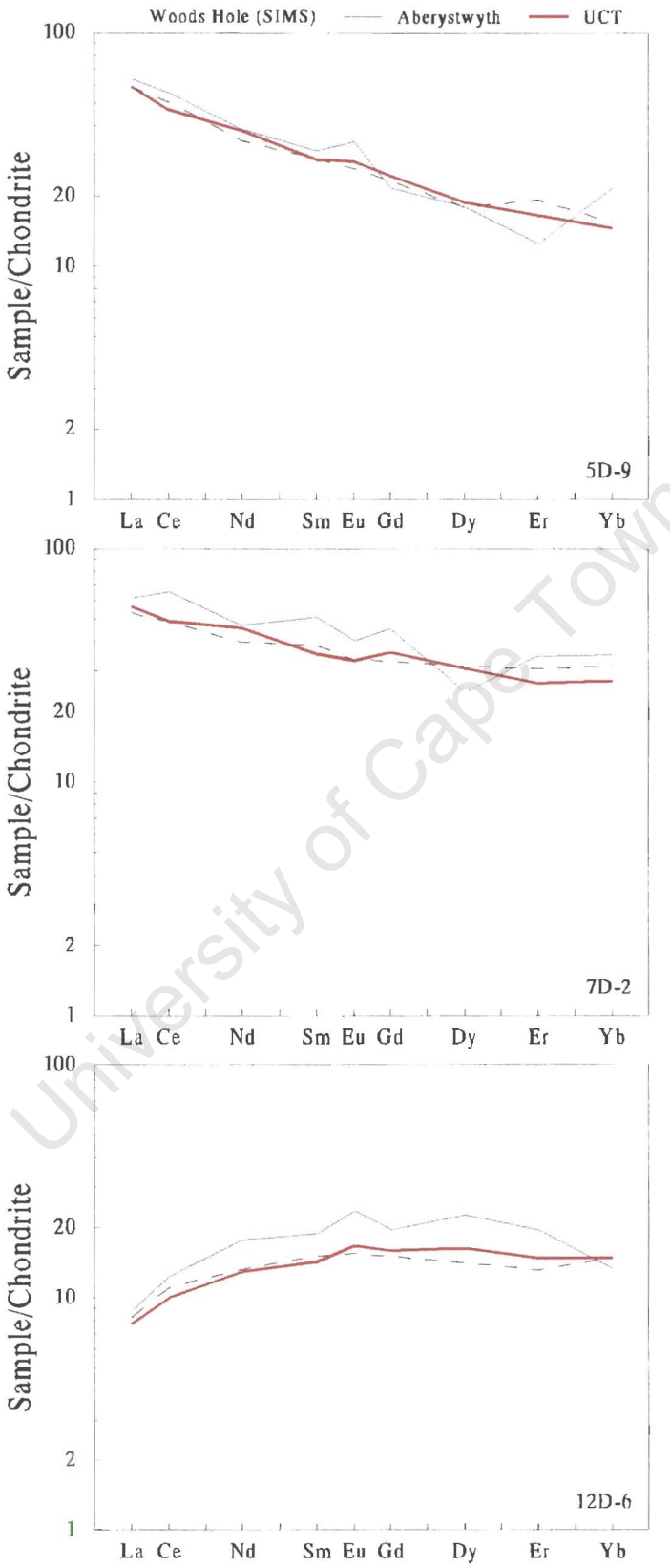

University of Cape Town

Figure 3.3: Representative chondrite-normalised (Sun & McDonough, 1989) rare earth-element data for quenched igneous glass shards obtained by SIMS (Woods Hole Oceanographic Institution), and by LA-ICP-MS at the University of Wales at Aberystwyth and at UCT.

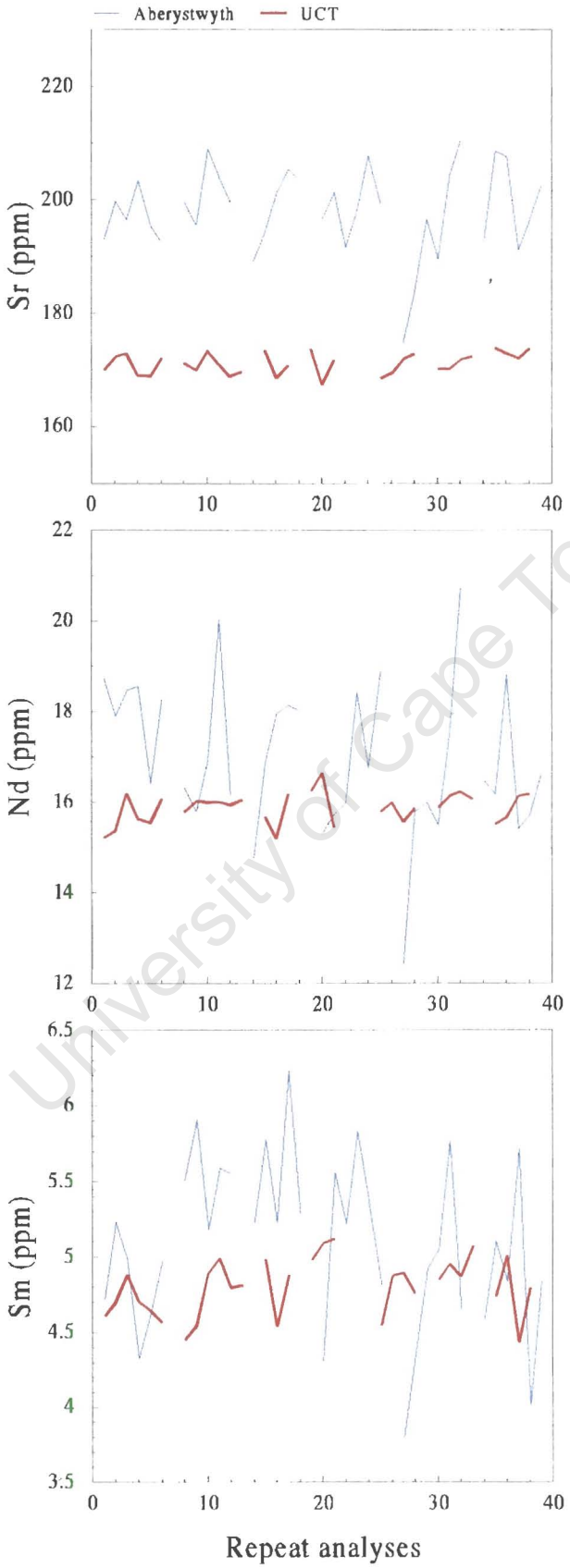

University of Cape Town

Figure 3.4: Representative trace-element data for repeat analyses of the Vulcan 40-56 quenched igneous glass shards obtained by LA-ICP-MS at the University of Wales at Aberystwyth and at UCT. All values in ppm. Breaks in lines indicate sample changes, spanning time intervals of a few minutes or more than a day..

erratic and off-set from the patterns based on the SIMS and UCT data. An important factor influencing the Aberystwyth data was instrumental drift during the analyses. The Vulcan 40-56 glass shards were analysed repeatedly at regular intervals throughout the data-gathering sessions at Aberystwyth and UCT. Assuming homogeneity of the glass shards from this single sample, these analyses can then be used to assess the stability of each instrument during data-gathering sessions and between sessions. The reproducibility of representative trace-element values using the facility at Aberystwyth and UCT are assessed in fig. 3.4. The values for repeat analyses using the Aberystwyth facility vary substantially, while the results for the same elements from the facility at UCT vary within a much narrower range. The systematic off-set between Aberystwyth and UCT data observed in especially the plot of Sr values for repeat analyses in fig. 3.4 is due to the use at UCT of the later, more comprehensive, compilation of trace-element values for the relevant NIST standards during data-reduction (Pearce *et al.*, 1997). The NIST 612 value of 76.15ppm for Sr (Pearce *et al.*, 1997) was used for Sr calibration and reduction of the UCT analysis, while the NIST certified value of 515.5ppm for NIST 610 was used for the Aberystwyth analyses (Pearce *et al.*, 1997). Instrumental drift therefore introduced significant scatter into the data-set obtained using the facility at Aberystwyth, while the instrument at UCT remained relatively stable throughout the analysis of the set of quenched igneous glass shards. In subsequent chapters, only the data obtained using the UCT LA-ICP-MS facility were used.

University of Cape Town

CHAPTER 4: REGIONAL VARIATIONS

In geochemical and petrogenetic studies of the eruptive products of mid-ocean ridge volcanism, the purpose of these detailed investigations is the explanation of fundamental characteristics observed in MORB, as revealed in quantitative compositional data or petrographic observations. In general, presentation of such data takes the form of discussions of major-element, trace-element, radiogenic-isotope, or noble-gas data for quenched igneous-glass or bulk-rock samples, and the modal mineralogy, petrography, or compositions of phenocrysts present in these basalts (examples from studies of the Mid-Atlantic Ridge: Devey *et al.*, 1994; Douglass *et al.*, 1999; Douglass *et al.*, 1995; Fontignie & Schilling, 1996; Humphris *et al.*, 1985; Kurz *et al.*, 1998; le Roex *et al.*, 1987; le Roex *et al.*, 1996; Michael *et al.*, 1994; Moreira *et al.*, 1995; Niu & Batiza, 1994; Schilling *et al.*, 1985). The investigation of so-called "along-ridge" variations in MORB compositional or mineralogical data convey the geographical extent of distinctive compositional features, and delineate coherent subsets of the data which share primary characteristics. This chapter will therefore aim to present the fundamental characteristics of the data obtained in this study, and discuss any observed local and regional primary systematics in MORB characteristics.

Due to the large number of dredges and samples encompassed by this study, the following discussion will deal with the data subdivided into 6 geographic groupings, based on the "along-ridge" extent of the compositional influence of the two proximal mantle plumes on the incompatible trace-element compositions of recovered MORB. In order of latitude, with dredge station numbers in brackets, these groupings are: northern N-MORB (45D-39D, excluding 42D), northern Discovery-influenced MORB (42D, 37D-30D), central N-MORB (28D-26D), southern Discovery-influenced MORB (25D, 2D-9D), southern N-MORB (10D-13D), and Shona-influenced MORB (14D-24D, and A2-4, A6, A7, A9, A10) (see fig. 3.1 for further geographical reference). The compositional details of these subdivisions will be discussed in detail in sections 4.3 & 4.4, and chapter 5, although these subdivisions will be used in sections 4.1 & 4.2.

The compositional data, obtained as described in chapter 3, are tabulated in full in appendix B and the current chapter will present representative extracts from this extensive data-set. The petrographic descriptions and point-counted modal mineralogies of the polished thin-

University of Cape Town

sections are presented in appendix C.

4.1 PETROGRAPHY

The results of optical microscopy conducted on polished thin sections of selected samples of MORB recovered from the SMAR in this study, will be presented and discussed in this section. The initial discussion will focus on the observed, quantitative modal mineralogy of these basalts, and especially possible latitudinal variations within these data. The influence of the two proximal mantle plumes on the presence of phenocrysts phases and their relative proportions will be assessed.

The remainder of this section will deal with the discussion of each observed phenocrysts phase, in terms of size-range, habit, inclusions, etc. Variations in these phenocrysts characteristics will also be assessed in relation to the possible influence of the two proximal mantle plumes on crystallisation beneath this section of the SMAR.

Modal mineralogy. The modal mineralogy of MORB from this section of the SMAR exhibit hardly any significant variations "along-ridge", see fig. 4.1. If sample-density is taken into account, then basalts recovered from mantle plume-influenced ridge segments span a similar range in phenocryst abundance as those recovered from uninfluenced ridge segments. The majority of the samples are aphyric in nature and contain <10% total phenocrysts, see plates 4.1-4.4, with a few sparsely phyric samples, though still a significant number, containing 10-20% total phenocrysts, see plates 4.5-4.6, and only three highly phyric samples which contain >20% total phenocrysts, see plates 4.7-4.8.

The vast majority of the samples contain <3% modal olivine phenocrysts, with only a few northern and southern Discovery- and Shona-influenced MORB containing 3-10% modal olivine phenocrysts. According to modal abundance, plagioclase is the dominant phenocryst phase present in these basalts. The plagioclase mode varies mostly between 0- 20%, with three samples containing significantly higher plagioclase modes of up to 40%. Variations in plagioclase modal abundance exhibit no significant latitudinal systematics or associations with the influence of the proximal mantle plumes. The occurrence of clinopyroxene as a phenocryst phase in these basalts is rare, but it is not confined to depleted or mantle plume-influenced basalts (also see fig. 4.2). The extremely rare presence of spinel microphenocrysts is indicated in fig. 4.2 and when present

University of Cape Town

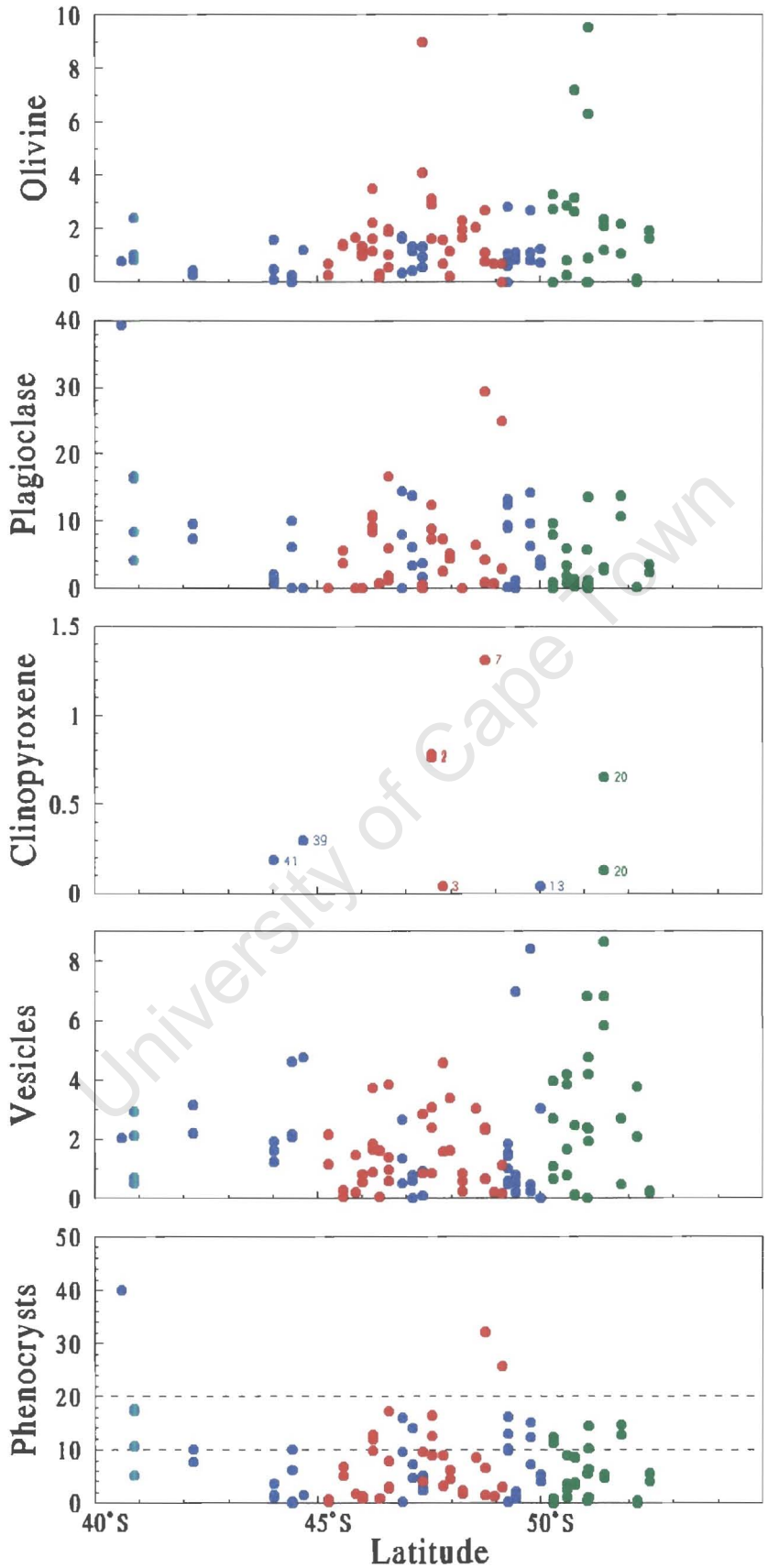

University of Cape Town

Figure 4.1: Modal mineralogy versus latitude. Point-counted phenocryst abundances presented as percentages. Blue markers: N-MORB; red markers: Discovery-influenced MORB; green markers: Shona-influenced MORB. Labels on plot of clinopyroxene occurrence indicate dredge numbers.

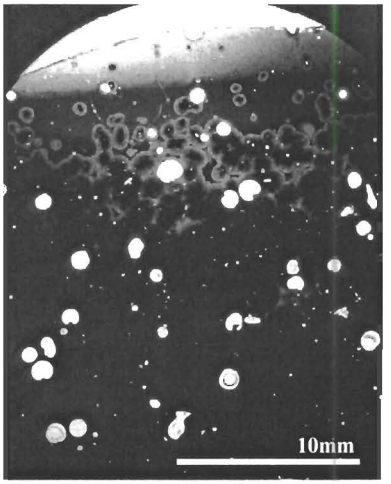

Plate 4.1: Aphyric, glassy and vesicular basalt (23D-4).

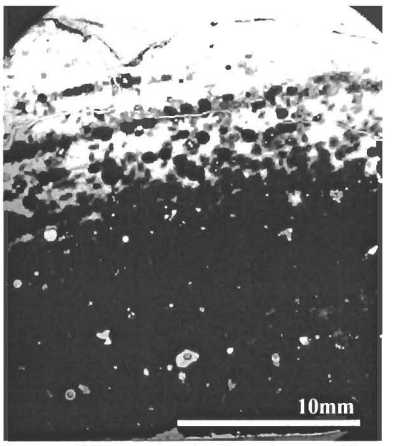

Plate 4.2: Aphyric basalt, grading from quenched igneous-glass rim to dark devitrified matrix (11D-10).

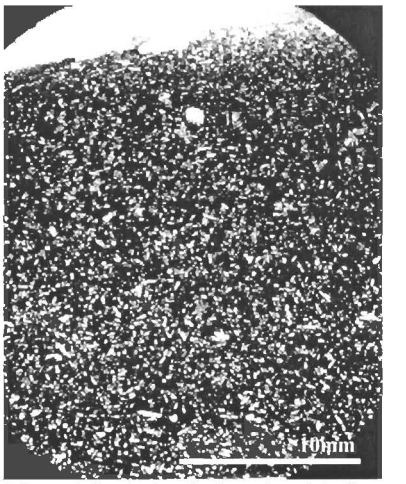

Plate 4.3: Aphyric basalt with fine plagioclase laths in dark, devitrified groundmass (26D-1).

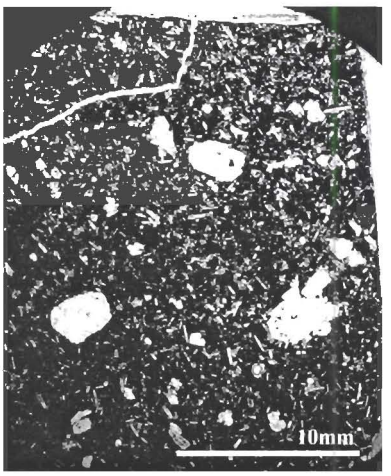

Plate 4.4: Slightly porphyritic basalt, with large, rounded plagioclase phenocrysts set in matrix of fine plagioclase laths and dark groundmass (12D-1).

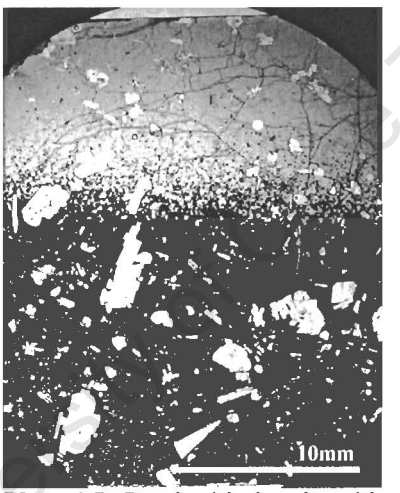

Plate 4.5: Porphyritic basalt, with plagioclase phenocrysts and lesser olivine phenocrysts. Quenched igneous-glass rim contains clusters of plagioclase and olivine microphenocrysts (10D-9).

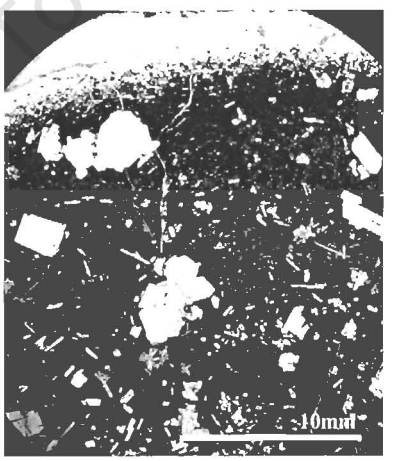

Plate 4.6: Porphyritic basalt, with large plagioclase phenocrysts set in a devitrified matrix (28D-2).

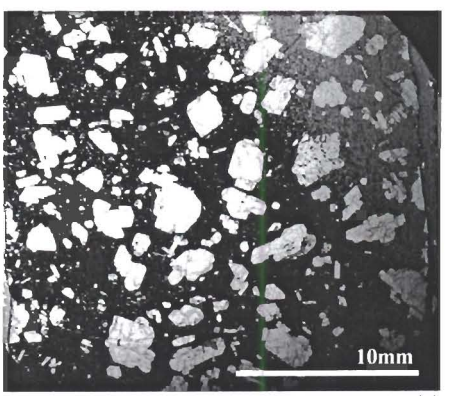

Plate 4.7: Coarsely porphyritic basalt, with large plagioclase and lesser olivine and clinopyroxene phenocrysts (7D-3).

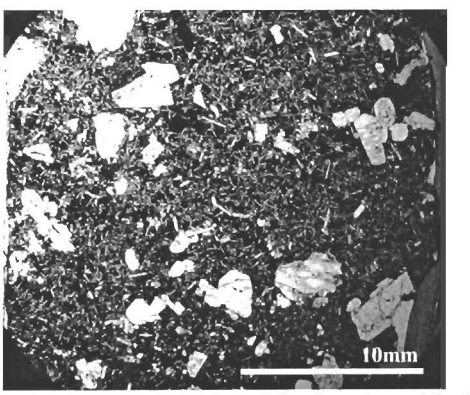

Plate 4.8: Coarsely porphyritic basalt, with large plagioclase phenocrysts in a matrix of dense, fine plagioclase laths (44D-1).

they are closely associated with, or occur as inclusions in, olivine phenocrysts in northern and southern Discovery- and Shona-influenced MORB. The northern and southern Discovery-, and Shona-influenced MORB dominate the samples containing abundant vesicles, but a number of N-MORB are still present amongst these highly vesicular basalts.

Olivine phenocrysts. The observed maximum size of phenocryst phases in the basalts recovered from the SMAR, plotted against latitude in fig. 4.2, varies considerably. Olivine phenocrysts are observed to range from microphenocrysts (≤250μm) to rare megacrysts (≤5mm). Some samples contain two distinct populations of olivine phenocrysts in terms of size, with large isolated subhedral to anhedral megacrysts and euhedral to subhedral microphenocrysts in glomerocrysts with small plagioclase laths or in so-called "bow-tie"-clusters with radiating plagioclase needles or micro-laths, see plates 4.9-4.11. The habit of anhedral olivines ranges from rounded and embayed, probably due to resorption, see plates 4.14 & 4.15, to skeletal, probably due to quenching of interrupted rapid growth, see plate 4.16. Euhedral to anhedral olivines grains are frequently heavily fractured, see plate 4.12. As is illustrated in fig. 4.3 and fig. 4.4, olivine phenocrysts are rarely observed to be resorbed, optically zoned or to contain any type of inclusions, see plate 4.13.

Olivine phenocrysts containing quenched igneous-glass inclusions are limited to samples from only seven dredges, although when such olivine phenocrysts were observed they constituted a large percentage of the total olivine mode, see fig. 4.3. The occurrence of olivine phenocrysts containing quenched igneous-glass inclusions seems to be mostly confined to samples from dredges recovered from mantle plume-influenced ridge segments. The qualitatively observed occurrence of resorption of phenocrysts, quenched igneous-glass inclusions in phenocrysts, and optical zoning of phenocrysts in samples from individual dredges are indicate at their latitudinal locations in fig. 4.4. No systematic variations can be deduced from this representation, except possibly the confirmation of the restriction of olivine phenocrysts containing quenched igneous-glass inclusions to dredges which sampled mantle plume-influenced ridge segments and the lack of observed zoned olivine phenocrysts.

Plagioclase phenocrysts. Observed plagioclase phenocrysts range in size from microlaths (≤250μm) to megacrysts (≤1cm). As for olivine phenocrysts, some samples contain two distinct populations of plagioclase phenocryst in terms of size, with isolated large, resorbed and/or

University of Cape Town

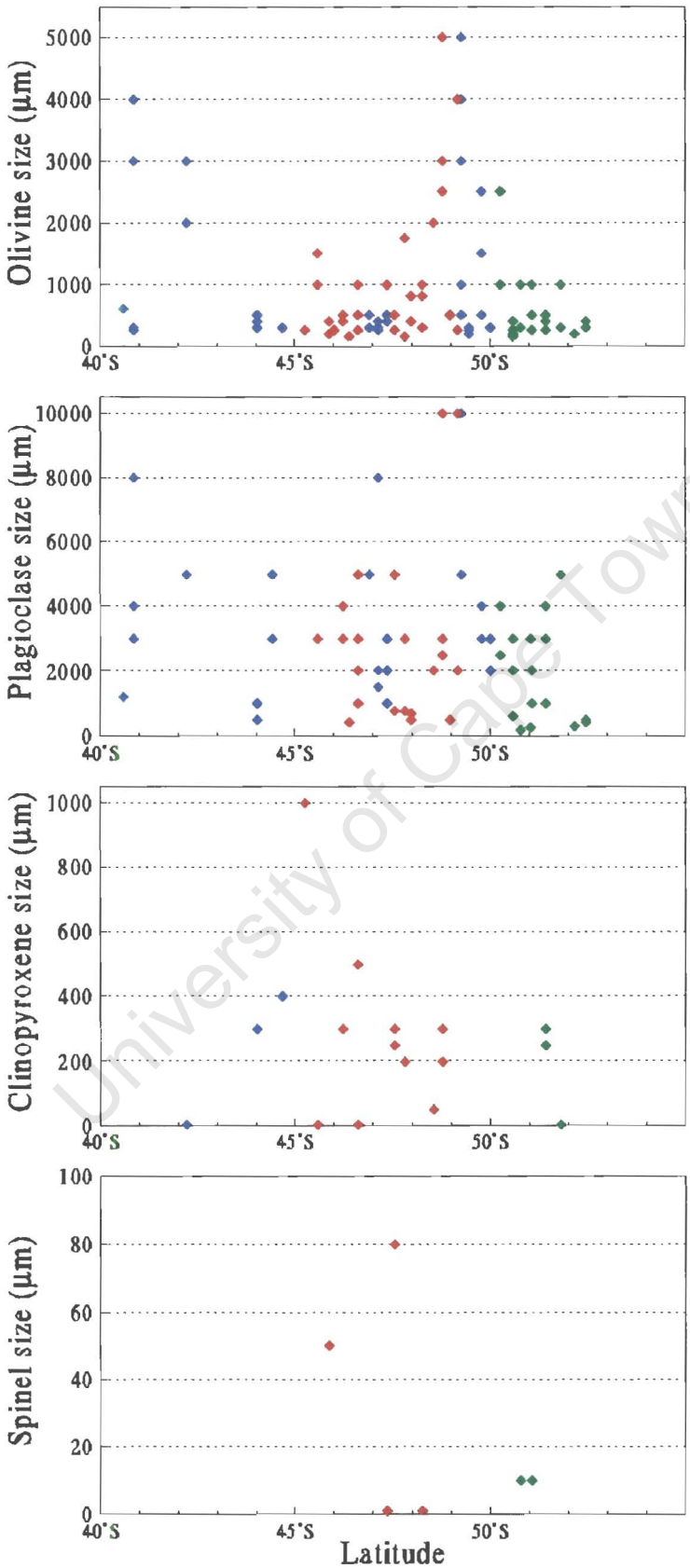

University of Cape Town

Figure 4.2: Phenocryst size versus latitude. For clinopyroxene and spinel, data points along x-axis indicates trace presence of phase. Blue markers: N-MORB, red markers: Discovery-influenced MORB, green markers: Shona-influenced MORB.

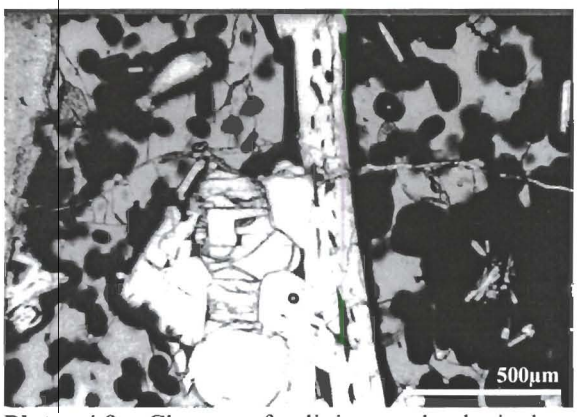

Plate 4.9: Cluster of olivine and plagioclase microphenocrysts in a quenched igneous-glass rim (3D-1).

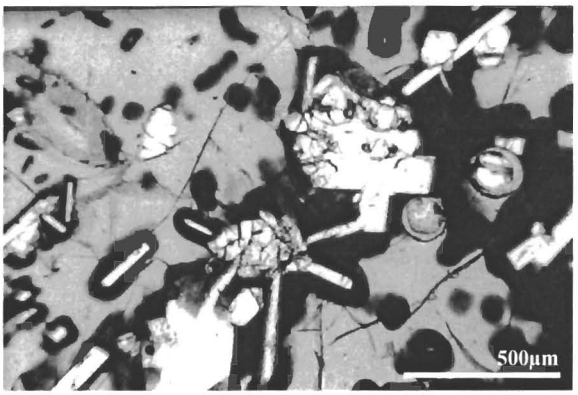

Plate 4.10: Clusters of olivine and plagioclase microphenocrysts in a quenched igneous-glass rim (12D-3).

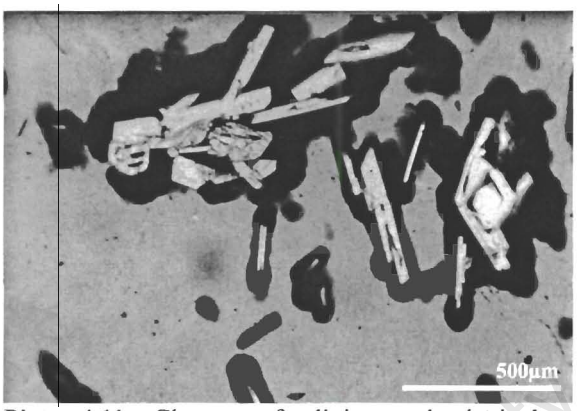

Plate 4.11: Clusters of olivine and plagioclase microphenocrysts in a quenched igneous-glass rim (20D-3).

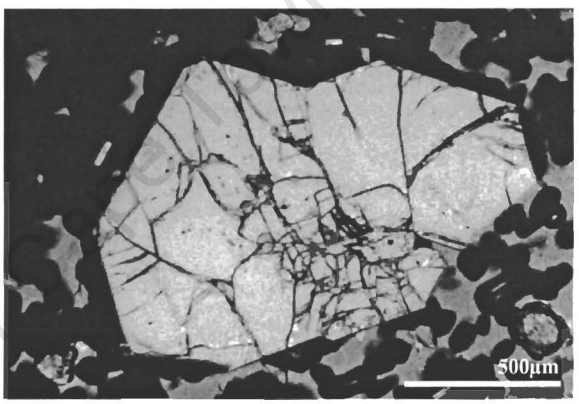

Plate 4.12: Euhedral, fractured olivine phenocrysts in partially devitrified quenched igneous-glass (3D-1).

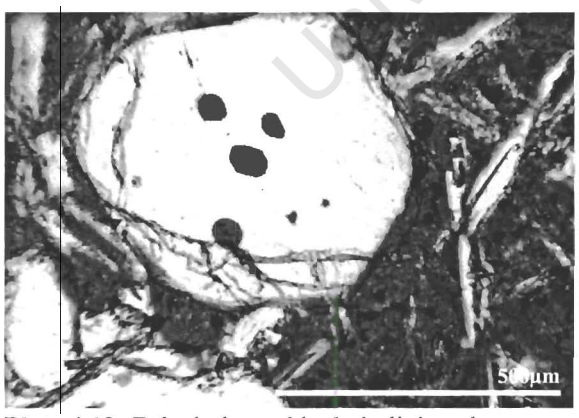

Plate 4.13: Euhedral to subhedral olivine phenocryst with quenched igneous-glass inclusions (17D-1).

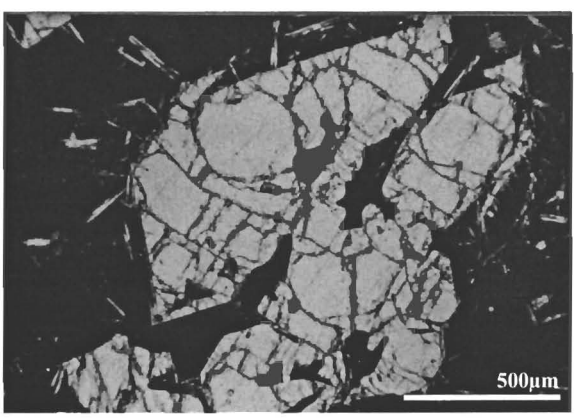

Plate 4.14: Euhedral to subhedral and partially resorbed olivine phenocryst (25D-8).

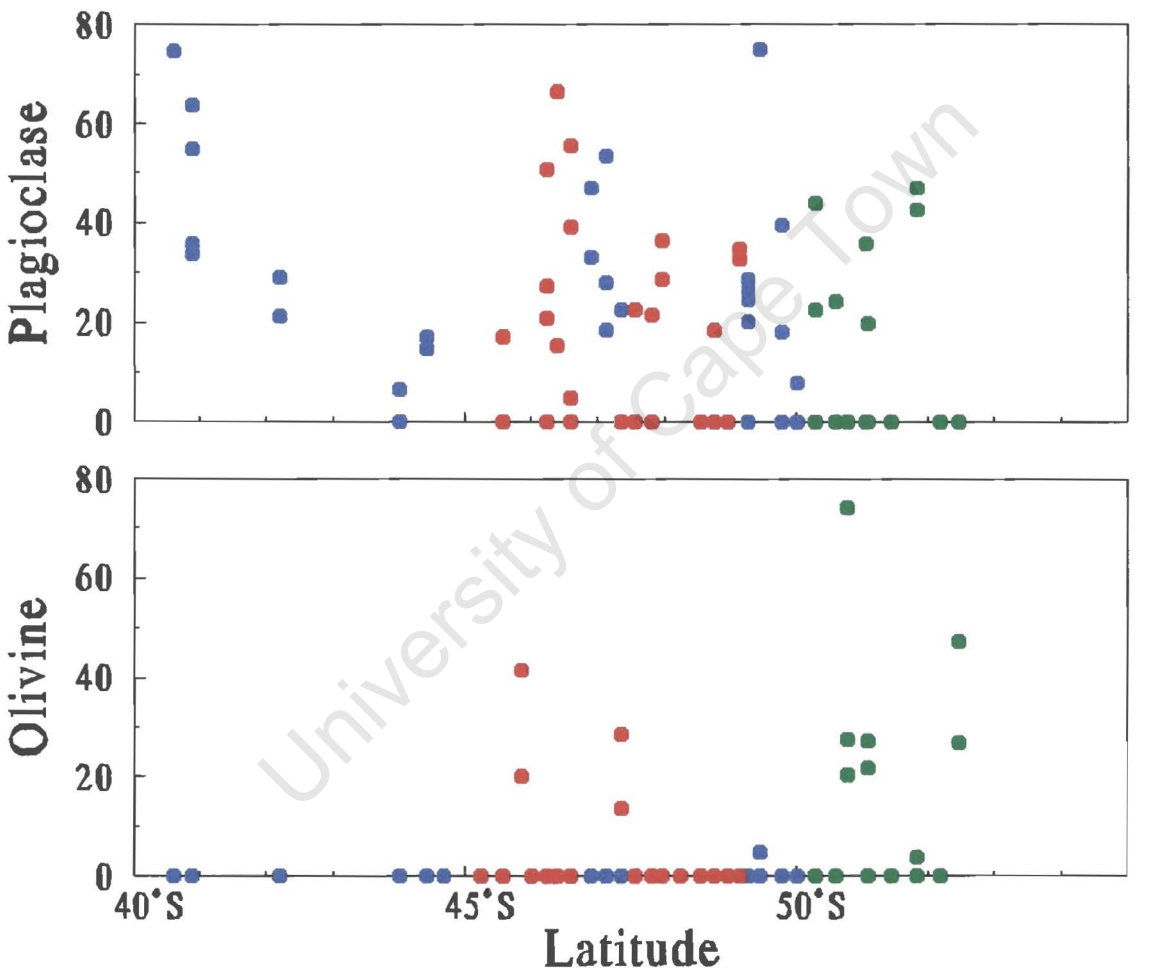

University of Cape Town

Figure 4.3: Modal percentages of olivine and plagioclase phenocrysts in individual dredges which contain quenched igneous-glass inclusions versus latitude. Blue markers: N-MORB, red markers: Discovery-influenced MORB, green markers: Shona-influenced MORB.

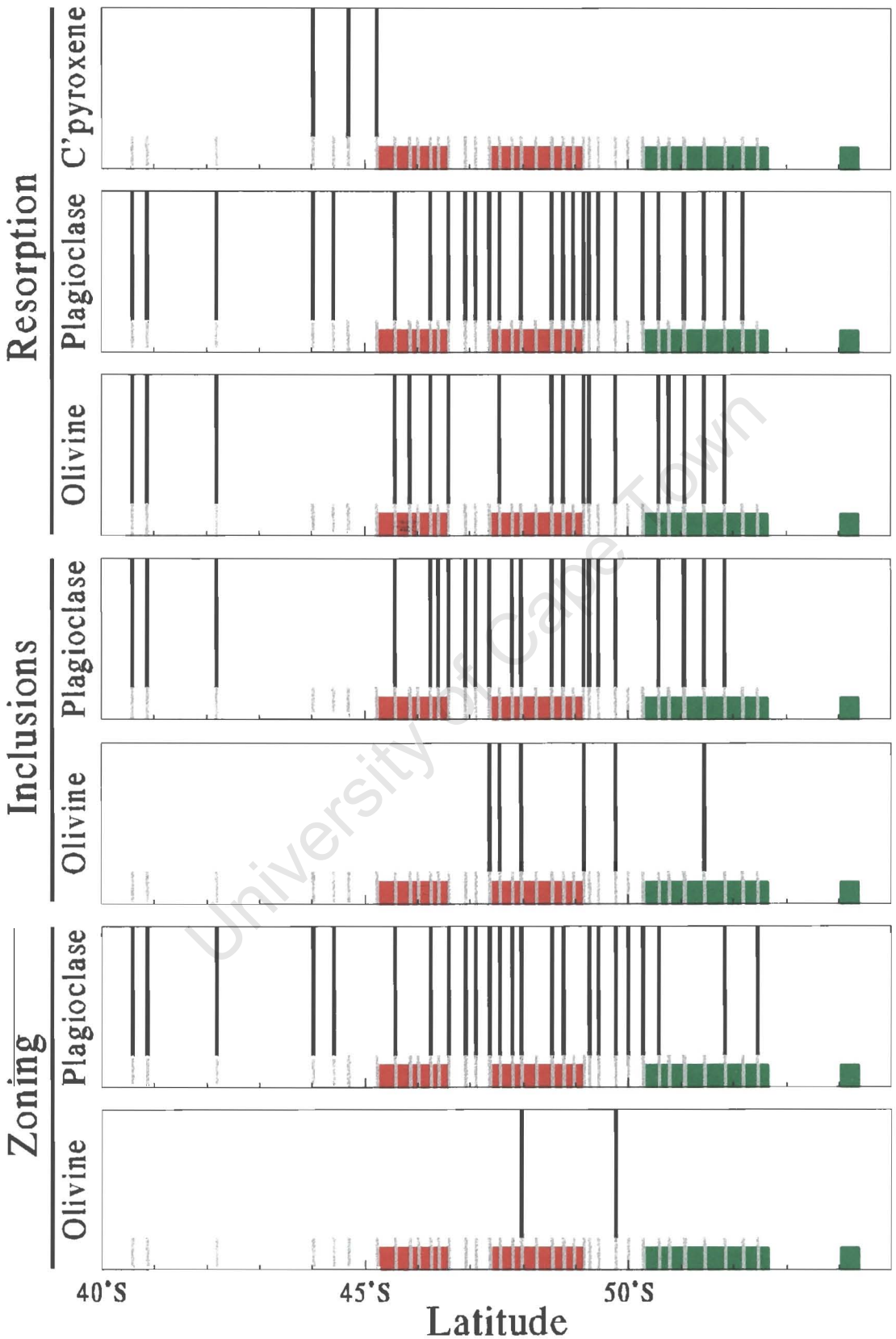

University of Cape Town

Figure 4.4: Phenocrysts characteristics observed in thin sections versus latitude. Grey bars: dredge locations; black bars: presence of relevant characteristic; red and green fields: latitudinal extend of Discovery- and Shona-influenced ridge segments.

optically zoned megacrysts and smaller, euhedral phenocrysts or microlaths associated with olivine or clinopyroxene phenocrysts, see plates 4.9-4.11. Some large anhedral plagioclase phenocrysts have grain boundaries with olivine and clinopyroxene phenocrysts filling embayments. These mafic phases have either become partially enclosed by the plagioclase phenocrysts during its growth, or these mafic phases grew at the expense of the plagioclase phenocrysts. It is not possible to distinguish between these two possibilities within the scope of this study. Large plagioclase phenocrysts frequently have quenched igneous glassy intrusions, due to resorption, breaching grain boundaries. Small plagioclase grains regularly have skeletal habits, resulting from rapid quenching during crystal growth. Inclusions in plagioclase phenocrysts generally occur in three distinct habits: arranged parallel to crystallographic planes or euhedral grain boundaries, randomly orientated and commonly associated with glassy intrusions, or confined to concentric bands correlated with optical zoning, see plates 4.17-4.19.

Resorption, zoning and inclusions combine in some plagioclase phenocrysts to map complex growth histories. It is fairly common for larger plagioclase phenocrysts to display zoning, or bands of inclusions, parallel to crystallographic planes, which are terminated or non-parallel to the grain boundaries due to partial resorption of the original grain, see plates 4.20 & 4.21. Subsequent cessation of resorption and renewed growth then result in some plagioclase phenocrysts having outer "mantles" of secondary growth with zoning, or bands of inclusions, parallel to the new grain boundaries, but off-set with regard to the zoning, or bands of inclusions in the previously resorbed "cores", see plate 4.17. In some rare cases, a second stage of resorption can results in this secondary zoning, or bands of inclusions, again being terminated by grain boundaries.

The point-counted percentages of the plagioclase phenocryst modes in individual dredges containing quenched igneous-glass inclusions are shown in fig. 4.3. The occurrence of plagioclase phenocrysts containing quenched igneous-glass inclusions has no discernable latitudinal systematics, although this characteristic is extremely common amongst samples from all the dredges. The qualitatively observed occurrence of resorption, quenched igneous glassy inclusions, and optical zoning in plagioclase phenocrysts, plotted against latitude in fig. 4.4, have no systematic variation or correlation with the influence of the proximal mantle plumes.

Clinopyroxene, spinel and minor phenocryst-phases. The size-range of clinopyroxene

University of Cape Town

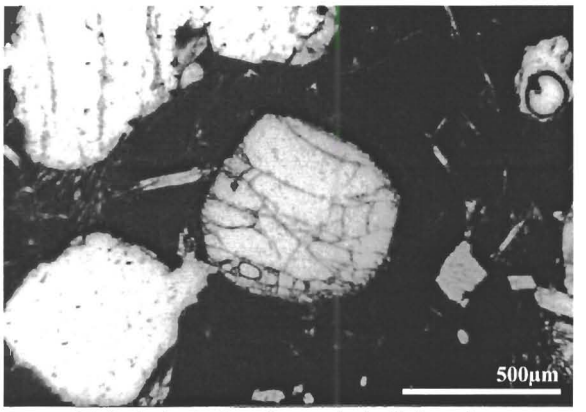

Plate 4.15: Anhedral and rounded olivine phenocryst (26D-5).

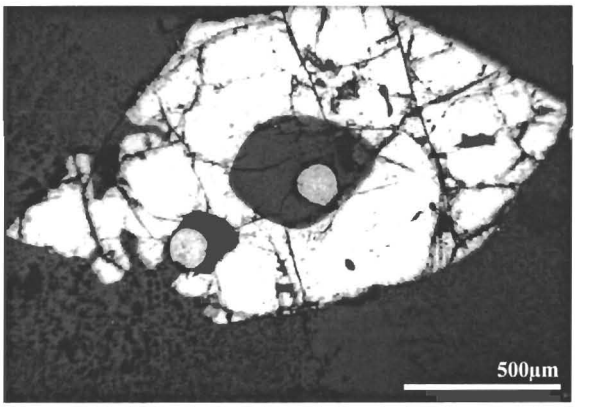

Plate 4.16: Euhedral and partially skeletal or resorbed olivine phenocryst, with two vesicles present, in a dark, uniform matrix (19D-2).

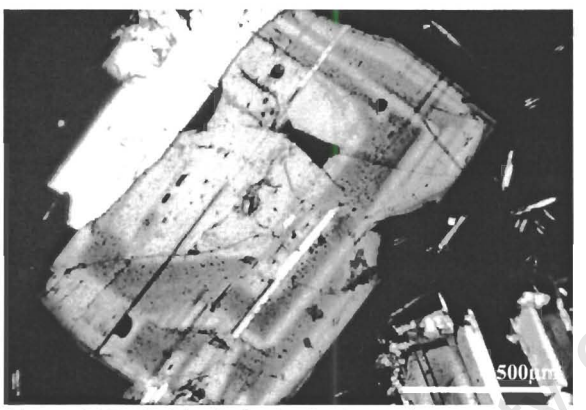

Plate 4.17: Subhedral plagioclase phenocryst with two generations of optical zoning, quenched igneous-glass inclusions associated with specific bands of optical zoning and partially resorbed grain edges (12D-3: cross-polarises light).

Plate 4.18: Euhedral to subhedral plagioclase phenocryst with a band of quenched igneous-glass inclusions coincident with a band of the concentric optical zoning (4D-7: cross-polarised light).

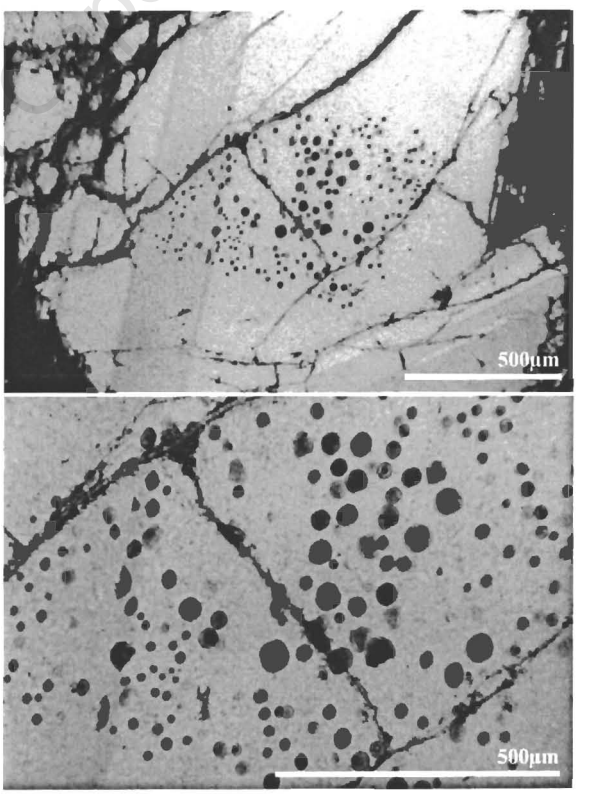

Plate 4.19: Top plate: subhedral, fractured plagioclase phenocryst with quenched igneous-glass inclusions concentrated exclusively in the core. Bottom plate: higher magnification view of the semi-randomly orientated quenched igneous-glass inclusions (27D1).

University of Cape Town

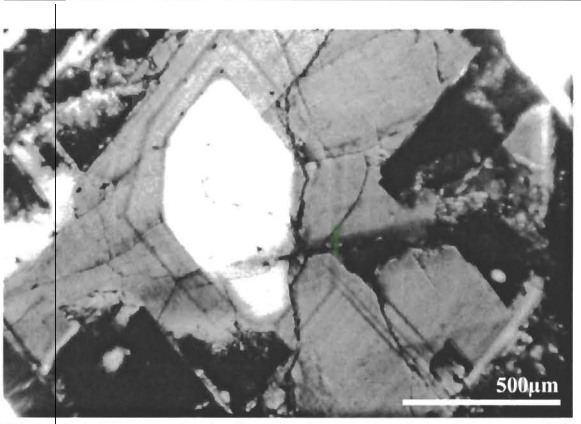

Plate 4.20: Anhedral plagioclase phenocryst with clear, euhedral core, surrounded by concentric optical zoning now interrupted by heavily resorbed grain edges (10D-1: cross-polarised light).

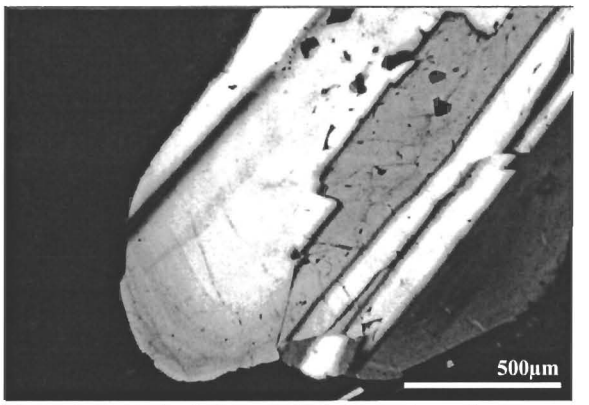

Plate 4.21: Anhedral, rounded plagioclase phenocryst with fine, concentric optical zoning truncated by resorbed grain edges (20D-3: cross-polarised light).

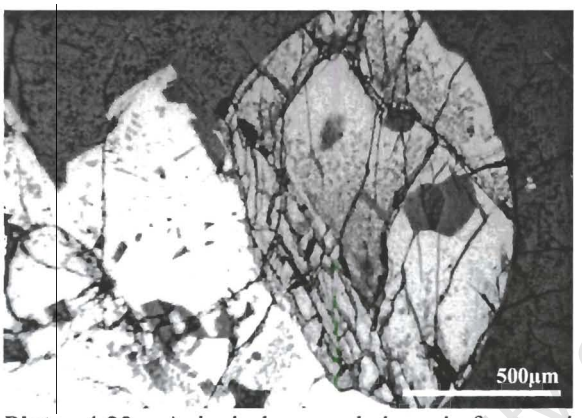

Plate 4.22: Anhedral, rounded and fractured clinopyroxene phenocryst, with quenched igneous-glass inclusion, adjacent to anhedral plagioclase phenocryst (2D-1: reflected & transmitted light).

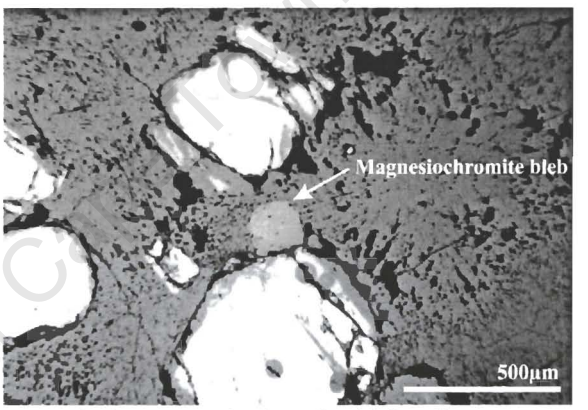

Plate 4.23: Magnesiochromite bleb adjacent to an olivine phenocryst (19D-7: reflected & transmitted light).

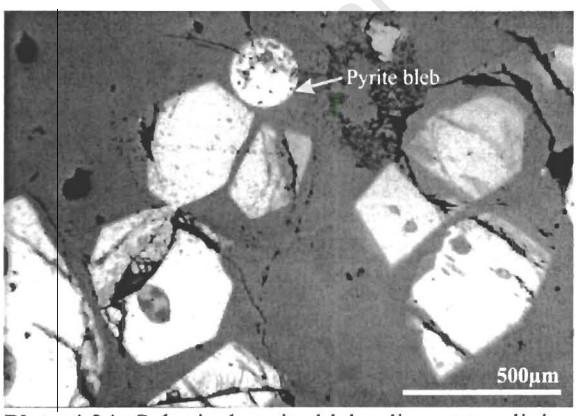

Plate 4.24: Spherical pyrite bleb adjacent to olivine phenocryst (19D-7: reflected & transmitted light).

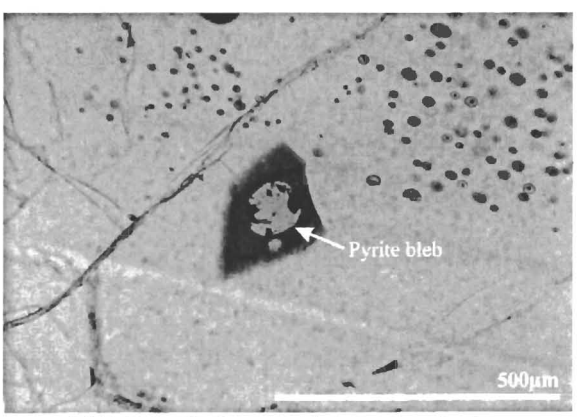

Plate 4.25: Spherical pyrite bleb in quenched igneous-glass inclusion, in a plagioclase phenocryst (45D-2: reflected & transmitted light).

phenocrysts is restricted to ≤500μm for all but one phenocryst, see plate 4.22. Clinopyroxene phenocrysts range from euhedral, through subhedral, to anhedral and severely rounded grains. When present as phenocrysts, clinopyroxenes are predominantly associated with olivine and plagioclase phenocrysts in small clusters. Some clinopyroxene phenocrysts observed in northern N-MORB and northern Discovery-influenced MORB exhibited evidence of having experienced resorption, but the rare occurrence of clinopyroxene as a phenocryst phase prevented any possible delineation of latitudinal systematics.

As stated previously, spinels are extremely rare and range in size from 10-80μm. The observed grains are euhedral to anhedral, with cubic spinel crystals occurring as inclusions in olivines. Extremely rare opaque microphenocrysts were observed in some low Mg# basalts. These microphenocrysts proved to be magnesiochromites grains and pyrite blebs. Both phases commonly occur as inclusions in plagioclase and olivine phenocrysts or closely associated with olivine microphenocryst clusters, see plates 4.23-4.25.

Summary. Although the total modal mineralogies of the recovered MORB from this section of the SMAR do not exhibit systematic variations with latitude, olivine phenocrysts are slightly more abundant in basalts recovered from mantle plume-influenced ridge segments. The majority of the MORB from the SMAR are aphyric to sparsely phyric with <10-20% total phenocrysts, with <3% olivine phenocrysts, <20% plagioclase phenocrysts, rare clinopyroxene and spinel, as well as occasional sulphide blebs.

Olivine and plagioclase phenocrysts exhibit no distinct evidence of latitudinal systematics in terms of size, habit, resorption, optical zoning, or inclusions. Therefore, it seems the Discovery and Shona mantle plumes have very little observable influence on the abundance and physical characteristics of the phenocrysts present in these MORB.

4.2 MINERALOGY

Representative sub-sets of the compositions of observed phenocryst phases in the MORB recovered from the SMAR in this study will be presented in this section, and the complete data-set of phenocryst compositions will be discussed. The variations within and between the compositions of phenocryst phases in N-MORB and the various mantle plume-influenced MORB will be assessed. Any differences observed between the compositions of phenocrysts and

University of Cape Town

microphenocrysts will be stressed and discussed. The degree to which the observed phenocryst phases are in equilibrium with the host-quenched igneous glasses and aphyric bulk-rock samples will investigated. The results of geothermometry will also be addresses, specifically the differences between calculated equilibrium and liquidus temperatures for plagioclase and olivine phenocrysts. All these variables will be assessed in the sub-groups defined earlier and the latitudinal variations in these variables will be highlighted and discussed.

Olivine. A representative subset of olivine-phenocryst compositions are listed in table 4.1 (the complete data-set of olivine-phenocryst compositions are listed in appendix B, table B.1), arranged according to increasing latitudinal locations of the dredge stations from which the samples were recovered. The observed forsterite compositions of olivine phenocrysts and microphenocrysts are plotted against latitude in fig.4.5, olivine compositions from samples recovered from ridge segments unaffected by mantle plumes in blue, those from samples from Discovery-influenced ridge segments in red, and from Shona-influenced ridge segments in green.

University of Cape Town

The majority of the observed compositions of olivine phenocrysts and microphenocrysts in the northern N-MORB (dredges 45-39, excluding dredge 42) samples varies between Fo_{83-85}. The compositions of the olivine phenocrysts in sample 45D-2 are exceptionally high, at Fo_{87-89} for this region. Except for the northernmost dredge, dredge 45, samples from the remaining northern N-MORB contain phenocrysts as well as microphenocrysts and the observed compositions of the olivines in these two populations are indistinguishable, see fig. 4.5. The calculated equilibrium olivine forsterite compositions plotted in fig. 4.5 indicate that the olivine phenocrysts and microphenocrysts in these northern N-MORB, and even the exceptionally high forsterite contents of olivine phenocrysts in dredge 45, are in general in equilibrium with the host quenched igneous glasses at low pressures.

The observed compositions of olivine phenocrysts and microphenocrysts in northern Discovery-influenced MORB (dredges 42, 37-30) varies predominantly between Fo_{84-86}, with higher compositions of Fo_{87-88} in olivine phenocrysts in samples from dredge 37. In most of these samples, the compositions of olivine microphenocrysts are slightly lower than the compositions of co-existing olivine phenocrysts, see fig. 4.5. The comparisons between calculated equilibrium and observed olivine forsterite compositions in fig. 4.5 indicate that the majority of the olivine phenocrysts and microphenocrysts in these basalts are in equilibrium with their host quenched

Table 4.1: Representative olivine phenocryst compositions (EMP) in oxide-weight percentages, with all iron reported as Fe^{2+}. The size of phenocrysts analysed varied between phenocrysts (pheno) and microphenocryst (micro).

Sample	45D-2		43D-1	41D-2	37D-3	36D-5	32D-2	30D-1	28D-3	28D-9	26D-5		3D-1	7D-1	
Size	pheno	pheno	micro	micro	pheno	micro	micro	micro	micro	micro	micro	pheno	micro	pheno	pheno
Lat. (°S)	40.59	40.59	42.19	44.02	45.23	45.57	46.23	46.59	46.90	46.90	47.35	47.35	47.80	48.76	48.76
SiO_2	40.95	40.97	40.15	40.03	40.83	39.99	39.79	40.10	40.13	39.12	38.75	40.33	40.47	39.54	39.83
TiO_2	< 0.039	< 0.039	< 0.039	< 0.039	< 0.039	< 0.039	< 0.039	< 0.039	< 0.039	< 0.039	< 0.039	< 0.039	< 0.039	< 0.039	< 0.039
Al_2O_3	< 0.038	< 0.038	0.07	< 0.038	< 0.038	0.09	< 0.038	0.09	< 0.038	0.10	0.07	< 0.038	< 0.038	0.06	< 0.038
Cr_2O_3	< 0.044	< 0.044	< 0.044	< 0.044	< 0.044	< 0.044	< 0.044	< 0.044	< 0.044	< 0.044	< 0.044	< 0.044	< 0.044	< 0.044	< 0.044
FeO	11.33	10.64	15.12	14.37	11.29	14.82	14.65	12.65	12.80	14.01	17.59	10.01	12.20	12.08	12.39
MnO	0.19	0.20	0.29	0.22	0.13	0.21	0.23	0.21	0.18	0.21	0.30	0.13	0.15	0.20	0.24
MgO	47.53	47.70	44.90	45.53	47.40	45.06	44.64	46.47	45.92	45.31	41.95	48.20	46.52	47.42	47.38
CaO	0.29	0.32	0.30	0.30	0.30	0.30	0.30	0.30	0.34	0.31	0.32	0.28	0.30	0.27	0.26
NiO	0.24	0.16	0.15	0.17	0.26	0.17	0.10	0.15	0.15	0.20	0.10	0.26	0.15	0.22	0.20
Total	100.53	99.99	100.98	100.62	100.21	100.64	99.71	99.97	99.52	99.26	99.08	99.21	99.79	99.79	100.30
Fo	87.83	88.55	83.72	84.62	87.86	84.09	84.16	86.43	86.18	84.85	80.61	89.21	86.90	87.12	86.81

Sample	7D-2				10D-2	10D-3	12D-3	13D-2	15D-2	19D-9		20D-3	23D-1	22D-4	
Size	pheno	pheno	micro	micro	pheno	micro	pheno	micro	micro	pheno	micro	pheno	micro	micro	micro
Lat. (°S)	48.76	48.76	48.76	48.76	49.25	49.25	49.76	49.99	50.58	51.06	51.06	51.43	52.16	52.46	52.46
SiO_2	38.94	39.06	37.90	37.97	39.78	39.10	40.06	40.03	39.47	39.85	39.97	38.80	38.36	37.63	37.42
TiO_2	< 0.039	< 0.039	< 0.039	< 0.039	< 0.039	< 0.039	< 0.039	< 0.039	< 0.039	< 0.039	< 0.039	< 0.039	< 0.039	< 0.039	< 0.039
Al_2O_3	< 0.038	< 0.038	< 0.038	< 0.038	< 0.038	0.05	< 0.038	< 0.038	< 0.038	< 0.038	< 0.038	< 0.038	< 0.038	< 0.038	< 0.038
Cr_2O_3	< 0.044	< 0.044	< 0.044	< 0.044	< 0.044	< 0.044	< 0.044	< 0.044	< 0.044	0.09	< 0.044	< 0.044	< 0.044	< 0.044	< 0.044
FeO	18.54	18.89	24.48	24.90	14.69	15.89	11.56	12.42	16.35	12.11	13.52	17.65	21.47	25.84	26.22
MnO	0.26	0.29	0.33	0.37	0.26	0.29	0.19	0.17	0.27	0.16	0.23	0.26	0.40	0.40	0.37
MgO	41.83	41.49	37.17	36.55	44.55	44.32	47.01	46.96	43.87	47.12	46.53	41.85	39.60	36.40	36.09
CaO	0.28	0.25	0.30	0.32	0.31	0.31	0.28	0.31	0.30	0.33	0.30	0.32	0.30	0.29	0.26
NiO	0.10	< 0.052	0.11	< 0.052	0.18	0.15	0.23	0.23	0.20	0.13	0.16	0.12	0.11	0.12	0.10
Total	99.95	99.98	100.29	100.11	99.77	100.11	99.33	100.12	100.46	99.79	100.71	99.00	100.24	100.68	100.46
Fo	79.78	79.40	72.67	72.05	84.00	82.87	87.49	86.72	82.30	87.13	85.64	80.53	76.25	71.11	70.68

Fo: forsterite content as percentage

University of Cape Town

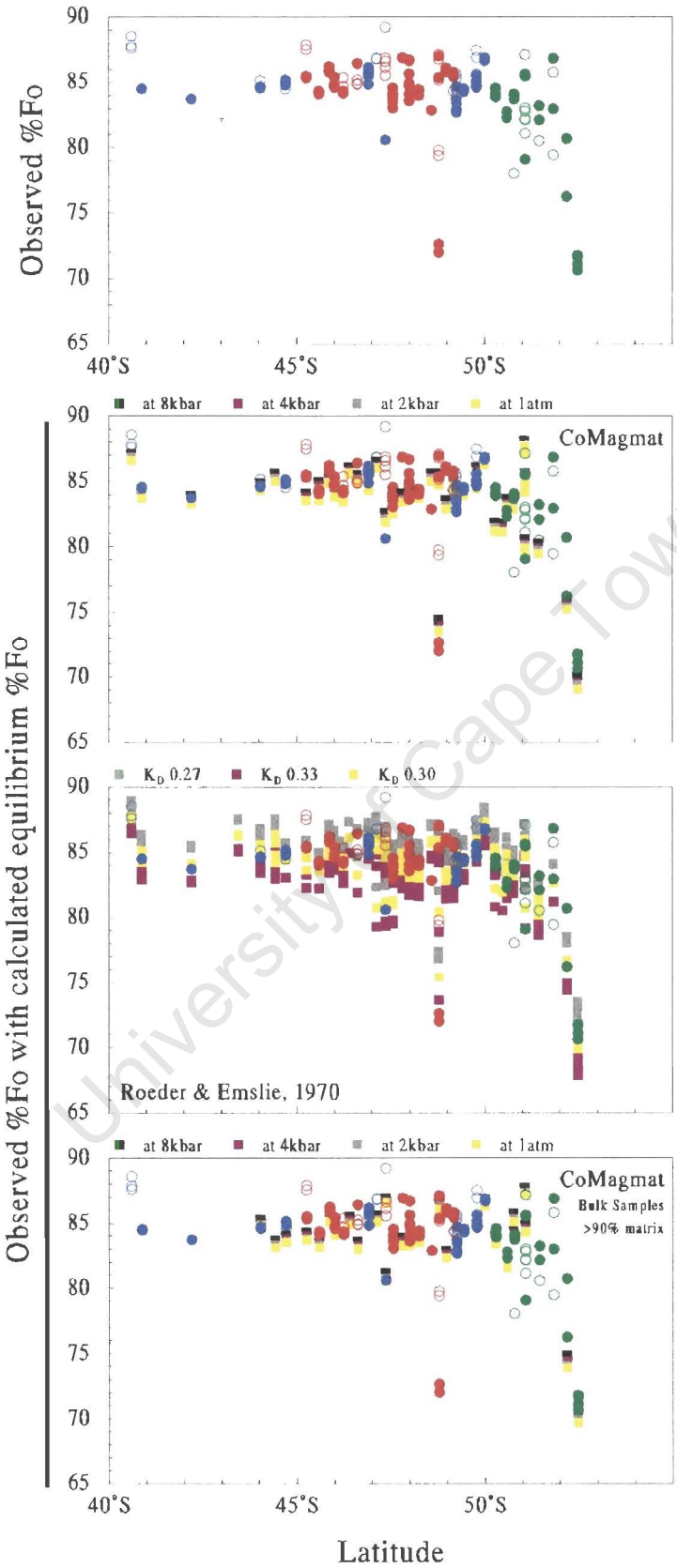

University of Cape Town

Figure 4.5: Observed forsterite (Fo) percentages of olivine phenocrysts (open circles) and microphenocrysts (filled circles) in individual dredges versus latitude. Equilibrium olivine Fo percentages were calculated for quenched igneous glasses and aphyric bulk-rock samples using CoMagmat (Ariskin *et al.*, 1993) and for quenched igneous glasses according to Roeder & Emslie (1970).

igneous glasses and aphyric bulk-rock compositions. In this instance the high forsterite, Fo_{87-88}, olivine phenocrysts in samples from dredge 37 are clearly not in equilibrium with the quenched igneous-glass or bulk-rock compositions.

The observed compositions of olivine phenocrysts and microphenocrysts in central N-MORB (dredges 28-26) are mostly restricted to Fo_{85-86}. However, in the southernmost of these dredges, dredge 26, the microphenocrysts have low forsterite compositions, while the phenocrysts have the highest forsterite compositions, Fo_{89}, of all olivines in this study, see table 4.1. With the exception of the exceptionally high forsterite olivine phenocrysts in dredge 26, the olivine phenocrysts and microphenocrysts, even the low forsterite microphenocrysts in dredge 26, are in equilibrium with the host quenched igneous glasses and aphyric bulk-rock samples at low pressures, see fig. 4.5.

The observed compositions of olivine phenocrysts and microphenocrysts in southern Discovery-influenced MORB (dredges 25, 2-9) are predominantly confined to a broad range of Fo_{82-87}. However, olivine phenocrysts and microphenocrysts in basalts from dredge 7 span a considerably larger range. Microphenocrysts in sample 7D-2 have compositions of Fo_{72-73} and phenocrysts have compositions of Fo_{79-80}, while phenocrysts in sample 7D-1 have compositions of Fo_{86-87} (see fig. 4.5 and table 4.1). On the basis of olivine composition, the basalts recovered from dredge station 7 are heterogeneous and might be derived from at least two distinct parental magmas. However, the Mg# of the quenched igneous glass in sample 7D-2 is extremely low at 47.2 and therefore significantly more evolved than the quenched igneous glass from sample 7D-1 with Mg# of 63.6. These two samples therefore represent significantly different stages of magma evolution and this must be a factor when comparing the significantly different observed olivine compositions. The phenocrysts and microphenocrysts in these basalts are predominantly in equilibrium with the host quenched igneous glasses and aphyric bulk-rock samples, see fig. 4.5. Even the extremely low forsterite microphenocrysts in sample 7D-2 are in, or very close to, equilibrium with the host igneous-glass composition.

The observed compositions of olivine phenocrysts and microphenocrysts in southern N-MORB (dredges 10-13) span a range of compositions between Fo_{82-88}. The observed forsterite compositions of the olivine phenocrysts and microphenocrysts in basalts from these dredges increase progressively southward within this geographical section of the ridge, see fig. 4.5. The

University of Cape Town

olivine microphenocrysts have consistently lower forsterite contents relative to the compositions of co-existing phenocrysts. All the observed compositions of these olivine phenocrysts and microphenocrysts are in equilibrium with the relevant quenched igneous glasses at low pressures.

The observed compositions of olivine phenocrysts and microphenocrysts in Shona-influenced MORB (dredges 14D-24D, and A2-4, A6, A7, A9, A10) span a similar range as observed in southern Discovery-influenced MORB of Fo_{80-87}. As for southern Discovery-influenced MORB, a small number of olivine phenocrysts and especially microphenocrysts have extremely low forsterite compositions. Olivine microphenocrysts in basalts from dredge 22 have compositions as low as Fo_{70-72}, see table 4.1, but again these microphenocrysts occur in highly evolved samples with low Mg#'s, such as 22D-4 with a Mg# of 42.1. Regardless of the large variation in observed compositions of olivine phenocrysts and microphenocrysts, these olivines are in general remarkably in equilibrium with the relevant quenched igneous glasses and aphyric bulk-rock samples at low pressures.

Summary. The compositions of olivine microphenocrysts and phenocrysts are fairly restricted in N-MORB and most samples from mantle plume-influenced MORB, and span a range of $Fo_{\sim 82-87}$. Olivine phenocrysts have in general higher forsterite compositions than coexisting microphenocrysts, and in some case have compositions significantly higher than the general range of $Fo_{\sim 88-89}$. Some samples with low Mg#'s of ~40-42, restricted to mantle plume-influenced MORB, contain olivine microphenocrysts with forsterite compositions of $Fo_{\sim 70-73}$.

Olivine microphenocrysts are in general in, or close to, equilibrium with host-quenched igneous glasses and aphyric bulk-rock compositions at pressures ≤4kbar, even those microphenocrysts with extremely low forsterite compositions. Olivine phenocrysts are rarely observed to be in, or even close to, equilibrium with host-quenched igneous glasses or aphyric bulk-rock compositions.

Plagioclase. A representative subset of plagioclase-phenocryst compositions are listed in table 4.2 (the complete data-set of plagioclase-phenocryst compositions are listed in appendix B, table B.2), arranged according to increasing latitudinal locations of the dredge stations from which the samples were recovered. Observed anorthite compositions of plagioclase phenocrysts and microphenocrysts are plotted against latitude in fig. 4.6, plagioclase compositions from

University of Cape Town

samples recovered from ridge segments unaffected by mantle plumes in blue, those from samples from Discovery-influenced ridge segments in red, and from Shona-influenced ridge segments in green.

The observed compositions of plagioclase phenocrysts and microphenocrysts in northern N-MORB range from as high as An_{90} to as low as An_{68}, see table 4.2, and no clear predominance of either size-fraction amongst high- or low-An compositions is evident. The observed plagioclase compositions have no latitudinal systematics, see fig. 4.6. The phenocrysts with An_{90} compositions occur in sample 45D-2 in host-quenched igneous glass with Mg# of 67.2, while the phenocrysts and microphenocrysts with An_{68-69} compositions occur in samples 44D-3 and 41D-2 with Mg#'s of 62.1 and 63.0, respectively. These samples therefore do not differ greatly in terms of magma evolution due to crystallisation, although their plagioclase phenocrysts and microphenocrysts differ significantly in composition. In the previous section on the petrographic characteristics of these phenocrysts and microphenocrysts, the plagioclase phenocrysts were described as commonly exhibiting signs of disequilibrium, i.e. resorption. Comparing the observed compositions of the plagioclase phenocrysts in this region with the calculated equilibrium plagioclase compositions underscore this observation, see fig. 4.6. Plagioclase phenocrysts with high-An compositions are clearly not in equilibrium with the host-quenched igneous glasses at any realistic pressure, i.e. below 8kbar. The low-An plagioclase phenocrysts and microphenocrysts are in, or close to, equilibrium with quenched igneous glasses at low pressures, or at least <4kbar.

The observed compositions of plagioclase phenocrysts and microphenocrysts in northern Discovery-influenced MORB varies from An_{78-86} in phenocrysts to An_{68-74} in microphenocrysts, see table 4.2. There is therefore a distinct correlation between high-An compositions and larger size grains, opposed to low-An compositions and smaller size grains, see fig. 4.6. The observed plagioclase compositions plotted in fig. 4.6 do not exhibit any latitudinal trend. The plagioclase microphenocrysts are in equilibrium with the quenched igneous glasses at pressures <4kbar, but the larger phenocrysts are not in equilibrium with the quenched igneous glasses at any realistic pressure modelled. However, some of the plagioclase phenocrysts are in equilibrium with the aphyric bulk-rock compositions at low pressures. This might indicate some instances of closed system crystallisation, where the original, large high-An plagioclase phenocrysts did not get removed from the evolving magma.

University of Cape Town

Table 4.2: Representative plagioclase phenocryst compositions (EMP) in oxide-weight percentages, with all iron reported as Fe^{2+}. The size of phenocrysts analysed varied between phenocrysts (pheno) and microphenocryst (micro).

Sample	45D-2		44D-3	41D-2	36D-5	32D-2		31D-1	28D-2	28D-3	27D-1	26D-5	2D-3		3D-1
Size	pheno	micro	pheno	micro	micro	pheno	micro	pheno	pheno	pheno	pheno	pheno	pheno	pheno	pheno
Lat. (°S)	40.59	40.59	40.86	44.02	44.68	46.23	46.23	46.39	46.90	46.90	47.11	47.35	47.55	47.55	47.80
SiO_2	46.88	48.25	52.11	52.40	50.77	47.86	51.90	47.58	49.44	47.44	47.79	53.62	51.00	52.62	47.33
Al_2O_3	33.30	31.93	29.63	29.97	30.74	32.55	29.80	32.79	30.47	32.45	33.18	29.27	30.49	28.94	32.52
FeO	0.22	0.27	0.48	0.40	0.39	0.23	0.45	0.29	0.37	0.37	0.34	0.48	0.34	0.48	0.36
MgO	0.16	0.24	0.29	0.27	0.21	0.19	0.23	0.16	0.23	0.22	0.21	0.21	0.21	0.25	0.21
CaO	18.05	16.64	14.16	14.17	15.28	17.29	14.29	17.42	16.13	17.41	17.49	13.20	14.62	13.29	17.17
NA_2O	1.07	1.87	3.52	3.55	3.00	1.82	3.58	1.63	2.38	1.61	1.54	4.07	3.24	4.01	1.48
K_2O	< 0.024	< 0.024	< 0.024	< 0.024	< 0.024	< 0.024	0.06	< 0.024	< 0.024	< 0.024	< 0.024	< 0.024	0.08	0.10	< 0.024
Total	99.68	99.20	100.19	100.76	100.39	99.94	100.31	99.87	99.02	99.50	100.55	100.85	99.98	99.69	99.07
An	90.30	83.09	68.98	68.80	73.78	84.02	68.53	85.54	78.96	85.67	86.26	64.18	71.05	64.33	86.49

Sample	6D-1	7D-2	7D-3	9D-3	10D-3		12D-3	13D-2	14D-1	15D-2	17D-1	18D-6	19D-2	20D-3	22D-4
Size	pheno	pheno	pheno	pheno	pheno	micro	micro	micro	pheno	pheno	micro	pheno	micro	micro	micro
Lat. (°S)	48.55	48.76	48.76	49.15	49.25	49.25	49.76	49.99	50.27	50.58	50.76	51.05	51.06	51.43	52.46
SiO_2	49.88	53.14	48.41	48.74	49.10	53.41	50.60	48.90	47.87	46.85	51.63	47.65	52.90	50.59	54.84
Al_2O_3	31.77	29.33	32.47	32.33	31.94	28.85	30.75	31.73	32.82	33.29	30.22	32.66	28.85	31.02	28.32
FeO	0.41	0.59	0.35	0.32	0.28	0.49	0.37	0.33	0.36	0.36	0.45	0.32	0.54	0.38	0.60
MgO	0.24	0.16	0.17	0.23	0.18	0.25	0.23	0.22	0.18	0.17	0.24	0.19	0.19	0.23	0.17
CaO	15.52	12.97	17.35	16.13	16.74	13.25	15.05	16.17	16.92	17.77	14.31	17.36	12.89	15.20	12.13
NA_2O	2.32	3.69	1.57	1.87	1.94	3.97	3.00	2.12	1.42	1.03	3.13	1.32	3.78	2.72	4.55
K_2O	0.04	0.10	< 0.024	0.04	< 0.024	< 0.024	< 0.024	< 0.024	< 0.024	< 0.024	0.04	< 0.024	0.04	0.06	0.10
Total	100.18	99.98	100.32	99.66	100.18	100.22	100.00	99.47	99.57	99.47	100.02	99.50	99.19	100.20	100.71
An	78.50	65.61	85.95	82.49	82.64	64.85	73.51	80.85	86.78	90.54	71.47	87.89	65.17	75.25	59.20

An: anorthite content as percentage

University of Cape Town

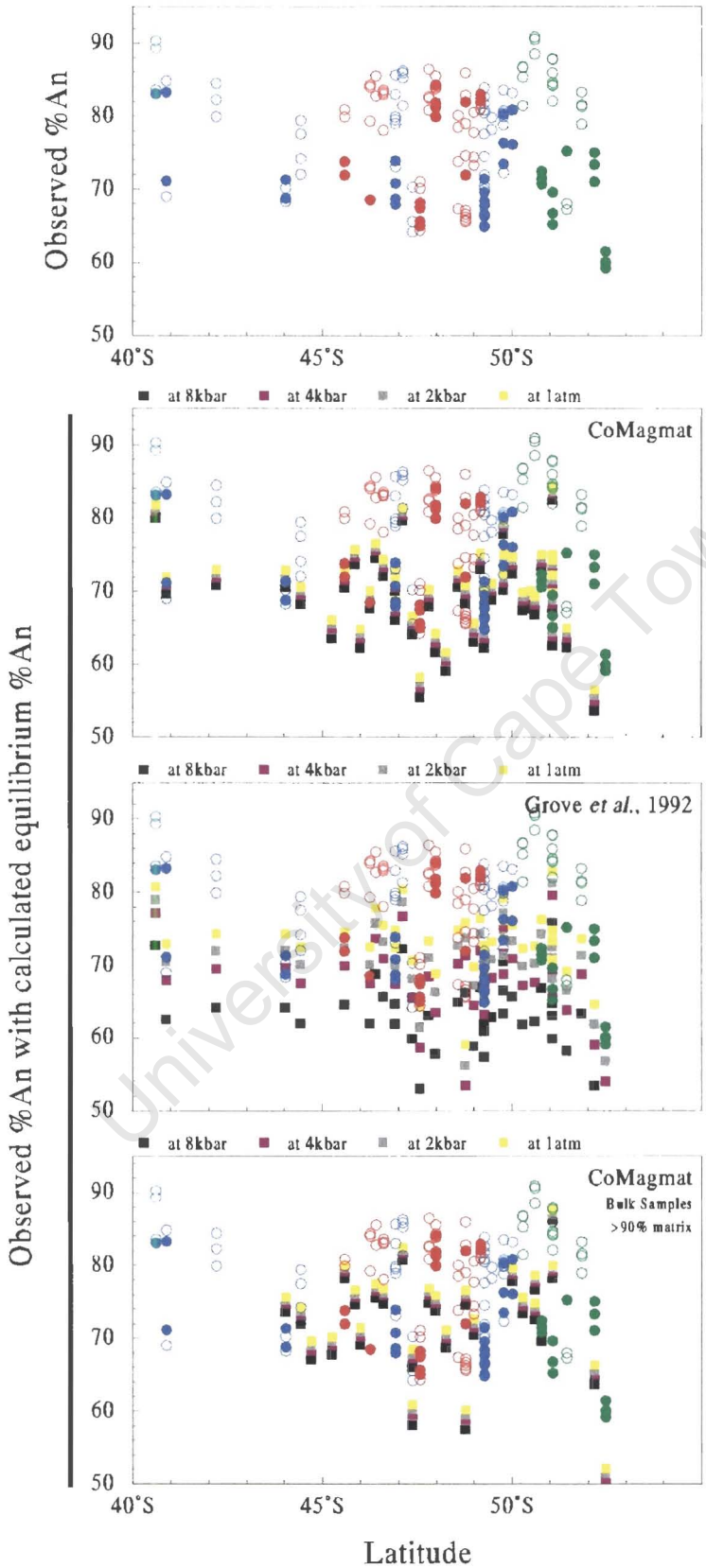

University of Cape Town

Figure 4.6: Observed anorthite (An) percentages of plagioclase phenocrysts (open circles) and microphenocrysts (filled circles) in individual dredges versus latitude. Equilibrium plagioclase An percentages were calculated for quenched igneous glasses and aphyric bulk-rock samples using CoMagmat (Ariskin *et al.*, 1993) and for quenched igneous glasses according to Grove *et al.* (1992).

The observed compositions of plagioclase phenocrysts and microphenocrysts in central N-MORB fall in the general range of An_{64-86}. Microphenocrysts are compositionally restricted to the low-An end of the spectrum, but phenocrysts compositions span the whole range observed, see fig. 4.6. The plagioclase phenocrysts in dredge 26, the southernmost dredge station in this geographical group, have exceptionally low An_{64-70} compositions, but are nevertheless in equilibrium with the host-quenched igneous glass and aphyric bulk-rock composition at pressures <4kbar. The majority of the remaining plagioclase phenocrysts and microphenocrysts are also in equilibrium with host-quenched igneous glass and aphyric bulk-rock compositions at similar pressures of <4kbar, see fig. 4.6. Although the plagioclase phenocrysts with the highest anorthite compositions amongst these samples are not in equilibrium with host-quenched igneous glass or aphyric bulk-rock compositions at any pressure <8kbar.

The observed plagioclase phenocryst and microphenocryst compositions in southern Discovery-influenced MORB fall between An_{64-87}, with no preferred concentration of microphenocrysts or phenocrysts at either end of this range. The plagioclase phenocrysts and microphenocrysts are mostly not in equilibrium with host-quenched igneous glass or aphyric bulk-rock compositions, see fig. 4.6. A minority of the low-An plagioclase phenocrysts and microphenocrysts are in, or close to, equilibrium with host-quenched igneous glass compositions at low pressures, but not convincingly in equilibrium with the aphyric bulk-rock compositions.

The observed plagioclase phenocryst and microphenocryst compositions in southern N-MORB range from An_{64} for microphenocrysts to An_{83}, mostly for phenocrysts, see table 4.2. The observed compositions of plagioclase phenocrysts and microphenocrysts in the northernmost dredge in this geographical region, dredge 10, span this range, while the dredges further to the south have much more restricted ranges of plagioclase compositions and also progressively higher anorthite contents, see fig. 4.6. The plagioclase microphenocrysts are generally in equilibrium with the host-quenched igneous glass compositions at pressures <4kbar, while the plagioclase phenocrysts with higher anorthite compositions are not in equilibrium with the quenched igneous glass compositions.

The observed compositions of plagioclase phenocrysts and microphenocrysts in Shona-influenced MORB span a considerable range from An_{59} for microphenocrysts in the highly evolved sample 22D-4, which has host-quenched igneous glass with Mg# of 42.1, in the south,

University of Cape Town

to An_{91} for phenocrysts in the moderately evolved sample 15D-2, which has host-quenched igneous glass with Mg# of 61.0. Although a few plagioclase phenocrysts have low anorthite compositions, the low-anorthite end of the compositional spectrum is dominated by plagioclase microphenocrysts, see fig. 4.6. The plagioclase phenocrysts are rarely in equilibrium with the host-quenched igneous glass or aphyric bulk-rock compositions, and when in equilibrium are restricted to pressures <2kbar. The plagioclase microphenocrysts are also not generally in equilibrium with host-quenched igneous glass or aphyric bulk-rock compositions, but more commonly than the plagioclase phenocrysts. Plagioclase microphenocrysts are in equilibrium with host-quenched igneous glass or aphyric bulk-rock compositions at low pressures <2kbar.

Summary. The observed compositions of plagioclase phenocrysts and microphenocrysts have no distinct latitudinal systematic variation, and the basalts recovered from mantle plume-influenced ridge segments do not contain plagioclase phenocrysts or microphenocrysts with significantly different compositions relative to plagioclase in N-MORB. As expected, plagioclase microphenocrysts have the lowest anorthite compositions and these occur in highly evolved basalts. Although not consistently in equilibrium, the plagioclase microphenocrysts are more commonly in equilibrium with host-quenched igneous glass or bulk-rock compositions at low pressures.

With rare exceptions, plagioclase phenocrysts, especially those with high anorthite compositions, were found not to be in equilibrium with host-quenched igneous glass or bulk-rock compositions at pressures <8kbar. This deduction agrees with observation of the habits of large plagioclase phenocrysts, described in the previous section. The phenocrysts were found to be severely rounded and resorbed and these petrographic observations also indicate disequilibrium with host-quenched igneous glass or groundmass.

Clinopyroxene and spinel. Clinopyroxene is rarely present in the MORB from the SMAR studied in this project, as discussed in the previous section, see fig. 4.1. A limited number of clinopyroxene microphenocrysts and a phenocrysts were analysed, compositions listed in table 4.3, and were restricted to the compositional range $Wo_{41-43}En_{48-52}Fs_{6-10}$. All these clinopyroxene microphenocrysts and phenocryst occurred in southern Discovery-influenced MORB, with the exception of the microphenocrysts from sample 20D-3 which is a Shona-influenced MORB. The small spinel microphenocrysts analysed and listed in table 4.4 are from

University of Cape Town

Table 4.3: Clinopyroxene phenocryst compositions (EMP) in oxide-weight percentages, with all iron reported as Fe^{2+}. The size of phenocrysts analysed varied between phenocrysts (pheno) and microphenocryst (micro).

Sample	2D-3		3D-1	6D-1	7D-3	20D-3
Size	micro	micro	micro	micro	pheno	micro
Lat. (°S)	47.55	47.55	47.80	48.55	48.76	51.43
SiO_2	50.76	52.90	52.56	51.92	52.37	52.45
TiO_2	0.96	0.53	0.31	0.42	0.30	0.53
Al_2O_3	4.29	1.98	2.93	3.60	3.30	1.95
Cr_2O_3	1.08	0.78	0.47	1.19	1.25	0.44
FeO	5.86	5.74	4.85	4.73	4.19	5.87
MnO	0.14	0.14	< 0.06	0.15	< 0.06	0.19
MgO	16.56	18.25	17.73	17.75	17.83	17.98
CaO	19.61	19.11	20.13	20.21	20.92	19.55
Na_2O	0.30	0.27	0.27	0.25	0.24	0.24
K_2O	< 0.023	< 0.023	< 0.023	< 0.023	< 0.023	< 0.023
Total	99.56	99.70	99.25	100.22	100.40	99.20
Wo	41.43	38.93	41.44	41.49	42.71	39.66
En	48.67	51.72	50.77	50.69	50.61	50.74
Fs	9.90	9.35	7.78	7.82	6.68	9.60

Wo, En, Fs: wollastonite, enstatite, and ferrosilite content as percentages

University of Cape Town

Table 4.4: Spinel microphenocryst compositions (EMP) in oxide-weight percentages, with Fe_2O_3 calculated by stoichiometry (Droop, 1987). The phenocrysts analysed were all microphenocrysts (micro) in size.

Sample	34D-3		19D-7		
Size	micro	micro	micro	micro	micro
Lat. (°S)	45.85	45.85	51.06	51.06	51.06
SiO_2	< 0.038	< 0.038	< 0.038	0.09	2.01
TiO_2	0.38	0.37	0.74	0.68	1.38
Al_2O_3	40.01	39.74	32.84	32.82	26.88
Cr_2O_3	23.73	23.72	28.33	28.60	27.42
FeO	12.05	12.16	14.76	14.84	20.56
Fe_2O_3	4.94	5.06	7.80	7.16	7.64
MnO	0.14	< 0.078	0.19	0.20	0.23
MgO	16.92	16.96	14.96	14.84	12.18
CaO	0.06	0.07	< 0.027	< 0.027	0.28
Total	98.25	98.19	99.64	99.24	98.59
Mg#	0.71	0.71	0.64	0.64	0.51
Cr#	0.28	0.29	0.37	0.37	0.41

Mg#: atomic Mg^{2+}/(atomic Mg^{2+}+atomic Fe^{2+})
Cr#: atomic Cr^{3+}/(atomic Cr^{3+}+atomic Al^{3+})

northern Discovery-influenced MORB, sample 34D-3, and Shona-influenced MORB, sample 19D-7. All the analyses of spinel microphenocrysts yielded total iron as ferrous iron and the FeO and Fe_2O_3 concentrations listed in table 4.4 were calculated based on stoichiometry. (Droop, 1987). The compositions in table 4.4 underscore the division between these two samples, with the spinel microphenocrysts from sample 34D-3 having higher Mg#'s of 0.71, and lower Cr#'s of 0.28-0.29 relative to those from sample 19D-7 with Mg#'s of 0.51-0.64, and Cr#'s of 0.37-0.41. The more opaque spinel microphenocrysts in sample 19D-7 can therefore be considered as having compositions which class them as magnesiochromites.

Sulphide. Sulphide blebs occur as rare inclusions in, or adjacent to, olivine (19D-7) and plagioclase (45D-2) phenocrysts, see plates 4.24-25. Quantitative analysis of these blebs proved problematic due to their small size and fine-scale compositional heterogeneities. Semi-quantitatively, sulphide blebs ranged in iron content between 39-55wt%, in nickel content between 8-28wt%, and in sulphur content between 35-38wt%.

Geothermometry. The calculated olivine and plagioclase equilibrium and liquidus temperatures (Ariskin *et al.*, 1993; Longhi *et al.*, 1978; Nielsen & Dungan, 1983; Roeder, 1974; Roeder & Emslie, 1970) are plotted against latitude in fig. 4.7. The calculated equilibrium olivine temperatures are more varied and extend to lower values in northern and southern Discovery-influenced, and Shona-influenced MORB, relative to N-MORB. This observation is not surprising, as the basalts recovered from mantle plume-influenced ridge segments have in general lower Mg#'s relative to N-MORB, and are therefore more evolved which implies that crystallisation continued for longer periods in these mantle plume-influenced basalts and thus proceeded to lower temperatures prior to eruption. The calculated equilibrium temperatures of the most Mg-rich olivines, which are not necessarily in equilibrium with their host-quenched igneous glass, extend to lower values for southern Discovery-influenced MORB, but otherwise agree with the temperatures obtained from olivines in equilibrium with their host-quenched igneous glasses.

The calculated liquidus temperatures are not well constrained, but again the dredges which sampled mantle plume-influenced ridge segments have the most internal variation. The northern and southern Discovery- and Shona-influenced MORB yield temperatures lower than basalts recovered from mantle plume-unaffected ridge segments. Comparing the equilibrium and

University of Cape Town

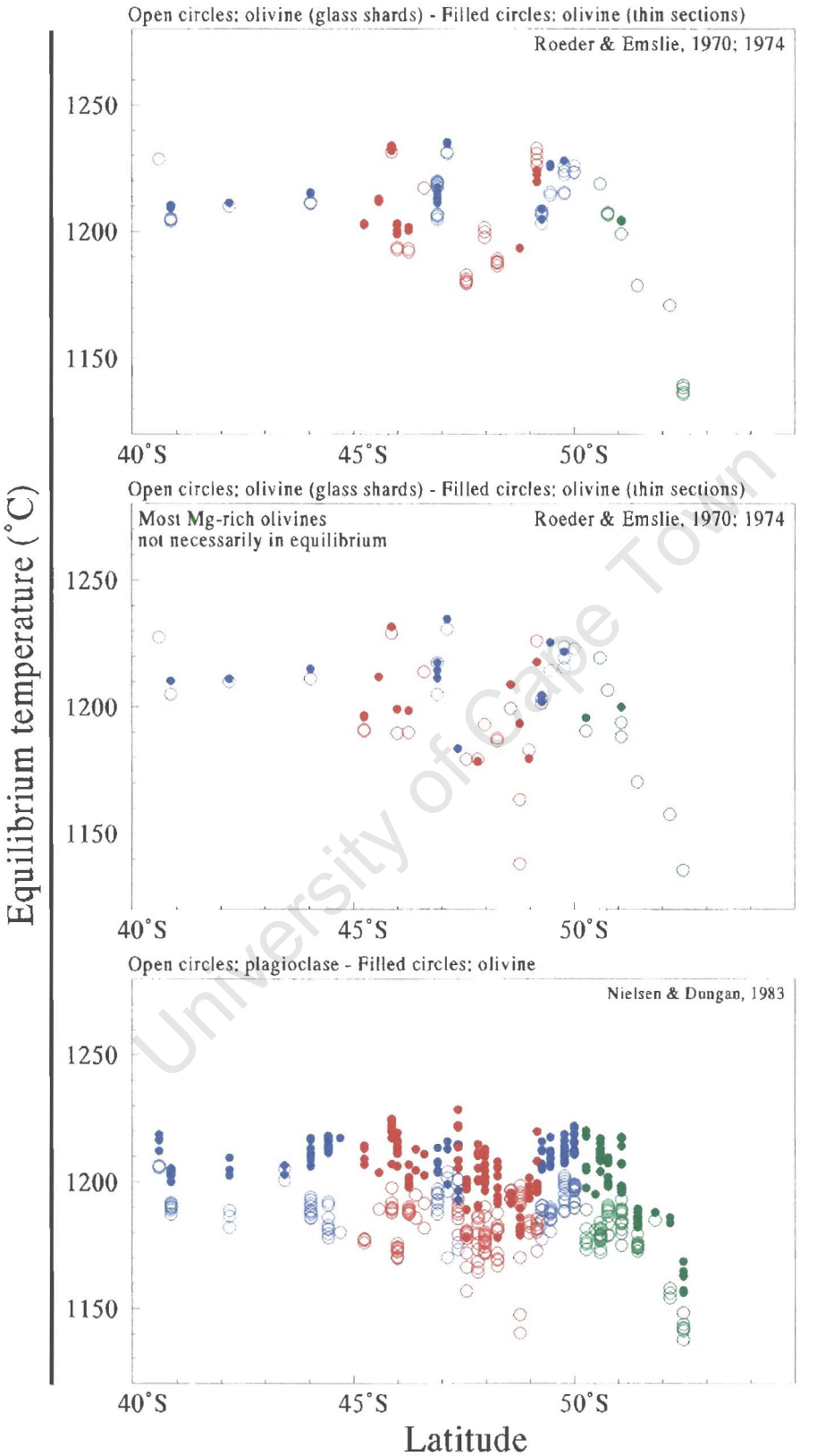

University of Cape Town

Figure 4.7: Olivine and plagioclase equilibrium and liquidus temperatures (°C) versus latitude. Calculations referenced on each diagram; CoMagmat reference Ariskin *et al.* (1993); and "glass shard": calculated using quenched igneous-glass compositions from glass separates, "thin section": calculated using quenched igneous-glass compositions from the immediate vicinity of phenocrysts in polished thin sections.

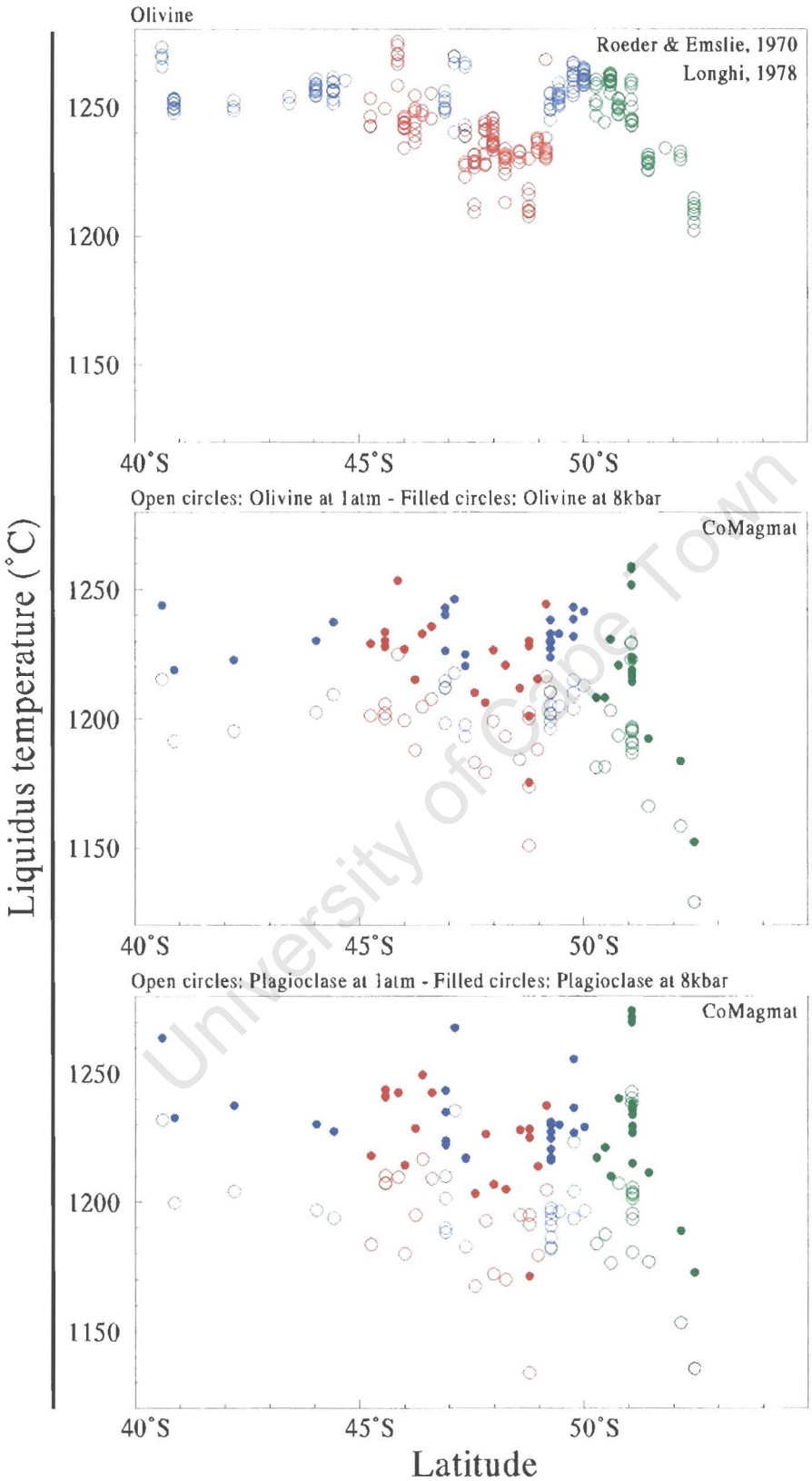

University of Cape Town

Figure 4.7 (continued)

liquidus temperatures indicates that olivine phenocrysts in N-MORB were at equilibrium with their host-quenched igneous glasses at temperatures higher than the calculated 1atm liquidus temperatures and closer to the calculated 4-6kbar liquidus temperatures. The olivines from the northern and southern Discovery- and Shona-influenced MORB were at equilibrium with their host-quenched igneous glass at lower pressures than those in N-MORB, but still at temperatures mostly higher than the calculated 1atm liquidus temperatures and closer to the calculated 2-4kbar liquidus temperatures. This indicates cessation of olivine crystallization in basalts recovered from mantle plume-unaffected ridge segments at pressures of 4-6kbar and in basalts recovered from Discovery- and Shona-influenced ridge segments at 2-4kbar.

4.3 BULK-ROCK COMPOSITIONS

This section will briefly present representative bulk-rock compositions of MORB from the SMAR. The major discussion of the compositional characteristics of these bulk-rock data, in terms of classification, mantle plume-influence, and phenocryst crystallisation or accumulation, will be conducted in conjunction with the compositional data for the quenched igneous glasses in the next section. Here, the focus will be on an overview of the actual, absolute compositions of bulk-rock samples from the different geographical groups.

University of Cape Town

Table 4.5 contains a sub-set of thirty bulk-rock compositions representative of the larger data-set of sixty-two bulk-rock compositions listed in appendix B, table B.6. The samples are listed in latitudinal order from the north to the south and contain examples of basalts from the northern, central and southern N-MORB, the northern and southern Discovery-influenced MORB, and the Shona-influenced MORB.

Major-element data. The bulk-rock compositions of samples of northern (45D-2, 44D-3, 41D-1 and 40D-5), central (28D-9, 27D-1, 27D-2 and 26D-1) and southern (10D-8, 11D-2, 12D-2 and 13D-1) N-MORB in table 4.5 are representative of the compositional diversity, or lack thereof, amongst N-MORB recovered from the SMAR. In terms of some major-elements concentrations, these N-MORB are quite homogeneous, e.g. SiO_2 of 48.35-51.12wt%, TiO_2 of 0.65-1.69wt%, and MgO of 7.01-8.67wt%, while the concentrations of Al_2O_3, 14.86-22.10wt%, and CaO, 10.05-13.66wt%, vary significantly. The maxima in the concentrations Al_2O_3 and CaO occur in highly phyric samples, such 45D-2 listed in table 4.5.

Table 4.5: Representative major- and trace-element (XRF) compositional data for bulk-rock samples. Major-element concentrations in oxide-weight percentages, and trace-element concentrations in ppm. MBSL: dredging depth in average metres below sea-level. Mg#: atomic Mg^{2+}/(atomic Mg^{2+} + atomic Fe^{2+}), using $Fe_2O_3/FeO=0.15$. %Matr.: percentage matrix from point-counted thin sections. LOI: loss on ignition

Sample	45D-2	44D-3	41D-1	40D-5	37D-2	34D-3	32D-2	30D-2	28D-9	27D-1	27D-2	26D-1	25D-1	2D-1	3D-3
Lat. (°S)	40.59	40.86	44.02	44.41	45.23	45.85	46.23	46.59	46.90	47.11	47.11	47.35	47.35	47.55	47.80
Long. (°W)	16.77	16.79	16.08	15.91	15.08	14.19	13.56	13.39	13.45	13.40	13.40	13.40	10.32	10.19	10.15
MBSL	3203	3067	3522	3488	3534	3443	3108	3153	3417	3081	3081	3857	2032	2494	2549
SiO_2	48.35	50.18	50.79	50.96	50.37	48.98	50.63	50.49	50.11	49.01	49.32	50.29	54.15	51.47	50.87
TiO_2	0.66	1.24	1.27	1.50	1.69	1.19	1.49	1.51	1.39	0.90	0.98	1.69	1.33	1.91	1.38
Al_2O_3	22.10	16.51	15.71	15.27	15.54	16.09	15.76	15.83	15.54	18.11	17.41	14.86	14.85	15.41	16.00
Fe_2O_3	0.86	1.27	1.24	1.38	1.32	1.38	1.32	1.33	1.31	1.14	1.32	1.47	1.16	1.23	1.21
FeO	5.74	8.47	8.26	9.20	8.80	9.18	8.81	8.84	8.74	7.62	8.77	9.82	7.70	8.21	8.09
MnO	0.11	0.17	0.17	0.18	0.17	0.17	0.18	0.18	0.18	0.16	0.16	0.20	0.13	0.16	0.16
MgO	7.01	7.69	8.21	8.12	8.01	9.25	7.72	7.72	8.31	8.30	8.84	7.27	8.78	6.53	7.19
CaO	13.66	12.10	11.29	11.08	10.49	10.72	11.16	11.21	11.21	11.97	10.98	10.87	8.10	10.47	11.54
Na_2O	1.88	2.11	2.62	2.49	2.92	2.61	2.40	2.55	2.48	2.20	2.49	2.91	2.82	2.69	2.70
K_2O	0.04	0.09	0.14	0.13	0.48	0.15	0.24	0.24	0.16	0.09	0.09	0.15	0.28	0.77	0.40
P_2O_5	0.05	0.11	0.12	0.15	0.23	0.09	0.17	0.16	0.14	0.06	0.07	0.16	0.14	0.29	0.16
LOI	0.04	0.04	0.06	0.04	0.09	0.07	0.04	0.07	0.07	0.07	0.04	0.10	0.05	0.11	0.12
H_2O^-	0.21	0.15	0.51	0.24	0.54	0.36	0.39	0.29	0.26	0.34	0.37	0.50	0.31	0.84	0.84
Total	100.72	100.12	100.40	100.73	100.62	100.24	100.30	100.41	99.90	99.97	100.83	100.28	99.79	100.09	100.66
Mg#	68.5	61.8	63.9	61.1	61.9	64.2	61.0	60.9	62.9	66.0	64.3	56.9	67.0	58.6	61.3
%Matr.	58	89	95	95	98	98	86	96	97	85	95	97	93	90	95
Sc	24	39	36	40	35	36	36	41	41	35	32	40	22	36	37
V	134	248	241	275	245	210	228	291	252	177	163	296	150	245	252
Cr	320	336	328	320	294	414	299	286	333	304	339	227	449	198	262
Co	39	48	47	49	48	53	46	50	48	48	53	47	48	43	46
Ni	144	120	142	146	157	200	118	124	145	157	202	108	289	71	99
Cu	61	74	56	59	58	60	58	60	63	75	70	58	51	47	58
Zn	45	73	73	86	83	82	78	87	80	59	75	89	93	90	77
Rb	< 1.5	< 1.5	< 1.5	1.60	7.80	< 1.5	5.20	2.50	1.90	< 1.5	< 1.5	1.50	5.00	13.4	5.80
Sr	110	106	108	107	195	105	160	119	128	117	132	119	209	295	134
Y	17.4	31	34	39	36	32	32	40	35	26	27	44	20	30	31
Zr	41	80	84	101	122	72	95	114	97	61	64	121	80	159	97
Nb	< 2.5	3.30	3.30	3.50	10.1	< 2.5	7.50	4.60	4.10	< 2.5	< 2.5	< 2.5	5.20	15.2	6.40
Ba	< 3.7	< 3.7	7.00	9.00	82	< 3.7	49	15.0	15.7	< 3.7	< 3.7	8.40	57	171	62

University of Cape Town

Table 4.5 (cont.)

Sample	7D-1	7D-2	7D-3	9D-3	10D-8	11D-2	12D-2	13D-1	15D-2	15D-4	17D-1	18D-6	19D-3	20D-2	22D-3
Lat. (°S)	48.76	48.76	48.76	49.15	49.25	49.44	49.76	49.99	50.58	50.58	50.76	51.05	51.06	51.43	52.46
Long. (°W)	10.07	10.07	10.07	9.91	8.14	7.97	8.03	7.88	6.43	6.43	6.34	6.20	6.16	5.78	4.57
MBSL	3218	3218	3218	3892	2637	3868	3874	3555	2980	2980	2943	1991	1743	1719	3059
SiO_2	50.98	52.59	50.33	50.71	50.44	50.70	50.67	50.96	49.93	50.36	49.14	49.03	50.19	50.78	50.38
TiO_2	1.43	2.42	0.87	1.53	1.51	1.40	1.09	1.07	1.39	1.27	1.46	0.89	1.27	1.82	2.62
Al_2O_3	16.74	14.21	18.51	15.35	15.27	15.30	17.40	15.88	14.75	15.65	15.09	18.10	15.80	14.73	13.17
Fe_2O_3	1.02	1.69	0.99	1.33	1.32	1.35	1.10	1.15	1.48	1.27	1.39	1.10	1.18	1.41	1.79
FeO	6.78	11.26	6.62	8.86	8.77	8.97	7.31	7.63	9.88	8.46	9.23	7.33	7.88	9.40	11.94
MnO	0.13	0.22	0.14	0.18	0.18	0.18	0.15	0.16	0.19	0.17	0.18	0.15	0.16	0.19	0.23
MgO	7.42	5.74	7.35	7.90	7.83	8.04	7.70	8.56	7.84	8.26	9.39	8.84	7.55	6.87	5.02
CaO	10.38	9.50	12.81	11.14	11.05	11.32	12.48	12.50	11.59	11.71	10.80	12.15	12.52	11.15	8.92
Na_2O	2.77	2.79	2.07	2.18	2.91	2.49	2.02	2.39	1.94	2.23	2.60	2.17	2.40	2.47	2.97
K_2O	1.27	0.73	0.23	0.16	0.16	0.12	0.10	0.07	0.16	0.20	0.31	0.10	0.38	0.37	0.59
P_2O_5	0.30	0.33	0.09	0.14	0.14	0.12	0.09	0.08	0.13	0.13	0.14	0.05	0.14	0.20	0.36
LOI	0.14	-1.71	0.06	0.11	0.07	0.08	0.03	0.04	0.09	0.07	0.09	0.05	0.15	0.07	0.17
H_2O^-	0.95	0.91	0.39	0.75	0.75	0.47	0.46	0.56	0.38	0.44	0.60	0.59	0.70	0.32	2.30
Total	100.30	102.38	100.45	100.34	100.37	100.52	100.60	101.04	99.73	100.21	100.45	100.55	100.32	99.78	100.46
Mg#	66.1	47.6	66.4	61.4	61.4	61.5	65.2	66.7	58.6	63.5	64.5	68.2	63.1	56.6	42.9
%Matr.	96	91	67	74	98	92	76	92	93	87	91	94	97	87	96
Sc	29	40	33	36	38	43	36	39	43	38	37	32	40	43	39
V	178	373	199	148	260	280	236	241	305	258	242	168	249	305	363
Cr	262	73	39	322	270	308	391	430	331	379	375	333	367	197	77
Co	39	45	42	46	46	48	44	48	49	49	57	53	47	44	43
Ni	123	58	112	136	132	144	150	129	127	145	229	200	101	69	51
Cu	55	43	62	72	56	61	60	69	74	65	65	93	88	62	37
Zn	67	112	58	50	79	82	65	64	86	75	79	63	72	90	128
Rb	22	13.7	3.50	2.40	< 1.5	< 1.5	< 1.5	< 1.5	2.70	2.10	3.20	< 1.5	5.10	5.70	10.4
Sr	373	142	135	139	115	109	103	96	94	105	136	114	164	181	126
Y	22	53	21	24	37	35	27	27	33	30	34	21	26	33	63
Zr	137	185	57	53	104	90	67	64	83	76	102	48	82	118	222
Nb	20	13.5	3.30	2.60	< 2.5	< 2.5	< 2.5	< 2.5	3.90	4.20	5.20	< 2.5	6.70	9.40	14.9
Ba	290	152	32	22	4.30	< 3.7	< 3.7	< 3.7	8.00	12.0	22	< 3.7	40	58	109

University of Cape Town

The bulk-rock major-element compositions of northern Discovery-influenced MORB vary within much smaller ranges relative to the compositional variations in the bulk-rock major-element compositions of the southern Discovery-influenced MORB, and basalts from both groups are heterogeneous in terms of bulk-rock compositions. The SiO_2, TiO_2, and Al_2O_3 concentrations in the northern Discovery-influenced MORB vary between 48.98-50.89wt%, 1.16-1.69wt%, and 15.54-17.23wt% respectively, while in the southern Discovery-influenced MORB SiO_2, TiO_2, and Al_2O_3 vary between 50.33-54.15wt%, 0.87-2.42wt%, and 14.21-18.51wt% respectively. The southern Discovery-influenced MORB also define a significantly larger range in Mg#'s of bulk-rock compositions of 47.6-67.0, relative to the northern Discovery-influenced MORB with bulk-rock Mg#'s of 60.9-64.2.

Although the bulk-rock major-element compositions of Shona-influenced MORB are significantly heterogeneous, the concentrations of SiO_2 in these basalts are relatively restricted to a range of 49.00-51.03wt%. The concentrations of TiO_2 and Al_2O_3 vary between 0.89-2.62wt% and 13.17-18.10wt%, respectively, in Shona-influenced MORB. The remaining major-element oxides in these basalts also vary significantly, with FeO, MgO and CaO spanning ranges of 7.31-11.94wt%, 5.02-9.39wt%, and 8.92-12.85wt%. The Mg#'s of these bulk-rock samples vary from 42.9 to 68.2, and the large compositional variations observed especially in FeO, MgO, Al_2O_3 and CaO are due to the significant range in evolution, i.e. crystallisation and phenocrysts removal or accumulation, of these samples.

Trace-element data. As will be discussed in greater detail in the following section, the bulk-rock compositions of northern, central and southern N-MORB are depleted in incompatible trace elements, with concentrations of Rb <3.2ppm, Nb <4.2ppm and Ba <15.7. The concentrations of Sr and Zr in these N-MORB are restricted to ranges of 96-132ppm and 41-121ppm, respectively, which will be shown to be significantly lower than in the mantle plume-influenced basalts.

As in the bulk-rock major-element compositions of the northern and southern Discovery-influenced MORB, the incompatible trace-element concentrations in the southern Discovery-influenced MORB are significantly higher and more heterogeneous relative to the northern Discovery-influenced MORB. The concentrations of Rb, Nb and Ba in the bulk-rock samples of southern Discovery-influenced MORB range between 2.4-22ppm, 2.6-20ppm and 22-290ppm,

University of Cape Town

respectively, while in bulk-rock samples of northern Discovery-influenced MORB these incompatible trace elements range between <1.5-15ppm, <2.5-16.9ppm and <3.7-157ppm, respectively. The Sr and Zr concentrations in the bulk-rock samples of southern Discovery-influenced MORB range between 134-373ppm and 53-185ppm, but between 105-260ppm and 72-133ppm in the bulk-rock samples of northern Discovery-influenced MORB. The bulk-rock compositions of Discovery-influenced MORB are therefore significantly more enriched in incompatible trace elements relative to the compositions N-MORB, while the bulk-rock compositions of southern Discovery-influenced MORB define the most-enriched and most-diverse of this spectrum of mantle plume-influenced basalts.

The incompatible trace-element concentrations in bulk-rock samples of Shona-influenced MORB are higher than in N-MORB, but do not in general reach the enrichment observed in Discovery-influenced MORB. The concentrations of Rb, Nb and Ba in the bulk-rock samples of Shona-influenced MORB vary between <1.5-10.4ppm, <2.5-14.9ppm, and <3.7-109ppm. The bulk-rock concentrations of Sr in Shona-influenced MORB are also lower relative to Discovery-influenced MORB, at between 94-181ppm, but Zr concentrations of between 48-222ppm in Shona-influenced MORB span a larger range and to higher values relative to Discovery-influenced MORB.

Summary. The bulk-rock samples of MORB recovered from the SMAR span a range of major-element and trace-element compositions, variable due to the compositional influences of the proximal mantle plumes on the mantle source-regions from which these basalts were derived, the occurrence of both highly evolved, with low Mg#'s of 42-50, and only slightly evolved, with high Mg#'s of 65-68, basalts, and the affects of phenocryst accumulation on bulk-rock compositions.

The incompatible trace-element compositions of these basalts are the most decisive indicators of significant compositional heterogeneities between samples recovered from ridge segments affected or unaffected by the proximal mantle plumes. The bulk-rock compositions of basalts recovered from Discovery- and Shona-influenced ridge segments are highly and variably enriched in incompatible trace elements, with for example Ba concentrations <15.7ppm in N-MORB samples compared to <290ppm in mantle plume-influenced samples.

University of Cape Town

4.4 QUENCHED IGNEOUS-GLASS COMPOSITIONS

This section will present and discuss the major- and trace-element compositions of the quenched igneous glasses of MORB recovered from the SMAR. A representative subset of the complete data-set, given in appendix B, table B.5, of quenched igneous-glass compositions are listed in table 4.6. During the detailed discussion of characteristic variations or influences of petrogenetic processes on the compositions of the quenched igneous glasses, the compositions of the bulk-rock samples of these basalts will also be included.

The igneous classification of these MORB recovered from the SMAR will be discussed using established systems as well as comparisons with published data for MORB recovered from other mid-ocean ridges. Observed variations in major- and trace-element compositions of these basalts will discussed and assessed in general terms of petrogenetic processes and the compositional influences of the proximal mantle plumes.

University of Cape Town

4.4.1 Classification

This section will address the major-element classification of the rock samples recovered from the SMAR into the basaltic igneous system. The trace-element compositions of these samples will further be used to define and contrast the relative enrichment of specific incompatible trace elements and specific ratios of highly incompatible/moderately incompatible trace elements, and classify samples as either depleted or N-MORB, or enriched or E-MORB.

Major-element compositions. MORB recovered from this section of the southern Mid-Atlantic Ridge are predominantly tholeiitic basalts according to the total-alkali versus silica (TAS) classification (Le Maitre, 1989; MacDonald & Katsura, 1964) in fig. 4.8, which shows the data for the quenched igneous-glass and bulk-rock samples. The data extend in some cases into the basaltic andesite field for both quenched igneous-glass and bulk-rock samples. The CIPW normative compositions of these MORB are dominantly olivine-normative, although a significant number of samples are quartz-normative, see fig. 4.8.

Trace-element compositions. The variations in the concentrations of incompatible elements relative to moderately incompatible elements (Sun & McDonough, 1989), expressed as ratios in fig. 4.9a, are considerable in these MORB. The compositional characteristics observed span the range from the extremely incompatible-element depleted to the extremely

Table 4.6: Representative major- (EMP) and trace-element (LA-ICP-MS) compositional data for quenched igneous glasses. Major-element concentrations: oxide-weight percentages, all iron reported as Fe^{2+}, and trace-element concentrations: ppm. MBSL: dredge depth in average metres below sea-level. Mg#: atomic Mg^{2+}/(atomic Mg^{2+} + atomic Fe^{2+}), using $Fe_2O_3/FeO=0.15$.

Sample	45D-1	44D-6	42D-1	40D-5	34D-6	33D-5	32D-3	31D-1	30D-1	28D-6	27D-1	27D-2	26D-1	25D-1	2D-1
Lat. (°S)	40.59	40.86	43.43	44.41	45.85	45.99	46.23	46.39	46.59	46.90	47.11	47.11	47.35	47.35	47.55
Long. (°W)	16.77	16.79	16.17	15.91	14.19	14.08	13.56	13.46	13.39	13.45	13.40	13.40	13.40	10.32	10.19
MBSL	3203	3067	3449	3488	3443	3381	3108	2822	3153	3417	3081	3081	3857	2032	2494
SiO_2	49.30	50.11	49.42	51.54	49.25	49.97	51.33	49.61	50.08	50.61	48.90	50.57	50.08	53.98	51.66
TiO_2	0.92	1.38	1.22	1.54	1.25	1.66	1.51	1.40	1.31	1.26	0.99	1.73	1.84	1.43	2.14
Al_2O_3	16.77	15.31	16.97	14.72	16.39	15.65	15.49	16.56	15.85	15.63	16.79	14.19	14.63	15.79	14.92
FeO	8.80	9.73	8.96	10.19	10.28	9.16	9.70	8.89	9.51	8.96	9.38	11.26	11.26	8.39	9.86
MnO	0.16	0.17	0.18	0.16	0.22	0.19	0.14	0.15	0.15	0.20	0.16	0.15	0.16	0.14	0.16
MgO	9.47	8.21	8.39	8.22	9.10	7.76	7.55	8.19	8.36	8.23	8.98	7.02	7.06	7.51	6.24
CaO	12.32	12.11	11.21	11.12	11.10	10.41	11.19	11.25	11.55	12.11	11.83	10.86	11.07	8.69	10.42
Na_2O	2.35	2.70	2.75	2.76	2.81	3.34	3.05	2.94	2.89	2.79	2.57	3.15	3.09	3.41	3.35
K_2O	0.04	0.08	0.36	0.09	0.08	0.70	0.30	0.51	0.16	0.07	0.05	0.11	0.12	0.28	0.76
P_2O_5	0.08	0.14	0.14	0.14	0.10	0.30	0.18	0.16	0.11	0.11	0.08	0.14	0.15	0.11	0.25
Total	100.21	99.94	99.58	100.48	100.58	99.14	100.44	99.66	99.97	99.97	99.73	99.18	99.46	99.73	99.76
Mg#	68.5	63.1	65.5	62.0	64.2	63.2	61.2	65.1	64.0	65.0	66.0	55.8	55.9	64.4	56.2
Sc	39	49	33	43	43	37	44	37	43	45	45	48	48	23	38
Ni	156	86	123	113	142	122	85	113	97	94	133	66	73	132	43
Rb	0.47	1.02	6.16	1.52	1.03	14.2	4.57	8.32	2.10	0.81	0.53	1.44	1.23	4.72	13.7
Sr	96	101	183	97	99	238	146	195	119	111	103	105	109	199	263
Y	24	36	23	36	31	30	32	26	29	28	26	42	43	18	30
Zr	55	88	73	96	73	129	99	101	80	79	65	123	125	79	159
Nb	1.06	2.45	7.60	2.44	1.79	16.1	7.39	9.22	3.02	1.25	1.08	2.66	2.50	5.45	15.6
Ba	6.06	13.1	79	16.8	11.9	157	63	102	27	12.5	7.29	15.9	17.4	60	183
La	1.99	3.48	6.07	3.56	2.65	11.9	6.35	8.60	3.76	3.00	2.51	4.57	4.74	5.53	15.9
Ce	6.11	9.35	13.4	10.0	7.70	24	14.2	17.7	9.45	8.33	7.38	13.3	13.4	11.4	32
Nd	5.96	9.71	9.16	10.2	7.86	15.5	10.8	12.0	9.03	8.45	7.55	13.4	13.2	9.77	19.8
Sm	2.18	3.21	2.62	3.42	2.87	4.35	3.28	3.19	2.87	2.78	2.56	4.23	4.80	3.57	4.91
Eu	0.81	1.18	1.14	1.18	0.57	1.40	1.23	1.25	1.07	1.04	0.97	1.38	1.30	1.36	1.76
Gd	2.88	5.00	3.57	5.21	3.94	5.13	4.71	4.21	4.39	3.92	4.21	6.01	6.02	4.28	5.39
Dy	3.83	5.75	3.73	5.57	4.74	5.07	5.50	4.34	4.94	4.82	4.46	7.15	7.86	3.48	5.35
Er	2.30	3.40	2.28	3.34	3.06	2.98	3.05	2.44	2.93	2.78	2.82	4.30	4.50	1.63	2.73
Yb	2.42	3.37	2.17	3.65	3.27	2.88	3.06	2.41	2.75	3.04	2.88	4.15	4.39	1.58	2.67
Ta	0.11	0.17	0.54	0.19	0.11	1.01	0.32	0.63	0.19	0.07	< 0.06	0.16	0.16	0.32	1.03
Pb	< 0.18	< 0.18	0.42	0.71	< 0.18	1.35	0.79	1.01	0.53	< 0.18	< 0.18	< 0.18	< 0.18	0.56	1.68
Th	0.11	0.24	0.65	0.20	0.13	1.39	0.62	0.87	0.26	0.15	0.12	0.21	0.27	0.52	1.59
U	0.02	0.04	0.14	0.05	< 0.02	0.33	0.13	0.20	0.06	0.03	< 0.02	0.05	0.02	0.09	0.34

University of Cape Town

Table 4.6 (cont.)

Sample	3D-2	4D-3	7D-1	7D-2	9D-2	10D-2	11D-4	12D-2	13D-1	14D-5	18D-2	19D-1	19D-4	23D-1	22D-3
Lat. (°S)	47.80	47.97	48.76	48.76	49.15	49.25	49.44	49.76	49.99	50.27	51.05	51.06	51.06	52.16	52.46
Long. (°W)	10.15	10.08	10.07	10.07	9.91	8.14	7.97	8.03	7.88	7.06	6.20	6.16	6.16	5.34	4.57
MBSL	2549	2895	3218	3218	3892	3860	3868	3874	3555	3347	1991	1743	1743	2609	3059
SiO_2	51.34	51.24	51.23	51.89	51.99	51.47	50.39	51.92	51.02	51.68	50.87	49.58	50.63	50.84	51.37
TiO_2	1.77	1.57	1.53	2.52	1.75	1.46	1.45	1.25	1.13	1.66	1.22	1.58	1.42	2.35	2.68
Al_2O_3	14.32	15.26	16.40	13.15	15.00	15.50	15.34	14.85	15.41	13.99	14.58	15.75	15.14	13.55	13.35
FeO	9.80	9.03	7.88	12.47	9.71	9.60	10.18	9.43	8.63	10.98	9.30	11.58	9.52	12.64	13.58
MnO	0.14	0.14	0.14	0.15	0.14	0.15	0.15	0.15	0.16	0.14	0.14	0.16	0.19	0.15	0.16
MgO	7.53	7.60	6.79	5.51	7.34	7.79	8.03	8.42	8.76	7.55	8.45	7.19	7.97	6.09	4.83
CaO	10.48	11.07	10.52	9.24	10.08	11.07	11.49	12.13	12.58	11.36	12.56	9.90	12.55	9.99	9.17
Na_2O	3.08	2.70	3.15	3.25	3.20	3.04	2.82	2.58	2.43	2.67	2.53	3.17	2.71	3.03	3.18
K_2O	0.52	0.40	1.22	0.64	0.51	0.08	0.06	0.04	0.04	0.08	0.19	0.12	0.26	0.30	0.52
P_2O_5	0.22	0.21	0.27	0.29	0.28	0.12	0.12	0.09	0.08	0.12	0.10	0.12	0.15	0.27	0.36
Total	99.20	99.22	99.13	99.11	100.00	100.28	100.03	100.86	100.24	100.23	99.94	99.15	100.54	99.21	99.19
Mg#	60.9	63.0	63.6	47.2	60.5	62.1	61.5	64.4	67.3	58.2	64.8	55.7	62.9	49.4	41.9
Sc	38	40	30	43	36	41	45	44	43	48	44	34	46	47	46
Ni	86	78	70	38	101	92	113	107	111	77	68	112	71	47	33
Rb	8.86	6.32	19.0	12.5	9.21	0.72	0.49	0.44	0.29	1.02	2.89	1.38	3.65	4.35	9.47
Sr	172	151	347	129	165	100	104	91	88	86	144	161	144	111	117
Y	30	26	19	47	35	33	35	29	25	35	23	25	26	51	62
Zr	133	99	126	174	149	91	91	73	61	93	76	87	86	162	218
Nb	10.5	8.36	21	13.8	10.5	1.33	1.36	1.22	0.93	2.62	5.28	3.33	7.16	8.15	14.9
Ba	111	90	305	156	114	9.26	6.69	6.94	4.34	11.1	41	18.2	51	52	106
La	10.9	8.19	17.8	13.4	11.6	2.94	2.79	2.51	1.80	3.37	5.44	3.87	6.53	8.43	14.6
Ce	24	18.5	34	30	25	8.81	8.99	7.37	6.10	9.96	12.2	10.3	14.6	21	33
Nd	16.5	12.4	18.2	21	17.7	9.89	9.25	8.03	6.52	9.84	9.08	9.17	10.0	17.9	24
Sm	4.49	3.47	4.16	5.42	4.83	3.51	3.34	2.97	2.20	3.48	2.82	3.21	3.22	5.26	6.98
Eu	1.43	1.30	1.56	1.92	1.55	1.25	1.26	1.02	1.06	1.29	1.03	1.20	1.12	2.06	2.24
Gd	4.82	4.04	3.85	7.37	6.18	5.09	5.09	4.05	3.81	5.30	3.53	4.13	3.78	7.61	9.62
Dy	5.19	4.40	3.74	7.77	6.17	5.29	5.27	4.52	4.13	6.02	3.93	4.38	4.67	8.00	9.62
Er	3.09	2.57	1.76	4.39	3.69	3.41	3.56	2.80	2.31	3.65	2.21	2.58	2.51	4.91	5.98
Yb	2.95	2.56	1.73	4.60	3.38	3.55	3.23	2.74	2.50	3.80	2.26	2.11	2.52	5.09	5.82
Ta	0.62	0.51	1.27	0.87	0.65	0.12	0.13	0.10	< 0.06	0.17	0.35	0.22	0.39	0.56	0.93
Pb	1.09	0.63	1.69	1.25	1.10	0.40	0.43	0.26	0.49	0.60	0.26	0.40	0.40	0.92	1.46
Th	1.04	0.73	1.90	1.08	0.96	0.14	0.13	0.10	0.06	0.19	0.48	0.27	0.55	0.77	1.42
U	0.22	0.16	0.42	0.27	0.19	0.04	0.04	0.02	< 0.02	0.05	0.14	0.06	0.14	0.20	0.32

University of Cape Town

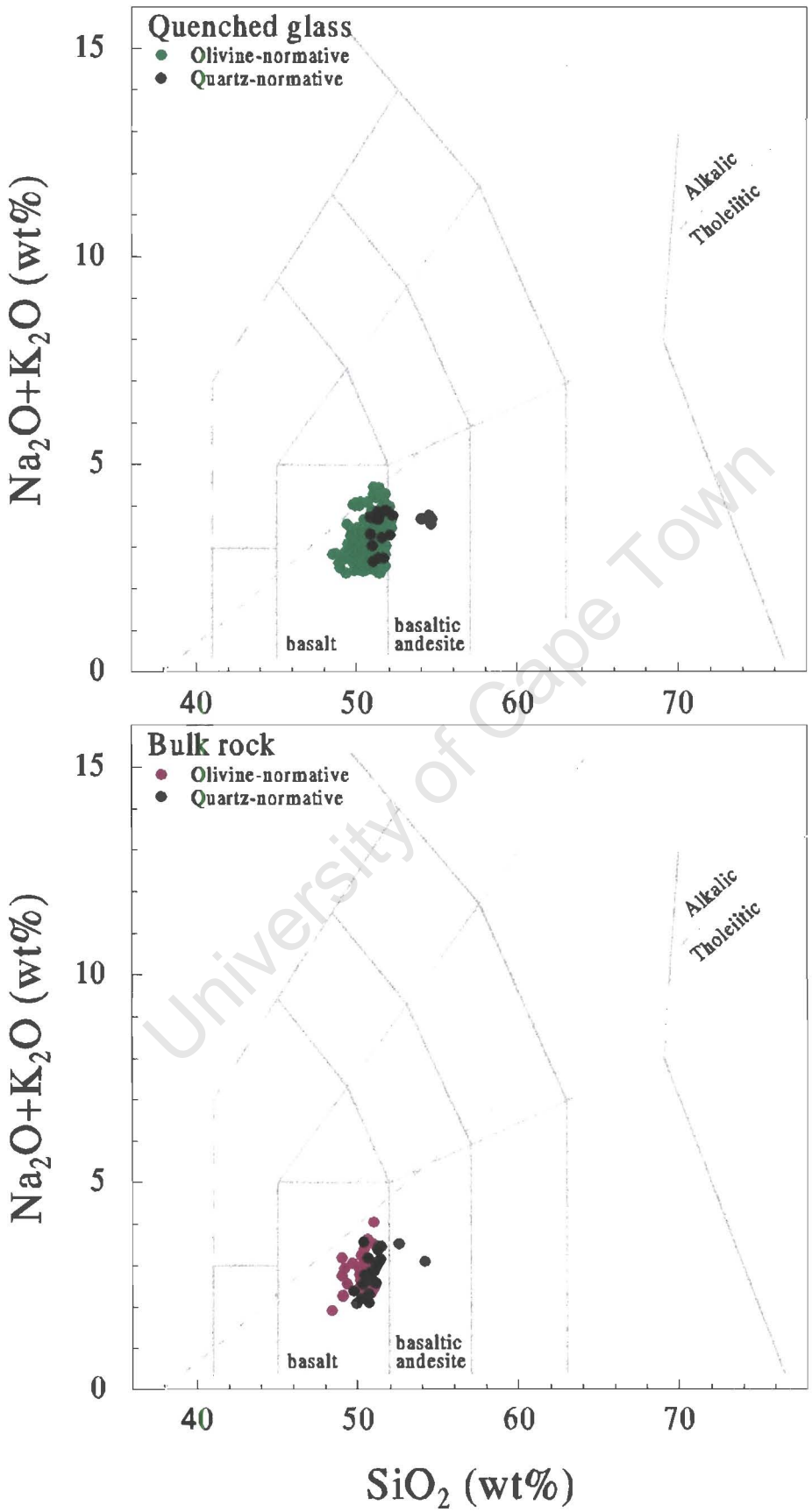

University of Cape Town

Figure 4.8: Total-alkali vs. silica (TAS) classification of southern Mid-Atlantic Ridge basalts (Le Maitre, 1989). Alkalic and tholeiitic subdivision after MacDonald and Katsura (1964).

incompatible-element enriched ends of the documented spectrum of MORB compositions (le Roex, 1987). The maximum values observed for Nb/Zr, Zr/Y, $(La/Sm)_N$ and K/Ti in compositions of quenched igneous glasses from northern, central and southern N-MORB of 0.03, 2.91, 0.79 and 0.14, are within the compositional range of "typical" N-MORB values of 0.03-0.05, 2.64-2.91, 0.61-1.00, and 0.1-0.3 (after le Roex, 1987; Michael *et al.*, 1989; Smith *et al.*, 1998; Sun & McDonough, 1989).

In contrast the values of these ratios in northern Discovery-influenced MORB varies from 0.02-0.13, 2.26-4.34, 0.60-1.98, and 0.07-0.62. Therefore, although some basalts recovered the northern Discovery-influenced ridge segments are compositionally similar to depleted MORB, see sample 34D-6 in table 4.6, the majority are definitely compositionally enriched in terms of incompatible trace elements and the values for these ratios are significantly higher than the ranges mentioned for "typical" N-MORB. A similar scenario is observed in the compositions of quenched igneous glass from southern Discovery-influenced MORB. The values for Nb/Zr, Zr/Y, $(La/Sm)_N$, and K/Ti in these samples range between 0.05-0.17, 2.25-6.88, 0.97-2.94, and 0.22-1.15. Again, a small number of samples recovered from the southern Discovery-influenced ridge segments are compositionally depleted MORB, but the vast majority have incompatible trace-element characteristics of highly-enriched, mantle plume-influenced E-MORB. The incompatible trace-element enrichment of the southern Discovery-influenced MORB is much stronger and pronounced in comparison with the compositions of northern Discovery-influenced MORB.

University of Cape Town

The values for Nb/Zr, Zr/Y, $(La/Sm)_N$, and K/Ti in Shona-influenced MORB vary within respective ranges of 0.03-0.09, 2.58-3.79, 0.62-1.53, and 0.07-0.29, again containing compositions similar to "typical" N-MORB to incompatible trace-element enriched MORB. Although the majority of these compositions are therefore E-MORB, the incompatible trace-element enrichments in these Shona-influenced MORB are not as high as in either of the groups of Discovery-influenced MORB.

Although the incompatible-element enrichment discussed above might, to some degree, be due to the highly evolved nature of some of the basalts, crystallization alone can not account for the observed scale of the enrichment. This is evident from the lack of correlation between trace-element ratios or absolute concentrations, and Mg# as indicator of evolution, highly

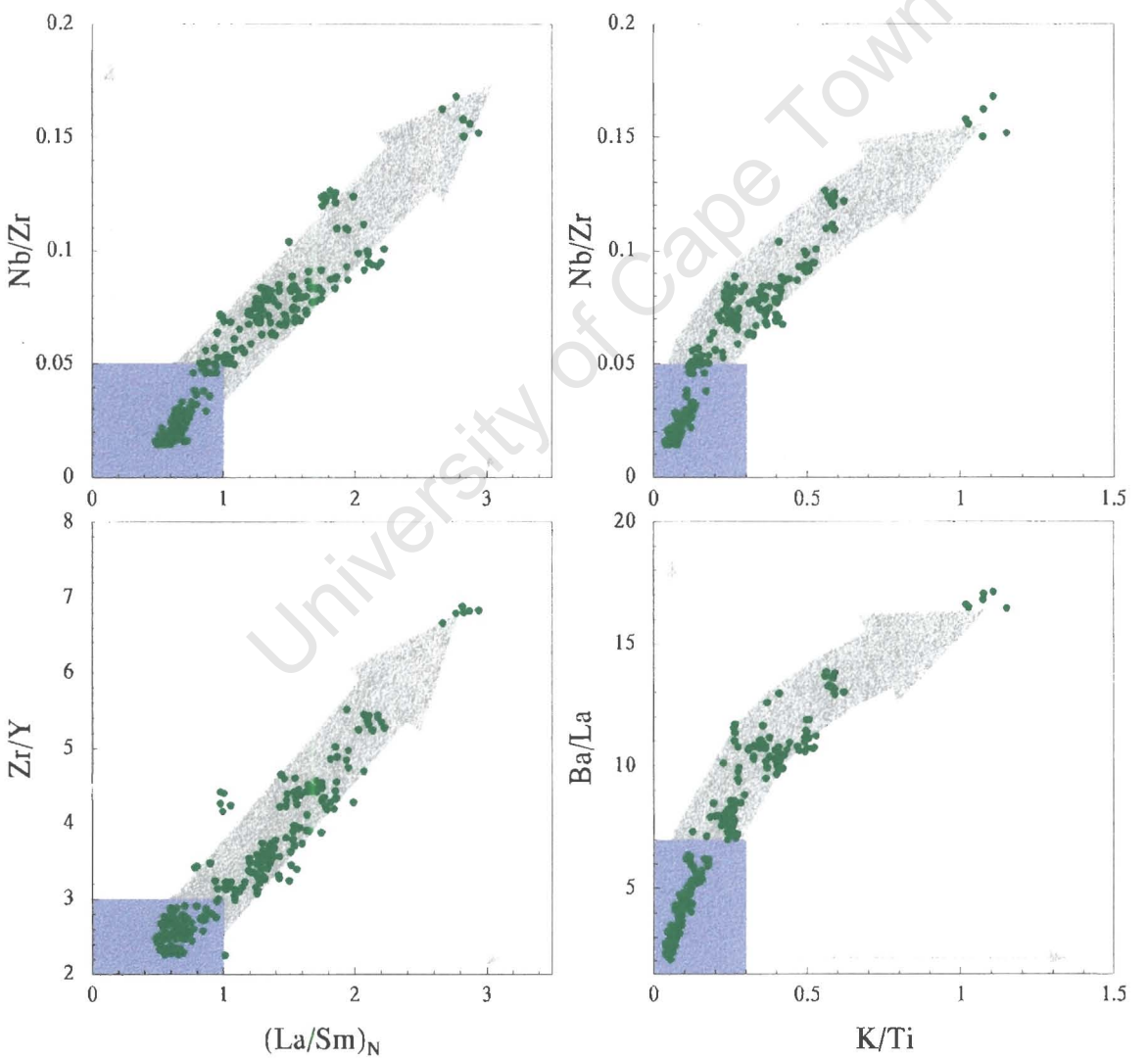

University of Cape Town

Figure 4.9a: Highly incompatible-element/moderately incompatible-element ratios (using the order of relative incompatibility and chondrite values from Sun & McDonough, 1989) vs. $(La/Sm)_N$ and K/Ti. Blue filled areas indicate depleted or N-MORB compositions; light grey arrows indicate increasing relative enrichment of incompatible elements towards enriched or E-MORB compositions (le Roex, 1987; Sun & McDonough, 1989.

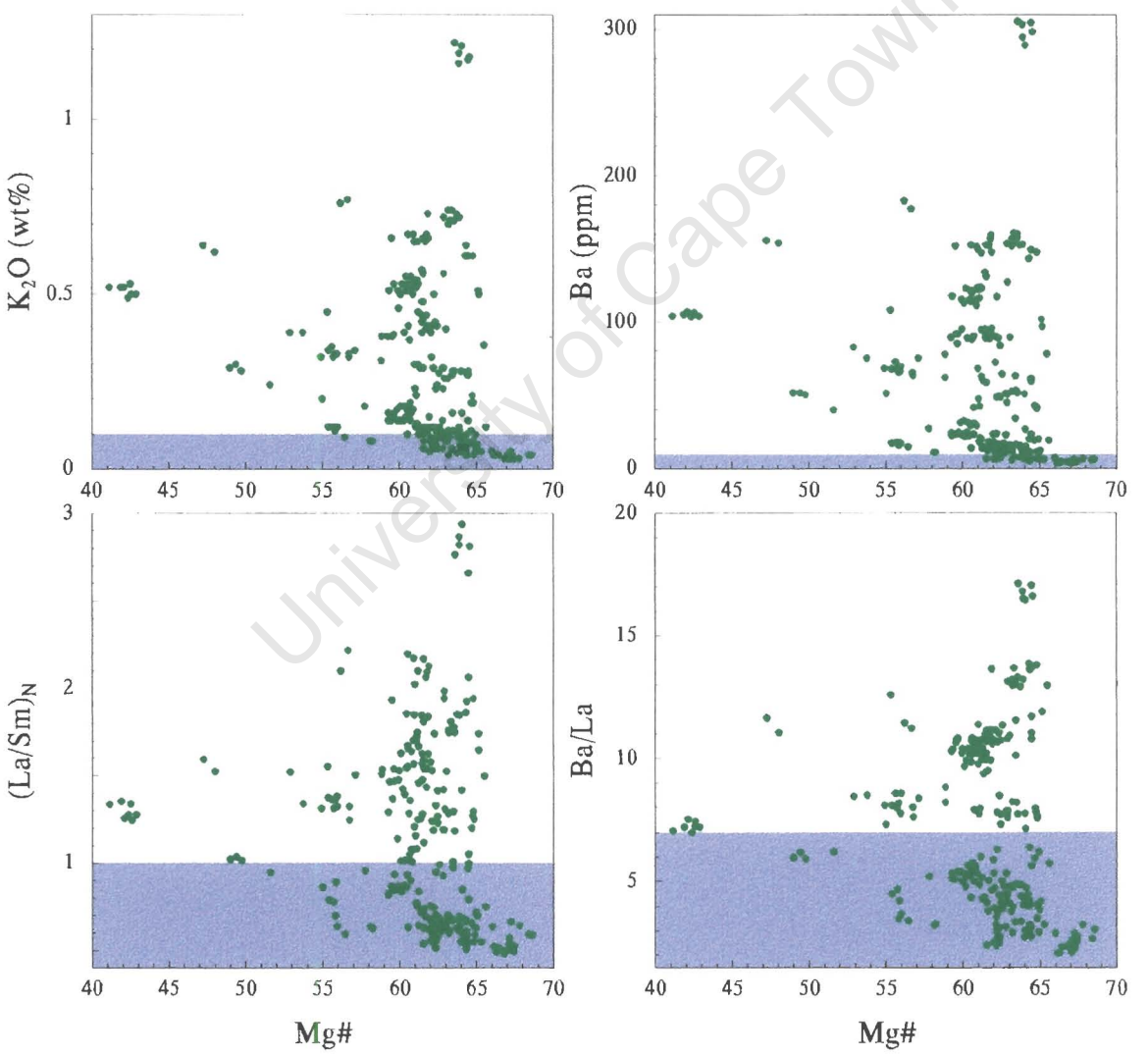

University of Cape Town

Figure 4.9b: Highly incompatible-element/moderately incompatible-element (using the order of relative incompatibility of Sun & McDonough, 1989) ratios vs. Mg# (Fe_2O_3/FeO=0.15). Blue filled areas indicate depleted or N-MORB compositions (le Roex, 1987; Sun & McDonough, 1989).

evolved basalts having low Mg#'s, in fig. 4.9b. The basalts with the strongest incompatible-element enriched characters occur amongst sample with high Mg#'s, see for example sample 7D-1, in table 4.6, with Mg# of 63.6 and Ba concentration of 305ppm.

Summary. The samples recovered from the SMAR in this study are therefore predominantly tholeiitic basalts, with a small number having basaltic andesite-affinities (dredge 25). The trace-element characteristics of these basalts range from incompatible trace-element depleted N-MORB to highly incompatible trace-element enriched E-MORB. This compositional continuum is evident in terms of ratios of highly incompatible/moderately incompatible trace elements, such as Nb/Zr 0.01-0.17, Zr/Y 2.25-6.88, $(La/Sm)_N$ 0.48-2.94, and K/Ti 0.04-1.15 , as well as absolute concentrations of incompatible trace elements, such as Ba 4.03-305ppm, and K_2O 0.03-1.22wt%. The incompatible trace-element enrichment in these basalts is not the result of crystallisation, as the highest levels of enrichment is observed in samples with high Mg#'s of 63-66.

4.4.2 Major-element variations

This section will deal with the variations observed in the major-element compositions of the quenched igneous-glass and bulk-rock compositions of the MORB recovered from the SMAR in this study. The complete data-set will first be discussed in general, focussing on specific major-element oxides or ratios. The general discussion will be followed by a more detailed discussion of the major-element variations observed in the compositions of northern, central and southern N-MORB, northern and southern Discovery-influenced MORB, and Shona-influenced MORB.

General observations. The MgO-content of the MORB recovered from the SMAR varies from comparatively high values of 9-9.6 wt% to low values of 4.6-5 wt%, correspondingly Mg#'s vary from 41.1-68.5. Variations in the concentrations of the other major elements can be observed on MgO-variation diagrams in fig. 4.10, and the observed trends are broadly consistent with crystallisation of olivine, plagioclase and calcic pyroxene (Langmuir *et al.*, 1992; Niu & Batiza, 1994; Stakes *et al.*, 1984). The characteristics of these trends are that as the MgO concentrations decrease in the quenched igneous glasses, concurrent increases are observed in the concentrations of TiO_2 from 0.92-2.86wt%, FeO^* from 7.68-14.16wt%, Na_2O from 2.35-3.52wt%, K_2O from 0.03-1.22wt% and P_2O_5 from 0.06-0.40wt%. However, decreases are

University of Cape Town

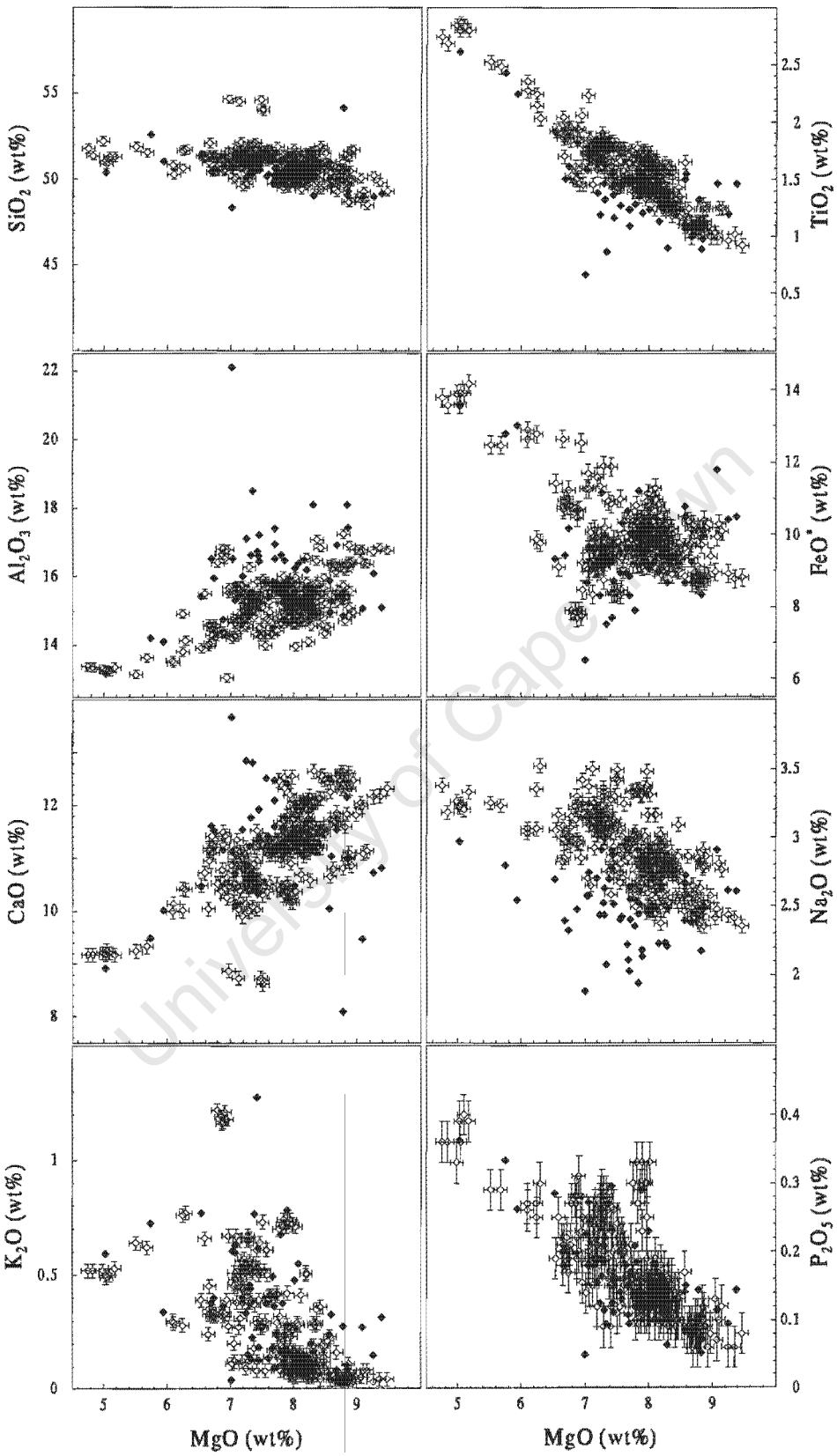

Figure 4.10: MgO-variation diagrams of all the quenched igneous glasses (open symbols, with 2σ error bars) and bulk-rock samples (filled symbols).

observed in the concentrations of CaO from 12.65-8.61wt% and Al_2O_3 from 17.25-13.05wt% as MgO concentrations decrease. The SiO_2 concentrations remain fairly constant, at 48.49-52.22wt%, with the exception samples from dredge 25, which are off-set to higher SiO_2 concentrations of 53-55wt% at MgO concentrations of 6.5-7.5wt%, with decreasing MgO concentrations.

N-MORB. The MgO-variation diagrams for compositions of quenched igneous glasses from N-MORB, in fig. 4.11a, indicate that the data are clustered towards the primitive, high-MgO, 7.02-9.47wt%, end of the field defined by the compositions of all the basalts recovered from the SMAR. This is especially evident for TiO_2 and K_2O, due to the previously discussed incompatible-element depleted nature of these basalts. The concentrations of SiO_2 are restricted to a range of 48.66-51.92wt%, while CaO and Al_2O_3 concentrations decrease from 12.64-10.58wt% and 17.25-14.19wt%, respectively, coincident with the decrease in MgO concentrations. Simultaneously, the concentrations of TiO_2, FeO*, Na_2O, K_2O and P_2O_5 increase from 0.92-1.84wt%, 8.61-11.32wt%, 2.35-3.15wt%, 0.03-0.15wt%, and 0.06-0.18wt%, respectively. These systematic variations with decreasing MgO concentrations are consistent with the effects of crystallisation as discussed earlier, but define only broad trends at best in fig. 4.11a. It should be noted that any "trends" observed on these diagrams should be viewed with caution. The dredge locations are all separated by significant geographical distances and sample different ridge segments.

The affects of crystallisation on the compositions of quenched igneous glasses from N-MORB are examined further using CaO/Al_2O_3 ratios plotted against Mg#'s in fig. 4.12. The calculated phenocryst-crystallisation vectors indicate the influence of individual phenocryst phases or combinations in terms of CaO/Al_2O_3 and Mg#. The data for N-MORB quenched igneous glasses in fig. 4.12 are inconclusive. The majority of data for quenched igneous glasses from N-MORB have CaO/Al_2O_3 values which vary between ~0.7-0.8, while Mg#'s vary between ~60-69. No broad trend is apparent in the CaO/Al_2O_3 and Mg# data for N-MORB, but data for samples from most individual dredges, which vary outside the 2σ errors, are orientated parallel to the plagioclase-crystallisation vector.

The MgO concentrations in the bulk-rock samples of N-MORB span a range of 7.01-8.84wt%, which is similar to that for quenched igneous glasses of 7.02-9.07wt%. This overlap

University of Cape Town

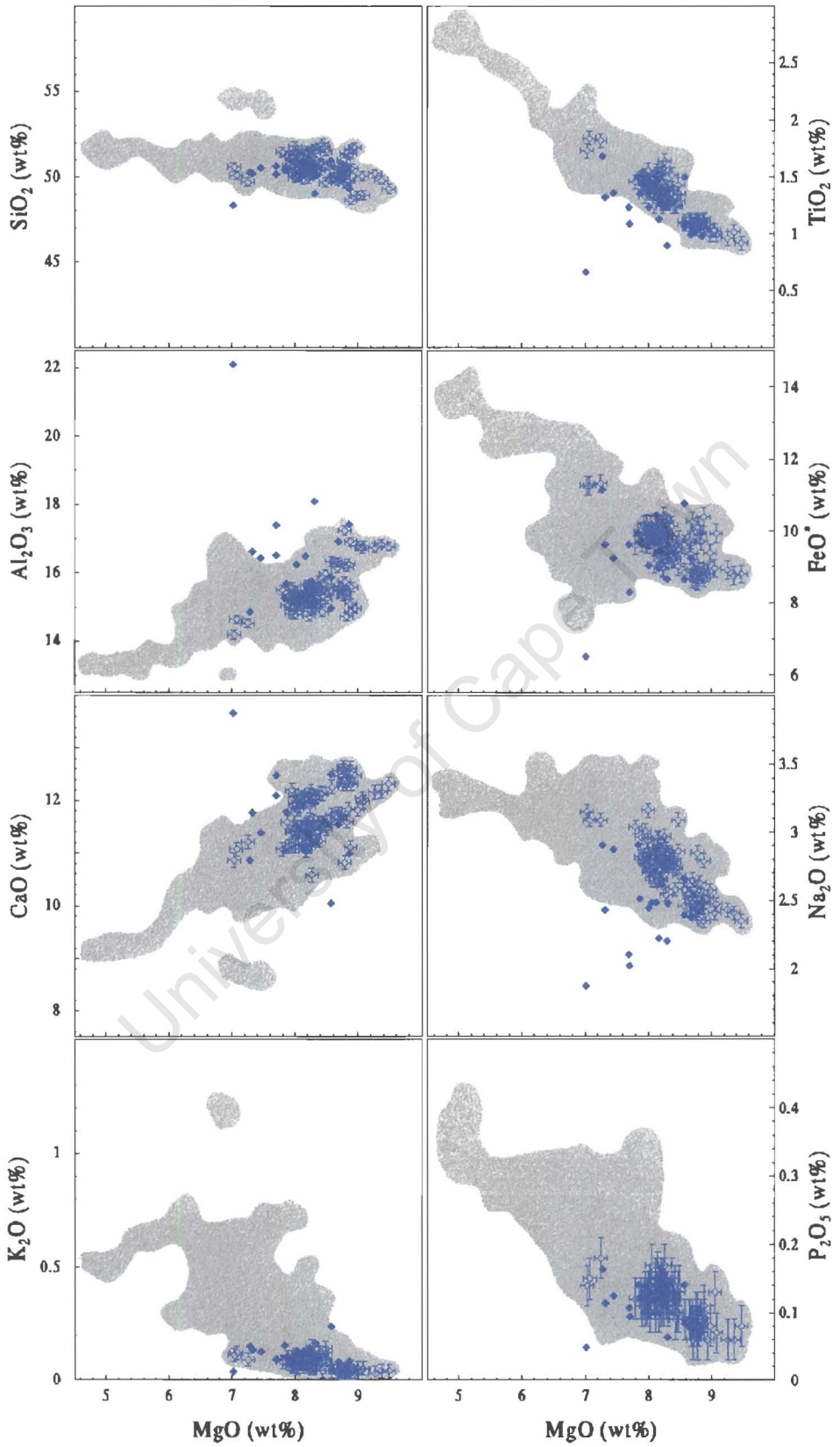

University of Cape Town

Figure 4.11a: MgO-variation diagrams for northern, central and southern N-MORB. Grey filled fields indicate spread of all data (see fig. 4.11); open symbols: quenched igneous glasses; filled symbols: bulk-rock samples; bars indicate 2σ errors.

in terms of MgO concentrations between bulk-rock samples and quenched igneous glasses of N-MORB are evident in fig. 4.11a. However, what is also clear from fig. 4.11a is that the bulk-rock major-element compositions of N-MORB have some significant differences with the data for the quenched igneous glasses. The concentrations of TiO_2, 0.66-1.69wt%, and Na_2O, 1.88-2.91wt%, and FeO* to a lesser degree, 5.74-9.49wt%, in the bulk-rock samples are off-set, at constant MgO concentrations, to lower values relative to the data for quenched igneous glasses, 0.92-1.84wt%, 2.35-3.16wt%, and 8.61-11.32wt%, respectively. The concentrations of Al_2O_3, 14.86-22.10wt%, and to a smaller extent for CaO, 10.05-13.66wt%, are off-set to higher values at constant MgO concentrations, relative to the data for quenched igneous glasses, 14.19-17.25wt% and 10.58-12.64wt%.

Discovery-influenced MORB. The major-element compositional data for Discovery-influenced MORB presented on MgO-variation diagrams, in fig. 4.11b, span a large range of the major-element variations observed in this study. Some of the obvious anomalous quenched igneous-glass compositions plotting separate from the fields for the complete data-set are from samples of the southern Discovery-influenced MORB. Basalts from dredges 25, see composition of sample 25D-1 and 7D-1 in table 4.6, account for high concentrations of SiO_2, ~54-55wt% and low concentrations of CaO, ~8.6-8.8wt%, while basalts from dredge 7 account for high concentrations of K_2O, ~1.1-1.2wt%. Remaining Discovery-influenced MORB define relatively coherent trends of increasing concentrations of SiO_2, 48.49-51.50wt%, and TiO_2, 0.99-2.52wt%, with decreasing MgO concentrations, 9.15-5.51wt%. Concentrations of Na_2O, 2.58-3.52wt%, K_2O, 0.06-0.74wt%, and P_2O_3, 0.08-0.33wt%, in quenched igneous glasses from Discovery-influenced MORB define more diffuse increasing trends with concurrent decreasing MgO concentrations, in fig. 4.11b. FeO* concentrations in quenched igneous-glass compositions of Discovery-influenced MORB do not define any clear trends and vary between ~7-11wt%, with a few samples with high FeO* concentrations, ~12.5wt%, at the lowest MgO concentrations.

The quenched igneous-glass compositions of basalts from the southern Discovery-influenced MORB define the lower MgO end of the data presented in fig. 4.11b. The MgO concentrations in southern Discovery-influenced MORB decline from 8.67wt% to 5.51wt%, while in northern Discovery-influenced MORB MgO concentrations decline from 9.15-7.41wt%. The Mg#'s mirror this division, with quenched igneous-glass compositions of southern Discovery-influenced MORB having Mg#'s of 64.8-47.2, in contrast to the 65.5-59.9 Mg#'s in

University of Cape Town

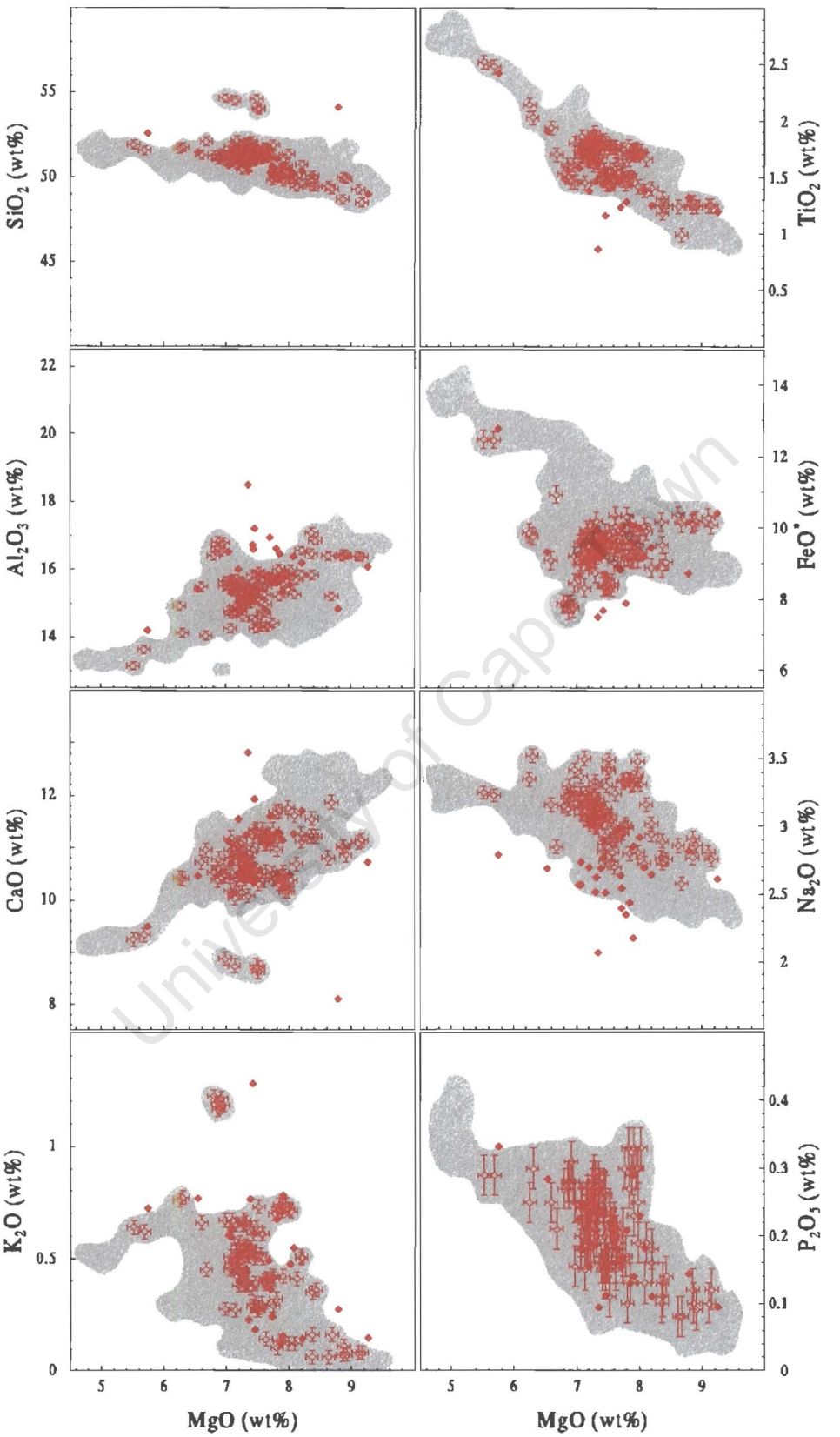

University of Cape Town

Figure 4.11b: MgO-variation diagrams for northern and southern Discovery-influenced MORB. Grey filled fields indicate spread of all data (see fig. 4.10); open symbols: quenched igneous glasses; filled symbols: bulk-rock samples; bars indicate 2σ errors.

quenched igneous glasses of northern Discovery-influenced MORB. The ranges in major-element compositions in Discovery-influenced MORB in general, discussed above, are therefore composed of two distinct geographically defined groups, when excluding the anomalous samples from dredges 25 & 7. The high-concentration ends of the SiO_2, 49.27-52.14wt%, and TiO_2, 0.99-2.52wt%, increasing trends with decreasing MgO concentrations are composed of southern Discovery-influenced MORB samples. There is more overlap between these two groups in the more diffuse increasing trends with decreasing MgO concentrations defined by the concentrations of Na_2O, K_2O, and P_2O_5. Nevertheless, quenched igneous-glass compositions of southern Discovery-influenced MORB still dominate the high-concentration ends for Na_2O, $\leq$3.52wt%, K_2O, $\leq$0.76wt%, and P_2O_5, $\leq$0.30wt%. The low-concentration ends of the decreasing Al_2O_3, $\geq$13.15wt%, and CaO, $\geq$9.24wt%, trends with decreasing MgO concentrations are defined by southern Discovery-influenced MORB, while concentrations of Al_2O_3 and CaO do not decline below 14.97wt% and 10.16wt%, respectively, in northern Discovery-influenced MORB.

The CaO/Al_2O_3 and Mg# data for quenched igneous glasses from Discovery-influenced MORB in fig. 4.12 vary mostly between Mg#'s of ~58-66 and CaO/Al_2O_3 values of ~0.6-0.8. Data for basalts from individual do not vary substantially outside of the 2σ errors, but when slight trends are defined by samples from dredges these are aligned between the olivine and plagioclase crystallisation vectors.

The major-element data of bulk-rock samples of Discovery-influenced MORB presented in fig. 4.11b overlap with the data for quenched igneous glasses in terms of MgO concentrations, 5.74-9.25wt% and 5.51-9.15wt% respectively. The bulk-rock compositions of samples 7D-1 &7D-3, see table 4.5, define the high Al_2O_3, 18.51wt%, CaO, 12.81wt%, and K_2O, 1.27wt%, data points in fig. 4.11b, while the bulk-rock composition of sample 25D-1, see table 4.5, defines the high SiO_2, 54.15wt%, and low CaO, 8.10wt%, data point. The bulk-rock major-element data for the remaining samples mostly overlap with the data for quenched igneous glasses, but slight off-sets are present to lower values for TiO_2 and FeO* and to higher values for Al_2O_3 and CaO relative to data for quenched igneous glasses, at constant MgO concentrations. The concentrations for Na_2O in the bulk-rock samples of Discovery-influenced MORB define an increasing trend with decreasing MgO concentrations off-set to lower Na_2O values relative to data for quenched igneous glasses, at constant MgO concentrations.

University of Cape Town

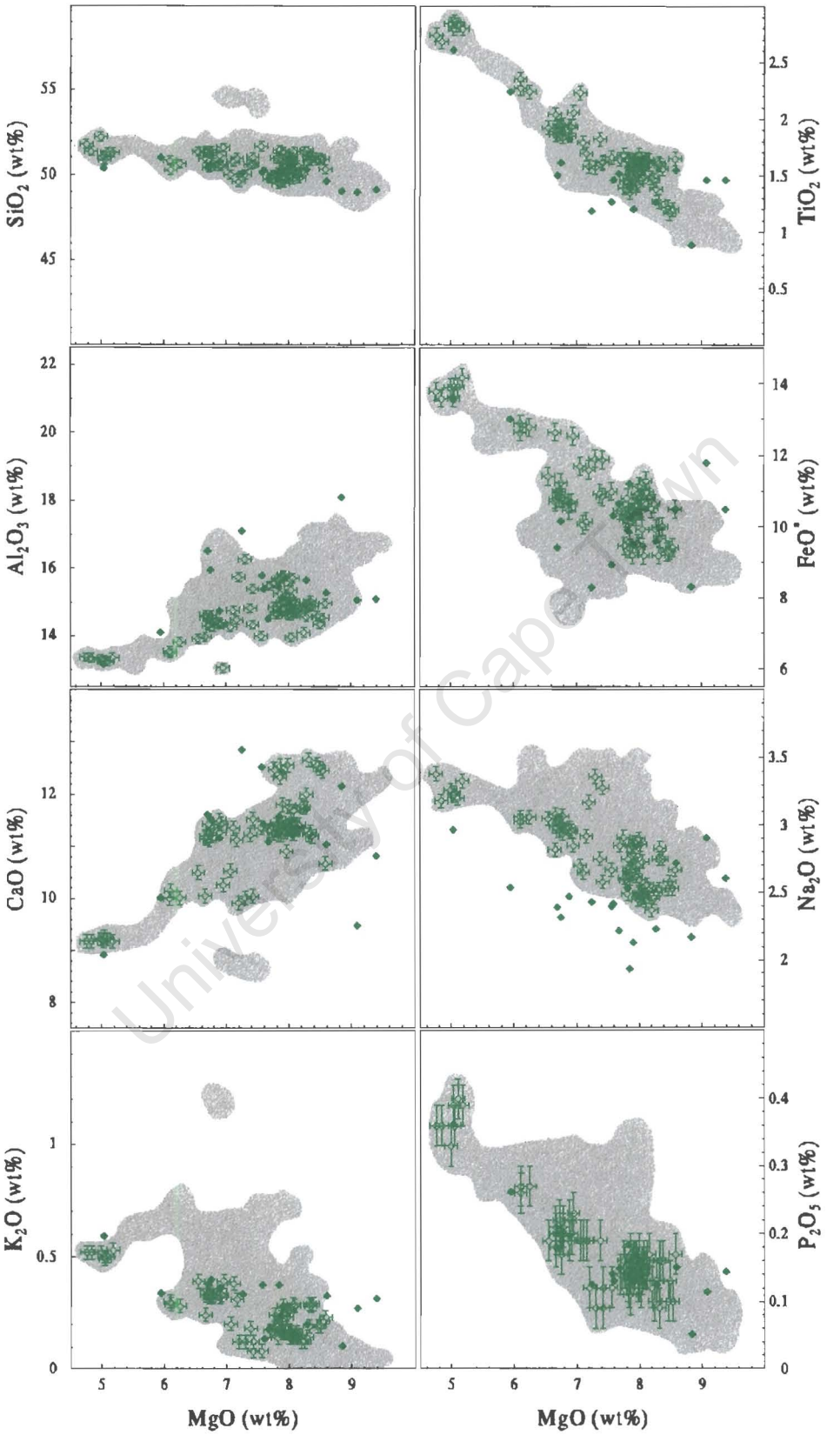

University of Cape Town

Figure 4.11c: MgO-variation diagrams for Shona-influenced MORB. Grey filled fields indicate spread of all data (see fig. 4.10); open symbols: quenched igneous glasses; filled symbols: bulk-rock samples; bars indicate 2σ errors.

Shona-influenced MORB. The major-element compositional data presented in fig. 4.11c for the quenched igneous glasses of Shona-influenced MORB also span most of the observed range of major-element variations for all quenched igneous glasses from MORB recovered from the SMAR. The MgO concentrations in the quenched igneous glass for Shona-influenced MORB decrease from 8.57-4.75wt% and define the lower-end of the total observed range, in contrast to MgO concentrations in quenched igneous glass from Discovery-influenced MORB which decrease from 9.15-5.51wt%. The two sets of mantle plume-influenced MORB therefore span overlapping ranges in MgO content, but the Shona-influenced MORB are more highly evolved. This is also evident in the Mg#'s of the quenched igneous glass of Shona-influenced MORB which decrease from 64.8-41.1, in contrast to the decrease of 65.5-47.20 for Mg#'s in quenched igneous glass for Discovery-influenced MORB.

The other major-element data for quenched igneous glass from Shona-influenced MORB define more coherent trends on the MgO-variation diagrams in fig. 4.11c. Trends of increasing concentrations concurrent with decreasing MgO concentrations are observed for SiO_2, 49.45-52.22wt%, TiO_2, 1.17-2.86wt%, FeO*, 9.19-14.16wt%, Na_2O, 2.37-3.38wt%, K_2O, 0.08-0.53wt%, and P_2O_3, 0.09-0.40wt%. The concentration-ranges for Na_2O and K_2O in these quenched igneous glass for Shona-influenced MORB are clearly off-set to lower values, at constant MgO concentrations, compared to the data for quenched igneous glasses for Discovery-influenced MORB. The two sets of mantle plume-influenced MORB therefore define distinctly different trends for Na_2O and K_2O. The increasing trend for FeO* against decreasing MgO in quenched igneous glasses of Shona-influenced MORB also contrast with the data for Discovery-influenced MORB, which do not define any significant trend for FeO* versus MgO in fig. 4.11b. Trends of decreasing concentrations with decreasing MgO concentrations are observed for Al_2O_3, 16.27-13.05wt%, and CaO, 12.65-9.17wt%, in the compositional data for quenched igneous glasses from Shona-influenced MORB.

The CaO/Al_2O_3 and Mg# data for quenched igneous glasses from the Shona-influenced MORB in fig, 4.12 vary over a substantial range of CaO/Al_2O_3 values, ~0.55-0.9, and Mg#'s, ~40-66. These data define a broad trend of decreasing CaO/Al_2O_3 values with concurrent decreasing Mg# values, thus generally consistent with the presence of clinopyroxene in the fractionating solid assemblage. However, data for basalts from individual dredges are still orientated between the olivine and plagioclase crystallisation vectors.

University of Cape Town

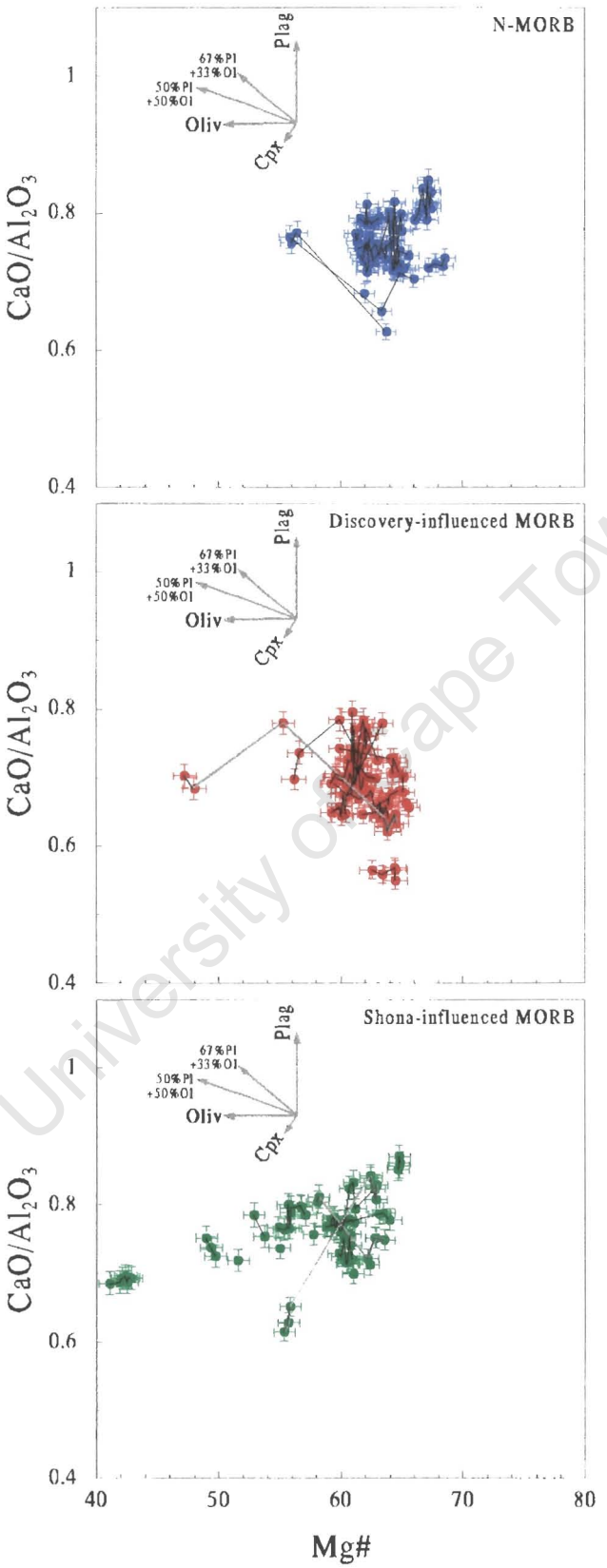

University of Cape Town

Figure 4.12: CaO/Al_2O_3 versus Mg# (Fe_2O_3/FeO=0.15) diagrams for quenched igneous glasses with black lines linking all samples from single dredges and grey lines linking samples from single dredges which are definitely not genetically related (see text), and bars indicate 2σ errors. Calculation of phenocryst-crystallisation vectors inverse of the calculation for phenocryst accumulation described in the caption to fig. 4.14a.

The major-element data for the limited number of bulk-rock samples of Shona-influenced MORB, presented in fig. 4.11c, are quite scattered. These data extend from high MgO concentrations of 9.39wt%, compared to 8.57wt% for quenched igneous glasses, to MgO concentrations of 5.02wt%, which are similar to the 4.75wt% for the quenched igneous glasses. Data for most bulk-rock samples overlap significantly with data for quenched igneous glasses, but are generally more scattered around the trends defined by the quenched igneous-glass data. The Na_2O concentrations in bulk-rock samples of Shona-influenced MORB are systematically off-set to lower values, at constant MgO concentrations, relative to the data for quenched igneous glasses.

Summary. The variations of major-element oxides versus MgO concentrations in fig. 4.11a-c are broadly consistent with the effects of crystallisation on the evolving magma. As MgO concentrations decrease, the concentrations of SiO_2 remain fairly constant or increase slightly. The concentrations of TiO_2, FeO*, Na_2O, K_2O, and P_2O_5 in quenched igneous glasses of MORB from the SMAR define trends of progressively increasing values with decreasing MgO concentrations, while Al_2O_3 and CaO concentrations define trends of progressively lower values.

The major-element data for quenched igneous glasses from N-MORB are clustered at the high-MgO end of the complete range of compositions observed. Compositional variations are limited in the major-element data for the quenched igneous glasses of N-MORB, although these data define short trends of especially increasing TiO_2 and Na_2O and decreasing Al_2O_3 and CaO with decreasing MgO. The major-element data for bulk-rock samples of N-MORB are more varied and extend to especially high values in Al_2O_3 and CaO concentrations, and low values in TiO_2, FeO* and Na_2O.

The quenched igneous glasses from Discovery-influenced MORB have major-element compositions which span almost the complete range of MgO concentrations observed, just excluding the lowest MgO concentrations. Some significant outliers are observed towards higher values for SiO_2 and K_2O, and towards lower values for CaO. These anomalous compositions are restricted to samples from dredges 25 & 7. Otherwise, the general major-element compositions of quenched igneous glasses of Discovery-influenced MORB define trends of increasing SiO_2, TiO_2, Na_2O, K_2O and P_2O_5 with decreasing MgO, and decreasing Al_2O_3 and CaO. The data for

University of Cape Town

FeO* are more scattered and do not define any significant trend with decreasing MgO concentrations. Quenched igneous glasses from northern Discovery-influenced MORB are concentrated in the high-MgO end of the spectrum of all Discovery-influenced MORB, while southern Discovery-influenced MORB define the low-MgO end of this continuum of quenched igneous glass compositions. The bulk-rock major-element compositions of samples from dredges 25 & 7 again define the most-extreme outliers relative to the quenched igneous-glass compositions, while the remaining bulk-rock compositions of Discovery-influenced MORB do not plot significantly removed from the quenched igneous-glass data. An exception to this is the Na_2O concentrations in the bulk-rock samples which define a trend of increasing concentrations with decreasing MgO, off-set, to lower values at constant MgO values, from a similar trend in the quenched igneous-glass data.

The major-element compositions of quenched igneous glasses from Shona-influenced MORB also almost span the complete range of observed MgO concentrations, but exclude the high-MgO end of this spectrum. The compositions of quenched igneous glasses define trends of increasing SiO_2, TiO_2, FeO*, Na_2O, K_2O and P_2O_5 with decreasing MgO, and decreasing Al_2O_3 and CaO. The Na_2O and K_2O concentrations define trends at slightly shallower angles relative to the data for quenched igneous glasses from Discovery-influenced MORB. The major-element compositions of bulk-rock samples of Shona-influenced MORB have some samples with MgO concentrations higher than that from the quenched igneous-glass compositions. Otherwise the major-element compositions of the bulk-rock samples overlap in general with the data for quenched igneous glass. An exception, again, are the concentrations of Na_2O in the bulk-rock samples which define a similar trend of increasing concentrations with decreasing MgO values as observed in the quenched igneous-glass data, but off-set to lower values at constant MgO concentrations from the quenched igneous-glass trend.

The variations of the CaO/Al_2O_3 and Mg# data for quenched igneous glasses from samples of N-MORB, Discovery-influenced MORB and Shona-influenced MORB from individual dredges are variably orientated between the trends defined by the compositional affects of olivine and plagioclase crystallisation. The data for quenched igneous glasses from Shona-influenced MORB define a broad trend consistent with the presence of clinopyroxene in the fractionating solid assemblage at some earlier stage of magma evolution.

University of Cape Town

4.4.3 Trace-element variations

The trace-element compositions of the quenched igneous glasses of MORB recovered from the SMAR have received some attention during the discussion of the compositional classification of these basalts in section 4.4.1. Therefore, having established the presence of incompatible trace-element depleted and enriched compositions amongst MORB recovered from the SMAR, the first issue addressed in this section will be the geographical systematics of these incompatible trace-element compositional variations. Secondly, the origin of the incompatible trace-element enriched MORB will be investigated further, especially in terms of the extent of the compositional influences of the proximal mantle plumes.

It has been well established along much of the length of the Mid-Atlantic Ridge, that regional variations in ratios of highly to moderately incompatible trace-elements coincide with major anomalous elevation of ridge segments. These bathymetric anomalies occur at similar latitudes as on-ridge or near-ridge ocean-islands, which have been accepted as surface expressions of mantle plumes, composed of incompatible trace-element enriched and isotopically distinct mantle material upwelling from great depth, for a considerable time, e.g. Gough/Tristan da Cunha (Fontignie & Schilling, 1996; Hanan *et al.*, 1986; Humphris *et al.*, 1985), the Azores (White & Bryan, 1977; White & Schilling, 1978), Iceland (Schilling *et al.*, 1983, and references therein) and Ascension and St. Helena islands (Fontignie & Schilling, 1996; Hanan *et al.*, 1986).

University of Cape Town

The concept of mantle plume-influenced, incompatible trace-element enriched MORB assumes that the fundamental incompatible-element enrichment is due to mixing between end-member mantle sources, i.e. the ambient incompatible trace-element depleted MORB mantle, and an incompatible trace-element enriched mantle plume source. If this assumption holds true, then the incompatible trace-element data for the MORB recovered from the SMAR in this study must define mixing curves on ratio-ratio plots. These curves can be linear or hyperbolic on ratio-ratio plots, depending on the relative incompatibility of the two elements chosen as numerator and denominator (Langmuir *et al.*, 1978). This model of mantle plume-mid-ocean ridge compositional interaction will be evaluated in the second part of this section, with the enriched mantle plume source, along this section of the SMAR, being either the Discovery or Shona mantle plumes.

Latitudinal variations. The geographical distribution of N-MORB and incompatible

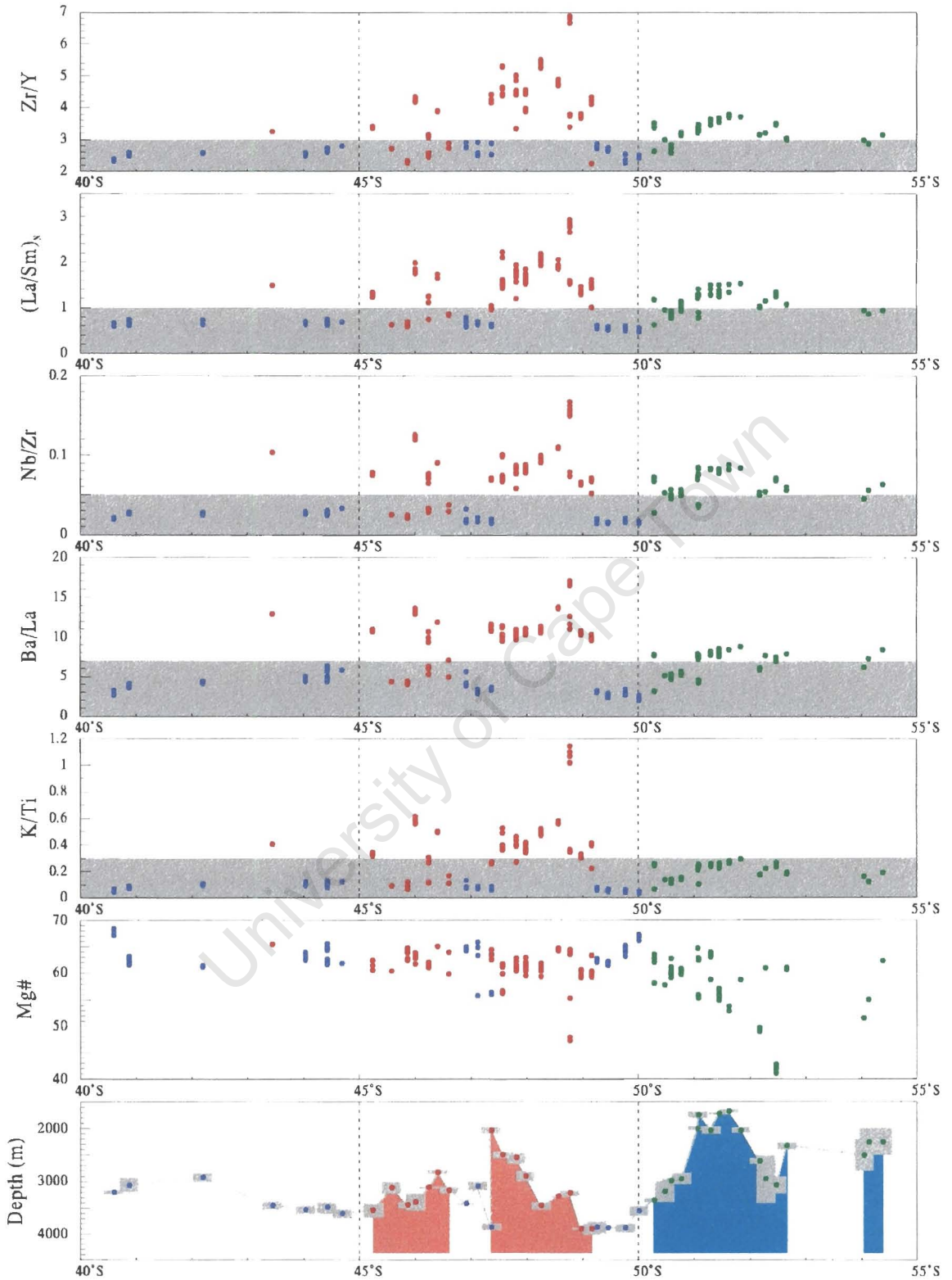

University of Cape Town

Figure 4.13: Highly/moderately (after Sun & McDonough, 1989) incompatible trace-element ratios, Mg# of quenched igneous glasses (Fe_2O_3/FeO=0.15), and depth of ridge segments sampled in metres below sea-level vs latitude. Blue symbols: northern, central, and southern N-MORB; red symbols: northern and southern Discovery-influenced MORB; green markers: Shona-influenced MORB; light grey filled area: N-MORB compositional space (le Roex, 1987; Sun & McDonough, 1989); grey line: average bathymetry of ridge; grey bars: depth range sampled by relevant dredge.

trace-element enriched MORB, along the section of the SMAR studied, is delineated in fig. 4.13 by plotting the characteristic incompatible trace-element ratios, used during the classification of these basalts, versus the latitudinal location of the dredge stations. The dredges which yielded incompatible trace-element enriched MORB are clearly defined by high values for ratios of highly to moderately incompatible trace-elements in fig. 4.13, with values for Zr/Y >3, $(La/Sm)_N$ >1, Nb/Zr >0.05, Ba/La >7 and K/Ti >0.3 (after le Roex, 1987; Michael *et al.*, 1989; Smith *et al.*, 1998; Sun & McDonough, 1989). The latitudinal extent of the occurrence of incompatible trace-element enriched basalts correlate with elevated and varied bathymetry of ridge segments, which in turn have been linked to the proximal mantle plumes (Douglass *et al.*, 1999; Douglass *et al.*, 1995; Small, 1995). The radiogenic isotope data for the same samples have been used to delineate the latitudinal influence of the proximal mantle plumes on the compositions of the erupted MORB, and these data mirror the correlation observed between the most incompatible trace-element enriched MORB and the anomalously elevated ridge segments (Douglass *et al.*, 1999).

The data presented in fig. 4.13 indicate consistency of the incompatible trace-element depletion of the northern, central and southern N-MORB. With the exception of the central N-MORB, the remaining N-MORB were all recovered from ridge segments with fairly deep and constant bathymetry. Significant and rapid compositional changes occur across the large off-set Falkland-Agulhas Fracture Zone (at ~47.5°S), between central N-MORB and southern Discovery-influenced MORB, and the lesser off-set transform (at ~49.2°S) between southern Discovery-influenced MORB and southern N-MORB. These structural features seem to act as, or define, compositional barriers in the mantle beneath the SMAR.

The northern Discovery-influenced MORB are composed of incompatible trace-element enriched basalts, as well as some incompatible trace-element depleted basalts. At one particular case, dredge 32, both groups of compositionally distinct basalts were recovered at a single location. The incompatible trace-element enrichment in northern Discovery-influenced MORB extent to values of ≤0.13 for Nb/Zr, ≤4.34 for Zr/Y, ≤13.7 for Ba/La, ≤1.98 for $(La/Sm)_N$, and ≤0.62 for K/Ti. In contrast, the southern Discovery-influenced MORB are composed entirely of incompatible trace-element enriched basalts, the degree of enrichment is significantly higher compared to northern Discovery-influenced MORB. The extent of the incompatible trace-element enrichment in these southern Discovery-influenced MORB is indicated by the high

University of Cape Town

values of ≤0.17 for Nb/Zr, ≤6.88 for Zr/Y, ≤17.1 for Ba/La, ≤2.94 for $(La/Sm)_N$, and ≤1.15 for K/Ti observed.

The incompatible trace-element characteristics of the Shona-influenced MORB in fig. 4.13 range from mostly enriched for some ratios, e.g. ≤0.09 for Nb/Zr, ≤3.79 for Zr/Y, and ≤1.53 for $(La/Sm)_N$, while for other ratios the compositions are distinctly more depleted in nature, e.g. ≤8.82 for Ba/La, and ≤0.29 for K/Ti. The incompatible trace-element enrichment in Shona-influenced MORB also do not nearly reach the high levels observed in Discovery-influenced MORB. Although some Shona-influenced MORB are the most-evolved basalts recovered in this study, with Mg#'s of ≥41.1, these basalts are still not the most-enriched in incompatible trace elements, thus further indicating the secondary role magma evolution has in the origin of the incompatible trace-element enrichment observed in MORB from the SMAR.

The high degree of variability in MORB erupted along the Discovery-influenced ridge segments could indicate the sparsity of significantly long-lived magma chambers, which could serve to homogenise magma compositions. The Shona-influenced ridge segments are significantly more elevated relative to the Discovery-influenced ridge segments. This could be due to higher heat-flow beneath the Shona-influenced ridge segments, relative to Discovery-influenced ridge segments, resulting in higher degrees of melting to form the thicker, shallower crust, therefore more dilution of the incompatible-element enrichment, due to the plume, by higher degrees of melting of the ambient depleted mantle, longer-lived magma chambers beneath the ridge segments result in eruption of more evolved basalts with more homogeneous compositions. This possible higher heat-flow beneath the Shona-influenced ridge segments relative to the Discovery-influenced ridge segments, could be due to the postulated proximal or ridge-centred present-day location of the Shona hotspot, while the Discovery hotspot is more distal, ~425km, from the ridge segments experiencing its influence (Douglass *et al.*, 1999; Douglass *et al.*, 1995; Small, 1995).

Mantle plume-influence. The incompatible trace-element data for MORB recovered from the SMAR define hyperbolic correlations in fig. 4.14, where the ratio on the *y*-axis is defined as moderately incompatible element/highly incompatible element and plotted against La/Sm or K/Ti on the *x*-axis. To eliminate the possibility that these hyperbolic trends are pure coincidence, the selected "companion plots" (Langmuir *et al.*, 1978) are also given in fig. 4.14.

University of Cape Town

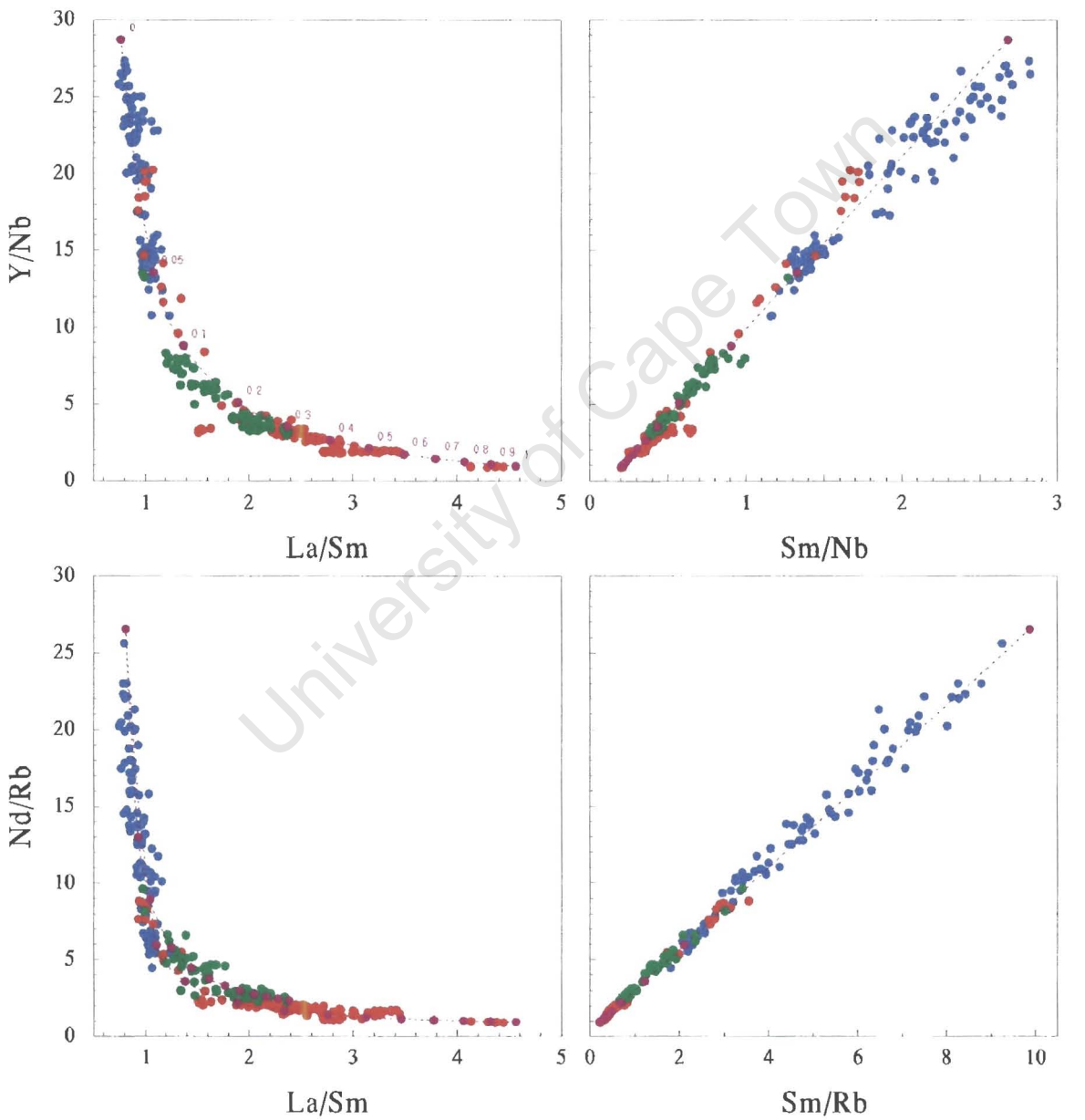

University of Cape Town

Figure 4.14: Moderately/highly (after Sun & McDonough, 1989) incompatible trace-element ratios vs. La/Sm and K/Ti; and "companion plots" (See text for discussion). Mixing trajectories calculated with samples 13D-8,10,14 as depleted end-members; 7D-5 (Discovery) and 21D-1 (Shona) as enriched end-members; and the equations of Langmuir *et al.* (1978). Labels on trajectories indicate fraction of enriched end-member in relevant mixture. Blue markers: N-MORB; red markers: Discovery-influenced MORB; green markers: Shona-influenced MORB.

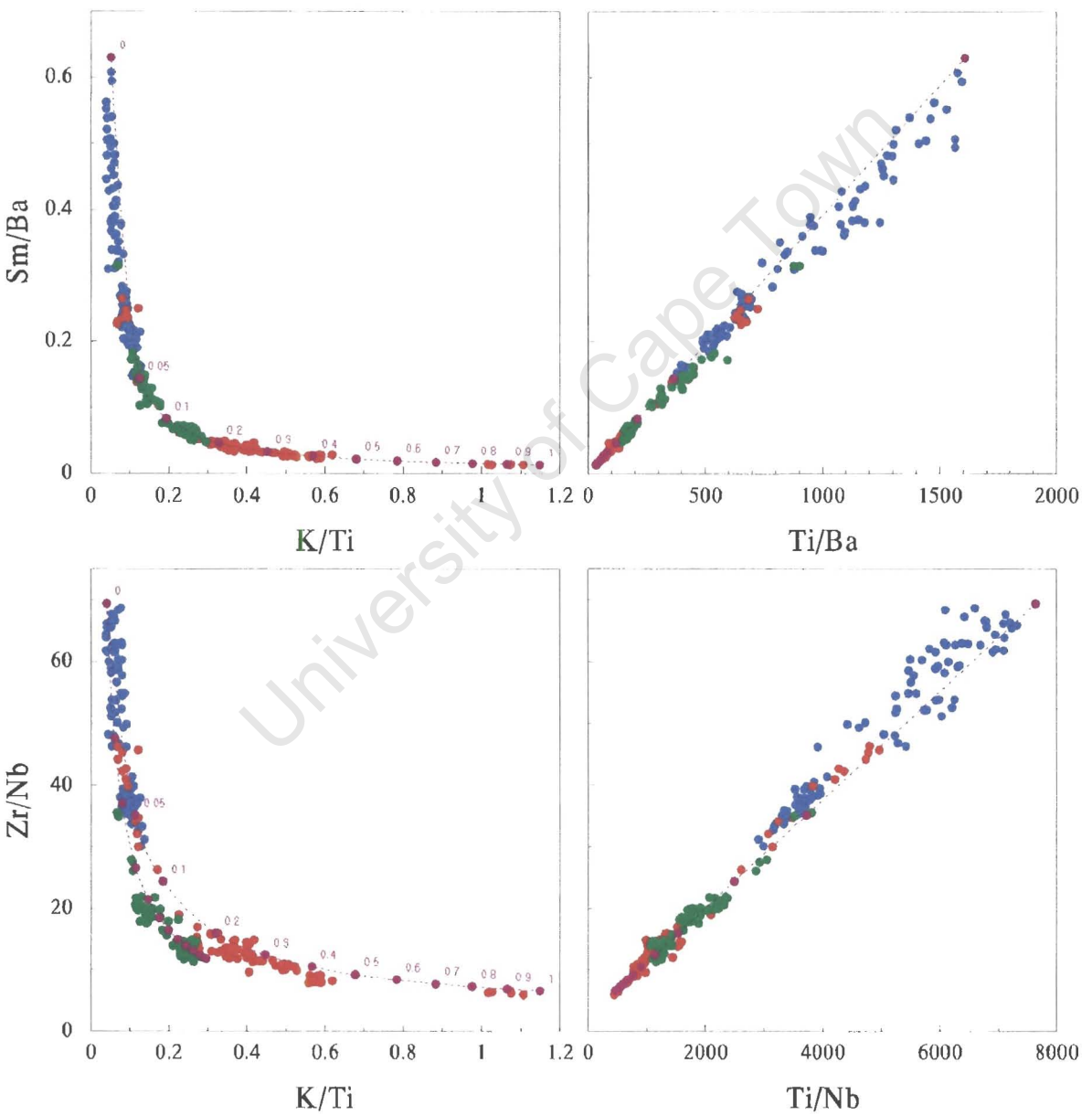

University of Cape Town

Figure 4.14 (continued).

These plots use one of the original ratios versus the ratio of the denominators of the two original ratios. When two incompatible elements are normalized to a third, binary mixing results in linear correlations. If the hyperbolic correlations on the initial plots are due to mixing, then linear trends should occur on these "companion plots" (Langmuir *et al.*, 1978). The "companion plots" in fig. 4.14 exhibit linear trends, confirming the validity of the original hyperbolic correlations.

Also plotted in fig. 4.14 are calculated mixing trajectories on each diagram between a depleted end-member and a Discovery (sample 7D-5) and Shona (sample 21D-1) incompatible trace-element enriched end-member. All the MORB samples used in these calculations of mixing trajectories are representative of the most unevolved samples from the respective geochemical domains, with Mg#'s of the incompatible trace-element depleted MORB ranging from 66-67, the Discovery-influenced sample 7D-5 with Mg# of 64, and the Shona-influenced sample 21D-1 with Mg# of 58.

The excellent agreement between the tightly defined hyperbolic curves of trace-element compositions of MORB recovered from the SMAR and the calculated mixing trajectories in fig. 4.14 corroborates the conclusions drawn from the radiogenic isotope data (Douglass *et al.*, 1999). Therefore, the observed variations in the incompatible trace-element compositions of the MORB recovered from the SMAR are due to varying degrees of binary mixing between magmas derived from an incompatible trace-element depleted mantle source, the ambient MORB mantle, and magmas derived from, possibly two, incompatible trace-element enriched mantle sources with different characteristics, the Discovery and Shona mantle plume-derived components.

This mixing could occur between incompatible trace-element depleted magmas and incompatible trace-element enriched magmas, derived during separate melting events of separate mantle source-regions. The previously discussed lack of compositional homogeneity of basalts, coupled with geophysical studies of slow-spreading ridges (Batiza *et al.*, 1988; Detrick *et al.*, 1990), argue against the presence of shallow-level, long-lived, ridge-centred magma chambers which are the only reasonable sites for secondary mixing of various magmas. The alternative is the derivation of magmas with various degrees of incompatible trace-element enrichment from compositional heterogeneous mantle source-regions. The mixing between the incompatible trace-element depleted MORB mantle and incompatible trace-element enriched mantle plume-derived material therefore occur prior to the mantle entering the melting regions beneath the

University of Cape Town

ridge segments. The mantle which enters these melting regions experienced subsolidus mixing and the depleted MORB mantle is probably "variably veined" with incompatible trace-element enriched zones (Hirschmann & Stolper, 1996; le Roex, 1987).

Summary. The latitudinal distribution of incompatible trace-element depleted and enriched MORB mirrors the patterns observed in radiogenic isotope data (Douglass *et al.*, 1999) and the occurrence of incompatible trace-element enriched MORB are clearly associated with the geographic extent of the influence of the Discovery and Shona mantle plumes, respectively. The northern Discovery-influenced MORB include some N-MORB, and the southern Discovery-influenced MORB are significantly more enriched in incompatible trace elements. The Shona-influenced MORB are not as enriched in incompatible trace elements relative to Discovery-influenced MORB, although the Shona-influenced ridge segments have significantly shallower bathymetry.

The compositional influences of the Discovery and Shona mantle plumes on the mantle source regions beneath ridge segments of the SMAR are consistent with a model of variable subsolidus mixing between incompatible trace-element depleted and enriched mantle domains. Mantle melting beneath the mantle plume-influenced ridge segments therefore sample heterogeneous, two-component source-regions simultaneously.

University of Cape Town

4.4.4 Major-element systematics of quenched igneous glass-bulk-rock sample pairs

It is clear from the data presented in fig. 4.10 & 4.11a-c that most of the compositions of bulk-rock samples plot significantly separated from the compositions of quenched igneous glasses from the same basalts. The quenched igneous glass-bulk-rock sample pairs for MORB recovered from the SMAR are plotted and joined on fig. 4.15a-c. Also plotted are vectors (Staudigel & Bryan, 1981, see caption of fig. 4.15a for details of calculation), which indicate the compositional effect of adding plagioclase, olivine or clinopyroxene to hypothetical quenched igneous glasses.

The following discussion will therefore focus on detailing the variations between the compositions of the quenched igneous glasses and bulk-rock samples for N-MORB, Discovery-influenced MORB and Shona-influenced MORB. The systematics of the quenched igneous glass-bulk-rock pairs for each of these group, and differences between these, will be discussed.

The term "companion" will be used in the following discussion to refer to the quenched igneous glass from the same basalt as the bulk-rock sample under discussion.

N-MORB. The quenched igneous glass-bulk-rock data for N-MORB recovered from the SMAR are plotted as linked symbols in fig. 4.15a. These N-MORB data pairs form two main trends which can, respectively, be accounted for by the addition of <10% to >30% plagioclase phenocrysts (An_{90-70}), and the addition of ~10-13% plagioclase and ~4% olivine phenocrysts.

The addition of plagioclase phenocrysts is the most important of the two processes capable of linking the compositions of quenched igneous glasses to their respective bulk-rock sample compositions. The compositions of the majority of N-MORB bulk-rock samples are significantly enriched, by >2wt%, in Al_2O_3 relative to companion quenched igneous-glass compositions. These bulk-rock compositions also have significantly lower MgO concentrations, ~1-2wt%, compared with the compositions of companion quenched igneous glasses, see fig. 4.15a. These major-element characteristics, as well as slightly lower SiO_2, TiO_2, FeO* and higher CaO, result in the orientation of the majority of the N-MORB quenched igneous glass-bulk-rock pairs aligned with the plagioclase-addition vectors on the MgO-variation diagrams in fig. 4.15a.

The data for the quenched igneous glass-bulk-rock pairs of two samples, both central N-MORB (27D-2 & 26D-1), are orientated roughly orthogonal to the rest of the data in the Al_2O_3 versus MgO diagram in fig. 4.15a. The bulk-rock compositions of these samples have higher Al_2O_3, MgO, fairly constant CaO, and lower SiO_2, TiO_2 and FeO* concentrations relative to the compositions of the companion quenched igneous glasses. The resulting orientation of these two quenched igneous glass-bulk-rock pairs are consistent with a small addition of plagioclase and olivine phenocrysts in the case of 26D-1, but the large off-set observed between the bulk-rock and quenched igneous-glass compositions of 27D-2 necessitates the addition approximately 4% olivine and ~10-13% plagioclase phenocrysts to the bulk system.

The addition of significant quantities of plagioclase phenocrysts and/or lesser quantities of olivine phenocrysts to the bulk systems of these N-MORB indicates the lack of separation between early formed phenocrysts and the evolving magma. This can be due to rapid crystallization, transport and eruption of the magma without significant time-intervals during

University of Cape Town

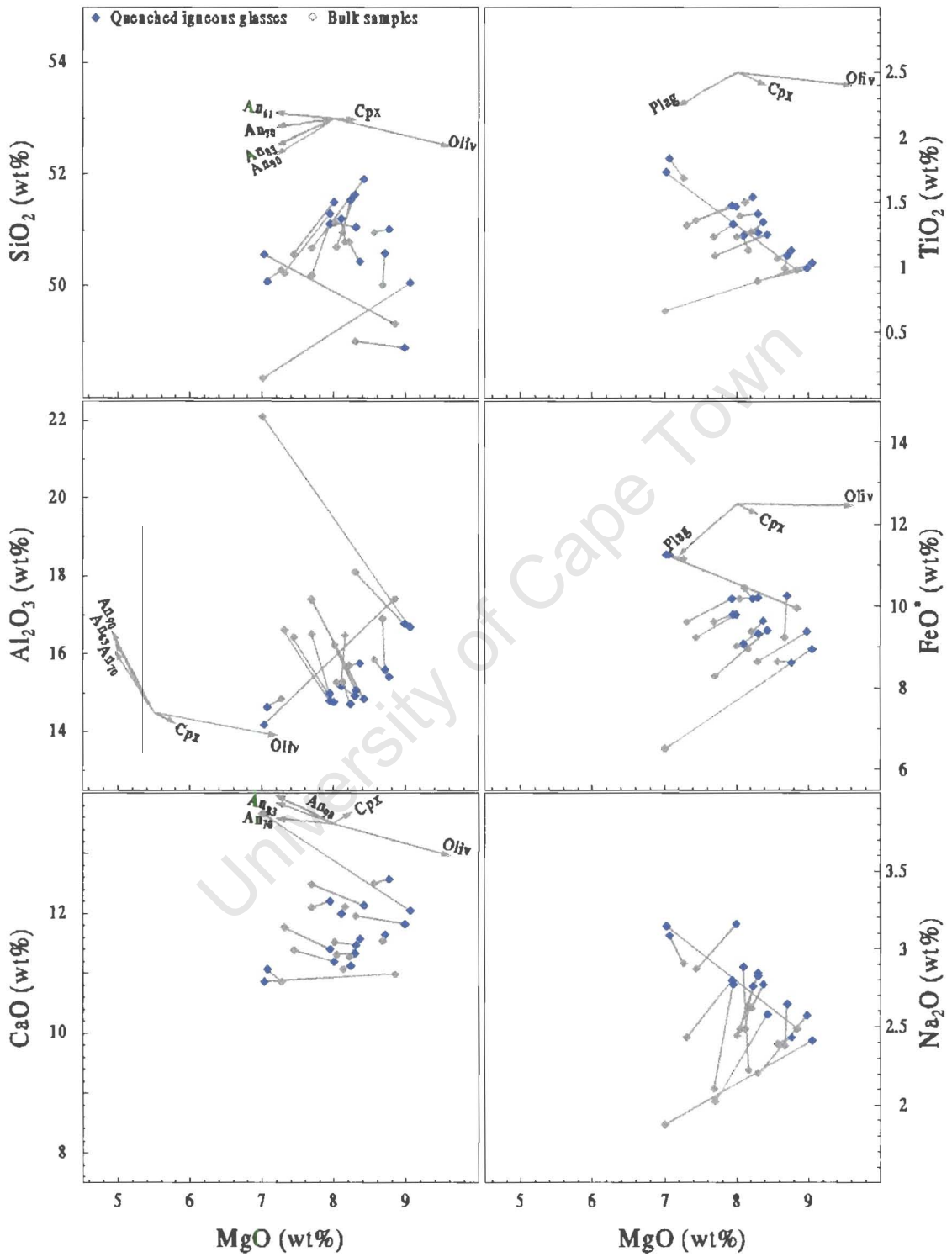

University of Cape Town

Figure 4.15a: MgO-variation diagrams for quenched igneous glass-bulk-rock sample pairs for N-MORB. Vectors on selected diagrams indicate addition of 10% plagioclase, 4% olivine or 2% clinopyroxene. The vectors were calculated after Staudigel and Bryan (1981), using: plagioclase phenocryst compositions from sample 45D-2 ($An_{90,83}$), and sample 44D-3 (An_{70}); olivine phenocryst composition from sample 45D-2; clinopyroxene phenocryst composition from sample 7D-3; and hypothetical quenched igneous-glass compositions.

which formed phenocrysts could be fractionated from the magma.

Discovery-influenced MORB. The major-element compositional data for the quenched igneous glass-bulk-rock sample pairs of Discovery-influenced MORB define no clear trends on the MgO-variation diagrams in fig. 4.15b. The quenched igneous glass-bulk-rock pairs can be roughly divided into two groups, the first with MgO concentrations in bulk-rock samples *lower* than in the companion quenched igneous glasses, and the second with MgO concentrations in the bulk-rock samples *higher* than in the companion quenched igneous glasses. In the case of the first group, the main compositional influence seems to be the addition of varying amounts of varying-An plagioclase phenocrysts, with the trend for An_{70} being more appropriate for the majority of samples.

For the second group, the picture is more complex. In some of the MgO-variation diagrams, e.g. the FeO*-MgO plot, the data for quenched igneous glass-bulk-rock pairs are aligned parallel to the calculated olivine- or clinopyroxene-addition vector. The data do not allow to distinguish sufficiently between the compositional affects of additing these two mafic phenocryst phases. It is also very likely that a combination of both olivine and clinopyroxene phenocrysts could be responsible for the compositional differences between the bulk-rock samples and companion quenched igneous glasses. The significantly higher Al_2O_3 concentrations in bulk-rock samples, especially for samples with low MgO concentrations, compared with companion quenched igneous glasses further necessitate the addition of plagioclase phenocrysts to the bulk systems.

University of Cape Town

Therefore, the observed variations in the major-element data for the quenched igneous glass-bulk-rock pairs of Discovery-influenced MORB indicate a complex history of phenocrysts addition beneath these ridge segments samples. Besides a processes of accumulation of plagioclase phenocrysts, especially those with lower anorthite content, the data also necessitate the addition of variable combinations of plagioclase, olivine and clinopyroxene phenocrysts. In contrast with the data for quenched igneous glass-bulk-rock pairs for N-MORB from the SMAR, the data for Discovery-influenced MORB indicate variable accumulation of phenocrysts phases throughout the crystallisation-evolution of magmas.

Shona-influenced MORB. The major-element compositional data for the quenched

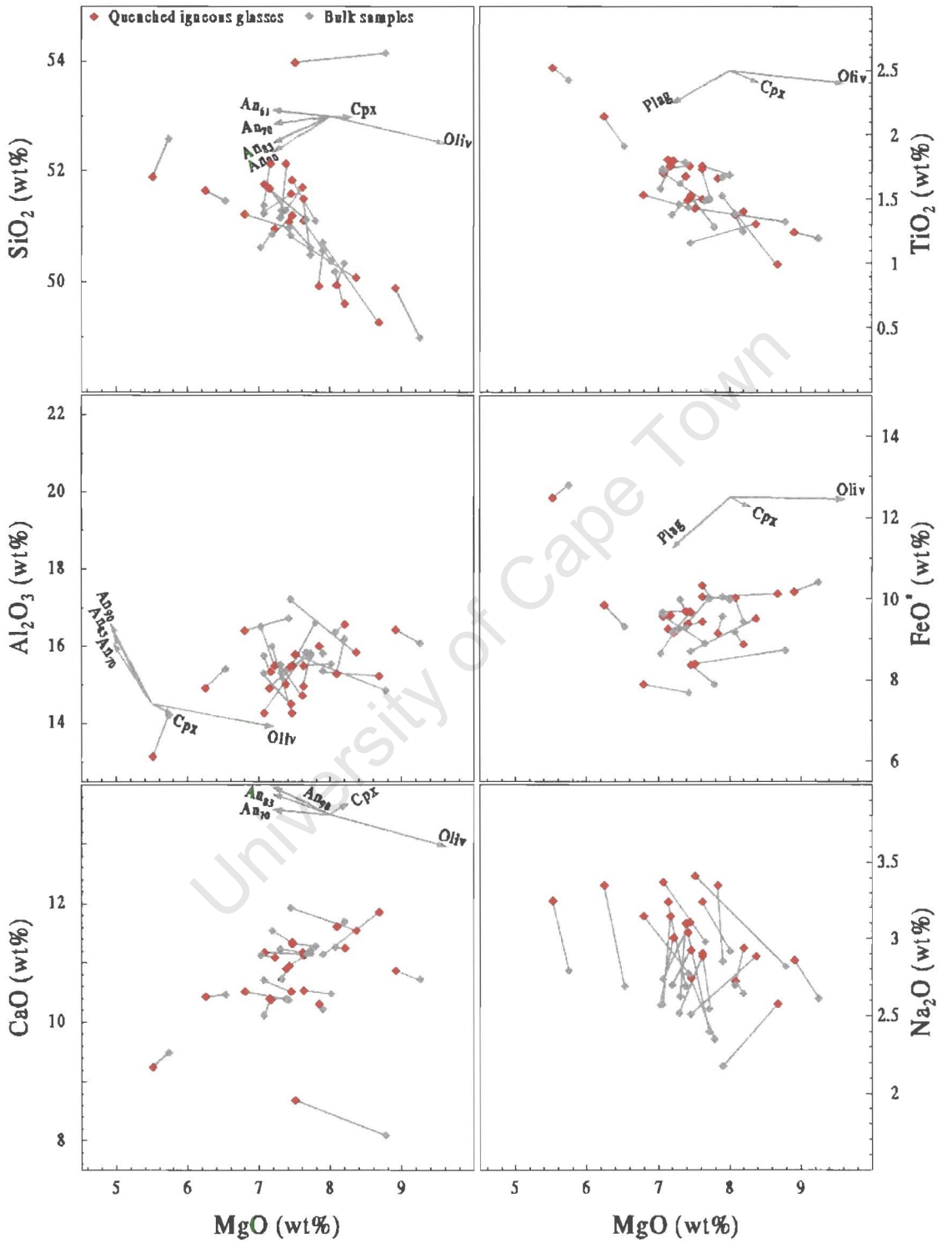

Figure 4.15b: MgO-variation diagrams for quenched igneous glass-bulk-rock sample pairs for Discovery-influenced MORB. Vectors on selected diagrams indicate addition of 10% plagioclase, 4% olivine or 2% clinopyroxene. See caption to fig. 4.15a for details of vector calculation.

University of Cape Town

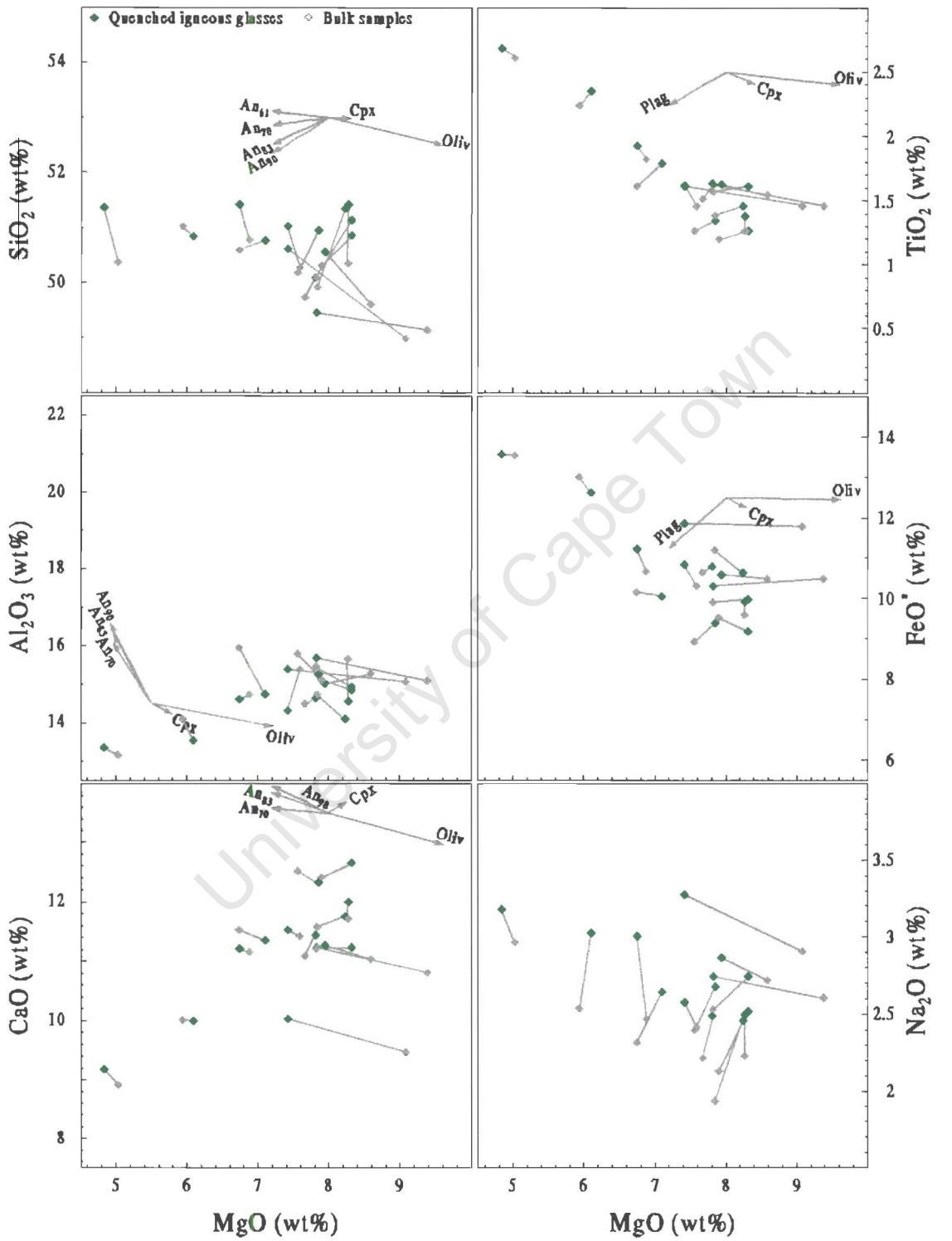

University of Cape Town

Figure 4.15c: MgO-variation diagrams for quenched igneous glass-bulk-rock sample pairs for Shona-influenced MORB. Vectors on selected diagrams indicate addition of 10% plagioclase, 4% olivine or 2% clinopyroxene. See caption to fig. 4.15a for details of vector calculation.

igneous glass-bulk-rock sample pairs from Shona-influenced MORB display two distinct orientations on the MgO-variation diagrams in fig. 4.15c. As for the quenched igneous glass-bulk-rock pairs from Discovery-influenced MORB, the quenched igneous glass-bulk-rock pairs from Shona-influenced MORB can be divided in terms of differences in MgO concentrations between the bulk-rock samples and companion quenched igneous glasses. A number of basalts have MgO concentrations in the bulk-rock samples *lower* than in the companion quenched igneous glasses, some basalts have *roughly equal* MgO concentrations in the bulk-rock samples and companion quenched igneous glasses, and a third set of basalts have MgO concentrations in the bulk-rock samples *higher* than in the companion quenched igneous glasses.

The bulk-rock samples from the first group of pairs have lower SiO_2, slightly lower TiO_2, roughly constant FeO*, slightly higher CaO, and higher Al_2O_3 compared with the compositions of the companion quenched igneous glasses. These pairs are not orientated parallel to a single, specific phenocrysts accumulation vector, but it is clear that the addition of ~10% plagioclase phenocrysts dominated in these systems. The mafic phenocryst phases were also being added to the system at this stage, but played a much lesser role than plagioclase phenocrysts.

The bulk-rock samples and companion quenched igneous glasses from the second group of pairs *mirror* the major-element differences described for quenched igneous glass-bulk-rock pairs from the first group. However, these differences are more subdued and these pairs are aligned between the calculated phenocrysts-addition vectors for plagioclase and the mafic phases. Prior to eruption, these magmas therefore experienced variable addition of <10% plagioclase phenocrysts and <4% mafic phases.

The bulk-rock samples from the third group of pairs have *slightly to substantially lower* SiO_2, TiO_2, Al_2O_3 and CaO concentrations, and *roughly equal* FeO* concentrations relative to the compositions of companion quenched igneous glasses. The orientations of these quenched igneous glass-bulk-rock pairs on the MgO-variation diagrams in fig. 4.15c are significantly aligned with that of the calculated olivine phenocryst-addition vectors. The major-element systematics of the third group of quenched igneous glass-bulk-rock pairs are therefore dominated by the addition of ~4% olivine phenocrysts, and the concurrent addition of small quantities of plagioclase and clinopyroxene phenocrysts can not be discounted.

University of Cape Town

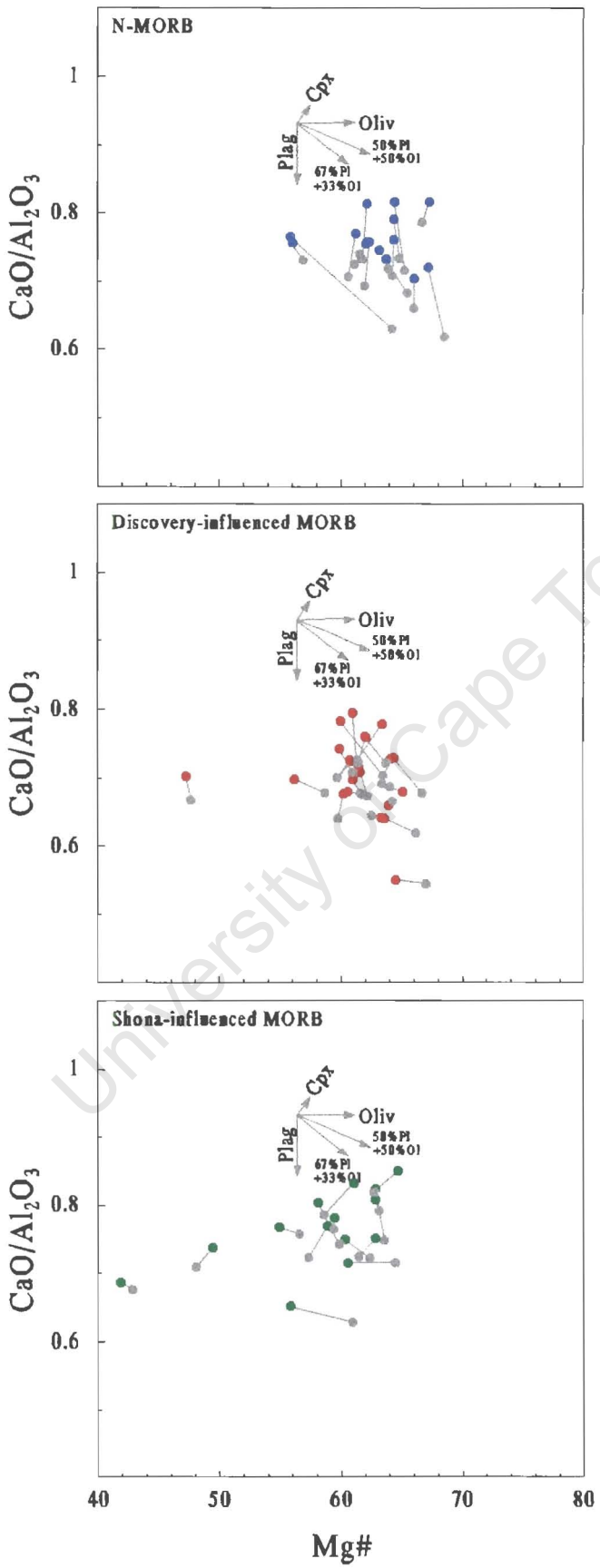

University of Cape Town

Figure 4.16: CaO/Al_2O_3 versus Mg# diagrams for quenched igneous glass-bulk-rock sample pairs for MORB from the SMAR. Vectors on diagrams indicate addition of 10% plagioclase, 4% olivine, 2% clinopyroxene, or olivine:plagioclase mixtures as indicated. See caption to fig. 4.15a for details of vector calculation.

Summary. The correlation between the orientation of quenched igneous glass-bulk-rock sample pairs and calculated phenocryst addition vectors are also evident on the relevant CaO/Al_2O_3 versus Mg# diagram in fig. 4.16. Additional vectors for 10% addition of a mix of phenocrysts with plagioclase:olivine ratios of 50:50 and 67:33 are also plotted on each of these diagrams.

The compositional differences between the bulk-rock samples and companion quenched igneous glasses of N-MORB, recovered from the SMAR, are quite apparent in fig. 4.16. The majority of bulk-rock samples have been compositional affected by the sole addition of >10% plagioclase phenocrysts, while a small number of bulk-rock samples had up to 33% of the phenocrysts added to them composed of olivine phenocrysts. The orientations of quenched igneous glass-bulk-rock pairs from Discovery-influenced MORB are quite varied in fig. 4.16. The majority of bulk-rock samples have had >10% of plagioclase phenocrysts added to them, while the rest have experienced the addition of a variable mixture of plagioclase and olivine phenocrysts. The proportions of olivine phenocryst in these mixtures range from <33% to substantially >50%. Similarly, the orientations of quenched igneous glass-bulk-rock pairs from Shona-influenced MORB in fig. 4.16 indicate that plagioclase and olivine phenocrysts have been added to the systems to variable extents and in variable proportions. Addition of olivine phenocrysts played a larger role in the Shona-influenced MORB systems relative to Discovery-influenced MORB or N-MORB. The total extent of phenocryst-addition necessitated to account for the differences between bulk-rock samples and companion quenched igneous glasses in Shona-influenced MORB is <10%. The proportions of olivine phenocrysts in the mixtures added to these systems ranged between <33% to >80%.

University of Cape Town

4.5 REGIONAL SUMMARY

The following section will give a brief overview of the preceding discussions of the petrography, mineralogy and bulk-rock and quenched igneous-glass compositions of MORB recovered from the SMAR.

Petrography. The basalts recovered from the SMAR are predominantly observed to be aphyric to sparsely phyric, with <10-20% total phenocrysts. The modal mineralogies of these basalts are dominated by the presence of plagioclase phenocrysts which generally constitute ≤20%, although a small number of samples contain ≤40% plagioclase phenocrysts. Olivine

phenocrysts are present at much lower abundances of ≤3%, although in some of the Shona-influenced MORB olivine phenocrysts constitute the major phenocryst phase observed. Clinopyroxenes are predominantly present as rare microphenocrysts in mantle plume-influenced basalts. Spinel microphenocrysts are also rare, occur predominantly associated with or included in olivine phenocryst, and are also mostly confined to mantle plume-influenced MORB. Rare sulphide blebs are present as isolated microphenocrysts or inclusions in plagioclase and olivine phenocrysts.

Large plagioclase phenocrysts are frequently resorbed and rounded, exhibit optical zoning, and contain quenched igneous-glass inclusions in cores or in bands associated with optical zoning. Plagioclase microphenocrysts are frequently skeletal in habit. Large olivine phenocrysts are rare, but when present are also frequently resorbed and might contain quenched igneous-glass inclusions.

The observed modal mineralogies and phenocryst characteristics of MORB from the SMAR do not exhibit any clear latitudinal variations. Olivine phenocrysts are slightly more abundant in mantle plume-influenced MORB, but otherwise the Discovery and Shona mantle plumes were not observed to have influenced the abundance or physical characteristics of phenocrysts in the MORB recovered from the SMAR.

University of Cape Town

Mineralogy. The compositions of olivine microphenocrysts and phenocrysts are fairly restricted in N-MORB and most samples from mantle plume-influenced MORB, and span a range of $Fo_{\sim 82\text{-}87}$. Olivine phenocrysts have in general higher forsterite compositions than coexisting microphenocrysts, and in some case have compositions of $Fo_{\sim 88\text{-}89}$, significantly higher than the general range. Some samples with low Mg#'s of ~40-42, restricted to mantle plume-influenced MORB, contain olivine microphenocrysts with forsterite compositions of $Fo_{\sim 70\text{-}73}$.

Olivine microphenocrysts are in general in, or close to, equilibrium with host-quenched igneous glasses and aphyric bulk-rock compositions at pressures ≤4kbar, even those microphenocrysts with extremely low forsterite compositions. Olivine phenocrysts are rarely observed to be in, or even close to, equilibrium with host-quenched igneous glasses or aphyric bulk-rock compositions.

The observed compositions of plagioclase phenocrysts and microphenocrysts have no distinct latitudinal systematic variation, and the basalts recovered from mantle plume-influenced ridge segments do not contain plagioclase phenocrysts or microphenocrysts with significantly different compositions relative to plagioclase in N-MORB. As expected, plagioclase microphenocrysts have the lowest anorthite compositions and these occur in highly evolved basalts.

Although not consistently in equilibrium, the plagioclase microphenocrysts are more commonly in equilibrium with host-quenched igneous glass or bulk-rock compositions at low pressures. With rare exceptions, plagioclase phenocrysts, especially those with high anorthite compositions, were found not to be in equilibrium with host-quenched igneous glass or bulk-rock compositions at pressures <8kbar.

The rare presence of clinopyroxene and spinel as phenocrysts or microphenocrysts in MORB from the SMAR resulted in only limited compositional data being available for these phases. Nonetheless, clinopyroxene microphenocryst compositions were restricted to a range of $Wo_{41-43}En_{48-52}Fs_{6-10}$, while the two populations of spinel microphenocrysts have Mg#'s of 0.71, 0.51-0.64 and Cr#'s of 0.28-0.29, 0.37-0.41. Qualitative results for sulphide blebs show iron content varying between 39-55wt%, nickel content between 8-28wt%, and sulphur between 35-38wt%.

Compositional variations. In terms of the major-element compositions of bulk-rock samples and quenched igneous glasses of the MORB recovered from the SMAR, these samples are predominantly olivine-normative tholeiitic basalts with a few exceptions classified as quartz-normative basaltic andesites. The trace-element compositions of these basalts span a range from incompatible trace-element depleted ($Nb/Zr \leq 0.03$, $Zr/Y \leq 2.91$, $(La/Sm)_N \leq 0.79$, $K/Ti \leq 0.14$) to incompatible trace-element enriched ($Nb/Zr \leq 0.17$, $Zr/Y \leq 6.88$, $(La/Sm)_N \leq 2.94$, $K/Ti \leq 1.15$).

The variations observed in the major-element data of the quenched igneous glasses and bulk-rock samples are broadly consistent with the effects of crystallisation on evolving magmas. Therefore, as MgO concentrations decrease SiO_2 concentrations remain fairly constant, while the concentrations of TiO_2, FeO*, Na_2O, K_2O and P_2O_5 increase and Al_2O_3 and CaO decrease. The co-variations of CaO/Al_2O_3 ratios and Mg#'s of these basalts are also broadly consistent

University of Cape Town

with crystallisation. These major-element variations are most pronounced in the compositions of Shona-influenced MORB, while Discovery-influenced MORB define less-consistent trends and N-MORB compositions are mostly restricted to the high MgO-content end of the observed spectrum.

The geographic distribution of the previously-defined incompatible trace-element enriched basalts are restricted to ridge segments with anomalously shallow bathymetry, at the same latitude as the Discovery and Shona mantle plumes. MORB recovered from Discovery-influenced ridge segments have the highest observed incompatible trace-element enrichment and show the most variability in compositions. The basalts recovered from Shona-influenced ridge segments are enriched in incompatible trace elements to a lower degree and show significant, but less pronounced variability. Incompatible trace-element depleted basalts were predominantly recovered from ridge segments with deep and consistent bathymetry, as well as from some of the northern Discovery-influenced ridge segments.

The compositional continuum from incompatible trace-element depleted to enriched MORB observed from the SMAR are consistent with subsolidus mixing between the ambient MORB mantle and mantle material derived from the proximal Discovery and Shona mantle plumes. The result of this process of mixing between compositionally enriched and depleted mantle domains is the melting of heterogeneous mantle source regions beneath segments of the SMAR.

The differences between the major-element compositions of bulk-rock samples and companion quenched igneous glasses of N-MORB are predominantly due to addition of plagioclase phenocrysts to the bulk magma systems. The compositions of bulk-rock samples of Discovery-influenced MORB differ significantly from that of companion quenched igneous glasses and necessitate the addition of >10% plagioclase phenocrysts to bulk magma systems. The addition of <10% of a mixture of plagioclase and <30% to >50% olivine phenocrysts are necessary to account for the differences between bulk-rock samples and companion glasses for some of the Discovery-influenced MORB. The compositional relationship between bulk-rock samples and companion quenched igneous glasses from Shona-influenced MORB require addition of <10% of variable proportions of plagioclase and olivine phenocrysts to bulk magma systems. The addition of olivine phenocrysts to bulk magma systems are more significant in

University of Cape Town

Shona-influenced MORB and olivine can constitute <33% to >80% of the total amount of phenocrysts required to account for the compositional differences between bulk-rock samples and companion quenched igneous glasses.

University of Cape Town

CHAPTER 5: GEOCHEMICAL CHARACTERISTICS OF MANTLE SOURCE-REGIONS

The aim of this chapter is to further examine the incompatible element characteristics of MORB from the SMAR, briefly discussed in the previous chapter. The presence and latitudinal distribution of identified enrichments and depletions in incompatible trace-element concentrations in the concentrations of these MORB will be evaluated with respect to published radiogenic isotope data, obtained on a subset of these samples (Douglass *et al.*, 1999), in order to link these incompatible trace-element characteristics to mantle source-region compositions. The incompatible trace-element characteristics of the above-delineated mantle source-regions will be defined and evaluated relative to accepted mantle compositional end-members. The nature and possible origins of any observed anomalies will be explored.

The advantages attached to the use of oceanic basalt to probe the geochemical characteristics of the underlaying mantle are: the relatively large mantle volumes represented by the erupted material; and the much smaller risk of significant crustal contamination during magma transport towards the surface, relative to volcanic rocks from island arcs and continental regions (Hofmann, 1997). A variety of so-called "geochemical tracers" can been used to investigate observed basaltic compositional characteristics and deduce possible compositions and origins of mantle source-regions from which MORB and OIB were derived (e.g. Hofmann, 1997). The most commonly used and accepted indicators of heterogeneous mantle source-regions are heavy radiogenic isotope ratios, e.g. $^{87}Sr/^{86}Sr$, $^{143}Nd/^{144}Nd$ and $^{206,207,208}Pb/^{204}Pb$ (Hart, 1988; Hofmann, 1997). The concentration ratios of certain extremely incompatible elements have also been used to probe mantle source-regions, when it has been argued that these ratios are insensitive, within acceptable limits, to changes due to melting or crystallisation processes envisaged being active beneath mid-ocean ridges. This may be the case if these elements are perfectly incompatible, or if the two elements involved have identical partition coefficients during all magmatic processes beneath mid-ocean ridges (e.g. Hofmann, 1997; Hofmann *et al.*, 1986). The validity of using incompatible element ratios in a similar fashion to isotopic ratios does not remain unquestioned (Simms & DePaolo, 1997), but regardless of limitations, selected ratios can provide an added dimension to further explore questions not completely answered by isotopic data alone (Sun & McDonough, 1989).

University of Cape Town

5.1 INCOMPATIBLE TRACE-ELEMENT CHARACTERISTICS OF MANTLE SOURCE-REGIONS

Correlation between incompatible trace-element and radiogenic isotope data in MORB from the SMAR. In chapter 4, a range of incompatible trace-element enriched MORB were identified and, due to their recovery from ridge segments located over the bathymetric "highs" associated with the proposed present-day latitudinal locations of the Discovery and Shona mantle plumes, these compositional characteristics were previously ascribed to melts having been derived from a blend of the ambient depleted mantle and incompatible trace-element enriched domains introduced into the sub-ridge mantle by the above-mentioned mantle plumes. However, trace-element data in MORB are not generally viewed as unequivocally representative of the compositions of the mantle source-regions from which they were derived without the support of radiogenic isotope data.

The possibility that the incompatible trace-element enriched MORB recovered from both Discovery- and Shona-influenced ridge segments, were derived, through exotic petrogenetic processes, e.g. autometasomatism, from ambient, depleted mantle sources, is refuted by their correlation with the radiogenic isotope "mantle plume-signatures", reported by Douglass *et al.* (1999). The mantle plume-influenced MORB with enriched incompatible trace-element compositions, e.g. containing low values for Y/Nb of $\leq \sim 8$, Zr/Nb of $\leq \sim 25$ and Sm/Ba of $\leq \sim 0.1$ and high values for La/Sm of $\geq \sim 1.1$, K/Ti of $\geq \sim 0.15$ and Nd/Rb of $\geq \sim 4$, are also the basalts with the highest radiogenic isotope values, e.g. high $^{87}Sr/^{86}Sr$ ratios of $\geq \sim 0.7036$ and low $^{143}Nd/^{144}Nd$ ratios of $\leq \sim 0.5129$ for Discovery-influenced samples and high $^{206}Pb/^{204}Pb$ ratios of $\geq \sim 18.4$ for Shona-influenced MORB, which is illustrated in fig. 5.1a-c.

The observed incompatible trace-element diversity in the MORB recovered from the SMAR is therefore unequivocally linked to distinct radiogenic isotope-defined mantle source-regions. The trace-element compositional diversity observed in these basalts can therefore be used to investigate the compositional characteristics of the MORB mantle source-regions beneath the SMAR.

Trace-element characteristics of mantle source-regions beneath the SMAR. The trace-element data from these MORB from the SMAR are combined with OIB data from the South Atlantic in fig. 5.2. It is evident from the trends defined by incompatible trace-element enriched

University of Cape Town

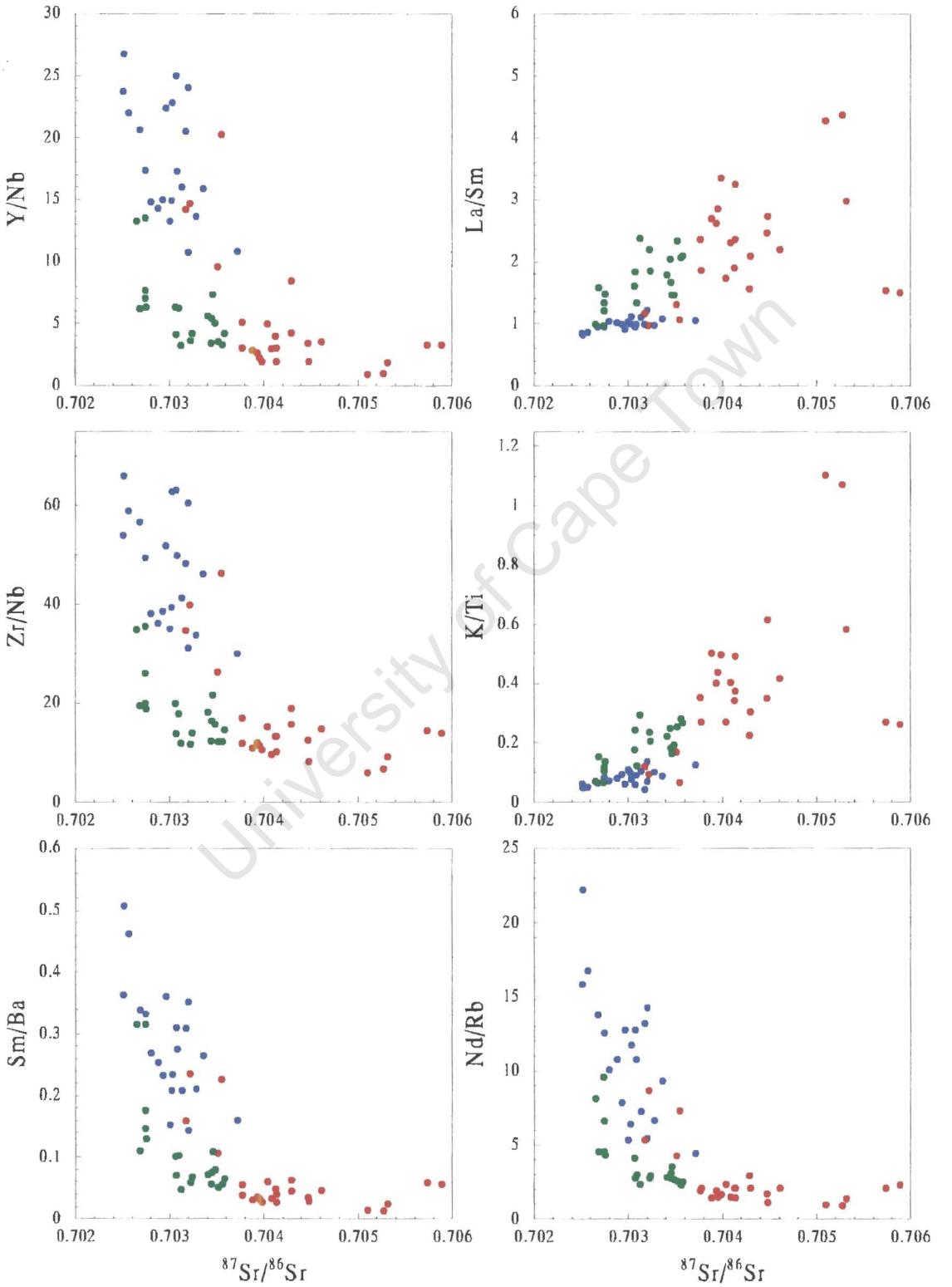

University of Cape Town

Figure 5.1a: Incompatible trace-element ratios versus $^{87}Sr/^{86}Sr$ (Douglass *et al.*, 1999). Blue markers: N-MORB; red markers: Discovery-influenced MORB; and green markers: Shona-influenced MORB.

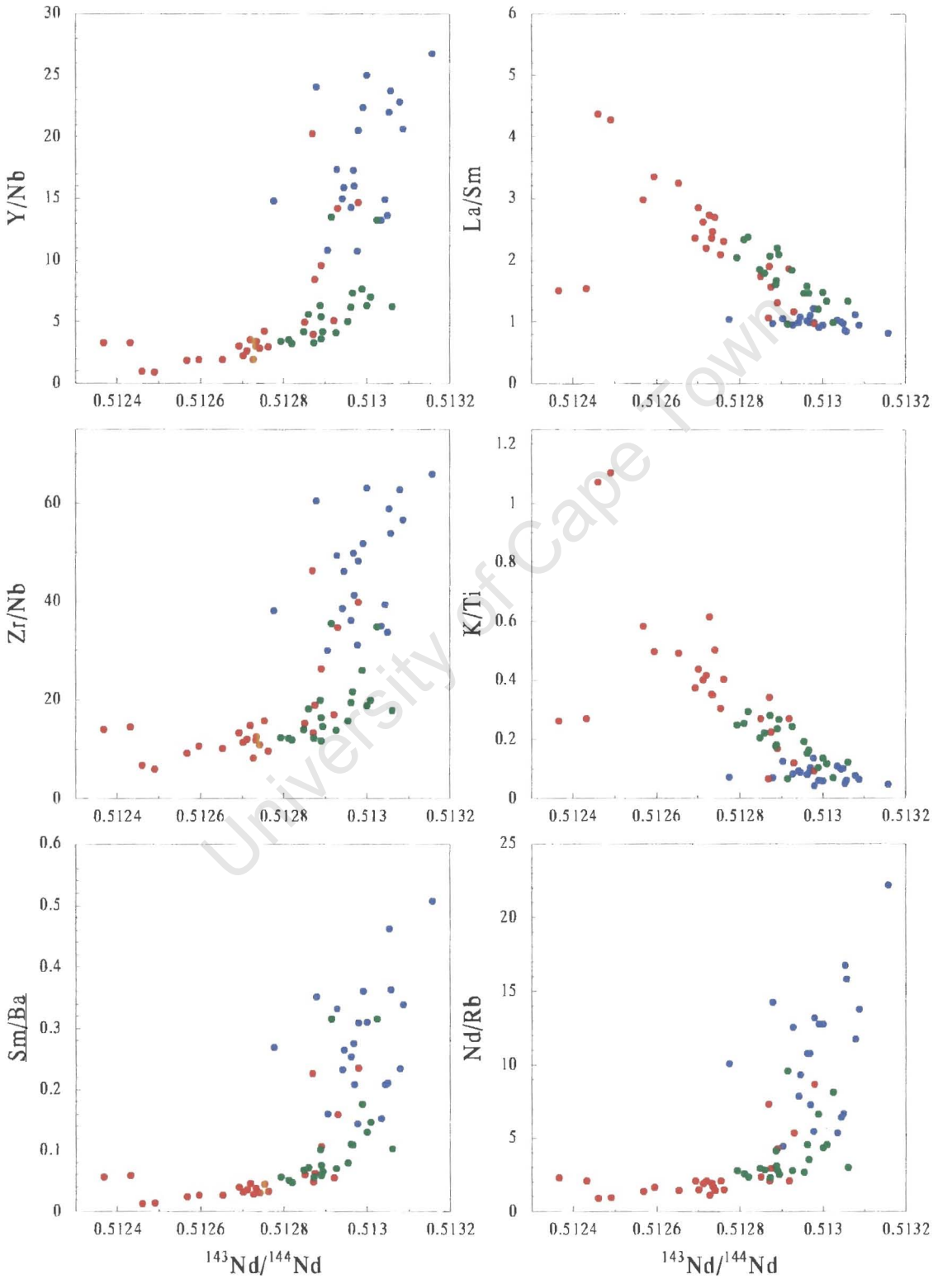

University of Cape Town

Figure 5.1b: Incompatible trace-element ratios versus $^{143}Nd/^{144}Nd$ (Douglass *et al.*, 1999). Blue markers: N-MORB; red markers: Discovery-influenced MORB; and green markers: Shona-influenced MORB.

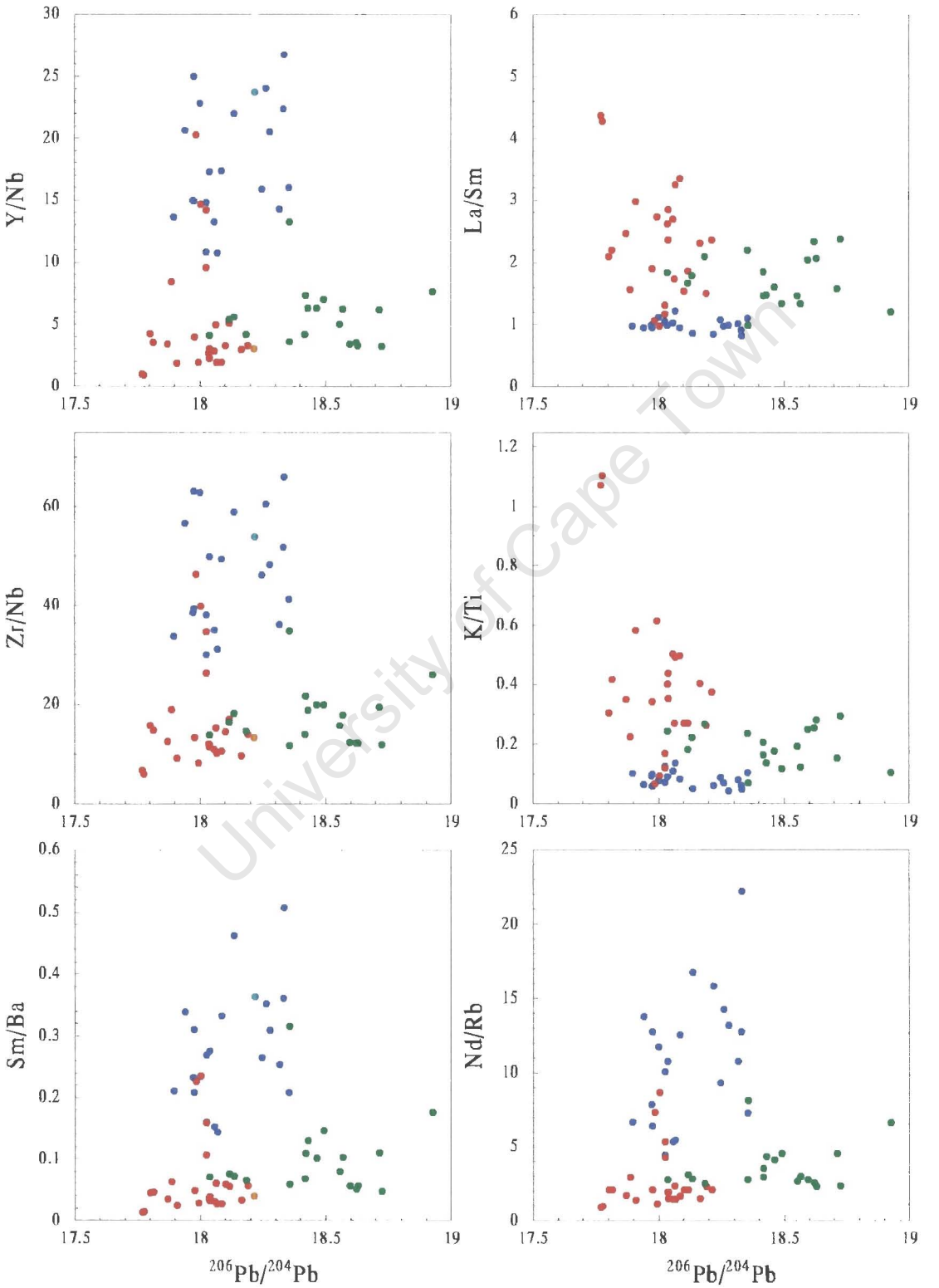

University of Cape Town

Figure 5.1c: Incompatible trace-element ratios versus $^{206}Pb/^{204}Pb$ (Douglass *et al.*, 1999). Blue markers: N-MORB; red markers: Discovery-influenced MORB; and green markers: Shona-influenced MORB.

basalts that the Discovery-influenced MORB are predominantly associated with EM-type OIB (e.g. Walvis Ridge, Tristan da Cunha, and Gough), while Shona-influenced MORB are associated with HIMU-type OIB (e.g. St. Helena and Bouvet). These incompatible trace element data therefore corroborate the radiogenic isotope data, which cast Discovery-influenced MORB and Shona-influenced MORB in terms of magmas derived from mantle source-regions which have had compositional influence from mantle plumes belonging to these recognised mantle end-members (Douglass *et al.*, 1999; Zindler & Hart, 1986). The compositional influences of mantle plumes on proximal MORB mantle source-regions have been demonstrated by numerous studies, e.g. the impact of the Ascension, St. Helena and Tristan da Cunha/Gough mantle plumes on MORB from ~8°-10°S, ~14°-18°S, and ~34°-40°S on the Mid-Atlantic Ridge, respectively (Fontignie & Schilling, 1996; Hanan *et al.*, 1986; Humphris *et al.*, 1985; Schilling *et al.*, 1985).

Incompatible trace-element enriched basalts from northern Discovery-influenced MORB (from dredges 37, 33 & 32) plot at significantly lower Ba/Nb values, see fig. 5.2, relative to the majority of Discovery-influenced MORB which were recovered from ridge segments south of the Falkland/Agulhas Fracture Zone. The Nb concentrations in these northern Discovery-influenced MORB are significantly higher at constant Ba concentrations relative to examples of southern Discovery-influenced MORB. Northern Discovery-influenced basalts from dredge 37 have Nb and Ba concentrations of ~9.0-9.3ppm and ~84-90ppm, respectively, while southern Discovery-influenced basalts from dredge 2 have Nb and Ba concentrations of ~7.9-8.7ppm and ~92-96ppm. Northern Discovery-influenced MORB from dredge 33 have Nb and Ba concentrations of ~15.3-16.6ppm and ~152-161ppm, while southern Discovery-influenced basalts from dredge 5 have Nb and Ba concentrations of ~13.1-14.0ppm and 150-157ppm. This is also observed for northern Discovery-influenced basalts from dredge 32 which have Nb and Ba concentrations of ~6.3-6.8ppm and ~59-73ppm, while southern Discovery-influenced MORB from dredge 25 have Nb and Ba concentrations of ~5.5-5.7ppm and ~60-65ppm. Therefore, the incompatible trace-element enriched northern Discovery-influenced MORB have Nb concentrations significantly higher than southern Discovery-influenced MORB with similar concentrations of Ba and La (values not given, see table B.6, appendix B).

On both diagrams A & B in fig. 5.2, the data for N-MORB are off-set to higher Ba/Nb ratios (~4.3-10.1) than "typical" N-MORB (~2.7-4.0), and the La/Nb ratios (~1.2-2.4) for most of these basalts are also moderately high compared with data for "typical" N-MORB (~1.1-1.2)

University of Cape Town

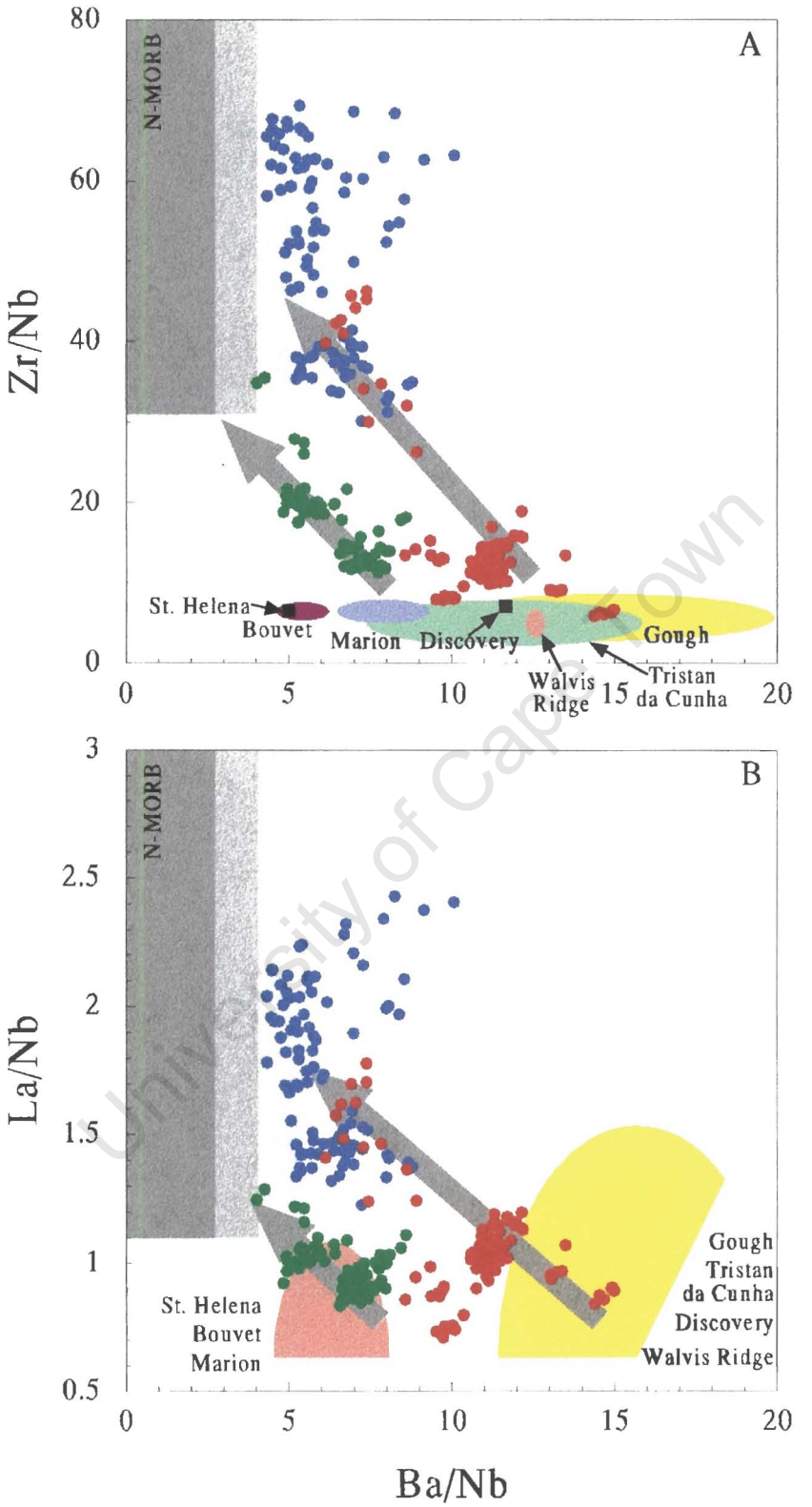

University of Cape Town

Figure 5.2: Zr/Nb & La/Nb versus Ba/Nb diagrams for all MORB from the SMAR, with data for typical N-MORB (Sun & McDonough, 1989) and OIB from the South Atlantic (Weaver, 1991; le Roex 1985; le Roex *et al.*, 1990; le Roex, unpublished data). In diagram A, compositions for St. Helena and Discovery are shown by black squares, as indicated by arrows, compositions of Bouvet, Marion, Tristan da Cunha, Walvis Ridge and Gough are defined by purple, light blue, light green, light red and yellow filled fields. In diagram B, compositions of OIB are indicated by two filled fields, with compositions of St. Helena, Bouvet and Marion enclosed by the light red field, and compositions of Gough, Tristan da Cunha, Discovery and Walvis Ridge enclosed by the yellow field.

(Hofmann, 1988; Sun & McDonough, 1989). The composition of "typical" N-MORB proposed by Sun & McDonough (1989) has Nb and Ba concentrations of 2.33ppm and 6.3ppm, respectively. N-MORB recovered from the SMAR with similar concentrations of Ba have significantly lower concentrations of Nb, e.g. N-MORB from dredge 45 have Nb and Ba concentrations of 1.06-1.17ppm and 5.75-6.58ppm, and N-MORB from dredge 11 have Nb and Ba concentrations of 1.25-1.43ppm and 6.61-7.75ppm. Therefore, the incompatible trace-element depleted basalts recovered from the SMAR have Nb concentrations significantly lower than would be expected for the observed Ba concentrations.

When considering a larger number of trace elements, the compositions of MORB recovered from the SMAR exhibit further compositional anomalies. The primitive-mantle normalised incompatible trace-element diagrams of MORB recovered from the SMAR, representative examples given in fig. 5.3, indicate the following departures from recognised compositions of typical N-, E-MORB and OIB (Hofmann, 1988; Sun & McDonough, 1989):

- Ba values for incompatible trace-element enriched Discovery-influenced MORB, and to a lesser extent incompatible trace-element enriched Shona-influenced MORB, are high;
- Significant negative Th anomalies exist in incompatible trace-element enriched Discovery-influenced MORB;
- Significant negative Nb anomalies are present in N-MORB, and Discovery-influenced MORB, with lower than expected Nb values for some Shona-influenced MORB;
- Ta values for some incompatible trace-element enriched Discovery-influenced MORB are lower than expected;.
- Sr and P values in all dredges are variable and in some basalts, especially Shona-influenced MORB, form significant negative anomalies;
- Some basalts have negative Eu anomalies (not shown, but chondrite-normalised REE patterns also show negative Eu anomalies in the same basalts);
- Basalts from dredge 25 and a subset from dredge 7 have highly depleted HREE abundances, and will be discussed in chapter 6.

The geographic distribution of the abovementioned anomalies are further illustrated in fig. 5.4. It is arguable that positive (>1) Ba/Ba* (see caption to fig. 5.4 for definition and calculation) anomalies are mostly concentrated in basalts recovered from ridge segments associated with the influence of the Discovery mantle plume, with less extreme anomalies in

University of Cape Town

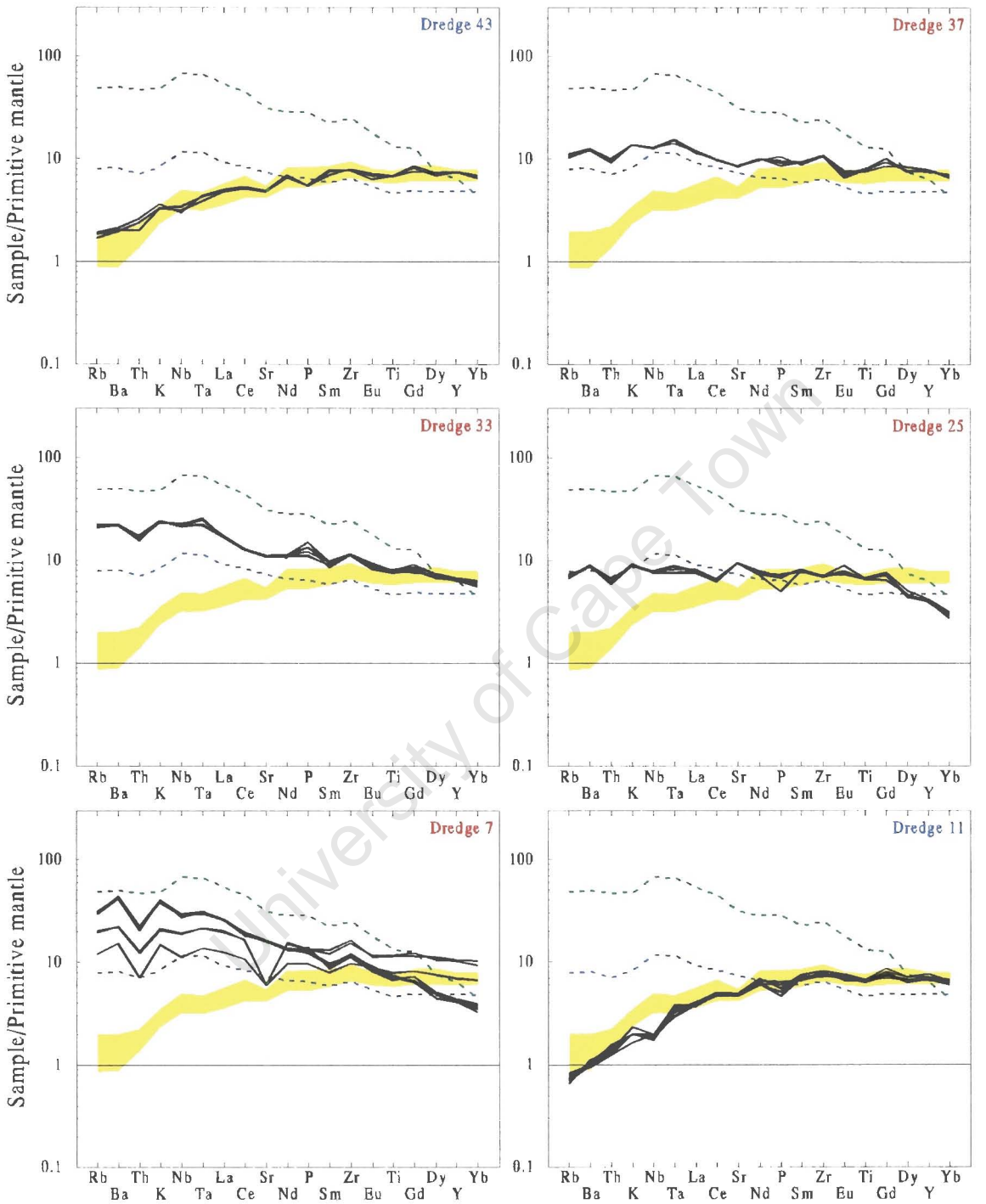

University of Cape Town

Figure 5.3: Primitive-mantle (Sun & McDonough, 1989) normalised incompatible trace-element diagrams, with elements in order of decreasing incompatibility (after Hofmann, 1997; Sun & McDonough, 1989), for representative MORB from the SMAR. Solid black lines: observed compositions of MORB from the SMAR; yellow field: typical compositional range for N-MORB (Hofmann, 1988; Sun & McDonough, 1989); blue dashed-line: typical composition of E-MORB; green dashed-line: typical composition of OIB (Sun & McDonough, 1989), all normalised to the primitive-mantle composition of Sun & McDonough (1989). Diagrams in order of increasing latitude of dredge-station location, with blue dredge numbers: N-MORB, red dredge numbers: Discovery-influenced MORB, green dredge numbers: Shona-influenced MORB. All plotted data > LLD + 2σ.

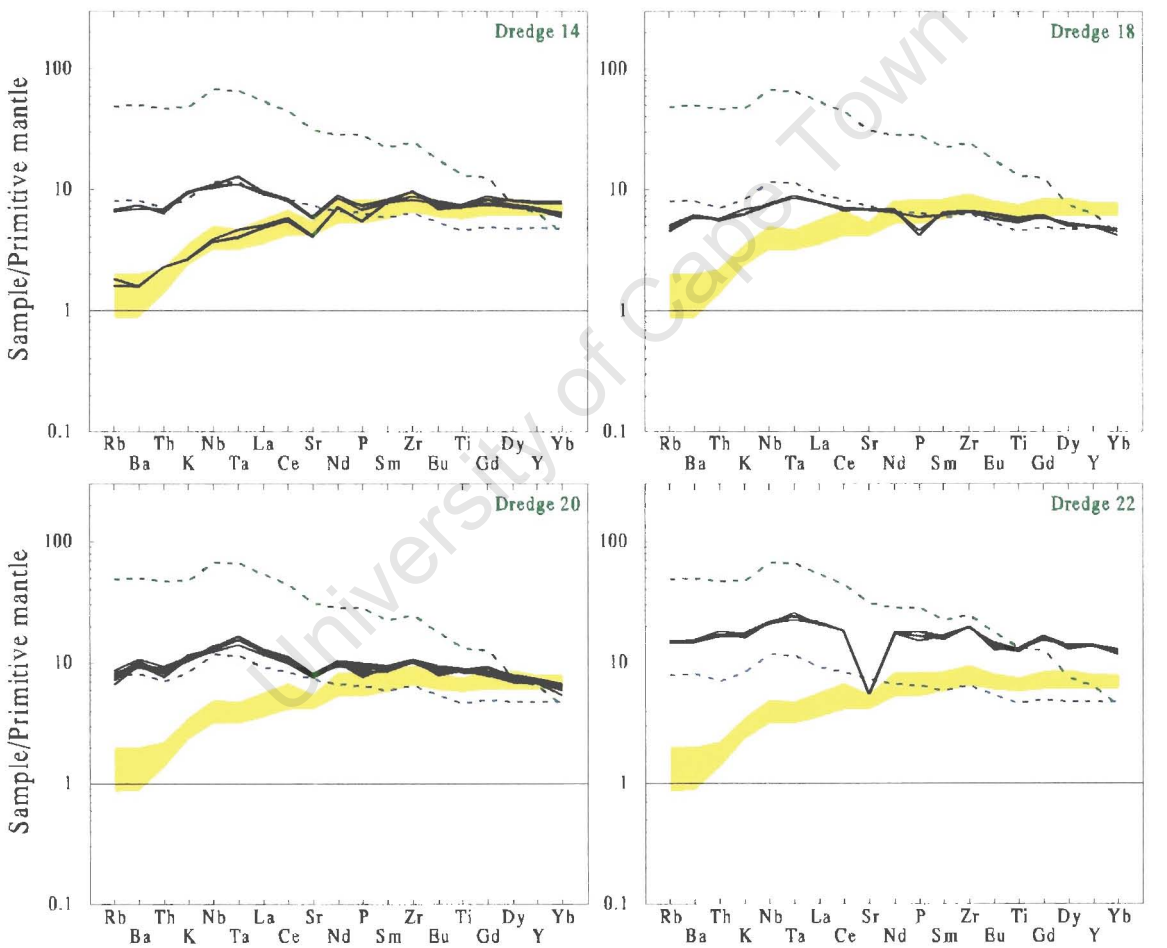

Figure 5.3 (cont.)

University of Cape Town

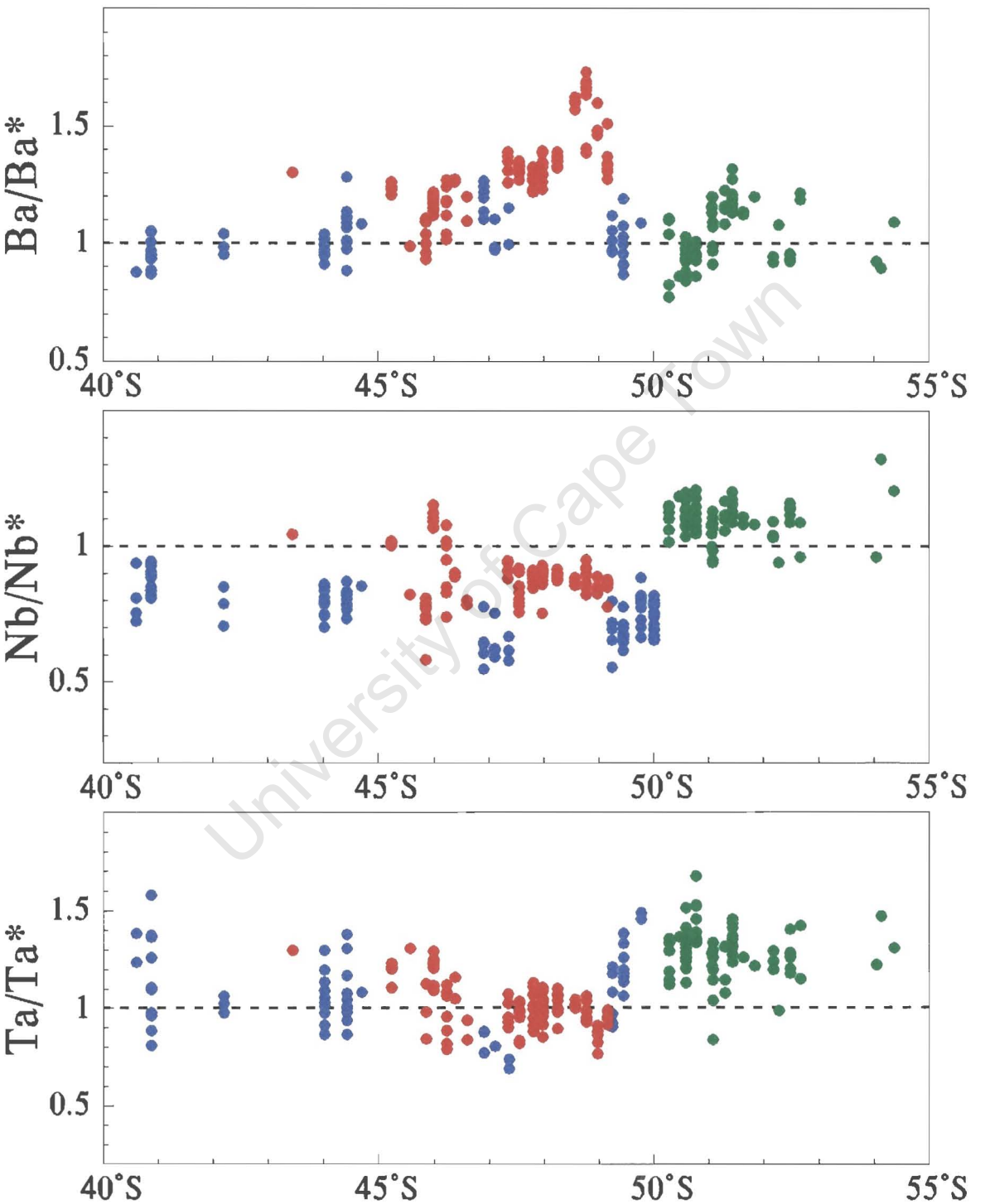

University of Cape Town

Figure 5.4: Diagrams of incompatible trace-element anomalies versus latitude. Anomalies quantified using the following formula: $Y/Y^{*}=(Y_{Observed})_N/[(X_{Observed})_N.(Z_{Observed})_N]^{½}$, were Y=element of interest; X, Z= "neighbour" elements on primitive-mantle normalised incompatible trace-element diagrams, such as in fig. 5.3. Selected X & Z for Ba: Rb, Th; for Nb: K, La; for Ta: K, La. All data plotted > LLD + 2σ.

basalts from Shona-influenced ridge segments. The negative (<1) Nb/Nb* anomalies are, on the other hand, clearly concentrated in N-MORB and basalts recovered from Discovery-influenced ridge segments. A definite geographical "break" occurs at the off-set transform (at ~50.1°S) which defines the northern limit of the Shona-influenced ridge segments. The negative Nb/Nb* anomaly is therefore almost completely absent in Shona-influenced MORB. The latitudinal distribution and magnitudinal significance of negative Ta/Ta* anomalies are less well-defined. N-MORB span a range from quite negative Ta/Ta* values, to highly positive values, Discovery-influenced MORB contain predominantly negative Ta/Ta* values, although significant positive values occur in some northern Discovery-influences MORB, while Shona-influenced MORB contain predominantly positive Ta/Ta* values, with only the odd negative value. The variation in magnitude, especially in N-MORB, could partially be due to the low absolute abundances of Ta in most of these basalts (0.06ppm-lower limit of detection plus 2σ error at 0.07ppm). The calculated Ta/Ta* values are therefore very sensitive to small variations in the measured absolute concentrations of Ta.

If two or more of the above trace element anomalies are due to a single process or mantle source-region characteristic, then there should exist correlations between these genetically related trace-element anomalies or between anomalies and proxies for petrogenetic processes accepted as possibly being active beneath mid-ocean ridges. The data presented in fig 5.5a indicate a positive correlation between Nb/Nb* and Ta/Ta* especially for Discovery- and Shona-influenced MORB, with the data for N-MORB slightly more scattered and plotting towards higher Ta/Ta* values. It is also clear that N-MORB and most of the Discovery-influenced MORB plot at Nb/Nb* values <1, while most Shona-influenced MORB and the incompatible trace-element enriched northern Discovery-influenced MORB from dredges 37, 33 & 32, discussed previously, plot at Nb/Nb* values >1.

The data for Ba/Ba* plotted against Nb/Nb* in fig. 5.5a are roughly confined to three overlapping groups. The data for N-MORB are roughly aligned with the theoretical trend for a negative correlation. The data for most Discovery-influenced MORB plot in a vertical trend of increasing Ba/Ba* values at restricted Nb/Nb* compositions. The data for most Shona-influenced MORB and the above-mentioned northern Discovery-influenced MORB also plot in a vertically aligned group of increasing Ba/Ba* values at constant Nb/Nb* compositions, but this group is located at lower average Ba/Ba* values relative to the trend for the main Discovery-

University of Cape Town

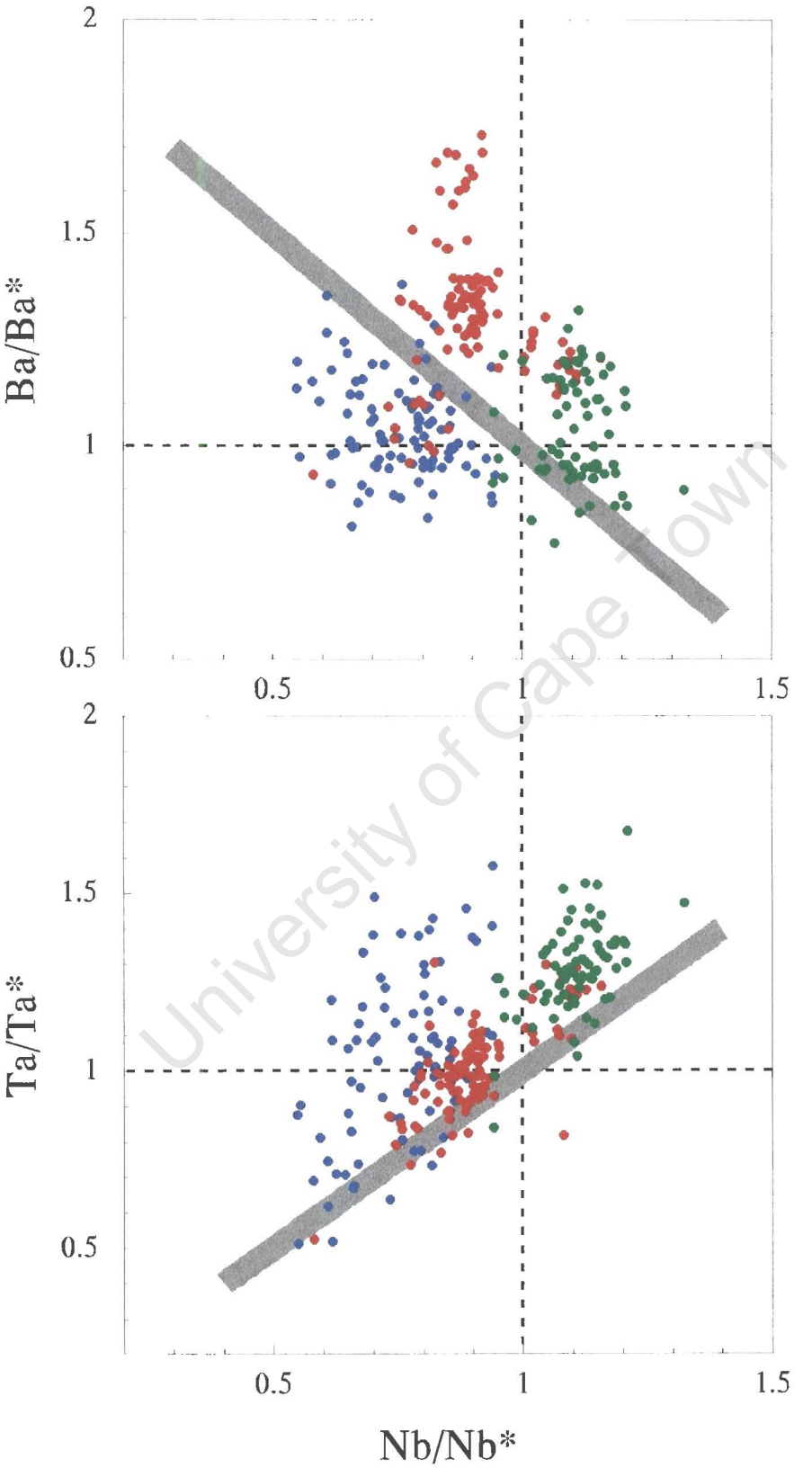

University of Cape Town

Figure 5.5a: Ba/Ba* and Ta/Ta* versus Nb/Nb* (for details of calculations see caption to fig. 5.4) for N-MORB (blue markers), Discovery-influenced MORB (red markers) and Shona-influenced MORB (green markers). Thick grey lines indicate negative and positive 1:1 correlations between Ba/Ba* and Nb/Nb*, and Ta/Ta* and Nb/Nb* respectively. All data plotted > LLD + 2σ.

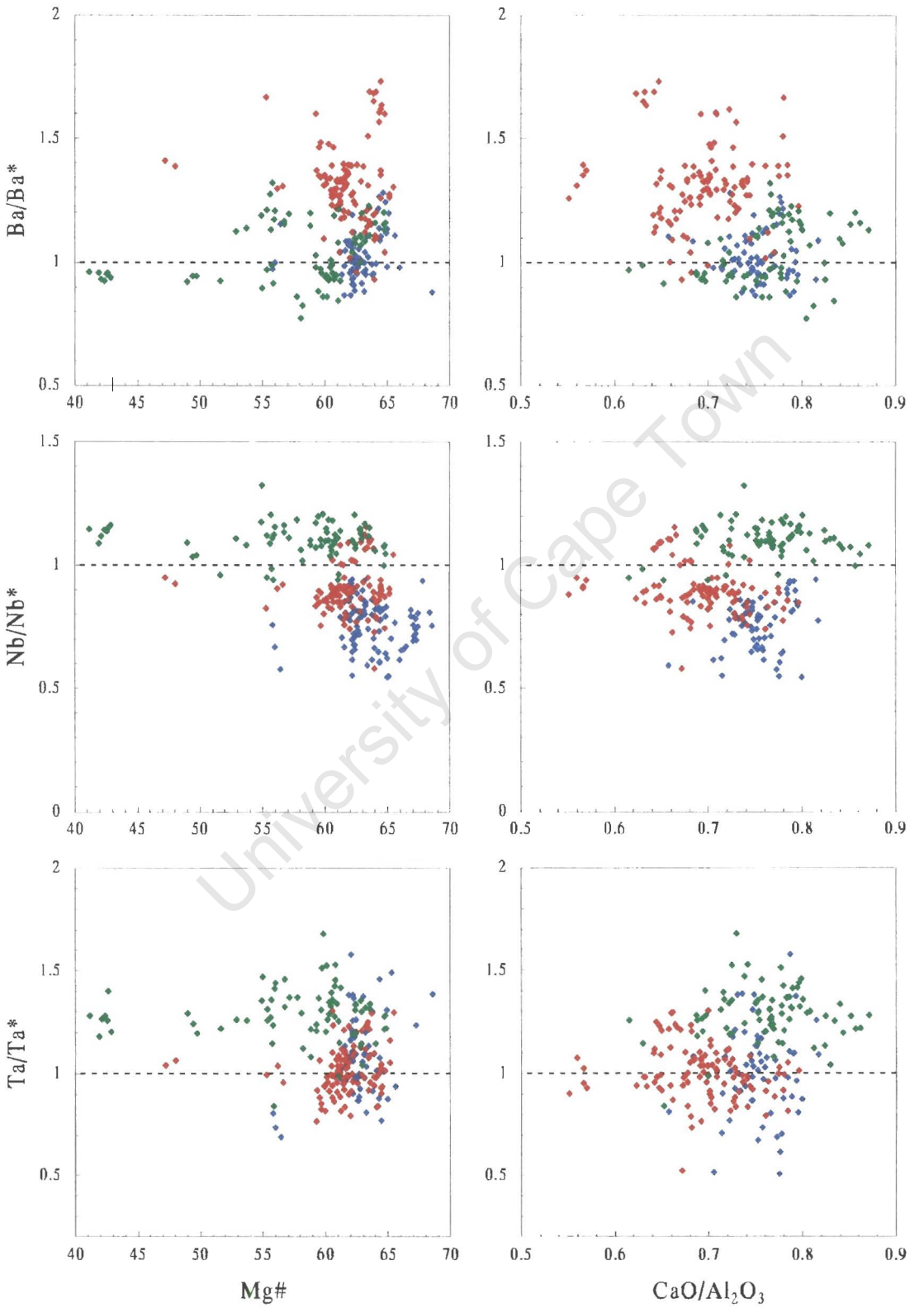

University of Cape Town

Figure 5.5b: Ba/Ba*, Nb/Nb* and Ta/Ta* (see caption to fig. 5.4 for details of calculation) versus Mg# (Fe_2O_3/FeO = 0.15) and CaO/Al_2O_3 for N-MORB (blue markers), Discovery-influenced MORB (red markers), and Shona-influenced MORB (green markers). All data plotted > LLD + 2σ.

influenced MORB.

The diagrams in fig. 5.5b indicate that the most-significant Ba/Ba*, Nb/Nb* and Ta/Ta* anomalies occur in basalts with high Mg#'s and a wide range of CaO/Al_2O_3 values. Mg# and CaO/Al_2O_3 can be viewed as proxies for phenocryst crystallisation, with progressive olivine or clinopyroxene crystallisation decreasing Mg#, while progressive plagioclase or clinopyroxene crystallisation will decrease CaO/Al_2O_3. Phenocryst crystallisation can therefore be eliminated as a possible origin of these incompatible trace-element anomalies. The negligible ability of phenocryst crystallisation to significantly affect the values of the above-mentioned three anomalies further is underscored by the limited range of Ba/Ba*, Nb/Nb*, and Ta/Ta* values in Shona-influenced MORB, although these basalts span an extensive range in Mg# and CaO/Al_2O_3 values.

The negative Sr and Eu anomalies observed in the compositions of some basalts, especially Discovery- and Shona-influenced MORB, can be accounted for through plagioclase crystallisation. These anomalies occur in basalts with low Mg#'s and CaO/Al_2O_3 values, which are indicative of plagioclase phenocrysts having been removed from the bulk magma systems. This also explains the linked occurrence of these anomalies, due to Sr and Eu being preferentially partitioned into plagioclase during crystallisation, the two elements are expected to vary sympathetically.

University of Cape Town

Summary. The observed range from incompatible trace-element enriched to depleted compositions in MORB from the SMAR correlate with radiogenic isotopic data for the same samples. This link confirms that the trace-element compositional characteristics observed in the basalts are due to the influences of the Discovery and Shona mantle plumes on the mantle source-regions from which these basalts were derived (Douglass *et al.*, 1999). The co-variations of the data for the Zr/Nb and La/Nb with Ba/Nb ratios of basalts recovered from the SMAR indicate that most of the Discovery-influenced MORB define a compositional trend from N-MORB towards the recognised compositions of some basalts from the Walvis Ridge, and Tristan da Cunha and Gough ocean islands. Most of the Shona-influenced MORB define a different trend from N-MORB towards the recognised compositions of basalts from the St. Helena, Bouvet and Marion ocean islands. Incompatible trace-element enriched basalts recovered from southern Discovery-influenced ridge segments have significantly lower Nb concentrations at

constant Ba concentrations relative to other Discovery-influenced MORB. N-MORB in general also have low Nb concentrations, relative to compositions of "typical" N-MORB.

The incompatible trace-element data for MORB recovered from the SMAR further exhibit significant anomalous primitive mantle-normalised Ba, Nb and Ta abundances relative to values expected based on concentrations of trace elements of similar compatibility. The positive Ba, and negative Nb and Ta anomalies occur predominantly in N-MORB and southern Discovery-influenced MORB. These anomalies exhibit some degree of internal correlation, but not with the Mg# or CaO/Al_2O_3 values for the basalts. These anomalies are therefore inherited from the compositions of the mantle source-regions from which the basalts were derived, and not the products of phenocryst crystallisation.

5.2 POSSIBLE ORIGINS OF OBSERVED INCOMPATIBLE TRACE-ELEMENT ANOMALIES IN MANTLE SOURCE-REGIONS

The anomalies in the primitive mantle-normalised Ba, Nb, and Ta abundances primarily observed in compositions of N-MORB and southern Discovery-influenced MORB were inherited from the mantle source-regions from which these basalts were extracted. The origins of these anomalies are therefore linked to the compositional evolution of the upper-oceanic mantle beneath these ridge segments.

This section will first assess the broad compositional evidence for the possible contamination of certain mantle source-regions beneath the SMAR by material with compositional characteristics similar to continental lithosphere and/or subducted sediment. Modelling of trace-element abundances will then be employed to further assess this process of mantle source-region contamination and attempt to quantify the degree of contamination required to account for the observed anomalies.

Compositional evidence for the presence of continental lithosphere and/or subducted sediment in MORB mantle source-regions beneath the SMAR. The primitive-mantle normalised incompatible trace-element data for representative N-MORB and southern Discovery-influenced MORB are presented in fig. 5.6. The previously discussed negative Nb anomalies are especially noticeable in the compositions of the N-MORB from dredges 43 & 11 in fig. 5.6, while the positive Ba anomalies are more prominent in the incompatible trace-element

University of Cape Town

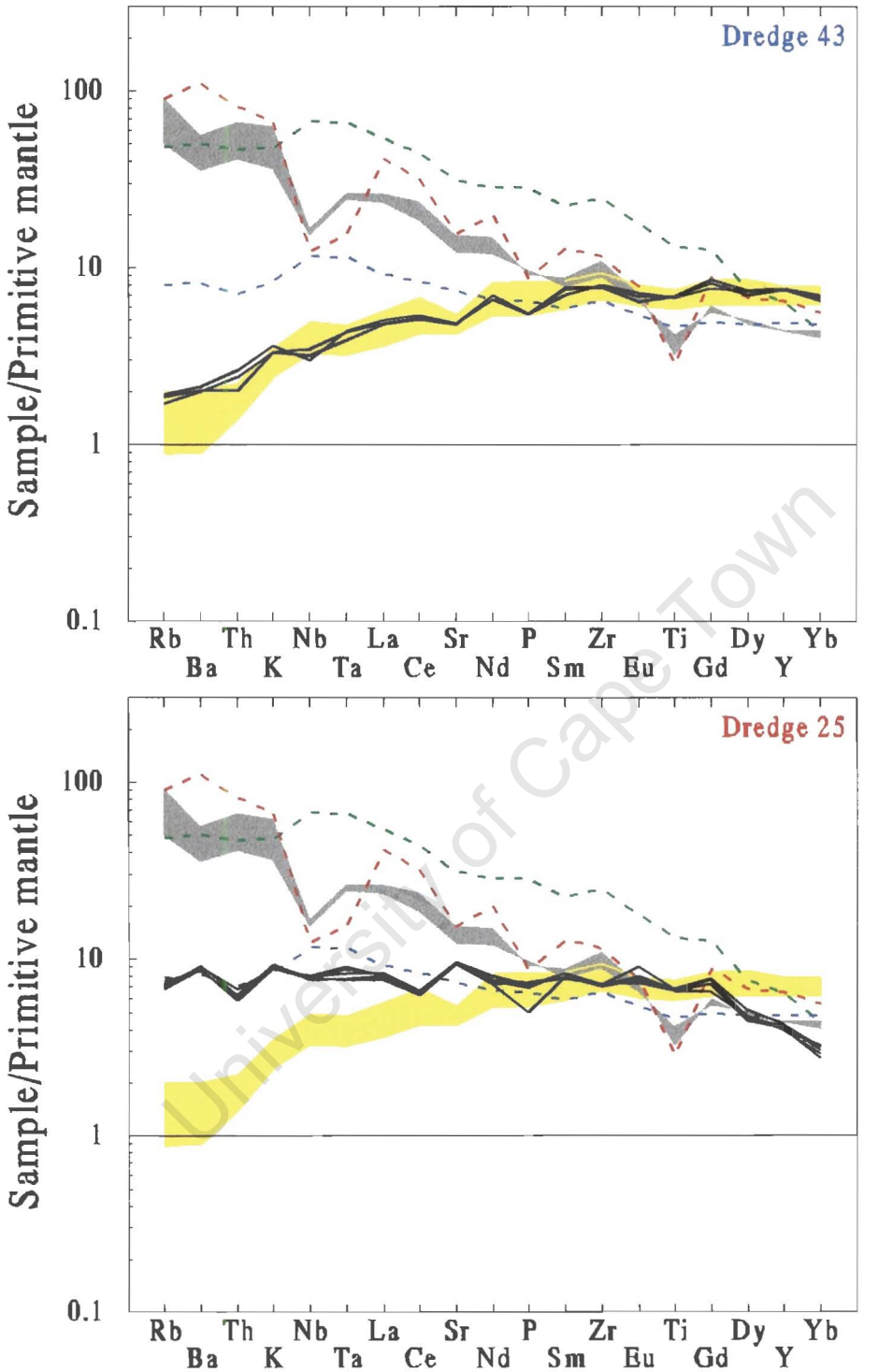

University of Cape Town

Figure 5.6: Primitive-mantle (Sun & McDonough, 1989) normalised incompatible trace-element diagrams, with elements in order of decreasing incompatibility (after Hofmann, 1997; Sun & McDonough, 1989), for selected MORB from the SMAR. Solid black lines: observed compositions of MORB from the SMAR; yellow field: typical compositional range for N-MORB (Hofmann, 1988; Sun & McDonough, 1989); blue dashed-line: typical composition of E-MORB; green dashed-line: typical composition of OIB (Sun & McDonough, 1989); grey field: typical compositional range for average continental crust (Hofmann, 1988; Rudnick & Fountain, 1995); red dashed-line: composition of average subducted sediment (Plank & Langmuir, 1998), all normalised to the primitive-mantle composition of Sun & McDonough (1989). Diagrams in order of increasing latitude of dredge-station location, with blue dredge numbers: N-MORB, and red dredge numbers: southern Discovery-influenced MORB. All plotted data > LLD + 2σ.

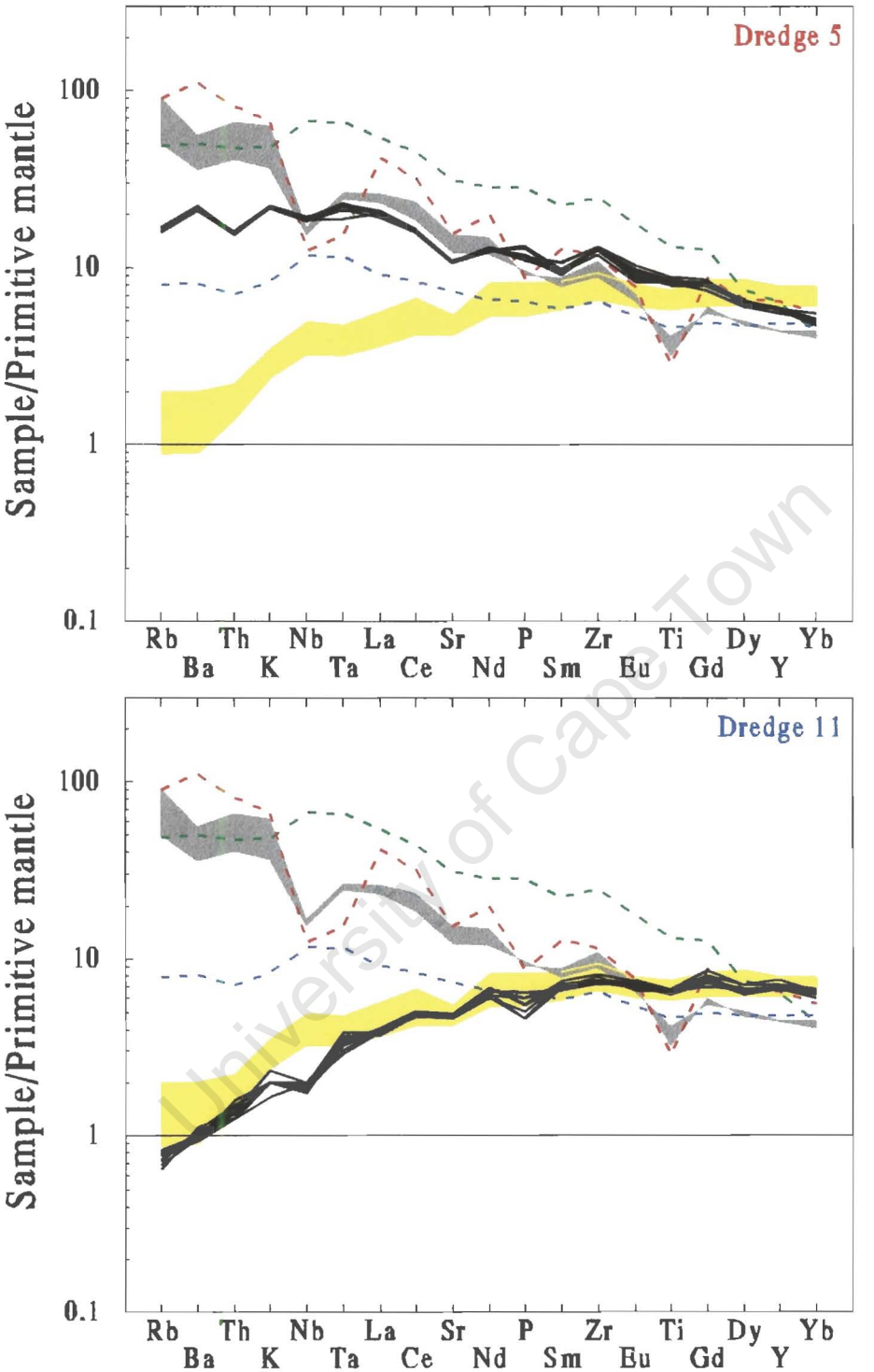

University of Cape Town

Figure 5.6 (cont.):

enriched compositions of the basalts from dredges 25 & 5.

The diagrams in fig. 5.6 are similar to those in fig. 5.3, but with the notable difference that the diagrams in fig. 5.6 also illustrate the compositions of average continental crust (Hofmann, 1988; Rudnick & Fountain, 1995) and average subducted sediment (Plank & Langmuir, 1998). The data for average continental crust in fig. 5.6 contain distinct negative anomalies for primitive mantle-normalised Ba, Nb and Ti abundances relative to trace elements of similar compatibility, and only moderate anomalously negative values for primitive mantle-normalised Ta abundances. The data for average subducted sediment exhibit a moderate anomalously positive value for primitive mantle-normalised Ba abundances relative to trace elements of similar compatibility; and distinct negative anomalies for primitive mantle-normalised Nb, Ta, Sr, P and Ti abundances. The observed primitive mantle-normalised incompatible trace-element abundance patterns for some N-MORB and southern Discovery-influenced MORB exhibit systematics in Nb, Ta, and to a lesser degree Ba, abundances which are similar to characteristic observed in the composition of average continental crust. However, primitive-mantle normalised incompatible trace-element patterns for other N-MORB and southern Discovery-influenced MORB feature anomalous Nb and especially Ta and Ba abundances which are in better agreement with the data presented for average subducted sediment.

University of Cape Town

The diagrams illustrating the latitudinal systematics of Ba/Ba*, Nb/Nb* and Ta/Ta* data for the MORB recovered from the SMAR plotted in fig. 5.4 are reproduced in fig. 5.7, but these diagrams now also contain the compositional values or ranges for the above ratios calculated for "typical" N-MORB, E-MORB, OIB, average continental crust and average subducted sediment from literature sources. The negative (<1) values observed in the Nb/Nb*, and to a lesser degree in the Ta/Ta*, compositions of N-MORB and Discovery-influenced MORB are displaced from the fields for "typical" N-MORB and E-MORB toward the fields and lines representing the compositions of average continental crust and average subducted sediment. The Nb/Nb* and Ta/Ta* values for Shona-influenced MORB are fairly restricted and cluster between the data for "typical" N-MORB, and E-MORB and OIB. Most N-MORB and Discovery-influenced MORB have positive (>1) Ba/Ba* values which plot above the fields for "typical" N-MORB, and even "typical" E-MORB and OIB, and the data for most N-MORB and Discovery-influenced MORB plot at anomalously high Ba/Ba* values towards and above the

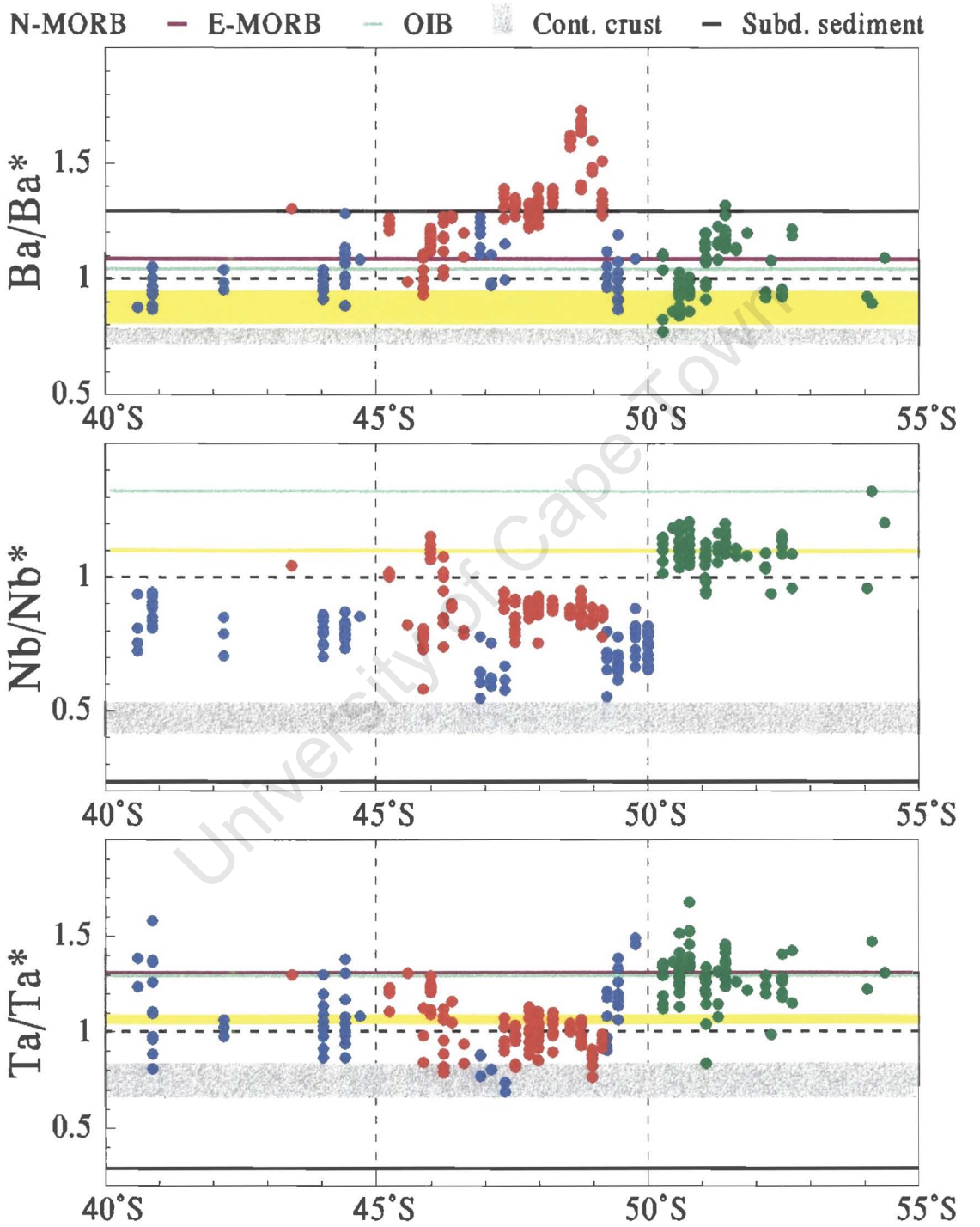

University of Cape Town

Figure 5.7: Diagrams of trace element anomalies versus latitude. Anomalies quantified using the following formula: $Y/Y^* = (Y_{Observed})_N / [(X_{Observed})_N \cdot (Z_{Observed})_N]^{½}$, were Y=element of interest; X, Z= "neighbour" elements on primitive-mantle normalised incompatible trace-element diagrams, such as in fig. 5.6. Selected X & Z for Ba: Rb, Th; for Nb: K, La; for Ta: K, La. "Typical" N-, E-MORB, OIB, average continental crust and average subducted sediment from same literature sources as in fig. 5.6. All data plotted > LLD + 2σ.

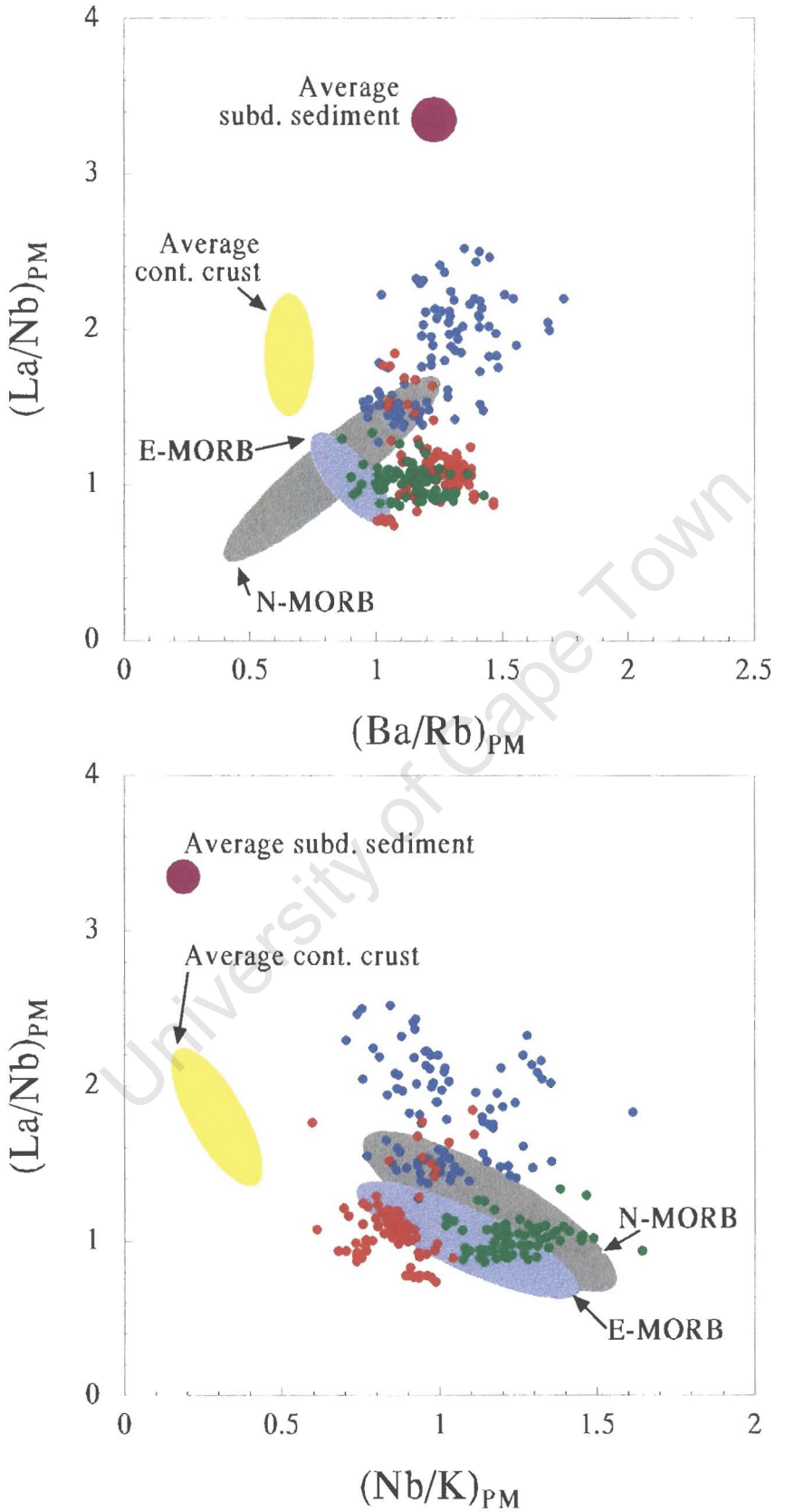

University of Cape Town

Figure 5.8: Primitive-mantle normalised (Sun & McDonough, 1989) La/Nb versus Ba/Rb and Nb/K for N-MORB (blue markers), Discovery-influenced MORB (red markers) and Shona-influenced MORB (green markers). Filled fields indicate compositions typical for the labelled components (see caption of fig. 5.6 for references). All data plotted > LLD + 2σ.

composition of average subducted sediment. The Ba/Ba* data for Shona-influenced MORB are mostly negative, more varied than the data for Nb/Nb* and plot around the compositions of "typical" N-, E-MORB and OIB, although some samples plot at positive values towards the composition of average subducted sediment.

The systematics of the Nb/Nb* and Ta/Ta* data for N-MORB and Discovery-influenced MORB in fig. 5.7 indicate that material with compositions similar to average continental crust or average subducted sediment could have influenced the compositions of the mantle source-regions from which these basalts were derived. However, the Ba/Ba* data for the N-MORB and Discovery-influenced MORB are significantly off-set towards the positive Ba/Ba* composition of average subducted sediment, and not towards the negative Ba/Ba* compositions of average continental crust.

The compositional data of MORB from the SMAR are further presented on more familiar primitive-mantle normalised incompatible trace-element ratio-ratio plots in fig. 5.8. The trace-element ratios selected illustrate the anomalously low Nb abundances in N-MORB and Discovery-influenced MORB, relative to trace elements with similar compatibility, resulting in high $(La/Nb)_{PM}$ and low $(Nb/K)_{PM}$ ratios. The depletion of Ba, relative to trace elements with similar compatibility, in the composition of average continental crust and the enrichment of Ba in the composition of average subducted sediment enable good separation between these two components using $(Ba/Rb)_{PM}$. The data for N-MORB and Discovery-influenced MORB plot towards the compositions of both average continental crust and average subducted sediment in the $(La/Nb)_{PM}$ versus $(Nb/K)_{PM}$ diagram, but on the $(La/Nb)_{PM}$ versus $(Ba/Rb)_{PM}$ diagram these basalts plot significantly towards the composition of average subducted sediment.

Quantitative evaluation of the proposed process of mantle source-region contamination. The data are first investigated using the concentration ratios of highly incompatible trace elements, e.g. Ce/Pb and Nb/U, as geochemical "tracers" of mantle source-region compositions, as pioneered by Hofmann (1986, 1997) and recently assessed by Simms & DePaolo (1997). Due to extremely low concentrations of U in the MORB recovered from the SMAR and the potential for U to be affected by alteration (LaTourrette & Burnet, 1992, and references therein), only Ce and Pb data are presented in fig. 5.9. The Nb and U data exhibit qualitatively similar systematics. It is evident from this diagram that MORB recovered from the

University of Cape Town

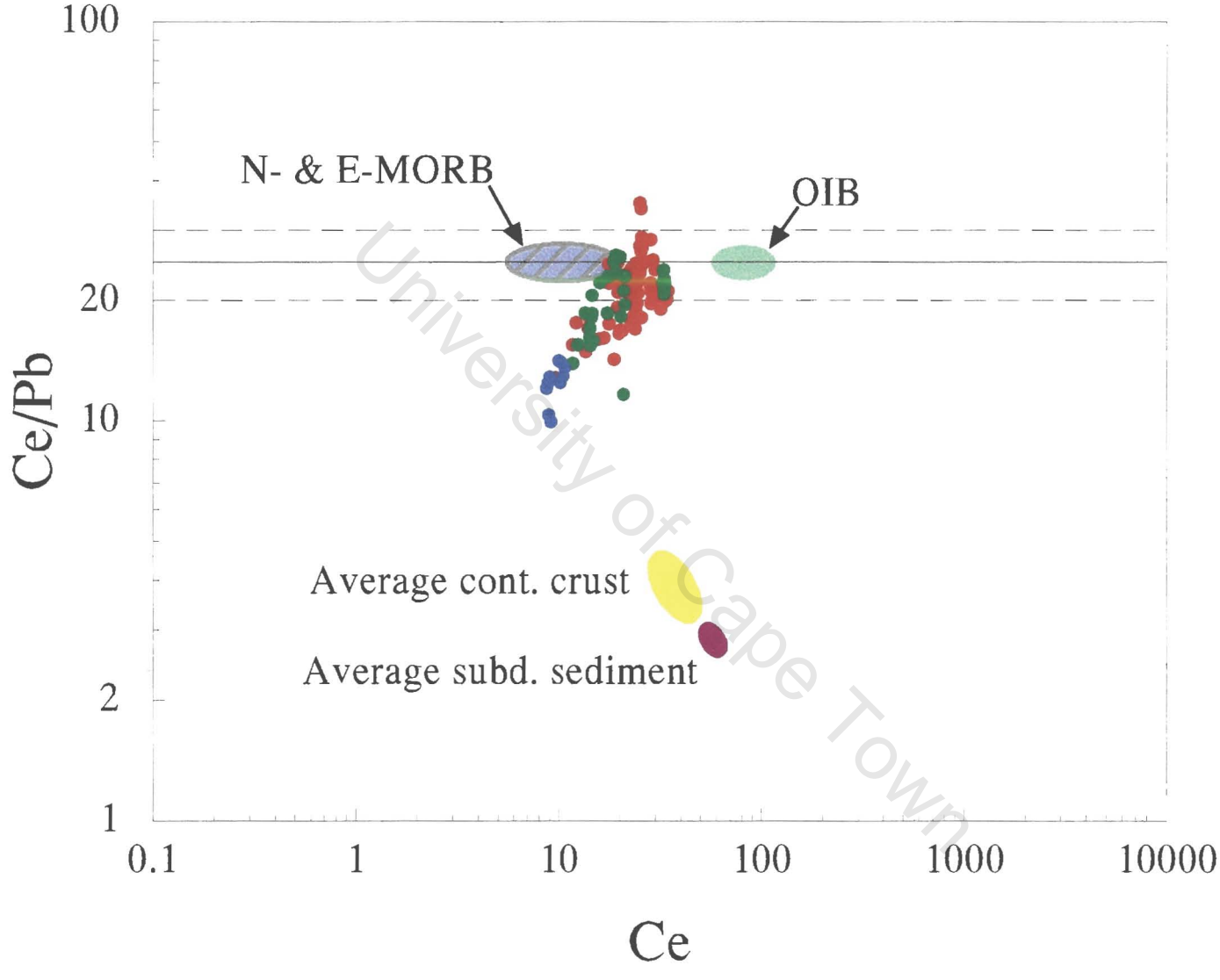

University of Cape Town

Figure 5.9: Ce/Pb versus Ce diagram for MORB from the SMAR. All literature data plotted for typical N- & E-MORB, OIB, average continental cryst and average subducted sediment from same references as in fig. 5.6. All data plotted > LLD + 2σ.

SMAR describe a trend extending below the mean Ce/Pb value of 25 ±5, defined as uniform and characteristic of global MORB, OIB and their respective mantle source-regions by Hofmann (1986), at low Ce concentrations. The extension of the data for these MORB beyond the global MORB and OIB fields to lower values of Ce/Pb could be due to the above-mentioned contamination of the relevant mantle source-regions, given the positions of compositional data for average continental crust and average subducted sediment in fig. 5.9.

The compositional effects of mixing between estimates of a MORB mantle source and average continental crust; and subsequent melting of resulting contaminated source-regions, are illustrated in fig. 5.10 (after Simms & DePaolo, 1997). The details of the calculations involved in the construction of the combined mixing and melting "grids" are given in the caption. To avoid any possible influences of phenocryst crystallisation on Ce and Pb concentrations, only samples with MgO > 6wt% were used and the remaining data were corrected to a reference value of 8wt% MgO (Simms & DePaolo, 1997). The data for MORB from the SMAR agree with a possible petrogenetic origin which involves: contamination of mantle source-regions with small degrees (<1.5%) of material with composition, at least in terms of Ce and Pb (as well as Nb & U), similar to average continental crust; and mean degrees of melting of these mantle source-regions, to yield magmas parental to the sampled MORB, ranging roughly between 10-20%. The data also agree best with melting during which Pb is slightly more compatible than Ce, leading to small, but significant, changes in Ce/Pb (diagram A compared to B). No conclusive distinction is possible in this modelling regarding the modal mineralogy of the mantle source-region (diagram A compared to C), although spinel-lherzolite is the generally accepted dominant mode of MORB mantle source-regions (Kinzler, 1997; Langmuir *et al.*, 1992). The parameters which define the above model are not well constrained and, consequently, the results should be viewed as semi-quantitative.

Again, these data alone are not conclusive regarding mantle source-region contamination, but taken in conjunction with the preceding primitive mantle-normalised incompatible trace-element anomalies and the radiogenic isotope data (Douglass *et al.*, 1999), a consistent structure is starting to emerge.

The compositional effects of either average continental crust or average subducted sediment being responsible for the contamination of the relevant mantle source-regions and the

University of Cape Town

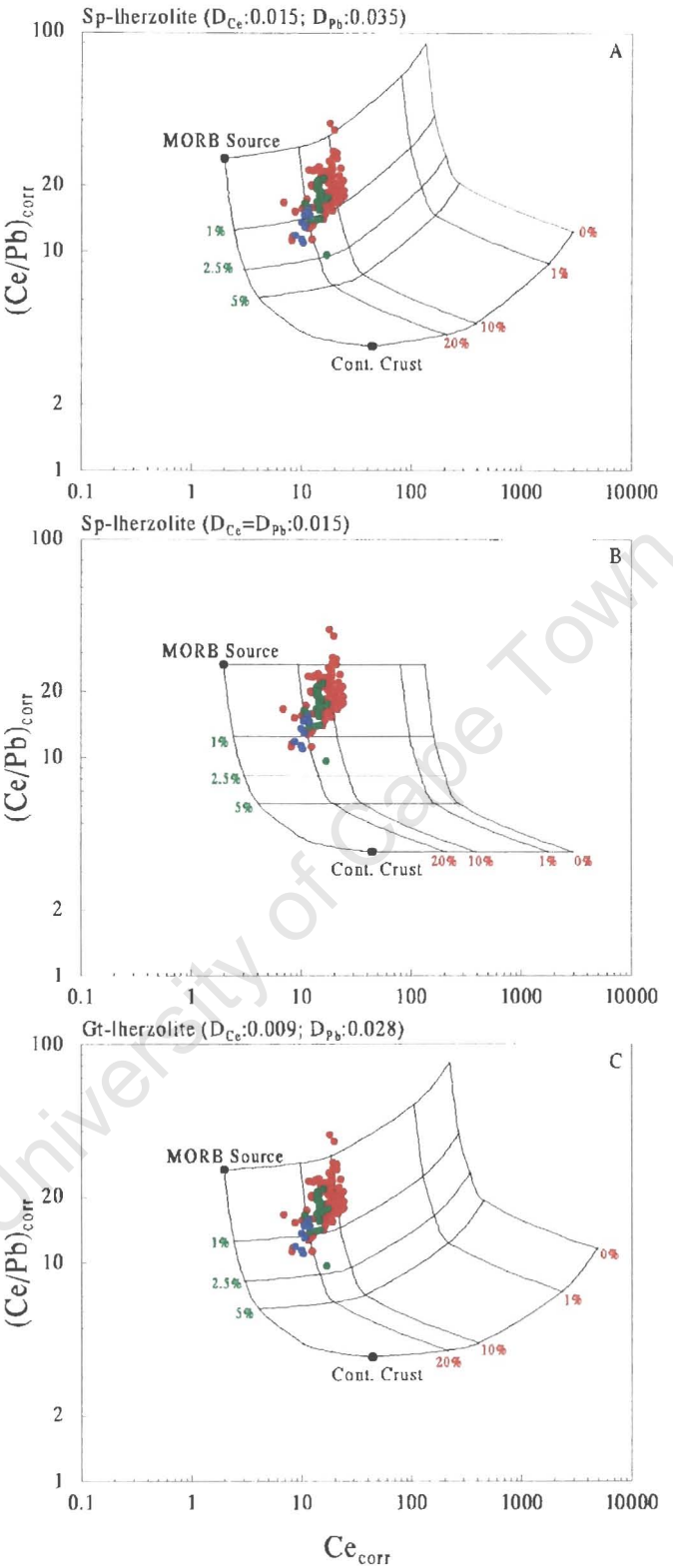

Figure 5.10: (Ce/Pb) versus Ce, with data corrected for fractionation to a value of 8wt% MgO. Mixing curves calculated using algorithm of Langmuir *et al.* (1978), dark-green labels indicate percentage contamination of MORB source by average continental crust. Data for compositions of MORB source and average continental crust; and source modal mineralogies for modelling of melting (spinel-lherzolite: olivine 46%; orthopyroxene 28%; clinopyroxene 18%; spinel 8% - and garnet-lherzolite: olivine 54%; orthopyroxene 17%; clinopyroxene 9%; garnet 20%), after Simms & DePaolo (1997). Melt compositions, dark-red labels indicate mean degrees of melting, modelled using the batch partial melting equation of Shaw (1970). Partition coefficients given in diagrams and taken from Simms & DePaolo (1997). All data plotted > LLD + 2σ.

University of Cape Town

possible role of mantle melting in the presence of residual garnet were further explored in terms of a wide range of incompatible trace-elements. Again, the modelling is fraught with assumptions and simplifications, but the essential results here are the general shapes of model-derived primitive mantle-normalised incompatible trace-element patterns, relative to the pattern observed for the compositions of "typical" N-MORB and E-MORB and the basalts from the SMAR.

The assumed compositions of the depleted MORB mantle (McKenzie & O'Nions, 1991; McKenzie & O'Nions, 1995) and average continental crust (Hofmann, 1988; Rudnick & Fountain, 1995) or average subducted sediment (Plank & Langmuir, 1998) used in this modelling are open to significant variations, as are the mantle modal mineralogies (Simms & DePaolo, 1997) and the incompatible trace-element partition coefficients (McKenzie & O'Nions, 1991; McKenzie & O'Nions, 1995), see table 5.1. Nonetheless, the results are summarised in diagrams in fig. 5.11a-b and indicate in fig. 5.11a that magmas, derived through mean degrees of batch partial melting (Shaw, 1970) between 10-20%, with mantle source-regions contaminated with <2.5% average continental crust contain primitive mantle-normalised Nb values significantly less than expected in "typical" N-, E-MORB and OIB. Compared to "typical" N-, E-MORB and OIB, similarly modelled magmas derived from mantle source-regions contaminated by <2.5% average subducted sediment, plotted in fig. 5.11b, contain not only significantly lower primitive mantle-normalised Nb values, but also significantly lower Ta values and slightly higher Ba values.

These modelled primitive mantle-normalised incompatible trace-element patterns are compared with the compositions of representative examples N-MORB and southern Discovery-influenced MORB in fig. 5.12, plotted previously in fig 5.6. The observed primitive mantle-normalised incompatible trace-element patterns in these MORB agree with patterns for magmas derived from mantle source-regions which contain a small degree (<2.5%) of material sharing compositional characteristics with both average continental crust and average subducted sediment. The patterns of the modelled magmas derived from spinel-lherzolite mantle source-regions are in agreement with most of these examples, but the observed patterns for the compositions of basalts recovered by dredge 25 are in better agreement with modelled magmas derived from a garnet-lherzolite mantle source-region. The presence of residual garnet during the mantle melting which produced basalts recovered from dredge 25, 7 and 6 will be

University of Cape Town

Table 5.1: Values, used in the calculations for fig. 5.11a-b, for the depleted mantle (McKenzie & O'Nions, 1991,1995), average continental crust (Hofmann, 1988; Rudnick & Fountain, 1995), average subducted sediment (Plank & Langmuir, 1998), partition coefficients (K_D's) (McKenzie & O'Nions, 1991,1995), and mantle modal mineralogies (Simms & DePaolo, 1997). All concentrations in ppm.

Element	Depleted mantle	Average crust	Average sub. sediment	K_D's Olivine	Opx	Cpx	Spinel	Garnet	Mantle modes (%)	Spinel-lherzolite	Garnet-lherzolite
Rb	0.062	39	57	0.00018	0.0006	0.001	0.0001	0.0007	**Olivine**	46	54
Ba	0.650	344	776	0.0003	0.0001	0.0005	0.0001	0.0005	**Opx**	28	17
Th	0.007	4.9	6.9	0.0001	0.0001	0.00026	0	0.0001	**Cpx**	18	9
K	20	13493	16935	0.00018	0.001	0.002	0.0001	0.001	**Spinel**	8	
Nb	0.390	11	9	0.005	0.005	0.02	0	0.07	**Garnet**		20
U	0.002	1.2	1.7	0.0001	0.0001	0.00036	0	0.0001			
Ta	0.018	0.9	0.6	0.005	0.005	0.02	0	0.04			
La	0.206	17	29	0.0004	0.002	0.054	0.01	0.01			
Ce	0.722	39	57	0.0005	0.003	0.098	0.01	0.01			
Pb	0.016	11.0	19.9	0.0001	0.0013	0.01	0	0.0005			
Sr	14.7	304	327	0.002	0.007	0.130	0.000	0.001			
Nd	0.815	19	27	0.001	0.0068	0.21	0.01	0.087			
P	51	916	829	0	0.03	0.03	0	0.1			
Sm	0.299	3.8	5.8	0.0013	0.01	0.26	0.01	0.217			
Zr	7.19	116	130	0.01	0.03	0.1	0	0.32			
Eu	0.115	1.2	1.3	0.0016	0.013	0.31	0.01	0.32			
Ti	1020	4757	3716	0.02	0.1	0.18	0.15	0.28			
Gd	0.419	3.5	5.3	0.0015	0.016	0.3	0.01	0.498			
Dy	0.525	3.6	5.0	0.0017	0.022	0.33	0.01	1.06			
Y	3.18	20	30	0.005	0.005	0.2	0	2.11			
Yb	0.347	2	3	0.0015	0.049	0.28	0.01	4.03			

University of Cape Town

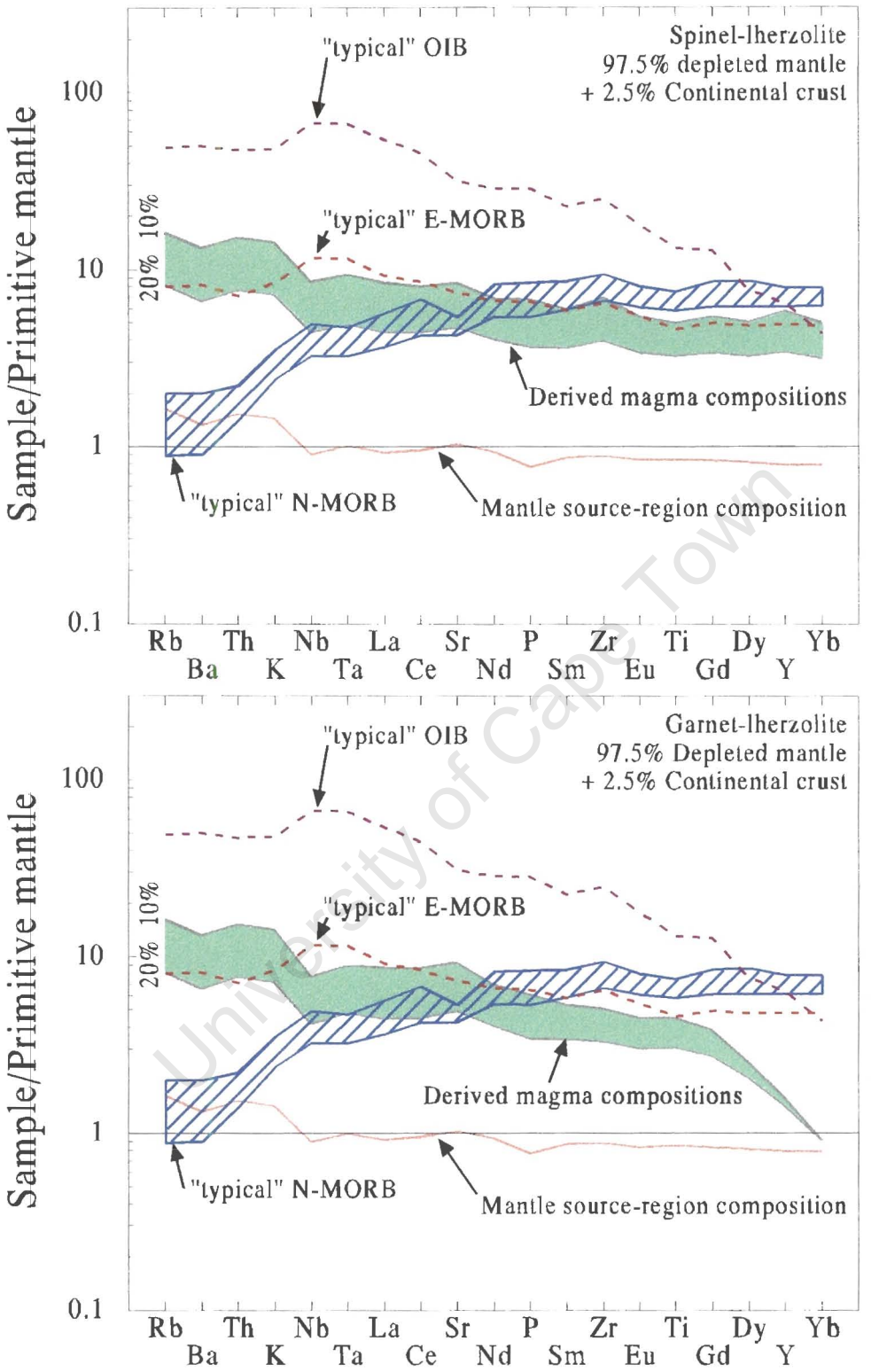

University of Cape Town

Figure 5.11a: Primitive mantle-normalised incompatible trace-element diagrams of mantle source-region compositions (pink line), derived from contaminating a depleted mantle composition (McKenzie & O'Nions, 1991; 1995) with average continental crust (Hofmann, 1988; Rudnick & Fountain, 1995), and magma compositions (green fields) derived from this mantle source-region through batch partial melting (Shaw, 1970) to 10%-20% (labelled grey lines). The mantle modes used are the same as referenced in fig. 5.10 (from Simms & DePaolo, 1997), and the partition coefficients are from McKenzie & O'Nions (1991, 1995). Compositions of "typical" N-MORB, E-MORB and OIB represented by labelled blue field, red dashed line and purple dashed lines, reproduced from and referenced in fig. 5.6

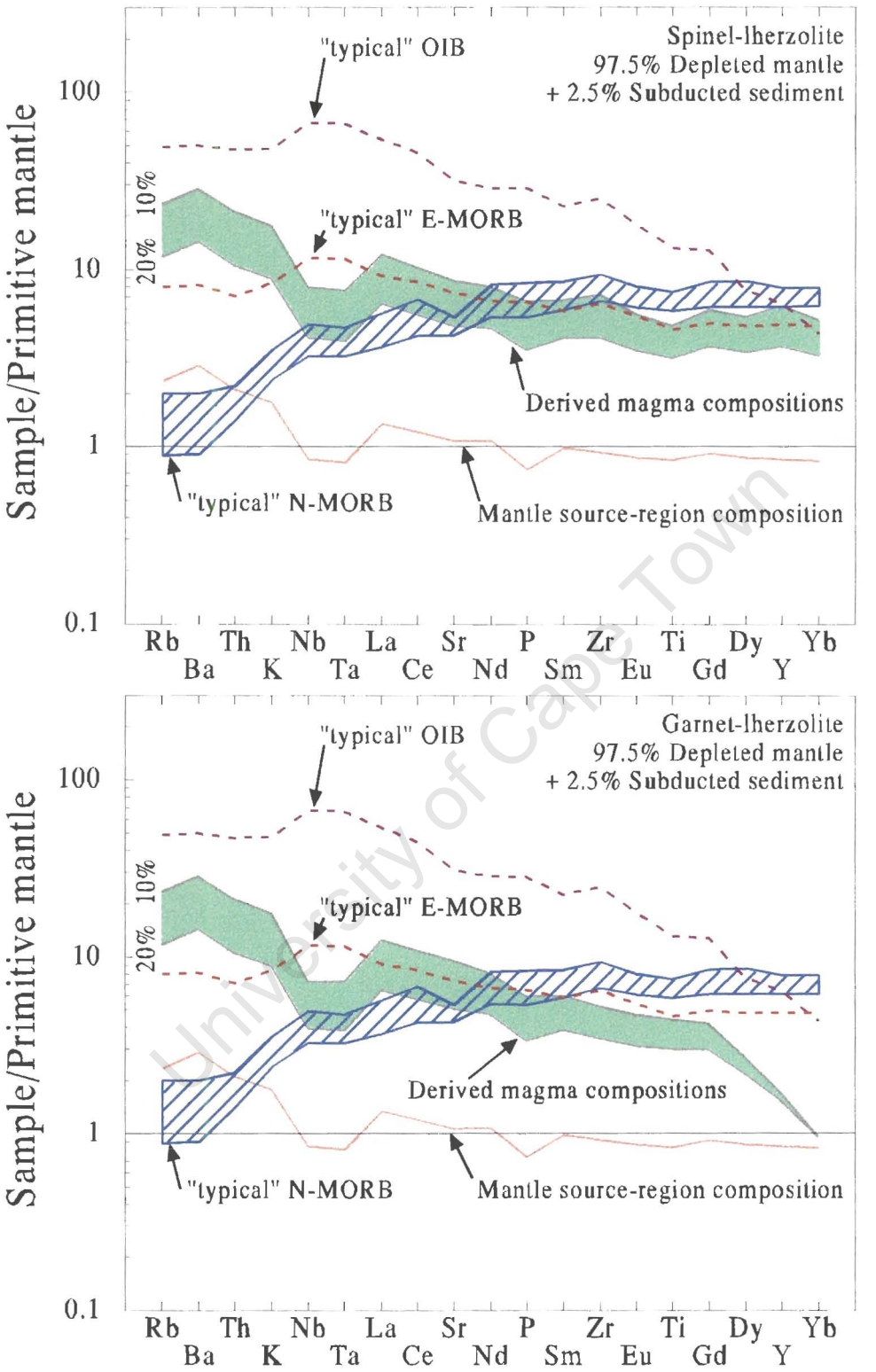

University of Cape Town

Figure 5.11b: Primitive mantle-normalised trace-element diagrams of mantle source-regions (pink lines) and batch partial melts (green fields) derived as in fig. 5.11a, but with source of contamination being average subducted sediment (Plank & Langmuir, 1998).

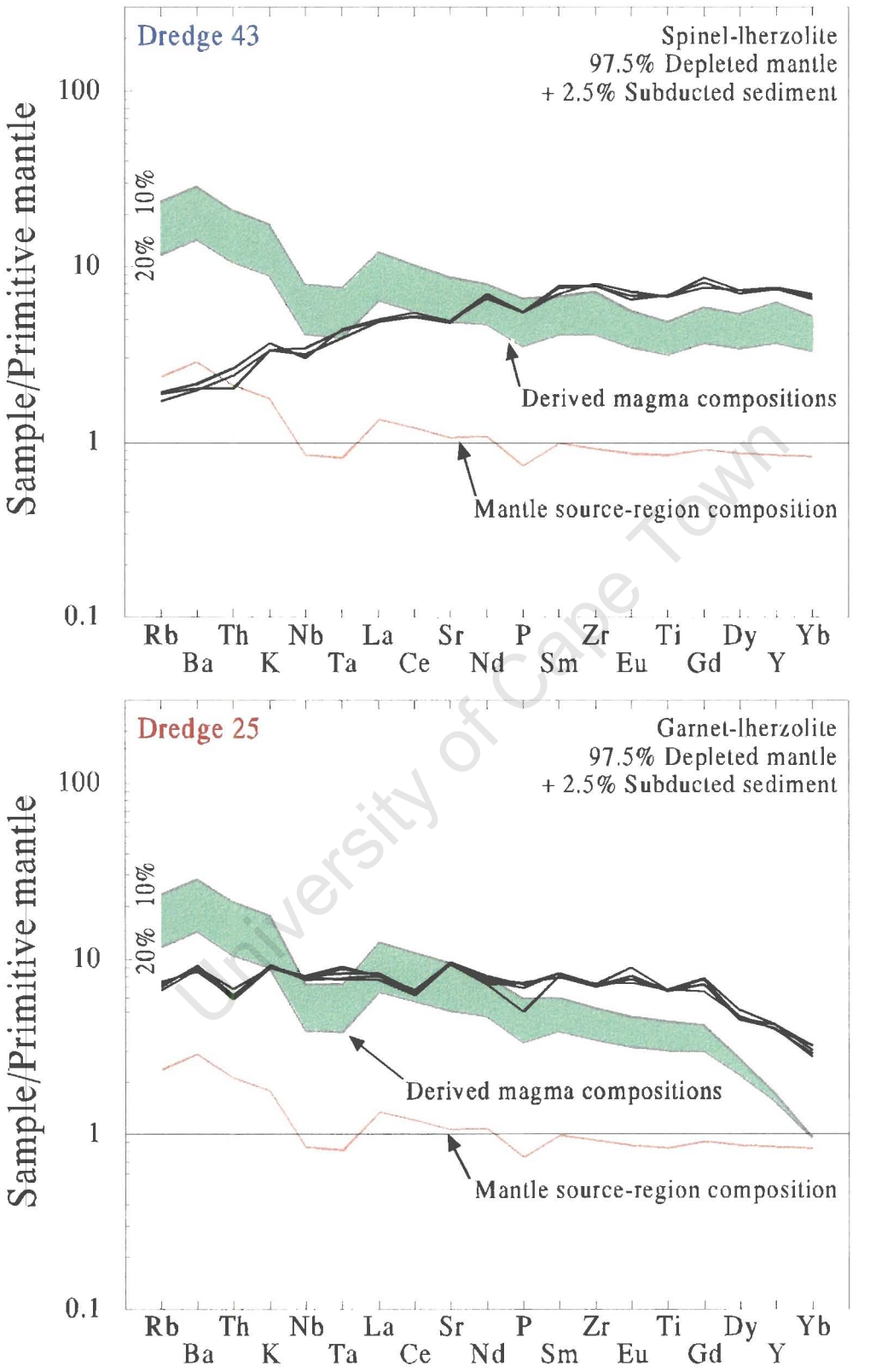

University of Cape Town

Figure 5.12: Primitive mantle-normalised (Sun & McDonough, 1989) incompatible trace-element diagrams comparing the compositions of representative N-MORB (blue dredge labels) and southern Discovery-influenced MORB (red dredge labels) with the modelled compositions of magmas produced by 10-20% melting (green fields) of spinel-lherzolite depleted mantle source-region, but garnet-lherzolite in the case of dredge 25, contaminated with 2.5% of average subducted sediment (see text and fig. 5.11a-b).

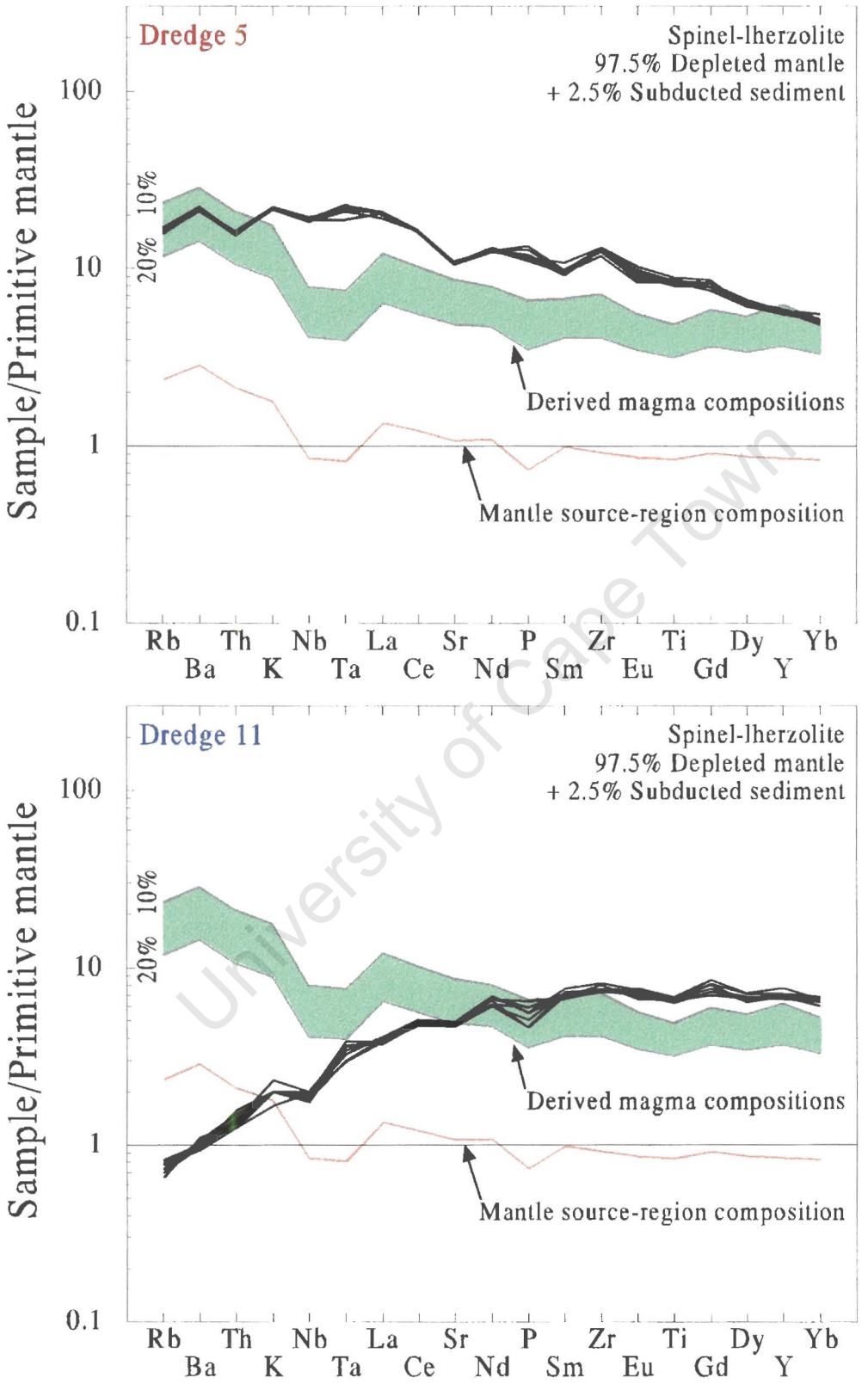

University of Cape Town

Figure 5.12 (cont.)

extensively addressed in chapter 6.

Summary. The observed anomalously low Nb, and to a lesser degree Ta, and high Ba abundances, relative to trace elements with similar compatibility, in the compositions of especially N-MORB and southern Discovery-influenced MORB are due to the compositional contamination of the mantle source-regions from which these basalts were derived. The composition of the likely contaminant share distinctive characteristics with the compositions of average continental crust and average subducted sediment.

The observed incompatible trace-element anomalies mentioned above can in general be accounted for by contaminating spinel-lherzolite mantle source-regions from which the basalts were derived with <2.5% of material with compositional characteristics of both average continental crust and average subducted sediment. The compositions of some of the basalts from the southern Discovery-influenced ridge segments, i.e. dredges 25, 7 & 6, exhibit observed depletions in HREE which are most-easily explained by the presence of residual garnet during the mantle melting from which these basalts were derived.

University of Cape Town

5.3 DISCUSSION

Trace-element characteristics of mantle source-regions beneath the SMAR. A number of studies of MORB and OIB from the South Atlantic Ocean have addressed the compositional interaction between mantle plumes and the ambient asthenospheric mantle beneath mid-ocean ridges (Douglass *et al.*, 1999; Douglass *et al.*, 1995; Fontignie & Schilling, 1996; Hanan *et al.*, 1986; Humphris *et al.*, 1985; le Roex *et al.*, 1987; Schilling *et al.*, 1985). The favoured and most successful tools used to define this compositional influence on MORB from the SMAR have been radiogenic isotope data, with incompatible trace-element data as support, or occasionally as primary means of investigation (e.g. Douglass *et al.*, 1999; Douglass *et al.*, 1995), or noble gas data to a much lesser degree (Kurz *et al.*, 1998; Moreira *et al.*, 1995). The geophysical observations of ridge-mantle plume interactions along the SMAR have, in addition, provided further support for the abovementioned geochemical studies (Small, 1995; Small *et al.*, 1994; Small *et al.*, 1995).

The radiogenic isotope and incompatible trace-element characteristics of South Atlantic mantle plumes are well-defined (e.g. Kempe & Schilling, 1974; le Roex, 1985; le Roex *et al.*,

1990; Weaver, 1991; Weaver *et al.*, 1987). The observed coupling between distinct radiogenic isotope data, ascribed to the compositional influences of specific mantle plumes on sub-ridge mantle source-regions, and incompatible trace-element enrichments in these MORB is therefore to be expected (Fontignie & Schilling, 1996; Humphris *et al.*, 1985).

The combined radiogenic isotope data and incompatible trace-element data presented in this chapter supports the observation made in the previous chapter regarding the inherently different compositions of the Discovery and Shona mantle plumes. The distinct mixing trajectories defined by the compositions of basalts recovered from the SMAR in the diagrams in fig 4.14 are due to two quite dissimilar enriched end-member compositions, represented by the Discovery and Shona mantle plumes, interacting with the ambient depleted MORB mantle beneath the SMAR. The Discovery mantle plume is compositionally similar to the EM mantle component, while the Shona mantle plume is compositionally associated with the HIMU mantle component. The compositions of basalts derived from the ambient MORB mantle have trace-element and radiogenic-isotope characteristics (Douglass *et al.*, 1999) which indicate some broad compositional contamination or "pollution" of the upper-oceanic mantle beneath the South Atlantic.

Proposed model of contamination of the upper oceanic mantle beneath the South Atlantic with delaminated subcontinental lithosphere. This discussion will first present compositional evidence from earlier studies of MORB from neighbouring and overlapping sections of the SMAR which extend the geographic area affected by the proposed process of contamination. A model will then be proposed, building on the work of Douglass *et al.* (1999), in which the upper oceanic mantle beneath the SMAR experienced low-degree compositional contamination by widely dispersed material derived from delaminated subcontinental lithosphere thermally eroded from beneath southern Africa during the breakup of Gondwana and the opening of the South Atlantic, and embedded and preserved in the surrounding asthenosphere.

The compositional characteristics of MORB from the SMAR to the north of the present section studied have indicated some degree of broad "pollution" of the mantle source-regions beneath the SMAR. This has been noted especially in radiogenic isotope data, which show decreasing trends southward from the St. Helena-influenced ridge-segments in $^{206}Pb/^{204}Pb$, $^{143}Nd/^{144}Nd$ and increasing $^{87}Sr/^{86}Sr$ (Fontignie & Schilling, 1996; Hanan *et al.*, 1986). The

University of Cape Town

radiogenic isotope data for the MORB from the section of the SMAR further southward, investigated in this study, extends these trends up to the Shona-influenced ridge-segments (Douglass *et al.*, 1999; see their fig. 3).

Although not specifically reported at the time, the incompatible trace-element data for bulk-rock MORB samples from the northern section of the SMAR have anomalous Ba/Nb ratios similar to the data for MORB from the presently studied section of the SMAR (Humphris *et al.*, 1985), see fig. 5.13. The same is true for MORB from the southernmost section of the SMAR, previously investigated by le Roex *et al.* (1987), also plotted in fig. 5.13. Quenched igneous glasses of the MORB from this earlier study were analysed in the present study and confirmed the bulk-rock data. Furthermore, Douglass & Schilling (1998) reported elevated Ba/Nb values for quenched igneous glasses from 3-46°S, including samples from Humphris *et al.* (1985), however, these data have not been published and could not be incorporated into fig. 5.13. The general overlap between incompatible trace-element characteristics of MORB from previous work on the SMAR between 32°-46°S (Humphris *et al.*, 1985) and 51°-54.5°S (le Roex *et al.*, 1987) with those for MORB from the ridge section between 40°-55°S is further illustrated in diagram A of fig. 5.14. Comparing data from bulk-rock samples (aphyric to moderately phyric, MgO > 6wt%) with data from quenched igneous glasses is not ideal, but nevertheless, the data from 32°-46°S are consistent with mixing between the enriched mantle material of the Tristan/Gough mantle plume with ambient depleted mantle which might have experienced some anomalous elevation of Ba/Nb. The bulk-rock data for basalts from 51°-54.5°S plot at significantly higher Ba/Nb values compared to quenched igneous-glass data for Shona-influenced MORB, some of which are from the same samples or ridge-segments. This might be due to bulk-rock samples used from le Roex *et al.* (1987) having at least moderate amounts of phenocrysts, although an explanation is not clear. Bulk-rock data for MORB from the two other mid-ocean ridges in the South Atlantic, the America-Antarctic Ridge (AAR) (le Roex *et al.*, 1985) and Southwest Indian Ridge (le Roex *et al.*, 1983), are presented in diagram B of fig. 5.14. These data are however dominated by the previously identified compositional influence of the Bouvet mantle plume (le Roex *et al.*, 1983; le Roex *et al.*, 1985).

The basalts recovered from the SMAR have incompatible trace-element and radiogenic isotope compositions which indicate that the ambient upper-oceanic mantle beneath the South Atlantic from ~30°S to at least as far south as the off-set transform at ~50°S, which defines the

University of Cape Town

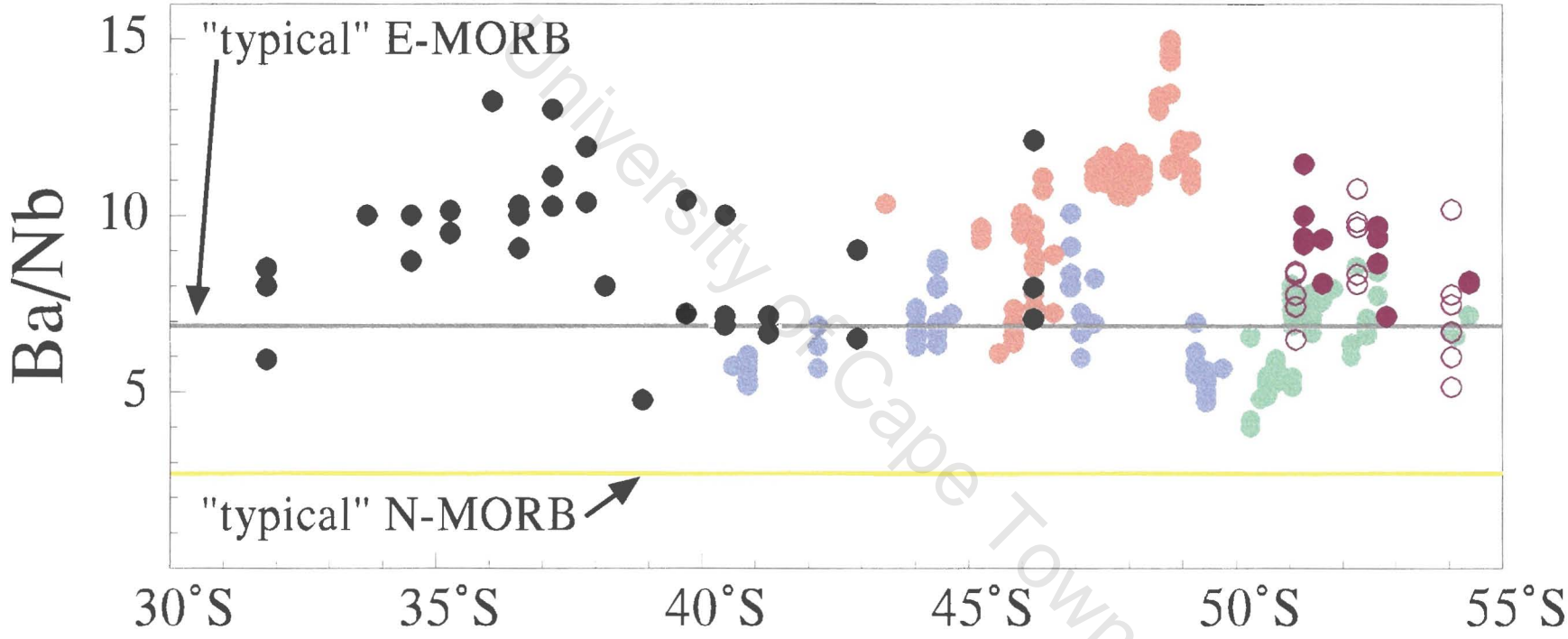

University of Cape Town

Figure 5.13: Ba/Nb versus latitude with N-MORB (light blue markers), Discovery-influenced MORB (light red markers) and Shona-influenced MORB (light green markers). Also plotted are MORB bulk-rock data from Humphris *et al.* (1985) as black markers and MORB bulk-rock data from le Roex *et al.* (1987) as purple markers, with filled markers from ridge axis and open markers from fracture zones. Compositions of "typical" N-MORB and "typical E-MORB represented by labelled lines (Sun & McDonough, 1989). All bulk-rock data from aphyric to moderately phyric samples (when specified), with MgO > 6wt%.

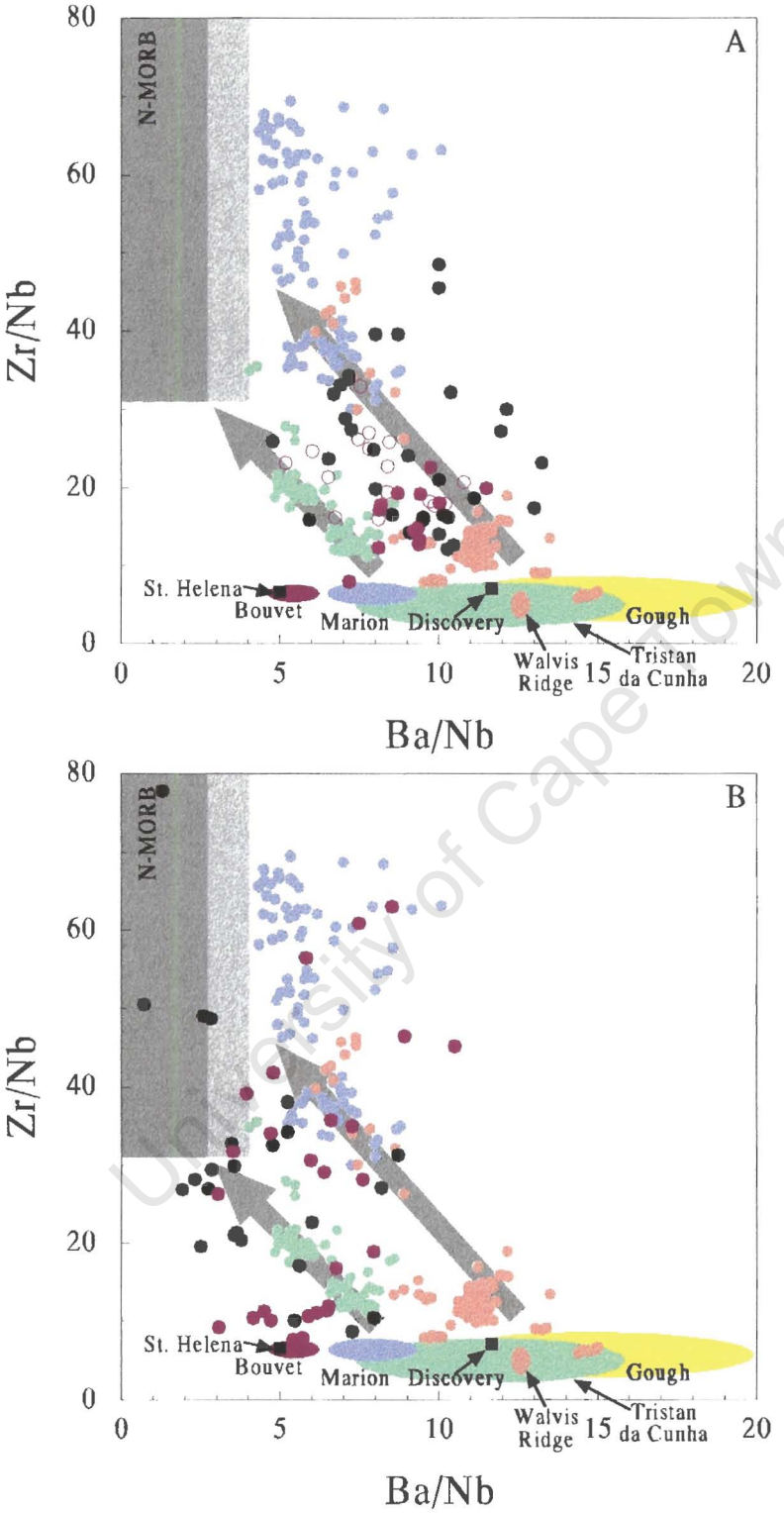

University of Cape Town

Figure 5.14: Zr/Nb versus Ba/Nb data for other MORB (bulk-rock samples with MgO > 6wt%; aphyric to moderately phyric, when specified) from the South Atlantic, compared with data for MORB data from the current study. N-MORB as light blue markers, Discovery-influenced MORB as light red markers, and Shona-influenced MORB as light green markers. Data for OIB from the South Atlantic and "typical" N-MORB also plotted, literature sources as in fig. 5.2. **A** Black markers: MORB from section of SMAR to the north (32°-46°S) of current study area; purple markers: MORB from southernmost end of SMAR - filled markers: from ridge axis; open markers: from fracture zones (literature sources as in fig 5.13). **B** Black markers: MORB from the America-Antarctic Ridge (le Roex *et al.*, 1985); purple markers: MORB from the Southwest Indian Ridge (le Roex *et al.*, 1983).

northern boundary of the Shona-influenced mantle source-regions, have been compositionally contaminated by a component other than proximal mantle plumes. The characteristic high Ba and low Nb and Ta abundances in the composition of the contaminant which affected the mantle source-regions of these MORB from the SMAR can best be accommodated by a combination of sub-continental lithosphere and subducted sediment. The required extent to which the ambient upper-oceanic mantle had to be the contaminated in order to impart the observed compositional characteristics is <2.5%.

Although subducted sediment is compositionally the most attractive contaminant, it is significantly impaired by the required presence of the contamination at shallow mantle levels beneath the mid-ocean ridge necessitated by the petrogenesis of MORB from relatively shallow mantle source-regions. However, the composition of the sub-continental lithosphere beneath southern Africa has been postulated to contain a significant subduction signature, i.e. relative enrichment in Ba, and depletions in Nb and Ta (Sun & McDonough, 1989). This would have been imprinted by melts derived from subducted slabs interacting with the surrounding mantle peridotite (Hart, 1988; Kelemen *et al.*, 1993). The assembly of Gondwana involved subduction of oceanic crust which was directed beneath what is now southern Africa (Grunow *et al.*, 1996; Unrug, 1996). The resulting subcontinental lithosphere would most-likely be quite varied in composition and encompass compositional characteristics of average continental crust and average subducted sediment.

University of Cape Town

The impact of mantle plumes on the overlaying continental lithosphere prior to continental breakup has been proposed as a process which can result in significant delamination of the subcontinental lithosphere (Hawkesworth *et al.*, 1986). The compositional and tectonic criteria for the origin of the contaminant is therefore best fulfilled by subcontinental lithosphere thermally eroded and delaminated beneath southern Africa and dispersed at shallow-levels into the sub-oceanic mantle.

Therefore, variously termed contamination or "pollution" of the ambient upper-oceanic mantle beneath the South Atlantic, as observed in and delineated by MORB and OIB in the preceding discussion, seems to correspond broadly with the latitudinal extent of the Dupal anomaly in the South Atlantic (Hart, 1984; Hart, 1988; Zindler & Hart, 1986). Where available, the radiogenic isotope and Ba/Nb data for MORB from approximately 15°-50°S allude to

variable degrees of low-level "background" contamination of the ambient depleted mantle beneath the SMAR. This supports the division of the Dupal anomaly into two distinct entities: one shallow in origin and composed of small proportions of widely dispersed material derived from delaminated subcontinental lithosphere, sampled predominantly by MORB and early mantle plume-related oceanic volcanism; the other deep in origin and sampled mostly by present mantle plume magmatism, i.e. the Tristan/Gough mantle plume (Milner & le Roex, 1996; Peate *et al.*, 1999).

Evaluation of the proposed model of mantle source-region contamination, relative to appropriate previous work. The model of contamination of the upper-oceanic mantle beneath a large portion of the South Atlantic with delaminated subcontinental lithosphere as discussed above and by Douglass *et al.* (1999) will be evaluated in this section.

The anomalies in the primitive mantle-normalised incompatible trace-element patterns shown by these N-MORB and Discovery-influenced MORB from the SMAR are unusual, not only locally, but also in the global compositional data for MORB. The only other MORB which have compositions with comparable anomalously high Ba and low Nb abundances are from 39°-41°E on the Southwest Indian Ridge (SWIR). These MORB from the SWIR also exhibit anomalous radiogenic isotope compositions (low $^{206}Pb/^{204}Pb$; high $^{87}Sr/^{86}Sr$) and incompatible trace-element anomalies in Ba and Nb values (Hamelin & Allègre, 1985; le Roex *et al.*, 1989; Mahoney *et al.*, 1992). Other oceanic basalts in the Indian and Atlantic Oceans have been observed to contain similar radiogenic isotope and incompatible trace-element anomalies, but none of these were erupted at mid-ocean ridges. These are basalts associated with volcanism attributed to influence of the Tristan da Cunha mantle plume (Milner & le Roex, 1996; Richardson *et al.*, 1982), the Crozet mantle plume (Mahoney *et al.*, 1996), and the Kerguelen mantle plume (Mahoney *et al.*, 1995).

Various hypotheses have been proposed to account for such anomalous compositional characteristics observed in oceanic basalts. Le Roex *et al.* (1989) favoured material derived from recycled oceanic lithosphere plus ancient pelagic sediment as the contaminant of the MORB mantle source-regions beneath 39°-41°E on the SWIR, over the tectonically more attractive origin from melting of delaminated subcontinental lithosphere stranded in the asthenospheric mantle. Radiogenic isotope data, on the other hand, have been used to advance the case for

University of Cape Town

stranded subcontinental lithosphere, thermally delaminated from Indo-Madagascar by the Marion mantle plume, as source for the contaminant material at 39°-41°E on the SWIR (Hamelin & Allègre, 1985; Mahoney *et al.*, 1992).

Similar arguments have been advanced to account for the radiogenic isotope characteristics of certain basalts from the Walvis Ridge in the South Atlantic (Milner & le Roex, 1996; Peate *et al.*, 1999). Following this model, the Tristan mantle plume caused thermal erosion of ancient continental lithospheric mantle at the time of continental breakup, which was then dispersed into the surrounding asthenosphere. Compositional contributions from this material during subsequent episodes of mantle melting resulted in erupted products inheriting very low $^{206}Pb/^{204}Pb$ and high $^{87}Sr/^{86}Sr$ characteristics, typical of subcontinental material.

In contrast to the basalts from 39°-41°E on the SWIR, the abovementioned basalts from the South Atlantic (Milner & le Roex, 1996; Peate *et al.*, 1999), exhibiting radiogenic isotope characteristics derived from some contribution of subcontinental lithosphere, are associated with early mantle plume volcanism, shortly after continental breakup, and were not erupted at mid-ocean ridges. Similarly, the origin of basalts from the Afanasy-Nikitin Rise in the Indian Ocean, which show compositional evidence for significant subcontinental lithosphere in their mantle source-regions, have been linked to early Crozet mantle plume volcanism (Mahoney *et al.*, 1996). Basalts from Broken Ridge and the Naturaliste Plateau in the Indian Ocean share the above compositional evidence for the presence of subcontinental lithosphere in their mantle source-regions. These basalts are likely to have been produced during the early phases of volcanism associated with the Kerguelen mantle plume (Mahoney *et al.*, 1995). The origin of material derived from the subcontinental lithosphere in the Indian Ocean is therefore intertwined with the breakup of Eastern Gondwana and the role of the thermal impact of these mantle plumes in this process.

None of the recent oceanic eruptive products of any of the abovementioned mantle plumes, including the Marion mantle plume, exhibit compositional characteristics of any nature which would require the contamination of their mantle source-regions by subcontinental lithosphere (le Roex *et al.*, 1990; le Roex *et al.*, 1989; Mahoney *et al.*, 1995; Mahoney *et al.*, 1996; Milner & le Roex, 1996). This observation could imply that these mantle plume-sources have undergone profound compositional changes through time, which seems unlikely (Mahoney

University of Cape Town

et al., 1996), or the influence of subcontinental lithosphere in these mantle-sources have significantly diminished with time. This seems more reasonable, as a finite amount of sub-continental lithosphere would be thermally eroded and dispersed in the asthenosphere or entrained by these mantle plumes during continental breakup.

Non-replenished amounts of sub-continental lithosphere and continuously upwelling enriched mantle material would therefore be sampled by subsequent melting associated with the respective mantle plumes. The mantle source-regions of the eruptive products of these mantle plumes would continuously be refined towards "pure" upwelling enriched mantle compositions associated with the much deeper mantle-sources of the respective mantle plumes.

Summary. The impact of mantle plumes, e.g. Tristan da Cunha, Discovery and to a lesser degree Shona, on the subcontinental lithosphere beneath Gondwana prior to the opening of the South Atlantic eroded material from the subcontinental lithosphere and dispersed this material into the surrounding asthenosphere. The subcontinental lithosphere derived from beneath southern Africa had compositions with specific characteristics, such as anomalously high Ba, and low Nb and Ta abundances.

Subsequent early volcanism associated with these mantle plumes yielded material partially derived from delaminated subcontinental lithosphere. However, with continued mantle plume-upwelling and melting, the proportion of delaminated subcontinental lithosphere in these mantle source-regions progressively decreased. The eruptive products of these mantle plumes therefore progressive contained less compositional characteristics inherited from delaminated subcontinental lithosphere.

The upper-oceanic mantle away from mantle plumes, however, preserved the dispersed material derived from delaminated subcontinental lithosphere longer, until entrained in the mantle upwelling beneath the mid-ocean ridges. Mantle melting at shallow-levels beneath ridge segments yielded magmas partially derived from the embedded delaminated subcontinental lithosphere. Due to the refractory, and possibly colder, nature of the embedded delaminated subcontinental lithosphere relative to ambient upper-oceanic mantle (Douglass *et al.*, 1999; Hawkesworth *et al.*, 1989), it tended to contribute to the magma being formed only at a late-stage and melts derived from it constituted relatively small proportions of the final magma.

University of Cape Town

Beneath mantle plume-influenced ridge segments, the added heat from the plumes resulted in higher proportions of the final magma having been derived from the embedded delaminated subcontinental lithosphere.

This would account for N-MORB containing only subtle evidence for the presence of subcontinental lithosphere in their mantle source-regions, predominantly in anomalous concentrations of Nb. This is due to the low absolute concentrations of Nb in the N-MORB which are readily affected by small degrees of contamination. The mantle plume-influenced MORB contain more diverse evidence of subcontinental lithosphere in their mantle source-regions, with significantly anomalous concentrations of Ba, Nb and Ta and radiogenic isotopes (Douglass *et al.*, 1999), reflecting the increased proportion of the melts derived from the subcontinental lithosphere.

Douglass *et al.* (1999) found radiogenic isotope evidence of subcontinental lithosphere in the mantle source-regions of mantle plume-influenced MORB from the SMAR, and the incompatible trace-element data presented here are evidence for the further presence of widely dispersed material derived from delaminated subcontinental lithosphere in the mantle source-regions of N-MORB from the SMAR. The required presence of subcontinental lithosphere in the mantle source-regions of N-MORB also further establishes the definite shallow-level nature of this broad upper-oceanic mantle contamination.

University of Cape Town

CHAPTER 6: MELTING PROCESSES BENEATH THE SOUTHERN MID-ATLANTIC RIDGE (40°-55°S)

The melting processes which give rise to magmas parental to the MORB recovered from the global mid-ocean ridge system are unobservable in nature and deciphering the details of these dynamic processes from the compositions of their basaltic eruptive products is a complex and ongoing endeavour. A large number of experimental, thermodynamic and empirical approaches have been formulated to approximate these melting processes, and deduce the nature and parameters of these melting processes (Asimow *et al.*, 1995a; Asimow *et al.*, 1995b; Baker *et al.*, 1995; Ghiorso & Carmichael, 1980; Ghiorso *et al.*, 1983; Ghiorso *et al.*, 1994; Ghiorso & Sack, 1995; Grove *et al.*, 1994; Hirschmann *et al.*, 1999a; Hirschmann *et al.*, 1999b; Hirschmann *et al.*, 1998; Iwamori *et al.*, 1995; Johnson & Dick, 1992; Johnson *et al.*, 1990; Kinzler, 1997; Kinzler & Grove, 1992a; Kinzler & Grove, 1992b; Kinzler & Grove, 1993; Langmuir *et al.*, 1992; McKenzie, 1985; McKenzie & Bickle, 1988; Niu, 1997; Niu, 1999; Niu & Batiza, 1991; Sack & Ghiorso, 1994a; Sack & Ghiorso, 1994b; Sack & Ghiorso, 1994c; Walter, 1999; Walter & Presnall, 1994; Walter *et al.*, 1995).

University of Cape Town

The following chapter will use the major- and trace-element compositions of MORB recovered from the SMAR to:

- evaluated any systematics observed or anomalies detected in the fractionation-corrected major-element compositions with regard to the so-called global trend (Klein & Langmuir, 1987; Klein & Langmuir, 1989), and the local trend, which is thought to be predominately a feature found in MORB from slower-spreading ridges (Langmuir *et al.*, 1992; Niu & Batiza, 1994).
- approximate the parameters, e.g. initial pressure and mean extent, of the melting processes through which these basalts were extracted from the mantle (Kinzler & Grove, 1993; Niu & Batiza, 1991; Niu & Batiza, 1994). Any variations or anomalous values observed will be emphasized and explanations proposed.
- propose a model which aims to reconcile apparently conflicting signals from major- and trace-element data regarding the possible role of residual garnet during mantle melting beneath the SMAR.

6.1 FRACTIONATION-CORRECTED MAJOR-ELEMENT COMPOSITIONS

6.1.1 Details and discussion of data recalculation

The use of major-element compositions to investigate the nature, such as initial pressures and mean degrees of melting, of MORB is based on the ability to correct the data for changes due to crystallisation processes, back to a reference value of 8wt% MgO (Klein & Langmuir, 1987; Klein & Langmuir, 1989; Langmuir *et al.*, 1992). These fractionation-corrected major-element compositions are then assumed to be characteristic of the melting events which formed these basalts. The initial methodology used was fitting straight-line regressions, approximating liquid lines of decent, to regionally averaged data on major-element oxide-MgO diagrams, and using the slopes of these regressions to correct data for individual major-element oxides back to the reference MgO value of 8wt% (Klein & Langmuir, 1987; Klein & Langmuir, 1989). This approach was modified to take into account the change in the slope of liquid lines of decent at the onset of clinopyroxene as a fractionating phase, although the differences in fractionation-corrected major-element values obtained did not differ significantly from the previous, simplified method (Langmuir *et al.*, 1992). A further refinement was the use of second or third degree polynomial regressions to approximate liquid lines of decent (Niu & Batiza, 1994).

The major-element compositions of MORB from the SMAR do not define distinct crystallisation trends within single dredges. This is not to say that the data are scattered or random, but rather the data for single dredges are predominantly confined to a single or two distinct clusters which respectively span compositional ranges hardly larger than the analytical errors of the analyses. The approach adopted here has been to use the three groups of samples defined in chapters 4 & 5 (N-MORB, Discovery-influenced MORB, and Shona-influenced MORB) and to obtain separate sets of linear regressions for major-element oxide-MgO variations for each group (after Klein & Langmuir, 1989). The rationale behind this approach being the already defined compositional differences between these three groups of samples. Also, the probable different physical environments, i.e. thermal regime, beneath the ridge segments from which these different groups of MORB were recovered, due to the different nature of the influences of the separate mantle plumes. The major-element compositions of the quenched-igneous glasses of these MORB groupings define broad trends which conform to different crystallisation-induced liquid lines of decent (Langmuir *et al.*, 1992), see fig. 6.1a-c, thus justifying the use of these groupings and the use of separate sets of linear regressions to

University of Cape Town

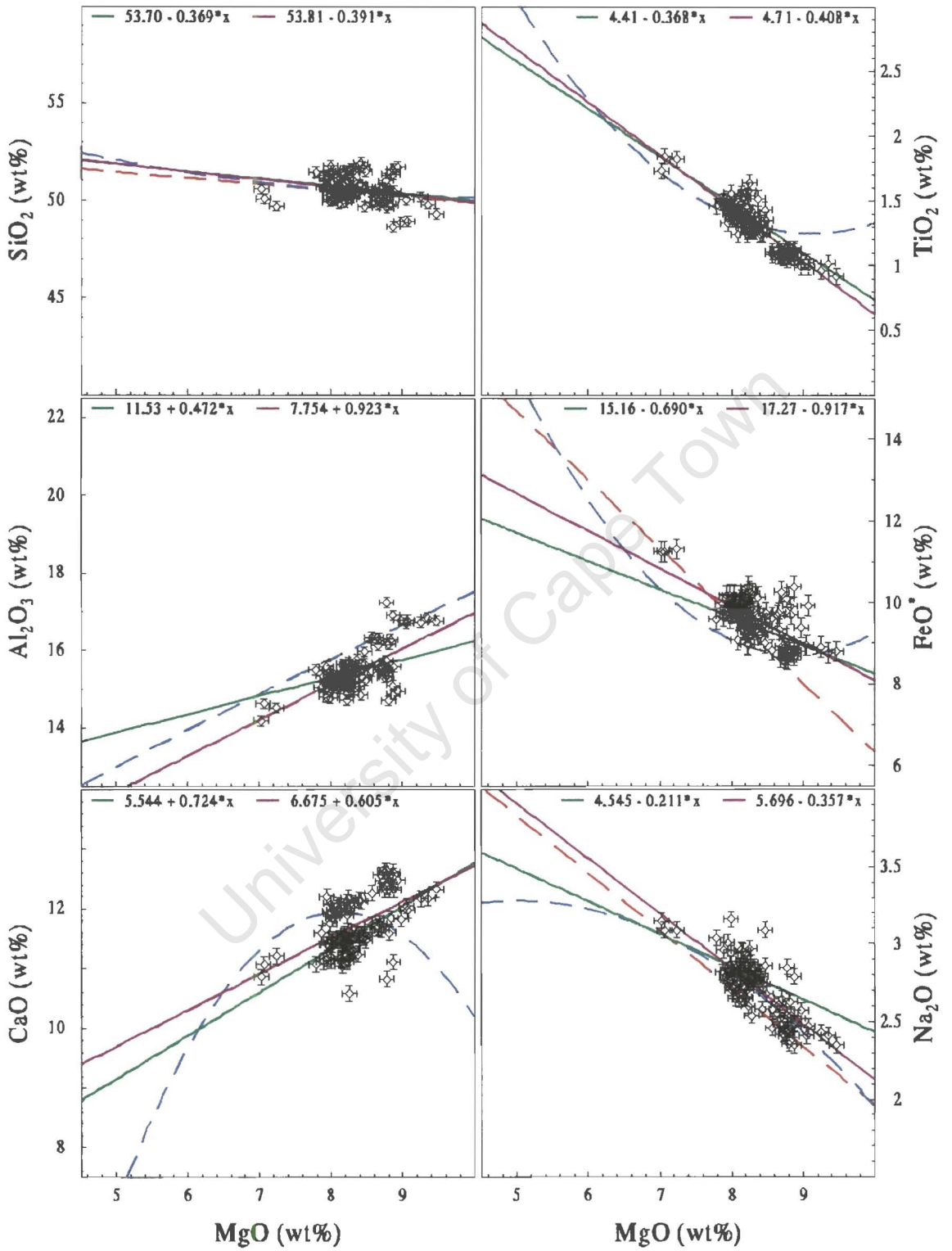

University of Cape Town

Figure 6.1a: MgO-variation diagrams for quenched igneous-glass compositions of N-MORB from the SMAR, with multiple regressions approximating liquid lines of decent. The red dashed lines are based on a global MORB data-set (Klein & Langmuir, 1987, 1989), the blue dashed lines are for MORB data from 26°S on the MAR (Niu & Batiza, 1994), the green lines are based on all the MORB quenched igneous-glass compositions from the current study, and the purple lines are based only on the plotted subset of data.

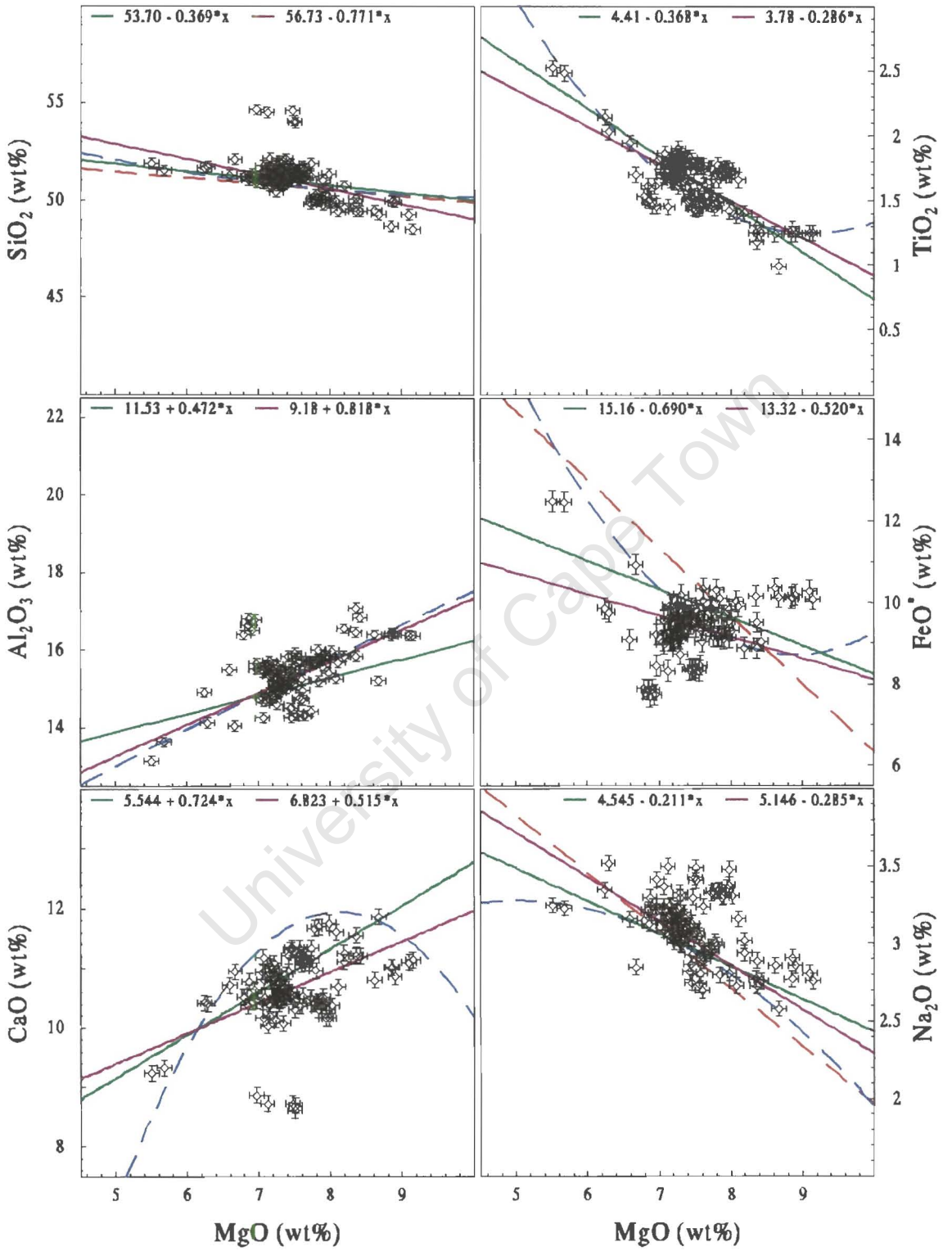

University of Cape Town

Figure 6.1b: MgO-variation diagrams for quenched igneous-glass compositions of Discovery-influenced MORB, with multiple regressions approximating liquid lines of decent. The red dashed lines are based on a global MORB data-set (Klein & Langmuir, 1987, 1989), the blue dashed lines are for MORB data from 26°S on the MAR (Niu & Batiza, 1994), the green lines are based on all the MORB quenched igneous-glass compositions from the current study, and the purple lines are based only on the plotted subset of data.

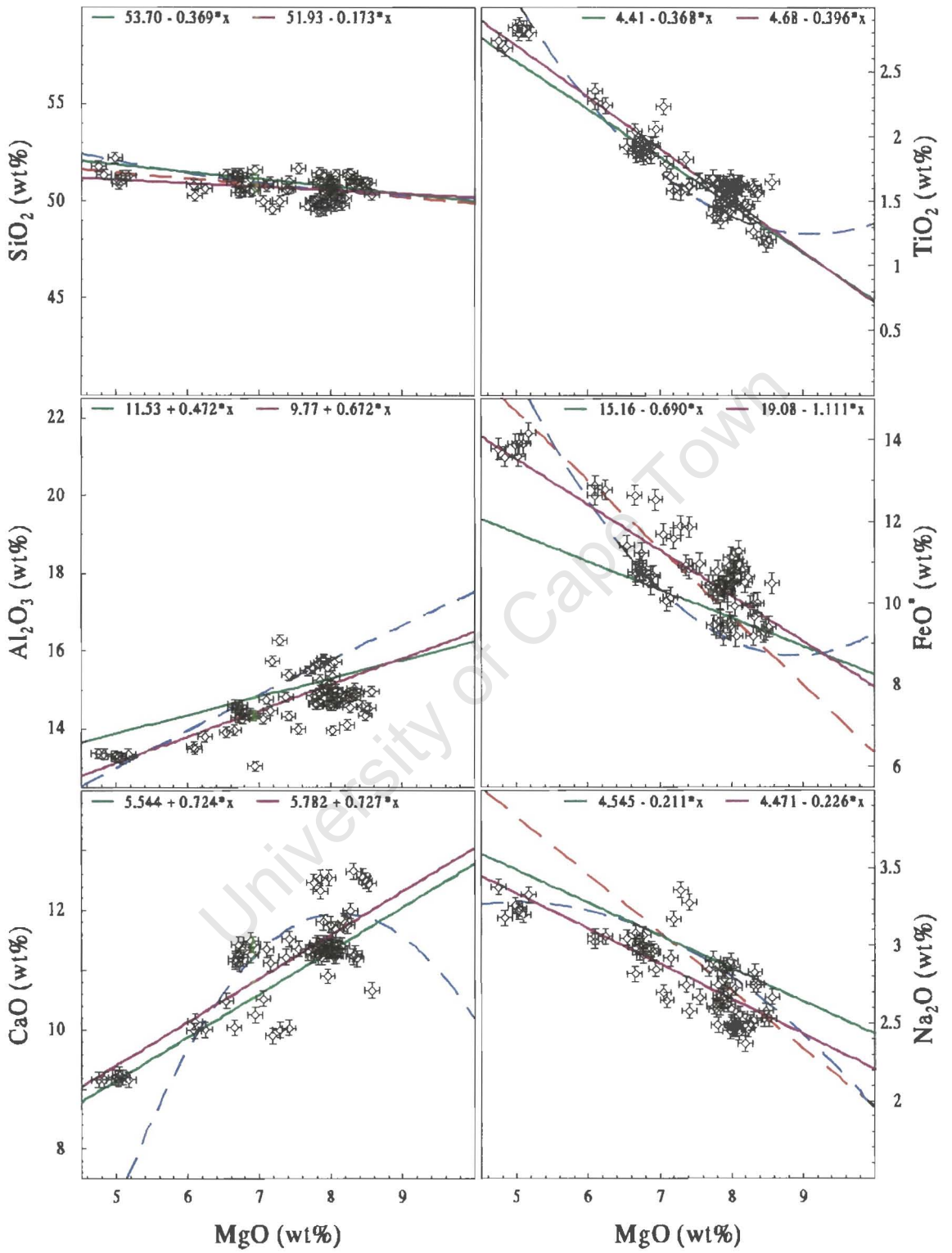

University of Cape Town

Figure 6.1c: MgO-variation diagrams for quenched igneous-glass compositions of Shona-influenced MORB, with multiple regressions approximating liquid lines of decent. The red dashed lines are based on a global MORB data-set (Klein & Langmuir, 1987, 1989), the blue dashed lines are for MORB data from 26°S on the MAR (Niu & Batiza, 1994), the green lines are based on all the MORB quenched igneous-glass compositions from the current study, and the purple lines are based only on the plotted subset of data.

approximate the compositional changes due to fractional crystallisation.

It is evident from fig. 6.1a-c that polynomial regressions (e.g. those used by Niu & Batiza, 1994 and plotted in fig. 6.1a-c) do not fit the trends for these data. The observed trends in the MORB data are broad and no change in slope can be reliably ascertained, therefore the single linear regression method (Klein & Langmuir, 1987) is applied, after empirical adjustments to the slopes (after Klein & Langmuir, 1989). The slopes of the regressions through the separate groups, plotted in fig. 6.1a-c, a MgO reference value of 8wt%, and the general equation (see equation 6.1) for correcting major-element data for the affects of crystallisation were therefore used to recalculated the major-element data for individual MORB samples.

$$Oxide_{reference\ value} = Oxide_{observed\ value} - (slope).(MgO_{observed\ value}) + (slope).(MgO_{reference\ value}) \quad \ldots\ldots\ldots \text{ equation 6.1}$$

6.1.2 The global trend

General observations for fractionation-corrected major-element data of MORB from the SMAR, and discussion of the origins of the global trend. The fractionation-corrected Na_2O ($Na_{8.0}$), FeO ($Fe_{8.0}$) and SiO_2 ($Si_{8.0}$) values of these MORB from the SMAR are generally off-set from the global trend (Klein & Langmuir, 1987; Klein & Langmuir, 1989; Langmuir *et al.*, 1992), towards higher $Na_{8.0}$ and/or higher $Fe_{8.0}$ values (fig. 6.2). The size of error bars (not shown) are small relative to the size of the markers in fig. 6.2, and subsequent figures, and will therefore be omitted for the sake of clarity.

The clear displacement of these MORB "above" the global trend in terms of the Na_8-Fe_8 co-variation, in fig. 6.2, is significantly larger than the errors in the data and therefore constitutes a real feature of the data. The global data-set used to identify the global trend, and plotted in fig. 6.2, is composed of regionally average basalt compositions. In most cases these averages span less than a hundred kilometres, and for some ridges with low sampling densities the average value can represent a few hundred to more than five hundred kilometres of ridge-segments (Klein & Langmuir, 1987). It is therefore to be expected, and it has been shown, that unaveraged data will contain substantially more scatter, but still exhibit the same correlations, though more

University of Cape Town

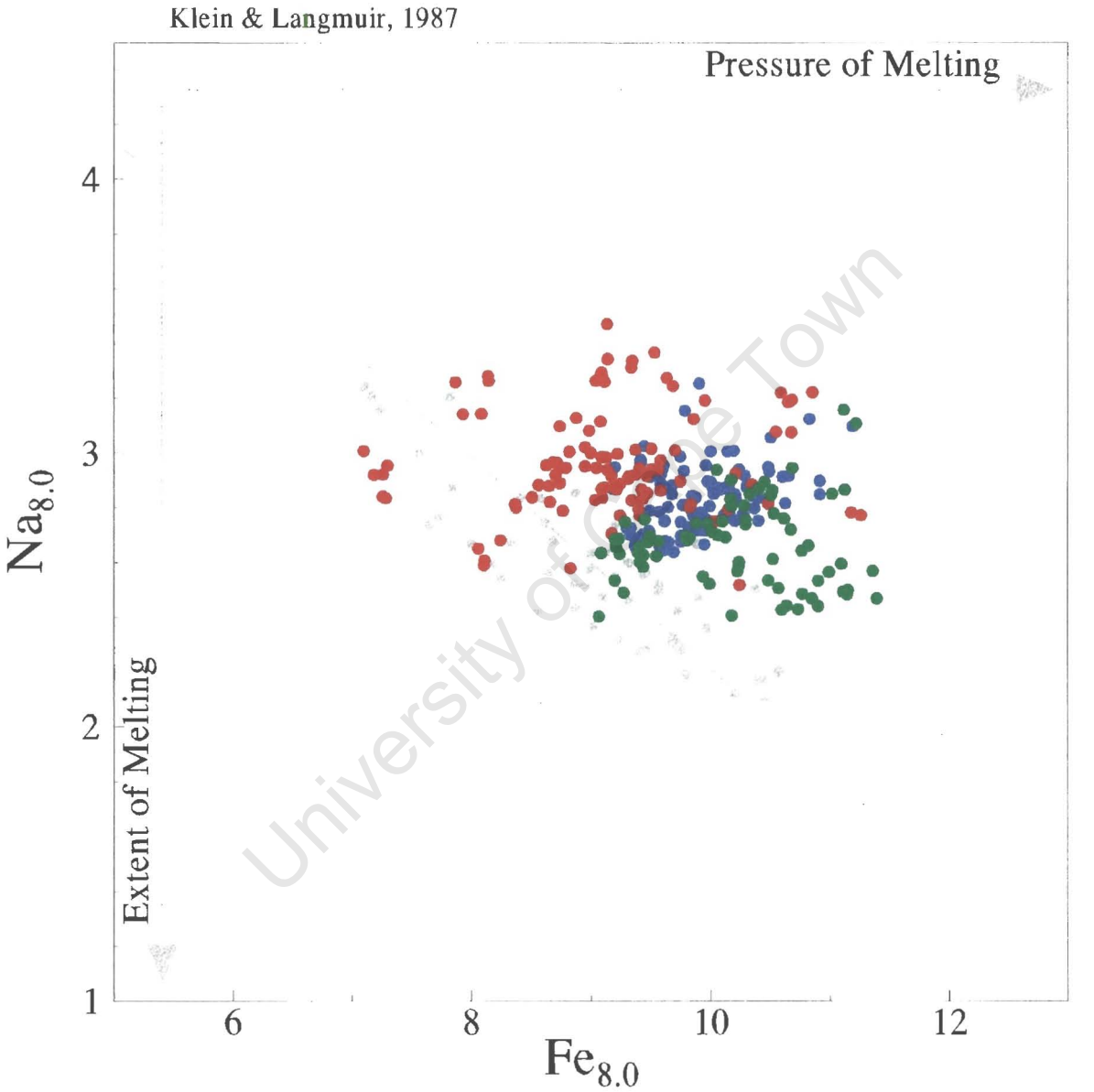

University of Cape Town

Figure 6.2: Fractionation-corrected Na_2O ($Na_{8.0}$) versus fractionation-corrected FeO ($Fe_{8.0}$) for all MORB from the SMAR, see text for details of calculation. Blue markers: N-MORB; red markers: Discovery-influenced MORB; green markers: Shona-influenced MORB; light grey markers: global MORB averages of Klein & Langmuir (1987); dashed line: so-called global trend after Klein & Langmuir (1987).

poorly defined, as the averaged data (Brodholt & Batiza, 1989).

The original explanation for the origin of the global trend is rooted in a model of a "variable temperature" mantle, see fig. 6.3, in which mantle temperatures beneath the mid-ocean ridge system vary by as much as 250°C to yield the global range in linked $Na_{8.0}$-$Fe_{8.0}$ values (Klein & Langmuir, 1987; Klein & Langmuir, 1989). In this model, the temperature of the mantle governs the depth at which the mantle solidus is intercepted and melting is initiated beneath the mid-ocean ridges. High mantle temperatures result in deep initiation of melting, while low mantle temperatures will result in melting commencing at shallower depths. The depth at which melting ceases is assumed not to vary significantly, correlating approximately with the base of the crust, and the mean extent of melting is positively correlated with the initial depth of melting, therefore both increase in unison. Higher mean extents of melting will yield thicker crust and thicker crust results in shallower ridge bathymetry. A coherent correlation has therefore been established between high mean pressures of melting (high $Fe_{8.0}$), high mean extents of melting (low $Na_{8.0}$), thick oceanic crust and shallow ridge bathymetry; as opposed to low mean pressures of melting (low $Fe_{8.0}$), low mean extents of melting (high $Na_{8.0}$), thin oceanic crust and deep ridge bathymetry. This correlation therefore results in the global trend (Klein & Langmuir, 1987; Klein & Langmuir, 1989; Langmuir *et al.*, 1992).

An alternative to the "variable temperature" mantle model as explanation for the global trend is the proposed "constant temperature" mantle model (Shen & Forsyth, 1995), see fig. 6.3. The basis of this model is that mantle temperature is generally constant globally beneath mid-ocean ridges and therefore the initial depth of melting is globally constant beneath mid-ocean ridges. In contrast with the "variable temperature" mantle model, the mean pressure of melting and the mean extent of melting are inversely correlated in this model. The origin of the global trend is proposed to be rooted in a combination of variations in the final depths of melting and mantle compositional heterogeneity. Shen & Forsyth (1995) cast doubt on the validity of $Fe_{8.0}$ as indicator of depth of melting due to a negative correlation observed between $Fe_{8.0}$ and K_2O/TiO_2. The importance of this correlation is that K_2O/TiO_2 has been proposed as indicator of mantle-source compositional heterogeneity. Therefore, a substantial portion of the variation in $Fe_{8.0}$ is argued to be due to mantle heterogeneity, and not an indication of depth of melting. To overcome this source-compositional effect, $Fe_{8.0}$ values were corrected to a reference value of 0.1 K_2O/TiO_2. This second level of data correction decreased the range of $Fe_{8.0}$ values, but the

University of Cape Town

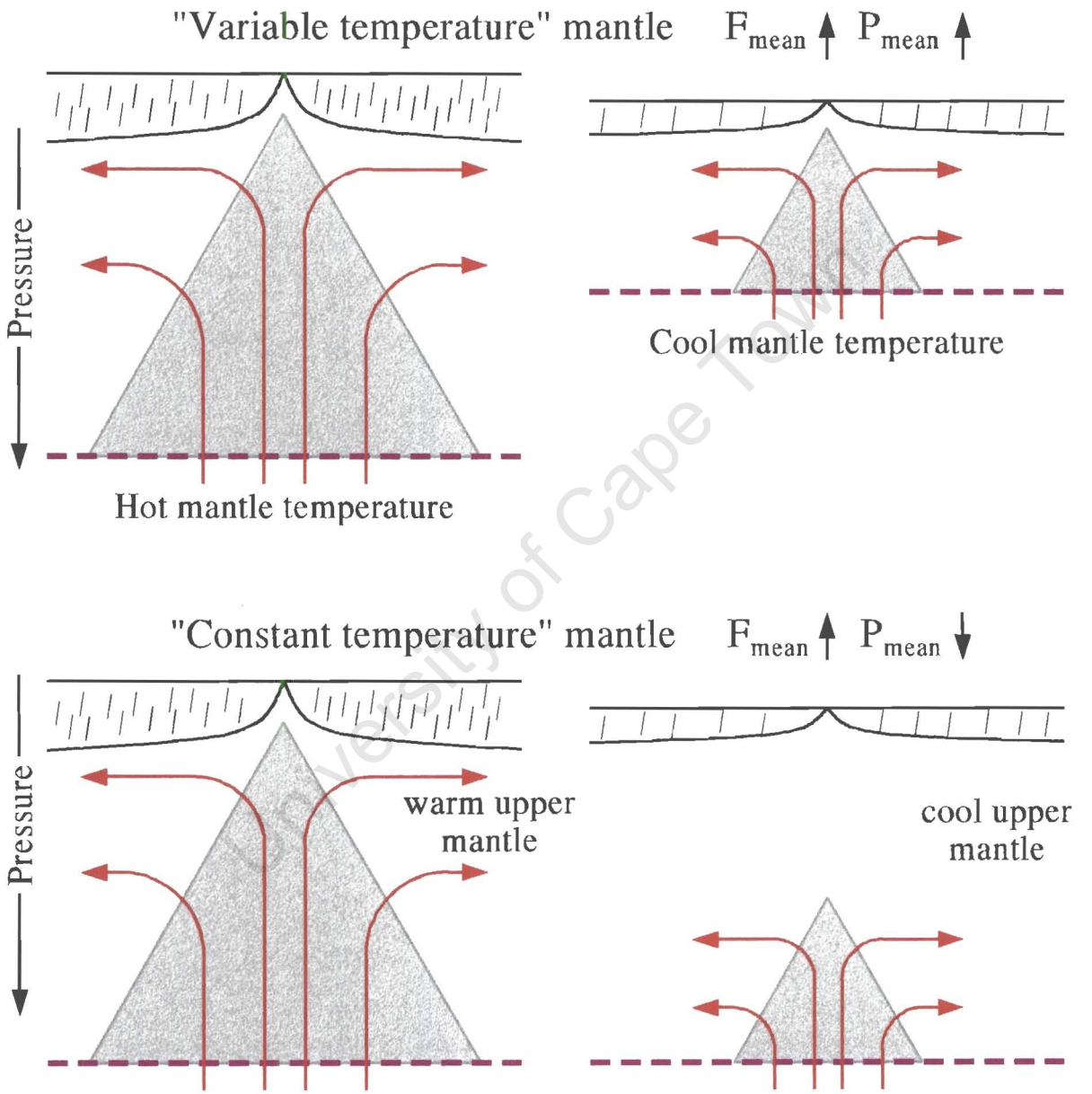

University of Cape Town

Figure 6.3: Schematic diagrams, after Kinzler (1997), illustrating the features of the two mantle melting models proposed to account for the global trend. Dashed purple line: depth of mantle melting initiation; filled grey triangles: melting regimes; curved red arrows: mantle flow-lines.

global trend is still observed in the data (Shen & Forsyth, 1995).

The "constant temperature" mantle model and the above methodology of correcting for source-compositional heterogeneities was assessed by Kinzler (1997). It was shown that major-element compositions of low-degree melts produced at high pressures and crystallised to 8wt% MgO do not fall within the global array of MORB data. Furthermore, the use of K_2O/TiO_2 as reference to correct MORB data for source-compositional heterogeneity does not deal adequately with the difference in partitioning behaviour of K_2O and TiO_2 during melting and crystallisation. The correction of MORB data to a constant K_2O/TiO_2 ratio therefore erases significant compositional variations which reflect true variations in pressure and extent of melting (Kinzler, 1997).

Observation and discussion of unusual features in the fractionation-corrected major-element data for MORB from the SMAR. Although the above-mentioned off-set of the data for these MORB from the global trend is a prominent feature of the data, a less obvious, but possibly more significant, apparent paradox is evident in fig. 6.2. The data for MORB recovered from Shona-influenced ridge segments extend to lower $Na_{8.0}$ and higher $Fe_{8.0}$ values with respect to the data for N-MORB. It is to be expected that the ridge segments affected by the Shona mantle plume will yield basalts which have low $Na_{8.0}$ and high $Fe_{8.0}$ values, consistent with derivation from mantle with above average temperatures. The thermal influence of the hotter mantle associated with the upwelling Shona mantle plume will result in deep initiation of melting and the volumes of magma from the resulting high extent of melting will form abnormally thick crust, giving rise to the observed shallow ridge bathymetry in this region. The data for N-MORB and Shona-influenced MORB conform to the basic framework of the "variable temperature" mantle model for the origin of the global trend.

The paradox alluded to is the behaviour of the data for the Discovery-influenced MORB with respect to the global trend. The data for these mantle-plume influenced basalts plot towards higher $Na_{8.0}$ (low extent of melting) and lower $Fe_{8.0}$ (shallow depths of melting) with respect to the data for N-MORB, therefore completely the opposite behaviour as expected for basalts derived from mantle material with above average temperature associated with the Discovery mantle plume. If the global trend is indeed due to a variation in mantle temperature as described above, then the paradox is why the basalts from the Discovery- and Shona-influenced ridge

University of Cape Town

segments respectively fall on opposite sides of N-MORB. Although the Discovery mantle plume is presently located significant away from the ridge segments (Douglass *et al.*, 1999; Douglass *et al.*, 1995), the mantle beneath these Discovery-influenced ridge segments, which are all anomalously elevated, should still have higher temperatures relative to ridge segments unaffected by mantle plumes.

As was shown and discussed in chapter 5, the range in incompatible trace-element concentrations in these MORB from the SMAR is correlated with a range in radiogenic isotope ratios. The basalts recovered from Discovery- and Shona-influenced ridge segments have distinct radiogenic isotope ratios and incompatible trace-element characteristics, respectively, relative to the N-MORB recovered from the ridge segments which have not experienced any observed mantle-plume influence (Douglass *et al.*, 1999; Douglass *et al.*, 1995). At least three broad, but distinct, mantle source-region have therefore been identified: normal depleted MORB mantle, Discovery-influenced incompatible trace-element and radiogenic isotope enriched mantle, and Shona-influenced incompatible trace-element and radiogenic isotope enriched mantle. The question is now whether the global trend and related major-element indicators of melting parameters are systematically associated with these identified mantle source-regions.

Due to the reservations raised by Shen & Forsyth (1995) regarding the sole use of $Fe_{8.0}$ as indicator of pressure of melting, and the use of $Fe_{8.0}$ and $Si_{8.0}$ by Kinzler (1997) to investigate the pressure of melting, the following discussion and series of diagrams will use Si_8/Fe_8 as proxy for initial pressure of melting, after Niu & Batiza (1991, 1994). As the initial pressures of melting of basalts decrease, so the Si_8/Fe_8 ratios for the basalts will increase.

It is clear from fig. 6.4a that the distinctly higher $^{87}Sr/^{86}Sr$ ratios of the Discovery-influenced MORB correlate with high Si_8/Fe_8 ratios, but no apparent correlation is observed between the isotope ratios and Na_8. In fig. 6.4b, the distinctly higher $^{206}Pb/^{204}Pb$ ratios of the Shona-influenced MORB show no clear linear correlation with Si_8/Fe_8 ratios or Na_8 values, and the Shona-influenced MORB overlap with the data for N-MORB. The observations from fig.6.4a-b is not surprising, as fig 6.2 already separated the three MORB compositional groupings in terms of initial pressure (Fe_8, or Si_8/Fe_8) and extent (Na_8) of melting. Whether major-element heterogeneity is the cause of the anomalous indications of pressure and extent of melting for Discovery-influenced MORB, or if it is due to some physical process linked to

University of Cape Town

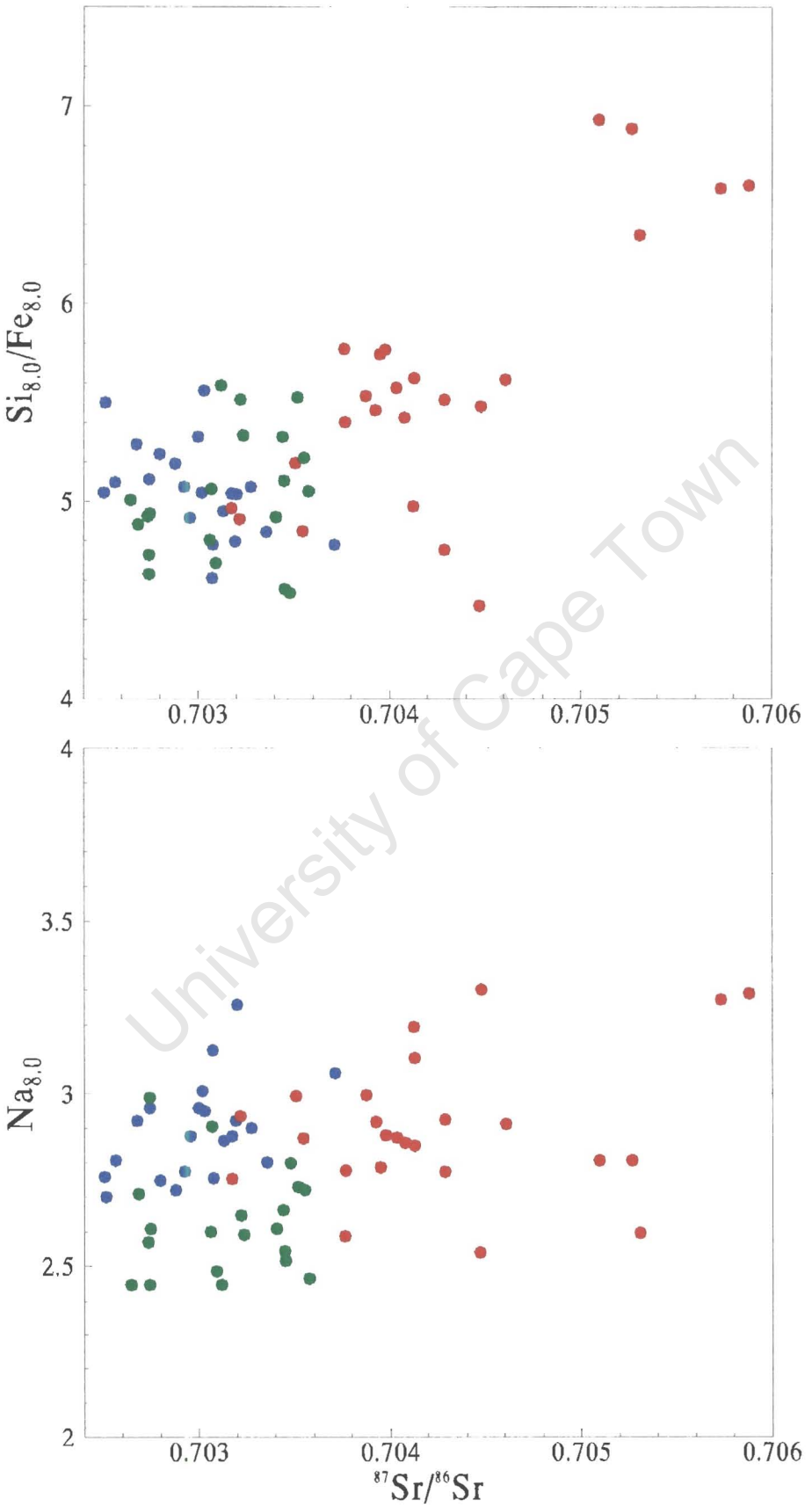

University of Cape Town

Figure 6.4a: Si_8/Fe_8 and Na_8 versus $^{87}Sr/^{86}Sr$ for N-MORB (blue markers), Discovery-influenced MORB (red markers) and Shona-influenced MORB (green markers). Radiogenic isotope data from Douglass *et al.* (1999).

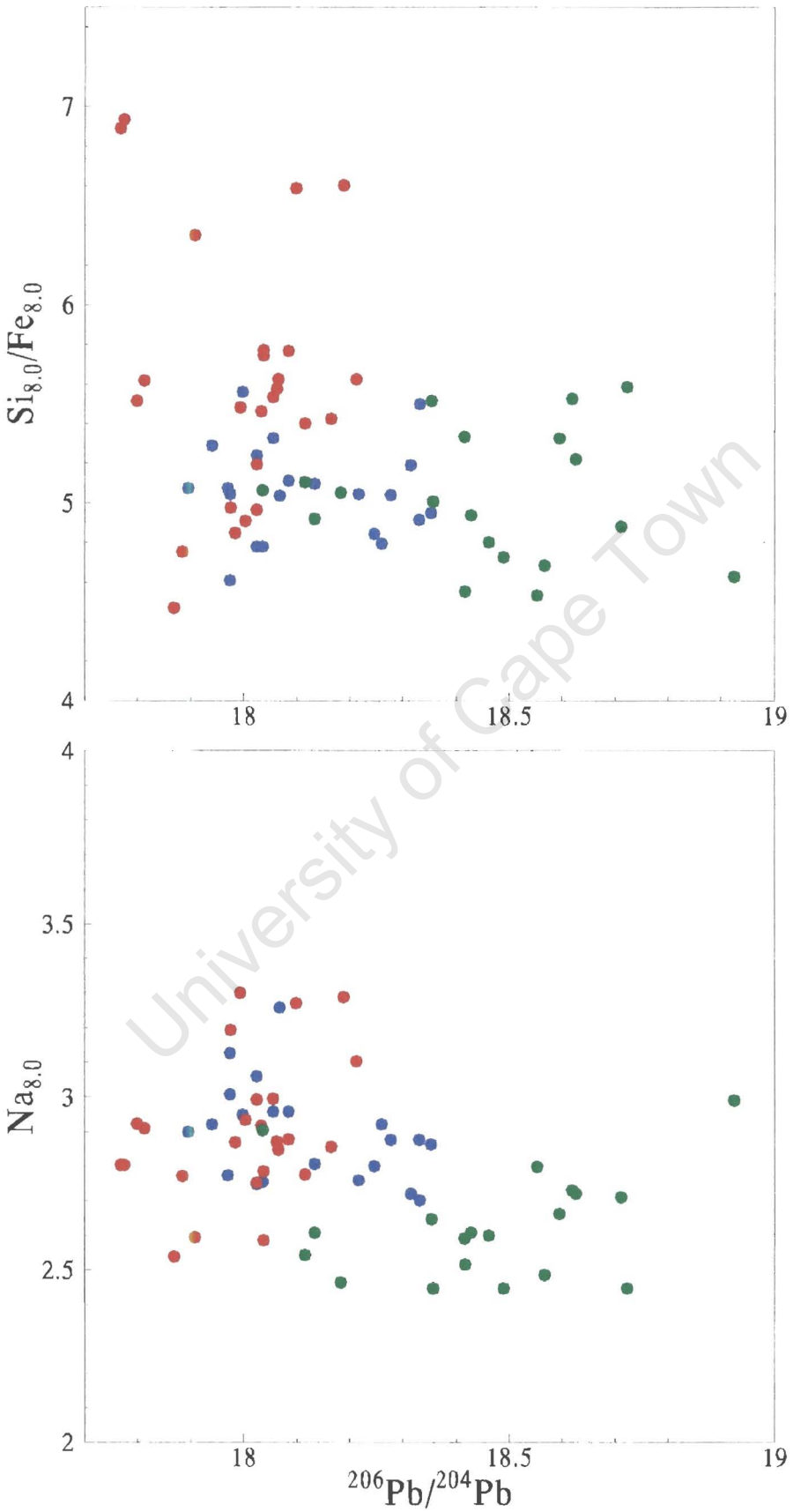

University of Cape Town

Figure 6.4b: Si_8/Fe_8 and Na_8 versus $^{206}Pb/^{204}Pb$ for N-MORB (blue markers), Discovery-influenced MORB (red markers) and Shona-influenced MORB (green markers). Radiogenic isotope data from Douglass *et al.* (1999).

melting in the mantle, is still not resolved. However, the Si_8/Fe_8 data confirms the observations from the global trend. It is therefore more likely that the Discovery-influenced MORB contain signatures of true pressures and extents of melting. This agrees with the conclusion reached by Brodholt & Batiza (1989), Kinzler (1997), Klein & Langmuir (1989) and Langmuir *et al.* (1992), that major-element heterogeneity in the mantle is a reality, but that it does not cause, or significantly impact on, the systematics of the global trend.

The point of discussion is therefore not whether the systematics observed in the pressure and extent of melting of these MORB are due entirely to the mantle source-region compositional differences identified in chapter 5. Rather, it is how to reconcile the observed compositional variations and melting parameters in a coherent model of melting beneath the SMAR. The trace-element data of the quenched igneous glasses of these MORB contain some further anomalous characteristics, which are correlated with the fractionation-corrected major-element indicators of the initial pressure and extent of melting, as well as with the distinct radiogenic-isotope defined mantle source-region domains. These trace-element characteristics deepen the contradictory nature of the Discovery-influenced MORB, but might also aid in resolving this paradox.

University of Cape Town

The above-mentioned anomalous trace-element characteristics are illustrated in fig. 6.5a-b. MORB with anomalously low concentrations of Sc and Yb, resulting in extremely high chondrite-normalized (Sm/Yb) ratios, constitute the high Si_8/Fe_8 and high Na_8 end-member of correlations predominantly defined by Discovery-influenced basalts. Low Yb concentrations, with concurrent high chondrite-normalized (Sm/Yb) ratios and low Sc concentrations in MORB are viewed as evidence for the formation of the parental magma during melting in the presence of residual modal garnet (Hirschmann, 1996; Hirschmann & Stolper, 1996; Shen & Forsyth, 1995). The high garnet partition coefficients for Yb and Sc relative spinel, see table 6.1, result in significantly higher bulk partition coefficients when melting occurs in the garnet-lherzolite stability field relative to the spinel-lherzolite stability field (Hirschmann & Stolper, 1996; Shen & Forsyth, 1995). These trace-element characteristics are therefore in conflict with the fractionation-corrected major-element evidence, which indicates shallow pressures of melting for these MORB. This is due to garnet being unstable at depths shallower than approximately 85km, i.e. 28-30kbar, and only magmas which formed during melting which commenced at depths greater than 28-30kbar should contain the above, or any other (e.g. U-Th or coupled

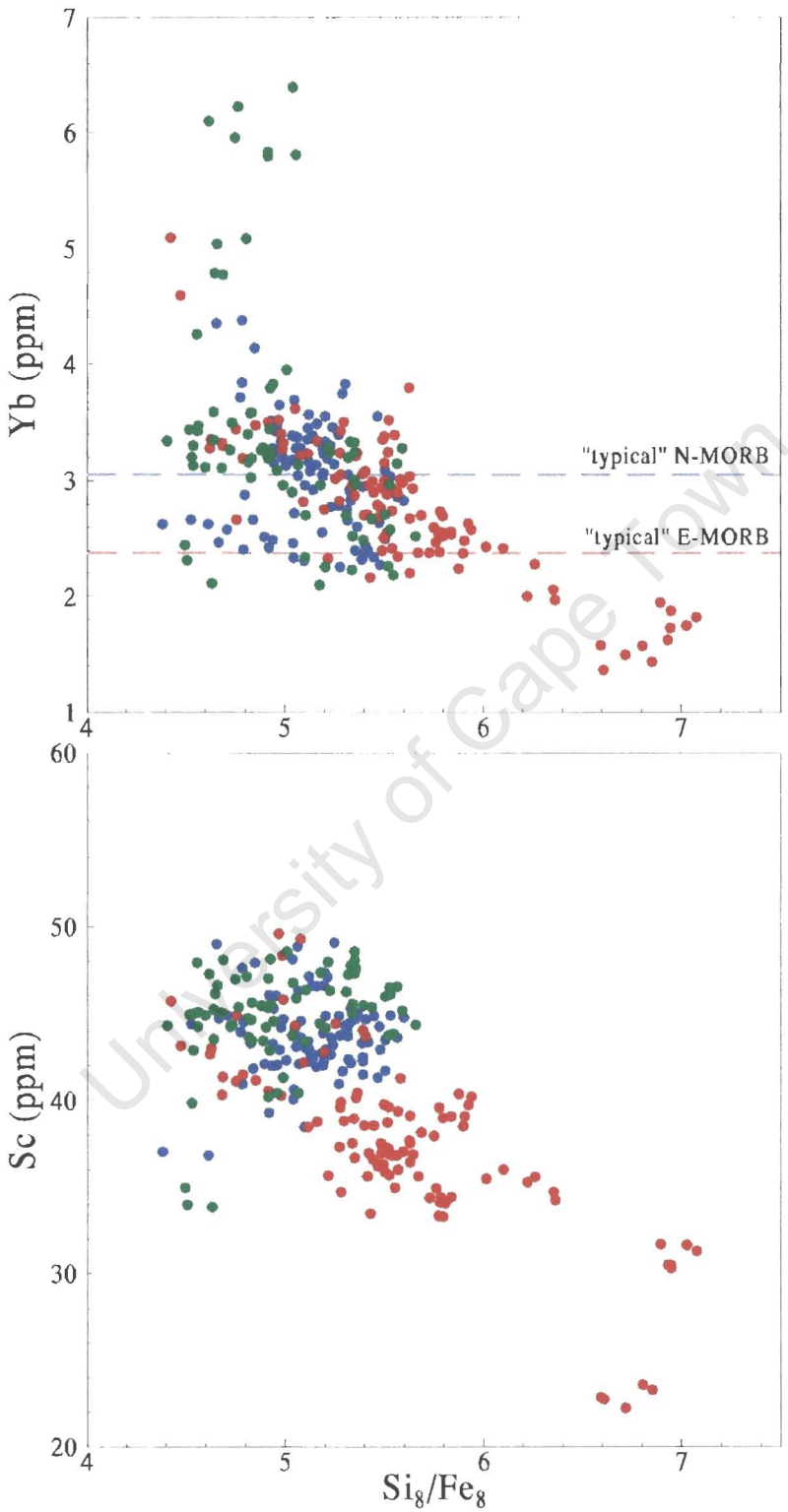

University of Cape Town

Figure 6.5a: Yb and Sc concentrations versus Si_8/Fe_8 of N-MORB (blue markers), Discovery-influenced MORB (red markers) and Shona-influenced MORB (green markers).

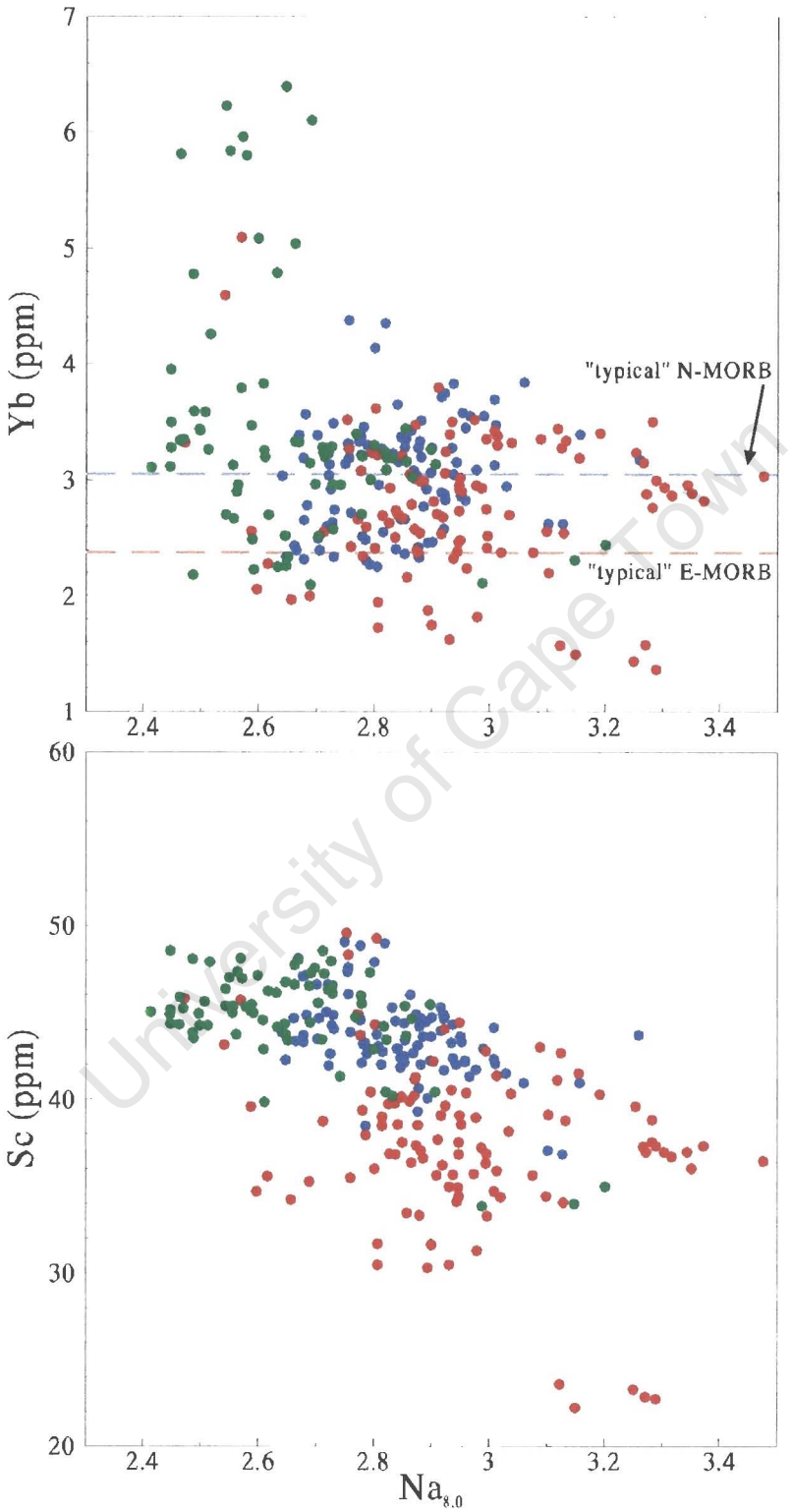

University of Cape Town

Figure 6.5b: Yb and Sc concentrations versus Na_8 of N-MORB (blue markers), Discovery-influenced MORB (red markers) and Shona-influenced MORB (green markers).

Sm-Nd - Lu-Hf isotopic systematics), evidence of residual garnet in their mantle source-region (Bourdon *et al.*, 1996; Hirschmann & Stolper, 1996; Kinzler, 1997; LaTourrette *et al.*, 1993; Robinson & Wood, 1998; Salters, 1996; Salters *et al.*, 1994; Shen & Forsyth, 1995).

If significant proportions of these melts were indeed directly derived from garnet-lherzolite stability field, then it might be argued that the major-element variations during garnet-lherzolite melting are different from those deduced for melts formed from spinel-lherzolite. Although the details of garnet-lherzolite melting beneath mid-ocean ridges have not received the same attention as spinel-lherzolite melting (Hirschmann & Stolper, 1996; Johnson *et al.*, 1990; Kinzler, 1997; Kinzler & Grove, 1992a; Kinzler & Grove, 1992b; Kinzler & Grove, 1993; Langmuir *et al.*, 1992; Niu, 1997; Niu & Batiza, 1991; Salters & Hart, 1989; Salters & Hart, 1991; Walter & Presnall, 1994; Walter *et al.*, 1995), preliminary data indicate that the systematics of the key major-element indicators of initial depth of melting (FeO and SiO_2) observed in melts formed in the spinel-lherzolite stability field persist in melts generated in the lower pressure portion of the garnet-lherzolite stability field (Kinzler, 1997).

Summary of observations. The fractionation-corrected major-element variations of these MORB from the SMAR conform broadly to the global trend as defined in previous work which used a global data-set of regional averages of basalt compositions (Klein & Langmuir, 1987; Klein & Langmuir, 1989; Langmuir *et al.*, 1992). The observed scatter in the data from this study is probably due to the use of individual analyses rather than averages. The data for the Shona-influenced MORB plot towards higher initial pressures and higher extents of melting relative to the data for N-MORB, consistent with the thicker crust in this region, expressed in the shallower ridge bathymetry. However, the data for Discovery-influenced MORB plot towards lower initial pressures and lower extents of melting relative to the data for N-MORB, which is opposite to what is expected and observed for the Shona-influenced MORB and MORB from most other mantle plume-influenced ridge segments (Langmuir *et al.*, 1992). The thicker crust in this area, also expressed as shallow ridge bathymetry, is in conflict with these below-average degrees of melting as indicated by the fractionation-corrected major-element data. A similar feature is evident for the Galapagos spreading centre, for which no explanation has yet been proposed (Langmuir *et al.*, 1992).

Some of the Discovery-influenced MORB contain anomalously high chondrite-

University of Cape Town

normalized Sm/Yb ratios and low Sc concentrations, which might suggest the presence of garnet as residual phase at some stage of the melting process which formed them. If a single episode of melting formed the magmas parental to the Discovery-influenced MORB and residual garnet is the cause of the low Yb and Sc concentrations, then the melting process must have been initiated at depths greater than at least 28kbar. This discrepancy between the melting parameters deduced from the fractionation-corrected major-element data, and what is expected for MORB from shallow bathymetry, mantle plume-influenced ridge segments, as well as the decoupling between the fractionation-corrected major-element data and the trace-element indicators of initial depth of melting will be addressed in a following section and a model proposed to reconcile these conflicting data.

6.1.3 The local trend

General observations. Further investigation of the Na_8-Fe_8 systematics of MORB from individual dredges show fine structure in what at first might seem scatter, when the data are viewed in the broad groupings based on previously defined criteria of mantle plume-influence. The diagrams in fig 6.6 show all the Na_8-Fe_8 data for the dredges in different colours as listed in the respective legends. Where one colour represents a number of dredges, the ranges in the data for the MORB from these dredges overlap and they are grouped together to avoid unnecessary visual clutter. Yellow lines represent local trends defined by the data, which are then reproduced in each diagram to evaluate whether the data from other dredges fall along the same or similar trends. The observed trends fall into two categories according to orientation. One set of trends occur approximately orthogonal to the global trend, and the second set of trends occur at much shallower angles relative to the global trend. The first group of trends are parallel to the so-called local trend in the global MORB data-set (Klein & Langmuir, 1989; Langmuir *et al.*, 1992). The local trend is observed predominantly in data for MORB from slower spreading mid-ocean ridges, and the presence of the local trend in these data is therefore not surprising (Klein & Langmuir, 1989; Langmuir *et al.*, 1992).

Evaluation of proposed models for the origin of the local trend. The origin of the local trend is not well-constrained and a number of scenarios have been proposed (Grove *et al.*, 1992; Kelemen *et al.*, 1997a; Kinzler, 1997; Kinzler & Grove, 1992b; Klein & Langmuir, 1987; Langmuir *et al.*, 1992; Niu & Batiza, 1991; Niu & Batiza, 1993; Niu & Batiza, 1994). The initial model advanced to account for the local trend (Klein & Langmuir, 1989), is that the basalts

University of Cape Town

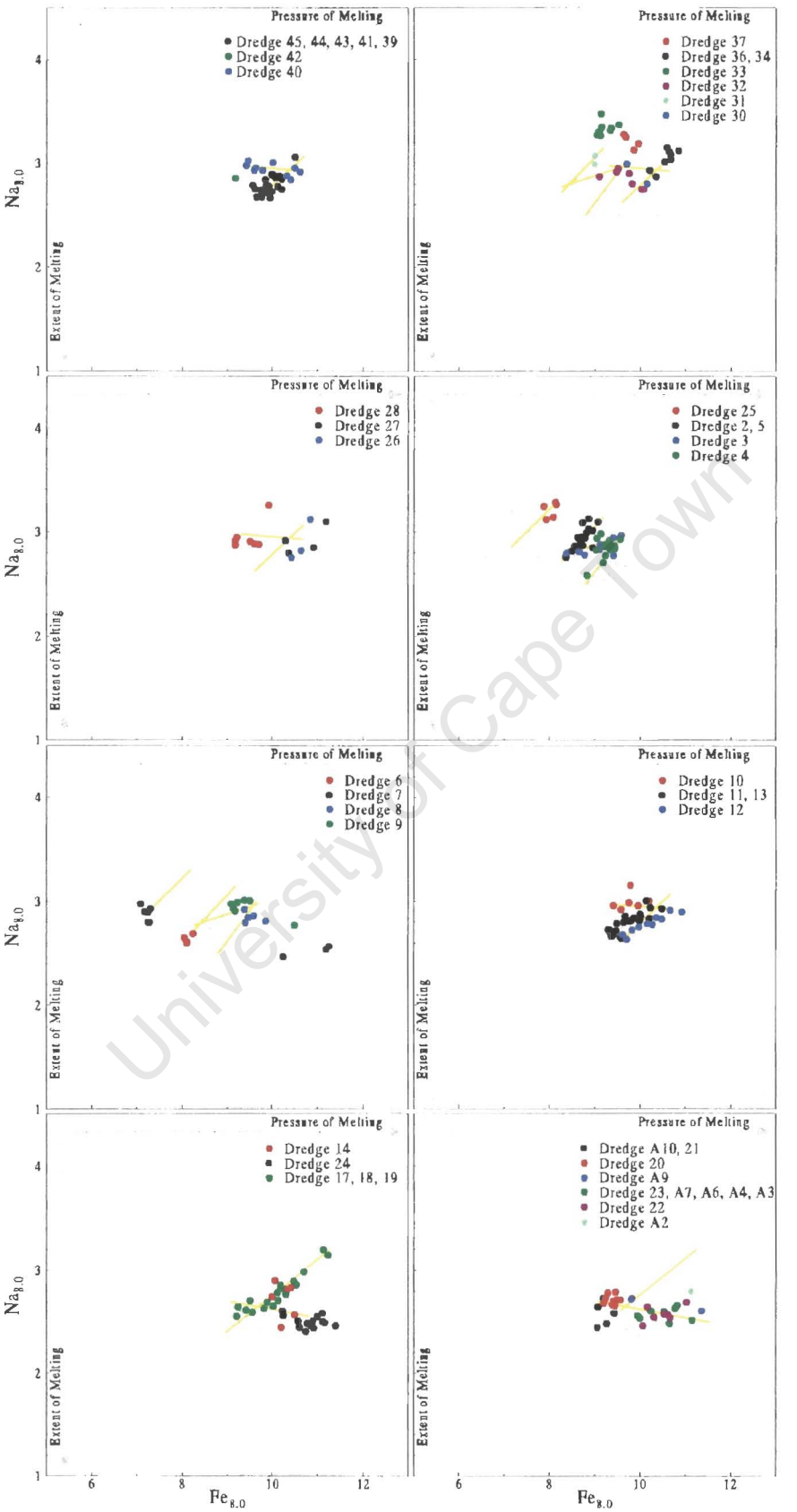

University of Cape Town

Figure 6.6: Na_8 versus Fe_8 for MORB from individual dredges, as indicated by different colours and defined in each legend. Yellow lines: observed local trends in the data; light grey dashed line: original global trend of Klein & Langmuir (1987, 1989); light grey markers: original global data-set of Klein & Langmuir (1987).

which constitute this trend represent the continuous sampling of instantaneous melts from throughout the melting column. The lack of the local trend in data for basalts from faster spreading mid-ocean ridges can thus be attributed to thorough homogenisation of these melts in shallow-level sub-axial magma chambers. The lack of extensive shallow-level sub-axial magma chambers beneath slower spreading mid-ocean ridges (Batiza *et al.*, 1988; Detrick *et al.*, 1990) would then result in the range of MORB compositions which define the local trend being erupted. The global trend would then be defined by the homogenised magmas, made up of all these instantaneous melts from throughout the melting column (Klein & Langmuir, 1989). This model is evaluated in fig 6.7a-b. It is evident from the modelled melting trajectories, with the compositions of the instantaneous melts after each increment of melting indicated, that the above model for the origin of the local trend does not conform to rigorous modelling of the melting process. The melting trajectories are too steep for eruption of magmas from different depths in the melting column to be the cause of the observed local trends, although the average pooled magmas from triangular melting regimes conform to the orientation and systematics of the global trend, as has previously been concluded (Kinzler, 1997; Langmuir *et al.*, 1992; Niu & Batiza, 1991).

An alternative proposed origin for the local trend, defined to account for the compositions of MORB from 26°S on the MAR, is the compositional affects of melting in diapiric bodies of mantle according to the net melting reaction: *melt A + pyroxene ⇒ melt B + olivine* (Kelemen *et al.*, 1997a; Niu & Batiza, 1993; Niu & Batiza, 1994). It was found that fractionation-corrected data for CaO and TiO_2 increase and decrease respectively with increasing $Si_{8.0}/Fe_{8.0}$, i.e. with progressive decompression and melting. Due to clinopyroxene, and to a lesser extent orthopyroxene, being the most important buffer phase in the mantle-source for both CaO and TiO_2 during melting, this complementary behaviour was viewed as evidence for the dissolution of pyroxene into the melt during decompression. Further positive correlations for Si_8/Fe_8, Ca_8 and a negative correlation for Ti_8 against fractionation-corrected Ni_8 was viewed as evidence for progressive olivine crystallisation concurrent with decompression and pyroxene dissolution (Niu & Batiza, 1994). The data for these MORB from the SMAR do not agree with this model. In fig. 6.8, only the plots of Ti_8 versus Si_8/Fe_8 and Ca_8 versus Ni_8 show rough correlations in agreement with the dissolution/crystallisation model. The data on the other diagrams exhibit none of the systematics required by the dissolution/crystallisation model. Therefore, the local trends in the data for these MORB from the SMAR are not due to

University of Cape Town

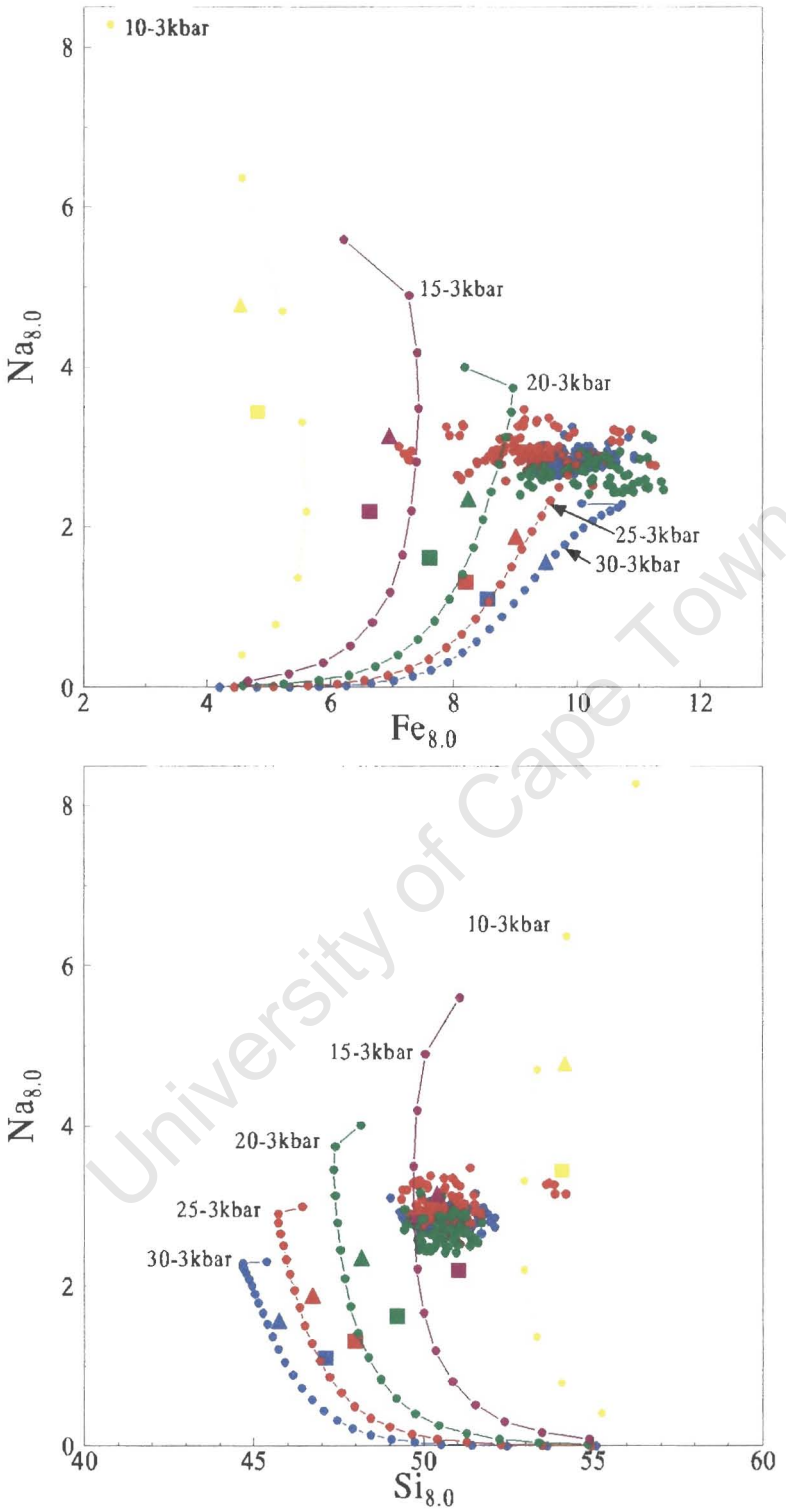

University of Cape Town

Figure 6.7a: Na_8 versus Fe_8 and Na_8 versus Si_8 for all the data for N-MORB (blue markers), Discovery-influenced MORB (red markers) and Shona-influenced MORB (green markers). Melting trajectories calculated using the algorithms of Kinzler (1997). Melting of the Hart & Zindler (1986) depleted I mantle composition was modelled at a series of initial pressures as labelled, with a constant final pressure of 3kbar, at a melt production-rate of 1%/kbar, with 99% of the melt removed per kbar (after Kinzler, 1997). Each increment of melting is represented by the solid circles on each trajectory. The filled squares represent the average pooled magmas for each trajectory assuming a columnar melting regime, and the filled triangles represent the average pooled magmas for each trajectory assuming a triangular melting regime (Kinzler, 1997).

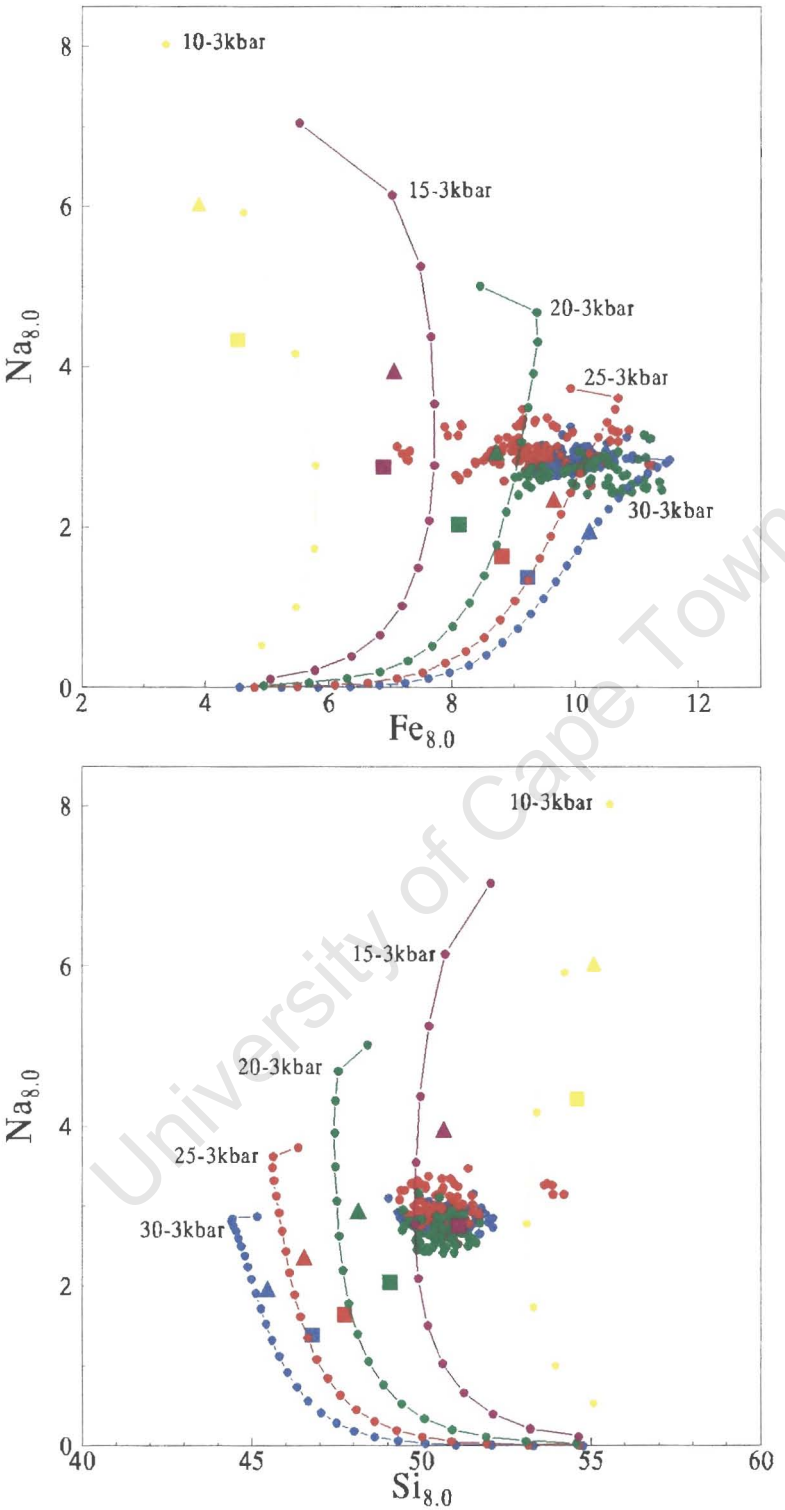

University of Cape Town

Figure 6.7b: Na_8 versus Fe_8 and Na_8 versus Si_8 for all the data for N-MORB (blue markers), Discovery-influenced MORB (red markers) and Shona-influenced MORB (green markers). Melting trajectories calculated using the algorithms of Kinzler (1997). Melting of the AP (abyssal peridotite) fertile 2 mantle composition (Kinzler, 1997) was modelled at a series of initial pressures as labelled, with a constant final pressure of 3kbar, at a melt production-rate of 1%/kbar, with 99% of the melt removed per kbar (after Kinzler, 1997). Each increment of melting is represented by the solid circles on each trajectory. The filled squares represent the average pooled magmas for each trajectory assuming a columnar melting regime, and the filled triangles represent the average pooled magmas for each trajectory assuming a triangular melting regime (Kinzler, 1997).

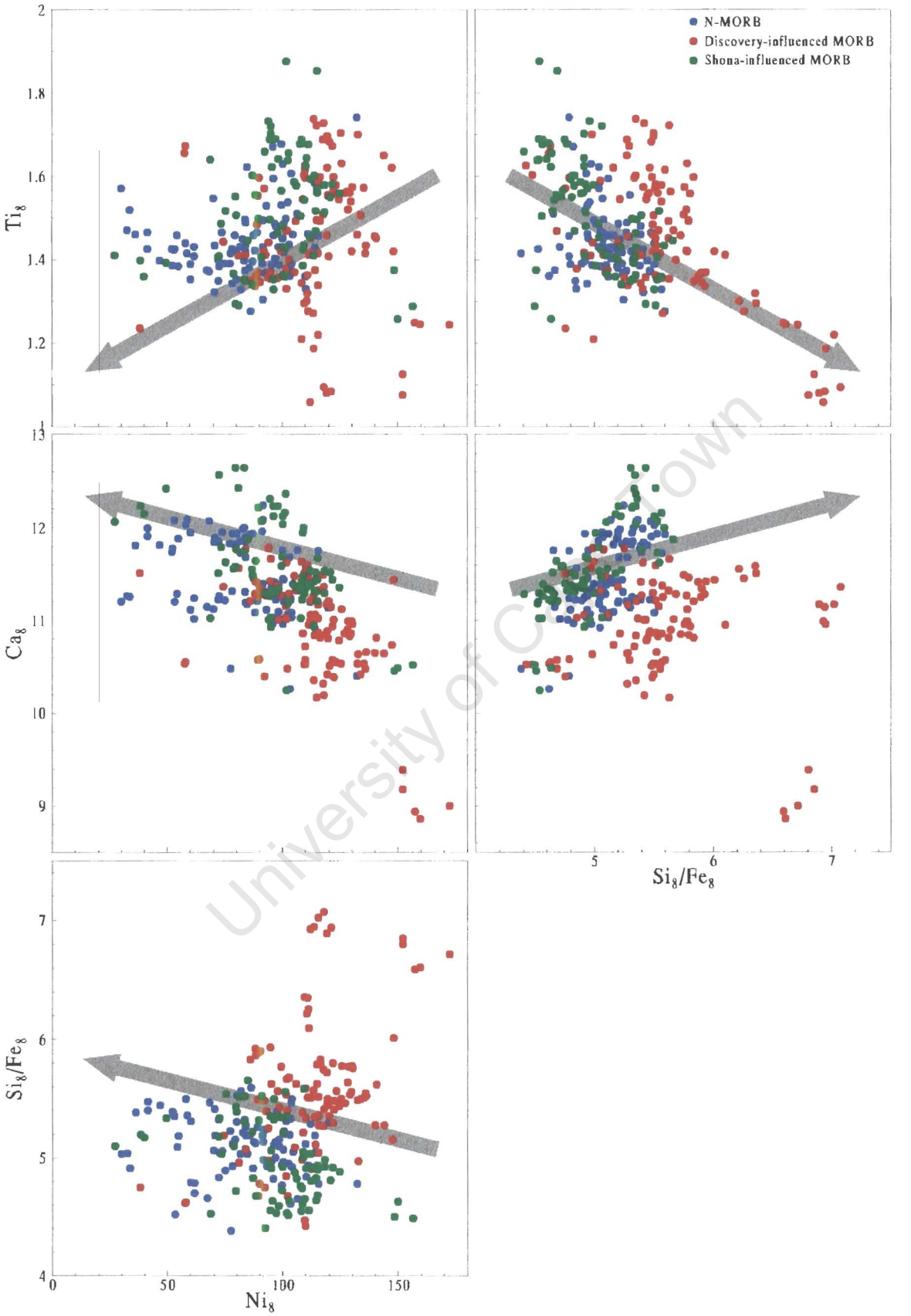

University of Cape Town

Figure 6.8: Fractionation-corrected Ti_8 and Ca_8 versus Ni_8 and Si_8/Fe_8, and Si_8/Fe_8 versus Ni_8 for MORB from the SMAR. Grey arrows indicate correlations expected for olivine crystallisation with progressive, indicated by directions of arrows, decompression and clinopyroxene dissolution into the melt (Niu & Batiza, 1994).

progressive dissolution of pyroxene and crystallisation of olivine during a net mantle melting reaction as proposed by Niu & Batiza (1994).

Another possible cause of the local trend in fractionation-corrected major-element data for MORB from slow-spreading ridges, such as the SMAR, is polybaric phenocryst crystallisation (Grove *et al.*, 1992; Kinzler & Grove, 1992b). The possibility of high-pressure phenocryst crystallisation is more probable at slow-spreading ridges, due to more efficient mantle cooling at slower spreading rates, the probable thicker lithospheric cap and the lack of evidence for shallow-level sub-axial magma chambers (Batiza *et al.*, 1988; Detrick *et al.*, 1990; Langmuir *et al.*, 1992). The results of crystallisation at 1atm and 8kbar presented in fig 6.9, were obtained with compositions of modelled average pooled magmas, see also fig. 6.7a-b, as starting compositions and using the CoMagmat algorithm of Ariskin *et al.* (1993). When compared to other methods available to model crystallisation and calibrated against experimental crystallisation studies, CoMagmat reproduces the behaviour of natural systems quite successfully, with minimal demand in terms of computer requirements and in a user-friendly format (Yang *et al.*, 1996).

The compositions of the average pooled magmas, derived by melting the HZ depleted 1 and AP fertile 2 mantle compositions of Kinzler (1997) between 20-3kbar and 15-3kbar in the preceding section, were modelled as starting compositions for crystallisation at 1atm and 8kbar as detailed above. The compositions of the resulting evolved magmas are plotted in fig. 6.9 upon reaching 8wt% MgO. The evolved 8wt%-MgO magmas derived through crystallisation at 1atm and 8kbar of the same starting composition are linked by a solid black line in fig. 6.9. The result is a series of sub-parallel lines defining the Na_8-Fe_8 compositions of magmas derived through crystallisation at 1atm-8kbar of the four starting compositions.

The natures of the low pressure and high pressure fractional crystallisation of all the starting compositions are qualitatively similar, and will only be discussed for the example of the average pooled magma derived from melting the AP fertile 2 mantle source, at 20-3kbar, as starting composition (dark green markers in fig. 6.9). The initial stages of the low pressure crystallisation of this starting composition involve only olivine, but after 4% crystallisation (at 10.20wt% MgO) plagioclase joins the liquidus assemblage. The crystallisation of these two phases continues until the remaining magma reaches a composition of 8wt% MgO after 37%

University of Cape Town

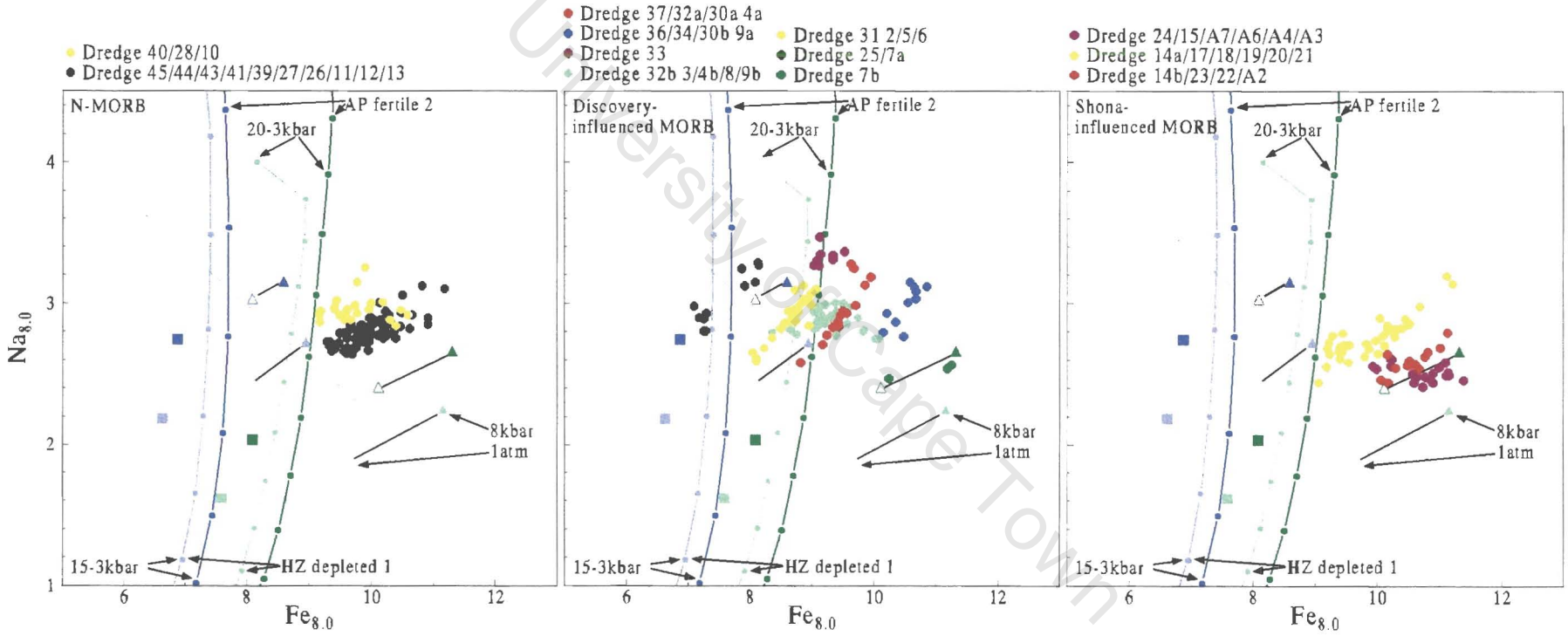

University of Cape Town

Figure 6.9: Na_8 versus Fe_8 for N-MORB (left diagram), Discovery-influenced MORB (middle diagram) and Shona-influenced MORB (right diagram). Subsets of samples defining local trends, are grouped by colours defined in legends. Dashed grey line: global trend (Klein & Langmuir, 1987, 1989). Coloured lines with markers: calculated melting trajectories (Kinzler, 1997) using starting compositions and pressure intervals as labelled, and a rate of melting of 1%/kbar with 90% melt removal/kbar. Filled square markers: pooled melts of modelled melting trajectories of same colour. Triangular markers linked by solid black lines: compositional range of pooled melts of same colour crystallised (Ariskin *et al.*, 1993) to 8wt% MgO between pressures ranging from 1atm to 8kbar (as labelled).

crystallisation. At high pressure, olivine again dominate the initial crystallisation and is joined in the liquidus assemblage by plagioclase after 3% crystallisation (at 10.29wt% MgO). However, after 18% crystallisation (at 9.49wt% MgO) clinopyroxene is added to the liquidus assemblage and the three-phase assemblage is removed from the magma until it reaches a composition of 8wt% MgO after 44% crystallisation. The extended crystallisation of the magma, i.e. 44% relative to 37%, and the significant presence of clinopyroxene in the liquidus assemblage at high pressure result in significantly higher Na_2O and FeO concentrations in the magma at 8wt%. Although not shown, the SiO_2 concentration of the magma at 8wt% MgO after high pressure crystallisation is also significantly lower.

The orientation of the modelled low pressure-high pressure crystallisation trends presented in fig 6.9 agree with the orientation of local trends in the data for MORB from the SMAR. This agreement therefore indicates that the initial pressure of melting beneath the SMAR varied at least from 15-20kbar, and major-element compositions of the mantle source-regions varied from depleted to fertile in nature. Significantly, crystallisation occurred beneath individual ridge segments of the SMAR over a range of pressures resulting in the observed local trends in the compositions of erupted basalts.

Increasing the rate of melting from 1%/kbar to 2%/kbar in the modelling of the composition of the starting magmas, result in lower Na_8 and higher Fe_8 concentrations in the instantaneous melts for each increment of melting. Subsequent increasing of the melting rate to 3%/kbar and 4%/kbar cause negligible changes in the compositions of instantaneous melts relative to those produced by melting at 2%/kbar. Variations in the rate of melting which produced the starting magmas, especially in the range between 1%/kbar to 2%/kbar, can therefore significantly shift the local trends, produced by subsequent crystallisation over a range of pressures, along the general orientation of the global trend.

The concentrations of Sr are fairly constant amongst basalts from the SMAR constituting subsets which define local trends in fig. 6.6. This is illustrated in fig. 6.10, where the Sr concentrations of basalts are plotted against their Na_8 and Fe_8 values. The data for samples from single dredges which define local trends in fig. 6.6, define horizontal trends in fig. 6.10, although the Sr data-set for MORB from the SMAR as a whole define broad positive and negative correlations with Na_8 and Fe_8 data respectively. The concentrations of Sr in basalts which define

University of Cape Town

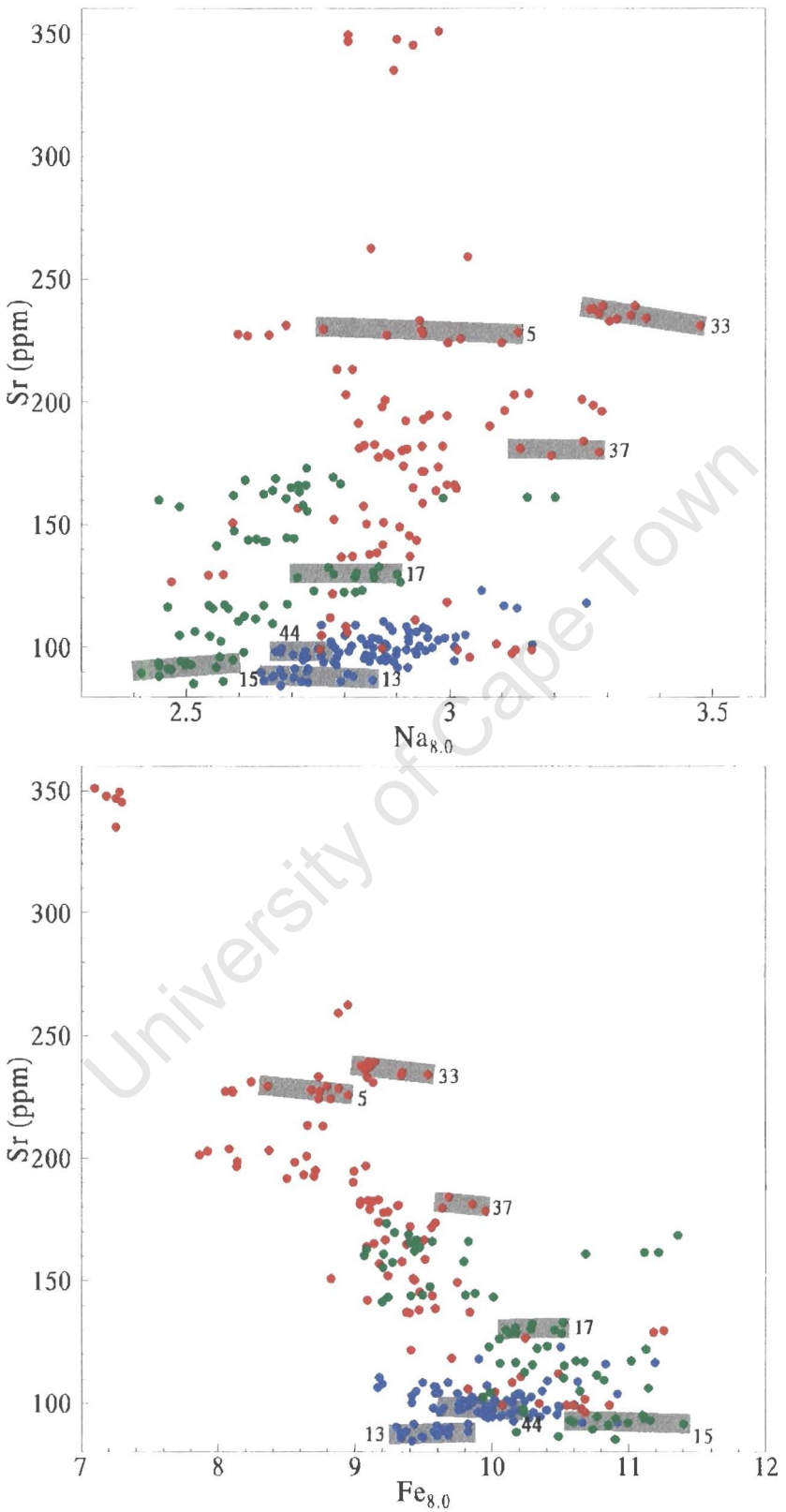

University of Cape Town

Figure 6.10: Sr concentrations versus Na_8 and Fe_8 for N-MORB (blue markers), Discovery-influenced MORB (red markers), and Shona-influenced MORB (green markers). Filled grey fields, labelled with dredge numbers, indicate samples from dredges which define local trends in fig 6.6.

local trends are therefore buffered within individual local trends. During mantle melting, Sr is incompatible (Langmuir *et al.*, 1992) and the broad positive and negative correlations with Na_8 and Fe_8 observed in fig. 6.10 are the expected results. Therefore, the first-order co-variation of Sr concentrations with Na_8 and Fe_8 is the result of the same variations in mantle melting processes proposed to account for the global trend (Langmuir *et al.*, 1992). However, the second-order of complexity in the Sr versus Na_8 and Fe_8 co-variation in which Sr concentrations are constant along local trends require a process which can buffer Sr concentrations while producing local trends in the Na_8-Fe_8 data. The most-likely process is crystallisation involving plagioclase, in addition to olivine and/or clinopyroxene. The presence of plagioclase in the liquidus assemblage during crystallisation yields bulk partition coefficients for Sr of ~ 1 (Langmuir *et al.*, 1992), due to the high partition coefficient of 2-1.4 for Sr in plagioclase (Dunn & Sen, 1994; McKenzie & O'Nions, 1991). The discussion of the nature of the low and high pressure crystallisation modelled in fig. 6.9 to produce local trends in the Na_8-Fe_8 data for MORB from the SMAR, record the presence of plagioclase in the liquidus assemblage at both low and high pressures shortly after initiation of crystallisation. The buffered concentrations of Sr observed in basalts which define local trends are therefore consistent with the earlier major-element modelling which advocates a role for phenocryst crystallisation in the origin of local trends.

Although the origin of the local trend in the global data-set is still a matter of debate, the data from the SMAR support a model in which crystallisation, probably at variable pressures, play an important role (Grove *et al.*, 1992; Kinzler & Grove, 1992b). Not only the major-element modelling, but also the co-variation of Sr concentrations with major-element parameters, illustrated by the buffered Sr concentrations in the MORB, support the influence of crystallisation on the origin of the local trend. This is contrary to what has been concluded previously using data for MORB quenched igneous glasses from the FAMOUS region on the MAR (Langmuir *et al.*, 1992).

6.2 VARIATIONS IN CALCULATED MELTING PARAMETERS

Discussion of different calculation methods. The fractionation-corrected major-element data for MORB can contain signatures related to the melting processes in the mantle from which the basaltic magmas were derived, as was discussed in the previous section. The broad major-element indicators of the initial pressures (Fe_8, and Si_8/Fe_8) and mean extents (Na_8, and Ca_8/Al_8) of melting, discussed previously, have been used in a number of studies to produced equations

University of Cape Town

aimed at quantifying the initial, final, or mean pressures and mean extents of melting (Kinzler & Grove, 1993; Langmuir *et al.*, 1992; Niu & Batiza, 1991). The results from the different approaches do not agree quantitatively, but do agree quite well qualitatively (Kinzler & Grove, 1993). The algorithms of Niu & Batiza (1991) were used to calculate the melting parameters plotted in fig. 6.11a (equations 7.2-7.4). The reasons for this choice are that these equations use a number of the fractionation-corrected major-element values from each MORB sample, unlike the algorithms (equations 7.5-7.8 of Kinzler & Grove (1993). They also do not require any further data manipulation, unlike the equations of Kinzler & Grove (1993) which necessitates the projection of the data orthogonally onto the idealized global trend, before the Na_8 and Fe_8 values should be used in the calculations.

The calculated melting parameters, using the equations of Niu & Batiza (1991), are plotted against latitude for these MORB from the SMAR in fig. 6.11a. For comparison, the melting parameters calculated using the equations of Kinzler & Grove (1993) are also plotted in against latitude in fig. 6.11b. The Na_8 and Fe_8 data used to calculated the parameters in fig. 6.11b were not projected orthogonally onto the idealized global trend, therefore the quantitative values are not reliable although the uncorrected data should not yield results qualitatively different from corrected data. The relationship between Na_8 and Fe_8 would be the same before and after projection onto the idealized global trend, only the absolute values would change and

$$F_{mean}(wt\%) = 19.202 - 5.175Na_{8.0} + 15.537\frac{Ca_{8.0}}{Al_{8.0}} \quad \text{equation 7.2}$$

$$P_{initial}(kbar) = 25.98 + 0.967F + 45.277\frac{1}{F} - 5.186\frac{Si_{8.0}}{Fe_{8.0}} \quad \text{equation 7.3}$$

$$P_{final}(kbar) = (1.3613P_{initial} + 3.9103) + \frac{(-1.3458P_{initial} - 13.592)}{F} + (-0.03015P_{initial} - 0.2929)F \quad \text{equation 7.4}$$

(Niu & Batiza, 1991)

$$F_{mean}(wt\%) = -8.746 + 0.205(Fe_{8.0})^2 + 0.405(Na_{8.0})^2 \quad \text{equation 7.5}$$

$$P_{mean}(kbar) = 3.18 + 0.630F_{mean} \quad \text{equation 7.6}$$

$$T_{initial}(^oC) = 1113 + 20.15F_{mean} \quad \text{equation 7.7}$$

$$Crust\ (km) = (2P_{mean} - 2P_{final} + 1) \times 0.033F_{mean} \quad \text{equation 7.8}$$

(Kinzler & Grove, 1993)

University of Cape Town

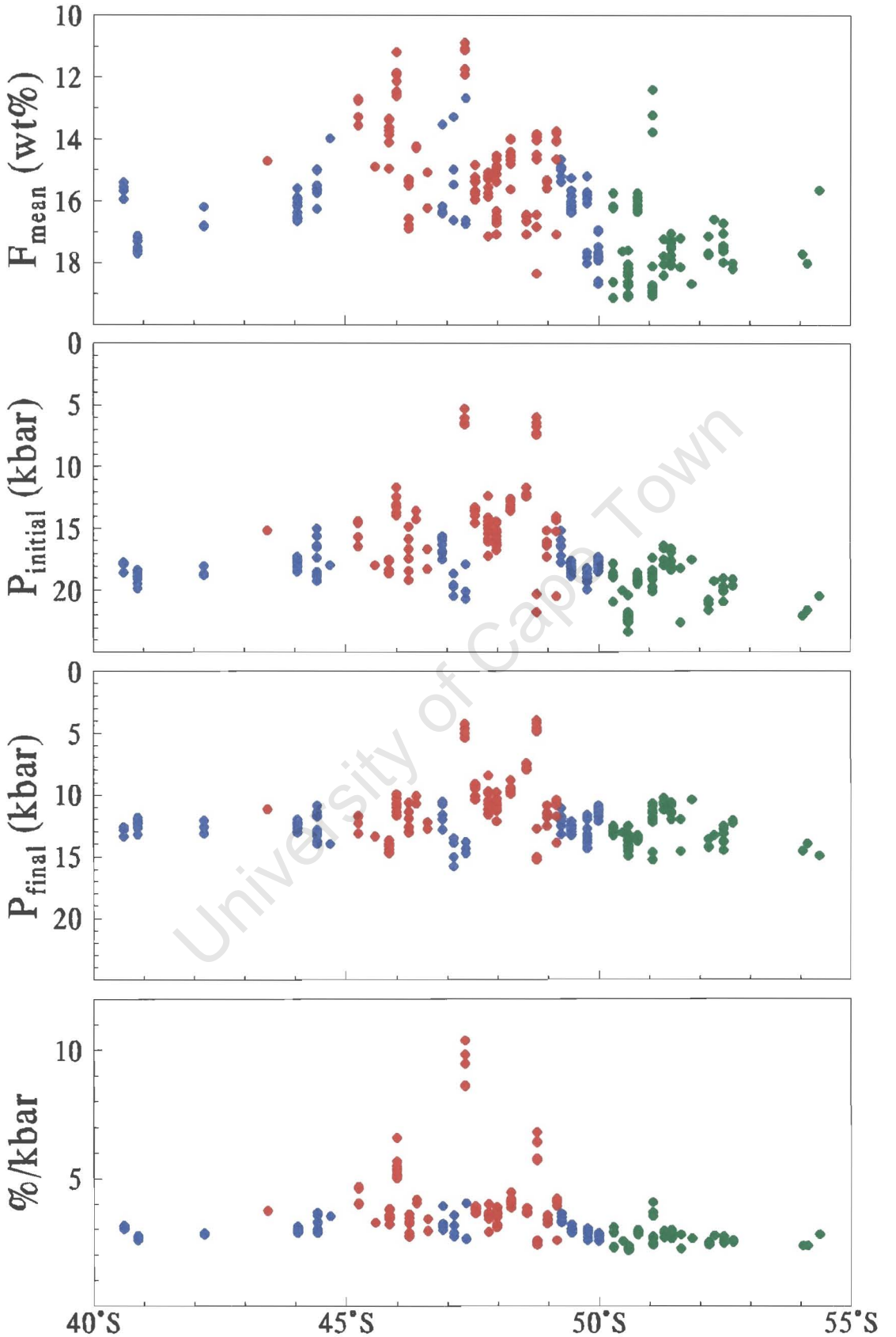

University of Cape Town

Figure 6.11a: F_{mean}, $P_{initial}$, P_{final} and rate of melting for N-MORB (blue markers), Discovery-influenced MORB (red markers) and Shona-influenced MORB (green markers), calculated using the equations of Niu & Batiza (1991), versus latitude (°S).

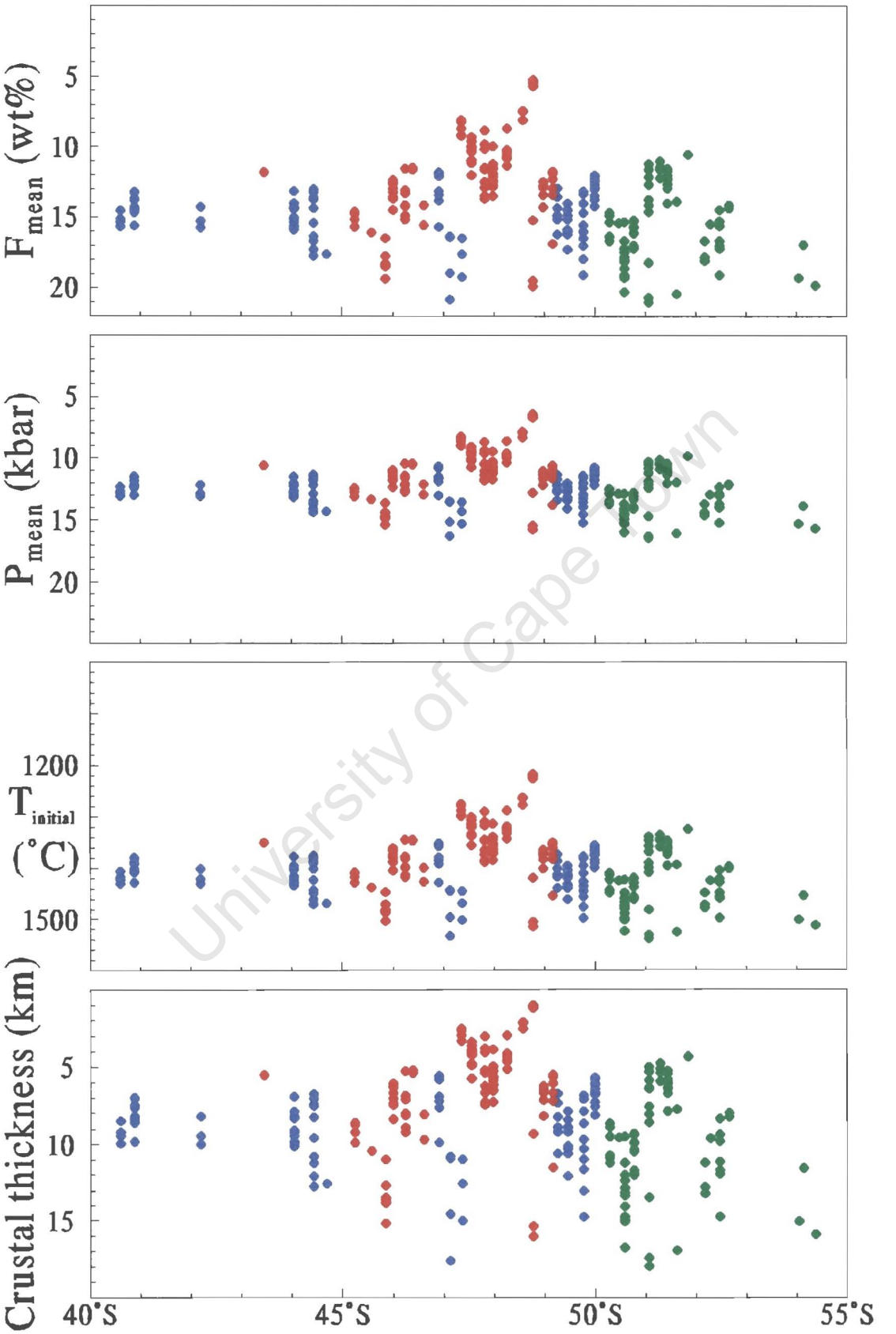

University of Cape Town

Figure 6.11b: F_{mean}, P_{mean}, $T_{initial}$ and crustal thickness for N-MORB (blue markers), Discovery-influenced MORB (red markers) and Shona-influenced MORB (green markers), calculated using the equations of Kinzler & Grove (1993), versus latitude (°S).

data for MORB which define local trends would collapse into single points on the global trend. The corrected data would therefore contain less scatter, but basalts which plotted at low Na_8 and high Fe_8 would still yield higher extents and higher degrees of melting relative to basalts which plotted at high Na_8 and low Fe_8. The calculated melting parameters in fig. 6.11a & b agree qualitatively and define similar "along-ridge" trends. The following discussion of the variations in the calculated melting parameters will therefore only focus on the data presented in fig. 6.11a.

Observed variations in calculated melting parameters of MORB from the SMAR. The along-ridge variations observed in fig. 6.11a correlate with the conclusions reached during the discussion of the data for these MORB relative to the global trend. The mean extents of the mantle melting which produced the Shona-influenced MORB are higher relative to the melting which yielded N-MORB. The melting beneath Shona-influenced ridge segments was also initiated at greater pressures relative to melting beneath ridge segments unaffected by mantle plumes. The Discovery-influenced MORB on the other hand, were derived from mantle melting at lower pressures and to smaller extents relative to the melting which yielded N-MORB. This is to be expected, as these melting parameters use the fractionation-corrected major-element data which define the global trend.

The calculated melting parameter do, however, yield some additional information regarding the melting processes by which these MORB were formed. The data for N-MORB indicate general mean extents of melting (14-17%) which decrease to ~11% in the proximity of the Discovery-influenced ridge segments, and which increase up to ~19% in the two dredges north of the first Shona-influenced ridge segments and the second dredge from the northern edge of the study area. The initial and final pressures of melting are fairly constant for N-MORB (~18±2kbar; and ~13±2kbar), but the basalts in the two dredges immediately north of the Falkland/Agulhas Fracture Zone, at ~47.5°S, yield slightly greater initial (~21kbar) and final (~16kbar) pressures of melting.

The data for Shona-influenced MORB conform to expectations for mantle plume-influenced basalts, and yield predominantly higher extents of melting (16-19%) than N-MORB and slightly greater initial pressures of melting (~20±3kbar). However, the final pressures of melting for Shona-influenced MORB are fairly constant (~13±2kbar) and overlap with the range for N-MORB. The rates of melting calculated for N-MORB and Shona-influenced MORB are

University of Cape Town

fairly constant at 2-4%/kbar, and the higher mean extents of melting for Shona-influenced MORB are therefore due to the deeper initiation of melting beneath these ridge segments.

The calculated melting parameters in fig. 6.11a confirm the anomalous character of the data for MORB from the Discovery-influenced ridge segments, especially the ridge segments to the south of the Falkland/Agulhas Fracture Zone, at ~47.5°S. In general, the Discovery-influenced MORB yield mean extents of melting (13-17%) lower than N-MORB, with a few dredges containing MORB which yield particularly low extents of melting (11-13%). The initial and final pressures of melting for Discovery-influenced MORB seem to define two distinct groups, one the northern Discovery-influenced MORB with13-20kbar and 10-15kbar, and the other the southern Discovery-influenced MORB with 13-17kbar and 8-12kbar. Some of the southern Discovery-influenced MORB extreme anomalous initial and final pressures of melting (5-7kbar; and 4-5kbar). This narrow interval of melting results in extreme rates of melting for the origin of these basalts (6-10%/kbar). Otherwise the rates of melting calculated for Discovery-influenced MORB also fall in the 2-4%/kbar range defined for the N-MORB and Shona-influenced MORB.

The anomalous character of the Discovery-influenced MORB, and particularly this subset of basalts from south of the Falkland/Agulhas Fracture Zone, is further illustrated in fig. 6.12 and fig. 6.13. There is a positive correlation between $^{87}Sr/^{86}Sr$ values and initial pressures of melting for Discovery-influenced MORB. The basalts with the highest $^{87}Sr/^{86}Sr$ values, and therefore the strongest Discovery mantle-plume signatures, also have the anomalously low values for initial pressures of melting. The mean extents of melting do not correlate as well as the initial pressures of melting with the $^{87}Sr/^{86}Sr$ values, but the lowest mean extents of melting are calculated for the basalts with the highest $^{87}Sr/^{86}Sr$ values. Therefore the mantle source-regions which have experienced the strongest influence of the Discovery mantle plume experienced melting at significantly shallower levels in the mantle, compared to all other MORB from the SMAR. However, these mantle source-regions have not experienced melting to anomalously lower extents of melting.

The Discovery-influenced basalts which yielded the anomalously low initial pressures of melting, also have anomalously low Sc concentrations (~22-32ppm) and high chondrite-normalised (Sun & McDonough, 1989) Sm/Yb ratios in fig. 6.13. The low Sc and Yb

University of Cape Town

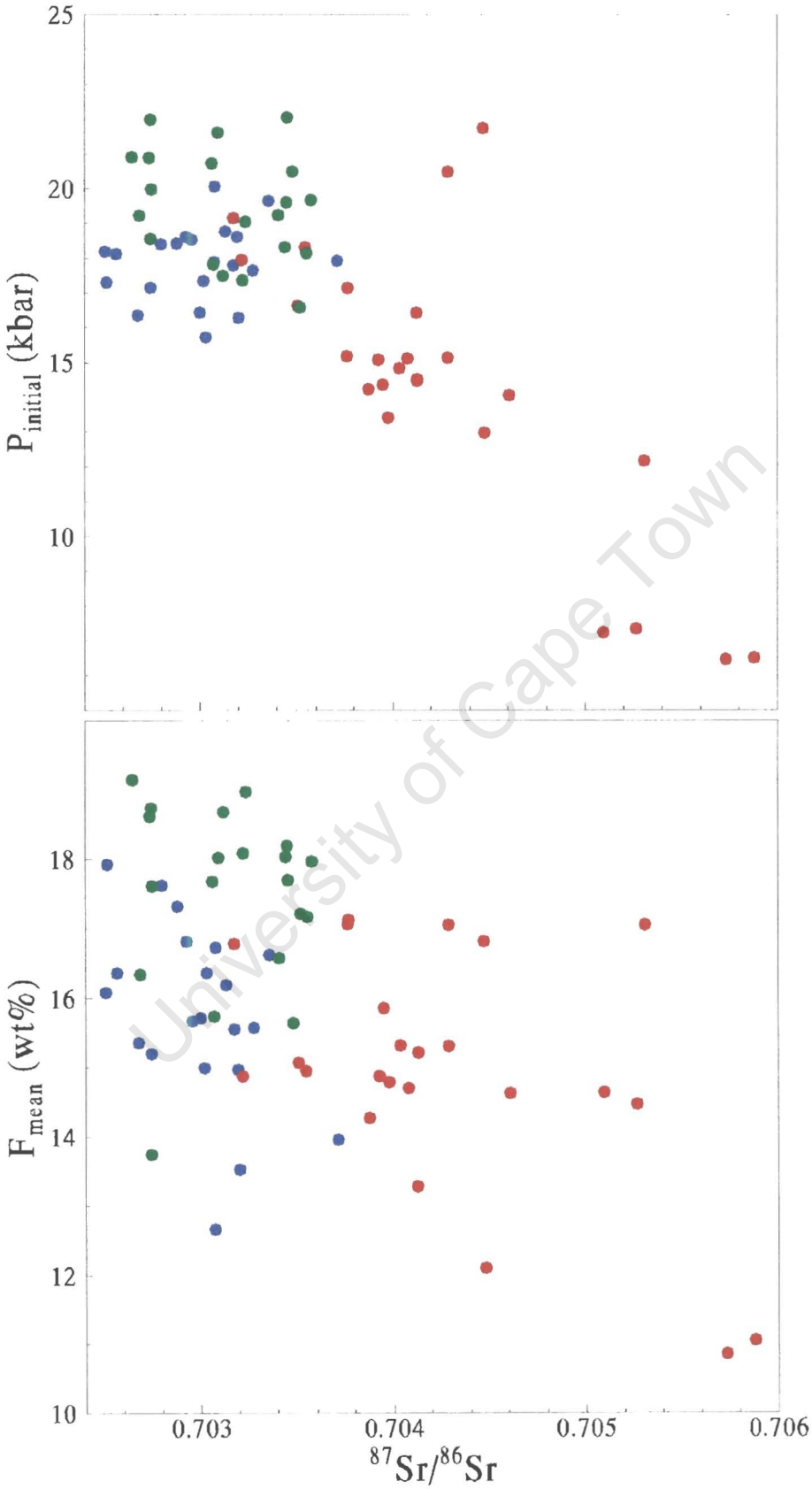

University of Cape Town

Figure 6.12: Calculated melting parameters (Niu & Batiza, 1991) (see text for discussion), versus $^{87}Sr/^{86}Sr$ (Douglass *et al.*, 1999) for N-MORB (blue markers), Discovery-influenced MORB (red markers) and Shona-influenced MORB (green markers).

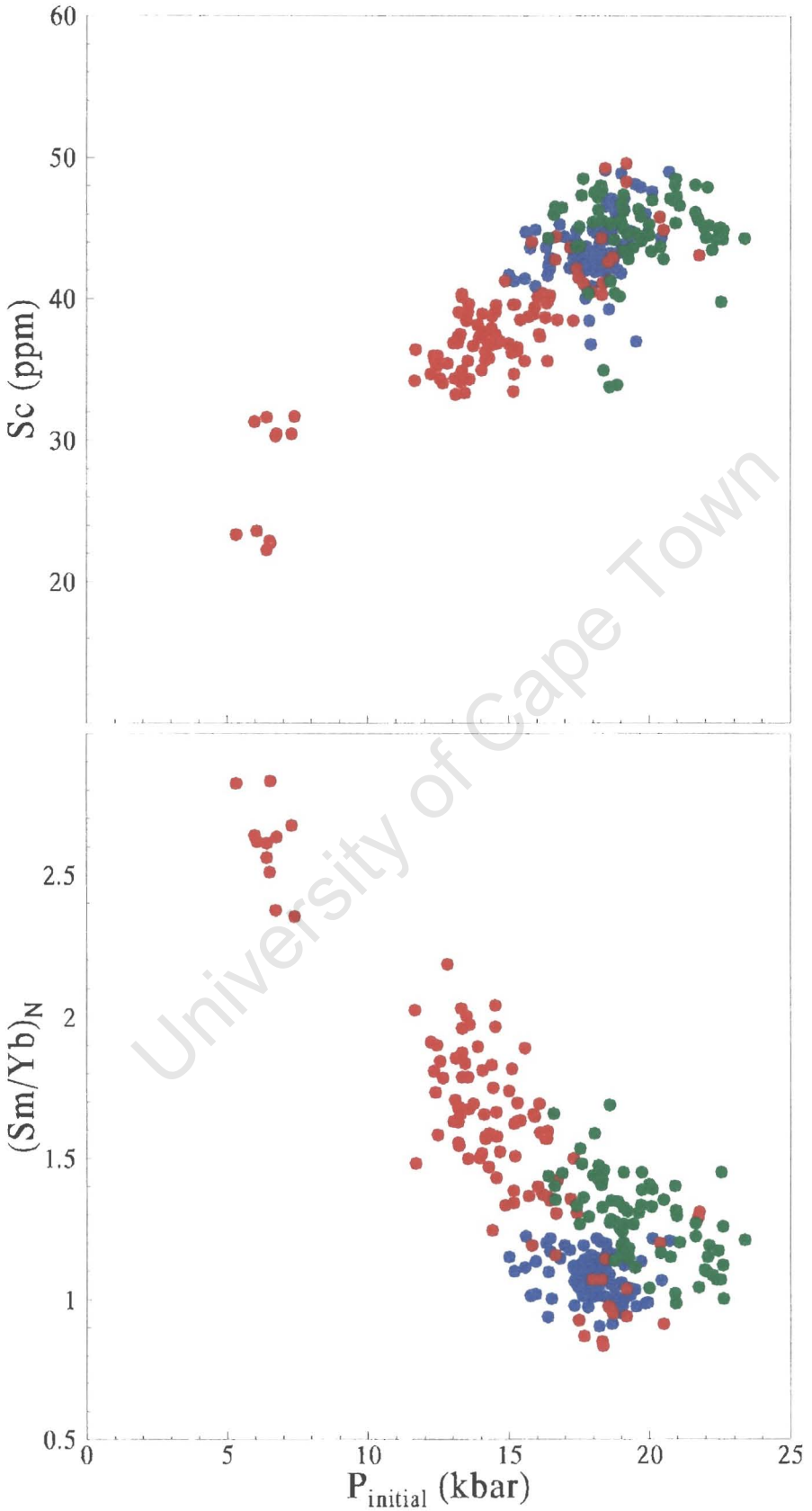

University of Cape Town

Figure 6.13: Sc concentrations and chondrite-normalised (Sun & McDonough, 1989) (Sm/Yb) ratios versus calculated initial pressures of melting (Niu & Batiza, 1991) for N-MORB (blue markers), Discovery-influenced MORB (red markers) and Shona-influenced MORB (green markers).

concentrations in these basalts were earlier discussed as evidence for the presence of residual garnet during the mantle melting process which yielded these basalts. It is therefore clear that these unusual MORB were not only derived from mantle source-regions which have been compositionally most-affected by the influence of the Discovery mantle plume, at anomalously low initial pressures of melting and at exceptionally high rates of melting, but that at some stage of the melting process garnet must have been a residual phase.

The paradox of the Discovery-influenced MORB can therefore be summarised as follows: these MORB exhibit fractionation-corrected major-element data and calculated melting parameters characteristic of magmas having been derived at anomalously low initial pressures from relatively low mean extents of melting, which is completely at odds with their recovery from shallow ridge segments and therefore regions of thick crust. These observations are further complicated by radiogenic isotope data which indicate that the basalts which formed at the lowest pressures were derived from mantle source-regions with compositions which have been influenced the most by the mantle plume. To conclude the enigmatic nature of these basalts, trace-element data seem to necessitate the presence of residual garnet in the mantle source-regions at some stage during the melting process.

University of Cape Town

6.3 RESIDUAL GARNET DURING MELTING BENEATH DISCOVERY-INFLUENCED RIDGE SEGMENTS

Basalts with conflicting trace-element and major-element indicators of initial pressures of melting are predominantly derived from material strongly associated with the Discovery mantle plume. The paradox in the composition of Discovery-influenced MORB discussed in the preceding sections is especially pronounced in all the basalts recovered from dredges 25 and 6, and a subset of basalts from dredge 7 (samples 1, 5-9). The trace-element characteristics (high $(Sm/Yb)_N$ ratios of 1.73-2.83 and low Sc concentrations of 22.2-32ppm) of these basalts are very-well correlated with anomalous radiogenic isotope data (high $^{87}Sr/^{86}Sr$ ratios of 0.705093-0.705878 and low $^{143}Nd/^{144}Nd$ ratios of 0.512365-0.512567), see fig. 6.14. The radiogenic isotope ratios for these basalts, and in particular the basalts from dredge 25, have been interpreted as the most representative of the Discovery mantle plume (Douglass *et al.*, 1999; Douglass *et al.*, 1995). Therefore the melting processes which produced these basalts primarily sampled the undiluted mantle plume-derived component in the mantle source-regions.

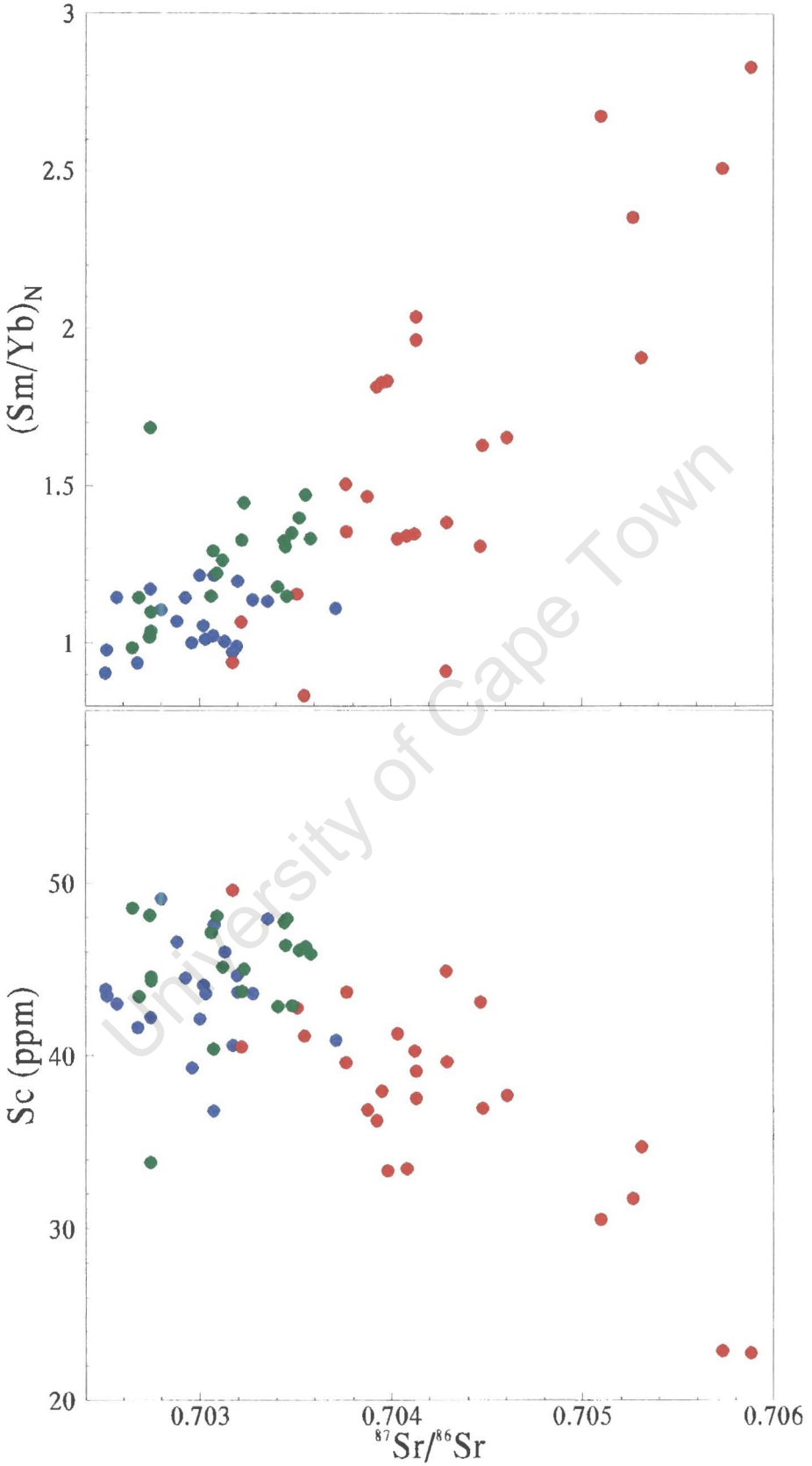

University of Cape Town

Figure 6.14: Chondrite-normalized (Sun & McDonough, 1989) Sm/Yb ratios and Sc concentrations versus $^{87}Sr/^{86}Sr$ ratios (Douglass *et al.*, 1999) for N-MORB (blue markers), Discovery-influenced MORB (red markers) and Shona-influenced MORB (green markers).

The correlation with the radiogenic isotope data in fig. 6.14 confirms that the trace-element characteristics of these MORB are inherited from the mantle source-regions through the melting processes. This conclusion is further reinforced by the clear correlation of the high $(Sm/Yb)_N$ ratios and low Sc concentrations of these basalts with high Si_8/Fe_8 in fig. 6.5a, with low calculated initial pressures of melting in fig. 6.13, and therefore with the melting environment.

The possible influence of crystallisation. The possibility that the trace-element characteristics, anomalously low Sc concentrations and high $(Sm/Yb)_N$ ratios, might be due to a process of crystallisation, is not supported by other compositional characteristics or forward modelling. Previously, constant Sr concentrations at variable Na_8 and Fe_8 values within dredges were used to indicate the influence crystallisation involving plagioclase at some stage during the petrogenetic history of basalts from the SMAR, see fig. 6.10. Basalts from a considerable number of dredges exhibited distinct evidence of having experienced significant crystallisation. Although the Sr concentrations of these anomalous basalts do not vary significantly, neither do their Na_8 or Fe_8 values. The Sr-Na_8-Fe_8 co-variations, which indicate crystallisation in basalts from other dredges, indicate a much reduced role for crystallisation in these basalts.

The Mg#'s of these basalts from dredge 25, 6 & 7 are high (62.5-64.7), while the CaO/Al_2O_3 ratios are low (0.55-0.73). In fig. 6.15, these basalts plot progressively removed from the rest of the basalts from the SMAR. From the more detailed discussion of the nature and role of crystallisation on the compositions of the basalts recovered from the SMAR in chapter 7, it is clear that the combined Mg#-CaO/Al_2O_3-Sc characteristics of these basalts could not be due to the affects of crystallisation. In fig. 7.7, crystallisation at constant pressures between 1atm and 8kbar of various starting composition, e.g. quenched igneous glasses and an aphyric bulk sample all with high Mg#'s and listed in table 7.2, can not reproduce magmas with Mg#'s, CaO/Al_2O_3 or Sc concentrations similar to these basalts. Using theoretical melt compositions as starting compositions (produced by forward-modelling the near-fractional melting of the Hart & Zindler (1986) depleted 1 and the AP fertile 2 mantle composition (Kinzler, 1997), at constant initial pressure of melting of 20kbar and melting terminating at 10kbar or at the point of clinopyroxene exhaustion in the source mode, and at melting rates of 1-4%/kbar (Kinzler, 1997), see chapter 7 for further details), crystallisation can also not reproduce magmas with the Mg#'s, CaO/Al_2O_3 or Sc concentrations similar to these basalts, see fig. 7.7.

University of Cape Town

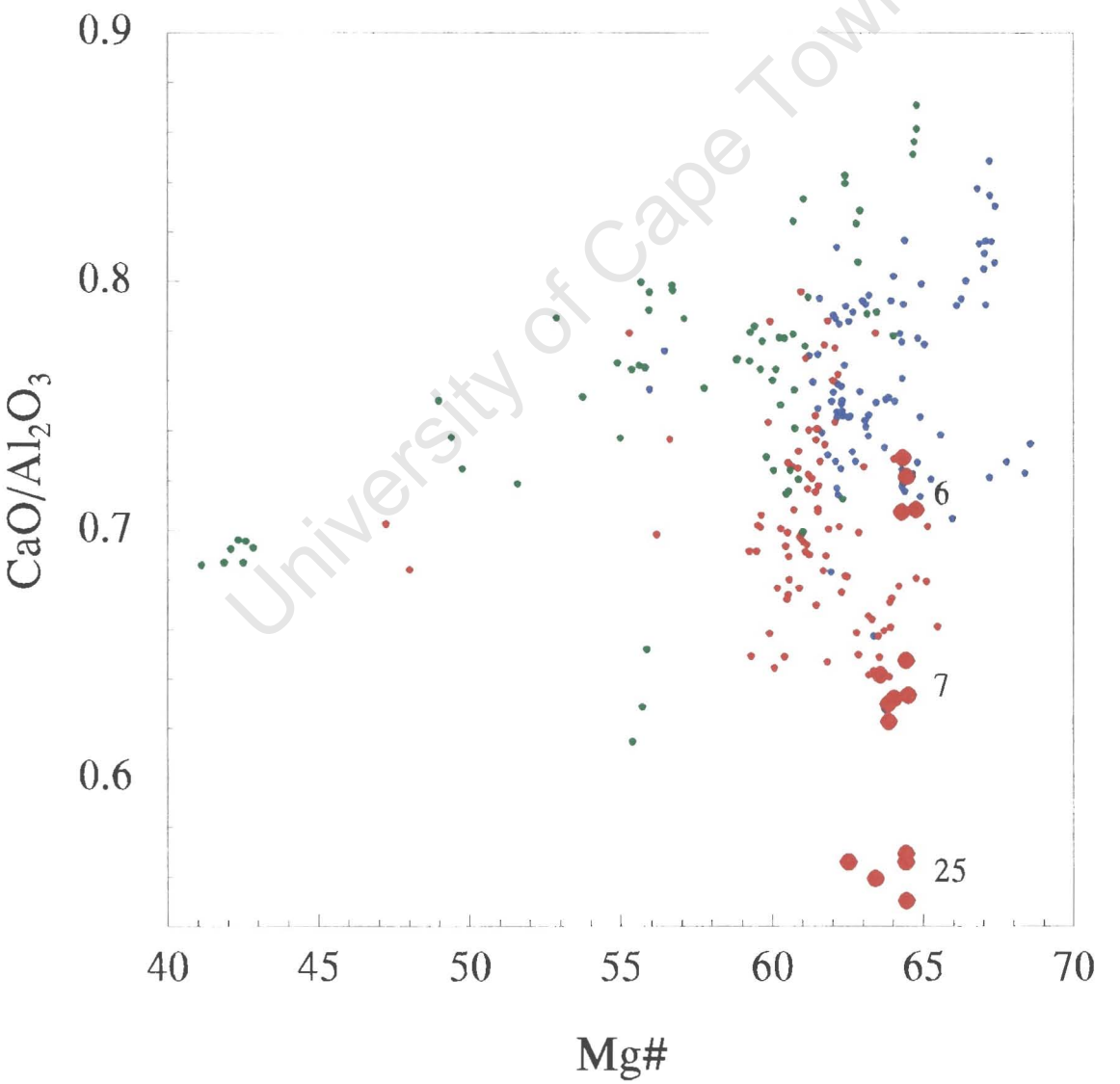

University of Cape Town

Figure 6.15: CaO/Al_2O_3 versus Mg# (atomic $Mg/(Mg+Fe^{2+})$) for N-MORB (blue markers), Discovery-influenced MORB (red markers) and Shona-influenced MORB (green markers), with the anomalous basalts from Discovery-influenced ridge segments indicated by the large markers labelled with the relevant dredge numbers.

Could the conflict between trace-element and major-element indicators of initial pressure of melting be due to analytical artifacts or inapplicable modelling? If the conflicts between the trace-element and fractionation-corrected major-element characteristics are not due to crystallisation, then a resolution would be if some of these characteristics are analytical artifacts or the products of algorithms applied beyond the scope of their calibration. The trace-element concentrations are unequivocally real features of the data and necessitate the presence of residual garnet during melting in the mantle source-regions of these basalts. Melts formed at depth in the garnet-lherzolite stability-field could have different major-element systematics from melts derived from spinel-lherzolite, which would make applying algorithms constructed using data for magmas derived from spinel-lherzolite inappropriate. However, preliminary data have indicated that the systematics of the essential major-element indicators of depth of melting, i.e. FeO and SiO_2, defined for melts generated in the spinel-lherzolite stability-field, persist in the melts formed in the lower pressure portion of the garnet-lherzolite stability-field (Kinzler, 1997). Therefore, the major-element characteristics are also real features of the data, and a model must be explored which can accommodate all these data characteristics.

An increased role for pyroxene, most-likely clinopyroxene, during the melting processes which yielded the MORB from the SMAR is indicated by the off-set of the data for these basalts from the global trend in fig. 6.2. The behaviour of the major elements during the melting of high-pyroxene mantle-source compositions are not well-understood at present (Hirschmann *et al.*, 1995; Yaoling Niu, pers. comm.; Tim Grove, pers. comm.), but one characteristic has been qualitatively defined. As the proportion of melt derived from pyroxene during melting increases, the resulting magma composition will be enriched in NaO and total FeO at similar initial pressures and extents of melting compared to magmas derived from "normal" mantle source-regions (Hirschmann *et al.*, 1995; Langmuir *et al.*, 1992). The fractionation-corrected compositional data for the MORB from the SMAR might therefore indicate a generally higher proportion of pyroxene in their mantle source-regions, relative to the global MORB compositional data-set.

Model A: Preferential melting of small proportions of garnet pyroxenite veins or layers, with compositions for average pyroxenite from xenoliths and alpine massifs or pyroxenite from typical subducted sediment, within mantle source-regions composed predominantly of spinel-lherzolite. A possible resolution to this paradox would be if these

University of Cape Town

anomalous basalts were derived from mantle source-regions which contained residual garnet in their modal mineralogy after melting at shallow depths. Garnet is stable to lower pressures in pyroxenite than in lherzolite and there is an increasing consensus that some MORB mantle source-regions might contain ~5% garnet pyroxenite as veins or layers intercalated with spinel-lherzolite (Hirschmann & Stolper, 1996, and references therein). The low-pressure limit of garnet stability in lherzolite has been defined as ~28-30kbar (Kinzler, 1997; Robinson & Wood, 1998), whereas the low-pressure limit for garnet stability in pyroxenite is typically 13-17kbar (Hirschmann & Stolper, 1996). If the enriched mantle component associated with the Discovery mantle plume is present beneath the SMAR as veins or layers of garnet pyroxenite in spinel-lherzolite, then preferential melting of these veins or layers at low pressures could possibly yield magmas with the observed anomalous compositional characteristics.

The quantitative investigation of the above model of the melting of a predominantly spinel-lherzolite mantle source-region containing ~5% garnet pyroxenite is limited to the trace-element characteristics as the behaviour of major elements during the melting of pyroxenitic material is poorly understood (Hirschmann *et al.*, 1995; Yaoling Niu, pers. comm.; Tim Grove, pers. comm.). The melting process was modelled as incremental, equilibrium batch melting (Gast, 1968; Shaw, 1970) with 90% of the melt formed during each step being removed, with spinel-lherzolite melting non-modally (Kinzler, 1997). Due to the currently unconstrained nature of pyroxenitic melting, the material was modelled to melt in modal proportions (Hirschmann & Stolper, 1996). The spinel-lherzolite melting was modelled using the algorithms of Kinzler (1997). The software program SPIMW10 (provided by Kinzler) to model spinel-lherzolite melting calculates the mineral-mode of the mantle residue after each increment of melting. These modes could therefore be used for the trace-element modelling to calculate new bulk partition coefficients after each increment of melting, thus accommodating the non-modal nature of the spinel-lherzolite melting and the dynamic nature of the change in melting coefficients with change in pressure.

The model of garnet-pyroxenite veins in the spinel-lherzolite mantle source-regions of MORB and the composite melts produced by melting of these mixed mantle source-regions, as proposed by Hirschmann & Stolper (1996), was explored using the above modelling methodology to assess the possible applicability of this model for the origin of the trace-element characteristics of the anomalous basalts from the Discovery-influenced ridge segments. The

University of Cape Town

basis of this model can be summarised as follows:

1. Melting of the garnet-pyroxenite (clinopyroxene and orthopyroxene) material is initiated at a depth Z_1, prior to the initiation of melting of the surrounding spinel-lherzolite;
2. Melting of the spinel-lherzolite is initiated at a depth Z_2, at a rate of 1.2%/kbar;
3. The rate of melting of the garnet-pyroxenite material below Z_2 is exceptionally high, 4.5-6%/kbar, and is termed super-adiabatic, due to the non-melting enclosing spinel-lherzolite providing excess heat for the melting of the garnet-pyroxenite material. In the adiabatically upwelling mantle, the garnet-pyroxenite material remains at relatively constant temperatures during melting. In contrast, the temperature of the non-melting enclosing spinel-lherzolite continues to increase adiabatically, and in an attempt to attain equilibrium, heat therefore flows from the spinel-lherzolite into the garnet-pyroxenite (Hirschmann & Stolper, 1996);
4. Due to the garnet-pyroxenite material not receiving excess heat above Z_2 from the now melting enclosing spinel-lherzolite, the rate of melting of the garnet-pyroxenite material decreases to 1.8%/kbar;
5. At a depth of approximately 15kbar, garnet is exhausted in the pyroxenite material and at shallower depths melting continues with only clinopyroxene and orthopyroxene in the mode;
6. The garnet-free pyroxenite is assumed to be more refractory and to melt at a reduce rate of 0.9%/kbar;
7. Melting is assume to proceed to a depth of approximately 3kbar;
8. The final melts would be composed of approximately 15% garnet-pyroxenite derived melt for Z_1-Z_2=5kbar, and about 20% for Z_1-Z_2=8kbar (Hirschmann & Stolper, 1996).

The various values for parameters used in the modelling are listed and referenced in table 6.1. It is difficult to critically assess the success of this modelling relative to the results of Hirschmann & Stolper (1996), since the partition coefficients for Yb used by these authors are not provided in the publication on their results. The modelling done here were conducted for Sc, Sm and Yb over the range of partition coefficients given in table 6.1.

The results of the melting calculations of a mantle source-region composed of 95% spinel-lherzolite and 5% AVG (average pyroxenite composition from xenoliths and alpine massifs, after Hirschmann & Stolper, 1996) garnet-pyroxenite are listed in table 6.2a. The

University of Cape Town

Table 6.1: Input parameters used in modelling melting to investigate geochemical evidence for residual garnet during melting in the source-regions of some MORB from Discovery-influenced ridge-segments.

	Gt-pyroxenite	Sp-lherzolite	
Mantle source-region composition[1]:	5%	95%	
Fraction of final melt[1]:			
Scenario A:			
(Z_1-Z_2=5kbar; rate=4.5%/kbar)	0.15	0.85	
Scenario B:			
(Z_1-Z_2=5kbar; rate=6%/kbar)	0.20	0.80	
Scenario C:			
(Z_1-Z_2=8kbar; rate=4.5%/kbar)	0.20	0.80	
Pyroxenite modal mineralogy[1]:	**Cpx**	**Opx**	**Garnet**
Before garnet-exhaustion	0.500	0.300	0.200
After garnet-exhaustion	0.625	0.375	
Starting compositions[1,2,3]:	**Sc**	**Sm**	**Yb**
AVG[1] pyroxenite	14.88	1.42	1.55
SOC[2] pyroxenite	14.88	2.32	3.05
Sp-lherzolite	12.00	0.317	0.432
Partition coefficients[1,4,5]:	**Sc**	**Sm**	**Yb**
Clinopyroxene	*3.000*-1.310	*0.350*-0.221	*0.467*-0.400
Orthopyroxene	*1.200*-0.330	*0.020*-0.020	0.100
Olivine	0.260-*0.170*	0.001	0.023-*0.030*
Spinel	0.240-*0.048*	0.001	0.005
Garnet	*4.000*-2.270	0.217	7.000

1. Hirschmann & Stolper, 1996: AVG - average pyroxenite from xenoliths and alpine massifs; SOC - pyroxenite from typical subducted oceanic crust; Sm & Yb values for different pyroxenite starting compositions and spinel-lherzolite.
2. McKenzie & O'Nions, 1995: Sc for pyroxenites from oceanic basalt source composition.
3. Hofmann, 1988: Sc for spinel-lherzolite taken from primitive mantle composition.
4. Niu *et al.*, 1996: partition coefficients in italics from this compilation, represents extremely high values for clinopyroxene, orthopyroxene and garnet partition coefficients.
5. Own compilation (Dunn & Sen, 1994; Hart & Dunn, 1993; le Roex *et al.*, 1996; McKenzie & O'Nions, 1991; Nielsen *et al.*, 1992; Niu *et al.*, 1996): Hirschmann & Stolper (1996) partition coefficients fall within the range of values used.

University of Cape Town

different scenarios are defined in table 6.1, and encompass variations in the rate of super-adiabatic melting and the extent of the pressure-interval of super-adiabatic melting. Firstly, none of the $(Sm/Yb)_N$ ratios of the final melts composed of all the steps of the different scenarios modelled (A: $(Sm/Yb)_N = \textit{0.984}$-0.882; B: $(Sm/Yb)_N = \textit{1.009}$-0.885; C: $(Sm/Yb)_N = \textit{0.989}$-0.872 - the values in italics were calculated using the partition coefficients compiled by Niu *et al.* (1996), as listed in table 6.1) come close to the observed values for $(Sm/Yb)_N$ in the actual basalts of 1.73-2.83. Although the Yb concentrations in these modelled final melts (A: Yb =

Table 6.2a: Results for the modelling of melting a spinel-lherzolite source-region containing 5% AVG garnet-pyroxenite, see text for details. All pressures in kbar, rates of melting in %/kbar, and concentrations in ppm. Values in italics were calculated using the partition coefficients compiled by Niu *et al.* (1996) listed in table 6.1.

AVG-pyroxenite				Melt				Source		
Scenario A	**Rate**	$P_{initial}$-P_{final}	F_{mean}	**Sc**	**Sm**	**Yb**	$(Sm/Yb)_N$	**Sc**	**Sm**	**Yb**
Step 1	4.5	30-26	0.187	*6.08*-12.60	*4.26*-5.64	*0.98*-4.58		*16.91*-15.41	*0.75*-0.42	*1.68*-0.84
Step 2	1.8	25-16	0.151	*6.74*-12.96	*2.50*-1.96	*1.05*-2.73		*18.72*-15.84	*0.44*-0.14	*1.79*-0.50
Step 3 (gt-out)	0.9	15-3	0.100	*8.33*-16.75	*1.61*-0.71	*4.85*-1.51		*19.89*-15.74	*0.31*-0.08	*1.45*-0.39
Steps 1-3			0.438	*6.82*-13.67	*3.05*-3.24	*1.89*-3.24	*1.789*-1.112			
Steps 1 & 2 only			0.337	*6.38*-12.76	*3.47*-4.00	*1.01*-3.75	*3.815*-1.183			
Scenario B										
Step 1	6.0	30-26	0.242	*6.25*-12.69	*3.82*-4.72	*1.00*-4.11		*17.67*-15.59	*0.63*-0.30	*1.73*-0.70
Step 2	1.8	25-16	0.151	*7.04*-13.11	*2.07*-1.42	*1.08*-2.28		*19.56*-16.03	*0.37*-0.10	*1.84*-0.42
Step 3 (gt-out)	0.9	15-3	0.100	*8.70*-16.95	*1.33*-0.51	*4.99*-1.26		*20.77*-15.93	*0.26*-0.06	*1.49*-0.32
Steps 1-3			0.493	*6.99*-13.69	*2.78*-2.86	*1.83*-2.97	*1.683*-1.069			
Steps 1 & 2 only			0.393	*6.56*-12.85	*3.15*-3.46	*1.03*-3.41	*3.396*-1.127			
Scenario C										
Step 1	4.5	33-26	0.282	*6.32*-12.73	*3.62*-4.29	*1.01*-3.90		*18.27*-15.73	*0.52*-0.20	*1.77*-0.58
Step 2	1.8	25-16	0.151	*7.28*-13.24	*1.71*-0.94	*1.10*-1.89		*20.22*-16.18	*0.30*-0.07	*1.88*-0.35
Step 3 (gt-out)	0.9	15-3	0.100	*8.99*-17.11	*1.10*-0.34	*5.10*-1.05		*21.47*-16.08	*0.21*-0.04	*1.52*-0.27
Steps 1-3			0.533	*7.10*-13.70	*2.60*-2.60	*1.80*-2.80	*1.603*-1.033			
Steps 1 & 2 only			0.432	*6.66*-12.91	*2.95*-3.13	*1.04*-3.20	*3.154*-1.084			
Sp-lherzolite										
Steps 2-3	1.2	25-3	0.221	*16.72*-26.44	*1.22*-1.20	*1.65*-1.66	*0.821*-0.803			
Step 2 only	1.2	25-15	0.113	*13.76*-25.49	*2.24*-2.38	*2.35*-2.49	*1.060*-1.063			
Final melts										
Scenario A (all steps)			0.182	*15.24*-24.52	*1.49*-1.51	*1.69*-1.90	*0.984*-0.882			
Scenario A (steps 1-2)			0.093	*12.65*-23.58	*2.42*-2.63	*2.15*-2.68	*1.255*-1.088			
Scenario B (all steps)			0.182	*14.78*-23.89	*1.53*-1.53	*1.69*-1.92	*1.009*-0.885			
Scenario B (steps 1-2)			0.094	*12.32*-22.96	*2.42*-2.60	*2.08*-2.68	*1.291*-1.079			
Scenario C (all steps)			0.182	*14.80*-23.89	*1.50*-1.48	*1.68*-1.89	*0.989*-0.872			
Scenario C (steps 1-2)			0.094	*12.34*-22.97	*2.38*-2.53	*2.09*-2.63	*1.269*-1.068			
Observed values				22.2-35.5	3.42-4.33	1.37-2.28	1.73-2.83			

University of Cape Town

Table 6.2b: Results for the modelling of melting a spinel-lherzolite source-region containing 5% SOC garnet-pyroxenite, see text for details. All pressures in kbar, rates of melting in %/kbar, and concentrations in ppm. Values in italics were calculated using the partition coefficients compiled by Niu *et al.* (1996) listed in table 6.1.

SOC-pyroxenite				**Melt**				**Source**		
Scenario A	**Rate**	$P_{initial}$-P_{final}	F_{mean}	**Sc**	**Sm**	**Yb**	$(Sm/Yb)_N$	**Sc**	**Sm**	**Yb**
Step 1	4.5	30-26	0.187	*6.08*-12.60	*6.97*-9.22	*1.93*-9.01		*16.91*-15.41	*1.23*-0.69	*3.31*-1.65
Step 2	1.8	25-16	0.151	*6.74*-12.96	*4.08*-3.20	*2.06*-5.38		*18.72*-15.84	*0.72*-0.23	*3.53*-0.98
Step 3 (gt-out)	0.9	15-3	0.100	*8.33*-16.75	*2.63*-1.15	*9.55*-2.98		*19.89*-15.74	*0.51*-0.13	*2.86*-0.76
Steps 1-3			0.438	*6.82*-13.67	*4.98*-5.30	*3.72*-6.38	*1.485*-0.923			
Steps 1 & 2 only			0.337	*6.38*-12.76	*5.68*-6.53	*1.99*-7.39	*3.167*-0.982			
Scenario B										
Step 1	6.0	30-26	0.242	*6.25*-12.69	*6.24*-7.72	*1.97*-8.09		*17.67*-15.59	*1.02*-0.50	*3.40*-1.38
Step 2	1.8	25-16	0.151	*7.04*-13.11	*3.39*-2.32	*2.12*-4.49		*19.56*-16.03	*0.60*-0.17	*3.63*-0.82
Step 3 (gt-out)	0.9	15-3	0.100	*8.70*-16.95	*2.18*-0.84	*9.81*-2.49		*20.77*-15.93	*0.42*-0.09	*2.94*-0.64
Steps 1-3			0.493	*6.99*-13.69	*4.54*-4.67	*3.61*-5.85	*1.398*-0.887			
Steps 1 & 2 only			0.393	*6.56*-12.85	*5.14*-5.65	*2.03*-6.71	*2.820*-0.936			
Scenario C										
Step 1	4.5	33-26	0.282	*6.32*-12.73	*5.91*-7.02	*1.98*-7.68		*18.27*-15.73	*0.84*-0.33	*3.47*-1.14
Step 2	1.8	25-16	0.151	*7.28*-13.24	*2.79*-1.54	*2.17*-3.72		*20.22*-16.18	*0.49*-0.31	*3.71*-0.68
Step 3 (gt-out)	0.9	15-3	0.100	*8.99*-17.11	*1.80*-0.56	*10.03*-2.06		*21.47*-16.08	*0.35*-0.06	*3.00*-0.53
Steps 1-3			0.533	*7.10*-13.70	*4.25*-4.25	*3.55*-5.51	*1.333*-0.858			
Steps 1 & 2 only			0.432	*6.66*-12.91	*4.82*-5.11	*2.05*-6.30	*2.618*-0.900			
Sp-lherzolite										
Steps 2-3	1.2	25-3	0.221	*16.72*-26.44	*1.22*-1.20	*1.65*-1.66	*0.821*-0.803			
Step 2 only	1.2	25-15	0.113	*13.76*-25.49	*2.24*-2.38	*2.35*-2.49	*1.060*-1.063			
Final melts										
Scenario A (all steps)			0.182	*15.24*-24.52	*1.78*-1.81	*1.96*-2.37	*1.011*-0.852			
Scenario A (steps 1-2)			0.093	*12.65*-23.58	*2.76*-3.01	*2.29*-3.23	*1.335*-1.035			
Scenario B (all steps)			0.182	*14.78*-23.89	*1.88*-1.89	*2.04*-2.50	*1.025*-0.843			
Scenario B (steps 1-2)			0.094	*12.32*-22.96	*2.82*-3.04	*2.28*-3.34	*1.372*-1.012			
Scenario C (all steps)			0.182	*14.80*-23.89	*1.83*-1.81	*2.03*-2.43	*1.000*-0.828			
Scenario C (steps 1-2)			0.094	*12.34*-22.97	*2.76*-2.93	*2.29*-3.25	*1.339*-1.000			
Observed values				22.2-35.5	3.42-4.33	1.37-2.28	1.73-2.83			

University of Cape Town

1.69-1.90ppm; B: Yb = *1.69*-1.92ppm; C: Yb = *1.68*-1.89ppm) fall within the observed range of 1.37-2.28ppm for this element, the concentration of Sm in these melts (A: Sm = *1.49*-1.51ppm; B: Sm = 1.53ppm; C: Sm = *1.50*-1.48ppm) are too low by approximately a factor of two compared to the observed range of 3.42-4.33ppm for Sm concentrations. The modelled values for Sc concentrations in the final melts (A: Sc = 15.24-24.52ppm; B: Sc = 14.78-23.89ppm; C: Sc = 14.80-23.89ppm) overlap the lower half of the observed range of Sc concentrations, 22.2-35.5ppm, in the basalts.

The results of the modelled melting of a mantle source-region composed of 95% spinel-lherzolite and 5% SOC (pyroxenite composition from subducted oceanic crust, after Hirschmann & Stolper, 1996) garnet-pyroxenite are listed in table 6.2b. Although the modelled $(Sm/Yb)_N$ ratios of the final melts are higher relative to the final melts in table 6.2a (A: $(Sm/Yb)_N$ = *1.011*-0.852; B: $(Sm/Yb)_N$ = *1.025*-0.843; C: $(Sm/Yb)_N$ = *1.000*-0.828), these ratios are still significantly lower than the observed values of $(Sm/Yb)_N$, 1.73-2.83, in the basalts. The Sm concentrations in the modelled melts (A: Sm = *1.78*-1.81ppm; B: Sm = *1.88*-1.89ppm; C: Sm = *1.83*-1.81ppm) are still too low compared to the observed concentrations of Sm, 3.42-4.33ppm, and the Yb concentrations (A: Yb = *1.96*-2.37ppm; B: Yb = *2.04*-2.50ppm; C: Yb = *2.03*-2.43ppm) now overlap and exceed the high end of the observed range of Yb concentrations, 1.37-2.28ppm. Due to the same Sc concentration in AVG and SOC garnet-pyroxenite, the results for Sc modelling in table 6.2b are the same as in table 6.2a.

The models for melting of a mantle source-region composed of 5% garnet-pyroxenite and 95% spinel-lherzolite, as proposed by Hirschmann & Stolper (1996) do not yield final melts with values for $(Sm/Yb)_N$ ratios as high as observed in these anomalous MORB from Discovery-influenced ridge segments. It therefore seems that residual garnet must be a more significant factor during the melting processes which produced these anomalous basalts.

Model A modified: Preferential melting of small proportions of garnet pyroxenite veins or layers, with compositions for average pyroxenite from xenoliths and alpine massifs or pyroxenite from typical subducted sediment, within mantle source-regions composed predominantly of spinel-lherzolite, with melting terminating within the garnet-stability field for pyroxenite. A modification of the above model which would increase the proportion of the final melt produced in the presence of residual garnet and agree more with the calculated melting

University of Cape Town

parameters in the preceding section, is to increase the final pressure of melting from the assumed value of 3kbar. To simplify the calculation, the final melts of the above modelled melting of garnet-pyroxenite were recalculated using the results of steps 1 and 2 only, and spinel-lherzolite melting was also terminated at 15kbar. All the melt derived from the pyroxenitic material would then have formed in the presence of residual garnet, and still constitute 15-20% of the final melts. Another result of this modification to the above model is the lowering of the mean extent of melting which produced the final melts, from ~18% to ~9%. The failure of the original model to reproduce the high $(Sm/Yb)_N$ ratios of the anomalous basalts, therefore fits with the calculated lower extents of melting for these basalts (17% - 10%) compared to the rest of the MORB from the SMAR (~19% - ~15%).

The results of this modified model of melting mantle source-regions composed of 5% garnet-pyroxenite and 95% spinel-lherzolite are also given in table 6.2a & b (see the rows labelled *Steps 1 & 2 only* for each scenario in table 6.2a & b). Although the final melts for AVG (A: $(Sm/Yb)_N = 1.255$-1.088; B: $(Sm/Yb)_N = 1.291$-1.079; C: $(Sm/Yb)_N = 1.269$-1.068) and SOC garnet-pyroxenite compositions now contain higher $(Sm/Yb)_N$ ratios (A: $(Sm/Yb)_N = 1.335$-1.035; B: $(Sm/Yb)_N = 1.372$-1.012; C: $(Sm/Yb)_N = 1.339$-1.000), these ratios still do not agree with the observed range of $(Sm/Yb)_N$, 1.73-2.83, in the anomalous basalts. The lower end of the concentration range for Yb in some of the final melts derived from AVG garnet-pyroxenite (A: Yb = *2.15*-2.68ppm; B: Yb = *2.08*-2.68ppm; C: Yb = *2.09*-2.63ppm) overlap slightly with the higher end of the range of observed concentrations for Yb, 1.37-2.28, in the anomalous basalts, but the final melts from SOC garnet-pyroxenite still have too high Yb concentrations (A: Yb = *2.29*-3.23ppm; B: Yb = *2.28*-3.34ppm; C: Yb = *2.29*-3.25ppm). The modelled concentrations for Sm in the final melts derived from AVG (A: Sm = *2.42*-2.63ppm; B: Sm = *2.42*-2.60ppm; C: Sm = *2.38*-2.53ppm) and SOC garnet-pyroxenite (A: Sm = *2.76*-3.01ppm; B: Sm = *2.82*-3.04ppm; C: Sm = *2.76*-2.93ppm) are however still too low, compared to the observed range of Sm concentrations, 3.42-4.33ppm, in these basalts. The range in concentrations for Sc in the modelled final melts (A: Sc = *12.65*-23.58ppm; B: Sc = *12.32*-22.96ppm; C: Sc = *12.34*-22.97ppm) still overlap with the observed range for Sc concentrations, 22.2-35.5ppm, in the anomalous basalts, but the extent of the overlap is less.

The greater amount of melt formed in the presence of residual garnet has therefore made a difference which brought the results for the modelled final melts closer to the observed

University of Cape Town

compositions of the anomalous MORB from Discovery-influenced ridge-segments. However, mantle source-regions composed of 5% garnet-pyroxenite, with broad compositions of average pyroxenite from xenoliths and alpine massifs or pyroxenite from typical subducted oceanic crust (Hirschmann & Stolper, 1996), and 95% spinel-lherzolite can not yield magmas with the trace-element characteristics observed in the anomalous basalts from Discovery-influenced ridge segments.

Further increasing the proportion of the final melt derived from the garnet-pyroxenite portion of the mantle source-region would yield magmas with higher $(Sm/Yb)_N$ ratios, but only up to a point. Significant residual garnet must remain after melting to impart the distinctive trace-element characteristics on the magma formed. If all of the garnet-pyroxenitic veins or layers melt, then the resulting melts would not have formed in the presence of residual garnet. Therefore, not all 5% of garnet-pyroxenite, with the compositions for average pyroxenite from xenoliths and alpine massifs or pyroxenite from typical subducted oceanic crust (Hirschmann & Stolper, 1996), can be melted in the mantle source-region, although they might melt to high extents. This conflicts with the generally accepted rule that at least 10% mean melting, initiated at an initial pressure of at least 30kbar, is required to produce the observed 6-7km thick oceanic crust (Langmuir *et al.*, 1992; Plank *et al.*, 1995), and the mean extents of melting calculated for these basalts earlier in this chapter (~19%-~10%). These values of mean extent of melting refers to ratio of mantle entering the melting region relative to the amount of material added to the oceanic crust. The mean extents of melting calculated, and listed in table 6.2a & b, for each step of garnet-pyroxenite melting refer only to the ratio between the 5% of the mantle source-region composed of garnet-pyroxenite and the amount of melt formed from it (Plank *et al.*, 1995). Therefore, to relate the garnet-pyroxenite mean extents of melting to the general definition, these values should be multiplied by 0.05, and the values for the spinel-lherzolite portions by 0.95. The calculated mean extents of melting of the final melts in table 6.2a & b took this effect into account and can be seen to decrease as a higher fraction of the melts are derived from the garnet-pyroxenite.

Model B: Derivation of these anomalous basalts from mantle source-regions composed of spinel-lherzolite pervaded by pyroxenitic veins or layers derived from low-degree melts of garnet-lherzolite, associated with the influence of the Discovery mantle-plume. It has been shown previously that these MORB with anomalous major- and trace-element characteristics

University of Cape Town

also contain the most-radiogenic Sr-isotope ratios and least-radiogenic Nd-isotope ratios, therefore the strongest Discovery mantle-plume compositional signatures. The origins of these MORB are consequently anomalous not only in terms of being derived from shallow-level melting processes and the probably presence of residual modal garnet at some stage during their melting history, but the compositions of the mantle source-regions from which they were derived are also exceptional. All three these aspects must therefore be addressed in unison, because they are most-probably all interrelated.

A conceptional model which encompasses all the above qualities is proposed below and will subsequently be investigated quantitatively. The mode in which mantle-plume derived material is injected and accommodated in the depleted MORB mantle beneath mid-ocean ridges in the proximity of mantle plumes, especially for the SMAR, has been proposed to be as small-degree melts which solidify as veins or layers in the ambient mantle (le Roex, 1987; le Roex *et al.*, 1987). If this is true for the mantle source-regions beneath the Discovery-influenced ridge-segments in the South Atlantic, then the basalts which are compositionally most-affected by the mantle plume must have been derived preferentially from vein-material relative to normal mantle. Therefore, it follows that these anomalous basalts from Discovery-influenced ridge-segments were either derived from mantle source-regions with exceptional proportions of vein-material, or the melting processes preferentially melted the vein-material at shallow mantle depths. The formation, and the preservation, of these veins or layers and the origin of the melts which formed them are not well-constrained at present and will be discussed later. It is proposed here that low-degree (2-5%) melts formed in the garnet-lherzolite stability-field within the mantle upwelling beneath the Discovery mantle plume due to the thermal and compositional influences of the mantle plume. These melts infiltrated the overlaying spinel-lherzolite mantle and solidified at depth to form pyroxenitic veins. Some of this veined spinel-lherzolite mantle flowed towards the SMAR and were entrained in the general mantle upwelling beneath ridge segments. As discussed for *Model A*, the pyroxenitic material intercepts its solidus at lower temperatures, therefore greater depths, compared to spinel-lherzolite and an interval of melting occurs, before the spinel-lherzolite solidus is reached, during which only the pyroxenitic material melts. As in *Model A*, the melting of the pyroxenitic material occur at accelerated "super-adiabatic" rates and it is not inconceivable that a large fraction, if not all, of the pyroxenitic vein-material could be depleted in mantle source-regions during melting beneath mid-ocean ridges. The melts derived from the pyroxenitic material would be exceptionally enriched in

University of Cape Town

incompatible trace-elements, due not only to the highly incompatible trace-element enriched nature of mantle-plume material. The low degrees of melting of this mantle-plume material would have yielded melts, which later formed the pyroxenitic material, containing very high concentrations of the highly incompatible trace elements. Various extents of "dilution" of melts derived from the pyroxenitic material with melts from the ambient spinel-lherzolite mantle would yield the range of compositions from normal-MORB to enriched-MORB observed in basalts recovered from the Discovery-influenced ridge segments (similar to a model proposed by Schilling *et al.* (1980) for MORB from 53-28°N on the MAR, adjacent to the Azores Plateau).

The trace-element compositions of melts at various stages and in various scenarios associated with the above conceptional model were modelled quantitatively. The modal mineralogies for garnet-lherzolite (le Roex *et al.*, 1996) and clinopyroxenite (Frey, 1980) used are given in table 6.3. The melting process was modelled as incremental, equilibrium batch melting with 90% of the melt formed during each step being removed, with garnet-lherzolite melting non-modally at a rate of 1%/kbar (Gast, 1968; Shaw, 1970). The source mineralogy of the residue of garnet-lherzolite melting was recalculated after each step, using the melting coefficients listed in table 6.3 (le Roex *et al.*, 1996). The non-modal melting of spinel-lherzolite was modelled as for *Modal A* at a rate of 1-2%/kbar, using the algorithms of Kinzler (1997) and the depleted mantle source-composition of Hart & Zindler (1986). The pyroxenitic material was assumed to melt completely, which will be discussed later, and mix with the melt derived from the spinel-lherzolite. Also listed in table 6.3 are the values of trace-element partition coefficients used (Dunn & Sen, 1994; Hart & Dunn, 1993; le Roex *et al.*, 1996; McKenzie & O'Nions, 1991; Nielsen *et al.*, 1992; Niu *et al.*, 1996), trace-element compositions of the initial garnet-lherzolite mantle (the primitive mantle composition of Hofmann, 1988) and initial spinel-lherzolite mantle (the MORB source composition of McKenzie & O'Nions, 1991; McKenzie & O'Nions, 1995).

The results of the modelling are listed in table 6.4 for the compositions of the melts derived from pyroxenitic material and spinel-lherzolite separately, and table 6.5a & b for the final mixed melts. In table 6.4, scenario A refers to melt derived from complete melting of pyroxenitic material formed from an initial small-degree (1.8%) fractional melt of garnet-lherzolite. Scenario B refers to melt derived from complete melting of pyroxenitic material also formed from a small-degree (2.7%) fractional melt of garnet-lherzolite, but the garnet-lherzolite had previously been slightly depleted by fractional removal of 1.8% of melt. Compositions of

University of Cape Town

Table 6.3: Data used for the modelling of the trace-element compositions of melts for ***Model B***. Modal mineralogy and melting coefficients for garnet-lherzolite (le Roex *et al.*, 1996), modal mineralogy for clinopyroxenite (Frey, 1980), trace-element partition coefficients (Dunn & Sen, 1994; Hart & Dunn, 1993; le Roex *et al.*, 1996; McKenzie & O'Nions, 1991; Nielsen *et al.*, 1992; Niu *et al.*, 1996), and mantle source compositions in ppm (primitive mantle (Hofmann, 1988); MORB source (McKenzie & O'Nions, 1991, 1995).

Modal Mineralogy	**Cpx**	**Opx**	**Oliv.**	**Garnet**					
Garnet-lherzolite	0.140	0.220	0.580	0.060					
Clinopyroxenite	0.900	0.050	0.050						
Melting coefficients	**Cpx**	**Opx**	**Oliv.**	**Garnet**					
Garnet-lherzolite	0.400	0.100	0.100	0.400					
Partition coefficients	**Sc**	**La**	**Sm**	**Yb**	**Rb**	**Sr**	**Nb**	**Ba**	**Ni**
Clinopyroxene	1.310	0.0536	0.221	0.40	0.0004	0.260	0.005	0.0007	2.0
Orthopyroxene	0.330	0.0005	0.020	0.10	0.0006	0.016	0.0025	0.000006	5.0
Olivine	0.260	0.0001	0.0007	0.023	0.0003	0.016	0.002	0.000005	10.0
Spinel	0.240	0.0006	0.0006	0.0045	0.0001	0.0001	0.0004	0.0001	5.0
Garnet	2.270	0.001	0.217	7.0	0.0007	0.20	0.0005	0.0005	1.10
Source compositions	**Sc**	**La**	**Sm**	**Yb**	**Rb**	**Sr**	**Nb**	**Ba**	**Ni**
Primitive mantle	14.88	0.614	0.387	0.414	0.535	18.21	0.618	6.049	2080
MORB source	12	0.206	0.299	0.347	0.062	14.7	0.390	0.650	2000

Table 6.4: Trace-element compositions of melts for ***Model B*** from pyroxenitic material and spinel-lherzolite, see text for details and definitions of scenario A & B. Rate of melting in %/kbar, pressures of melting in kbar, concentrations in ppm.

Pyroxenite					**Sc**	**La**	**Sm**	**Yb**	**Rb**	**Sr**	**Nb**	**Ba**	**Ni**
Scenario A					27.8	25.3	6.24	0.86	28.5	246	30.7	324	288
Scenario B					28.5	5.3	4.40	0.97	0.87	186	2.42	8.13	289
Sp-lherzolite	**Rate**	**$P_{initial}$**	**P_{final}**	**F_{mean}**	**Sc**	**La**	**Sm**	**Yb**	**Rb**	**Sr**	**Nb**	**Ba**	**Ni**
melt 1a	1	20	10	9.5	25.5	2.10	2.78	2.22	0.63	126	3.95	6.57	287
melt 1b	1	15	10	5.3	25.4	3.76	3.82	2.54	1.15	162	7.24	12.0	285
melt 2a	2	20	10	18.1	28.3	1.49	2.61	2.34	0.35	124	2.38	3.63	278
melt 2b	2	18	10	15.1	25.9	1.28	1.87	1.82	0.38	89	2.42	4.01	288
melt 2c	2	16.5	10.5	11.9	25.6	1.65	2.29	2.02	0.49	107	3.10	5.16	288
melt 2d	2	15	10	10.3	25.4	1.92	2.54	2.11	0.57	116	3.62	6.02	287

University of Cape Town

melts derived from melting of spinel-lherzolite are given for melting at a rate of 1%/kbar, from 20-10kbar and from 15-10kbar, also for melting at a rate of 2%/kbar, from 20-10kbar, 18-10kbar, 16.5-10.5kbar, and from 15-10kbar. The final mixed melts listed in table 6.5a & b are therefore firstly composed of mixtures of the scenario A pyroxenitic melt and the various spinel-lherzolite melts, and secondly between the scenario B pyroxenitic melt and the various spinel-lherzolite melts.

The compositions of the final mixed melts, examples are given for the fraction of the melt derived from pyroxenitic material of 0, 0.2, & 0.4, listed in table 6.5a & b agree much more with the observed compositions of the anomalous basalts from Discovery-influenced ridge segments. The concentrations of Sc, Sm and Yb in most mixed melts in table 6.5a composed of 20-40% pyroxenitic melt compare favourably with the observed range for these elements in these anomalous basalts, also listed in table 6.5a for comparison. The $(Sm/Yb)_N$ ratios of the final modelled melts listed in table 6.5a also fall within the range of $(Sm/Yb)_N$ in the anomalous basalts. It therefore seems as if the major- and trace-element characteristics of these anomalous basalts could be reconciled by melting at shallow mantle depths deriving a significant proportion (20-40%) of the final melt by complete melting of pyroxenitic material. The pyroxenitic material having formed from earlier small-degree melts (2-3%) of garnet-lherzolite mantle source-regions within the upwelling Discovery mantle plume.

A difficult point to address is whether material upwelling within the Discovery mantle plume might have anomalously low concentrations of Yb, and therefore high $(Sm/Yb)_N$ ratios are inherited from these source compositions by melts forming in the spinel-lherzolite stability-field. This would eliminate the necessity for residual garnet in the source-regions of the melts which later form the pyroxenite veins. Only the analysis of the single porphyritic basalt, containing large phenocrysts of plagioclase and some olivine and lesser clinopyroxene, recovered from the Discovery seamount is available (Kempe & Schilling, 1974; le Roex, unpublished data) to attempt to approximate the $(Sm/Yb)_N$ ratio of the Discovery mantle plume. Using the Sm/Yb ratio of this basalt, 5.2, the mantle mode for garnet-lherzolite and partition coefficients given in table 6.3, and 5% and 10% for F_{mean}, the source region of this basalt is calculated to have a $(Sm/Yb)_N$ value of 1.04-1.48. This value is significantly lower than the observed range of 1.73-2.83 for $(Sm/Yb)_N$ in the anomalous basalts. Proposed low-degree melts with the high $(Sm/Yb)_N$ ratios required to yield the observed values in basalts after dilution later

University of Cape Town

Table 6.5a: Trace-element compositions of final mixed melts for ***Model B*** with scenario A melts mixed with various spinel-lherzolite melts, all concentrations in ppm. Fraction refers to the contribution of pyroxenitic melt to the final mixed melts. C1 chondrite and primitive mantle values used to normalize Sm/Yb and La/Sm ratios, and Rb, Ba and Nb values respectively are from Sun & McDonough (1989).

Scenario A	Fraction	Sc	La	Sm	Yb	Rb	Sr	Nb	Ba	Ni	$(Sm/Yb)_N$	$(La/Sm)_N$	Rb_{PM}	Ba_{PM}	Nb_{PM}
plus melt 1a	0.0	25.5	2.10	2.78	2.22	0.63	126	3.95	6.57	287	1.39	0.49	0.99	0.94	5.54
	0.2	25.9	6.73	3.47	1.95	6.19	150	9.29	70.1	287	1.98	1.25	9.75	10.03	13.03
	0.4	26.4	11.36	4.16	1.68	11.76	174	14.63	134	287	2.76	1.76	18.52	19.12	20.5
plus melt 1b	0.0	25.4	3.76	3.82	2.54	1.15	162	7.24	12.04	285	1.67	0.64	1.81	1.72	10.15
	0.2	25.9	8.06	4.31	2.21	6.61	179	11.92	74.5	285	2.17	1.21	10.41	10.65	16.72
	0.4	26.4	12.36	4.79	1.87	12.07	196	16.61	137	286	2.85	1.67	19.01	19.59	23.3
plus melt 2a	0.0	28.3	1.49	2.61	2.34	0.35	124	2.38	3.63	278	1.24	0.37	0.55	0.52	3.34
	0.2	28.2	6.24	3.33	2.05	5.97	148	8.04	67.7	280	1.81	1.21	9.40	9.69	11.27
	0.4	28.1	11.00	4.06	1.75	11.59	172	13.69	132	282	2.58	1.75	18.26	18.86	19.21
plus melt 2b	0.0	25.9	1.28	1.87	1.83	0.38	90	2.41	4.01	288	1.14	0.44	0.60	0.57	3.39
	0.2	26.3	6.08	2.75	1.64	6.00	121	8.06	68.0	288	1.87	1.43	9.45	9.74	11.31
	0.4	26.6	10.87	3.62	1.44	11.61	152	13.71	132	288	2.79	1.94	18.29	18.90	19.23
plus melt 2c	0.0	25.6	1.65	2.29	2.02	0.49	106	3.10	5.16	288	1.26	0.47	0.78	0.74	4.35
	0.2	26.0	6.37	3.08	1.78	6.09	134	8.61	69.0	288	1.92	1.31	9.58	9.87	12.08
	0.4	26.4	11.09	3.87	1.55	11.68	162	14.13	133	288	2.77	1.85	18.39	19.00	19.81
plus melt 2d	0.0	25.4	1.92	2.55	2.12	0.57	116	3.62	6.02	287	1.34	0.49	0.90	0.86	5.08
	0.2	25.9	6.59	3.29	1.87	6.15	142	9.03	69.6	287	1.96	1.29	9.69	9.97	12.66
	0.4	26.4	11.25	4.03	1.61	11.73	168	14.44	133	288	2.77	1.80	18.47	19.07	20.3
Observed		22.2	5.25	3.42	1.37	4.27	196	5.45	59.6	65	1.73	0.97	6.72	8.53	7.65
values		-35.5	-18.04	-4.33	-2.28	-19.84	-351	-21.2	-305	-145	-2.83	-2.94	-31.2	-43.7	-29.8

University of Cape Town

Table 6.5b.: Trace-element compositions of final mixed melts for ***Model B*** with scenario B melts mixed with various spinel-lherzolite melts, all concentrations in ppm. Fraction refers to the contribution of pyroxenitic melt to the final mixed melts. C1 chondrite and primitive mantle values used to normalize Sm/Yb and La/Sm ratios, and Rb, Ba and Nb values respectively are from Sun & McDonough (1989).

Scenario B	Fraction	Sc	La	Sm	Yb	Rb	Sr	Nb	Ba	Ni	$(Sm/Yb)_N$	$(La/Sm)_N$	Rb_{PM}	Ba_{PM}	Nb_{PM}
plus melt 1a	0.0	25.5	2.10	2.78	2.22	0.63	126	395	6.57	287	1.39	0.49	0.99	0.94	5.54
	0.2	26.1	2.74	3.10	1.97	0.68	138	3.64	6.88	287	1.75	0.57	1.06	0.98	5.11
	0.4	26.7	3.38	3.43	1.72	0.73	150	3.34	7.19	288	2.21	0.64	1.14	1.03	4.68
plus melt 1b	0.0	25.4	3.76	3.82	2.54	1.15	162	7.24	12.04	285	1.67	0.64	1.81	1.75	10.15
	0.2	26.0	4.07	3.94	2.23	1.09	167	6.27	11.26	286	1.96	0.67	1.72	1.61	8.80
	0.4	26.7	4.38	4.05	1.91	1.04	172	5.31	10.47	287	2.36	0.70	1.64	1.50	7.45
plus melt 2a	0.0	28.3	1.49	2.61	2.34	0.35	124	2.38	3.63	278	1.24	0.37	0.55	0.52	3.34
	0.2	28.3	2.25	2.96	2.07	0.45	136	2.39	4.53	280	1.59	0.49	0.72	0.65	3.35
	0.4	28.4	3.02	3.32	1.79	0.56	148	2.40	5.43	283	2.06	0.59	0.88	0.78	3.36
plus melt 2b	0.0	25.9	1.28	1.87	1.83	0.38	90	2.41	4.01	288	1.14	0.44	0.60	0.57	3.39
	0.2	26.4	2.09	2.38	1.67	0.48	109	2.41	4.84	289	1.60	0.57	0.76	0.69	3.39
	0.4	26.9	2.89	2.88	1.48	0.58	128	2.42	5.66	289	2.16	0.65	0.91	0.81	3.39
plus melt 2c	0.0	25.6	1.65	2.29	2.02	0.49	106	3.10	5.16	288	1.26	0.47	0.78	0.74	4.35
	0.2	26.1	2.38	2.71	1.81	0.57	122	2.97	5.75	288	1.67	0.57	0.90	0.82	4.16
	0.4	26.7	3.11	3.13	1.60	0.64	138	2.83	6.35	288	2.18	0.64	1.02	0.91	3.97
plus melt 2d	0.0	25.4	1.92	2.55	2.12	0.57	116	3.62	6.02	287	1.34	0.49	0.90	0.86	5.08
	0.2	26.1	2.60	2.92	1.89	0.63	130	3.38	6.44	288	1.72	0.57	1.00	0.92	4.74
	0.4	26.7	3.28	3.29	1.66	0.69	144	3.14	6.86	288	2.21	0.64	1.09	0.98	4.40
Observed		22.2	5.25	3.42	1.37	4.27	196	5.45	59.6	65	1.73	0.97	6.72	8.53	7.65
values		-35.5	-18.04	-4.33	-2.28	-19.84	-351	-21.2	-305	-145	-2.83	-2.94	-31.2	-43.7	-29.8

University of Cape Town

during MORB melting, can not be extracted from spinel-lherzolite mantle source-regions with this calculate $(Sm/Yb)_N$ ratio of the Discovery mantle plume. Although the above calculation is poorly constrained, the result supports the previously deduced presence of residual garnet during the derivation of the low-degree melts, which later formed the proposed pyroxenite veins, from the mantle plume material

Although the basalts recovered by dredge 25, at the end of the Discovery-influenced ridge segment terminated by the Falkland-Agulhas Fracture Zone, at ~47.5°S, share the radiogenic isotope characteristics and evidence for residual garnet (low Sc concentrations, high $(Sm/Yb)_N$ ratios) with the anomalous basalts from dredge 6 & 7, the basalts from dredge 25 have REE and primitive-mantle normalized-incompatible trace-element patterns which show relatively less enrichment in their compositions of highly incompatible elements (e.g. Rb, Ba, Nb) and light REE (e.g. La). Therefore, the high $(La/Sm)_N$ and Rb_{PM}, Ba_{PM}, and Nb_{PM} values for the final mixed melts in table 6.5a might compare favourably with the observed range of these elements in the anomalous basalts from dredge 6 & 7 ($(La/Sm)_N$: 1.861-2.939; Rb_{PM}: 15.50-31.2; Ba_{PM}: 20.5-43.7; Nb_{PM}: 15.43-29.8), but not with the observed range for these elements in the anomalous basalts from dredge 25 ($(La/Sm)_N$: 0.970-1.050; Rb_{PM}: 6.72-7.43; Ba_{PM}: 8.53-9.25; Nb_{PM}: 7.65-8.04). The final mixed melts in table 6.5b have much lower values for $(La/Sm)_N$ and Rb_{PM}, Ba_{PM}, and Nb_{PM} for melts comprising 20-40% pyroxenitic melt, although these melts still have low Sc concentrations and high $(Sm/Yb)_N$ ratios. This is due to the composition of the pyroxenitic material being depleted in highly incompatible trace elements, after being formed from small-degree melts (2-3%) of a garnet-lherzolite mantle source-region from which 1.8% of melt was previously extracted (Scenario B). Regardless of the relatively unconstrained nature of the starting compositions, the modelled final mixed melts in table 6.5a & b exhibit the same relative behaviour for highly incompatible trace elements as observed in the anomalous basalts from dredges 25, and 6 & 7.

Therefore, it seems probable that the anomalous basalts from Discovery-influenced ridge segments were derived from melts composed of 20-40% pyroxenite-derived melt and 60-80% spinel lherzolite-derived melt. The pyroxenitic material probably melted completely, or to a very high mean extent (60-80% perfect fractional melts of the pyroxenitic material contain slightly lower concentrations of compatible elements such as Sc and Ni, and slightly higher concentrations of incompatible elements, such as La and Rb, but the general systematics and

University of Cape Town

ratios do not change significantly from the 100% melts). The trace-element compositions of the pyroxenitic material impart the trace-element characteristics for residual garnet during melting to the final mixed melts, after having formed from low-degree melts extracted from Discovery-mantle plume-influenced garnet-lherzolite mantle source-regions. The pyroxenitic material which contributed to the melts represented by the anomalous basalts from dredge 25, were formed by melts extracted from garnet-lherzolite mantle source-regions which were previously depleted by the removal of 2-3% of melt.

A possible constraint on the abundance of pyroxenitic material in mantle source-regions beneath sections of the SMAR. The abundance of pyroxenitic material in the mantle source-regions of MORB is relatively unconstrained. The abundances of pyroxenites in alpine massif outcrops were taken as a guide by Hirschmann & Stolper (1996) to conclude that pyroxenites might constitute 2-5% of the upper mantle. These abundances are probably more applicable for the mantle lithosphere and most-likely not representative of the occurrence of pyroxenites in the convecting mantle beneath mid-ocean ridges (Hirschmann & Stolper, 1996). Furthermore, in mantle plume-influenced mantle regions the abundance of pyroxenitic material embedded in the mantle might be enhanced, due to the generation of melt during the focussed and large-scale adiabatic mantle upwelling having the potential to generate significant segregations (Spray, 1989).

A possible means of approximating the abundance of pyroxenitic material in the mantle source-regions of these anomalous basalts from the Discovery-influenced ridge segments is provided by the mean extent of melting calculated on the basis of the major-element characteristics of these basalts (≈12%) in the previous section. Equation 6.9, given below, was constructed for this purpose. In this calculation, the pyroxenite was assumed to melt completely and the mean extents of melting of the spinel-lherzolite was varied between 10-17.5%. The fractions of liquid derived from pyroxenite and spinel-lherzolite must add-up to 1 and both be positive values. The same is true for the fractions of the source composed of pyroxenite and spinel-lherzolite. The equation was therefore solved iteratively for the fractions of the source composed of pyroxenite and spinel-lherzolite, at variable mean extents of melting of spinel-lherzolite (10%, 12.5%, 15%, and 17.5%) and variable fractions of the liquid composed of pyroxenitic melt (0.2, 0.3, 0.4, 0.5). The results are given in table 6.6.

University of Cape Town

$$(F_{p'xenite} \times frac^{liquid}_{p'xenite} \times frac^{source}_{p'xenite}) + (F_{sp-lh} \times frac^{liquid}_{sp-lh} \times frac^{source}_{sp-lh}) \approx 0.12 \quad \ldots\ldots \text{equation 6.9}$$

$F_{p'xenite,sp-lh}$ = *mean extent of melting of pyroxenite, spinel - lherzolite*

$frac^{liquid}_{p'xenite,sp-lh}$ = *fraction of liquid composed of pyroxenite or spinel - lherzolite melt*

$frac^{source}_{p'xenite,sp-lh}$ = *fraction of source comprised of pyroxenite or spinel - lherzolite*

From the preceding modelling of the compositions of the final mixed melts, it seems 20-40% of the final mixed melts must be derived from the pyroxenitic material. Due to the uncertainties involved in this modelling, regarding mantle modes, melting coefficients, mode and extent of melting and starting compositions, 30% was taken as the maximum contribution of the melts derived from pyroxenitic material to the final mixed melts. The increasing volumes of mantle which would have to be tapped by 2-3% melts in order to form the pyroxenitic material make it also unreasonable to expect the mantle source-regions to contain more than 20% pyroxenitic material. These conceptual constraints eliminate significant sections of the results in table 6.6. The only results which still seem valid are for fractions of pyroxenitic melt in the final melt of approximately 0.3 and mean extents of melting of the spinel-lherzolite with which it mixed varying between 12.5-15%. This scenario yields abundances of pyroxenite in the mantle source-regions of 7.5-15%.

Table 6.6: Matrix of fractions of mantle source-region composed of pyroxenitic material for spinel-lherzolite melts of various extents of melting, and various fractions of the final melt composed of melt derived from 100% of melting of the pyroxenitic material. See text and equation 7.9 for details.

	Fraction of final melt composed of melt derived from pyroxenitic material			
F_{mean} (sp-lherzolite)	0.2	0.3	0.4	0.5
17.5%	---	---	0.050	0.080
15.0%	---	0.075	0.095	0.106
12.5%	0.200	0.150	0.140	0.103
10.0%	0.333	0.220	0.175	0.155

University of Cape Town

6.4 DISCUSSION

6.4.1 Major-element systematics as indicators of melting parameters - the global trend.

Observations for MORB from the SMAR. The respective orientations of fractionation-corrected major-element data of N-MORB, Discovery-influenced MORB and Shona-influenced MORB conform to the orientation of the so-called global trend for $Na_{8.0}$-$Fe_{8.0}$-Si_8 data (Klein & Langmuir, 1987; Klein & Langmuir, 1989; Langmuir *et al.*, 1992). The data for these MORB contain more scatter relative to the averaged global data-set (Klein & Langmuir, 1987), but this is to be expected for unaveraged data (Brodholt & Batiza, 1989). Although the data conform to the orientation of the global trend, the unaveraged data for MORB from the SMAR plot systematically to significantly higher $Na_{8.0}$ and $Fe_{8.0}$ and are off-set "above" the global trend.

A number of models have been proposed to account for the origin of the global trend (Kinzler, 1997; Kinzler & Grove, 1993; Klein & Langmuir, 1987; Klein & Langmuir, 1989; Langmuir *et al.*, 1992; Shen & Forsyth, 1995), but the "variable temperature" mantle model still seems to offer the best explanation. Variations in the temperature of the upwelling beneath the mid-ocean ridges result in variable depths of initiation of melting, with fairly constant final depths of melting. Therefore hotter mantle starts melting at greater depth, melt to higher mean extents and form thicker crust which results in shallower bathymetry for the relevant mid-ocean ridges. The reverse is true for cooler mantle upwelling. This model is supported by the fractionation-corrected data for MORB recovered from SMAR ridge segments unaffected by hotspots, and from ridge segments affected by the Shona mantle plume. The data for Shona-influenced MORB indicate melting beneath these shallow bathymetry ridge segments being initiated at greater depths ($\leq$23kbar) compared with melting beneath ridge segments unaffected by mantle plumes (~18±3kbar), although the final depths of melting for these two groups of MORB are fairly constant (~13±2kbar). Therefore the greater initial depth of melting results generally in greater mean extents of melting beneath Shona-influenced ridge segments (16-19%) compared to melting beneath ridge segments unaffected by mantle plumes (14-18%), although the rate of melting is fairly constant for these two groups of MORB (2-4%/kbar).

The fractionation-corrected major-element data for MORB from Discovery-influenced ridge segments seem to contradict this explanation for the global trend and plot on the opposite side of N-MORB relative to the data for Shona-influenced ridge segments. Therefore at initial pressures of melting which predominantly range to much lower values (13-20kbar) and with

University of Cape Town

more varied final pressures of melting (8-15kbar), relative to N-MORB. Some anomalous samples yielded extremely low values of 5-7kbar for the initial pressures of melting and also anomalously low final pressures of melting, at 4-5kbar. The mean extents of melting beneath the Discovery-influenced ridge segments (14-17%) are in general similar to that beneath the ridge segments unaffected by mantle plumes, but the locations of shallow mantle melting also experienced melting to slightly lower extents (~12%). The rate of melting beneath most of the Discovery-influenced ridge segments is similar to the rate beneath Shona-influenced ridge segments and ridge segments unaffected by mantle plumes (2-4%/kbar). However, in the regions of anomalously shallow mantle melting, the rate of the melting must have been exceptionally high (>5%/kbar). Although the orientation of the fractionation-corrected major-element data for Discovery-influenced MORB correlates with the global trend, the position of these data relative to N-MORB seems to be in conflict with the origin of the global trend and the recovery of these mantle plume-influenced basalts from ridge segments with shallow bathymetry, and therefore thick oceanic crust which necessitates the generation of high volumes of melt in these regions.

The deduced melting parameters based on the major-element data for MORB from the SMAR, relative to accepted models for MORB generation and previous studies conducted in the South Atlantic. Fractionation-corrected $Na_{8.0}$-$Fe_{8.0}$-$Si_{8.0}$ data for the MORB from the SMAR follow previous observations for basalts from other areas of the global mid-ocean ridge system. As was stated above, the data for MORB from Shona-influenced ridge segments and for MORB from ridge segments unaffected by mantle plumes conform to the general concept of the origin of the global trend, i.e. significant variations in the temperature of the upwelling mantle beneath the ridge segments (Brodholt & Batiza, 1989; Kinzler, 1997; Klein & Langmuir, 1987; Klein & Langmuir, 1989; Langmuir *et al.*, 1992). Although no explanation had been proposed, the aberrant systematics of the MORB recovered from Discovery-influenced ridge segments have previously been observed in the global data-set, e.g. in the basalts recovered from ridge segments across the Galapagos platform (Langmuir *et al.*, 1992).

The pressure-dependent fractionation-corrected major-element have been taken to indicate the initial pressures of melting (Klein & Langmuir, 1987; Klein & Langmuir, 1989; Langmuir *et al.*, 1992; Niu & Batiza, 1991), however the possibility has been proposed that these fractionation-corrected major-element data might actually reflect the final depths of equilibrium between the melt and the solid residue and not the initial solidus depth (Niu, 1997; Niu & Batiza,

University of Cape Town

1994). Equilibrium between melt and solid residue, if present, would persist to shallower depths in higher temperature mantle regions, therefore especially beneath ridge segments affected by mantle plumes (Niu, 1997; Niu & Batiza, 1994). Therefore the pressure signature preserved in the fractionation-corrected major-element data for MORB from Discovery-influenced ridge segments might actually reflect melts in these regions remaining in equilibrium with the hotter, mantle plume-influenced solid residue to shallower depths.

Two observations conflict with this interpretation. Firstly, the present-day location of the Discovery mantle plume has been placed ~425km from the MAR, while the Shona mantle plume may be located on or very close to the MAR (Douglass *et al.*, 1999; Douglass *et al.*, 1995; Small, 1995; Small *et al.*, 1994; Small *et al.*, 1995). The mantle beneath Shona-influenced ridge segments are therefore expected to be affected more significantly by the thermal influence of the proximal mantle plume, relative to the mantle beneath Discovery-influenced ridge segments. The shallower bathymetry for Shona-influenced ridge segments, relative to the bathymetry of Discovery-influenced ridge segments, seem to support the greater influence of the mantle plume and associated higher heat flow in this region. Therefore it is expected that melts beneath Shona-influenced ridge segments should much more readily stay in equilibrium with the solid residue to shallow depths. The MORB recovered from these ridge segments should then also more readily preserve pressure-dependant major-element characteristics indicative of shallow mantle depths. This is not observed and the fractionation-corrected major-element data for MORB recovered from Shona-influenced ridge segments reflect deep mantle depths. It therefore seems unlikely that the pressure-dependant major-element characteristics in MORB from Discovery-influenced ridge segments reflect equilibrium between melts and solid residue at shallow mantle depths.

Furthermore, on a finer scale, basalts recovered from locations at the ends of Discovery-influenced ridge segments reflect the shallowest mantle depths in their fractionation-corrected major elements. If the pressure-dependant major-element characteristics in the data for these MORB from Discovery-influenced ridge segments did reflect equilibrium between melts and hot solid residue, then the magmas formed in the vicinity of transform faults would be expected to reflect deeper and not shallower mantle pressures relative to basalts from ridge-segment centres. This is due to the enhanced cooling of the mantle from the surface, to greater depths, in the proximity of transform faults (Langmuir & Bender, 1984; Shaw & Lin, 1996). This

University of Cape Town

observation therefore also negates the possibility that the anomalous shallow mantle pressures reflected by the fractionation-corrected major-element data for MORB from Discovery-influenced ridge segments refer to the final depths of equilibrium between melts and hot, solid mantle residue.

A possible factor which could systematically and notably affect the $Na_{8.0}$-$Fe_{8.0}$ compositional co-variations of basalts is an increase in the abundance of pyroxene, especially clinopyroxene, in the modal mineralogies of the mantle source-regions from which the primary melts were extracted. Although this affect has not been quantified, qualitative results indicate higher NaO and total FeO content in melts derived from more pyroxene-rich mantle source-regions (Hirschmann *et al.*, 1995; Langmuir *et al.*, 1992). Therefore, the presence of increasing amounts of pyroxenitic material in the MORB mantle source-regions beneath Discovery-influenced ridge segments, or increasing the proportion of the melts derived from pyroxenitic material in the mantle source-regions, especially in the vicinity of transform faults, could possibly play, an as yet unquantified, role in the observed fractionation-corrected major-element indications of shallow mantle pressures.

The total range of the mean extent of melting (~12-19%) beneath the ridge segments of the SMAR, calculated using the fractionation-corrected major-element data of the recovered MORB, coincides with accepted extents of melting for the origin of basalts in the mantle beneath mid-ocean ridge environment. Numerous experimental studies have attempted to simulate the MORB melting process (Baker *et al.*, 1995; Baker *et al.*, 1996; Baker & Stolper, 1994; Iwamori *et al.*, 1995; Kinzler, 1997; Kinzler & Grove, 1992a; Kinzler & Grove, 1992b; Kinzler & Grove, 1993; Walter & Presnall, 1994) or used the results of experimental work to construct algorithms aimed to calculate the compositions of melts generated during melting beneath mid-ocean ridges (Kinzler, 1997; Kinzler & Grove, 1992b; Kinzler & Grove, 1993; Niu & Batiza, 1991; Walter *et al.*, 1995). The consensus which emerges from all the above studies places the mean extent of melting experienced by the mantle beneath mid-ocean ridges in the range of ~6-20%.

A further constraint on the extent of melting beneath mid-ocean ridges is deduced from studies of abyssal peridotites, recovered mainly from deep lithospheric levels exposed on the walls of fracture zones between ridge segments. Trace-element compositions of discrete clinopyroxenes in abyssal peridotites, especially from the America-Antarctic and Southwest

University of Cape Town

Indian ridges in the South Atlantic, indicate that these residues of the melting process beneath adjacent mid-ocean ridges experienced 5-25% of near-fractional melting, with extremely efficient and continuous melt removal during the melting process (Johnson & Dick, 1992; Johnson *et al.*, 1990). Trace-element composition of clinopyroxenes in abyssal peridotites from the global mid-ocean ridge system also define a general pattern of increased extents of melting beneath ridge segments affected by mantle plumes (20-30%), relative to ridge segments unaffected by mantle plumes (10-20%) (Dick, 1989; Dick *et al.*, 1984; Johnson & Dick, 1992; Johnson *et al.*, 1990). The calculated extents of melting beneath ridge segments of the SMAR and the near-fractional nature of the melting therefore agree with deductions regarding melting beneath mid-ocean ridges in general, and especially beneath the proximal America-Antarctic and Southwest Indian ridges in the South Atlantic, drawn from studies of abyssal peridotites.

The major-element compositions of residual minerals, e.g. clinopyroxene and spinel, in abyssal peridotites have also been found to correlate and with the spreading rate of the ridges from which they were recovered. These correlated major-element compositions are the result of various extents of melting of the peridotites beneath mid-ocean ridges. Niu & Hékinian (1997) deduced that the extent of melting beneath ridge segments vary with spreading rate, with ~10% melting at slow-spreading rates and ~22% melting at the fast-spreading rate end of the observed range for mid-ocean ridges. The correlated variations in the reconstructed modal mineralogies and bulk major-element compositions of abyssal peridotites have also been used to investigate the melting process which extracted melts from these samples beneath mid-ocean ridges (Niu, 1997). This approach to the problem of melting beneath mid-ocean ridges yielded variable extents of melting (~10-22%) consistent with the above experimental work, other investigations of abyssal peridotites and the calculated mean extents of melting for the majority of MORB from the SMAR.

Using the thickness of the oceanic crust and a simple approach to mass conservation, limits can be placed on the extent of melting beneath mid-ocean ridges. The geophysical defined thickness of normal oceanic crust is 6-7km, although it would be significantly thicker in regions affected by mantle plumes (Niu, 1997; Niu *et al.*, 1996). The width of the upwelling mantle, for perfect passive upwelling, is related to spreading rate by equation 6.10 (Reid & Jackson, 1981).

University of Cape Town

$$U = \frac{2Vz^2}{\pi(x^2 + z^2)} \quad \text{..... equation 6.10}$$

U = *mantle upwelling rate*
V = *half - spreading rate*
z = *depth*
x = *distance away from ridge*

$U_{max} = 2V/\pi$ directly beneath the ridge-axis ($x = 0$) and $U \leq 2V/\pi$ in general, and for simplicity it is assumed that $U = U_{max}$ across the ridge (Niu, 1997). With complete melt extraction during melting, the mass of melt produced per unit time must equal the mass of oceanic crust formed on the same time scale. The equation 6.11 must be true (Niu, 1997).

$$2Vh = 2wUF \quad \text{..... equation 6.11}$$

U = *mantle upwelling rate*
V = *half - spreading rate*
h = *crustal thickness*
w = *half - width of the upwelling - melting zone, i.e. one side of the ridge axis*
F = *the extent of melting of the mantle that enters the melting region*

Therefore, for oceanic crust 6km thick, $w \geq 3\pi/F$ or $w \geq 9/F$ (Niu, 1997). For $F = 5\%$, 10%, 15% and 20%, melt produced at distances of 180km, 90km, 60km and 45km, respectively, from both sides of the ridge must be transported laterally towards the ridge axis to form 6km thick crust. Melt transport over long distances, > 70km, in the mantle beneath mid-ocean ridges is difficult (Cordery & Phipps Morgan, 1993; Turcotte & Phipps Morgan, 1992). Therefore the mean extent of melting is much more likely to be 10-20% , due to the short distances over which melts would have to be transported (~35km on both side of the ridge) to form oceanic crust 6km thick (Niu, 1997; Niu *et al.*, 1996). The calculated extents of melting beneath the ridge segments of the SMAR therefore also conform to these geophysical and mass balance constraints.

The abovementioned studies also placed constraints on the pressure interval of melting beneath mid-ocean ridges. The initial pressure of melting deduced from experimental work falls in the range of ~20-25kbar and the final pressure of melting varies between ~4-12kbar (Kinzler, 1997; Kinzler & Grove, 1992b; Kinzler & Grove, 1993; Niu & Batiza, 1991). With the exception

University of Cape Town

of the anomalous basalts from Discovery-influenced ridge segments with extremely shallow initial pressures of melting (5-7kbar), the calculated initial and final pressures for melting beneath ridge segments of the SMAR are within the accepted values from experimental work.

The shapes of REE patterns in discrete clinopyroxenes in some abyssal peridotites seem to necessitate these peridotites to have experienced variable extents of melting initiated within the garnet stability-field (Johnson *et al.*, 1990). Therefore, some evidence exists to support small degrees of melting occurring at depths within the garnet stability-field.

6.4.2 Major-element systematics orthogonal to the global trend - the local trend.

Observations for MORB from the SMAR. The local trend is observed predominantly in the fractionation-corrected major-element data for MORB from mid-ocean ridges at the slower end of the spreading rate spectrum (Klein & Langmuir, 1989; Langmuir *et al.*, 1992). The trends, orthogonal to the orientation of the global trend, observed in the $Na_{8.0}$-$Fe_{8.0}$ data for a significant proportion of the MORB from the SMAR and parallel to the orientation of the local trend, are therefore well-defined features for a ridge such as the SMAR (Brodholt & Batiza, 1989; Klein & Langmuir, 1987; Klein & Langmuir, 1989; Niu & Batiza, 1993; Niu & Batiza, 1994). The local trends in the fractionation-corrected major-element data are sub-parallel and defined by basalts from mantle plume-affected ridge segments, as well as from ridge segments unaffected by mantle plumes. Another set of trends in the fractionation-corrected major-element data are orientated at angles between the local trends and seem to connect high-$Na_{8.0}$-high-$Fe_{8.0}$ ends of trends to low-$Na_{8.0}$-low-$Fe_{8.0}$ of adjacent trends.

Evaluation of possible origins of the local trends in the MORB from the SMAR. The origin of the local trends and the reason for the predominant occurrence in the fractionation-corrected major-element data of MORB from slow-spreading ridges are still unresolved (Klein & Langmuir, 1989; Langmuir *et al.*, 1992; Niu, 1997; Niu & Batiza, 1994). Calculated major-element trajectories of different mantle melting scenarios (Kinzler, 1997), i.e. various initial pressures of melting, rates of melting, extents of melting and starting compositions, are orientated at significantly steeper angles relative to the observed local trends. The possibility that the local trends are defined by continuously sampled instantaneous melts from different levels in melting columns (Klein & Langmuir, 1989) is therefore not supported by the data from the SMAR. Neither do the expanded fractionation-corrected major- ($Ti_{8.0}$, $Ca_{8.0}$) and trace-element

University of Cape Town

($Ni_{8.0}$) data for the MORB from the SMAR support the proposed role of a net melting reaction in which pyroxene is progressively dissolved and olivine crystallised during melt transport through the mantle (Niu, 1997; Niu & Batiza, 1994).

Another proposed origin for the local trend in fractionation-corrected major-element data for MORB at slow-spreading ridges, is polybaric phenocryst crystallisation (Grove *et al.*, 1992; Kinzler & Grove, 1992b). If phenocryst crystallisation does occur beneath slower-spreading ridges, it is more likely to occur at higher pressures relative to crystallisation beneath faster-spreading ridges (Michael & Cornell, 1998). This is probably due to a combination of more efficient cooling from the surface, the probable thicker lithospheric cap, and the lack of long-lived, shallow-level sub-axial magma chambers at slower-spreading ridges (Batiza *et al.*, 1988; Detrick *et al.*, 1990; Grove *et al.*, 1992; Langmuir *et al.*, 1992; Michael & Cornell, 1998). Trends defined by the calculated major-element compositions of modelled accumulated melts (Kinzler, 1997) crystallised at pressure ranging between 1atm-8kbar (Ariskin *et al.*, 1993) are orientated approximately parallel to the local trends in the data for MORB from the SMAR. Unlike the data for MORB from the FAMOUS region (Langmuir *et al.*, 1992), the concentrations of Sr in the basalts from the SMAR which define local trends remain fairly constant at variable $Na_{8.0}$ and $Fe_{8.0}$. The concentration of Sr is buffered during crystallisation up to pressures of 8kbar, by the presence of plagioclase as a liquidus phase. The constant Sr concentrations in basalts over significant ranges in $Na_{8.0}$ and $Fe_{8.0}$ therefore indicate a considerable role for crystallisation in the formation of the observed local trends in the fractionation-corrected major-element data for MORB from the SMAR.

University of Cape Town

6.4.3 The possible role for compositionally distinct pyroxenitic material, derived from small degree melts formed in the garnet-lherzolite stability-field, during melting beneath Discovery-influenced ridge segments.

Observations for MORB from the SMAR. The basalts recovered in dredges 25, 6 and some from dredge 7 contain anomalous major-, trace-element and radiogenic isotope characteristics. The fractionation-corrected major-element data of these basalts are characteristic of melts which formed at anomalously low initial pressures of melting ($Si_{8.0}/Fe_{8.0}$: 6.2-7.1; $P_{initial}$: 5-7kbar) compared to the rest of the basalts from the SMAR ($Si_{8.0}/Fe_{8.0}$: 4.4-6.1; $P_{initial}$: 13-20kbar), and the generally accepted range for MORB generation (20-25kbar) (Kinzler, 1997; Kinzler & Grove, 1992b; Kinzler & Grove, 1993; Niu & Batiza, 1991). The derived mean extents of melting ($Na_{8.0}$: 2.6-3.3; $Ca_{8.0}/Al_{8.0}$: 0.55-0.73; F_{mean}: 10.9-17.1%) for the genesis of the

basalts from dredge 25, 6 & 7 are not exceptional when compared to that for other MORB from the SMAR (12-19%), and extent towards the lower end of the accepted range (6-20%) from general studies of MORB melting (Kinzler, 1997; Kinzler & Grove, 1992b; Kinzler & Grove, 1993; Niu & Batiza, 1991; Walter *et al.*, 1995).

The anomalous trace-element characteristics (Sc ≥ 22.2ppm & $(Sm/Yb)_N$ = 1.73-2.83 at Mg# of 63-65%) are not only exceptional compared with other basalts from the SMAR, but also relative to data for other MORB from mid-ocean ridges in the Atlantic Ocean (e.g. the Southwest Indian Ridge, le Roex *et al.*, 1983; le Roex *et al.*, 1989, Southern Mid-Atlantic Ridge, le Roex *et al.*, 1987, and Northern Mid-Atlantic Ridge, le Roex *et al.*, 1996), as illustrated in fig. 6.16. Although these anomalous trace-element characteristics are linked to the low initial pressures of melting, as was shown in fig. 6.5a & 6.13, they necessitate the presence of residual garnet at some stage during the mantle melting from which these basalts were derived. Major- and trace-element indicators of initial pressures of melting in these basalts are therefore in apparent conflict, because garnet is only stable in lherzolite at pressures above 28-30kbar (Kinzler, 1997; Robinson & Wood, 1998) while initial pressures of melting derived from the fractionation-corrected major-element compositions are significantly lower ($P_{initial}$: 5-7kbar).

The high $^{87}Sr/^{86}Sr$ ratios (0.705093-0.705878) and low $^{143}Nd/^{144}Nd$ ratios (0.512365-0.512567) of the above basalts, the strongest evidence of the compositional influence of the Discovery mantle plume (Douglass *et al.*, 1999; Douglass *et al.*, 1995), are further well-correlated with calculated initial pressures of melting for these basalts, see fig. 6.4a & 6.12, and with the anomalous trace-element characteristics. The petrogenesis of these anomalous basalts from Discovery-influenced ridge segments therefore not only involved unusual melting processes, but also mantle source-regions with exceptional compositions.

Preferred model for the genesis of the anomalous basalts from Discovery-influenced ridge segments: derivation at low pressures of significant fractions of the final melts from pyroxenitic material, formed by low-degree garnet-lherzolite melts associated with the influence of the Discovery mantle plume, embedded in the spinel-lherzolite mantle. The trace-element modelling conducted in section 6.3 indicates that the geochemical characteristics of these anomalous basalts from Discovery-influenced ridge segments are best explained by a two-stage melting model. The first stage of this sequence is situated within the upwelling Discovery

University of Cape Town

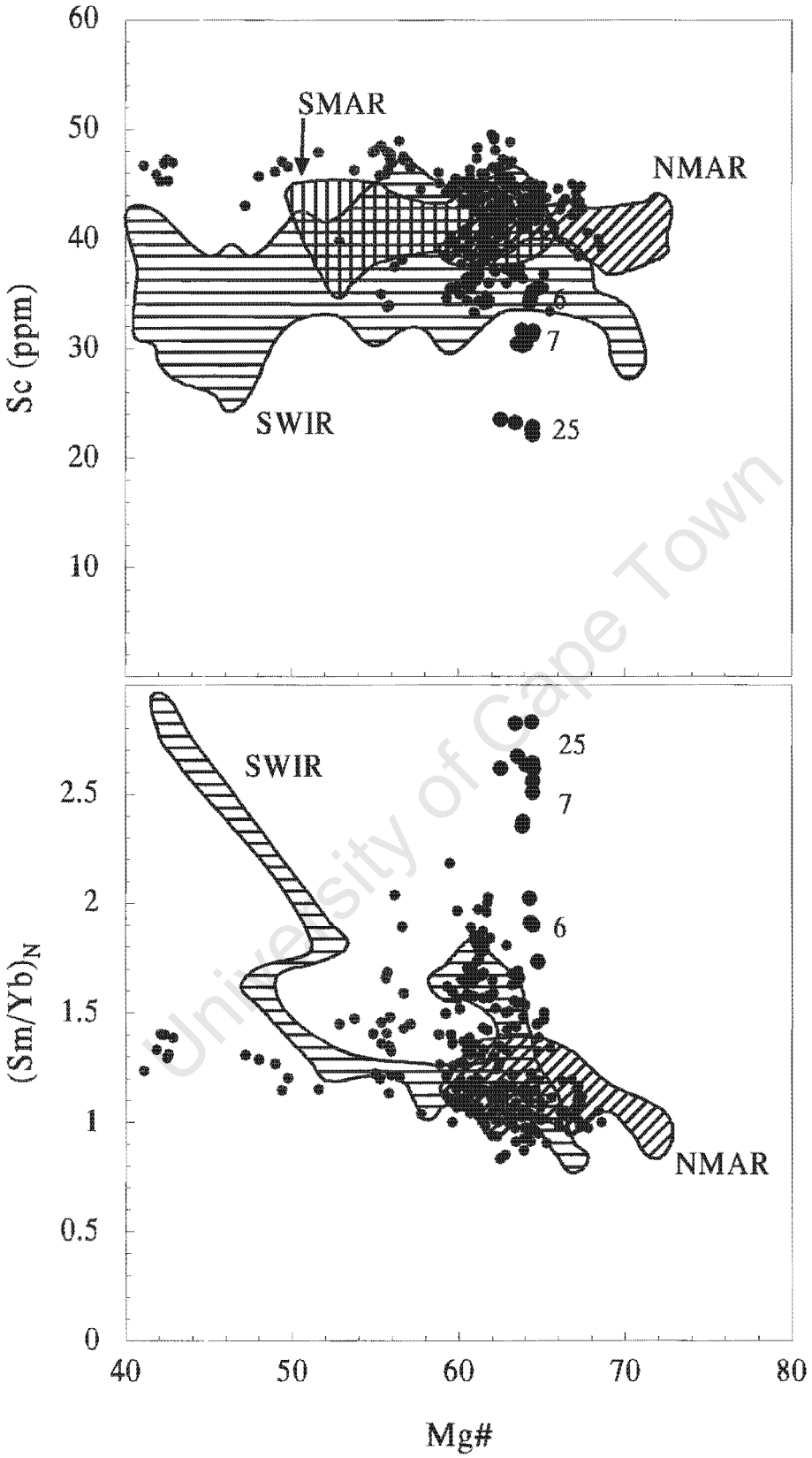

University of Cape Town

Figure 6.16: Sc concentrations (ppm) and chondrite-normalised (Sun & McDonough, 1989) Sm/Yb ratios versus Mg# for quenched igneous glasses of N-MORB (blue markers), Discovery-influenced MORB (red markers) and Shona-influenced MORB (green markers). Filled fields delineate extents of published data for MORB from the SWIR from le Roex *et al.* (1983) and le Roex *et al.* (1989), the NMAR from le Roex *et al.* (1996) and the SMAR from le Roex *et al.* (1987)

mantle plume and involves the formation of small-degree (1-2%) melts, at depths below the garnet-spinel transition (28-30kbar) (Kinzler, 1997; Robinson & Wood, 1998), from the incompatible trace-element and radiogenic-isotope enriched lherzolitic mantle. These melts would therefore have residual garnet present during their formation, contain low Sc concentrations, with middle REE (e.g. Sm) partitioned into the melt preferentially relative to the more compatible heavy REE (e.g. Yb), be significantly enriched in incompatible trace elements due to the enriched nature of the mantle-plume material from which they formed and the fact that the incompatible trace elements would preferentially partition into the early-formed low-degree melts, and inherit the radiogenic-isotope characteristics of the Discovery mantle plume.

Some of these small-degree melts are inefficiently focussed towards the central eruptive zone of the upwelling Discovery mantle plume, migrate only a short distance into the overlaying mantle before this upwelling mantle flows out of the melting regime and solidify as pyroxenitic veins or layers within the now cooler spinel-lherzolite mantle. The integrity of these veins or layers are maintained within the sub-oceanic mantle as it flows towards the shallower zone of upwelling beneath the mid-ocean ridge. This veined spinel-lherzolite mantle is entrained in the upwelling beneath the mid-ocean ridge and, due to the lower solidus temperature of the pyroxenitic material, the melting of the veins is initiated significantly prior to the melting of the spinel-lherzolite and proceed at exceptionally high rates. As the upwelling continues, the spinel-lherzolite solidus is reached and melting now involves both components of the upwelling mantle. Due to the high rates of melting of the pyroxenitic material and it's relatively low abundance in the upwelling mantle, it is exhausted before the spinel-lherzolite melting ceases. The higher volumes of melt derived from the spinel-lherzolite variably dilute the trace-element characteristics of the pyroxenitic melt during mixing prior to eruption of the final combined melt. The compositions of the final melts, erupted at the mid-ocean ridge, derived from the veined spinel-lherzolite mantle source-regions are dominated in the major-element characteristics by the spinel-lherzolite derived component and in the highly incompatible trace-element and radiogenic isotope characteristics by the vein-derived melts.

In the vicinity of transforms and fracture zones on the mid-ocean ridge, however, the thermal regime of the underlaying upwelling mantle is disturbed. Cooling from the top of the ocean crust is more effective, isothermal surfaces become depressed and rapid temperature changes occur within much shorter pressure intervals relative to the centres of ridge segments

University of Cape Town

(Langmuir & Bender, 1984; Shaw & Lin, 1996). The result is that, relative to ridge segments centres, mantle upwelling beneath transforms and fracture zone is diminished and the slower upwelling mantle intercepts the solidus of the pyroxenitic material and surrounding spinel-lherzolite, respectively, at lower pressures. The rapid temperature changes with decreasing pressure enhance the rate of melting of the pyroxenitic material and the shorter melting columns result in less melting of the spinel-lherzolite mantle. The final melts formed in the proximity of transforms and fracture zones are therefore derived from smaller extents of melting of the total upwelling mantle and composed of a higher proportion of melt derived from the vein component, relative to the final melts formed beneath ridge segments centres. The cooler thermal regime in the vicinity of transforms and fracture zones result in inefficient focussing of these lower extent, high vein-fraction final melts towards the main eruptive zones at the ridge segments centres. The cooler thermal regime also results in brittle failure occurring at deeper levels in the lithosphere, enhancing the formation of joints and fractures which aid the rapid ascend, and final eruption of these anomalous melts at the extremes of mid-ocean ridge segments.

If the upwelling mantle beneath mid-ocean ridge segments is veined, having been invaded by low-degree melts associated with proximal mantle plumes, then the basalts erupted at the ends of these ridge segments terminated by significant transforms or fracture zones probably contain higher fractions of melt derived from these veins relative to basalts erupted at ridge segment centres. The compositions of these basalts are therefore more influenced by the compositions of the veins, which would contain trace-element and radiogenic-isotope features characteristic of their original mantle source-regions and formation. Major-element compositions could also contain characteristic features imparted by the significantly higher proportion of clinopyroxene and orthopyroxene in the mineralogy of the mantle source-regions. This explains why basalts recovered from Discovery-influenced ridge segment ends in the immediate vicinity of the Falkland-Agulhas Fracture Zone and another significant transform, respectively, have the most-undiluted Discovery mantle plume-like radiogenic-isotope compositions, trace-element compositions indicative of residual garnet during melting, and fractionation-corrected major-element compositions characteristic of low initial pressures of melting and high proportions of pyroxene in their mantle source-regions (Langmuir & Bender, 1984; Sleep, 1984).

Evaluation of the preferred model for the origin of anomalous basalts from Discovery-influenced ridge segments, relative to studies of melt generation, migration and focussing in

University of Cape Town

the mantle. The existence of veined oceanic-mantle source-regions, especially beneath mid-ocean ridge segments affected by proximal mantle plumes, have been prosed in a number of studies based on the geochemical characteristics of basalts (Fontignie & Schilling, 1996; Hékinian *et al.*, 1995; Hirschmann & Stolper, 1996; le Roex, 1987; le Roex *et al.*, 1987; le Roex *et al.*, 1985; McKenzie & O'Nions, 1995; Niu *et al.*, 1999; Schilling *et al.*, 1994; Spray, 1989; Yang *et al.*, 1998). Although direct evidence for the relative abundance and composition of these veins in oceanic mantle source-regions is still lacking, pyroxene-rich rocks are present in a wide range of mantle samples (Hirschmann & Stolper, 1996). The origin of pyroxenitic veins in the oceanic asthenosphere still remain largely unconstrained, although a number of processes have been proposed. These vary from subduction of oceanic crust, delamination or foundering of mafic cumulates or restites from the lower continental crust, delamination of veined-subcontinental lithosphere, subduction of veined oceanic lithosphere, return of mantle wedge material, which became veined due to subduction zone processing, to the convecting mantle by corner flow, to metamorphic segregation (Hirschmann & Stolper, 1996; and references therein). Hirschmann & Stolper (1996) preferred the processes of subduction of oceanic crust, and recycling of lower crustal cumulates or restites, from the above list, for the formation of pyroxenitic veins in the oceanic asthenosphere. Although the process of vein-formation proposed in this study, i.e. pervasive infusion of overlaying mantle regions by low-degree melts associated with the influence of a mantle plume, was not assessed by Hirschmann & Stolper (1996) in their review of pyroxenite formation in the oceanic mantle, it has been advanced as a major mechanism affecting the sub-oceanic mantle (le Roex, 1987; le Roex *et al.*, 1987; Niu *et al.*, 1999; Spray, 1989).

University of Cape Town

Furthermore, this process of vein-formation is supported by a number of studies beyond the conceptual stage. The upwelling mantle material associated with the Discovery mantle plume is not only compositionally enriched in incompatible trace elements and radiogenic isotopes, but also significantly hotter and probably contains more volatiles, e.g. CO_2 and H_2O, and alkalis than the mantle upwelling beneath the SMAR (Hofmann, 1997; Kempe & Schilling, 1974; le Roex, 1987; McKenzie & O'Nions, 1995; Sobolev & Chaussidon, 1996). The effect of the much higher temperature of the upwelling material (~200-300°C) (McKenzie & O'Nions, 1995) associated with the mantle plume, and to a lesser degree the volatiles and alkalis, would be the earlier, deeper initiation of melting relative to melting of the colder upwelling mantle beneath mid-ocean ridge segments.

Although higher concentrations of volatiles and alkalis in the Discovery mantle plume might not be significant, and are definitely secondary in importance to the higher mantle temperatures of the plume (McKenzie & O'Nions, 1995), the effects ascribed to increased volatiles and alkalis in upwelling mantle also agree with the model proposed here. The initial extents of melting at depth within the mantle plume are small (<5%) until the temperature of the upwelling mantle is sufficient to generate significant melt for equivalent volatile-depleted mantle material (Hirschmann *et al.*, 1999a). The presence of significant volatiles and alkalis in the composition of the upwelling mantle would result in small-degree melts forming at great depth in a "dehydration"-zone of limited vertical extent, but distinct from later extensive melting of the anhydrous mantle at shallower depths over a much larger range in pressure. This deep zone of "dehydration"-melting is almost certainly located in the garnet-lherzolite stability-field (Hirschmann *et al.*, 1999a; Phipps Morgan & Morgan, 1999; Schilling *et al.*, 1980).

The possibility that significant amounts of small-degree melts might form from melting of garnet-lherzolite beneath mid-ocean ridges, and thus not involve mantle plumes, is inhibited by the extremely high potential temperatures (>1450°C) required (Robinson & Wood, 1998). These high potential temperatures are not unreasonable for a mantle plume (McKenzie & O'Nions, 1991) and the formation of small-degree melts at depths within the garnet-stability field from Discovery mantle-plume material as proposed in this study is quite feasible.

Assuming upwelling is passive and the shape of the melting regime is triangular (Plank & Langmuir, 1992), it is evident, although the relative initial depths of melting are not well constrained, that the volume of mantle involved in the initial melting of garnet-lherzolite is significantly larger than that involved in later melting of spinel-lherzolite mantle at shallower depths, see fig. 6.17 (Hirschmann *et al.*, 1999a). The flow direction of the solid mantle residue and the small-degree melts formed are decoupled, with the solid residue flowing out of the melting regime as indicated in fig. 6.17, whereas the melts are focussed towards the centre of the upwelling mantle plume into a smaller volume of mantle than that from which they were extracted (Kelemen *et al.*, 1995a; Kelemen *et al.*, 1995b; Magde *et al.*, 1996; Magde *et al.*, 1997). In this way, mantle volumes which exit the side of the melting regime after residing in the melting regime for a considerable time could have experienced numerous injections of these small-degree melts and contain significant abundances of pyroxenitic veins or layers. The occurrence and abundance (~7.5-15%) of pyroxenitic material in the mantle source-regions

University of Cape Town

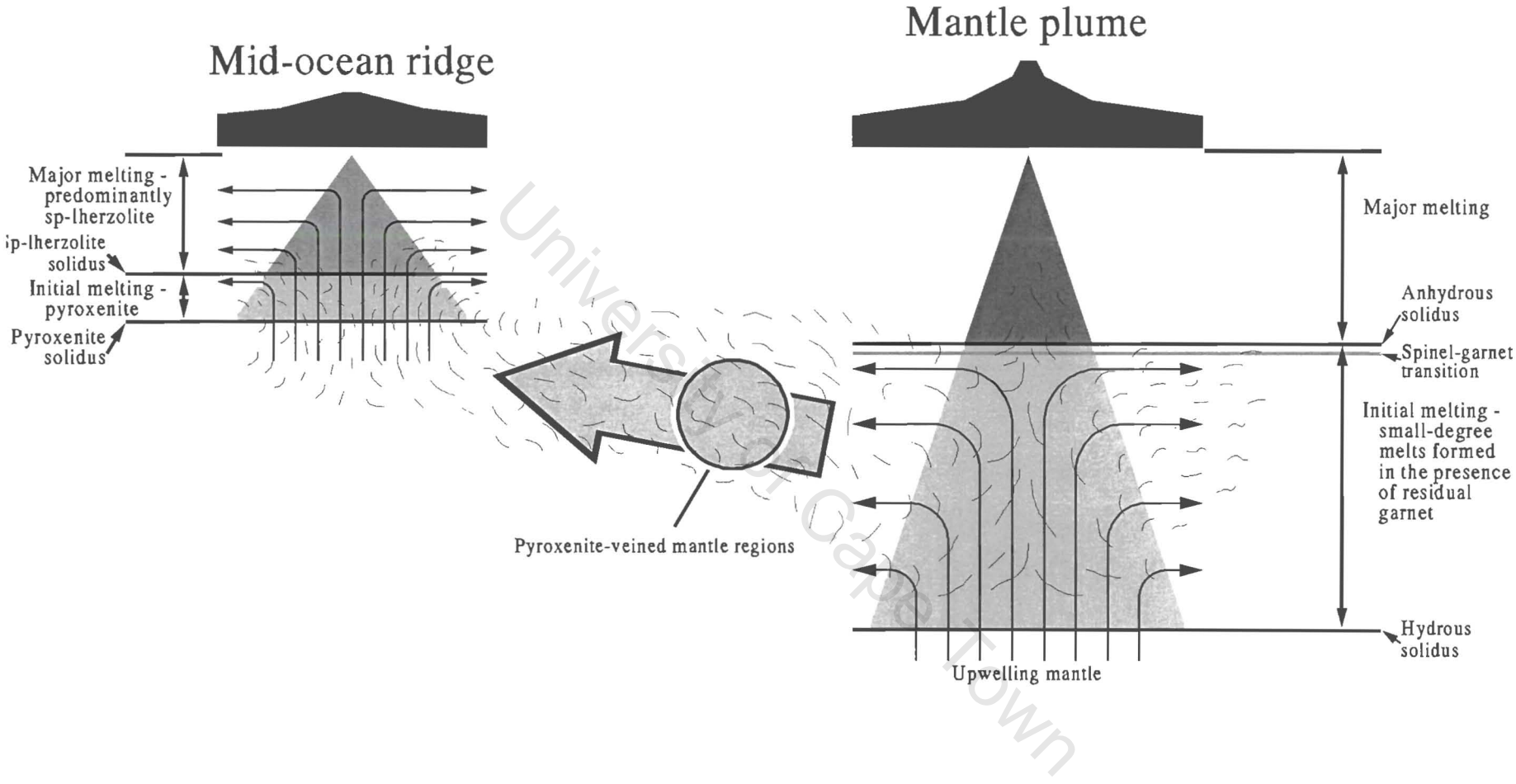

University of Cape Town

Figure 6.17: Schematic representation of the formation of pyroxenite-veined mantle regions from solidified small-degree melts formed during deep melting in the upwelling of incompatible-element and radiogenic-isotope enriched material beneath a mantle plume. Some of the pyroxenite-veined mantle regions flow towards the mid-ocean ridge and become entrained in the shallower mantle upwelling zone beneath the ridge. The lower temperature pyroxenite solidus is intercepted prior to the higher temperature spinel-lherzolite solidus during the adiabatic mantle upwelling beneath the ridge. An initial phase of melting of the pyroxenite veins therefore precedes the major phase of melting of the spinel-lherzolite. Schematics based on diagrams of Hirschmann *et al.* (1999c) and Kelemen *et al.* (1995a).

envisaged beneath some Discovery-influenced ridge segments in the model proposed for the origin of the anomalous basalts recovered from these ridge segments in this study, is difficult to evaluate quantitatively but seem reasonable.

The survival of pyroxenitic veins or layers in the mantle during horizontal mantle flow towards the SMAR from the locations of the Discovery mantle plume does not pose a significant problem. The proposed present-day location of the Discovery mantle plume is ~425km from the SMAR (Douglass *et al.*, 1999; Douglass *et al.*, 1995), within the limits of previous models of linked mantle flow between mantle plumes and the SMAR delivering mantle material from the plumes to the mantle upwelling beneath ridge segments (Schilling *et al.*, 1985). The dispersal of Discovery mantle-plume material in the oceanic mantle, started at ~35Ma (Douglass *et al.*, 1999), is proposed to have began arriving beneath the SMAR south of the Falkland-Agulhas Fracture Zone at ~13Ma (Douglass *et al.*, 1999), on this time scale mantle convection could not have significantly compromised the integrity of the proposed pyroxenitic veins (Dickin, 1995; Niu & Batiza, 1997; Niu *et al.*, 1996; Phipps Morgan & Morgan, 1999; Spray, 1989). The observed presence of pyroxenite dykes and sills in the mantle sections of ophiolites, e.g. the Oman ophiolite (Kelemen *et al.*, 1995a), also supports the survival of these features in the oceanic mantle.

The details of melting a two-component mantle source-region beneath mid-ocean ridges are not well-constrained, especially when pyroxenitic material is involved (Hirschmann *et al.*, 1995; Yaoling Niu, pers. comm.; Tim Grove, pers. comm.). The melting of particularly spinel-lherzolite mantle to produce the basalts recovered from the global mid-ocean ridge system has received considerable attention, in terms of experimental work, the modal mineralogies and compositions of abyssal peridotites, mantle xenoliths from oceanic volcanism, and theoretical thermodynamics (Asimow *et al.*, 1995a; Asimow *et al.*, 1995b; Baker *et al.*, 1995; Baker & Stolper, 1994; Elthon, 1989; Fujii, 1989; Ghiorso *et al.*, 1994; Ghiorso & Sack, 1995; Grove *et al.*, 1994; Hirschmann *et al.*, 1999a; Hirschmann *et al.*, 1999b; Hirschmann *et al.*, 1998; Iwamori *et al.*, 1995; Johnson & Dick, 1992; Johnson *et al.*, 1990; Kinzler, 1997; Kinzler & Grove, 1992a; Kinzler & Grove, 1992b; Kinzler & Grove, 1993; Niu, 1997; Niu & Batiza, 1991; Sack & Ghiorso, 1994a; Sack & Ghiorso, 1994b; Sack & Ghiorso, 1994c; Takahashi *et al.*, 1993; Walter & Presnall, 1994; Walter *et al.*, 1995; Yang *et al.*, 1998). The proposed melting of spinel-lherzolite beneath the SMAR is not exceptional and conforms to the current understanding of

University of Cape Town

this subject as discussed in section 6.4.1. The proposed melting of pyroxenitic material in mantle source-regions beneath Discovery-influenced ridge segments of the SMAR, however, requires further comment.

The pyroxenitic veins or layers in the spinel-lherzolite mantle would have anomalous compositions, relative to ambient spinel-lherzolite, inherited from the small-degree melts from which they formed, as discussed previously. A particular anomalous characteristic, relative to the ambient depleted spinel-lherzolite, of the compositions of these veins is the high volatile and alkali content (Niu *et al.*, 1999; Sobolev & Chaussidon, 1996; Sun & McDonough, 1989). This has a significant influence on the melting of the pyroxenitic veins. The solidus of pyroxenite is 50-100°C lower than the solidus for spinel-lherzolite (Hirschmann & Stolper, 1996), and this difference is enhanced by the presence of significant amounts of volatiles and alkalis (Hirschmann *et al.*, 1999a). Therefore, in the upwelling mantle beneath mid-ocean ridge segments, if pyroxenitic veins are present these would commence melting significantly earlier and deeper (~5-8kbar) than the surrounding spinel-lherzolite. Considering that the temperature interval between the solidus and liquidus of pyroxenite at 20-30kbar is 150-200°C, compared to 400-500°C for spinel-lherzolite, and all other upwelling parameters are constant, e.g. similar adiabatic paths and solidus and liquidus slopes (Hirschmann & Stolper, 1996), then the pyroxenitic material would melt at rates 20-50% higher than the surrounding spinel-lherzolite (Hirschmann & Stolper, 1996; and references therein).

The rate of melting of the pyroxenitic veins would be enhanced during the pressure interval after the pyroxenite solidus was intercepted and before the spinel-lherzolite solidus is reached. This is due to the increasing temperature of the adiabatic upwelling of the enclosing solid spinel-lherzolite. In the pressure interval between the solidi of the pyroxenite and spinel-lherzolite, the partial melting of pyroxenite would cause it to cool relative to the still solid spinel-lherzolite. Heat would therefore flow into the pyroxenite from the surrounding spinel-lherzolite. The result would be increased melting per unit upwelling for the pyroxenitic veins and the inhibition of melting in the spinel-lherzolite, because it would now be heating-up at a slower rate. The rate of this "super-adiabatic" melting of pyroxenitic veins could exceed 4-6%/kbar (Hirschmann & Stolper, 1996; and references therein; Sleep, 1984).

A further factor affecting the melting, especially relevant to the locations of the dredges

University of Cape Town

which recovered the anomalous basalts from Discovery-influenced ridge segments, is the flow of mantle material across fracture zones (Douglass *et al.*, 1999; Sleep, 1996). The steep sublithospheric slopes across the Falkland-Agulhas Fracture Zone, as modelled by Douglass *et al.*, (1999) in their fig. 7, would most-likely induce flow of the mantle plume-influenced material southwards, the Discovery mantle plume being located north of this fracture zone, across the fracture zone. The mantle material would then encounter steep sublithospheric slopes orthogonal to the ridge axis, as the fracture zone is crossed, and flow of the mantle material would be induced towards the mid-ocean ridge. The change in pressure associated with the "cascade" of the less-dense mantle plume-influenced material across the fracture zone, upwards along the steep sublithospheric slope, would result in decompression melting. In the case of the Falkland-Agulhas Fracture Zone, the "excess" extent of melting due to this interaction between mantle flow and the fracture zone, would be an added ~1-5% for rates of melting ranging between 1.5-2%/kbar (Douglass *et al.*, 1999; Sleep, 1996). Dredges 25, 6 & 7 were located on the opposite-side of fracture zones, relative to the location the Discovery mantle plume. These are the only locations on Discovery-influenced ridge segments where the mantle flow from the mantle-plume location had to cross fracture zones at high angles and the mantle source-regions of basalts could have experienced the phenomena of sudden and fast upwelling superimposed on, and adding to, the rapid melting of volatile- and alkali-rich pyroxenitic veins enclosed in spinel-lherzolite.

The model proposed in this study for the origin of the anomalous basalts from Discovery-influenced ridge segments not only require extremely rapid rates of melting, discussed and substantiated above, but also low initial pressures of melting (5-7kbar) with melting spanning a narrow pressure interval. Even considering the extremely high rates of melting possible in the pyroxenitic veins, it seems improbable that melting would occur at such low initial pressures. Below approximately 8kbar, spinel is no longer stable in the lherzolitic mantle and is replaced by plagioclase (Yang *et al.*, 1998). The stability-field for plagioclase-lherzolite is equivalent to the thermal boundary layer above the mantle, especially beneath slow-spreading ridges where conductive cooling from the surface is an important process (Niu, 1999; and references therein). It would therefore be extreme unlikely for extensive melting beneath Discovery-influenced ridge segments to occur within the plagioclase-lherzolite stability-field.

The most-likely explanation for the extremely low calculated initial pressures of melting for these basalts lie in the behaviour of the major elements during melting of pyroxenite. As

University of Cape Town

previously stated, the behaviour of the major elements during melting of pyroxenite or pyroxene-rich rocks have received very little attention and remain largely unconstrained (Hirschmann *et al.*, 1995; Yaoling Niu, pers. comm.; Tim Grove, pers. comm.). However, qualitative observations have been made which are relevant to this study. The melts derived from pyroxenite or pyroxene-rich rocks are likely to be richer in Na_2O and FeO^*, total iron, than melts derived from lherzolitic mantle source-regions (Hirschmann *et al.*, 1995). If these high Na_2O melts are in equilibrium with later melting of surrounding spinel-lherzolite, then the resulting final liquids would contain significantly lower CaO/Al_2O_3 ratios and CaO concentrations (Hirschmann *et al.*, 1999b). The compositions of these anomalous basalts do contain anomalously low CaO/Al_2O_3 ratios, CaO concentrations, and high Na_2O and FeO^* concentrations. If this qualitative agreement with the above experimental and theoretical work is not coincidence, then the low CaO/Al_2O_3 ratios and high Na_2O concentrations should have opposite effects on the calculation of the mean extent of melting. This explains the acceptable calculated values for the mean extents of melting for these anomalous basalts. However, the high FeO^* concentrations would result in values of calculated initial pressures of melting for these anomalous basalts lower, by an unquantified amount, than in reality. The calculated values for the initial pressures of melting for these anomalous basalts should therefore be viewed as qualitative indicators of shallower melting relative to the rest of the SMAR, but quantitatively as unrealistic lower extremes. A point to note is that it seems unlikely that the compositional effects of pyroxenite-melting on major-element indicators would more than half the calculated initial pressures of melting. Therefore, even for pyroxenites, the initial pressures of melting beneath the areas of the ridge segments from which these anomalous basalts were recovered, are unlikely to result in the presence of garnet in any direct way during melting.

Although the absolute values calculated for the initial pressures of melting for these anomalous basalts may be unrealistically low, the indications are still that melting occurred at lower initial pressures than in adjacent regions and occurred over a smaller pressure interval. As stated previously, the anomalous Discovery-influenced basalts were recovered from dredges located at the ends of ridge segments terminated by the Falkland-Agulhas Fracture Zone and another significant transform fault. Shorter melting columns, with melting initiating at shallower levels, beneath the ends of ridge segments adjacent to transforms and fracture zones have been proposed by a number of previous studies (Bender *et al.*, 1984; Cannat & Seyler, 1995; Langmuir & Bender, 1984; Magde *et al.*, 1997; Michael & Bonatti, 1985; Niu & Batiza, 1994;

University of Cape Town

Phipps Morgan & Forsyth, 1988; Reynolds & Langmuir, 1997; Schilling *et al.*, 1994; Shaw & Lin, 1996; Shen & Forsyth, 1995; White *et al.*, 1992). The basis of what the above authors termed the transform fault effect (TFE) is the disruption of the thermal regime beneath ridge segments by cooling and/or spatial off-set associated with transform faults of fracture zones. Mantle upwelling beneath and up to 15-30km from transform faults and fracture zones have been proposed and modelled (Magde *et al.*, 1997) to be muted and significantly less active than at the centre of ridge segments. The cooler thermal regime in these mantle regions would result in the pyroxenite and spinel-lherzolite solidi being intercepted by the upwelling mantle at slightly lower pressures, but more importantly, the final depths of melting adjacent to transform faults and fracture zones are expected to be significantly deeper relative to ridge segment centres (Magde *et al.*, 1997), see fig. 6.18. Therefore, the shorter melting columns, lower extents of melting and lower initial pressures of melting proposed in the model for the origin of the anomalous basalts from Discovery-influenced ridge segments conform to the accepted notions of mantle upwelling and melting beneath ridge-segment ends adjacent to significant transform faults and fracture zones.

The only remaining part of the preferred model for the origin of the anomalous basalts from Discovery-influenced ridge segments which still require evaluation, is the extraction of the melts from the mantle source-region and their eruption at the ends of the ridge segments without being focussed towards the ridge segment centres, homogenised or significantly diluted by more extensive melting of spinel-lherzolite. Decoupling of melt migration from the direction of solid-mantle flow can effectively focus melts towards the centres of ridge segments. In this scenario, the melt migration is highly three-dimensional, while the solid-mantle flow is more two-dimensional (Magde *et al.*, 1996; Magde *et al.*, 1997). The melts are assumed to migrate vertically to the top of the melting region, independent of the direction of solid-mantle flow, and then along the local slope of this surface. The shape of this surface, controlled significantly by enhanced conductive cooling at transform faults and fracture zones, is concave with a thermal high beneath the centre of the ridge segment. As melts migrate along the top of the melting region, they are therefore focussed towards the centre of the ridge segment and away ~~from any~~ transform faults or fracture zones (Magde *et al.*, 1996; Magde *et al.*, 1997).

The mode of melt migration in the mantle has received considerable attention (Aharonov *et al.*, 1995; Hirth & Kohlstedt, 1995; Kelemen *et al.*, 1997a; Kelemen *et al.*, 1994; Kelemen *et*

University of Cape Town

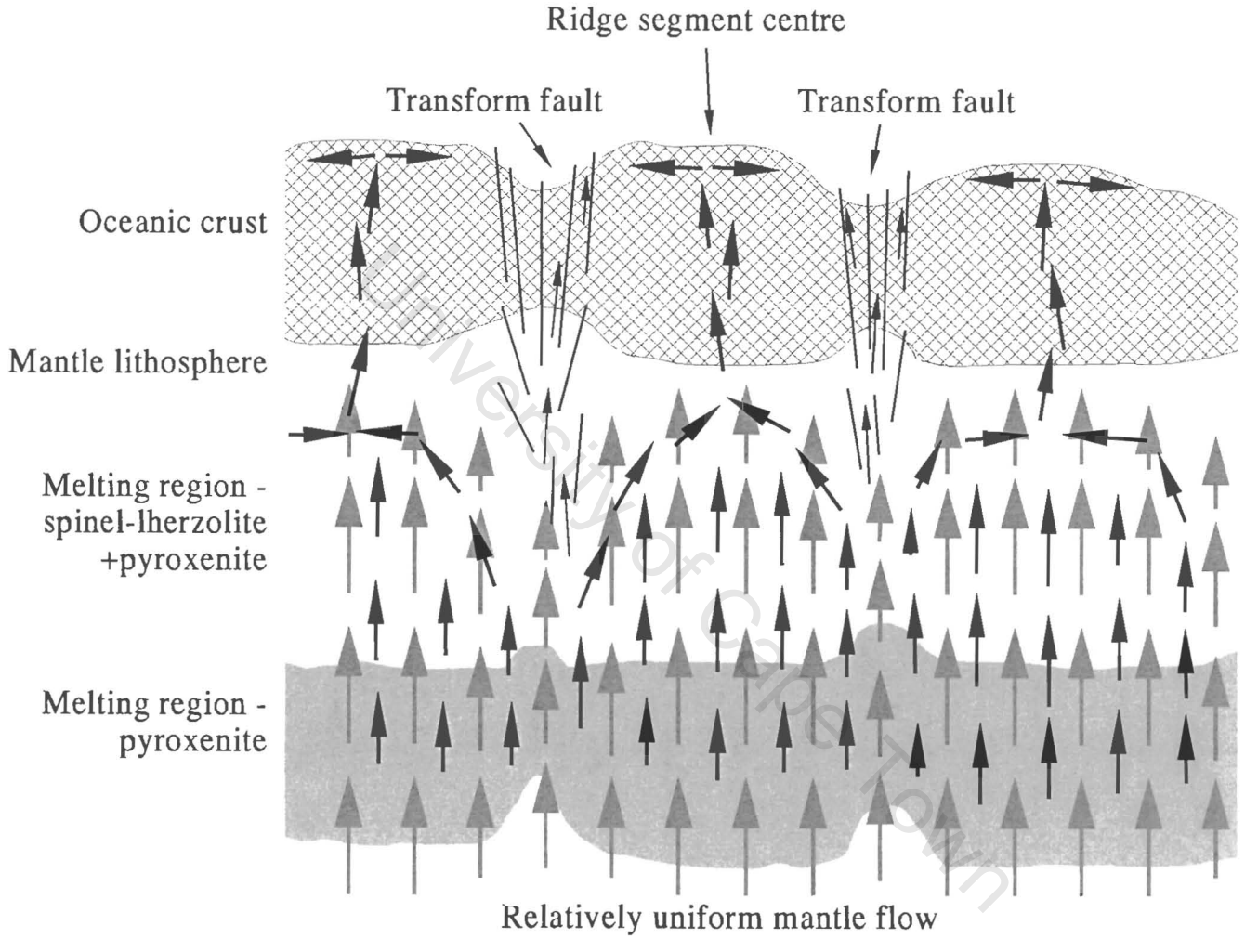

University of Cape Town

Figure 6.18: Schematic along-ridge section showing mantle-flow direction (grey arrows), melt-flow direction (black arrows), zone of pyroxenite-melting (dark grey filled area), zone of spinel-lherzolite plus pyroxenite-melting (light grey filled area), brittle fractures extending to greater depths at transform faults (black lines), small volumes of melt bypassing main melt-flow regime by migration along these fractures (thin black arrows). Schematic representation after Magde *et al.* (1997) and Reynolds & Langmuir (1997).

al., 1995a; Kelemen *et al.*, 1995b; and references therein; Kelemen & Aharonov, 1998; Kelemen *et al.*, 1997b; and references therein; Korenaga & Kelemen, 1997; Korenaga & Kelemen, 1998; Magde *et al.*, 1996; Magde *et al.*, 1997; Reiners, 1998; Seyler & Bonatti, 1997; Suhr, 1999). Two end-member modes of melt migration have been proposed, the one being diffuse, reactive porous flow in which small volumes (1-2%) of melts migrate along grain boundaries and stay in equilibrium with the solid mantle (Reiners, 1998; Seyler & Bonatti, 1997; Suhr, 1999). However, the observed disequilibrium between abyssal peridotites and MORB limits the importance of this process (Dick, 1989; Johnson & Dick, 1992; Johnson *et al.*, 1990; Kelemen & Aharonov, 1998; Kelemen *et al.*, 1997a; Kelemen *et al.*, 1995a). The second and more prominent mode of melt migration seems to be chemically isolated flow of melt, focussed in spatially significant, but restricted, conduits such as the dunites observed in ophiolite sections (Asimow & Stolper, 1999; Kelemen & Aharonov, 1998; Kelemen *et al.*, 1997a; Kelemen *et al.*, 1997b; Kelemen *et al.*, 1995a; Korenaga & Kelemen, 1997; Korenaga & Kelemen, 1998). These seemingly opposing views can be reconciled in a model where melt migration occurs predominantly in highly permeable and chemically isolated conduits, such as replacive dunites, while a smaller, but significant, fraction of the melt migrates by diffuse porous flow in the volumes of mantle between the major conduits (Aharonov *et al.*, 1995; Kelemen *et al.*, 1997a).

Although this dual-mode model of melt migration is probably dominant beneath ridge segments, the disrupted thermal regime in the vicinity of transform faults and fracture zones can also affect the mode of melt migration. The cooler mantle in these regions would allow the zone of brittle deformation to extend to greater depth and encourage the formation, in terms of size and frequency, of faults and cracks which could serve as conduits for melt migration, see fig. 6.18 (Kelemen *et al.*, 1997b; Shaw & Lin, 1996; Spiegelman & Kenyon, 1992; Turcotte & Phipps Morgan, 1992). Therefore, the structural weakening of the mantle and lower crust in the vicinity of transform faults and fracture zones, combined with the cooler thermal regime in these regions could result in the disruption of melt focussing towards the ridge segment centres. The high rates of melting in the narrow pressure interval would also supply enough melt per unit time to keep fractures open to serve as pathways for rapid melt ascend, bypassing standard sub-ridge magma-plumbing system, as required in the preferred model for the origin of the anomalous basalts from Discovery-influenced ridge segments.

Although significant sections of the preferred model for the origin of the anomalous

University of Cape Town

basalts from Discovery-influenced ridge segments are unconstrained, the general agreement with relevant studies of melting, mantle flow and melt migration is encouraging. The model proposed to account for the anomalous compositions of some basalts from Discovery-influenced ridge segments is conceptually in agreement with related studies and can reconcile the fractionation-corrected major-element, incompatible trace-element and radiogenic-isotope characteristics.

University of Cape Town

CHAPTER 7: CRYSTALLISATION PROCESSES BENEATH THE SOUTHERN MID-ATLANTIC RIDGE (40°-55°S)

The most-common and distinct process affecting the major-element compositions of magmas beneath mid-ocean ridges after segregation from the melting region, is crystallisation (Grove *et al.*, 1992). The slow-spreading rate and therefore low or episodic magma flux (Niu & Hékinian, 1997) beneath the SMAR probably result in rapid melt migration after segregation from the melting region and minimal magma residence-time at shallow-crustal levels prior to eruption, which negate the importance of chemical interaction between melts and the ambient mantle as proposed by some studies (Kelemen *et al.*, 1997; Kelemen *et al.*, 1995; Niu, 1997; Niu & Batiza, 1994; Reiners, 1998; Shimizu, 1994; Sobolev & Shimizu, 1993; Sobolev & Shimizu, 1994; Suhr, 1999). Reactive interaction between melts and ambient mantle is a difficult process to define using only MORB compositional data and is probably more significant beneath faster-spreading ridges (Michael & Cornell, 1998). Therefore, the following chapter will be restricted to the characterisation of crystallisation beneath the SMAR.

7.1 OBSERVED COMPOSITIONAL VARIATIONS IN MORB FROM THE SMAR DUE TO CRYSTALLISATION

Trends in major-element data for quenched igneous glasses and bulk-rock samples.

As discussed previous in chapter 4 and 6, the major-element data for the quenched igneous glasses and bulk-rock samples show broad trends on MgO-variation diagrams generally consistent with the crystallisation of various proportions of olivine, plagioclase and calcic pyroxene, see fig. 7.1. The TiO_2, FeO^*, Na_2O, K_2O and P_2O_3 concentrations increase with decreasing MgO content, whereas CaO and Al_2O_3 concentrations both decrease with decreasing MgO (Niu & Batiza, 1994; Reynolds & Langmuir, 1997; Stakes *et al.*, 1984). Olivine and plagioclase are ubiquitous during phenocryst crystallisation of magmas beneath mid-ocean ridges (Grove *et al.*, 1992; Langmuir *et al.*, 1992; Niu & Batiza, 1994; Reynolds & Langmuir, 1997; Stakes *et al.*, 1984) and both minerals are present as phenocrysts or microphenocrysts in almost all these MORB from the SMAR, see fig. 7.2. The differences in major-element compositions of related quenched igneous glass and bulk-rock samples were successfully modelled by accumulation of variable proportions of olivine and/or plagioclase phenocrysts in chapter 4.

University of Cape Town

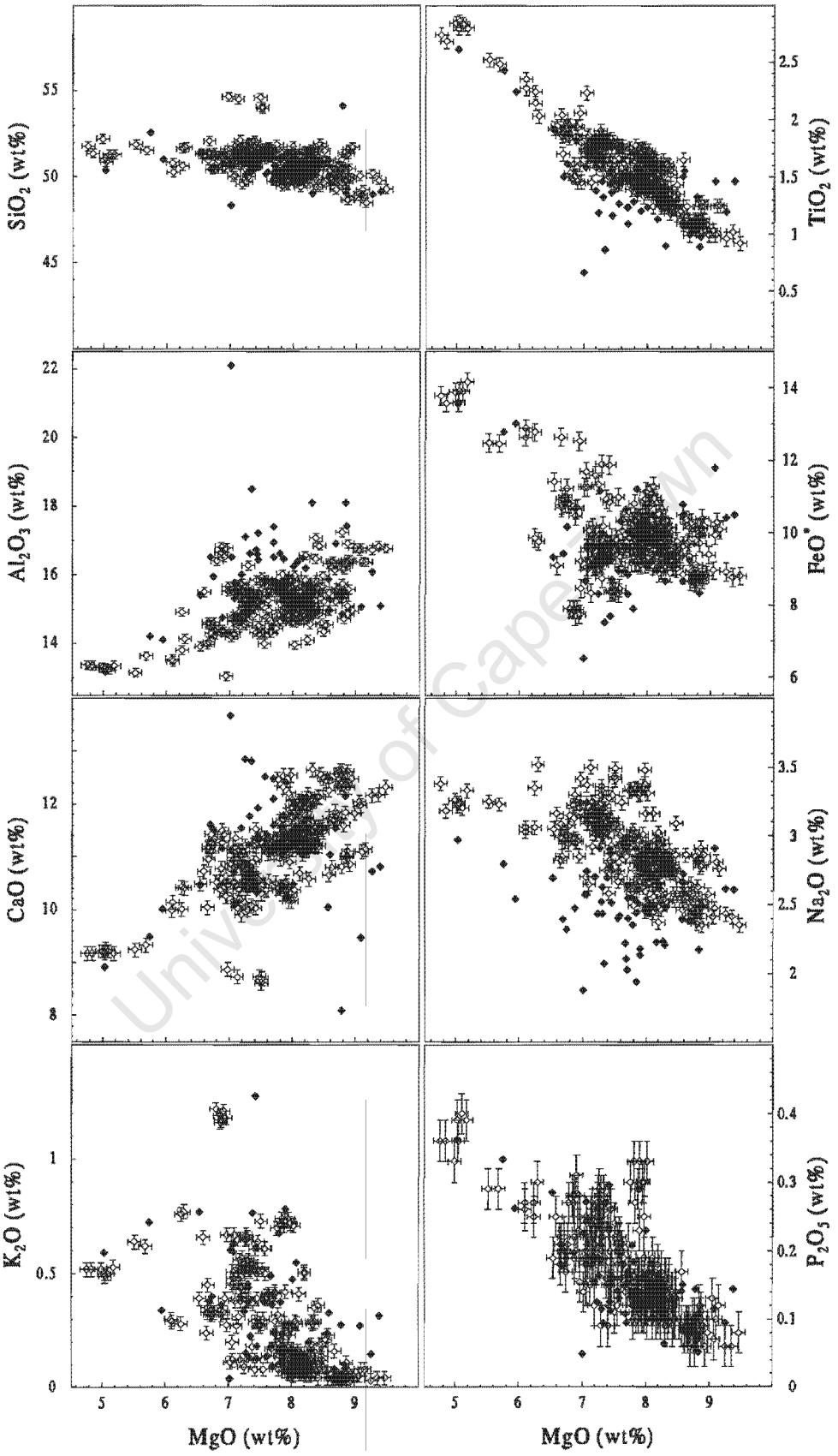

Figure 7.1: MgO-variation diagrams of all the quenched igneous glasses (open markers, with 2σ error bars) and bulk-rock samples (filled markers) of MORB from the SMAR.

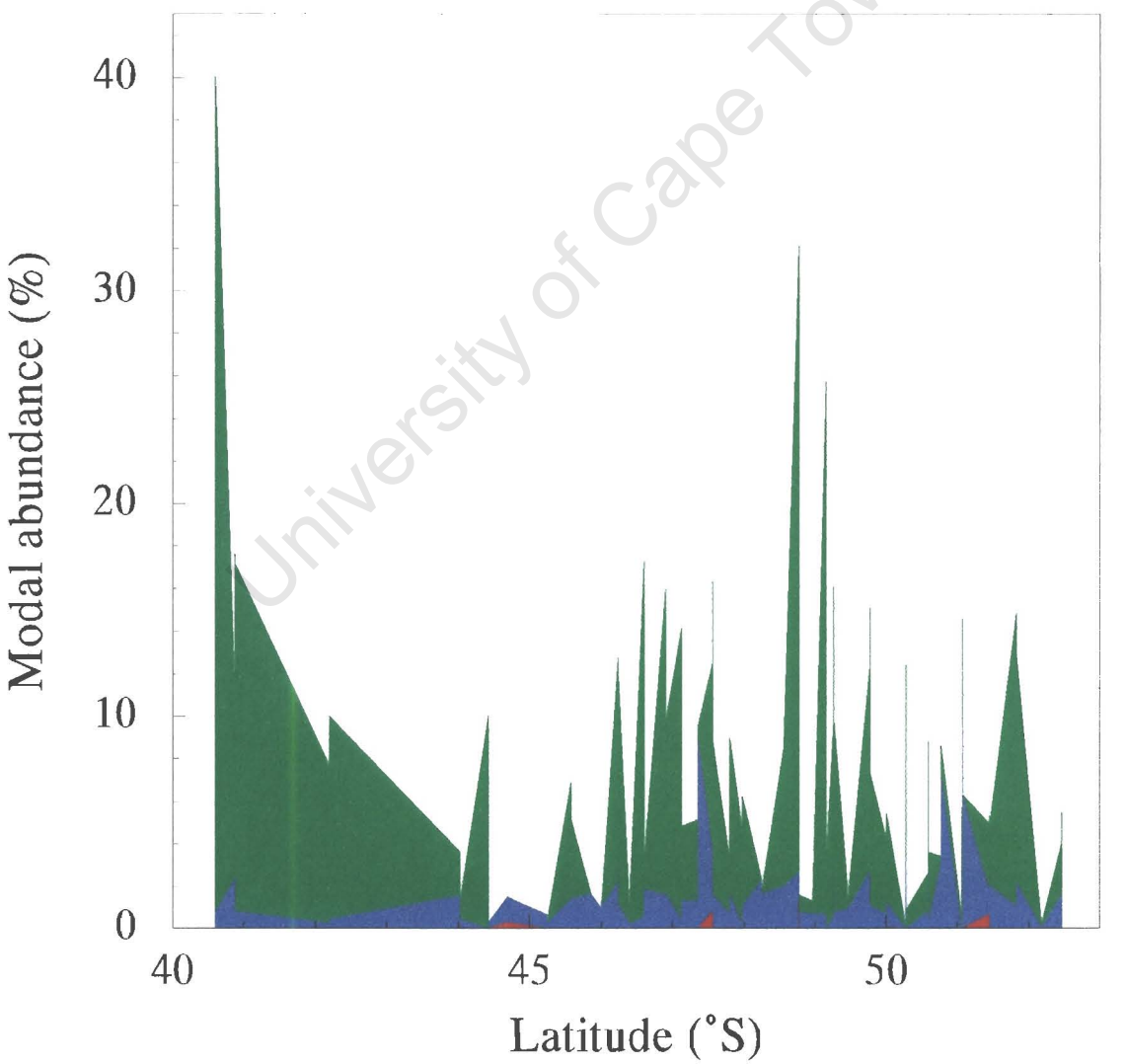

University of Cape Town

Figure 7.2: Modal abundances of plagioclase (green), olivine (blue), and clinopyroxene (red) as phenocryst or microphenocryst phases in modal mineralogical data for MORB from the SMAR versus latitude (°S) along the ridge.

The role of clinopyroxene during crystallisation beneath mid-ocean ridges is more ambiguous. The compositional characteristics of basalts recovered from mid-ocean ridge segments frequently require the presence of clinopyroxene during crystallisation, but it is not observed as a phenocrysts phase in many of these basalts (Michael & Cornell, 1998; Michael *et al.*, 1994). As is evident from fig. 7.2, clinopyroxene is also rarely present as phenocryst or microphenocryst phase in these basalts from the SMAR.

However, some of the major-element oxide variations in fig. 7.1 are consistent with, and in fact require, the presence of clinopyroxene during crystallisation. The decreasing Al_2O_3 and CaO, and increasing FeO^* and TiO_2 with decreasing MgO suggest the influence of crystallisation involving olivine, plagioclase and clinopyroxene. The co-variation of CaO with MgO is of particular importance in deducing the presence of clinopyroxene during crystallisation (Reynolds & Langmuir, 1997), due to the high CaO content of clinopyroxene relative to olivine and plagioclase (Niu & Batiza, 1994). The onset of clinopyroxene as a liquidus phase changes the slope of liquid-lines-of-descent on CaO versus MgO plots from slightly negative for olivine-plagioclase crystallisation, to positive for olivine-plagioclase-clinopyroxene crystallisation. The point at which this change of slope occurs shifts to higher MgO values as the pressure of crystallisation increases, while it is relatively insensitive to variations in the composition of the parental magma (Reynolds & Langmuir, 1997). The variations of CaO content against MgO content in quenched igneous glasses of the MORB from the SMAR are plotted in fig. 7.3, with compositional data from a number of representative dredges from mantle plume-affected and unaffected ridge segments highlighted. The negative slopes in fig. 7.3 for basalts from individual dredges, representative of all settings in this region of the SMAR, indicate the presence of clinopyroxene as a liquidus phase during crystallisation beneath these ridge segments. Negative slopes for CaO content versus MgO-content are also observed amongst basalts with high MgO content (8.2-9.3wt%), indicating the early saturation of these magmas with clinopyroxene during crystallisation, probably at high pressures.

Variations in trace-element data for quenched igneous glasses. The negative Sr and Eu anomalies in the primitive mantle-normalised incompatible trace-element plots of the compositions of some of these MORB from the SMAR were ascribed to plagioclase crystallisation in chapter 5. The constant Sr concentrations in basalts from some individual dredges, with concurrent co-variations in the $Na_{8.0}$ and $Fe_{8.0}$ values, defining local trends, for

University of Cape Town

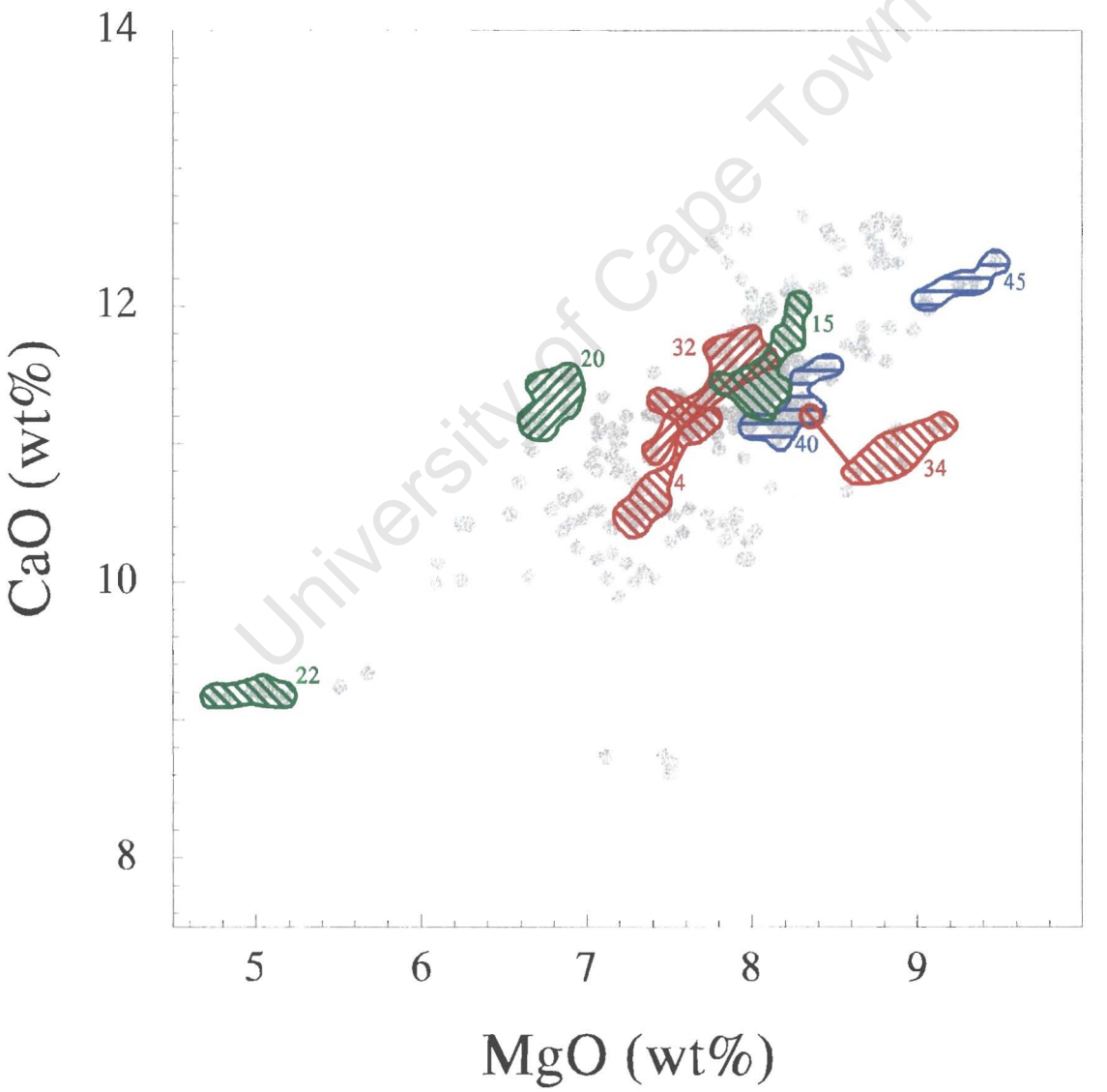

University of Cape Town

Figure 7.3: CaO concentrations versus MgO concentrations for all the quenched igneous glasses of MORB from the SMAR (grey markers), with selected subset of data from individual dredges, representative of all settings in this region of the SMAR and indicated by labels, delineated by diagonally lined fields. Blue fields: N-MORB; red fields: Discovery-influenced MORB; green fields: Shona-influenced fields.

these basalts were presented in chapter 6 as evidence of plagioclase crystallisation.

Due to the high partition coefficient of Ni in olivine (~10), see table 6.3, crystallisation of olivine phenocrysts rapidly decreases the concentration of Ni in the remaining magma. The compositional data for MORB from the SMAR presented in fig. 7.4 show initial, rapid decrease in Ni concentration with decreasing MgO content, followed by more gradual decrease in Ni with decreasing MgO content. This broad trend is with consistent initial olivine-dominated crystallisation, followed by crystallisation during which olivine is present in the liquidus assemblage in lesser proportions.

Sc is more compatible in clinopyroxene relative to olivine and plagioclase during crystallisation, see table 6.3, with values of partition coefficients for Sc in clinopyroxene ranging from 1.31-3.00. Therefore, with crystallisation, the concentration of Sc in the remaining magma will increase with decreasing MgO content, unless clinopyroxene is also present as a liquidus phase with olivine and plagioclase. The Sc content versus MgO content of all the quenched igneous glasses from MORB from the SMAR are plotted in fig. 7.5, with the same groups of samples from individual dredges demarcated by diagonally filled fields as in fig. 7.3. These fields are orientated without clear preference, but all trends where present are either negative or close to horizontal. This reinforces the conclusion reached earlier based on the data in fig. 7.3, that variable proportions of clinopyroxene were present in the liquidus assemblages during crystallisation beneath ridge segments of the SMAR, along with olivine and plagioclase.

Summary. From the preceding discussion, it can be concluded that there is qualitative evidence in the major- and trace-element compositions of MORB from the SMAR of the impact of crystallisation processes and their role in the evolution of the magmas prior to eruption. The compositional variations of MORB from the SMAR further indicate the presence during various stages of crystallisation of olivine, plagioclase and clinopyroxene.

7.2 FORWARD-MODELLING OF CRYSTALLISATION

None of the dredges in this study contain samples which define distinct and extensive liquid-lines-of-descent which can be used to approximate the details of the crystallisation process in the specific region sampled. The approach adopted in this section is to use the results of forward-modelling of crystallisation with various starting compositions and parameters to assess

University of Cape Town

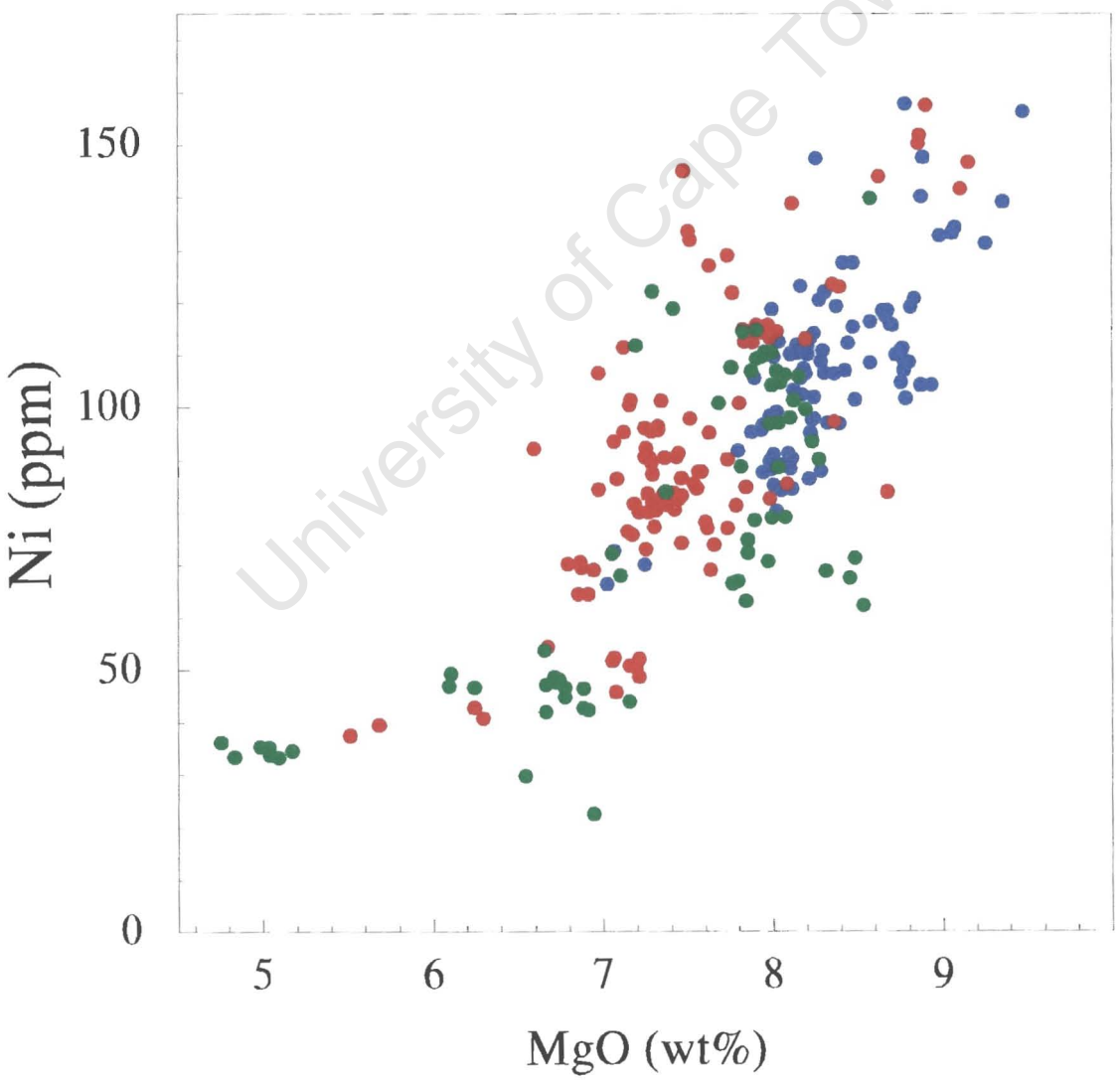

University of Cape Town

Figure 7.4: Ni content (ppm) versus MgO content (wt%) of all quenched igneous glasses of MORB from the SMAR. Blue markers: N-MORB; red markers: MORB from Discovery-influenced ridge segments; green markers: MORB from Shona-influenced ridge segments.

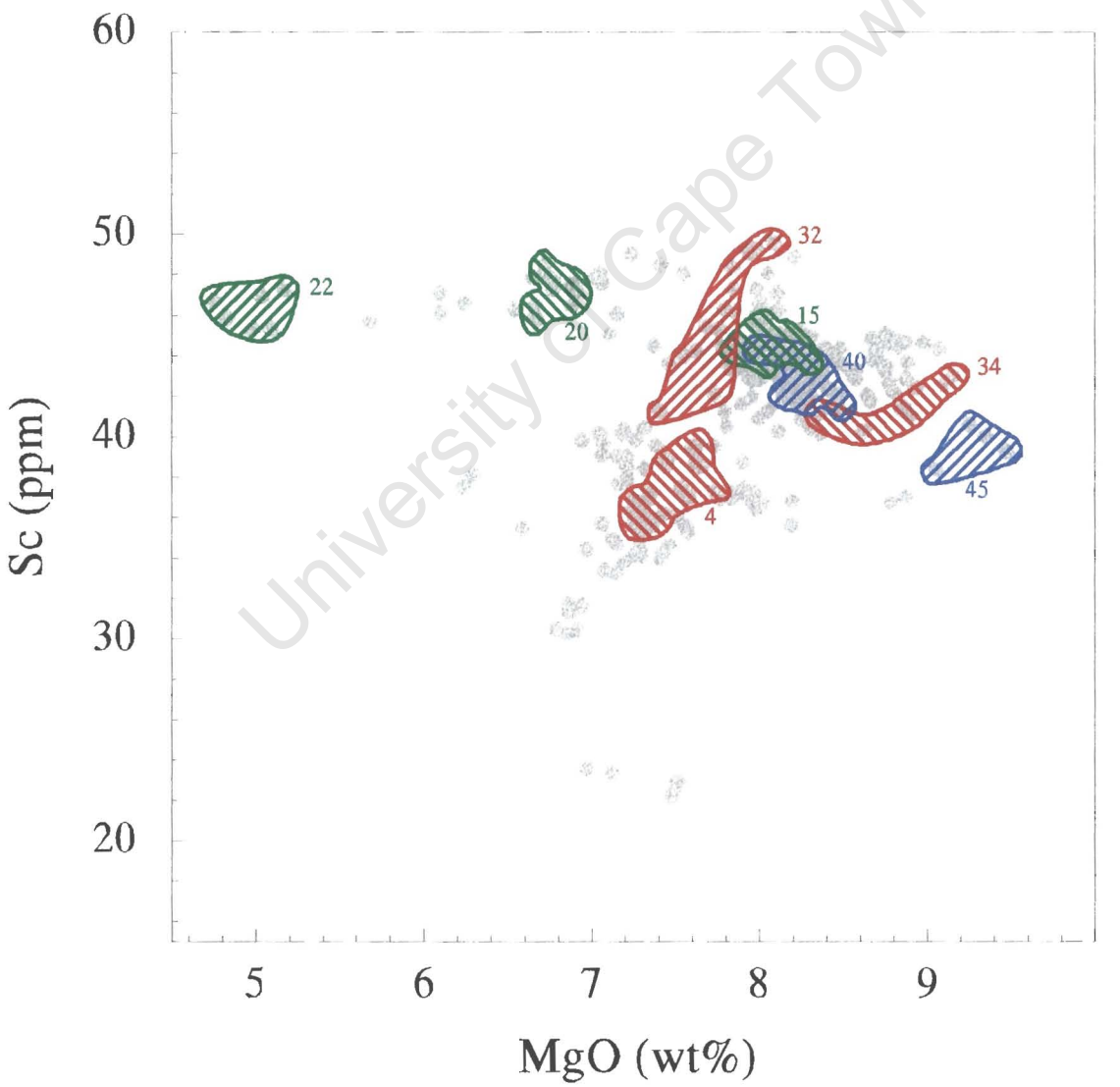

University of Cape Town

Figure 7.5: Sc concentrations (ppm) versus MgO concentrations (wt%) for quenched igneous glasses of the MORB from the SMAR (grey markers), with selected subset of data from individual dredges, indicated by labels, delineated by diagonally lined fields. Blue fields: N-MORB; red fields: Discovery-influenced MORB; green fields: Shona-influenced fields.

different scenarios which might account for the observed broad, general crystallisation-induced compositional variations in these MORB from the SMAR.

Starting compositions and modelling techniques. Primary melts of spinel-lherzolite mantle source-regions are inferred to have Mg#'s ≥70 (Frey *et al.*, 1993). The compositions of magmas used to model the compositional affects of crystallisation must therefore ideally conform to this criteria. In reality, MORB recovered from mid-ocean ridges rarely have such high Mg#'s (Grove *et al.*, 1992) and one approach commonly used is to select one or more basalts from the relevant study area with high Mg#'s (≥67 normally) as best approximations of primary magmas and use these as starting composition for forward-modelling of crystallisation (Frey *et al.*, 1993; le Roex *et al.*, 1996; Reynolds & Langmuir, 1997). A number of high Mg# quenched igneous glasses, as well as two aphyric, high Mg# bulk-rock samples, were selected from the data for MORB from the SMAR for use in modelling the results of different scenarios of crystallisation, see table 7.1.

The modelling of melting beneath the SMAR in the previous chapter yielded a number of theoretical primary melt compositions. The compositions of six modelled pooled melts, see table 7.1, were also used here to qualitatively assess the variations and trends observed in the compositions of MORB from the SMAR in terms of the affects of crystallisation on the compositions of theoretical mantle primary melts. The modelled primary melts were derived from two mantle compositions, using the major-element compositions of Hart & Zindler (1986) depleted 1 and AP fertile 2 (Kinzler, 1997) and the trace-element compositions of the MORB source of McKenzie & O'Nions (1995) (see table 6.3), at 20kbar for the initial pressure of melting, rates of melting varying from 1-3%/kbar as indicated, and 90% of melt formed during each step of fractional melting removed. The trace-element modelling and partition coefficients were discussed in the previous chapter.

The modelling of crystallisation was done using the CoMagmat modelling software of Ariskin *et al.* (1993). A number of widely used models for calculating liquid-lines-of-descent during crystallisation (Ariskin *et al.*, 1993, CoMagmat; Ghiorso & Sack, 1995, MELTS; Langmuir *et al.*, 1992, with modifications by Reynolds, 1995) were critically assessed and compared with results form experimental work by Yang *et al.* (1996). It was found that the resulting liquid-lines-of-descent of all these models, including the model proposed by Yang *et*

University of Cape Town

Table 7.1: Major- and trace-element compositions of high-Mg# quenched igneous glasses and bulk-rock samples, and theoretical primary melts used as starting compositions during the modelling of crystallisation (see text for discussion). Subscript G: quenched igneous glass; subscript B: bulk-rock sample. Theoretical primary melts labelled according to mantle major-element source and rate of melting. Therefore, HZ 1%: melt derived from Hart & Zindler (1986) depleted 1 mantle source at a rate of 1%/kbar; while AP 1%: melt derived from AP fertile 2 (Kinzler, 1997) at 1%/kbar.

	13D-1$_G$	13D-3$_G$	13D-14$_G$	45D-1$_G$	45D-2$_G$	45D-3$_G$	45D-4$_G$	13D-1$_B$	18D-6$_B$	HZ 1%	HZ 2%	HZ 3%	AP 1%	AP 2%	AP 3%
SiO_2	51.02	51.61	50.45	49.30	50.06	50.20	49.81	50.96	49.03	47.96	47.06	46.42	47.94	46.80	46.11
TiO_2	1.13	1.11	1.08	0.92	1.03	0.96	1.02	1.07	0.89	1.09	0.75	0.70	1.00	0.69	0.64
Al_2O_3	15.41	15.10	15.33	16.77	16.71	16.73	16.85	15.88	18.10	16.39	15.79	15.37	16.72	16.04	15.61
Cr_2O_3										0.10	0.12	0.13	0.08	0.09	0.10
FeO*	8.63	8.69	8.61	8.80	8.95	8.91	8.76	8.66	8.32	8.38	8.64	8.91	8.85	9.28	9.60
MgO	8.76	8.87	8.78	9.47	9.05	9.25	9.35	8.56	8.84	12.31	13.95	14.86	11.59	13.45	14.37
CaO	12.58	12.54	12.38	12.32	12.05	12.17	12.18	12.50	12.15	11.10	12.24	12.29	10.47	11.84	11.92
K_2O	0.04	0.03	0.03	0.04	0.05	0.03	0.04	0.07	0.10	0.07	0.03	0.03	0.07	0.03	0.03
Na_2O	2.43	2.48	2.45	2.35	2.41	2.43	2.41	2.39	2.17	2.62	1.41	1.30	3.28	1.77	1.62
Mg#	67.26	67.38	67.36	68.53	67.17	67.75	68.35	66.7	68.2	74.8	76.5	77.1	72.6	74.6	75.1
CaO/Al_2O_3	0.82	0.83	0.81	0.73	0.72	0.73	0.72	0.79	0.67	0.68	0.77	0.80	0.63	0.74	0.76
%matrix								91.5	94.3						
F_{mean}										9.5	18.1	19.7	9.5	18.1	19.7
Sc	43.5	42.9	44.8	39.3	38.5	40.6	40.1	39	32	25.3	26.0	26.2	24.9	25.6	25.8
Ni	111.5	104.3	101.8	156.5	133.4	131.4	139.3	129	200	288.0	292.0	295.0	286.6	290.6	293.6

University of Cape Town

al. (1996), agree quite well with each other and the experimental study, with the exception of MELTS which yielded anomalous results (Yang *et al.*, 1996). The use of the CoMagmat modelling software is therefore adopted, as other models (Langmuir *et al.*, 1992, with modifications by Reynolds, 1995; Yang *et al.*, 1996) would yield similar results.

Results of forward-modelling of crystallisation. The starting compositions discussed above and listed in table 7.1, were used to model the liquid-lines-of-descent for 50% isobaric crystallisation at 1atm, 2kbar, 4kbar, 6kbar and 8kbar. A number of the starting compositions are very similar and their results for modelled crystallisation do not differ significantly, therefore, results presented here will be from a sub-set of starting compositions representative of all those modelled. The representative results for major elements are plotted on MgO-variation diagrams in fig. 7.6a-f, and on CaO/Al_2O_3 versus Mg# diagrams in fig 7.7a-f. The results for Sc and Ni are also plotted versus Mg# in fig. 7.7a-f. The sequential change in the mineralogy of the liquidus assemblages of the modelled crystallisation at the different pressures of the individual starting compositions, including those not plotted in fig. 7.6a-f & 7.7a-f, are listed in table 7.2 & 7.3.

Due to the compositional data plotted on the diagrams in fig 7.6a-f-o & 7.7a-f representing MORB from a wide geographical region and radiogenic isotope and trace-element data discussed in chapter 5 indicating distinctly different mantle source-regions beneath these sections of the SMAR, the main objectives of the forward modelling of crystallisation conducted here are restricted to:

- evaluating the variations in major-element compositions observed in these MORB from the SMAR in terms of crystallisation models of the above discussed starting compositions;
- assessing the role of clinopyroxene as part of the liquidus assemblage during the crystallisation of these basalts; and
- preliminary delimitation of the pressure interval of crystallisation beneath the SMAR.

The quenched igneous glass samples from dredge 13 all initially fractionate plagioclase at pressures between 1atm and 4kbar, and only the results for sample 13D-1 will be discussed. Subsequent crystallisation involves plagioclase, olivine and clinopyroxene in variable proportions. The appearance of clinopyroxene as part of the liquidus assemblage occurs

University of Cape Town

Table 7.2: Modal mineralogy of liquid-lines-of-descent plotted in fig. 7.6 & 7.7 (see text for discussion). The MgO wt% and percentage crystallisation of the magma when a new phase joins the mode of the liquidus assemblage are given in brackets. The phase are listed in relative order of abundance in the liquidus assemblage.

Starting composition	Pressure of crystallisation	Mineralogy of liquidus assemblage
13D-1 glass	1atm	plag (8.74/1) ⇒ plag + oliv (7.68/19) ⇒ plag + cpx + oliv
	2kbar	plag (8.80/1) ⇒ plag + oliv (8.19/12) ⇒ plag + oliv + cpx
	4kbar	plag (8.82/1) ⇒ plag + oliv (8.66/4) ⇒ plag + oliv + cpx (8.55/6) ⇒ cpx + plag (8.35/11) ⇒ plag + cpx + oliv
	6kbar	cpx (8.68/1) ⇒ cpx + plag (8.32/16) ⇒ plag + cpx + oliv
	8kbar	cpx (8.32/6) ⇒ cpx + plag (7.48/32) ⇒ plag + cpx + oliv
13D-3 glass	1atm	plag + oliv (7.69/16) ⇒ plag + oliv + cpx (7.59/18) ⇒ cpx + plag (7.35/24) ⇒ plag + cpx + oliv
	2kbar	plag + oliv (8.18/9) ⇒ plag + cpx + oliv
	4kbar	plag + oliv (8.60/1) ⇒ plag + cpx + oliv
	6kbar	cpx (8.44/5) ⇒ cpx + plag (8.05/18) ⇒ plag + cpx + oliv
	8kbar	cpx (8.05/10) ⇒ cpx + plag (7.11/35) ⇒ plag + cpx + oliv
13D-14 glass	1atm	plag + oliv (7.65/20) ⇒ plag + cpx + oliv
	2kbar	plag (8.83/1) ⇒ plag + oliv (8.10/14) ⇒ plag + oliv + cpx (8.05/15) ⇒ cpx + plag (7.91/19) ⇒ plag + cpx + oliv
	4kbar	plag (8.88/1) ⇒ plag + oliv (8.58/6) ⇒ plag + cpx + oliv
	6kbar	cpx (8.78/1) ⇒ cpx + plag (8.49/13) ⇒ plag + cpx + oliv
	8kbar	cpx (8.42/6) ⇒ cpx + plag (7.75/28) ⇒ plag + cpx + oliv
45D-1 glass	1atm	plag (9.54/2) ⇒ plag + oliv (7.45/35) ⇒ plag + cpx + oliv
	2kbar	plag (9.60/2) ⇒ plag + oliv (7.91/30) ⇒ plag + cpx + oliv
	4kbar	plag (9.62/2) ⇒ plag + oliv (8.34/24) ⇒ cpx + plag (8.26/26) ⇒ plag + cpx + oliv
	6kbar	plag (9.57/3) ⇒ plag + oliv (8.89/15) ⇒ plag + cpx + oliv
	8kbar	plag (9.64/2) ⇒ plag + oliv (9.48/5) ⇒ cpx + plag (9.42/7) ⇒ plag + cpx + oliv
45D-2 glass	1atm	plag (9.16/2) ⇒ plag + oliv (7.19/33) ⇒ cpx + plag + oliv (6.97/37) ⇒ cpx + plag (6.82/40) ⇒ plag + cpx + oliv
	2kbar	plag (9.16/3) ⇒ plag + oliv (7.64/28) ⇒ plag + cpx + oliv
	4kbar	plag (9.20/3) ⇒ plag + oliv (8.13/21) ⇒ plag + cpx + oliv
	6kbar	plag (9.22/3) ⇒ plag + oliv (8.73/12) ⇒ plag + cpx + oliv
	8kbar	plag (9.20/2) ⇒ plag + oliv (9.06/7) ⇒ plag + cpx + oliv

University of Cape Town

Table 7.2 continued

Starting composition	Pressure of crystallisation	Mineralogy of liquidus assemblage
45D-3	1atm	plag (9.23/2) ⇒ plag + oliv (7.30/33) ⇒ plag + cpx + oliv
glass	2kbar	plag (9.32/2) ⇒ plag + oliv (7.74/28) ⇒ plag + oliv + cpx (7.67/29) ⇒ cpx + plag (7.45/34) ⇒ plag + cpx + oliv
	4kbar	plag (9.32/2) ⇒ plag + oliv (8.23/21) ⇒ plag + cpx + oliv
	6kbar	plag (9.30/3) ⇒ plag + oliv (8.82/12) ⇒ plag + cpx + oliv
	8kbar	plag (9.27/1) ⇒ plag + cpx (9.32/3) ⇒ plag + cpx + oliv
45D-4	1atm	plag (9.40/2) ⇒ plag + oliv (7.28/35) ⇒ plag + cpx + oliv
glass	2kbar	plag (9.46/2) ⇒ plag + oliv (7.74/30) ⇒ plag + cpx + oliv
	4kbar	plag (9.46/2) ⇒ plag + oliv (8.26/23) ⇒ plag + oliv + cpx (8.13/25) ⇒ cpx + plag (7.97/29) ⇒ plag + cpx + oliv
	6kbar	plag (9.48/3) ⇒ plag + oliv (8.81/15) ⇒ cpx + plag (8.73/17) ⇒ plag + cpx + oliv
	8kbar	plag (9.44/3) ⇒ plag + oliv (9.39/4) ⇒ cpx + plag (9.32/6) ⇒ plag + cpx + oliv
13D-1	1atm	plag (8.74/3) ⇒ plag + oliv (7.64/21) ⇒ cpx + plag + oliv (7.37/27) ⇒ cpx + plag (7.23/30) ⇒ plag + cpx + oliv
bulk-rock	2kbar	plag (8.78/3) ⇒ plag + oliv (8.07/15) ⇒ plag + cpx + oliv
	4kbar	plag (8.78/3) ⇒ plag + oliv (8.49/8) ⇒ cpx + plag (8.39/11) ⇒ plag + cpx + oliv
	6kbar	plag (8.63/1) ⇒ cpx + plag (8.49/12) ⇒ plag + cpx + oliv
	8kbar	cpx (8.47/2) ⇒ cpx + plag (7.50/32) ⇒ plag + cpx + oliv
18D-6	1atm	plag (9.58/7) ⇒ plag + oliv (7.10/42) ⇒ cpx + plag + oliv
bulk-rock	2kbar	plag (9.52/8) ⇒ plag + oliv (7.49/38) ⇒ cpx + plag (7.12/44) ⇒ plag + cpx + oliv
	4kbar	plag (9.54/8) ⇒ plag + oliv (8.00/32) ⇒ cpx + plag (7.89/34) ⇒ plag + cpx + oliv
	6kbar	plag (9.58/8) ⇒ plag + oliv (8.59/24) ⇒ plag + cpx + oliv
	8kbar	plag (9.58/8) ⇒ plag + oliv (9.23/14) ⇒ cpx + plag (9.42/7) ⇒ plag + cpx + oliv

University of Cape Town

progressively earlier in the process as the pressure of crystallisation is increased. The crystallisation sequences are listed in table 7.2. The liquid-lines-of-descent plotted in fig. 7.6a illustrate this progressive change in the liquidus assemblage with increasing pressure of crystallisation. Due to CaO being a major constituent of clinopyroxene, the trajectories for pressures of 1atm to 4kbar in the plots CaO versus MgO have sharp changes in slope at the onset of clinopyroxene crystallisation. The slopes change from negative to positive as CaO is removed in the crystallised clinopyroxene. The earlier appearance of clinopyroxene crystallisation at higher pressures are evident in the earlier change in slope at higher pressures. At pressures of 6-8kbar, clinopyroxene is the first liquidus phase in these samples and plagioclase joins the assemblage, followed by olivine at a later stage. Again, the sequences of crystallisation are listed in table 7.2. The liquid-lines-of-descent for these higher pressures of crystallisation therefore have positive slopes from the outset in the CaO versus MgO diagrams.

The modelled liquid-lines-of-descent crystallisation of the quenched igneous glasses from dredge 45 all start with plagioclase as the liquidus phase at all pressures modelled. The listed crystallisation sequences in table 7.2 and the representative liquid-lines-of-descent plotted in fig. 7.6b for sample 45D-1 show that the interval of plagioclase crystallisation is short, followed by crystallisation of plagioclase and olivine. Initially, MgO values increase, as plagioclase which is initially the sole liquidus phase does not contain MgO. The interval of plagioclase and olivine crystallisation becomes progressive shorter with increasing pressure and, as for the crystallisation of quenched igneous glasses from dredge 13, clinopyroxene joins the liquidus assemblage earlier as pressure is increased. The influence of clinopyroxene crystallisation is again evident in the change of the slopes of the crystallisation trends in the CaO versus MgO diagrams.

The two high MgO-content, aphyric bulk-rock starting compositions, samples 13D-1 and 18D-6, both initially crystallise plagioclase exclusively at pressures up to 4kbar, followed by an interval of plagioclase and olivine crystallisation. The 18D-6 bulk-rock starting composition crystallises plagioclase exclusively for a significant period and the liquid-lines-of-descent in fig. 7.6d exhibit initial trends to higher MgO and FeO, and lower Al_2O_3. The initial interval of plagioclase crystallisation for the 13D-1 bulk-rock starting composition is short and the crystallisation trends in fig. 7.6c show only slight initial trends to higher MgO and FeO, and lower Al_2O_3. The period of plagioclase and olivine crystallisation of the 18D-6 bulk-rock starting

University of Cape Town

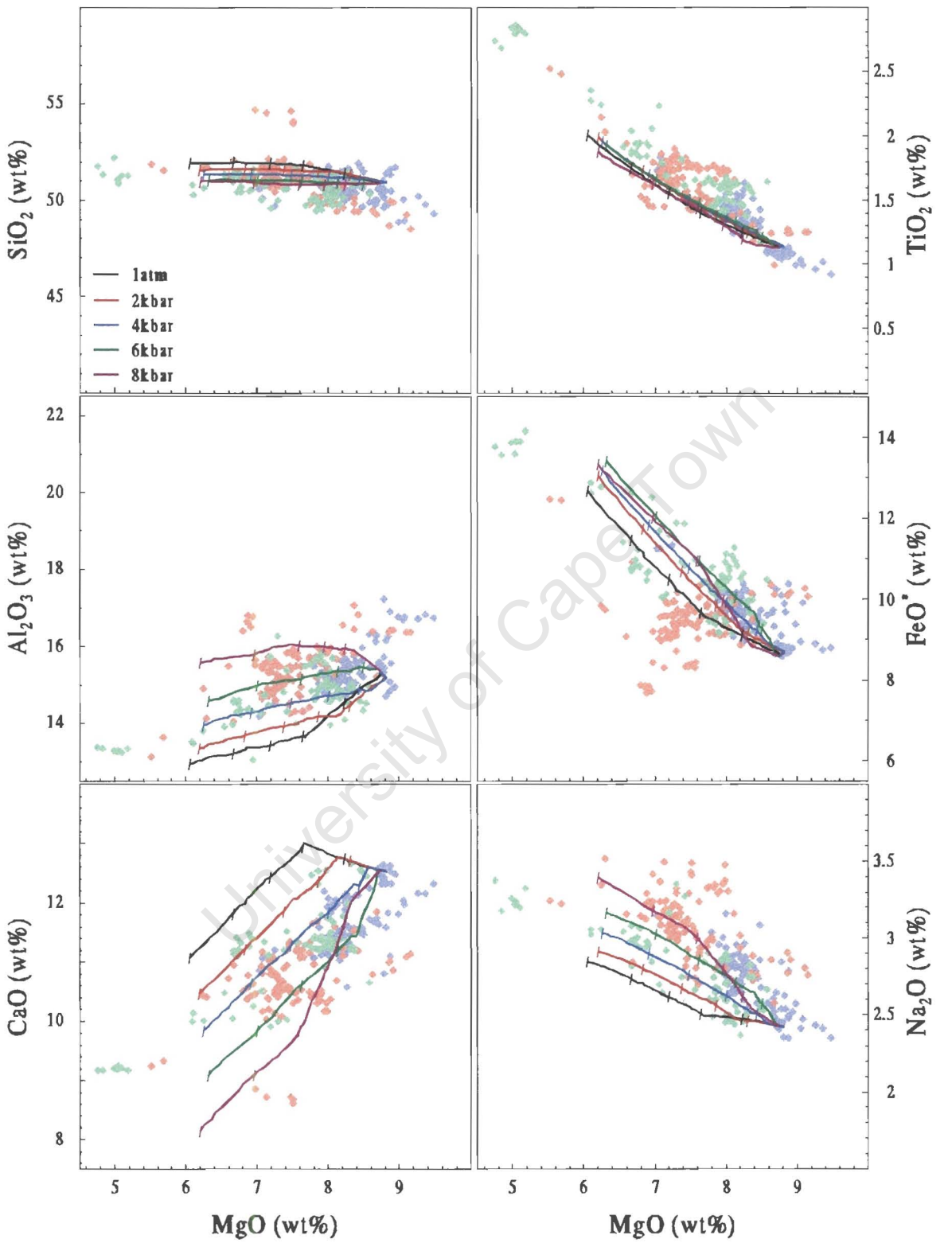

University of Cape Town

Figure 7.6a: MgO-variation diagrams of N-MORB (light blue markers), Discovery-influenced MORB (light red markers) and Shona-influenced MORB (light green markers), with superimposed liquid-lines-of-descent of modelled isobaric crystallisation (see legend), with tick-marks at 10% intervals. Starting composition: quenched igneous glass composition of sample 13D-1, listed in table 7.1. The phase compositions of the liquidus assemblages are listed in table 7.2.

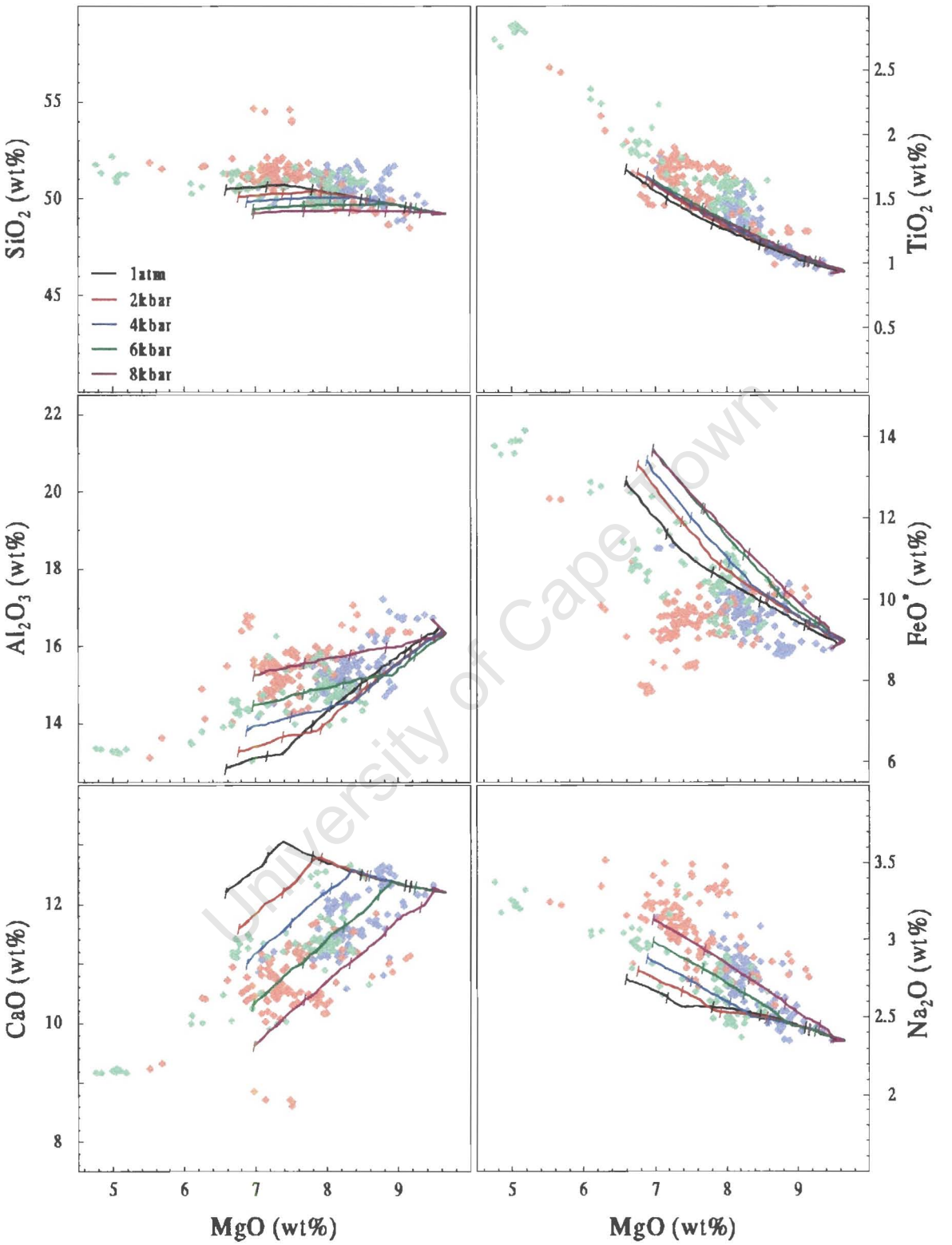

University of Cape Town

Figure 7.6b: MgO-variation diagrams of N-MORB (light blue markers), Discovery-influenced MORB (light red markers) and Shona-influenced MORB (light green markers), with superimposed liquid-lines-of-descent of modelled isobaric crystallisation (see legend), with tick-marks at 10% intervals. Starting composition: quenched igneous glass composition of sample 45D-1, listed in table 7.1. The phase compositions of the liquidus assemblages are listed in table 7.2.

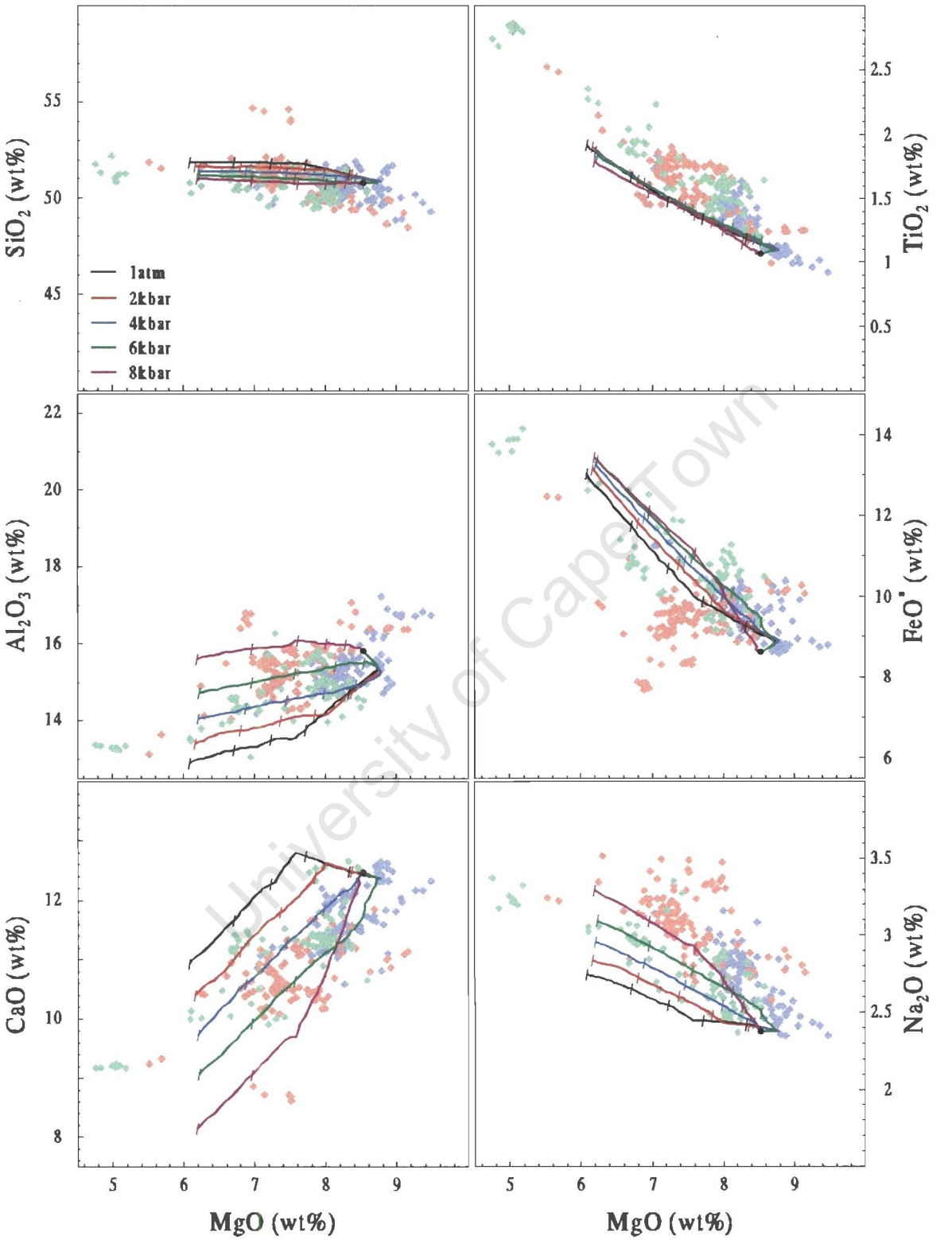

University of Cape Town

Figure 7.6c: MgO-variation diagrams of N-MORB (light blue markers), Discovery-influenced MORB (light red markers) and Shona-influenced MORB (light green markers), with superimposed liquid-lines-of-descent of modelled isobaric crystallisation (see legend), with tick-marks at 10% intervals. Starting composition: aphyric bulk-rock composition of sample 13D-1, listed in table 7.1. The phase compositions of the liquidus assemblages are listed in table 7.2.

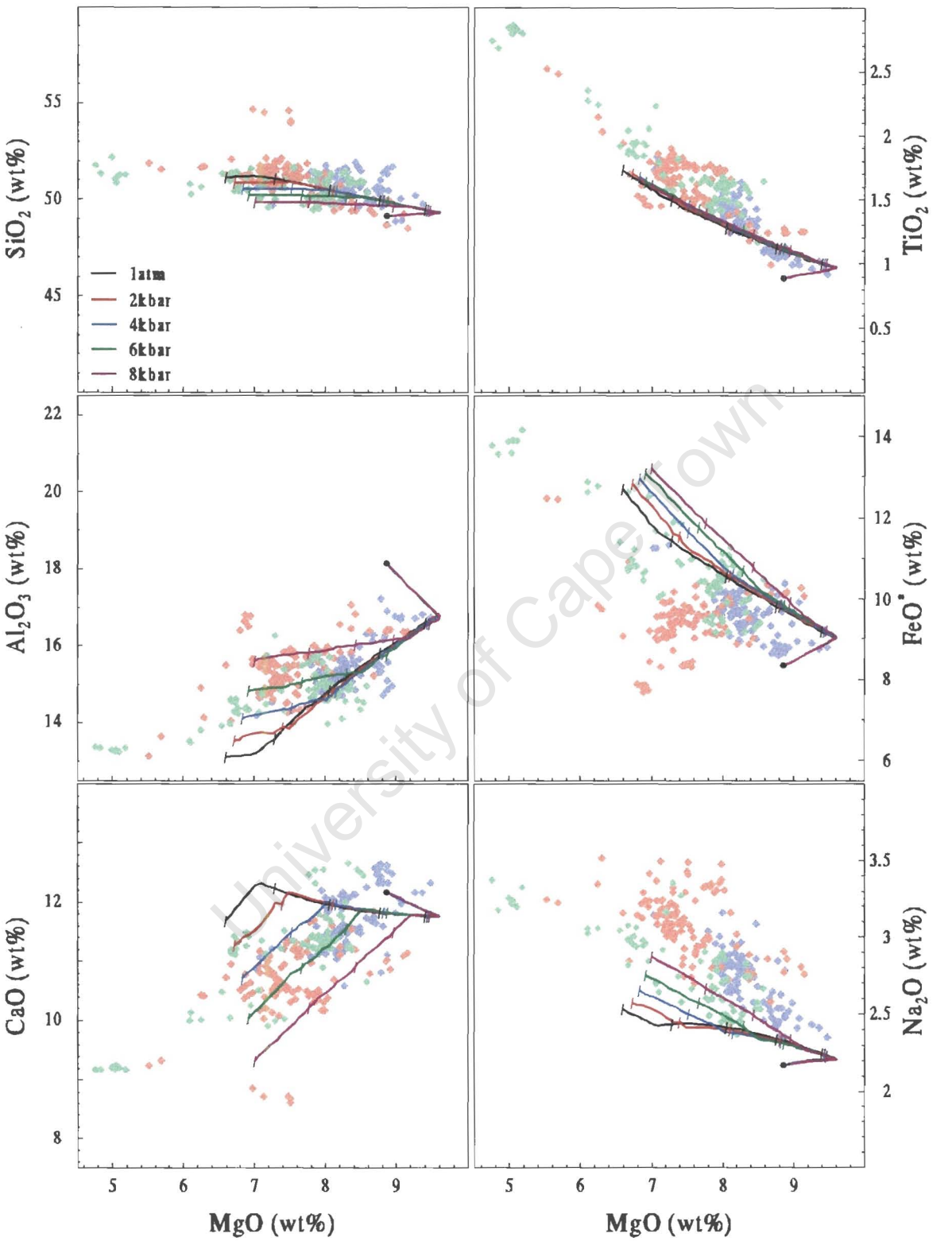

University of Cape Town

Figure 7.6d: MgO-variation diagrams of N-MORB (light blue markers), Discovery-influenced MORB (light red markers) and Shona-influenced MORB (light green markers), with superimposed liquid-lines-of-descent of modelled isobaric crystallisation (see legend), with tick-marks at 10% intervals. Starting composition: aphyric bulk-rock composition of sample 18D-6, listed in table 7.1. The phase compositions of the liquidus assemblages are listed in table 7.2.

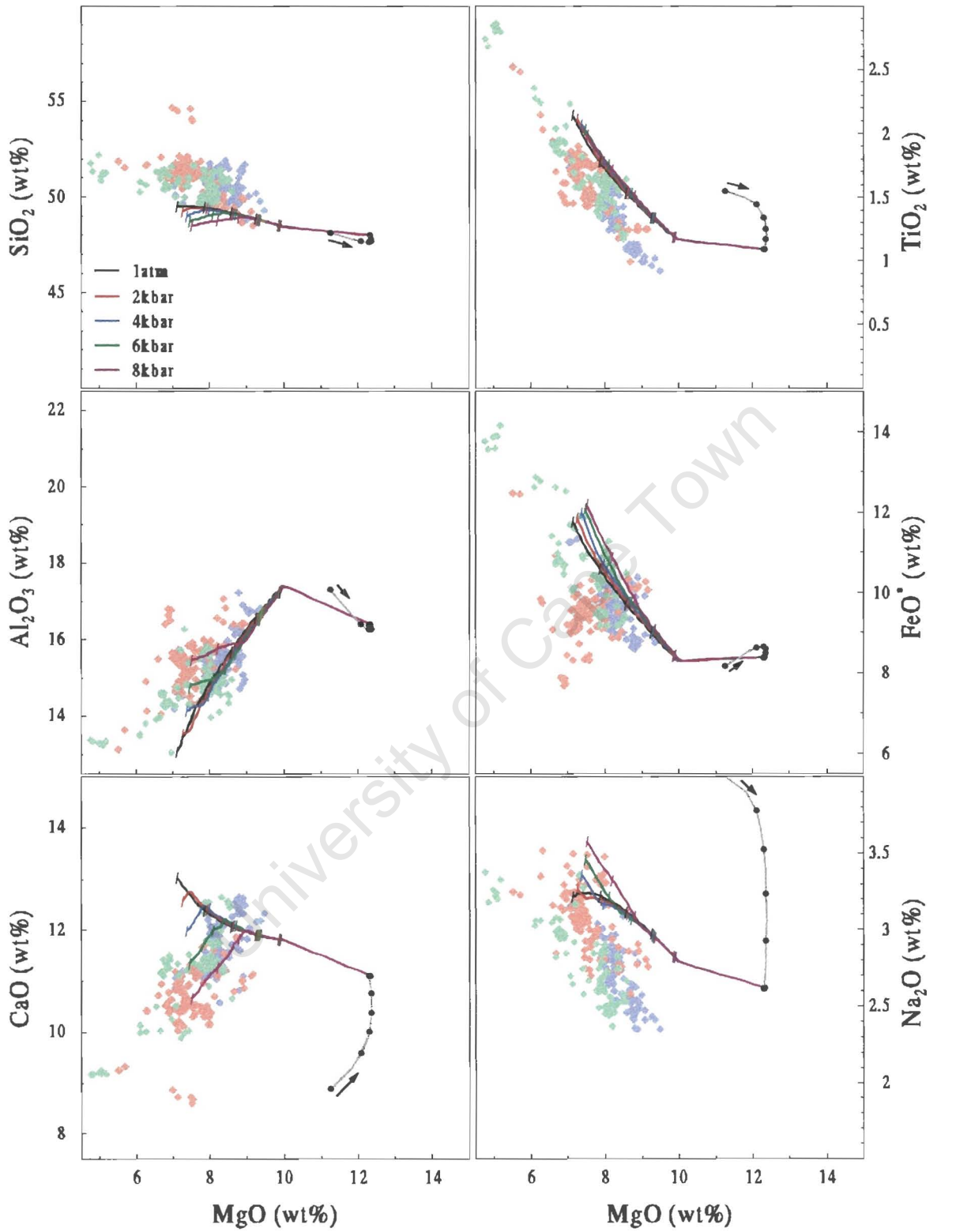

University of Cape Town

Figure 7.6e: MgO-variation diagrams of N-MORB (light blue markers), Discovery-influenced MORB (light red markers) and Shona-influenced MORB (light green markers), with superimposed liquid-lines-of-descent of modelled isobaric crystallisation (see legend), with tick-marks at 10% intervals. Starting composition: theoretical primary melt produced by melting the Hart & Zindler (1986) depleted mantle 1 composition with the melting algorithms of Kinzler (1997) from 20-10kbar, at a melting rate of 1%/kbar, listed in table 7.1. Melting trajectories as grey lines with black circles at 2% intervals and arrows indicating the direction of increasing melting. The phase compositions of the liquidus assemblages are listed in table 7.3.

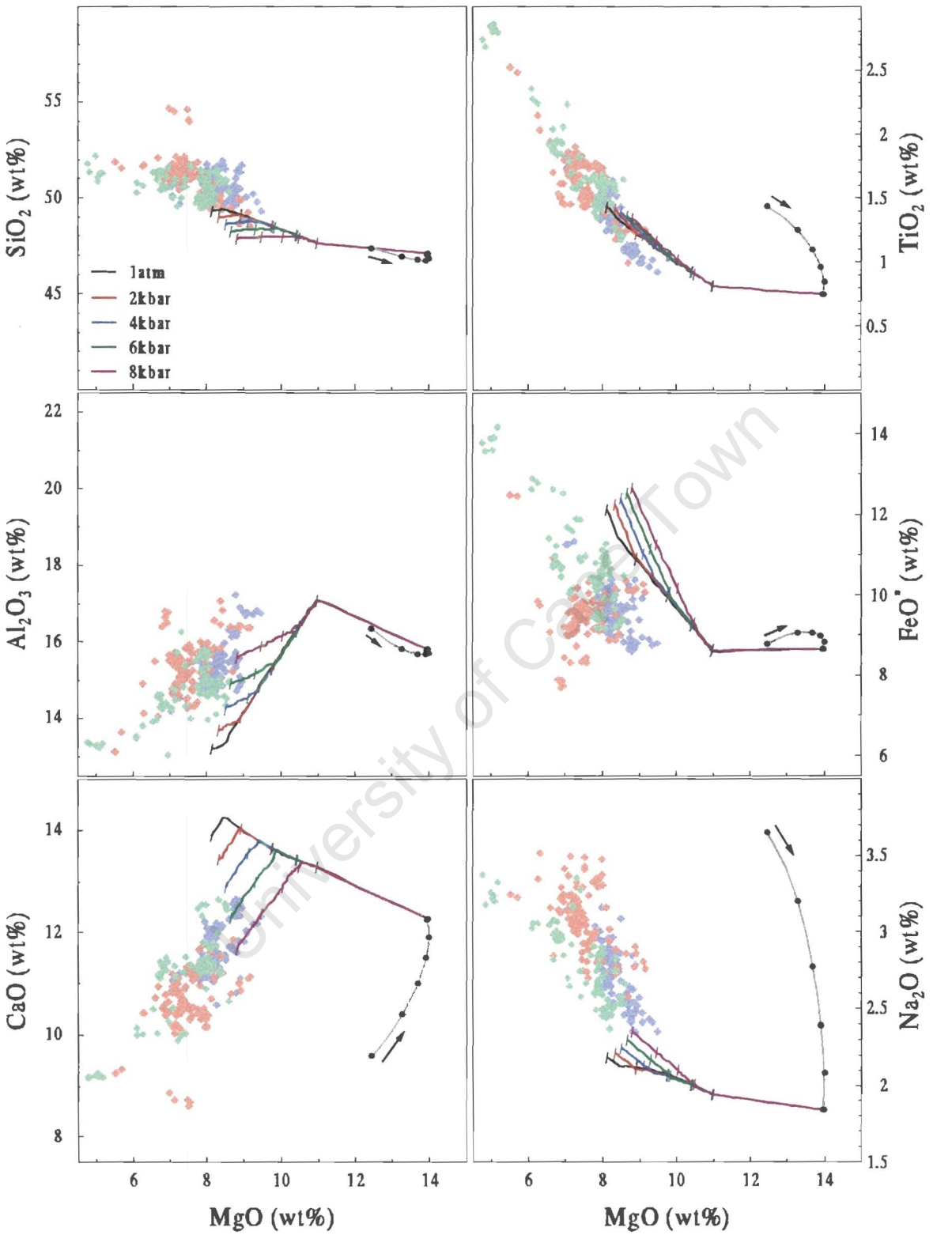

University of Cape Town

Figure 7.6f: MgO-variation diagrams of N-MORB (light blue markers), Discovery-influenced MORB (light red markers) and Shona-influenced MORB (light green markers), with superimposed liquid-lines-of-descent of modelled isobaric crystallisation (see legend), with tick-marks at 10% intervals. Starting composition: theoretical primary melt produced by melting the Hart & Zindler (1986) depleted mantle 1 composition with the melting algorithms of Kinzler (1997) from 20-10kbar, at a melting rate of 2%/kbar, listed in table 7.1. Melting trajectories as grey lines with black circles at 2% intervals and arrows indicating the direction of increasing melting. The phase compositions of the liquidus assemblages are listed in table 7.3.

composition is followed by clinopyroxene joining the liquidus assemblage, at progressively earlier stages as pressure is increased, see table 7.2 and the change in slope of the liquid-lines-of-descent in the CaO versus MgO diagram in fig. 7.6d. Clinopyroxene is more prominent in the crystallisation of the 13D-1 bulk-rock starting composition. The interval of plagioclase and olivine crystallisation at 1atm to 4kbar is significantly shorter compared to the crystallisation of the 18D-6 bulk-rock starting composition, see table 7.2. This interval also decreases rapidly with increasing pressure and is followed by crystallisation involving clinopyroxene. At 6kbar, plagioclase is joined after 1% crystallisation by clinopyroxene, and olivine is the third phase to join the liquidus assemblage after 12% crystallisation. At 8kbar, clinopyroxene is on the liquidus first, followed by concurrent crystallisation of plagioclase for a significant interval before olivine joins the liquidus assemblage.

Comparing the above discussed modelled liquid-lines-of-descent with the compositional data for the quenched igneous glasses of the MORB from the SMAR allows the evaluation of the broad influence of crystallisation on basalt petrogenesis in this region. The trends in the compositional data plotted in fig. 7.6a-f agree with the orientation of the modelled crystallisation trends of plagioclase, olivine and clinopyroxene. The negative trends in the TiO_2, FeO and Na_2O versus MgO diagrams for the quenched igneous glass data for N-MORB and MORB from Shona-influenced ridge segments are coincident with the modelled liquid-lines-of-descent using the selected high MgO quenched igneous glass and bulk-rock starting compositions. The majority of the N-MORB require ≤25% crystallisation to account for the compositional range observed, especially in terms of MgO content. The Shona-influenced MORB contain some samples with MgO concentrations <5wt% and more than the modelled 50% crystallisation is required to accommodate the compositional range of these basalts.

The data for MORB from Discovery-influenced ridge segments define trends off-set to lower FeO and higher Na_2O values relative to N-MORB and Shona-influenced MORB. The proposed high proportions of pyroxene in the modes of the mantle source-regions of these basalts are argued to result in melts with higher FeO and Na_2O concentrations compared to melts from normal lherzolitic source-regions (Hirschmann *et al.*, 1995; Langmuir *et al.*, 1992). High concentrations of Na_2O in melts have also been proposed to result in lower concentrations of CaO and lower values for CaO/Al_2O_3 in these melts (Hirschmann *et al.*, 1999). These abnormal compositional characteristics inherited during melting result in the observed off-sets in major-

University of Cape Town

element data. None of the incompatible trace-element enriched basalts recovered from Discovery-influenced ridge segments have high MgO concentrations, only some of the incompatible trace-element depleted basalts have high MgO concentrations. The same is true for incompatible trace-element basalts recovered from Shona-influenced ridge segments. While only N-MORB compositions were therefore used to model crystallisation, variations in major-element compositions of Discovery-influenced MORB are broadly parallel to the orientation of modelled crystallisation trends.

On the Al_2O_3 and CaO versus MgO diagrams in fig. 7.6a-f, especially for the quenched igneous glass starting composition of sample 45D-1 in fig. 7.6b, the onset of clinopyroxene crystallisation, and therefore the change in slope of the trends, occurs progressively earlier with increasing pressure, from at 35% crystallisation for 1atm to 15% for 6kbar. The liquid-lines-of-descent for preceding stages of plagioclase and olivine crystallisation for these pressures plot coincident. The result of the progressively earlier appearance of clinopyroxene on the liquidus are sets of evenly-spaced, parallel trends for three-phase crystallisation, spanning the various pressures. The compositional data for MORB from the SMAR define a broad positive trend in the CaO versus MgO diagrams, coincident with trends for samples from individual dredges, and no initial negative trends are observed. The observed trends of CaO versus MgO in the basalt compositions are therefore consistent with parallel trends of three-phase crystallisation of olivine, plagioclase and clinopyroxene for a range pressures, the breadth of the observed CaO-MgO trend is due to the range in degree of crystallisation at which clinopyroxene crystallisation is initiated over the range of pressure from 2-8kbar.

University of Cape Town

The role of clinopyroxene during crystallisation is further investigated in fig. 7.7a-d, were the data for the quenched igneous glasses and the modelled crystallisation trends are plotted in terms of CaO/Al_2O_3, Sc and Ni versus Mg#. Crystallisation of olivine will result in the decrease of the Mg# of the remaining liquid, but not significantly affect the CaO/Al_2O_3 ratio. Plagioclase crystallisation will increase the CaO/Al_2O_3 ratio of the remaining liquid, while leaving the Mg# largely unaffected. Clinopyroxene crystallisation will decrease both the CaO/Al_2O_3 ratio and Mg# of the remaining liquid. This is evident in the diagrams in fig. 7.7a-d, were the initial crystallisation of plagioclase result in vertical sections of liquid-lines-of-descent, e.g. in fig. 7.7d, while the crystallisation of plagioclase and olivine result in trends with negative slopes, as shown by the second stage of most crystallisation trajectories below 4kbar. The crystallisation of

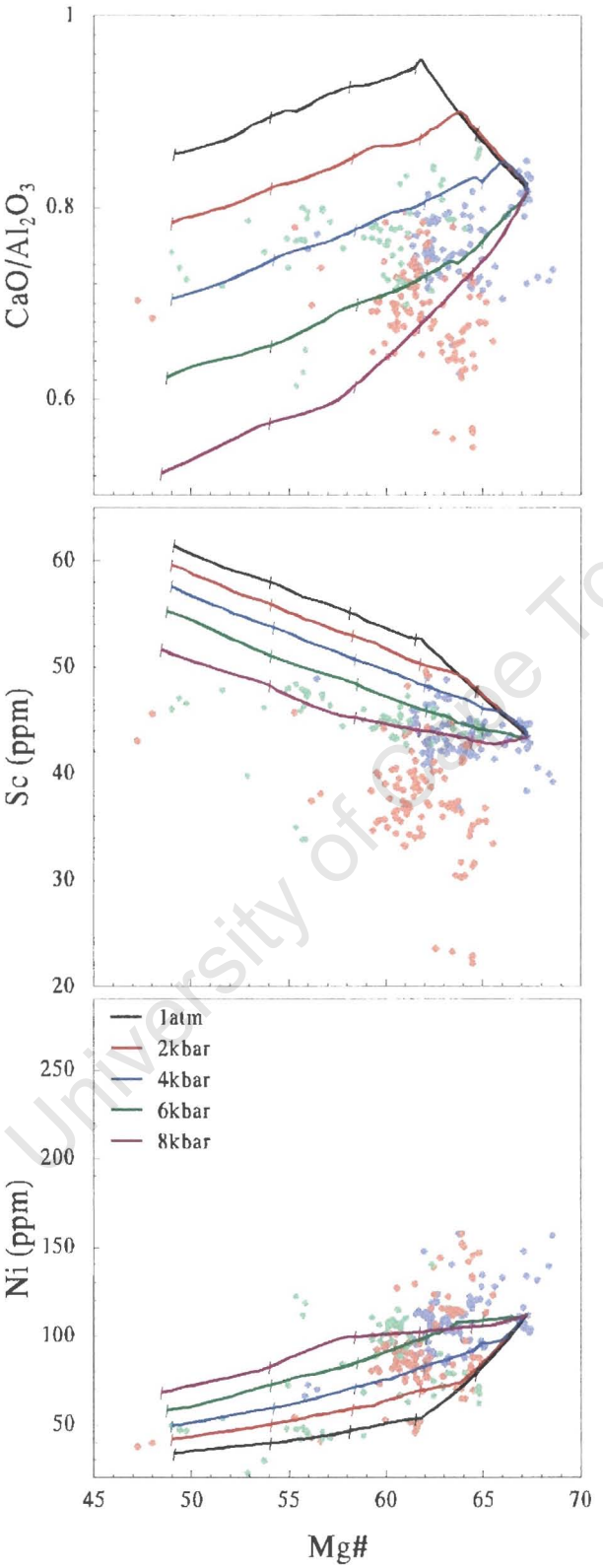

Figure 7.7a: CaO/Al_2O_3, Sc and Ni versus Mg# (atomic $Mg^{2+}/[Mg^{2+}+Fe^{2+}]$) of N-MORB (light blue markers), Discovery-influenced MORB (light red markers) and Shona-influenced MORB (light green markers), with superimposed liquid-lines-of-descent of modelled isobaric crystallisation (see legend), with tick-marks at 10% intervals. Starting composition: quenched igneous glass composition of sample 13D-1, listed in table 7.1. The phase compositions of the liquidus assemblages are listed in table 7.2.

University of Cape Town

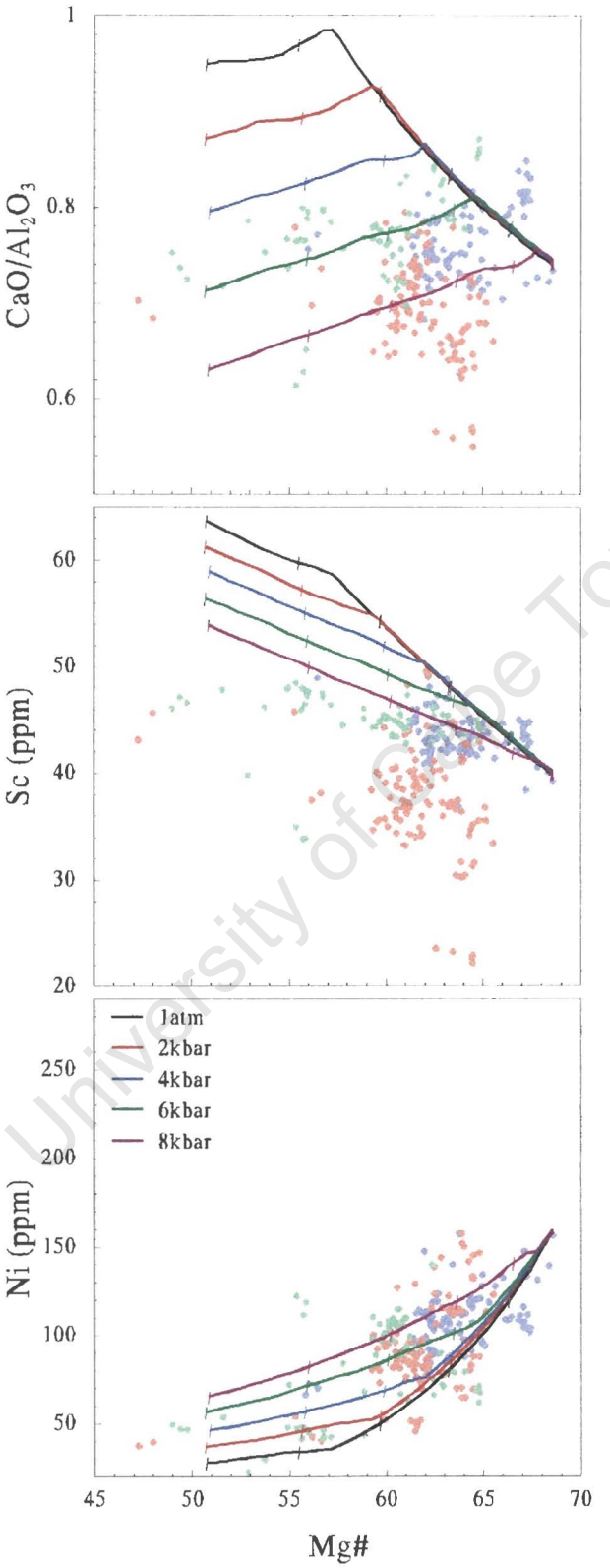

University of Cape Town

Figure 7.7b: CaO/Al_2O_3, Sc and Ni versus Mg# (atomic $Mg^{2+}/[Mg^{2+}+Fe^{2+}]$) of N-MORB (light blue markers), Discovery-influenced MORB (light red markers) and Shona-influenced MORB (light green markers), with superimposed liquid-lines-of-descent of modelled isobaric crystallisation (see legend), with tick-marks at 10% intervals. Starting composition: quenched igneous glass composition of sample 45D-1, listed in table 7.1. The phase compositions of the liquidus assemblages are listed in table 7.2.

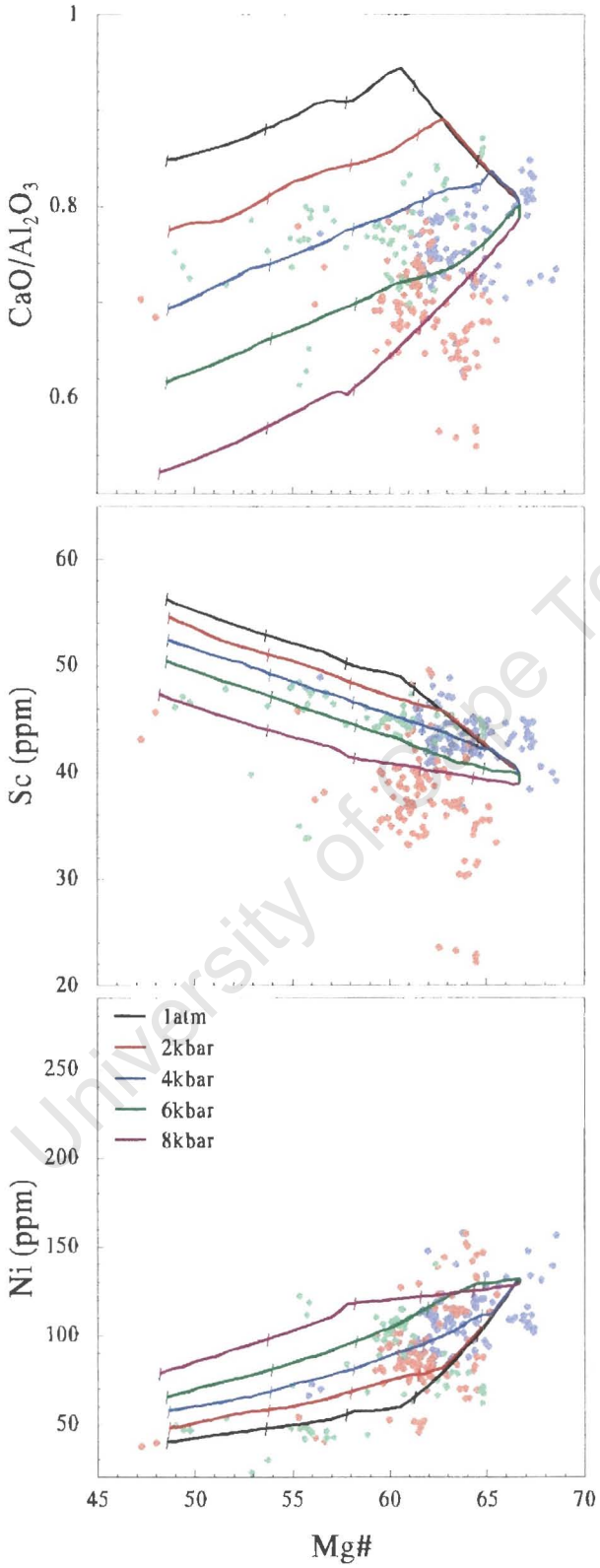

University of Cape Town

Figure 7.7c: CaO/Al_2O_3, Sc and Ni versus Mg# (atomic $Mg^{2+}/[Mg^{2+}+Fe^{2+}]$) of N-MORB (light blue markers), Discovery-influenced MORB (light red markers) and Shona-influenced MORB (light green markers), with superimposed liquid-lines-of-descent of modelled isobaric crystallisation (see legend), with tick-marks at 10% intervals. Starting composition: aphyric bulk-rock composition of sample 13D-1, listed in table 7.1. The phase compositions of the liquidus assemblages are listed in table 7.2.

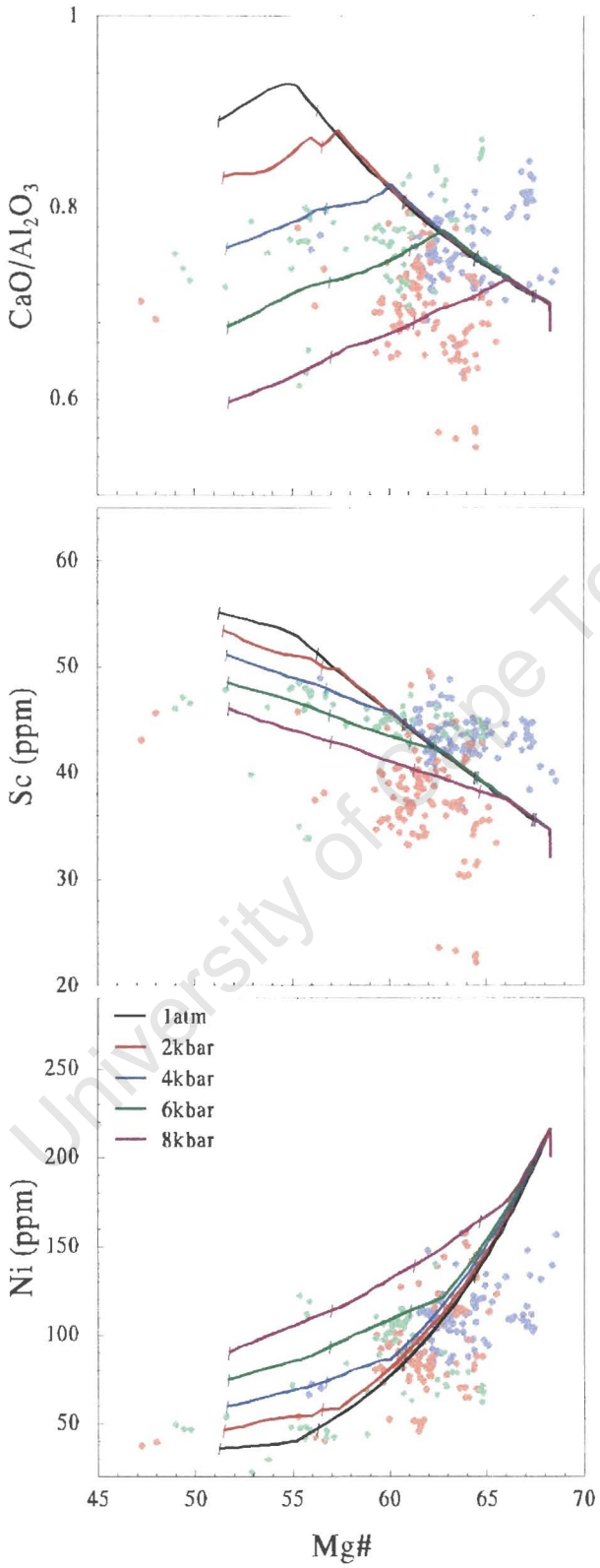

University of Cape Town

Figure 7.7d: CaO/Al_2O_3, Sc and Ni versus Mg# (atomic $Mg^{2+}/[Mg^{2+}+Fe^{2+}]$) of N-MORB (light blue markers), Discovery-influenced MORB (light red markers) and Shona-influenced MORB (light green markers), with superimposed liquid-lines-of-descent of modelled isobaric crystallisation (see legend), with tick-marks at 10% intervals. Starting composition: aphyric bulk-rock of sample 18D-6, listed in table 7.1. The phase compositions of the liquidus assemblages are listed in table 7.2.

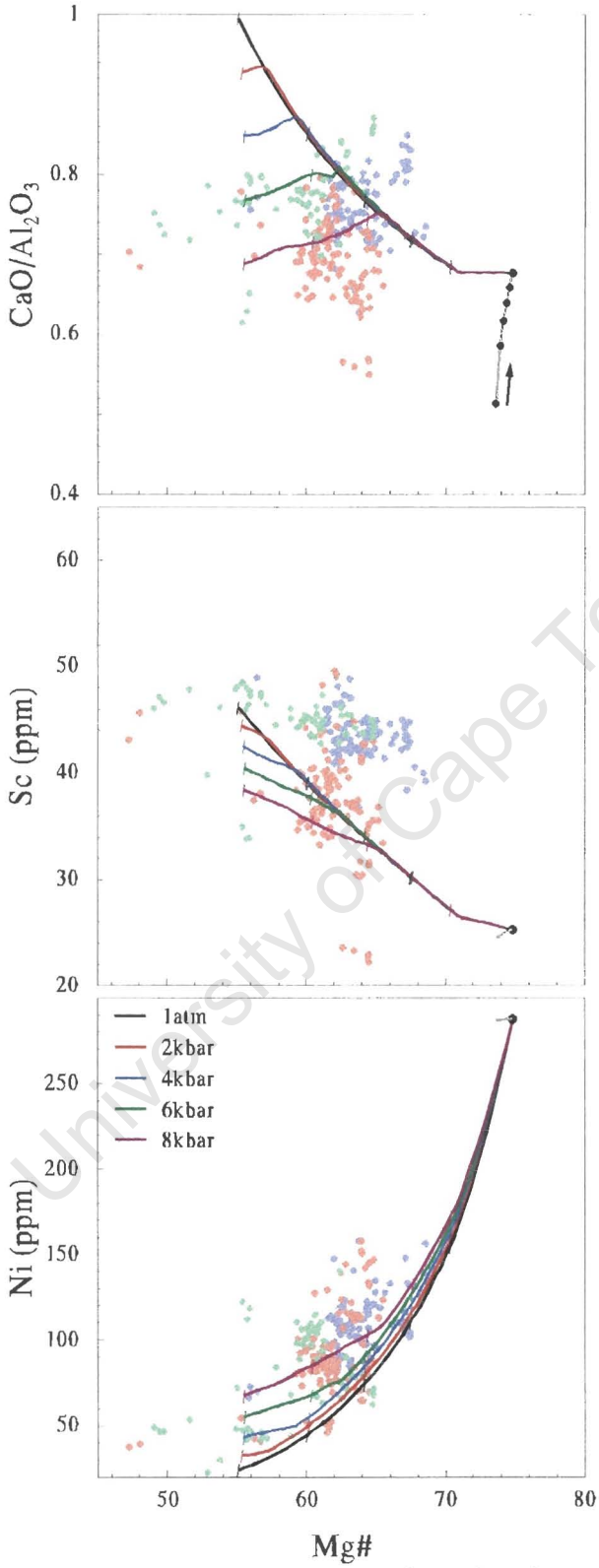

University of Cape Town

Figure 7.7e: CaO/Al_2O_3, Sc and Ni versus Mg# (atomic $Mg^{2+}/[Mg^{2+}+Fe^{2+}]$) of N-MORB (light blue markers), Discovery-influenced MORB (light red markers) and Shona-influenced MORB (light green markers), with superimposed liquid-lines-of-descent of modelled isobaric crystallisation (see legend), with tick-marks at 10% intervals. Starting composition: theoretical primary melt produced by melting the Hart & Zindler (1986) depleted mantle 1 composition with the melting algorithms of Kinzler (1997) from 20-10kbar, at a melting rate of 1%/kbar, listed in table 7.1. Melting trajectories as grey lines, black circles at 2% intervals and an arrow indicating the direction of increasing melting. The phase compositions of the liquidus assemblages are listed in table 7.3.

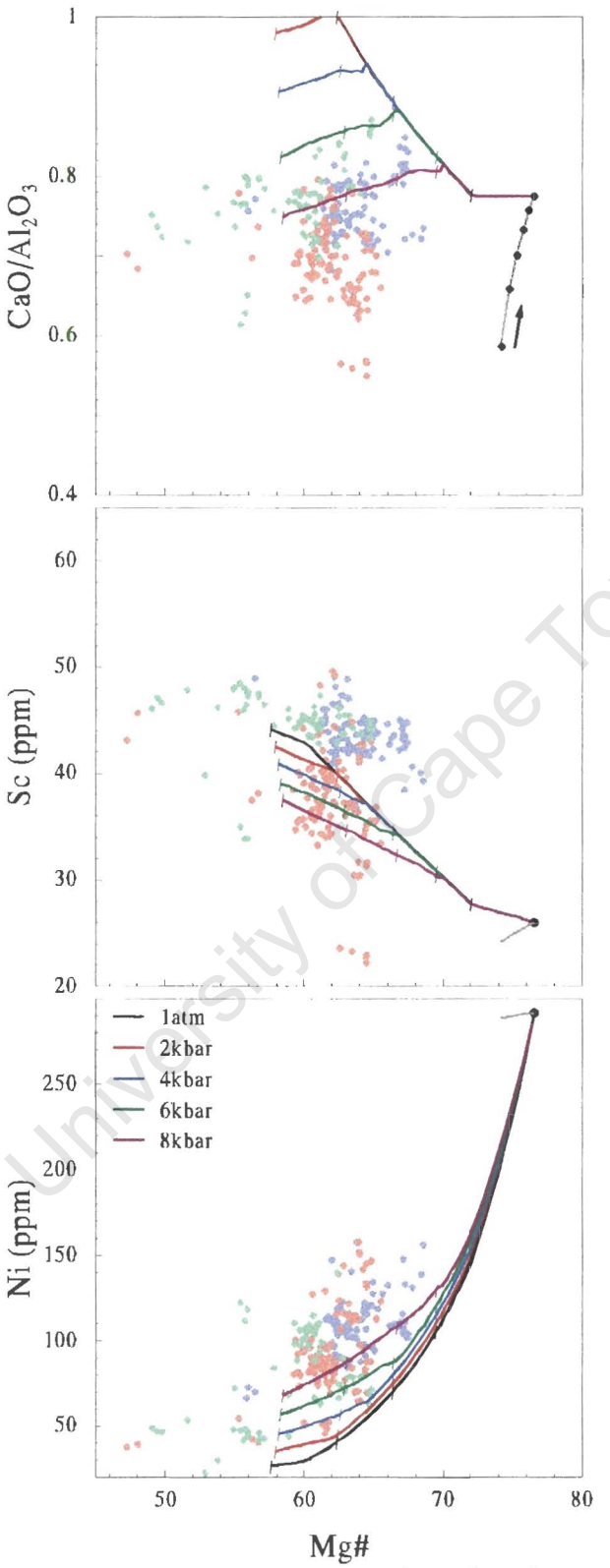

University of Cape Town

Figure 7.7f: CaO/Al_2O_3, Sc and Ni versus Mg# (atomic $Mg^{2+}/[Mg^{2+}+Fe^{2+}]$) of N-MORB (light blue markers), Discovery-influenced MORB (light red markers) and Shona-influenced MORB (light green markers), with superimposed liquid-lines-of-descent of modelled isobaric crystallisation (see legend), with tick-marks at 10% intervals. Starting composition: theoretical primary melt produced by melting the Hart & Zindler (1986) depleted mantle 1 composition with the melting algorithms of Kinzler (1997) from 20-10kbar, at a melting rate of 2%/kbar, listed in table 7.1. Melting trajectories as grey lines, black circles at 2% intervals and an arrow indicating the direction of increasing melting. The phase compositions of the liquidus assemblages are listed in table 7.3.

clinopyroxene is involved in the final stage of most liquid-lines-of-descent, while at high pressures clinopyroxene is crystallised from the start, resulting in positive slopes of liquid-lines-of-descent, or the final sections, in the CaO/Al_2O_3 versus Mg# diagrams.

As in the CaO versus MgO diagrams, the data for the quenched igneous glasses from N-MORB and MORB from Shona-influenced ridge segments are broadly orientated along the positive slopes of the modelled liquid-lines-of-descent in the CaO/Al_2O_3 versus Mg# diagrams in fig. 7.7a-d. The data for MORB from Discovery-influenced ridge segments plot off-set to lower CaO/Al_2O_3 values, which, as discussed earlier, might result from anomalous proportions pyroxenitic material in the mantle source-regions from which these melts were extracted. Nevertheless, the orientation of the data for the quenched igneous glasses in the CaO/Al_2O_3 versus Mg# diagrams in fig. 7.7a-d are consistent with modelled crystallisation in which clinopyroxene was formed along with olivine and plagioclase.

The restriction of Sc values to a constant range of approximately 40-50ppm for N-MORB and MORB from Shona-influenced ridge segments is also consistent with clinopyroxene being part of the liquidus assemblage during crystallisation of these basalts. Sc is compatible in clinopyroxene, but incompatible in olivine and plagioclase. This is illustrated by the initial negative slopes of the modelled liquid-lines-of-descent in the Sc versus Mg# diagrams in fig. 7.7a-d, especially fig. 7.7d, during crystallisation of plagioclase and/or olivine, followed by significantly shallower slopes after clinopyroxene joined the liquidus assemblage. The value of the partition coefficient for Sc in clinopyroxene in the literature ranges as high as 3.0 (Niu *et al.*, 1996), while the value used in the modelling of crystallisation here was 1.31 (Hart & Dunn, 1993). Increasing the value for this partition coefficient would rotate the slopes of the sections of the trends during which clinopyroxene crystallised closer to horizontal in the Sc versus Mg# diagrams in fig. 7.7a-d. The position of the data for the quenched igneous glasses in the Sc versus Mg# diagrams therefore reinforce the necessity of clinopyroxene during crystallisation of these basalts.

It is evident (fig. 7.7a-d) that the anomalously low Sc values (~22-24ppm) for the basalts recovered from dredge 25 could not result from crystallisation of the selected starting compositions. The variable mixing of melts derived from the ambient depleted mantle and a Discovery mantle plume-derived component in the form of intercalated pyroxenitic material was

University of Cape Town

proposed as the origin of the spectrum of variable enriched MORB compositions recovered from the Discovery-influenced ridge segments, see chapters 5 and 6. Mixing of melts similar to the low-Sc dredge 25 basalts with the ambient mantle giving rise to N-MORB with 40-50ppm Sc, as discussed in chapters 5 & 6 is believed to have led to Discovery-influenced MORB with Sc concentrations of 30-40ppm. Although the Sc concentrations of the general Discovery-influenced MORB are lower than the modelled liquid-lines-of-descent, these compositions also defined a broadly constant range which is systematically lower then the range for N-MORB and Shona-influenced MORB. No MORB with appropriately high-MgO quenched igneous glass or bulk-rock compositions for use as starting compositions for modelling of crystallisation were recovered from Discovery-influenced ridge segments. However, taking the calculated crystallisation trends in the Sc versus Mg# diagrams in fig. 7.7a-d as generic, then a starting composition with ~10ppm less Sc than the current starting compositions would be sufficient to produce liquid-lines-of-descent which explain the broad band of Discovery-influenced MORB on these diagrams.

The major-element oxide variations, as well as CaO/Al_2O_3, Mg# and Sc variations, of the quenched igneous glass of the MORB from the SMAR are consistent with these basalts having experienced variable degrees of crystallisation involving plagioclase, olivine and, in most cases, clinopyroxene at a range of pressures. In fig. 7.7a-d, the co-variation of the Ni content and Mg# of the quenched igneous glasses are also clearly accounted for by the crystallisation of olivine, see especially fig. 7.7b.

In fig. 7.6a-d & 7.7a-d, the data for the majority of the quenched igneous glasses are located on the high-pressure side of the liquid-lines-of-descent for crystallisation at 2kbar. The data for quenched igneous glasses from N-MORB and Shona-influenced MORB are bounded at high pressure by the 4-6kbar liquid-lines-of-descent in these diagrams. The data for quenched igneous glasses from Discovery-influenced ridge segments plot toward pressures of crystallisation higher than 8kbar in some diagrams, e.g. Na_2O versus MgO and CaO/Al_2O_3 and Sc versus Mg#, while located at pressures below 1atm in the FeO versus MgO diagrams. As discussed in chapter 6, these basalts from dredge 25, 6 & 7 were derived from mantle source-regions containing significant proportions of Discovery mantle plume-derived pyroxenitic material, which yield melts during melting with lower FeO and Sc, and higher Na_2O than melts derived from the ambient lherzolitic mantle. Therefore, although the data for N-MORB and

University of Cape Town

Shona-influenced MORB indicate pressures of crystallisation ranging between 2kbar and 4-6kbar, based on these modelled liquid-lines-of-descent in fig. 7.6a-d & 7.7a-d, the pressures of crystallisation of Discovery-influenced MORB can not be deduced from these diagrams.

The derivation of the high-MgO quenched igneous glass compositions from theoretical primary melt compositions through crystallisation. The forward modelling of the crystallisation of the theoretical primary melts derived through the melting of proposed mantle source-regions, as discussed in chapter 6, can be used to bridge the gap between these modelled products of mantle melting and the most-primitive MORB recovered from the SMAR. As was discussed earlier, all the MORB recovered from the SMAR contain compositional evidence of having experienced crystallisation and none have compositions generally thought of as typical of primary products of MORB mantle melting. The mantle source-regions beneath the SMAR have also been shown to be heterogeneous in terms of isotopic, trace- and major-element compositions, therefore the compositional trends derived from the modelled crystallisation of the theoretical primary melts are more significant qualitatively for their general shape and orientation, than for any quantitative conclusions.

The compositions of these theoretical primary melts are listed in table 7.1 and liquid-lines-of-descent for the melts derived from the Hart & Zindler (1986) depleted mantle 1 composition are plotted along with the data for the quenched igneous glasses in fig. 7.6e & f, and fig. 7.7e & f. The crystallisation trends presented on these diagrams are representative of those calculated using the other theoretical primary melt compositions in table 7.1. The changing mineralogy of the liquidus assemblage during the crystallisation of each starting composition are listed in table 7.3. All starting compositions initially crystallisation only olivine to 7-11% crystallisation, followed by crystallisation of plagioclase and olivine. At 1atm and 2kbar, some of the starting compositions, e.g. AP 1%, do not saturate with clinopyroxene before the modelling was terminated at 50% crystallisation and the interval of plagioclase and olivine crystallisation continues to the 50% cut-off point. For the remaining starting compositions, clinopyroxene joins the liquidus assemblage eventually and the three-phase crystallisation of plagioclase, clinopyroxene and olivine continues to 50% crystallisation. As pressure is increased, clinopyroxene joins the liquidus assemblage at progressive earlier steps, e.g. for HZ 2% it joins plagioclase and olivine after 44% crystallisation at 1atm and after 18% crystallisation at 8kbar.

University of Cape Town

Table 7.3: Modal mineralogy of liquid-lines-of-descent, plotted in fig. 7.6 & 7.7, calculated using theoretical primary melts as starting compositions (see text for discussion). The MgO wt% and percentage crystallisation of the magma when a new phase joins the mode of the liquidus assemblage are given in brackets. The phase are listed in relative order of abundance in the liquidus assemblage. HZ: Hart & Zindler (1986) depleted mantle 1; AP: AP fertile 2 of Kinzler (1997); percentages refer to melting rate used.

Starting composition	Pressure of crystallisation	Mineralogy of liquidus assemblage
HZ 1%	1atm	oliv (10.13/7) ⇒ plag + oliv
	2kbar	oliv (10.12/7) ⇒ plag + oliv (7.49/46) ⇒ plag + cpx + oliv
	4kbar	oliv (10.12/7) ⇒ plag + oliv (7.89/41) ⇒ plag + cpx + oliv
	6kbar	oliv (10.12/7) ⇒ plag + oliv (8.37/35) ⇒ cpx + plag (8.27/37) ⇒ plag + cpx + oliv
	8kbar	oliv (10.11/7) ⇒ plag + oliv (8.99/26) ⇒ plag + cpx + oliv
HZ 2%	1atm	oliv (11.16/9) ⇒ plag + oliv (8.54/44) ⇒ cpx + plag + oliv
	2kbar	oliv (11.16/9) ⇒ plag + oliv (8.91/40) ⇒ cpx + plag + oliv
	4kbar	oliv (11.15/9) ⇒ plag + oliv (9.38/35) ⇒ cpx + plag (9.29/37) ⇒ plag + cpx + oliv
	6kbar	oliv (11.15/9) ⇒ plag + oliv (9.89/28) ⇒ cpx + plag + oliv
	8kbar	oliv (11.15/9) ⇒ plag + oliv (10.55/18) ⇒ cpx + plag (10.48/20) ⇒ cpx + plag + oliv
HZ 3%	1atm	oliv (11.44/11) ⇒ plag + oliv (8.78/45) ⇒ cpx + plag + oliv
	2kbar	oliv (11.44/11) ⇒ plag + oliv (9.17/41) ⇒ cpx + plag + oliv
	4kbar	oliv (11.43/11) ⇒ plag + oliv (9.62/36) ⇒ cpx + plag + oliv
	6kbar	oliv (11.43/11) ⇒ plag + oliv (10.16/29) ⇒ cpx + plag + oliv
	8kbar	oliv (11.43/11) ⇒ plag + oliv (10.7/20) ⇒ cpx + plag (10.66/22) ⇒ plag + oliv + cpx (10.41/27) ⇒ cpx + plag (10.32/30) ⇒ cpx + plag + oliv
AP 1%	1atm	oliv (9.42/7) ⇒ plag + oliv
	2kbar	oliv (9.41/7) ⇒ plag + oliv
	4kbar	oliv (9.41/7) ⇒ plag + oliv (7.03/47) ⇒ plag + cpx + oliv
	6kbar	oliv (9.41/7) ⇒ plag + oliv (7.45/41) ⇒ cpx + plag (7.34/43) ⇒ plag + cpx + oliv
	8kbar	oliv (9.40/7) ⇒ plag + oliv (8.01/32) ⇒ cpx + plag + oliv
AP 2%	1atm	oliv (11.00/8) ⇒ plag + oliv (7.89/49) ⇒ cpx + plag
	2kbar	oliv (11.00/8) ⇒ plag + oliv (8.29/45) ⇒ cpx + plag + oliv
	4kbar	oliv (10.99/8) ⇒ plag + oliv (8.76/40) ⇒ cpx + plag + oliv
	6kbar	oliv (10.99/8) ⇒ plag + oliv (9.26/34) ⇒ plag + cpx + oliv
	8kbar	oliv (10.99/8) ⇒ plag + oliv (9.82/26) ⇒ cpx + plag (9.76/28) ⇒ plag + cpx + oliv

University of Cape Town

Table 7.3 continued

Starting composition	Pressure of crystallisation	Mineralogy of liquidus assemblage
AP 3%	1atm	oliv (10.96/11) ⇒ plag + oliv
	2kbar	oliv (10.96/11) ⇒ plag + oliv (8.54/46) ⇒ cpx + plag + oliv
	4kbar	oliv (10.96/11) ⇒ plag + oliv (9.02/41) ⇒ cpx + plag + oliv
	6kbar	oliv (11.28/10) ⇒ plag + oliv (9.51/35) ⇒ plag + cpx + oliv
	8kbar	oliv (11.28/10) ⇒ plag + oliv (10.10/27) ⇒ plag + cpx + oliv

University of Cape Town

In terms of the major-element oxides, the modelled crystallisation of all the theoretical primary melts produce magmas with SiO_2 concentrations too low compared to the observed data, but in agreement with the general observed trend in the data. The calculated trends of the crystallisation of HZ 1% for FeO pass through the high MgO quenched igneous glass data for N-MORB and Shona-influenced MORB, but as discussed earlier the MORB from Discovery-influenced ridge segments are off-set to lower FeO. The liquid-lines-of-descent of HZ 2% for FeO agree with the trend in the observed data, but are off-set to higher MgO. The crystallisation trends for TiO_2 also agree with the trend in the observed data.

The calculated trends in the Al_2O_3, CaO and Na_2O versus MgO diagrams are more intricate due to the significant affect of liquidus plagioclase and clinopyroxene on these major elements. The initial phases of olivine crystallisation result in negative slopes of the trends in the Al_2O_3 versus MgO diagrams in fig. 7.6e & f, with the slopes changing sharply to positive as plagioclase joins olivine in the liquidus assemblage. The slopes change again to much shallower positive orientations when clinopyroxene joins plagioclase and olivine. The liquid-lines-of-descent for HZ 1%, in fig 7.6e, pass through the observed data in the Al_2O_3 versus MgO diagrams, and whereas the crystallisation trends of the HZ 2% starting composition do not pass through the observed data, their orientation do agree with the trend of the observed data. In the CaO versus MgO diagrams in fig 7.6e, crystallisation trends for HZ 1% also pass through the observed data, at CaO values lower than the highest observed compositions. The 6-8kbar liquid-lines-of-descent for HZ 2% in fig. 7.6f pass through the observed data at high CaO, high MgO values and at that stage are crystallising plagioclase, clinopyroxene and olivine. These trends are therefore also in agreement with the orientation of the observed data. The high pressure liquid-lines-of-descent for HZ 3% and AP 3%, not shown, also approach the high CaO, high MgO end of the observed data, but do not agree with the observed data as well as the trends for HZ 2%, and AP 2%, not shown. In the Na_2O versus MgO diagrams, the trends for crystallisation of the HZ 1% starting compositions are at Na_2O values significantly too high to yield the observed most-primitive quenched igneous glass compositions. The liquid-lines-of-descent for the HZ 2-3% and AP 2-3%, only those for HZ 2% shown in fig. 7.6f, are at much lower Na_2O values and pass close to or through the most-primitive end of the observed data at all pressures of crystallisation.

The least-evolved high-MgO quenched igneous glasses used previously as starting

University of Cape Town

compositions to the model crystallisation of the MORB from the SMAR are therefore products of significant crystallisation of the magmas formed by mantle melting. The modelling of the crystallisation of theoretical primary mantle melts also agree with the conclusion reached in chapter 6, that these basalts formed at melting rates of 2-3%/kbar, because the trends observed in the compositions of the basalts are well-aligned with trend of the modelled crystallisation of the theoretical primary melts formed at rates of 2-3%/kbar. The primary melts produced by mantle melting beneath the SMAR experienced substantial (30-40%) crystallisation to reach the least-evolved compositions of the sampled MORB. This crystallisation occurred at 6-8kbar and initially involved only olivine, then plagioclase and olivine, and finally plagioclase, clinopyroxene and olivine.

Summary. The compositional trends calculated using high-MgO basalts from the SMAR as starting compositions are qualitatively orientated parallel to the observed data for MORB from the SMAR. Crystallisation trajectories which are aligned with the observed trends in the data initial involve either olivine or plagioclase, followed by co-crystallisation of both these phase before clinopyroxene joins the liquidus assemblage. At progressively higher pressures of crystallisation, clinopyroxene joins the liquidus assemblage earlier and for some starting compositions clinopyroxene is a liquidus phase from the onset or very earlier stages of crystallisation at pressure >6kbar. Regardless of the starting composition used, the observed trends in the data for MORB from the SMAR necessitate clinopyroxene as a liquidus phase at some stage during crystallisation.

University of Cape Town

The majority of quenched igneous glasses fall on the high-pressure side of liquid-lines-of-descent for crystallisation at 2kbar. The data for N-MORB and Shona-influenced MORB are bounded at high pressure by the 4-6kbar liquid-lines-of-descent, whereas basalts from Discovery-influenced ridge segments are located toward pressures higher than 8kbar for some elements, e.g. Na_2O versus MgO and CaO/Al_2O_3 and Sc versus Mg#, while falling at pressures below 1atm for FeO versus MgO. The data for N-MORB and Shona-influenced MORB indicate pressures of crystallisation ranging between 2kbar and 4-6kbar, but the pressures of crystallisation of Discovery-influenced MORB could not be deduced.

The compositions of modelled primary melts, derived by mantle melting at rates of 2-3%/kbar, underwent substantial (30-40%) crystallisation to reach the least-evolved compositions

of the sampled MORB. Furthermore, this crystallisation occurred at high pressures (6-8kbar), with olivine as the initial liquidus phase, joined at 8-10% crystallisation by plagioclase and clinopyroxene joins these two liquidus phase after 20-30% crystallisation.

7.3 PRESSURES OF CRYSTALLISATION

Methods used to calculate the pressures at which the MORB from the SMAR experienced crystallisation. Both the methods discussed below and employed here to deduce the pressures at which the MORB from the SMAR experienced crystallisation are dependent on the basalts having been in saturated with olivine, plagioclase and clinopyroxene. The modelled liquid-lines-of-descent calculated in the previous section indicated that the major- and trace-element variations observed in the compositional data for the basalts from the SMAR are consistent with the presence of clinopyroxene in the liquidus assemblage. On the CaO versus MgO diagrams discussed in the previous section, the data for the quenched igneous glasses define positive trends, with no indication of preceding negative slopes. This observation therefore alludes to these basalts having been erupted after clinopyroxene joined plagioclase and olivine as a liquidus phase. For the following modelling of the pressures of crystallisation, the quenched igneous glasses with MgO content <8.3wt% were assumed to have been in equilibrium with plagioclase, olivine and clinopyroxene during crystallisation. This assumption is in agreement with the conclusions from the previous section and the MgO value used is consistent with that used in other studies to delimit basalts saturated with clinopyroxene (Michael & Cornell, 1998; Michael pers. comm.; Reynolds & Langmuir, 1997; Smith *et al.*, 1998).

University of Cape Town

The first method employed to determine the pressures at which these MORB from the SMAR experienced crystallisation is that developed by Grove *et al.* (1992). A series of equations were constructed based on experimental studies which can be used to calculated the locations of the olivine-plagioclase-augite-low Ca pyroxene-melt (OPALM), olivine-plagioclase-augite-melt (OPAM) and olivine-plagioclase-melt saturation boundaries for basalts at given pressures. The OPAM boundaries in the quartz-olivine-clinopyroxene pseudo-ternary diagrams plotted in fig. 7.8 were sketched parallel to the boundaries determined for the Serocki lava ALV-1690-20, after Grove *et al.* (1992). Plotting the composition of the basalt in question and these predicted boundaries, calculated at various pressures for this composition, on olivine-plagioclase-clinopyroxene and quartz-olivine-clinopyroxene pseudo-ternary diagrams allows the graphical assessment of the pressure at which the basalt crystallised. The diagrams in fig. 7.8 illustrate the

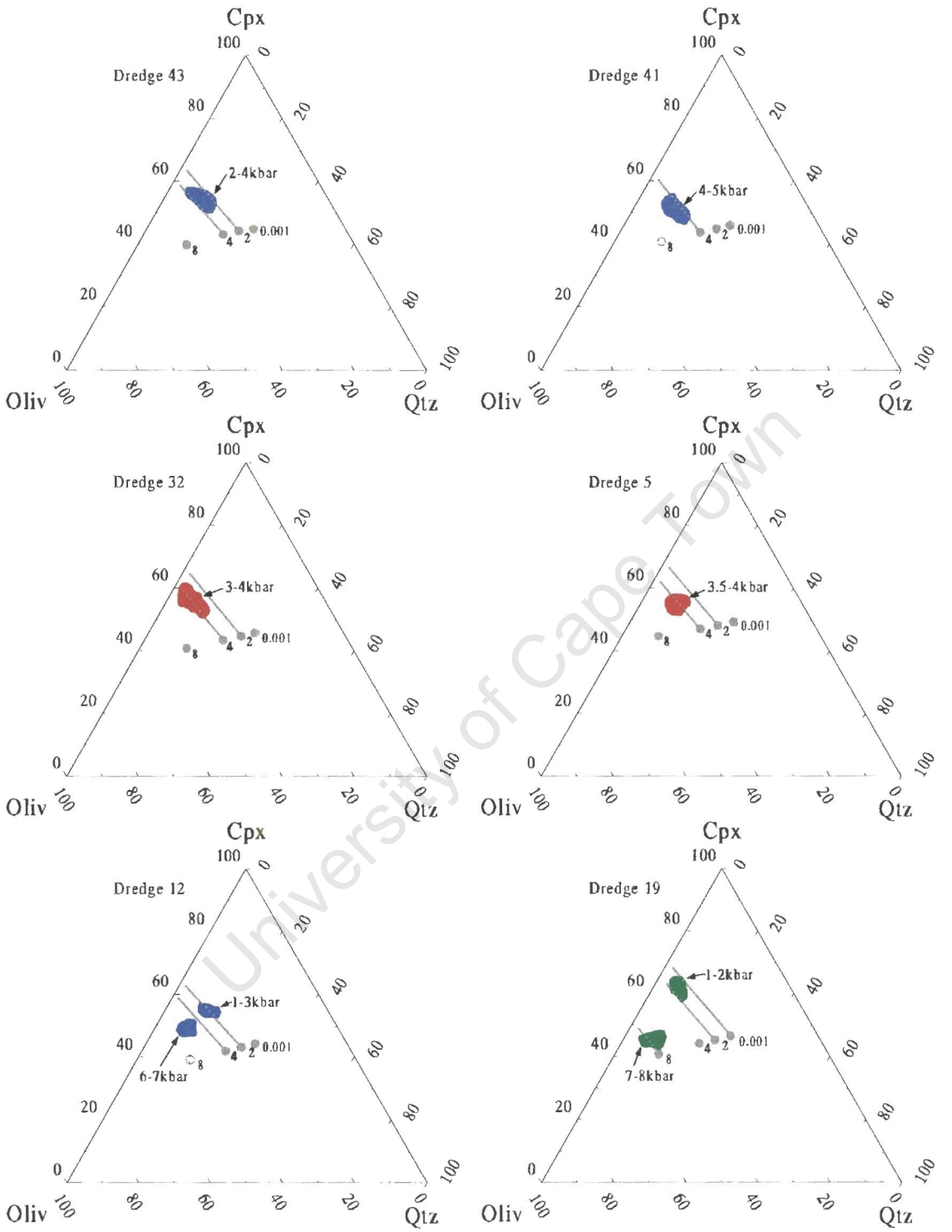

University of Cape Town

Figure 7.8: Quartz (Qtz)-olivine (Oliv)-clinopyroxene (Cpx) pseudo-ternary diagrams with the predicted olivine-plagioclase-augite-low Ca-pyroxene-melt points (grey markers; OPALM points) at 1atm and 2-8kbar (as labelled), and olivine-plagioclase-augite boundaries (grey lines) where relevant (Grove *et al.*, 1992; see text for discussion) of representative dredges. The OPALM points were calculated using related quenched igneous glass and aphyric bulk-rock pairs with homogeneous compositions. The blue fields: N-MORB; red fields: Discovery-influenced MORB; green fields: Shona-influenced MORB.

typical graphical presentation and determination of the pressure of crystallisation using this method of Grove *et al.* (1992).

The second method used in this study to determine the pressures of crystallisation of these MORB from the SMAR employs the algorithms of Yang *et al.* (1996) as rearranged and discussed by Michael & Cornell (1998). These algorithms are given below as equations 7.1 & 7.2, with pressures calculated in kilobars and the molar quantities (i.e. XAl) calculated according to the method of Grove *et al.* (1992). These equations are applicable only if the basalts have experienced saturation of clinopyroxene at some stage during crystallisation. The MgO values at which clinopyroxene can reliably be considered to have crystallised from a basaltic composition was taken as <8wt% by Michael & Cornell (1998) for a global data-set and as <8.3wt% by Reynolds & Langmuir (1997) for basalts south of the Kane fracture zone on the northern MAR. As discussed above, the quenched igneous glass for MORB from the SMAR with MgO content <8.3wt% were taken to have saturated with clinopyroxene during crystallisation. It must be noted that a single pressure is calculated for each basalt, when in reality crystallisation probably follows a polybaric path in reaching the final erupted composition. A magma might crystallise plagioclase, clinopyroxene and olivine at high pressure, but ascend to shallower depths prior to eruption where clinopyroxene is no longer stable. The magma would then evolve towards the low pressure cotectic by crystallisation of olivine and plagioclase and probably the dissolution of clinopyroxene. If the residence time at shallow levels is too short to allow the magma to reach the cotectic prior to eruption, then the composition of the sampled basalt will yield a pressure of crystallisation intermediate between the original high pressure crystallisation and later shallow level crystallisation. The pressures obtained using the above method are therefore minima for the onset of crystallisation and maxima for the completion of crystallisation for each sample (Michael & Cornell, 1998).

$$P_{Al} = [XAl - 0.236 - 0.109(XNa) - 0.593(XK) + 0.35(XTi) + 0.299(XFe) + 0.13(XSi)] / 0.00218 \quad \text{..... equation 7.1}$$

$$P_{Ca} = [XCa - 1.133 + 0.569(XNa) + 0.776(XK) + 0.672(XTi) + 0.214(XFe) + 3.355(XSi) - 2.83(XSi^2)] / -0.00339 \quad \text{..... equation 7.2}$$

(Michael & Cornell, 1998, after Yang *et al.*, 1996)

University of Cape Town

Before using equations 7.1 & 7.2, the quenched igneous glass major-element data had to be corrected for inter-laboratory differences between the electron microprobe at MIT used to analyse the experimental material on which the equations are based, and the electron microprobe at the University of Cape Town used to analyse the quenched igneous glasses in this study. The correction factors listed in table 7.4 were calculated based on the composition of the ALV-1690-20 quenched igneous glass as obtained using the MIT microprobe (Grove *et al.*, 1990) and the UCT microprobe in this study. Using the corrected data and the above two equations yielded two values for the pressure of crystallisation for each basalt. The values obtained from these two equations are similar, but Michael & Cornell (1998) found equation 7.2 to be the most-robust and insensitive to analytical uncertainties. Therefore only the pressures based on the P_{Ca} equation (eq. 7.2) are used in the diagram in fig. 7.9.

Table 7.4: Composition of the ALV-1690-20 quenched igneous glass as analysed by the electron microprobe at MIT (average of 106 analyses) (Grove *et al.*, 1990) and UCT (average of 5 analyses), with calculated factors used to correct the UCT data to for the inter-laboratory differences between the two instruments.

	MIT	UCT	Correction factors
SiO_2	49.90	49.35	1.0111
TiO_2	1.71	1.82	0.9402
Al_2O_3	15.50	15.38	1.0079
FeO	9.92	10.15	0.9775
MgO	7.68	7.98	0.9625
CaO	10.80	10.97	0.9849
K_2O	0.14	0.14	0.9933
Na_2O	3.13	3.09	1.0113
P_2O_5	0.18	0.18	1.0229

Calculated pressures of crystallisation for the MORB from the SMAR. The calculated pressures of crystallisation for the MORB from the SMAR, obtained using both the above methods, are plotted against latitude in fig. 7.9. In diagram A in fig. 7.9, only pressures calculated for quenched igneous glasses with MgO content of 6.5-8.3% were plotted, in order to avoid comparing the pressures of crystallisation of highly evolved basalts with much lesser evolved basalts (Michael & Cornell, 1998). The pressures of crystallisation obtained using the two methods agree quite well, considering the errors on both methods are of the order of 1kbar (Michael & Cornell, 1998). From the latitudinal variations in fig. 7.9 it is evident that crystallisation occurred predominantly in a pressures range of 2-6kbar. Beneath Discovery-

University of Cape Town

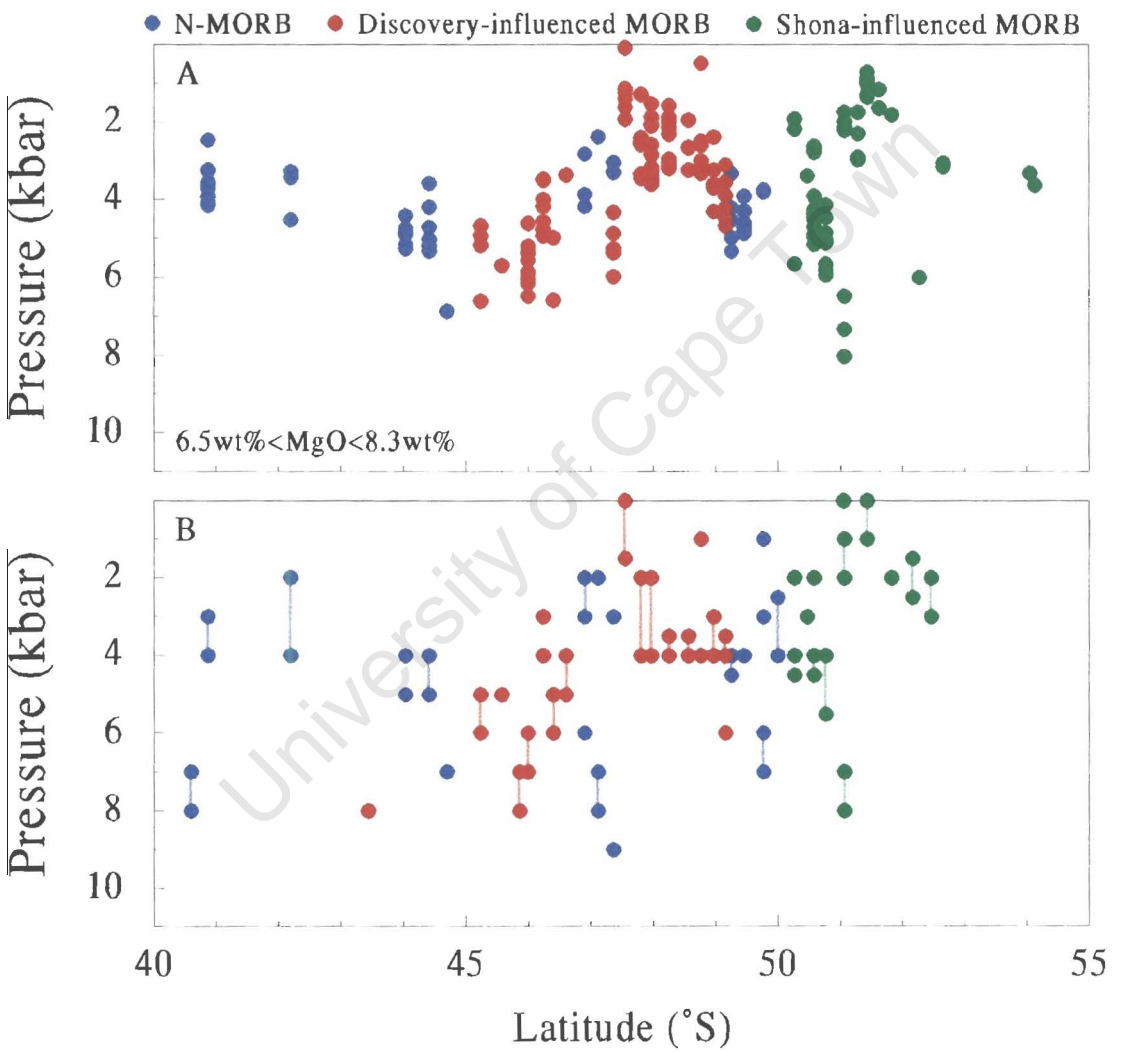

University of Cape Town

Figure 7.9: Calculated pressures of crystallisation versus latitude. **A** Pressures calculated after Michael & Cornell (1998) as discussed in the text, with only the values for quenched igneous glasses with MgO content between 6.5-8.3wt%. **B** Pressures obtained using the approach of Grove *et al.*, (1992) as discussed in the text and illustrated in fig. 7.8. Marker colours defined in the legend, markers connected by lines in **B** indicate a range of pressure obtained from a cluster of basalts, see fig. 7.8.

influenced ridge segments to the north of the Falkland-Agulhas Fracture Zone, crystallisation occurred at slightly higher pressures. To the south of this fracture zone, the basalts recovered from Discovery-influenced ridge segments experienced crystallisation at much shallower pressures of 1atm-4kbar. However, basalts from dredge 25, immediately south of the Falkland-Agulhas Fracture Zone, and dredge 9, the southernmost Discovery-influenced dredge, experienced crystallisation at pressures up to 6kbar. The Shona-influenced MORB span a considerable range of pressures of crystallisation, with the basalts at the northern extreme of the Shona-anomaly having experienced crystallisation at pressures of 2-8kbar. The central and southern zones of the Shona-anomaly sampled in this study yielded basalts which experienced crystallisation at much shallower pressures of 1atm-4kbar.

The variations of the calculated pressures of crystallisation with MgO content of the quenched igneous glasses, plotted in fig. 7.10, indicate distinct differences between the evolution of the N-MORB and the mantle plume-influenced MORB. The data for N-MORB, with the exception of a few outliers, form a vertical cluster at approximately 8wt% MgO and between 3-6kbar. This indicates that crystallisation beneath the ridge segments unaffected by the mantle plumes occurred at depths in the oceanic mantle (Grove *et al.*, 1992), did not proceed for sufficiently long to result in highly evolved basalts and if a second phase of crystallisation did occur at shallow depths, it was of insufficient magnitude to significantly mask the compositional effects of the prior high pressure crystallisation.

The crystallisation beneath the mantle plume-influenced ridge segments commenced at higher pressures of ~7kbar, excluding the two basalts from dredge 19 which yielded pressures of 8-9kbar, and occurred over a continuous spectrum of pressures to a final, shallow level of 1atm-1kbar. Although the crystallisation of the Discovery-influenced MORB occurred over a much larger range of pressures (1atm-~7kbar) compared with the N-MORB (3-6kbar), the crystallisation did not result in magmas with extensively more evolved compositions (8wt%≥MgO≥7wt%, compared to MgO~8wt% for N-MORB). This is an indication that individual episodes of crystallisation beneath the Discovery-influenced ridge segments were only slightly longer-lived than beneath the ridge segments unaffected by mantle plumes, even though it occurred over a much larger range of pressures. The Shona-influenced MORB experienced crystallisation over a similar range as the Discovery-influenced MORB (1atm-~7kbar), but the process of crystallisation was substantially longer-lived and produced more evolved basalt

University of Cape Town

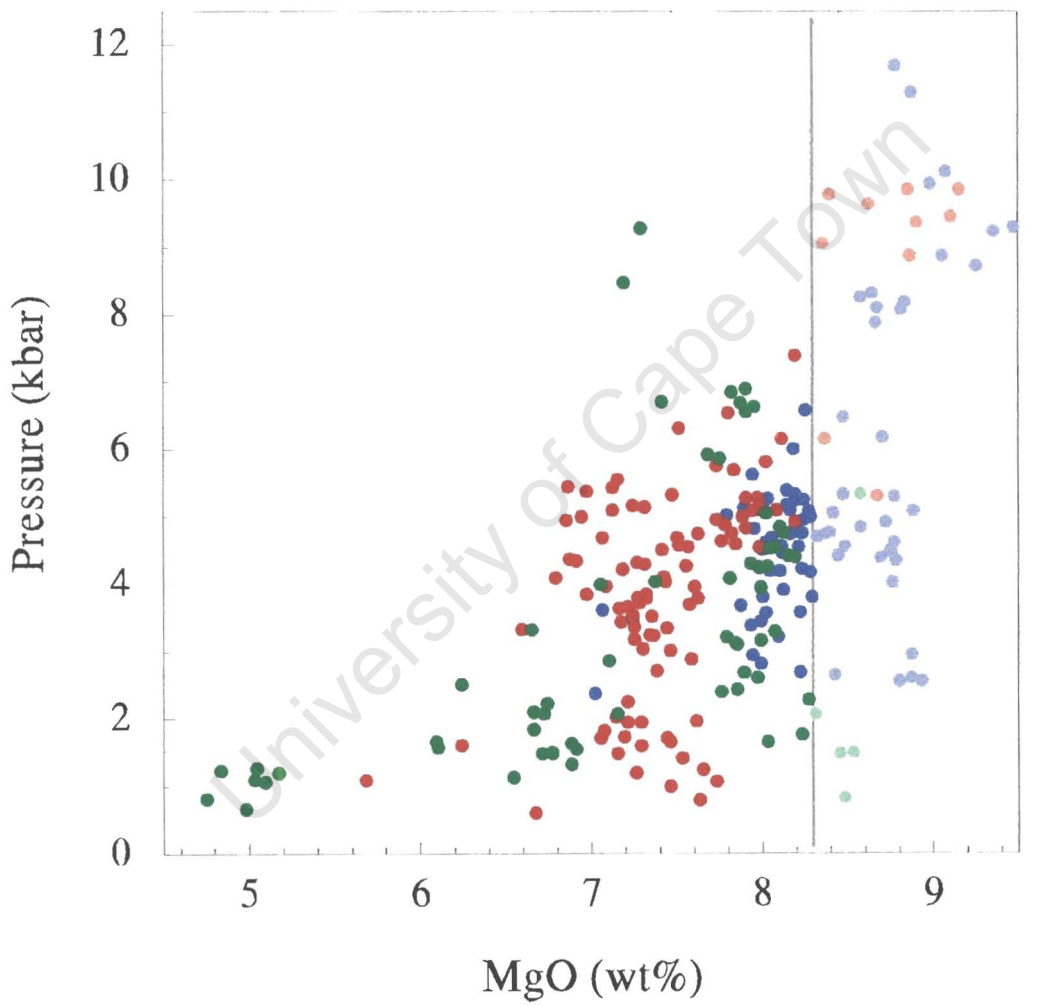

University of Cape Town

Figure 7.10: Pressure of crystallisation (Michael & Cornell, 1998) versus MgO content for quenched igneous glasses of MORB from the SMAR. Blue markers: N-MORB; red markers: Discovery-influenced MORB; green markers: Shona-influenced MORB. Grey line at 8.3wt% MgO, and lighter shades of the previously defined marker colours indicate MORB with MgO content >8.3wt% and therefore might not have been saturated with clinopyroxene during crystallisation.

compositions (~5-8wt% MgO). The trend in the data of the Shona-influenced MORB of decreasing pressures of crystallisation with decreasing MgO content and apparent levelling of the trend at low MgO concentrations agree with the observations from the global data-set of Michael & Cornell (1998). These features indicate that multi-phase crystallisation of plagioclase, clinopyroxene, and olivine occurred continuously as the magma bodies ascended and those that rose to the shallowest levels had enough time to evolve to higher degrees (Michael & Cornell, 1998).

Petrographic and mineral-chemical indications of the pressures of crystallisation beneath the ridge segments of the SMAR sampled. As mentioned previously, clinopyroxene is a rare phenocryst phase in the MORB recovered from the SMAR. The basalts in which clinopyroxene is present were predominantly recovered from mantle plume-influenced ridge segments, and the compositions of these basalts are only occasionally evolved (e.g. dredge 20 with Mg#'s≈55). More frequently, the basalts containing clinopyroxene as phenocryst or microphenocryst phases yielded low calculated pressures of crystallisation (1atm-2kbar for dredge 2, 3, 7, 20). The few N-MORB containing clinopyroxene yielded higher pressures of crystallisation (4-6kbar for dredge 39, 13) and these clinopyroxene phenocrysts exhibit resorption features and some grains are severely rounded, while the clinopyroxene in the mantle plume-influenced MORB are euhedral to subhedral. These observations support the deduction reached in the previous section that extensive crystallisation, reaching clinopyroxene saturation, occurred at shallow oceanic crustal levels (Grove *et al.*, 1992) beneath the mantle plume-influenced ridge segments, resulting in recovered basalts containing clinopyroxene grains with equilibrium textures. However, beneath ridge segments unaffected by the mantle plumes extensive crystallisation involving clinopyroxene occurred at oceanic mantle levels (Grove *et al.*, 1992) and the high relative density of clinopyroxene inhibits considerable transport of phenocrysts to shallow oceanic crustal levels (le Roex *et al.*, 1996). The clinopyroxene phenocrysts which did get entrained and transported to shallow depths are then out of equilibrium with the magma at these lower pressures and are resorbed. The anhedral and rounded clinopyroxenes observed in the N-MORB from the SMAR are interpreted to reflect grains which survived this process of resorption at shallow depths beneath the ridge segments.

The petrographic characteristics and occurrence of plagioclase and olivine phenocrysts are not indicative of specific pressures of crystallisation. The compositions of these phenocrysts

University of Cape Town

were discussed in chapter 5 and specifically the pressure at which they are in equilibrium with the relevant host quenched igneous glass or aphyric bulk-rock sample. It was concluded that some of the plagioclase microphenocrysts and phenocrysts are in equilibrium with host quenched igneous glasses at pressures of 1atm-4kbar, but the distribution of these equilibrium plagioclase grains span basalts recovered from all ridge segments. The majority of olivine phenocrysts and microphenocrysts are in equilibrium with the host quenched igneous glasses and bulk-rock samples at pressures >2kbar, with some high forsterite olivine phenocrysts not in equilibrium with host compositions at any pressure between 1atm-8kbar. The differences between calculated equilibrium olivine compositions are small and impede any clearer distinction of pressures of equilibrium or any associated latitudinal variations.

Comparison of the calculated equilibrium and liquidus temperatures of olivine phenocrysts and microphenocrysts, using the compositions of quenched igneous glasses and bulk-rock samples, provides some indication of the pressures of crystallisation (chapter 4). The values of calculated equilibrium and liquidus temperatures for olivine phenocrysts and microphenocrysts in basalts from ridge segments unaffected by mantle plumes are similar at pressures of 4-6kbar, whereas these values for olivines in basalts from mantle plume-affected ridge segments approach equality at pressures of 2-4kbar. Therefore final olivine crystallisation in N-MORB occurred at oceanic mantle depths (4-6kbar) beneath ridge segments which yielded only N-MORB, relative to beneath Discovery- and Shona-influenced ridge segments where olivine crystallisation ceased at oceanic crustal depths (2-4kbar).

University of Cape Town

7.4 DISCUSSION

The nature and setting of crystallisation processes beneath ridge segments of the SMAR. The variations in the major- and selected trace-element compositions of the quenched igneous glasses and bulk-rock samples discussed in this chapter, as well as chapters 4 & 6, confirm the influence of crystallisation of plagioclase, olivine and clinopyroxene on the compositions of basalts recovered from the SMAR. The differences in major-element compositions of quenched igneous glass-bulk-rock sample pairs are consistent with variable accumulation of observed plagioclase, olivine and very minor clinopyroxene phenocrysts. The presence of large (>2.5mm), resorbed plagioclase phenocrysts, some having high anorthite content (An_{85-90}) or distinct compositional zoning, not in equilibrium with the host compositions, indicate open system crystallisation, incomplete mixing or rapid change in the physical

environment (i.e. decreasing pressure with rapid ascent of magmas) prior to eruption of significant numbers of basalts along the SMAR. The resorbed texture of significant proportions of olivine phenocrysts and rare clinopyroxene phenocrysts also support the above description of crystallisation beneath the SMAR.

Modelling of crystallisation of high-MgO quenched igneous glass compositions, high-MgO aphyric bulk-rock samples, and theoretical primary melt compositions yielded liquid-lines-of-descent at various pressures which qualitatively indicated the sequence and pressures of crystallisation. The major- and selected trace-element variations of the quenched igneous glass from the SMAR are consistent with initial crystallisation of olivine, followed by plagioclase and olivine crystallisation. Three-phase crystallisation of plagioclase, clinopyroxene and olivine is indicated in all these basalts by the trend of decreasing CaO content with decreasing MgO content, the decreasing CaO/Al_2O_3 ratios with decreasing Mg#'s, and the fairly constant Sc contents (40-50ppm in N-MORB and Shona-influenced MORB; 30-40ppm in Discovery-influenced MORB) with decreasing Mg#'s. The variable appearance of clinopyroxene as a liquidus phase, indicated by the above criteria, indicates crystallisation occurring at greater mean depths beneath ridge segments unaffected by the mantle plumes, while crystallisation beneath ridge segments affected by the Discovery or Shona mantle plume occurred predominantly at shallower depths.

The different methods of assessing the pressures of crystallisation beneath the SMAR all yield the same result. Crystallisation beneath the ridge segments unaffected by the mantle plumes occurred predominantly at pressures of 3-6kbar, therefore initiated within the oceanic mantle. Beneath ridge segments affected by the Discovery mantle plume, crystallisation occurred predominantly at 4-6kbar, north of the Falkland-Agulhas Fracture Zone, and 1atm-4kbar, south of the Falkland-Agulhas Fracture Zone. Crystallisation beneath the northern-most Shona-influenced ridge segments occurred over a pressure range of approximately 2-8kbar. The crystallisation beneath Shona-influenced ridge segments further south occurred at shallower depths of 1atm-3kbar.

Evaluation of the details of crystallisation beneath the SMAR in terms of previous studies and related work. The observed variations in the major- and trace-element compositions of quenched igneous glasses from the SMAR and ascribed to crystallisation have been reported

University of Cape Town

for basalts from a number of other regions. The increasing FeO concentrations with decreasing MgO content requires crystallisation of olivine (Frey *et al.*, 1993), while the decreasing Al_2O_3 concentrations with decreasing MgO content necessitate the segregation of plagioclase and the decreasing CaO concentrations with decreasing MgO content require clinopyroxene crystallisation (Frey *et al.*, 1993; Stakes *et al.*, 1984; Tormey *et al.*, 1987). The restricted range in the Sc concentrations of the quenched igneous glasses observed here and attributed to the presence of a significant clinopyroxene fraction (30-50%) in the liquidus assemblage concur with previous observations and proposed explanations (Frey *et al.*, 1993; le Roex *et al.*, 1996).

The assessment of the MgO concentrations of the quenched igneous glasses at which it can be concluded that clinopyroxene is present is also consistent with the conclusions reached in studies of MORB from other ridges. In the study of Michael & Cornell (1998) in which MORB from a global data-set were investigated, only basalts with a MgO concentration <8wt% were considered to be reliably saturated with clinopyroxene. In studies of MORB from the AMAR and FAMOUS Valleys on the northern MAR, le Roex *et al.* (1996) and Stakes *et al.* (1984) placed clinopyroxene in the liquidus assemblage in basalts with MgO concentrations <~8.3wt% and <~8.35wt%, respectively. Reynolds & Langmuir (1997) concluded that clinopyroxene is part of the liquidus assemblage in basalts, from south of the Kane fracture zone on the northern MAR, with MgO concentrations <8.3wt%. The conclusion reached in the current study that the compositional variations observed in MORB with MgO concentrations <8.3wt% are consistent with crystallisation involving clinopyroxene is therefore reasonable.

The dominance of plagioclase in the modal mineralogies of these basalts and the general absence of clinopyroxene phenocrysts are not uncommon features of MORB which contain compositional evidence of clinopyroxene crystallisation. This so-called "pyroxene paradox" have been observed in a number of studies (Batiza & Niu, 1992; le Roex *et al.*, 1996; Stakes *et al.*, 1984) and the proposed explanation is based on the contrast in the densities of the ferromagnesian minerals, i.e. olivine and clinopyroxene, relative to the density of plagioclase and that of the magma from which they formed. In general, olivine and clinopyroxene phenocrysts have densities higher than that of the magma, while plagioclase is less dense than the magma (Batiza & Niu, 1992). Therefore, as magmas ascend from the depth of crystallisation, olivine and especially clinopyroxene phenocrysts would sink and be segregated from the magmas, while plagioclase would float, stay suspended and become entrained in the ascending

University of Cape Town

magmas (Batiza & Niu, 1992; le Roex *et al.*, 1996; Stakes *et al.*, 1984). Therefore the observed modal mineralogy does not necessarily represent the cotectic proportions of the liquidus phases and the qualitative presence of a phase is petrogenetically more significant (Bryan, 1983; Stakes *et al.*, 1984). The rare occurrence of clinopyroxene in these MORB from the SMAR is therefore not a counter to the deduction from the compositional variations of the quenched igneous glasses for the involvement of clinopyroxene during crystallisation.

The general sequence of phases during the proposed crystallisation beneath the SMAR of olivine, followed by plagioclase and olivine, and then plagioclase, clinopyroxene and olivine is typical for MORB (Batiza & Niu, 1992; Bryan, 1983; Bryan & Dick, 1982; Fisk *et al.*, 1982; Frey *et al.*, 1993; Grove *et al.*, 1992; Langmuir *et al.*, 1992; le Roex *et al.*, 1996; Michael *et al.*, 1994; Reynolds & Langmuir, 1997; Shi, 1992; Shi, 1993; Stakes *et al.*, 1984; Yang *et al.*, 1996). The range in deduced, from the modelled liquid-lines-of-descent, and calculated pressures of crystallisation is also consistent with pressures of crystallisation from other ridges (Grove *et al.*, 1992; le Roex *et al.*, 1996; Michael & Cornell, 1998; Reynolds & Langmuir, 1997; Smith *et al.*, 1998) and the proposed role of magma flux in determining the primary depth of crystallisation beneath ridges (Michael & Cornell, 1998; Sinton & Detrick, 1992; Smith & Cann, 1993), as discussed below.

University of Cape Town

The deeper crystallisation, at oceanic mantle depths of 3-6kbar, beneath ridge segments unaffected by the Discovery or Shona mantle plumes is consistent with low magma flux, cold crust and upper mantle and a deeper brittle-ductile transition (Michael & Cornell, 1998). The thicker brittle cap at these ridge segments would result in the halt of the ascending magma at depth, before reaching a level of neutral buoyancy (Smith & Cann, 1993). The increasing magma flux and higher temperatures beneath the ridge segments affected by the Discovery and Shona mantle plumes would result in high-temperature isotherms at shallow levels, weaker crust, although the crust is substantially thicker than beneath ridge segments unaffected by mantle plumes, and mantle (Michael & Cornell, 1998), and the halt of ascending mantle at shallower, oceanic crustal levels of 1atm-3kbar, when a level of neutral buoyancy is reached (Smith & Cann, 1993). However, the thicker crust beneath these mantle plume-influenced ridge segments could result in deeper initiation of crystallisation in some instances, as observed especially beneath ridge segments from the northern section of the Shona anomaly, if there was a tendency for the ascending magma to pond at the density contrast between the crust and the mantle (Smith

& Cann, 1993).

Crystallisation, especially during the initial phase of olivine crystallisation, at depths within oceanic mantle beneath ridge segments is supported by studies of abyssal peridotites. It has been found that abyssal peridotites are not pure residues of mantle melting, but contain excess modal olivine (Dick, 1989; Niu, 1997; Niu, 1999; Niu *et al.*, Submitted). This excess modal olivine is proposed to be the result of crystallisation of olivine during ascend of cooling magmas through the upper oceanic mantle after segregation from the melting region (Niu, 1997; Niu, 1999) as a consequence of the expansion of the olivine phase field with decreasing pressure (Niu, 1997; Niu, 1999).

As discussed in chapter 5 & 6, geophysical and petrogenetic studies have found no evidence for the presence of long-lived, steady-state, shallow-level magma chambers beneath the segments of slower-spreading, low magma flux ridges such as the SMAR (Batiza *et al.*, 1988; Batiza & Niu, 1992; Batiza *et al.*, 1996; Detrick *et al.*, 1990; Michael & Cornell, 1998; Sinton & Detrick, 1992). In the terminology of Sinton & Detrick (1992), when ascending magma beneath these low flux ridge segments are halted, the "magma chambers" formed are dominated by the crystal mush zone and an eruptable magma lens is unlikely to exist in any steady-state sense. The dimensions and life-time of these bodies would be highly variable, due to the intermittent nature of the magma supply (Sinton & Detrick, 1992; Smith & Cann, 1993). The eruptions of basalt at slow-spreading ridges are closely linked to tectonic events and injections of fresh, primitive magmas from the mantle into the highly crystalline mush zone (Sinton & Detrick, 1992; Smith & Cann, 1993). The erupted magmas at ridges characterised by low magma supply therefore frequently include crystals from the slowly cooling mush zone and are highly phyric, with large phenocrysts out of equilibrium with the magma and showing signs of resorption (Sinton & Detrick, 1992).

The above discussion agrees with the proposed model of crystallisation beneath ridge segments of the SMAR unaffected by the mantle plumes, where crystallisation ~~occurred~~ at depths within the oceanic mantle (3-6kbar) and probably predominantly at the base of the lithosphere. The "magma chambers" are dominated by the highly crystalline mush zone and the absence of any significant melt lens. Intermittently, the arrival of a new batch of magma coupled with tectonic activity induce the formation of conduits through which magmas containing

University of Cape Town

xenocrysts incorporated from the mush zone, especially less-dense plagioclase crystals, ascend rapidly to shallow-levels where insignificant crystallisation occurs prior to eruption of the magmas. At ridge segments affected by the Discovery or Shona mantle plumes, crystallisation occurred predominantly at oceanic crustal depths (1atm-3kbar) due to the higher temperatures in the crust and lithosphere in these regions. Although the magma flux is higher than beneath the ridge segments unaffected by the mantle plumes, it is too low to sustain long-lived magma bodies, but the small batches of ascending magmas are able to form small, short-lived shallow-crustal magma chambers. These magma chambers are also predominantly composed of the mush zone, but melt lenses are present, although discontinuous and small. The combination of small magma volumes, longer residence time and slower cooling results in the magmas from these ridges attaining higher degrees of differentiation prior to eruption, relative to magmas from the ridge segments unaffected by the mantle plumes (Michael & Cornell, 1998; Sinton & Detrick, 1992; Smith & Cann, 1993).

University of Cape Town

CHAPTER 8: CONCLUSIONS

Preceding chapters have detailed the compositional characteristics of 271 basalts recovered from the SMAR between 40°-55°S, during cruise 9309 of the R/V Maurice Ewing in 1993. Radiogenic isotope (Douglass *et al.*, 1999) and noble gas (Moreira *et al.*, 1995) studies of subsets of these samples have been concluded, and the work presented in this thesis focussed on the major- and trace-element compositions of bulk-rock and quenched igneous-glass samples, as well as the petrography and mineralogy of constituent phenocryst phases. These data were used to classify and describe general variations in MORB compositions, investigate the major- and trace-element characteristics of MORB mantle source-regions beneath the SMAR, and define the melting and crystallisation processes active beneath these ridge segments.

Regional variations. The basalts investigated in this study are aphyric to sparsely phyric (<10-20% total phenocrysts) and dominated by large, resorbed or rounded and optically zoned plagioclase phenocrysts (≤20%, few samples ≤40%; An_{80-90}) frequently containing inclusions of quenched igneous glass. Less-abundant plagioclase microphenocrysts ($An_{\geq 60}$) are frequently skeletal and occur in basalts with low Mg#'s. Olivine is the second-most abundant phenocryst (≤3%) and occurs mainly as microphenocrysts (Fo_{82-87}, with Fo_{70-73} in low Mg# basalts). Large olivine phenocrysts (Fo_{88-89}) are less-abundant and frequently rounded or resorbed. Clinopyroxene and spinel occur as rare microphenocryst phases, and occasional sulphide blebs are also present.

The major-element compositions of bulk-rock samples and quenched igneous glasses of MORB recovered from the SMAR, classify the samples as predominantly olivine-normative tholeiitic basalts with a few exceptions classified as quartz-normative basaltic andesites. Their trace-element compositions range from incompatible trace-element depleted (Nb/Zr ≤0.03, Zr/Y ≤2.91, $(La/Sm)_N$ ≤0.79, K/Ti ≤0.14) to incompatible trace-element enriched (Nb/Zr ≤0.17, Zr/Y ≤6.88, $(La/Sm)_N$ ≤2.94, K/Ti ≤1.15). The basalts with enriched incompatible trace-element compositions are also enriched in radiogenic isotopes (Douglass *et al.*, 1999) and were recovered from ridge segments with anomalously shallow bathymetry associated with the influence of two proximal mantle plumes, Discovery and Shona. Compositional trajectories defined by incompatible trace-element ratios support mixing between ambient depleted MORB mantle and enriched material derived from these two, isotopically distinct mantle plumes.

University of Cape Town

Mantle-plume compositional characteristics. The radiogenic-isotope compositions of 66 basaltic glasses led Douglass *et al.* (1999) to classify the Discovery and Shona mantle plumes as carrying EM- and HIMU-type mantle end-member components, respectively. The trace-element compositional characters of neither have been well-documented (Kempe & Schilling, 1974; le Roex *et al.*, 1987) with most of the information coming from studies of a limited number of MORB from mantle plume-influenced ridge segments (Douglass *et al.*, 1995; le Roex *et al.*, 1987); one sample is available from the Discovery seamount (Kempe & Schilling, 1974; le Roex, unpublished data).

The extensive trace-element data for bulk-rock and quenched igneous-glass samples of basalts from the SMAR support the above classification of these mantle plumes. The co-variations of the data for Zr/Nb and La/Nb with Ba/Nb ratios of basalts recovered from the SMAR indicate that most of the Discovery-influenced MORB define a compositional trend from N-MORB towards the recognised compositions of some basalts from the Walvis Ridge, and Tristan da Cunha and Gough ocean islands. Most of the Shona-influenced MORB define a different trend from N-MORB towards the recognised compositions of basalts from the St. Helena, Bouvet and Marion ocean islands. Incompatible trace-element enriched basalts recovered from southern Discovery-influenced ridge segments have significantly lower Nb concentrations at constant Ba concentrations relative to other Discovery-influenced MORB. N-MORB in general also have low Nb concentrations at constant Ba concentrations, relative to compositions of "typical" N-MORB.

Subcontinental lithosphere in mantle source-regions beneath the SMAR. Some basalts from the SMAR, particularly Discovery-influenced MORB, have unusually low $^{206}Pb/^{204}Pb$, $^{143}Nd/^{144}Nd$ and high $^{87}Sr/^{86}Sr$ background ratios which Douglass *et al.* (1999) proposed are due to the compositional influence of subcontinental lithosphere present in the mantle source-regions of these basalts. In the present investigation, these basalts and most N-MORB, as alluded to above, were further found to have anomalously high Ba, and low Nb and Ta abundances, relative to other elements with similar compatibility, compared to compositions of "typical" N-MORB or incompatible trace-element enriched MORB.

These trace-element features necessitate the presence of <2.5% of subcontinental lithosphere in the mantle source-regions of these basalts, and further are indicative of a

University of Cape Town

subduction zone-derived component to this subcontinental material. This is consistent with the inferred composition of the subcontinental lithosphere beneath southern Africa (Sun & McDonough, 1989) which after thermal erosion by mantle plumes impacting underneath western Gondwana became dispersed in the ambient, upper oceanic asthenosphere during the opening of the South Atlantic.

This variously termed contamination or "pollution" of the ambient upper-oceanic mantle beneath the South Atlantic, as observed in and delineated by MORB and OIB, seems to correspond broadly with the latitudinal extent of the Dupal anomaly in the South Atlantic (Hart, 1984; Hart, 1988; Zindler & Hart, 1986). Where available, the radiogenic isotope and Ba/Nb data for MORB from approximately 15°-50°S allude to variable degrees of low-level "background" contamination of the ambient depleted mantle beneath the SMAR. This supports the possible division of the Dupal anomaly into two distinct entities: one shallow in origin and composed of material derived from the subcontinental lithosphere broadly dispersed within the upper-oceanic asthenosphere, sampled predominantly by MORB and early mantle plume-related oceanic volcanism; the other deep in origin and sampled mostly by present mantle plume magmatism, i.e. the Tristan/Gough mantle plume (Milner & le Roex, 1996; Peate *et al.*, 1999).

Douglass *et al.* (1999) found radiogenic isotope evidence of subcontinental lithosphere in the mantle source-regions of mantle plume-influenced MORB from the SMAR and proposed the presence of this material as discreet so-called "rafters". The incompatible trace-element data presented here extend the possible presence of material with subcontinental lithosphere affinities to mantle source-regions of most MORB recovered from the SMAR. However, the wider occurrence of this material might rather favour the presence of delaminated subcontinental lithosphere as dispersed residual heterogeneities not completely rehomogenised by convective stirring of the upper-oceanic mantle (after Rehkämper & Hofmann, 1997). Furthermore, although not specifically reported at the time, the incompatible trace-element data for bulk-rock MORB samples from the study of Humphris *et al.* (1985), at 32°-46°S on the SMAR, and le Roex *et al.* 1987), at 51°-54.5°S on the SMAR, have anomalous Ba/Nb ratios similar to the data for MORB from the presently studied section of the SMAR. Therefore, the signal of upper-mantle "pollution" is wide-spread along the SMAR and supports the above model for the presence of a low percentage of broadly dispersed material derived from delaminated subcontinental lithosphere beneath a large area of the South Atlantic.

University of Cape Town

Prior this study, samples with compositional characteristics presented as evidence for delaminated subcontinental lithosphere in the mantle source-regions of oceanic basalts were predominantly restricted to early products of mantle plumes (Mahoney *et al.*, 1995; Mahoney *et al.*, 1996; Milner & le Roex, 1996; Peate *et al.*, 1999) and, in one location at 39°-41°E on the SWIR, MORB associated with the influence of the Marion mantle plume (Hamelin & Allègre, 1985; le Roex *et al.*, 1989; Mahoney *et al.*, 1992). Rehkämper & Hofmann (1997) reported radiogenic isotope and trace-element results for 9 basalt glasses from the Central Indian and Carlsberg Ridges, which they interpreted to indicate the contamination of the upper-oceanic mantle beneath the Indian Ocean by small percentages of recycled, altered oceanic crust along with variable amounts of ancient pelagic sediment. Although the trace-element characteristics of MORB from the SMAR concur with the physical aspect of the model proposed by Rehkämper & Hofmann (1997) for occurrence of anomalous material in the upper-oceanic mantle beneath the Indian Ocean, Douglass *et al.* (1999) concluded that recycled, altered oceanic crust along with variable amounts of ancient pelagic sediment as contaminant beneath the SMAR can not produce the radiogenic isotope values observed.

Global and local trends observed in the compositions of MORB from the SMAR. Internal variations in the sub-sets of fractionation-corrected major-element data (Na_8-Fe_8) for N-MORB, Discovery-influenced MORB and Shona-influenced MORB conform respectively to the orientation of the global trend. Data for Shona-influenced MORB indicate deeper (≤23kbar) initiation of melting relative to data for N-MORB (~18±3kbar), but final depths of melting for these two groups are fairly constant (~13±2kbar). This is consistent with the origin of the global trend through variable temperatures of the upwelling mantle, with hotter, mantle plume-influenced upwelling mantle melting at greater initial depths relative to normal, ambient mantle (Kinzler, 1997; Kinzler & Grove, 1993; Klein & Langmuir, 1987; Klein & Langmuir, 1989; Langmuir *et al.*, 1992). The greater initial depth of melting results generally in greater mean extents of melting beneath Shona-influenced ridge segments (16-19%), compared to melting beneath ridge segments unaffected by mantle plumes (14-18%), and yield thicker crust indicated by the shallower bathymetry of these ridge segments, although the rate of melting is fairly constant for these two groups of MORB (2-4%/kbar).

However, the data for Discovery mantle plume-influenced MORB indicate initiation of melting ranging towards shallower depths (13-20kbar) relative to N-MORB (~18±3kbar), and

University of Cape Town

with more varied final pressures of melting (8-15kbar). Some anomalous samples yielded extremely low values of 5-7kbar for the initial pressures of melting, and anomalously low final pressures of melting, at 4-5kbar. The mean extents of melting beneath the Discovery-influenced ridge segments (14-17%) are in general similar to that beneath the ridge segments unaffected by mantle plumes, but the samples derived from shallow mantle melting also experienced melting to slightly lower extents (~12%). The rates of melting beneath most of the Discovery-influenced ridge segments are similar to rates beneath Shona-influenced ridge segments and ridge segments unaffected by mantle plumes (2-4%/kbar). However, in the regions of anomalously shallow mantle melting, the calculated rates of the melting are exceptionally high (>5%/kbar). Although the broad orientation of the Na_8-Fe_8 data for Discovery-influenced MORB correlates with the global trend, the higher Na_8-lower Fe_8 values and therefore lower initial pressures and mean extents of melting calculated for these basalts relative to N-MORB are in conflict with the generally accepted origin of the global trend, and the recovery of these mantle plume-influenced basalts from ridge segments with shallow bathymetry, and therefore thick oceanic crust necessitating the generation of high volumes of melt in these regions. The mantle source-regions beneath Discovery-influenced ridge segments are interpreted to be veined with pyroxenitic material and the effect of melting of these veins on the major-element compositions of the erupted basalts could account for the anomalous depths and extents of melting calculated for Discovery-influenced MORB.

University of Cape Town

A similar contradiction between calculated melting parameters, using fractionation-corrected major-element compositions, has been observed for basalts recovered from the Galapagos spreading centre (Langmuir *et al.*, 1992). However, no other plausible explanation has previously been proposed to account for these observed anomalous values of derived melting parameters for mantle plume-influenced MORB.

Within each sub-set of N-MORB, Discovery-influenced MORB and Shona-influenced MORB, groups of individual basalt compositions define local trends orthogonal to the global trend. The origin of these local trends and the reason for their predominant occurrence in fractionation-corrected major-element data of MORB from slow-spreading ridges are still unresolved (Klein & Langmuir, 1989; Langmuir *et al.*, 1992; Niu, 1997; Niu & Batiza, 1994). Calculated major-element trajectories of different mantle melting scenarios (i.e. various initial pressures of melting, rates of melting, extents of melting, starting compositions) are orientated

at significantly steeper angles relative to the observed local trends. The possibility that the local trends are defined by continuously sampled instantaneous melts from different levels in melting columns (Klein & Langmuir, 1989) is therefore not supported by the data from the SMAR. Neither do the expanded fractionation-corrected major- (Ti_8, Ca_8) and trace-element (Ni_8) data for the MORB from the SMAR support the proposed role of a net melting reaction in which clinopyroxene and orthopyroxene are progressively dissolved and olivine crystallised during melt transport through the mantle (Niu, 1997; Niu & Batiza, 1994).

Trends defined by the calculated major-element compositions of modelled accumulated melts crystallised to 8wt% MgO at pressure ranging between 1atm-8kbar are orientated approximately parallel to the local trends observed in the data for MORB from the SMAR. Unlike the data for MORB from the FAMOUS region (Langmuir *et al.*, 1992), the concentrations of Sr in the basalts from the SMAR which define local trends remain fairly constant at variable $Na_{8.0}$ and $Fe_{8.0}$. The buffered Sr concentrations in basalts over significant ranges in $Na_{8.0}$ and $Fe_{8.0}$ therefore indicate a considerable role for plagioclase crystallisation in the formation of the observed local trends in the fractionation-corrected major-element data for MORB from the SMAR. Evaluation of the different proposed origins for local trends in the global data-set agrees with the work of Grove *et al.* (1992) and indicates that crystallisation of olivine, plagioclase and clinopyroxene at pressures between 1atm and at least 6kbar is the only process which can presently account for these trends in the data for MORB from the SMAR.

Pyroxenite veins in mantle source-regions. Some Discovery-influenced basalts, recovered from near the ends of ridge segments terminated by the Falkland-Agulhas Fracture Zone (at ~47.5°S) and another, unnamed but significantly off-set transform (at ~48.4°S), have high $^{87}Sr/^{86}Sr$ ratios (0.705093-0.705878) and low $^{143}Nd/^{144}Nd$ ratios (0.512365-0.512567), and were viewed by Douglass *et al.* (1999) as carrying the strongest signal of the compositional influence of the Discovery mantle plume. These samples also have anomalous trace-element compositions (low Sc concentrations ≥22.2ppm & high $(Sm/Yb)_N$ = 1.73-2.83, due mainly to low Yb concentrations of ≥1.37ppm at Mg# of 63-65) which are not only exceptional compared with other basalts from the SMAR, but also relative to data for other MORB from mid-ocean ridges in the Atlantic Ocean (e.g. the Southwest Indian Ridge, le Roex *et al.*, 1983; le Roex *et al.*, 1989, Southern Mid-Atlantic Ridge, le Roex *et al.*, 1987, and Northern Mid-Atlantic Ridge, le Roex *et al.*, 1996). These trace-element compositions necessitate the presence of residual

University of Cape Town

garnet at some stage during the mantle melting from which these basalts were derived.

The fractionation-corrected major-element data for these basalts from dredge 25, 6 & 7 ($Si_{8.0}/Fe_{8.0}$: 6.2-7.1) yielded initial pressures of melting of 5-7kbar, which are exceptionally low compared to the rest of the basalts from the SMAR ($Si_{8.0}/Fe_{8.0}$: 4.4-6.1; initial pressures of melting: 13-20kbar), and the generally accepted range for MORB generation (20-25kbar) (Kinzler, 1997; Kinzler & Grove, 1992; Kinzler & Grove, 1993; Niu & Batiza, 1991). The mean extents of melting calculated from the fractionation-corrected major-element compositions ($Na_{8.0}$: 2.6-3.3; $Ca_{8.0}/Al_{8.0}$: 0.55-0.73) are 10.9-17.1% for the genesis of the basalts from dredge 25, 6 & 7, which are not exceptional when compared to that for other MORB from the SMAR (12-19%), and extend towards the lower end of the accepted range (6-20%) of MORB melting in general (Kinzler, 1997; Kinzler & Grove, 1992; Kinzler & Grove, 1993; Niu & Batiza, 1991; Walter *et al.*, 1995). Major- and trace-element indicators of initial pressures of melting in these basalts are therefore in apparent conflict, in that residual garnet is required by the trace-element variations and it is only stable in lherzolite at pressures above 28-30kbar (Kinzler, 1997; Robinson & Wood, 1998) whereas initial pressures of melting calculated from the fractionation-corrected major-element compositions are significantly lower at 5-7kbar.

To address this dichotomy, a model is proposed wherein these anomalous basalts were primarily derived by melting of pyroxenite veins reflecting frozen small-degree melts (2-3%), associated with the upwelling Discovery mantle plume, which formed within the garnet-lherzolite stability-field. These pyroxenite veins therefore carried the radiogenic-isotope values of the Discovery mantle plume, and trace-element compositions reflecting the presence of residual garnet during melting. Mantle flow delivered the pyroxenite-veined mantle to proximal ridge segments where it became entrained in the general sub-ridge upwelling. Due to subdued upwelling and the suppressed thermal regime beneath the sections of ridge segments in the vicinity of fracture zones and off-set transforms, mantle melting in these regions occurred at shallow-levels over restricted pressure intervals. This melting preferentially consumed the pyroxenite veins, due to their low-temperature solidus relative to ambient spinel-lherzolitic mantle, and this tectonic setting favoured ineffective melt-focussing towards the central eruptive zones of the ridge segments, with consequent little homogenisation with melts derived from the ambient spinel-lherzolitic mantle, leading to the eruption of magmas with exceptionally undiluted pyroxenite-derived compositions. These magmas then contain major-element

University of Cape Town

compositions indicative of low initial pressures of melting, but anomalous radiogenic-isotope and trace-element characteristics inherited from pyroxenite veins derived from melts formed in the presence of residual garnet at depth in the mantle plume-upwelling regime.

Although the concept of "variably-veined" mantle source-regions have previously been proposed for mantle plume-influenced MORB (e.g. le Roex *et al.*, 1987 for Shona-influenced MORB from 51°-54.5°S on the SMAR; le Roex *et al.*, 1983 for Bouvet-influenced MORB from between the Bouvet Triple Junction and 11°E on the SWIR; Niu *et al.*, 1999 for enriched basalts from the East Pacific Rise), the above radiogenic-isotope, major- and trace-element data for basalts from dredges 25, 6 & 7 are the best evidence yet presented for the presence of separate, vein-like domains of material derived from a proximal mantle plume in mantle source-regions beneath mid-ocean ridges. The presence of pyroxenite veins in MORB mantle source-regions and a role of residual garnet during MORB melting have recently received attention (Hirschmann & Stolper, 1996; and references therein), but previously proposed origins of pyroxenite veins in MORB mantle source-regions can not successfully encompass and account for the wide spectrum of compositional and tectonic variables presented in this study.

Previously proposed models to account for residual garnet during MORB melting either placed the onset of melting beneath mid-ocean ridges at great depth in the garnet-lherzolite stability-field (LaTourrette *et al.*, 1993; Salters, 1996; Salters *et al.*, 1994; Salters & Hart, 1989; Salters & Hart, 1991), which would produce significantly thicker oceanic crust than observed (Hirschmann & Stolper, 1996), or required the presence of garnet-pyroxenite veins in MORB mantle source-regions (Hirschmann & Stolper, 1996), although none of the mechanisms proposed by Hirschmann & Stolper (1996) for the formation of these veins are applicable for the SMAR. The two-stage model of melting proposed in this study accounts for both the origin of pyroxenite veins in MORB mantle source-regions and the compositional signal of residual garnet during melting observed in these basalts, without appealing to extraordinary processes or parameters of MORB petrogenesis.

High pressures of crystallisation beneath the SMAR. Qualitative modelling of observed variations of major-element and selected trace-element data for MORB from the SMAR indicates significant crystallisation involving olivine, plagioclase and clinopyroxene at variable pressures. The compositions of theoretical primary melt compositions (Kinzler, 1997) require

University of Cape Town

30-40% crystallisation, of initially only olivine and later three-phase crystallisation of olivine, plagioclase and clinopyroxene, at pressures of 6-8kbar to attain compositions similar to basalts with high-MgO concentrations recovered from the SMAR.

The general decreasing trends in CaO concentrations and CaO/Al_2O_3 ratios with decreasing MgO concentrations and Mg#'s, and the relatively constant Sc concentrations with decreasing Mg#'s of basalts from the SMAR necessitate the presence of clinopyroxene on the liquidus during crystallisation beneath the SMAR, although clinopyroxene is rarely observed as a phenocryst phase. The pressures of crystallisation obtained from semi-quantitative comparisons between modelled crystallisation trends and observed variations in basalt compositions, and quantitative methods (Grove *et al.*, 1992; Michael & Cornell, 1998) all agree, and indicate relatively high pressures of crystallisation beneath the SMAR. Basalts recovered from ridge segments unaffected by mantle plumes experienced crystallisation predominantly at pressures of 3-6kbar. Beneath ridge segments affected by the Discovery mantle plume north of the Falkland-Agulhas Fracture Zone (at ~47.5°S), crystallisation occurred mainly at 4-6kbar, whereas south of this fracture zone crystallisation occurred at 1atm-4kbar beneath Discovery-influenced ridge segments. Basalts recovered from the northern-most Shona-influenced ridge segments experienced crystallisation at 2-8kbar, while further south Shona-influenced MORB underwent crystallisation at 1atm-3kbar.

The high calculated pressures of crystallisation beneath the SMAR agree with recent studies by Michael & Cornell (1998) of global variations of crystallisation pressures with spreading rate, and Grove *et al.* (1992) of localised regions of the northern MAR and EPR. The calculated high pressures of crystallisation for N-MORB and some mantle plume-influenced MORB agree with low magma supply beneath these slow-spreading ridge segments and the absence of long-lived, shallow, sub-axial magma chambers. Whereas the calculated pressures of crystallisation ranging to lower pressures beneath mantle plume-influenced ridge segments are consistent with slightly higher, but variable, magma supply from the hotter upwelling mantle below and the possible occurrence of transient magma bodies at shallower levels beneath the ridge axes. This comprehensive study of pressures of crystallisation beneath a slow-spreading mid-ocean ridge further confirms the contrast with faster spreading ridges, e.g. the EPR, where crystallisation occurs predominantly at low pressures in long-lived axial magma chambers (Michael & Cornell, 1998).

University of Cape Town

Summary. The ambient depleted MORB mantle beneath the South Atlantic have experienced at least two modes of compositional modification, prior to the eruption of the MORB recovered from the SMAR in this study. During the breakup of western Gondwana and the opening of the South Atlantic, mantle plumes such as Tristan da Cunha/Gough, Discovery and Shona thermally eroded small-degrees of subcontinental lithosphere, with compositions containing subductions-zone imprints, from beneath what is now southern Africa and subsequently this material became widely dispersed in the ambient upper-oceanic mantle. During MORB melting beneath the SMAR, only low proportions of the final melts are derived from this volumetrically small component. However, during MORB melting beneath mantle plume-influenced ridge segments, slightly higher proportions of the final magmas are being drawn from this material derived from delaminated subcontinental lithosphere. Secondly, material derived from the Discovery and Shona mantle plumes, respectively, variably infiltrated ambient upper-oceanic mantle which later became entrained in upwelling and MORB melting beneath proximal ridge segments, resulting in erupted MORB along the SMAR with compositions spanning a continuum from depleted to variably enriched in radiogenic-isotope ratios and incompatible trace-element abundances.

The nature of the material derived from the Discovery mantle plume is in the form of pyroxenite veins formed from frozen, small-degree melts which infiltrated the surrounding lherzolitic mantle after forming in the upwelling beneath the mantle plume. A significant proportion of these small-degree melts formed within the garnet-stability field. In this manner, variably-veined mantle formed, which, after subsequent mantle flow, became entrained in the general upwelling and melting beneath proximal ridge segments and the erupted basalts at these ridge segments are variable mixtures of melts derived from these pyroxenite veins and the ambient spinel-lherzolite mantle. Basalts erupted near the ends of some ridge segments have compositions dominated by the melts derived from pyroxenite veins, and carry the strongest radiogenic-isotope signals of the Discovery composition and preserve the trace-element compositions of the pyroxenite veins which were characteristically affected by the presence of residual garnet during the formation of the small-degree melts which formed them.

Crystallisation beneath the SMAR involved olivine, plagioclase and clinopyroxene in the liquidus assemblage at some stage of the process, although clinopyroxene is rarely presently as a phenocryst phase in the erupted basalts and occurs as scarce rounded remnant grains in some

University of Cape Town

samples. Beneath ridge segments unaffected by the two mantle plumes, crystallisation occurred predominantly at pressures of 3-6kbar, before the magma rapidly ascended and erupted without significant residence or crystallisation at shallow-levels beneath the ridge axis. Beneath northern Discovery-influenced ridge segments, which erupted depleted and enriched basalts, not containing the strongest Discovery-influence, crystallisation occurred at 4-6kbar, whereas beneath southern Discovery-influenced ridge segments, which erupted only strongly mantle plume-influenced basalts, crystallisation occurred at 1atm-4kbar. Except for a few samples from the northern extreme of the Shona-influenced ridge segments which experienced crystallisation at 2-8kbar, Shona-influenced MORB experienced crystallisation at 1atm-3kbar. Therefore, beneath the ridge segments most-affected by the Discovery and Shona mantle plumes respectively, magmas experienced crystallisation at shallow-levels, possibly in transient magma chambers. Otherwise the low-magma supply beneath the SMAR, linked to the slow-spreading rate of this mid-ocean ridge, resulted in crystallisation predominantly at depths >4kbar.

University of Cape Town

REFERENCES

Aharonov E., Whitehead J. A., Kelemen P. B., & Spiegelman M. (1995) Channeling instability of upwelling melt in the mantle. *Journal of Geophysical Research* **100**, 20433-20450.

Albee A. L. & Ray L. (1970) Correction factors for electron probe microanalyses of silicates, oxides, carbonates, phosphates and sulphates. *Analytical Chemistry* **42**, 1408-1414.

Ariskin A. A., Frenkel M. Y., Barmina G. S., & Nielsen R. L. (1993) Comagmat: A FORTRAN program to model magma differentiation processes. *Computers & Geosciences* **19**, 1155-1170.

Asimow P. D. (1999) A model that reconciles major- and trace-element data from abyssal peridotites. *Earth and Planetary Science Letters* **169**, 303-319.

Asimow P. D., Hirschmann M. M., Ghiorso M. S., O'Hara M. J., & Stolper E. M. (1995a) The effects of pressure-induced solid-solid phase transitions on decompression melting of the mantle. *Geochimica et Cosmochimica Acta* **59**, 4489-4506.

Asimow P. D., Hirschmann M. M., Ghiorso M. S., & Stolper E. M. (1995b) Isentropic melting processes in the mantle (abstract). In *Plume2*, Vol. 3 (ed. D. L. Anderson, S. R. Hart, and A. W. Hofmann), pp. 12-14. Alfred-Wegener-Stiftung.

Asimow P. D. & Stolper E. M. (1999) Steady-state mantle-melt interactions in one dimension: I. Equilibrium transport and melt focussing. *Journal of Petrology* **40**, 475-494.

Baker M. B., Hirschmann M. M., Ghiorso M. S., & Stolper E. M. (1995) Compositions of near-solidus peridotite melts from experiments and thermodynamic calculations. *Nature* **375**, 308-311.

Baker M. B., Hirschmann M. M., Wasylenki L. E., Stolper E. M., & Ghiorso M. S. (1996) Reply to Falloon *et al.*, 1996. *Nature* **381**, 286.

Baker M. B. & Stolper E. M. (1994) Determining the composition of high-pressure mantle melts using diamond aggregates. *Geochimica et Cosmochimica Acta* **58**, 2811-2827.

Batiza R., Melson W. G., & O'Hearn T. (1988) Simple magma supply geometry inferred beneath a segment of the Mid-Atlantic Ridge. *Nature* **335**, 428-431.

Batiza R. & Niu Y. (1992) Petrology and magma chamber processes at the East Pacific Rise ~9°30'N. *Journal of Geophysical Research* **97**, 6779-6797.

Batiza R., Niu Y., Karsten J. L., Boger W., Potts E., Norby L., & Butler R. (1996) Steady and non-steady state magma chambers below the East Pacific Rise. *Geophysical Research Letters* **23**, 221-224.

Bence A. E. & Albee A. L. (1968) Empirical correction factor for the electron microanalysis of silicates and oxides. *Journal of Geology* **76**, 382-403.

Bender J. F., Langmuir C. H., & Hanson G. N. (1984) Petrogenesis of basalt glasses from the Tamayo Region, East Pacific Rise. *Journal of Petrology* **25**, 213-254.

Bourdon B., Zindler A., Elliot T., & Langmuir C. H. (1996) Constraints on mantle melting at mid-ocean ridges from global ^{238}U-^{230}Th disequilibrium data. *Nature* **384**, 231-235.

Brodholt J. P. & Batiza R. (1989) Global systematics of unaveraged mid-ocean ridge basalt compositions: Comment on "Global correlations of ocean ridge basalt chemistry with axial depth and crustal thickness" by E. M. Klein and C. H. Langmuir. *Journal of Geophysical Research* **94**, 4231-4239.

Bryan W. B. (1983) Systematics of modal phenocryst assemblages in submarine basalts: Petrologic implications. *Contributions to Mineralogy and Petrology* **83**, 62-74.

Bryan W. B. & Dick H. J. B. (1982) Contrasted abyssal basalt liquidus trends: evidence for mantle major element heterogeneity. *Earth and Planetary Science Letters* **58**, 15-26.

Cannat M. & Seyler M. (1995) Transform tectonics, metamorphic plagioclase and amphibolization in ultramafic rocks of the Vema transform fault (Atlantic Ocean). *Earth and Planetary Science Letters* **133**, 283-298.

Castillo P. (1988) The Dupal anomaly as a trace of the upwelling lower mantle. *Nature* **336**, 667-670.

Cohen R. S. & O'Nions R. K. (1982) Identification of recycled continental material in the mantle from Sr, Nd and Pb isotope investigations. *Earth and Planetary Science Letters* **61**, 73-84.

Cordery M. J. & Phipps Morgan J. (1993) Convection and melting at mid-ocean ridges. *Journal of Geophysical Research* **98**, 19477-19503.

Danyushevsky L. V., Sobolev A. V., & Dmitriev L. V. (1996) Estimation of the pressure of crystallization and H_2O content of MORB and BABB glasses: calibration of an empirical technique. *Mineralogy and Petrology* **57**, 185-204.

Detrick R. S., Mutter J. C., Buhl P., & Kim I. I. (1990) No evidence from multichannel reflection data for a crustal magma chamber in the MARK area on the Mid-Atlantic Ridge. *Nature* **347**, 61-64.

Devey C. W., Garbe-Schönberg C.-D., Stoffers P., Chauvel C., & Mertz D. F. (1994) Geochemical effects of

University of Oslo Library

dynamic melting beneath ridges: Reconciling major and trace element variations in Kolbeinsey (and global) mid-ocean ridge basalts. *Journal of Geophysical Research* **99**, 9077-9095.

Dick H. J. B. (1989) Abyssal peridotites, very slow spreading ridges and ocean ridge magmatism. In *Magmatism in the Ocean Basins*, Vol. 42 (ed. A. D. Saunders and M. J. Norry), pp. 71-105. Geological Society Special Publications.

Dick H. J. B., Fisher R. L., & Bryan W. B. (1984) Mineralogic variability of the uppermost mantle along mid-ocean ridges. *Earth and Planetary Science Letters* **69**, 88-106.

Dickin A. P. (1995) *Radiogenic isotope geology*. Cambridge University Press.

Douglass J. & Schilling J.-G. (1998) New trace element analyses of the Southern Mid-Atlantic Ridge (3-46°S). (abstract). *Eos Transactions of the American Geophysical Union Fall Meeting Supplement* **79**, F943.

Douglass J., Schilling J.-G., & Fontignie D. (1999) Plume-ridge interactions of the Discovery and Shona mantle plumes with the southern Mid-Atlantic Ridge (40°-55°S). *Journal of Geophysical Research* **104**, 2941-2962.

Douglass J., Schilling J.-G., & Kingsley R. H. (1995) Influence of the Discovery and Shona mantle plumes on the southern Mid-Atlantic Ridge: rare earth evidence. *Geophysical Research Letters* **22**, 2893-2896.

Droop G. T. R. (1987) A general equation for estimating Fe^{3+} concentrations in ferromagnesian silicates and oxides from microprobe analyses, using stoichiometric criteria. *Mineralogical Magazine* **51**, 431-435.

Duncan A. R., Erlank A. J., & Betton P. J. (1984) Appendix 1: Analytical techniques and database descriptions. In *Petrogenesis of the volcanic rocks of the Karoo Province*, Vol. 13 (ed. A. J. Erlank), pp. 389-395. The Geological Society of South Africa.

Dunn T. & Sen C. (1994) Mineral/matrix partition coefficients for orthopyroxene, plagioclase, and olivine in basaltic to andesitic systems: A combined analytical and experimental study. *Geochimica et Cosmochimica Acta* **58**, 717-733.

Elthon D. (1989) Pressure of origin of primary mid-ocean ridge basalts. In *Magmatism in the Ocean Basins*, Vol. 42 (ed. A. D. Saunders and M. J. Norry), pp. 125-136. Geological Society Special Publication.

Fisk M. R., Bence A. E., & Schilling J.-G. (1982) Major element chemistry of Galápagos Rift Zone magmas and their phenocrysts. *Earth and Planetary Science Letters* **61**, 171-189.

Fontignie D. & Schilling J.-G. (1996) Mantle heterogeneities beneath the South Atlantic: a Nd-Sr-Pb isotope study along the Mid-Atlantic Ridge (3°S-46°S). *Earth and Planetary Science Letters* **142**, 209-221.

Frey F. A. (1980) The origin of pyroxenites and garnet pyroxenites from Salt Lake crater, Oahu, Hawaii: Trace element evidence. *American Journal of Science* **280-A**, 427-447.

Frey F. A., Walker N., Stakes D., Hart S. R., & Nielsen R. (1993) Geochemical characteristics of basaltic glasses from the AMAR and FAMOUS Axial Valleys, Mid-Atlantic Ridge (36°-37°N): Petrogenetic implications. *Earth and Planetary Science Letters* **115**, 117-136.

Fujii T. (1989) Genesis of mid-ocean ridge basalts. In *Magmatism in the Ocean Basins*, Vol. 42 (ed. A. D. Saunders and M. J. Norry), pp. 137-146. Geological Society Special Publication.

Gast P. W. (1968) Trace element fractionation and the origin of tholeiitic and alkaline magma types. *Geochimica et Cosmochimica Acta* **32**, 1057-1086.

Ghiorso M. S. & Carmichael I. S. E. (1980) A regular solution model for met-aluminous silicate liquids: application to geothermometry, immiscibility, and source regions of basic magmas. *Contributions to Mineralogy and Petrology* **71**, 323-342.

Ghiorso M. S., Carmichael I. S. E., Rivers M. L., & Sack R. O. (1983) The Gibbs Free Energy of mixing of natural silicate liquids; an expanded regular solution approximation for the calculation of magmatic intensive variables. *Contributions to Mineralogy and Petrology* **84**, 107-145.

Ghiorso M. S., Hirschmann M. M., & Sack R. O. (1994) New software models thermodynamics of magmatic systems. *Eos Transactions of the American Geophysical Union* **75**(49), 571, 575, 576.

Ghiorso M. S. & Sack R. O. (1995) Chemical mass transfer in magmatic processes IV. A revised and internally consistent thermodynamic model for the interpolation and extrapolation of liquid-solid equilibria in magmatic systems at elevated temperatures and pressures. *Contributions to Mineralogy and Petrology* **119**, 197-212.

Grove T. L., Kinzler R. J., & Bryan W. B. (1990) Natural and experimental phase relations of lavas from Serocki Volcano. In *Proceedings of the Ocean Drilling Program, Scientific Results*, Vol. 106/109 (ed. R. Detrick, J. Honnorez, W. B. Bryan, T. Juteau, and e. al.), pp. 9-17. Ocean Drilling Program.

Grove T. L., Kinzler R. J., & Bryan W. B. (1992) Fractionation of mid-ocean ridge basalts (MORB). *American Geophysical Union Geophysical Monograph* **71**, 281-310.

Grove T. L., Kinzler R. J., & Gaetani G. A. (1994) Using constraints from experimental petrology studies to model mantle melting processes under anhydrous and hydrous conditions (abstract). *Mineralogical Magazine* **58A**, 354-355.

Grunow A., Hanson R., & Wilson T. (1996) Were aspects of Pan-African deformation linked to Iapetus opening? *Geology* **24**, 1063-1066.

Hamelin B. & Allègre C. J. (1985) Large-scale regional units in the depleted upper mantle revealed by an isotope study of the South-West Indian Ridge. *Nature* **315**, 196-199.

Hanan B. B., Kingsley R. H., & Schilling J.-G. (1986) Pb isotope evidence in the South Atlantic for migrating ridge-hotspot interaction. *Nature* **322**, 137-144.

Hart S. R. (1984) A large-scale isotope anomaly in the Southern Hemisphere mantle. *Nature* **309**, 753-757.

Hart S. R. (1988) Heterogeneous mantle domains: signatures, genesis and mixing chronologies. *Earth and Planetary Science Letters* **90**, 273-296.

Hart S. R. & Dunn T. (1993) Experimental cpx/melt partitioning of 24 trace elements. *Contributions to Mineralogy and Petrology* **113**, 1-8.

Hartnady C. J. H. & le Roex A. P. (1985) Southern ocean hotspot tracks and the Cenozoic absolute motion of the African, Antarctic and South American plates. *Earth and Planetary Science Letters* **75**, 245-257.

Hawkesworth C. J., Kempton P. D., Mattey D. P., Palacz Z. A., Rogers N. W., & van Calsteren P. W. C. (1989) Intra-mantle fractionation vs. lithosphere recycling: Evidence from sub-continental mantle. In *Crust/Mantle Recycling at Convergence Zones* (ed. S. R. Hart and L. Gulen), pp. 227-237. Kluwer Acad.

Hawkesworth C. J., Mantovani M. S. M., Taylor P. N., & Palacz Z. (1986) Evidence from the Parana of south Brazil for a continental contribution to Dupal basalts. *Nature* **322**, 356-359.

Hékinian R., Bideau D., Hébert R., & Niu Y. (1995) Magmatism in the Garrett transform fault (East Pacific Rise near 13°27'S). *Journal of Geophysical Research* **100**, 10163-10185.

Hirschmann M. M. (1996) Reading garnet's signature. *Nature* **384**, 215-217.

Hirschmann M. M., Asimow P. D., Ghiorso M. S., & Stolper E. M. (1999a) Calculation of peridotite partial melting from thermodynamic models of minerals and melts. III. Controls on isobaric melt production and the effect of water on melt production. *Journal of Petrology* **40**, 831-851.

Hirschmann M. M., Baker M. B., & Stolper E. M. (1995) Partial melting of mantle pyroxenite (abstract). *Eos Transactions of the American Geophysical Union Fall Meeting Supplement* **76**, F696.

Hirschmann M. M., Ghiorso M. S., & Stolper E. M. (1999b) Calculation of peridotite partial melting from thermodynamic models of minerals and melts. II. Isobaric variations in melts near the solidus and owing to variable source composition. *Journal of Petrology* **40**, 297-313.

Hirschmann M. M., Ghiorso M. S., Wasylenki L. E., Asimow P. D., & Stolper E. M. (1998) Calculation of peridotite partial melting from thermodynamic models of minerals and melts. I. Review of methods and comparison with experiments. *Journal of Petrology* **39**, 1091-1115.

Hirschmann M. M. & Stolper E. M. (1996) A possible role for garnet pyroxenite in the origin of the "garnet signature" in MORB. *Contributions to Mineralogy and Petrology* **124**, 185-208.

Hirth G. & Kohlstedt D. L. (1995) Experimental constraints on the dynamics of the partially molten upper mantle: deformation in the diffusion creep regime. *Journal of Geophysical Research* **100**, 1981-2001.

Hofmann A. W. (1988) Chemical differentiation of the Earth: the relationship between mantle, continental crust, and oceanic crust. *Earth and Planetary Science Letters* **90**, 297-314.

Hofmann A. W. (1997) Mantle geochemistry: the message from oceanic volcanism. *Nature* **385**, 219-229.

Hofmann A. W., Jochum K. P., Seufert M., & White W. M. (1986) Nb and Pb in oceanic basalts: new constraints on mantle evolution. *Earth and Planetary Science Letters* **79**, 33-45.

Humphris S. E. & Thompson G. (1983) Geochemistry of rare earth elements in basalts from the Walvis Ridge: implications for its origin and evolution. *Earth and Planetary Science Letters* **66**, 223-242.

Humphris S. E., Thompson G., Schilling J.-G., & Kingsley R. H. (1985) Petrological and geochemical variations along the Mid-Atlantic Ridge between 46°S and 32°S: Influence of the Tristan da Cunha mantle plume. *Geochimica et Cosmochimica Acta* **49**, 1445-1464.

Iwamori H., McKenzie D., & Takahashi E. (1995) Melt generation by isentropic mantle upwelling. *Earth and Planetary Science Letters* **134**, 253-266.

Jeffries T. E., Perkins W. T., & Pearce N. J. G. (1995) Measurements of trace elements in basalts and their phenocrysts by laser probe microanalysis inductively coupled plasma mass spectrometry (LPMA-ICP-MS). *Chemical Geology* **121**, 131-144.

Johnson K. T. M. & Dick H. J. B. (1992) Open system melting and temporal and spatial variation of peridotite and basalt at the Atlantis II fracture zone. *Journal of Geophysical Research* **97**, 9219-9241.

Johnson K. T. M., Dick H. J. B., & Shimizu N. (1990) Melting in the oceanic mantle: an ion probe study of diopsides in abyssal peridotites. *Journal of Geophysical Research* **95**, 2661-2678.

Kamenetsky V. S., Eggins S. M., Crawford A. J., Green D. H., Gasparon M., & Falloon T. J. (1998) Calcic melt inclusions in primitive olivine at 43°N MAR: evidence for melt-rock reaction/melting involving clinopyroxene-rich lithologies during MORB generation. *Earth and Planetary Science Letters* **160**, 115-

University of Cape Town

132.

Kelemen P. B. & Aharonov E. (1998) Periodic formation of magma fractures and generation of layered gabbros in the lower crust beneath oceanic spreading ridges. In *Faulting and Magmatism at Mid-Ocean Ridges*, Vol. 106 (ed. W. R. Buck, P. T. Delaney, K. J. A., and Y. Lagabrielle), pp. 267-290. American Geophysical Union.

Kelemen P. B., Hirth G., Shimizu N., Spiegelman M., & Dick H. J. B. (1997a) A review of melt migration processes in the adiabatically upwelling mantle beneath oceanic spreading ridges. *Philosophical Transactions of the Royal Society of London* **355**, 283-318.

Kelemen P. B., Koga K., & Shimizu N. (1997b) Geochemistry of gabbro sills in the crust-mantle transition zone of the Oman ophiolite: implications for the origin of the oceanic lower crust. *Earth and Planetary Science Letters* **146**, 475-488.

Kelemen P. B., Shimizu N., & Dunn T. (1993) Relative depletion of niobium in some arc magmas and the continental crust: partitioning of K, Nb, La and Ce during melt/rock reaction in the upper mantle. *Earth and Planetary Science Letters* **120**, 111-134.

Kelemen P. B., Shimizu N., & Salters V. J. M. (1994) Focussed flow of melt in the upper mantle: Extraction of MORB beneath oceanic spreading ridges (abstract). *Mineralogical Magazine* **58A**, 466-467.

Kelemen P. B., Shimizu N., & Salters V. J. M. (1995a) Extraction of mid-ocean-ridge basalt from the upwelling mantle be focussed flow of melt in dunite channels. *Nature* **375**, 747-753.

Kelemen P. B., Whitehead J. A., Aharonov E., & Jordahl K. A. (1995b) Experiments on flow focussing in soluble porous media, with applications to melt extraction from the mantle. *Journal of Geophysical Research* **100**, 475-496.

Kempe D. R. C. & Schilling J.-G. (1974) Discovery tablemount basalt: Petrology and geochemistry. *Contributions to Mineralogy and Petrology* **44**, 101-115.

Kinzler R. J. (1997) Melting of mantle peridotite at pressures approaching the spinel to garnet transition: Application to mid-ocean ridge basalt petrogenesis. *Journal of Geophysical Research* **102**, 853-874.

Kinzler R. J. & Grove T. L. (1992a) Primary magmas of mid-ocean ridge basalts 1. Experiments and methods. *Journal of Geophysical Research* **97**, 688-6906.

Kinzler R. J. & Grove T. L. (1992b) Primary magmas of mid-ocean ridge basalts 2. Applications. *Journal of Geophysical Research* **97**, 6907-6926.

Kinzler R. J. & Grove T. L. (1993) Corrections and further discussion of the primary magmas of mid-ocean ridge basalts, 1 and 2. *Journal of Geophysical Research* **98**, 22339-22347.

Klein E. M. & Langmuir C. H. (1987) Global correlations of ocean ridge basalt chemistry with axial depth and crustal thickness. *Journal of Geophysical Research* **92**, 8089-8115.

Klein E. M. & Langmuir C. H. (1989) Local versus global variations in ocean ridge basalt composition: a reply. *Journal of Geophysical Research* **94**, 4241-4252.

Korenaga J. & Kelemen P. B. (1997) Origin of gabbro sills in the Moho transition zone of the Oman ophiolite: implications for magma transport in the oceanic lower crust. *Journal of Geophysical Research* **102**, 27729-27749.

Korenaga J. & Kelemen P. B. (1998) Melt migration through the oceanic lower crust: a constraint from melt percolation modelling with finite solid diffusion. *Earth and Planetary Science Letters* **156**, 1-11.

Kurz M. D., le Roex A. P., & Dick H. J. B. (1998) Isotope geochemistry of the oceanic mantle near the Bouvet triple junction. *Geochimica et Cosmochimica Acta* **62**, 841-852.

Langmuir C. H. & Bender J. F. (1984) The geochemistry of oceanic basalts in the vicinity of transform faults: observations and implications. *Earth and Planetary Science Letters* **69**, 107-127.

Langmuir C. H., Klein E. M., & Plank T. (1992) Petrological systematics of mid-ocean ridge basalts: constraints on melt generation beneath ocean ridges. *American Geophysical Union Geophysical Monograph* **71**, 183-280.

Langmuir C. H., Vocke R. D., & Hanson G. N. (1978) A general mixing equation with application to Icelandic basalts. *Earth and Planetary Science Letters* **37**, 380-392.

LaTourrette T. Z. & Burnet D. S. (1992) Experimental determination of U and Th partitioning between clinopyroxene and natural and synthetic basaltic liquid. *Earth and Planetary Science Letters* **110**, 227-244.

LaTourrette T. Z., Kennedy A. K., & Wasserberg G. J. (1993) Thorium-Uranium fractionation by garnet: evidence for a deep source and rapid rise of oceanic basalts. *Science* **261**, 739-742.

Le Maitre R. W. (1989) *A classification of igneous rocks and glossary on terms*. Blackwell Scientific Publications.

le Roex A. P. (1985) Geochemistry, mineralogy and magmatic evolution of the basaltic and trachytic lavas from Gough Island, South Atlantic. *Journal of Petrology* **26**, 149-186.

le Roex A. P. (1987) Source regions of mid-ocean ridge basalts: evidence for enrichment processes. In *Mantle Metasomatism* (ed. M. A. Menzies and C. J. Hawkesworth), pp. 389-422. Academic Press.

University of Cape Town

le Roex A. P., Cliff R. A., & Adair B. J. I. (1990) Tristan da Cunha, South Atlantic: Geochemistry and petrogenesis of a basanite-phonolite lava series. *Journal of Petrology* **31**, 779-812.

le Roex A. P. & Dick H. J. B. (1981) Petrography and geochemistry of basaltic rocks from the Conrad fracture zone on the America-Antarctica Ridge. *Earth and Planetary Science Letters* **54**, 117-138.

le Roex A. P., Dick H. J. B., Erlank A. J., Reid A. M., Frey F. A., & Hart S. R. (1983) Geochemistry, mineralogy and petrogenesis of lavas erupted along the Southwest Indian Ridge between the Bouvet Triple Junction and 11 degrees East. *Journal of Petrology* **24**, 267-318.

le Roex A. P., Dick H. J. B., & Fisher R. L. (1989) Petrology and geochemistry of MORB from 25°E to 46°E along the Southwest Indian Ridge: Evidence for contrasting styles of mantle enrichment. *Journal of Petrology* **30**, 947-986.

le Roex A. P., Dick H. J. B., Gulen L., Reid A. M., & Erlank A. J. (1987) Local and regional heterogeneity in MORB from the Mid-Atlantic Ridge between 54.5°S and 51°S: Evidence for geochemical enrichment. *Geochimica et Cosmochimica Acta* **51**, 541-555.

le Roex A. P., Dick H. J. B., Reid A. M., Frey F. A., Erlank A. J., & Hart S. R. (1985) Petrology and geochemistry of basalts from the American-Antarctic Ridge, Southern Ocean: implications fro the westward influence of the Bouvet mantle plume. *Contributions to Mineralogy and Petrology* **90**, 367-380.

le Roex A. P., Frey F. A., & Richardson S. H. (1996) Petrogenesis of lavas from the AMAR Valley and Narrowgate region of the FAMOUS Valley, 36°-37°N on the Mid-Atlantic Ridge. *Contributions to Mineralogy and Petrology* **124**, 167-184.

le Roex A. P., Milner S. C., & Mahoney J. J. (1995) Tristan and Marion mantle plumes: Evidence for the source of the EM-1 mantle component. In *Plume 2*, Vol. 3 (ed. D. L. Anderson, S. R. Hart, and A. W. Hofmann), pp. 85-87. Alfred-Wegener-Stiftung.

Lin J. & Phipps Morgan J. (1992) The spreading rate dependence of three-dimensional mid-ocean ridge gravity structure. *Geophysical Research Letters* **19**, 13-16.

Long J. V. P. (1995) Microanalysis from 1950-1990s. In *Microprobe techniques in the Earth Sciences* (ed. P. J. Potts, J. F. W. Bowless, S. J. B. Reed, and M. R. Cave). Chapman & Hall.

Longhi J., Walker D., & Hays J. F. (1978) The distribution of Fe and Mg between olivine and lunar basaltic liquids. *Geochimica et Cosmochimica Acta* **42**, 1545-1558.

MacDonald G. A. & Katsura T. (1964) Chemical composition of Hawaiian lavas. *Journal of Petrology* **5**, 82-133.

Magde L. S., Kincaid C., Sparks D. W., & Detrick R. S. (1996) Combined laboratory and numerical studies of the interaction between buoyant and plate-driven upwelling beneath segmented spreading centers. *Journal of Geophysical Research* **101**, 22107-22122.

Magde L. S., Sparks D. W., & Detrick R. S. (1997) The relationship between buoyant mantle flow, melt migration, and gravity bull's eyes at the Mid-Atlantic Ridge between 33°N and 35°N. *Earth and Planetary Science Letters* **148**, 59-67.

Mahoney J., le Roex A. P., Peng Z., Fisher R. L., & Natland J. H. (1992) Southwestern limits of Indian Ocean Ridge mantle and the origin of low $^{206}Pb/^{204}Pb$ mid-ocean ridge basalt: Isotope systematics of the Central Southwest Indian Ridge (17°-50°E). *Journal of Geophysical Research* **97**, 19771-19790.

Mahoney J. J., Jones W. B., Frey F. A., Salters V. J. M., Pyle D. G., & Davies H. L. (1995) Geochemical characteristics of lavas from Broken Ridge, the Naturaliste Plateau and southernmost Kerguelen Plateau: Cretaceous plateau volcanism in the southeast Indian Ocean. *Chemical Geology* **120**, 315-345.

Mahoney J. J., White W. M., Upton B. G. J., Neal C. R., & Scrutton R. A. (1996) Beyond EM-1: Lavas from Afanasy-Nikitin Rise and the Crozet Archipelago, Indian Ocean. *Geology* **24**, 615-618.

McKenzie D. (1985) The extraction of magma from the crust and mantle. *Earth and Planetary Science Letters* **74**, 81-91.

McKenzie D. & Bickle M. J. (1988) The volume and composition of melt generated by extension of the lithosphere. *Journal of Petrology* **29**, 625-679.

McKenzie D. & O'Nions R. K. (1983) Mantle reservoirs and ocean island basalts. *Nature* **301**, 229-231.

McKenzie D. & O'Nions R. K. (1991) Partial melt distributions from inversions of rare earth element concentrations. *Journal of Petrology* **32**, 1021-1091.

McKenzie D. & O'Nions R. K. (1995) The source regions of ocean island basalts. *Journal of Petrology* **36**, 133-159.

Michael P. J. (1995) Regionally distinctive sources of depleted MORB: Evidence from trace elements and H_2O. *Earth and Planetary Science Letters* **131**, 301-320.

Michael P. J. & Bonatti E. (1985) Peridotite composition from the North Atlantic: regional and tectonic variations and implications for partial melting. *Earth and Planetary Science Letters* **73**, 91-104.

Michael P. J., Chase R. L., & Allan J. F. (1989) Petrologic and geologic variations along the Southern Explorer Ridge, Northeast Pacific Ocean. *Journal of Geophysical Research* **94**, 13895-13918.

University of Cape Town

Michael P. J. & Cornell W. C. (1998) Influence of spreading rate and magma supply on crystallization and assimilation beneath mid-ocean ridges: Evidence from chlorine and major element chemistry of mid-ocean ridge basalts. *Journal of Geophysical Research* **103**, 18325-18356.

Michael P. J., Forsyth D. W., Blackman D. K., Fox P. J., Hanan B. B., Harding A. J., Macdonald K. C., Neumann G. A., Orcutt J. A., Tolstoy M., & Weiland C. M. (1994) Mantle control of a dynamically evolving spreading center: Mid-Atlantic Ridge 31-34°S. *Earth and Planetary Science Letters* **121**, 451-468.

Milner S. C. & le Roex A. P. (1996) Isotope characteristics of the Okenyenya igneous complex, northwestern Namibia: constraints on the composition of the early Tristan plume and the origin of the EM1 mantle component. *Earth and Planetary Science Letters* **141**, 277-291.

Moreira M., Staudacher T., Sarda P., Schilling J.-G., & Allègre C. J. (1995) A primitive plume neon component in MORB: The Shona ridge-anomaly, South Atlantic (51-52°S). *Earth and Planetary Science Letters* **133**, 367-377.

Nielsen R. L. (1988a) A model for the simulation of combined major and trace element liquid lines of descent. *Geochimica et Cosmochimica Acta* **52**, 27-38.

Nielsen R. L. (1988b) TRACE.FOR: a program for the calculation of combined major and trace-element liquid lines of descent for natural magmatic systems. *Computers & Geosciences* **14**, 15-35.

Nielsen R. L. (1989) Phase equilibria constraints on liquid lines of descent generated by paired assimilation and fractional crystallization: Trace elements and Sr and Nd isotopes. *Journal of Geophysical Research* **94**, 787-794.

Nielsen R. L. (1990) Simulation of igneous differentiation processes. In *Modern methods of igneous petrology: understanding magmatic processes*, Vol. 24 (ed. J. Nicholls and J. K. Russel), pp. 65-105. Mineralogical Society of America.

Nielsen R. L. & Dungan M. A. (1983) Low pressure mineral-melt equilibria in natural anhydrous mafic systems. *Contributions to Mineralogy and Petrology* **84**, 310-326.

Nielsen R. L., Gallahan W. E., & Newberger F. (1992) Experimentally determined mineral-melt partition coefficients for Sc, Y and REE for olivine, orthopyroxene, pigeonite, magnetite and ilmenite. *Contributions to Mineralogy and Petrology* **110**, 488-499.

Niu Y. (1997) Mantle melting and melt extraction processes beneath ocean ridges: Evidence from abyssal peridotites. *Journal of Petrology* **38**, 1047-1074.

Niu Y. (1999) Comments on some misconceptions in igneous and experimental petrology and methodology: a reply. *Journal of Petrology* **40**, 1195-1203.

Niu Y. & Batiza R. (1991) An empirical method for calculating melt compositions produced beneath mid-ocean ridges: Application for axis and off-axis (seamounts) melting. *Journal of Geophysical Research* **96**, 21753-21777.

Niu Y. & Batiza R. (1993) Chemical variation trends at fast and slow spreading mid-ocean ridges. *Journal of Geophysical Research* **98**, 7887-7902.

Niu Y. & Batiza R. (1994) Magmatic processes at a slow spreading ridge segment: 26°S Mid-Atlantic Ridge. *Journal of Geophysical Research* **99**, 19719-19740.

Niu Y. & Batiza R. (1997) Trace element evidence from seamounts for recycled oceanic crust in the Eastern Pacific mantle. *Earth and Planetary Science Letters* **148**, 471-483.

Niu Y., Collerson K. D., Batiza R., Wendt J. I., & Regelous M. (1999) Origin of enriched-type mid-ocean ridge basalts at ridges far from mantle plumes: The East Pacific Rise at 11°20'N. *Journal of Geophysical Research* **104**, 7067-7087.

Niu Y. & Hékinian R. (1997a) Basaltic liquids and harzburgitic residues in the Garrett Transform: a case study at fast-spreading ridges. *Earth and Planetary Science Letters* **146**, 243-258.

Niu Y. & Hékinian R. (1997b) Spreading-rate dependence of the extent of mantle melting beneath ocean ridges. *Nature* **385**, 326-329.

Niu Y., Langmuir C. H., & Kinzler R. J. (Submitted) The origin of abyssal peridotites: a new perspective. *Earth and Planetary Science Letters*.

Niu Y., Waggoner D. G., Sinton J. M., & Mahoney J. J. (1996) Mantle source heterogeneity and melting processes beneath seafloor spreading centers: the East Pacific Rise. 18°-19°S. *Journal of Geophysical Research* **101**, 27711-27734.

Norrish K. & Hutton J. T. (1969) An accurate X-ray spectrographic method for the analysis of a wide range of geological samples. *Geochimica et Cosmochimica Acta* **33**, 431-453.

Pearce N. J. G., Perkins W. T., Westgate J. A., Gorton M. P., Jackson S. E., Neal C. R., & Chenery S. P. (1997) A compilation of new and published major and trace element data for NIST SRM 610 and NIST SRM 612 glass reference materials. *Geostandards Newsletter* **21**, 115-144.

Pearce N. J. G., Westgate J. A., & Perkins W. T. (1996) Developments in the analysis of volcanic glass shards by

University of Cape Town

laser ablation ICP-MS: quantitative and single internal standard-multi-element methods. *Quaternary International* **34-36**, 213-227.

Peate D. W., Hawkesworth C. J., Mantovani M. S. M., Roders N. W., & Turner S. P. (1999) Petrogenesis and stratigraphy of the high-Ti/Y Urubici magma type in the Paraná flood basalt province and implications for the nature of 'Dupal'-type mantle in the South Atlantic region. *Journal of Petrology* **40**, 451-473.

Perkins W. T. & Pearce N. J. G. (1995) Mineral microanalysis by laserprobe inductively coupled plasma mass spectrometry. In *Microbeam Techniques in the Earth Sciences* (ed. P. J. Potts, J. F. W. Bowless, S. J. B. Reed, and M. R. Cave), pp. 291-325. Chapman & Hall.

Phipps Morgan J. & Forsyth D. W. (1988) Three-dimensional flow and temperature perturbations due to a transform offset: Effects on oceanic crustal and upper mantle structure. *Journal of Geophysical Research* **93**, 2955-2966.

Phipps Morgan J. & Morgan W. J. (1999) Two-stage melting and the geochemical evolution of the mantle: a recipe for mantle plum-pudding. *Earth and Planetary Science Letters* **170**, 215-239.

Plank T. & Langmuir C. H. (1992) Effects of the melting regime on the composition of the oceanic crust. *Journal of Geophysical Research* **97**, 19749-19770.

Plank T. & Langmuir C. H. (1998) The chemical composition of subducted sediment and its consequences for the crust and mantle. *Chemical Geology* **145**, 325-394.

Plank T., Spiegelman M., Langmuir C. H., & Forsyth D. W. (1995) The meaning of "mean F": Clarifying the mean extent of melting at ocean ridges. *Journal of Geophysical Research* **100**, 15045-15052.

Rehkämper M. & Hofmann A. W. (1997) Recycled ocean crust and sediment in Indian Ocean MORB. *Earth and Planetary Science Letters* **147**, 93-106.

Reid I. & Jackson H. R. (1981) Oceanic spreading rate and crustal thickness. *Marine Geophysical Research* **5**, 165-172.

Reiners P. W. (1998) Reactive melt transport in the mantle and geochemical signatures of mantle-derived magmas. *Journal of Petrology* **39**, 1039-1061.

Reynolds J. R. (1995) Segment-scale systematics of mid-ocean ridge magmatism and geochemistry. PhD, Columbia University.

Reynolds J. R. & Langmuir C. H. (1997) Petrological systematics of the Mid-Atlantic Ridge south of Kane: Implications for ocean crust formation. *Journal of Geophysical Research* **102**, 14915-14946.

Reynolds J. R., Langmuir C. H., Bender J. F., Kastens K. A., & Ryan W. B. F. (1992) Spatial and temporal variability in the geochemistry of basalts from the East Pacific Rise. *Nature* **359**, 493-499.

Richardson S. H., Erlank A. J., Duncan A. R., & Reid D. L. (1982) Correlated Nd, Sr and Pb isotope variation in Walvis Ridge basalts and implications for the evolution of their mantle source. *Earth and Planetary Science Letters* **59**, 327-342.

Robinson J. A. C. & Wood B. J. (1998) The depth of the spinel to garnet transition at the peridotite solidus. *Earth and Planetary Science Letters* **164**, 277-284.

Roeder P. L. (1974) Activity of iron and olivine solubility in basaltic liquids. *Earth and Planetary Science Letters* **23**, 397-410.

Roeder P. L. & Emslie R. F. (1970) Olivine-liquid equilibrium. *Contributions to Mineralogy and Petrology* **29**, 275-289.

Rudnick R. L. & Fountain D. M. (1995) Nature and composition of the continental crust: a lower crustal perspective. *Reviews of Geophysics* **33**, 267-309.

Sack R. O. & Ghiorso M. S. (1994a) Thermodynamics of multicomponent pyroxenes: I. Formulation of a general model. *Contributions to Mineralogy and Petrology* **116**, 277-286.

Sack R. O. & Ghiorso M. S. (1994b) Thermodynamics of multicomponent pyroxenes: II. Phase relations in the quadrilateral. *Contributions to Mineralogy and Petrology* **116**, 287-300.

Sack R. O. & Ghiorso M. S. (1994c) Thermodynamics of multicomponent pyroxenes: III. Calibration of $Fe^{2+}(Mg)_{-1}$, $TiAl_2(MgSi_2)_{-1}$, $TiFe_2^{3+}(MgSi_2)_{-1}$, $AlFe^{3+}(MgSi)_{-1}$, $NaAl(CaMg)_{-1}$, $Al_2(MgSi)_{-1}$ and $Ca(Mg)_{-1}$ exchange reactions between pyroxenes and silicate melts. *Contributions to Mineralogy and Petrology* **118**, 271-296.

Salters V. J. M. (1996) The generation of mid-ocean ridge basalts from the Hf and Nd isotope perspective. *Earth and Planetary Science Letters* **141**, 109-123.

Salters V. J. M., Bourdon B., & Elliot T. E. (1994) Constraints on the MORB melting regime based on the Lu-Hf and Sm-Nd systematics (abstract). *Mineralogical Magazine* **58A**, 799-800.

Salters V. J. M. & Hart S. R. (1989) The Hf-paradox, and the role of garnet in the MORB source. *Nature* **342**, 420-422.

Salters V. J. M. & Hart S. R. (1991) The mantle sources of ocean ridges, islands and arcs: the Hf-isotope connection. *Earth and Planetary Science Letters* **104**, 364-380.

Schilling J. G., Bergeron M. B., & Evans R. (1980) Halogens in the mantle beneath the North Atlantic.

University of Cape Town

Philosophical Transactions of the Royal Society of London **A297**, 147-178.

Schilling J. G., Thompson G., Kingsley R., & Humphris S. (1985) Hotspot-migrating ridge interaction in the South Atlantic. *Nature* **313**, 187-191.

Schilling J.-G., Hanan B. B., McCully B., Kingsley R. H., & Fontignie D. (1994) Influence of the Sierra Leone mantle plume on the equatorial Mid-Atlantic Ridge: A Nd-Sr-Pb isotopic study. *Journal of Geophysical Research* **99**, 12005-12028.

Schilling J.-G., Zajac M., Evans R., Johnson T., White W., Devine J. D., & Kingsley R. (1983) Petrologic and geochemical variations along the Mid-Atlantic Ridge from 29°N to 73°N. *American Journal of Science* **283**(510-586).

Scott D. R. & Stevenson D. J. (1989) A self-consistent model of melting, magma migration and buoyancy-driven circulation beneath mid-ocean ridges. *Journal of Geophysical Research* **94**, 2973-2988.

Seyler M. & Bonatti E. (1997) Regional-scale melt-rock interaction in lherzolitic mantle in the Romanche Fracture Zone (Atlantic Ocean). *Earth and Planetary Science Letters* **146**, 273-287.

Shaw D. M. (1970) Trace element fractionation during anatexis. *Geochimica et Cosmochimica Acta* **34**, 237-243.

Shaw W. & Lin J. (1996) Models of ocean ridge lithosphere deformation: Dependence on crustal thickness, spreading rate and segmentation. *Journal of Geophysical Research* **101**, 17977-17993.

Shen Y. & Forsyth D. W. (1995) Geochemical constraints on initial and final depths of melting beneath mid-ocean ridges. *Journal of Geophysical Research* **100**, 2211-2237.

Shi P. (1992) Basalt evolution at low pressure: implications from an experimental study in the system CaO-FeO-MgO-Al_2O_3-SiO_2. *Contributions to Mineralogy and Petrology* **110**, 139-153.

Shi P. (1993) Low-pressure phase relationships in the system Na_2O-CaO-FeO-MgO-Al_2O_3-SiO_2 at 1100°C, with implications for the differentiation of basaltic magmas. *Journal of Petrology* **34**, 743-762.

Shi P. & Libourel G. (1991) The effects of FeO on the system CMAS at low pressure and implications for basalt crystallization processes. *Contributions to Mineralogy and Petrology* **108**, 129-145.

Shimizu N. (1994) Depths of melting and melt extraction beneath mid-ocean ridges as recorded in melt inclusions (abstract). *Mineralogical Magazine* **58A**, 829-830.

Shimizu N. & Hart S. R. (1982) Applications of the ion microprobe to geochemistry and cosmochemistry. *Annual Review of Earth and Planetary Science* **10**, 483-526.

Shimizu N. & le Roex A. P. (1986) The chemical zoning of augite phenocrysts in alkaline basalts from Gough Island, South Atlantic. *Journal of Volcanology and Geothermal Research* **29**, 159-188.

Silver P. G. (1998) Coupling of South American and African plate motion and plate deformation. *Science* **279**, 60-63.

Simms K. W. W. & DePaolo D. J. (1997) Inferences about mantle magma sources from incompatible element concentration ratios in oceanic basalts. *Geochimica et Cosmochimica Acta* **61**, 765-784.

Singh S. C., Kent G. M., Collier J. S., Harding A. J., & Orcutt J. A. (1998) Melt to mush variations in crustal magma properties along the ridge crest at the southern East Pacific Rise. *Nature* **394**, 874-878.

Sinton J. M. & Detrick R. S. (1992) Mid-ocean ridge magma chambers. *Journal of Geophysical Research* **97**, 197-216.

Sleep N. H. (1984) Tapping of magmas from ubiquitous mantle heterogeneities: an alternative to mantle plumes? *Journal of Geophysical Research* **89**, 10029-10041.

Sleep N. H. (1996) Lateral flow of hot plume material ponded at sublithospheric depths. *Journal of Geophysical Research* **101**, 28065-28083.

Small C. (1995) Observations of ridge-hotspot interactions in the Southern Ocean. *Journal of Geophysical Research* **100**, 17931-17946.

Small C., Chen Y. J., & Schilling J.-G. (1994) A preliminary view of the Shona anomaly from Hydrosweep, gravity and magnetic data (abstract). *Eos Transactions of the American Geophysical Union Spring Meeting Supplement* **75**(16), 330.

Small C., Chen Y. J., & Schilling J.-G. (1995) Interactions between the Shona hotspot and the Mid-Atlantic Ridge (abstract). *Eos Transactions of the American Geophysical Union Fall Meeting Supplement* **76**(46), F541.

Smith D. K. & Cann J. R. (1993) Building the crust at the Mid-Atlantic Ridge. *Nature* **365**, 707-715.

Smith S. E., Casey J. F., Bryan W. B., Dmitriev L., Silantyev S., & Magakyan R. (1998) Geochemistry of basalts from the Hayes Transfrom region of the Mid-Atlantic Ridge. *Journal of Geophysical Research* **103**, 5305-5329.

Smith W. H. F. & Sandwell D. T. (1997) Global sea floor topography from satellite altimetry and ship depth soundings. *Science* **277**, 1956-1962.

Sobolev A. V. & Chaussidon M. (1996) H_2O concentrations in primary melts from supra-subduction zones and mid-ocean ridges: implications for H_2O storage and recycling in the mantle. *Earth and Planetary Science Letters* **137**, 45-55.

University of Cape Town

Sobolev A. V. & Shimizu N. (1993) Ultra-depleted primary melt included in an olivine from the Mid-Atlantic Ridge. *Nature* **363**, 151-154.

Sobolev A. V. & Shimizu N. (1994) The origin of typical NMORB: The evidence from a melt inclusion study (abstract). *Mineralogical Magazine* **58A**, 862-863.

Spiegelman M. & Kenyon P. (1992) The requirements for chemical disequilibrium during magma migration. *Earth and Planetary Science Letters* **109**, 611-620.

Spray J. G. (1989) Upper mantle segregation processes: evidence from alpine-type peridotites. In *Magmatism in the Ocean Basins*, Vol. 42 (ed. A. D. Saunders and M. J. Norry), pp. 29-40. Geological Society Special Publications.

Stakes D., Shervais J. W., & Hopson C. A. (1984) The volcanic-tectonic cycle of the FAMOUS and AMAR valleys, Mid-Atlantic Ridge (36°47'N): Evidence from basalt glass and phenocryst compositional variations for a steady state magma chamber beneath the valley midsections, AMAR 3. *Journal of Geophysical Research* **89**, 6995-7028.

Staudigel H. & Bryan W. B. (1981) Contrasting glass-whole rock compositions and phenocryst re-distribution, IPOD Sites 417 and 418. *Contributions to Mineralogy and Petrology* **78**, 255-262.

Suhr G. (1999) Melt migration under oceanic ridges: inferences from reactive transport modelling of upper mantle hosted dunites. *Journal of Petrology* **40**, 575-599.

Sun S.-s. & McDonough W. F. (1989) Chemical and isotopic systematics of oceanic basalts: implications for mantle composition and processes. In *Magmatism in the Ocean Basins*, Vol. 42 (ed. A. D. Saunders and M. J. Norry), pp. 313-345.

Takahashi E., Shimazaki T., Tsuzaki Y., & Yoshida H. (1993) Melting study of a peridotite KLB-1 to 6.5 GPa. and the origin of basaltic magmas. *Philosophical Transactions of the Royal Society of London* **342**, 105-120.

Tormey D. R., Grove T. L., & Bryan W. B. (1987) Experimental petrology of normal MORB near the Kane Fracture Zone: 22°-25°N, Mid-Atlantic Ridge. *Contributions to Mineralogy and Petrology* **96**, 121-139.

Turcotte D. L. & Phipps Morgan J. (1992) The physics of magma migration and mantle flow beneath a mid-ocean ridge. *American Geophysical Union Geophysical Monograph* **71**, 155-182.

Unrug R. (1996) The assembly of Gondwanaland. *Episodes* **19**, 11-20.

van Heerden L. (1987) The geochemistry, mineralogy and igneous petrology of some fracture zone basalts from the southern Mid-Atlantic Ridge. M.Sc., Cape Town.

Walter M. J. (1999) Comments on 'Mantle melting and melt extraction processes beneath ocean ridges: evidence from abyssal peridotites' by Yaoling Niu. *Journal of Petrology* **40**, 1187-1193.

Walter M. J. & Presnall D. C. (1994) Melting behaviour of simplified lherzolite in the system CaO-MgO-Al_2O_3-SiO_2-Na_2O from 7 to 35 kbar. *Journal of Petrology* **35**, 329-359.

Walter M. J., Sisson T. W., & Presnall D. C. (1995) A mass proportion method for calculating melting reactions and application to melting of model upper mantle lherzolite. *Earth and Planetary Science Letters* **135**, 77-90.

Weaver B. L. (1991) The origin of ocean island basalt end-member compositions: trace element and isotopic constraints. *Earth and Planetary Science Letters* **104**, 381-397.

Weaver B. L., Wood D. A., Tarney J., & Joron J.-L. (1987) Geochemistry of ocean island basalts from the South Atlantic: Ascension, Bouvet, St. Helena, Gough and Tristan da Cunha. In *Alkaline Igneous Rocks*, Vol. 30 (ed. J. G. Fitton and B. G. J. Upton), pp. 253-267.

White R. S., McKenzie D., & O'Nions R. K. (1992) Oceanic crustal thickness from seismic measurements and rare earth element inversions. *Journal of Geophysical Research* **97**, 19683-19715.

White W. M. & Bryan W. B. (1977) Sr-isotope, K, Rb, Cs, Sr, Ba and rare-earth geochemistry of basalts from the FAMOUS area. *Geological Society of America Bulletin* **88**, 571-576.

White W. M. & Schilling J.-G. (1978) The nature and origin of geochemical variation in Mid-Atlantic basalts from the North Atlantic. *Geochimica et Cosmochimica Acta* **42**, 1501-1516.

Yang H.-J., Kinzler R. J., & Grove T. L. (1996) Experiments and models of anhydrous, basaltic olivine-plagioclase-augite saturated melts from 0.001 to 10 kbar. *Contributions to Mineralogy and Petrology* **124**, 1-18.

Yang H.-J., Sen G., & Shimizu N. (1998) Mid-ocean ridge melting: Constraints from lithospheric xenoliths at Oahu, Hawaii. *Journal of Petrology* **39**, 277-295.

Zindler A. & Hart S. R. (1986) Chemical geodynamics. *Annual Review of Earth and Planetary Science* **14**, 493-571.

University of Cape Town

APPENDIX A: DREDGE STATION DETAILS

INTRODUCTION

The details of each dredge station is reproduced in table A.1, from the Cruise Report (EW9309) of the R/V Maurice Ewing, and for the Agulhas 32 samples from le Roex *et al.* (1987) in table A.2.

University of Cape Town

Table A.1: Dredge station details. Depth in metres below sea-level.

Station ID#	Lat. & Long.	Depth (m.b.s.l.)	Feature dredged	Rock recovery	Glass recovery	Weight (kg)
2D	47.55°S 10.19°W	2552-2435	Small volcano - centre of MAR rift valley floor - over Discovery gravity high	1. Pillow basalt fragments - one large with thick glassy crust 2. Very fresh glassy slabs	Abundant	247
3D	47.80°S 10.15°W	2654-2444	Centre of MAR rift valley floor - over Discovery gravity high	1. Pillow basalt fragments with variable amount of glass, Mn-coating and hydrothermal stains - probably 2-3 types 2. Small, rounded serpentinite cobble	Few nuggets	441
4D	47.97°S 10.08°W	2990-2800	East flank of volcanic ridge - centre of MAR rift valley floor - over Discovery gravity high	Very fresh glassy pillow basalts with abundant glass and crust	Abundant	182
5D	48.24°S 10.00°W	3525-3380	Volcanic ridge - centre of MAR rift valley floor - over Discovery gravity high	Pillow basalt fragments with minor glass retained	Minor chips	272
6D	48.55°S 10.17°W	3279-3255	Centre of MAR rift valley floor - over Discovery gravity high	One pillow basalt fragment with some glass retained	Minor chips	25
7D	48.76°S 10.07°W	3272-3163	Deep - MAR rift valley floor	1. Aphyric pillow basalt with some glass retained 2. Highly plagiophyric pillow basalt with glassy crust 3. Fresh highly plagiophyric basalt	1. Fresh station glass 2. Abundant aphyric glass nuggets	250
8D	48.96°S 9.97°W	3911-3876	Elongated volcano - centre of MAR rift valley floor - south end of Discovery gravity high	One small pillow basalt with minor glass retained	Poor-variolitic type	20
9D	49.15°S 9.91°W	4004-3780	Two small hills in centre of MAR rift valley floor - south end of Discovery gravity high	1. Extremely fresh, highly glassy slabs 2. Pillow fragments with some glass retained	Abundant nuggets	150
10D	49.25°S 8.14°W	3970-3750	MAR valley floor - nodal deep at RTI	1. Plagiophyric pillow basalts with some glass retained (tallus - older type) 2. Fresh, glassy, plagiophyric basalt from deep basin	Few nuggets	241
11D	49.44°S 7.97°W	3884-3852	Centre of MAR rift valley floor	Pillow and slabs of basalt with glass	Abundant glass nuggets	255
12D	49.76°S 8.03°W	3951-3797	Two small hills in centre of MAR rift valley floor	Plagiophyric basalt with glassy, striated crust	Abundant nuggets & chips - granular	250
13D	49.99°S 7.88°W	3646-3464	Small volcano in centre of MAR rift valley floor	Fresh, glassy pillow and slab, and a few aa type pieces	Abundant nuggets	218
14D	50.27°S 7.06°W	3387-3307	Volcanic ridge in centre of MAR rift valley floor	Pillow basalt with some glass and glassy crust retained with manganese coating	Minor chips	222
15D	50.58°S 6.43°W	3021-2939	Centre of MAR rift valley floor - north part of Shona gravity high	1. Very fresh and glassy pillow and slab basalt - some hydrothermal stains 2. One older pillow with some glass	Abundant nuggets	227
16D	50.83°S 6.43°W	2874-2863	Basin on flank of MAR axis	None		
17D	50.76°S 6.34°W	3050-2835	Small volcano in centre of MAR rift valley floor - north transition zone of Shona gravity high	Pillow basalt with some glass retained and thin manganese coating; traces of glob ooze	Few nuggets	181
18D	51.05°S 6.20°W	2029-1953	Elevated ridge axis over Shona gravity high (saddle point) - over axi-symmetric magnetic anomaly	Pillow and slab basalt with some glass retained and thin Mn-coating glacial erratics and pebbles	Minor	136

University of Cape Town

Table A.1: Dredge station details continued

Station ID#	Lat. & Long.	Depth (m.b.s.l.)	Feature dredged	Rock recovery	Glass recovery	Weight (kg)
19D	51.06°S 6.16°W	1800-1686	Elevated ridge axis Shona gravity high - east flank of MAR	Pillow basalt, highly vesicular with some glass retained and with thin Mn-coating; glacial erratics	Few glass fingers	227
20D	51.43°S 5.78°W	1739-1699	Elevated MAR axis over Shona gravity high - axial part	Two types of pillow and slab basalt: 1. Very fresh glassy crust (dark brown) 2. Older, with some light brown glassy crust	Few nuggets	45
21D	51.82°S 5.50°W	2070-1980	MAR elevated ridge axis - southern part of Shona gravity high	Highly plagiophyric basalt with minor brown glassy crust	Minor brown crust	227
22D	52.46°S 4.57°W	3222-2896	Centre of MAR rift valley floor - south of Shona gravity high	1. Very fresh, highly glassy basaltic slabs 2. Pillows 3. Pillow with minor glass 4. Older type with minor glass	Abundant glass nuggets	32
23D	52.16°S 5.34°W	2664-2554	Small hill in MAR rift valley floor - southern part of Shona gravity high	One large, very fresh. glassy basalt	Small slabs of very fresh, highly glassy basalt with dark brown crust	20
24D	50.46°S 6.53°W	3378-2988	MAR rift valley floor - northern rifted part of Shona gravity high	Two small, fist-size pillow plagiophyric basalts: one with very fresh glass; the other with no glass	Two small, very fresh, glassy slabs with dark brown crust	0.5
25D	47.35°S 10.32°W	2087-1977	Volcano in centre of MAR rifted valley floor - north end of Discovery gravity high	Small pillow fragments with very fresh and thick glass	1. Large glass nuggets 2. Large glass "scale" type	23
26D	47.35°S 13.40°W	3914-3800	MAR-Falkland RTI - central ridge in nodal deep	A few pillow basalt fragments with some glass retained	One small glass nugget	27
27D	47.11°S 13.40°W	3163-2998	Small volcano in centre of MAR rift valley floor	One large, fresh, highly plagiophyric glass with dark brown crust pillow basalt, and few smaller similar fragments	One small glass nugget, and glass chip with plagiophyric crust	136
28D	46.90°S 13.45°W	3433-3400	Small volcano in centre of MAR rift valley floor	Two types: 1. Very fresh, glassy born crust, highly plagiophyric pillow, basalts and slabs most abundant; 2. Aphyric pillow basalt fragments	Abundant very fresh, plagiophyric glass nuggets	196
29D	46.67°S 13.43°W	3860-3850	Empty dredge			
30D	46.59°S 13.39°W	3211-3095	Small ridge in centre of MAR rift valley floor	Three possible types: 1. Plagiophyric pillow basalt with fresh, granular glass and brown crust; 2. Older type, aphyric pillow basalt with black glass remaining; 3. Three small slabs with very fresh glass and dark brown crust, essentially aphyric	Minor chips of glass with brown crust	113
31D	46.39°S 13.46°W	2852-2792	Small volcano in centre of MAR rift valley floor	Two pillow fragments with some glass retained	"Scale" type glass from pillows	5

University of Cape Town

Table A.1: Dredge station details continued

Station ID#	Lat. & Long.	Depth (m.b.s.l.)	Feature dredged	Rock recovery	Glass recovery	Weight (kg)
32D	46.23°S 13.56°W	3121-3095	Small ridge in MAR rift valley floor at RTI (small transform)	Three possible types of pillow basalt fragments: 1. Highly plagiophyric with some glass and crust preserved; 2. "Grenade"-like plagiophyric, fresher, but very small; 3. Small, older slab with glass and palagonite	A few glass nuggets	136
33D	45.99°S 14.08°W	3550-3212	Volcanic ridge in MAR rift valley floor (20km long segment) (oblique section north of Discovery anomaly)	Two types: 1. Aphyric basalts, small grenade size pillow with very fresh glass (mostly peeled off); 2. Older pillow with minor glass remaining	Abundant glass nuggets with minor rock attached, also pure glass nuggets and "serpentinite" fragments	154
34D	45.85°S 14.19°W	3501-3384	Small volcanic ridge in MAR rift valley floor (short 20km long segment) (oblique section north of Discovery anomaly)	Fresh, glassy pillow basalt fragments, and small, fist-size pieces	Fresh nuggets, with some appearing kidney-like	100
35D	45.74°S 14.62°W	2842-2640	Steep-sided ridge in MAR rift valley floor	Lost dredge due to weight-hook failure		
36D	45.57°S 14.71°W	3229-3000	Small volcano in centre of MAR rift valley floor (short 25km long segment) (oblique section north of Discovery anomaly)	Five small pieces of pillow basalt with fresh black glass, also one glassy slab and one thin slab without glass	Glass limited, but good quality	5
37D	45.23°S 15.08°W	3668-3400	Small ridge in MAR rift valley floor (oblique section north of Discovery anomaly)	1. One large, fresh glassy pillow basalt with hydrothermal staining and small vesicles; 2. Smaller fragments, glassy and slightly older with traces of ooze; 3. Small, fist-size aphyric glass; 4. Small slab with glass and crust, and oldest-looking pillow with glass and manganese	Minor	91
38D	44.81°S 15.37W	3860-3639	Deep basin in MAR rift valley floor (short segment)	Lost dredge due to bomb failure		
39D	44.68°S 15.39°W	3685-3520	Small volcano in MAR rift valley floor (northern-most station in oblique part of MAR associated with Discovery anomaly)	One fist-size pillow basalt fragment	One fist-size glass piece coated with manganese	1
40D	44.41°S 15.91°W	3600-3376	Small volcanic ridge in centre of MAR rift valley floor	Several types of fresh pillow basalts with glass: 1. Plagiophyric - glassy and brown crust; 2. Aphyric pillow glassy basalt; 3. Aphyric, grey with some glass preserved	1. Plagiophyric-type with dark brown crust; 2. Aphyric nugget 3. Aphyric chip with some brown crust	155
41D	44.02°S 16.08°W	3600-3444	MAR rift valley floor (small ridge, east side)	Three possible types of pillow basalt fragments: 1. Fresh, glassy with dark brown crust, small slab, and traces of ooze; 2. Fresh, grey-type with minor glass remaining (fist-size); 3. Older-looking glassy with crust, and definitely older with minor glass and manganese staining	Few nuggets, some with brown crust	273

University of Cape Town

Table A.1: Dredge station details continued

Station ID#	Lat. & Long.	Depth (m.b.s.l.)	Feature dredged	Rock recovery	Glass recovery	Weight (kg)
42D	43.43°S 16.17°W	3522-3375	Small volcano in centre of MAR rift valley floor	One small piece of mud		0.5
43D	42.19°S 16.08°W	3000-2850	Small volcano in centre of MAR rift valley floor	Fresh, plagiophyric, glassy pillow basalts of various sizes with dark brown crust	One chip of glass with crown crust and thin coating of manganese	68
44D	40.86°S 16.79°W	3194-2939	Small volcano in centre of MAR rift valley floor	Two possible types of highly plagiophyric pillow basalts: 1. Large pillow with glassy, brown crust and manganese stains; 2. Small, loaf-like pillow basalt with very fresh, thick glass with dark brown crust	Fist-size plagiophyric glass with brown crust, and glass nuggets	259
45D	40.59°S 16.77°W	3233-3172	Small volcano in deep basin at centre of MAR rift valley floor	Fresh, highly plagiophyric pillow basalt with fresh glass (with flow striations) and large phenocrysts	Minor	145

University of Cape Town

Table A.2: Dredge station details for Agulhas 32 samples. Dredging depth in metres below sea-level.

Station ID#	Latitude & Longitude	Depth (mbsl)	General description
A2	54.37°S 1.20°W	2500-2000	Microporphyritic pillow basalt with quench glass. Microlites of olivine and Cr-spinel.
A3	54.12°S 1.97°W	2500-2000	Aphyric to highly porphyritic massive basalt and pillow basaltwith quench glass. Phenocrysts and microphenocrysts include olivine, plagioclase and Cr-spinel. Porphyritic varieties include both plagioclase phyric basalt and olivine phyric (picrite) basalt.
A4	54.03°S 2.13°W	2800-2200	Aphyric to coarsely porphyritic massive basalt and pillow basalt with quench glass. Plagioclase and olivine phenocrysts and microphenocrysts occur in all samples, with clinopyroxene and Cr-spinel microphenocrysts restricted to three and five samples respectively.
A6	52.65°S 4.38°W	2400-2250	Aphyric to sparsely plagioclase phyric basalt. Plagioclase and rare olivine and Cr-spinel microphenocrysts occur.
A7	52.27°S 4.83°W	3400-2500	Moderately phyric to highly plagioclase phyric massive basalt, pillow basalt with quench glass and diabase. Olivine, plagioclase and clinopyroxene phenocrysts and microphenocrysts occur in most samples. Cr-spinel occurs in one sample, while an equant FeNi sulphide microphenocryst occurs in the glass of another.
A9	51.62°S 5.60°W	1700-1650	Aphyric moderately vesicular pillow basalt with quench glass. Plagioclase, olivine and clinopyroxene phenocrysts and microphenocrysts occur.
A10	51.28°S 5.85°W	2100-1950	Aphyric to highly plagioclase phyric. Olivine, plagioclase and clinopyroxene occur as phenocrysts in all samples.

University of Cape Town

APPENDIX B: ANALYTICAL DATA

INTRODUCTION

This appendix presents the results of all the compositional data, in terms of mineralogy of phenocryst phases, compositions of quenched igneous-glass and bulk-rock samples, gathered during this study according to the techniques and methodologies described in chapter 3. The following is a list of the tables in this appendix, with details of their content:

Table B.1: Olivine phenocryst compositions (EMP);

Table B.2: Plagioclase phenocryst compositions (EMP);

Table B.3: Clinopyroxene phenocryst compositions (EMP);

Table B.4: Spinel microphenocryst compositions (EMP);

Table B.5: Quenched igneous-glass compositions (EMP & LA-ICP-MS);

Table B.6: Bulk-rock compositions (XRF).

The data in all the tables in this appendix are ordered according to increasing latitude of the dredge stations from which the samples were recovered. All analyses are labelled with the sample-name from which the material, e.g. phenocryst or quenched igneous glass, came, i.e. 45D-2 indicates the material came from the second basalt sample recovered by dredge 45. The labels of the samples used from the Agulhas 32 collection are preceded by "A". Where the result for an element was below the lower limits of detection for that technique, it is listed as "< LLD" (with the relevant value for the LLD given, as listed in tables in chapter 3).

University of Cape Town

Table B.1: Olivine phenocryst compositions (EMP) in oxide-weight percentages, with all iron reported as Fe^{2+}. The size of phenocrysts analysed varied between phenocrysts (pheno) and microphenocryst (micro).

Sample	45D-2			44D-3				43D-1	41D-2				39D-2		
Size	pheno	pheno	pheno	pheno	micro	micro	micro	micro	micro	micro	pheno	pheno	micro	micro	micro
Lat. (°S)	40.59	40.59	40.59	40.86	40.86	40.86	40.86	42.19	44.02	44.02	44.02	44.02	44.68	44.68	44.68
SiO_2	40.35	40.95	40.97	40.14	39.89	40.28	39.98	40.15	40.03	40.10	40.38	40.03	40.07	40.17	40.33
TiO_2	< 0.039	< 0.039	< 0.039	< 0.039	< 0.039	< 0.039	< 0.039	< 0.039	< 0.039	< 0.039	< 0.039	< 0.039	< 0.039	< 0.039	< 0.039
Al_2O_3	0.07	< 0.038	< 0.038	< 0.038	< 0.038	< 0.038	0.07	0.07	< 0.038	< 0.038	0.08	< 0.038	< 0.038	< 0.038	< 0.038
Cr_2O_3	< 0.044	< 0.044	< 0.044	< 0.044	< 0.044	< 0.044	< 0.044	< 0.044	< 0.044	< 0.044	< 0.044	< 0.044	0.08	0.08	< 0.044
FeO	11.56	11.33	10.64	14.40	14.39	14.54	14.44	15.12	14.37	14.27	13.82	14.41	13.96	13.69	13.73
MnO	0.22	0.19	0.20	0.20	0.25	0.19	0.24	0.29	0.22	0.24	0.23	0.24	0.25	0.21	0.20
MgO	47.43	47.53	47.70	45.20	45.46	45.53	45.43	44.90	45.53	45.66	45.71	45.61	45.12	45.52	45.14
CaO	0.31	0.29	0.32	0.32	0.34	0.32	0.33	0.30	0.30	0.32	0.30	0.29	0.27	0.24	0.26
NiO	0.17	0.24	0.16	0.15	0.20	0.12	0.17	0.15	0.17	0.20	0.15	0.17	0.18	0.23	0.23
Total	100.11	100.53	99.99	100.41	100.53	100.98	100.66	100.98	100.62	100.79	100.67	100.75	99.93	100.14	99.89
Fo	87.6	87.83	88.55	84.53	84.53	84.53	84.50	83.72	84.62	84.7	85.16	84.58	84.82	85.17	85.03

Sample	39D-2	37D-3				36D-5				34D-3				33D-4	
Size	pheno	pheno	pheno	micro	micro	micro	micro	pheno	pheno	micro	micro	pheno	pheno	micro	micro
Lat. (°S)	44.68	45.23	45.23	45.23	45.23	45.57	45.57	45.57	45.57	45.85	45.85	45.85	45.85	45.99	45.99
SiO_2	40.30	40.69	40.83	39.97	40.07	39.97	39.99	39.95	39.87	40.12	40.28	40.49	40.35	39.69	40.25
TiO_2	< 0.039	< 0.039	< 0.039	< 0.039	< 0.039	< 0.039	< 0.039	< 0.039	< 0.039	< 0.039	< 0.039	< 0.039	< 0.039	< 0.039	< 0.039
Al_2O_3	< 0.038	< 0.038	< 0.038	< 0.038	< 0.038	< 0.038	0.09	< 0.038	< 0.038	0.10	< 0.038	0.09	0.10	< 0.038	< 0.038
Cr_2O_3	0.09	< 0.044	< 0.044	< 0.044	< 0.044	< 0.044	< 0.044	< 0.044	< 0.044	0.08	< 0.044	< 0.044	0.08	< 0.044	< 0.044
FeO	14.25	11.68	11.29	13.41	13.35	14.53	14.82	14.52	14.61	13.08	12.79	13.08	12.80	13.66	13.60
MnO	0.19	0.17	0.13	0.24	0.20	0.25	0.21	0.26	0.23	0.16	0.23	0.16	0.20	0.17	0.26
MgO	44.97	47.40	47.40	45.32	45.46	45.08	45.06	45.18	45.03	45.75	46.15	45.92	46.54	45.92	45.79
CaO	0.26	0.32	0.30	0.32	0.27	0.28	0.30	0.30	0.31	0.30	0.30	0.26	0.28	0.31	0.27
NiO	0.23	0.20	0.26	0.21	0.20	0.16	0.17	0.17	0.14	0.24	0.16	0.17	0.24	0.15	0.14
Total	100.29	100.46	100.21	99.47	99.55	100.27	100.64	100.38	100.19	99.83	99.91	100.17	100.59	99.90	100.31
Fo	84.53	87.52	87.86	85.35	85.50	84.32	84.09	84.35	84.27	85.82	86.20	85.93	86.24	85.42	85.36

Fo: forsterite content as percentage

University of Cape Town

Table B.1 (cont.)

Sample	33D-4		32D-2				30D-1				28D-2				28D-3
Size	micro	micro	micro	micro	pheno	pheno	micro	pheno	pheno	pheno	pheno	pheno	micro	micro	micro
Lat. (°S)	45.99	45.99	46.23	46.23	46.23	46.23	46.59	46.59	46.59	46.59	46.90	46.90	46.90	46.90	46.90
SiO_2	40.02	39.93	39.79	39.89	40.21	40.05	40.10	39.71	39.25	39.84	39.92	39.62	39.94	40.01	40.13
TiO_2	< 0.039	< 0.039	< 0.039	< 0.039	< 0.039	< 0.039	< 0.039	< 0.039	< 0.039	< 0.039	< 0.039	< 0.039	< 0.039	< 0.039	< 0.039
Al_2O_3	0.07	0.08	< 0.038	< 0.038	< 0.038	< 0.038	0.09	< 0.038	< 0.038	< 0.038	0.06	0.06	0.06	< 0.038	< 0.038
Cr_2O_3	< 0.044	< 0.044	< 0.044	< 0.044	< 0.044	< 0.044	< 0.044	0.08	< 0.044	< 0.044	< 0.044	< 0.044	0.08	< 0.044	< 0.044
FeO	13.93	14.25	14.65	14.52	13.63	14.14	12.65	13.72	14.01	14.20	13.08	13.24	13.42	13.12	12.80
MnO	0.18	0.23	0.23	0.26	0.17	0.25	0.21	0.24	0.24	0.17	0.17	0.24	0.22	0.26	0.18
MgO	44.61	45.16	44.64	44.69	45.60	45.06	46.47	45.60	45.44	46.01	46.46	45.93	46.10	45.87	45.92
CaO	0.28	0.29	0.30	0.28	0.32	0.30	0.30	0.31	0.29	0.29	0.31	0.33	0.33	0.36	0.34
NiO	0.11	0.16	0.10	< 0.052	0.13	0.14	0.15	0.19	0.20	0.19	0.23	0.19	0.20	0.19	0.15
Total	99.20	100.10	99.71	99.64	100.06	99.94	99.97	99.85	99.43	100.70	100.23	99.61	100.35	99.81	99.52
Fo	84.83	84.61	84.16	84.35	85.37	84.69	86.43	85.18	84.87	84.93	86.00	85.69	85.59	85.76	86.18

Sample	28D-3					28D-9	27D-1		26D-5		25D-8				2D-3
Size	pheno	pheno	micro	micro	micro	micro	pheno	pheno	micro	pheno	pheno	pheno	pheno	pheno	micro
Lat. (°S)	46.90	46.90	46.90	46.90	46.90	46.90	47.11	47.11	47.35	47.35	47.35	47.35	47.35	47.35	47.55
SiO_2	39.89	39.61	40.09	39.74	39.69	39.12	40.25	40.37	38.75	40.33	40.31	40.06	40.23	40.43	39.75
TiO_2	< 0.039	< 0.039	< 0.039	< 0.039	< 0.039	< 0.039	< 0.039	< 0.039	< 0.039	< 0.039	< 0.039	< 0.039	< 0.039	< 0.039	< 0.039
Al_2O_3	< 0.038	< 0.038	< 0.038	< 0.038	< 0.038	0.10	0.07	0.07	0.07	< 0.038	0.07	< 0.038	< 0.038	< 0.038	< 0.038
Cr_2O_3	< 0.044	< 0.044	< 0.044	< 0.044	< 0.044	< 0.044	< 0.044	< 0.044	< 0.044	< 0.044	0.09	< 0.044	0.09	< 0.044	< 0.044
FeO	13.09	13.49	13.39	13.21	13.04	14.01	12.43	12.32	17.59	10.01	13.47	12.77	12.04	12.32	14.84
MnO	0.18	0.22	0.23	0.20	0.19	0.21	0.15	0.17	0.30	0.13	0.13	0.17	0.15	0.21	0.19
MgO	45.54	45.83	46.22	46.45	46.06	45.31	47.36	47.16	41.95	48.20	46.21	46.64	46.77	46.95	45.02
CaO	0.36	0.32	0.32	0.33	0.30	0.31	0.33	0.31	0.32	0.28	0.20	0.19	0.18	0.18	0.29
NiO	0.12	0.17	0.16	0.18	0.22	0.20	0.27	0.24	0.10	0.26	0.35	0.45	0.45	0.42	0.16
Total	99.18	99.64	100.41	100.11	99.50	99.26	100.86	100.64	99.08	99.21	100.83	100.28	99.91	100.51	100.25
Fo	85.84	85.48	85.67	85.90	85.93	84.85	86.80	86.85	80.61	89.21	85.53	86.14	86.84	86.62	84.08

Fo: forsterite content as percentage

University of Cape Town

Table B.1 (cont.)

Sample	2D-3							3D-1	4D-7						
Size	micro	micro	micro	micro	micro	micro	micro	micro	micro	micro	micro	micro	micro	micro	micro
Lat. (°S)	47.55	47.55	47.55	47.55	47.55	47.55	47.55	47.80	47.97	47.97	47.97	47.97	47.97	47.97	47.97
SiO_2	39.57	39.63	39.61	39.48	39.49	39.43	39.49	40.47	40.27	39.82	39.65	39.59	39.66	40.02	40.11
TiO_2	< 0.039	< 0.039	< 0.039	< 0.039	< 0.039	< 0.039	< 0.039	< 0.039	< 0.039	< 0.039	< 0.039	< 0.039	< 0.039	< 0.039	< 0.039
Al_2O_3	< 0.038	< 0.038	< 0.038	< 0.038	< 0.038	< 0.038	0.07	< 0.038	0.07	0.07	< 0.038	< 0.038	< 0.038	0.09	< 0.038
Cr_2O_3	< 0.044	< 0.044	< 0.044	< 0.044	< 0.044	< 0.044	< 0.044	< 0.044	< 0.044	< 0.044	< 0.044	< 0.044	< 0.044	< 0.044	< 0.044
FeO	14.43	15.34	15.32	14.67	14.79	15.09	15.61	12.20	12.34	14.14	14.84	14.25	15.25	13.37	12.33
MnO	0.22	0.23	0.21	0.29	0.23	0.18	0.27	0.15	0.16	0.18	0.21	0.20	0.18	0.15	0.21
MgO	44.99	44.63	44.58	44.97	44.52	44.59	44.05	46.52	46.50	45.80	45.09	45.67	44.74	46.03	46.63
CaO	0.31	0.33	0.32	0.31	0.32	0.32	0.34	0.30	0.27	0.29	0.26	0.30	0.28	0.27	0.28
NiO	< 0.052	0.11	0.14	0.16	0.16	0.15	0.13	0.15	0.24	0.17	0.17	0.20	0.20	0.25	0.19
Total	99.52	100.27	100.18	99.88	99.51	99.76	99.96	99.79	99.85	100.47	100.22	100.21	100.31	100.18	99.75
Fo	84.55	83.53	83.53	84.13	83.94	83.75	83.06	86.90	86.68	84.93	84.08	84.75	83.62	85.62	86.72

Sample	5D-4					6D-1	7D-1		7D-2				7D-3		
Size	pheno	micro	micro	micro	micro	micro	pheno	pheno	pheno	pheno	micro	micro	pheno	micro	micro
Lat. (°S)	48.24	48.24	48.24	48.24	48.24	48.55	48.76	48.76	48.76	48.76	48.76	48.76	48.76	48.76	48.76
SiO_2	40.03	39.56	40.01	39.60	39.93	39.90	39.54	39.83	38.94	39.06	37.90	37.97	39.27	39.76	39.42
TiO_2	< 0.039	< 0.039	< 0.039	< 0.039	< 0.039	< 0.039	< 0.039	< 0.039	< 0.039	< 0.039	< 0.039	< 0.039	< 0.039	< 0.039	< 0.039
Al_2O_3	< 0.038	< 0.038	< 0.038	< 0.038	< 0.038	0.08	0.06	< 0.038	< 0.038	< 0.038	< 0.038	< 0.038	0.05	0.05	0.06
Cr_2O_3	< 0.044	< 0.044	< 0.044	< 0.044	< 0.044	< 0.044	< 0.044	< 0.044	< 0.044	< 0.044	< 0.044	< 0.044	< 0.044	< 0.044	< 0.044
FeO	14.58	14.56	14.45	14.47	14.75	15.53	12.08	12.39	18.54	18.89	24.48	24.90	13.89	12.15	13.62
MnO	0.19	0.18	0.18	0.23	0.20	0.23	0.20	0.24	0.26	0.29	0.33	0.37	0.16	0.22	0.23
MgO	45.49	45.49	45.12	45.00	44.83	43.21	47.42	47.38	41.83	41.49	37.17	36.55	45.84	47.22	45.84
CaO	0.29	0.26	0.27	0.28	0.25	0.33	0.27	0.26	0.28	0.25	0.30	0.32	0.28	0.35	0.34
NiO	0.22	0.27	0.20	0.22	0.24	0.17	0.22	0.20	0.10	< 0.052	0.11	< 0.052	0.18	0.20	0.13
Total	100.80	100.32	100.23	99.80	100.20	99.45	99.79	100.30	99.95	99.98	100.29	100.11	99.67	99.95	99.64
Fo	84.40	84.39	84.44	84.32	84.03	82.87	87.12	86.81	79.78	79.40	72.67	72.05	85.17	87.01	85.39

Fo: forsterite content as percentage

University of Cape Town

Table B.1 (cont.)

Sample	7D-3	8D-1			9D-3				10D-1			10D-2	10D-3		
Size	micro	micro	micro	micro	micro	micro	pheno	pheno	micro	pheno	micro	pheno	pheno	pheno	micro
Lat. (°S)	48.76	48.96	48.96	48.96	49.15	49.15	49.15	49.15	49.25	49.25	49.25	49.25	49.25	49.25	49.25
SiO_2	39.57	40.29	40.17	40.01	39.98	40.25	39.64	39.95	39.17	39.24	39.21	39.78	39.50	39.51	39.10
TiO_2	< 0.039	< 0.039	< 0.039	< 0.039	< 0.039	< 0.039	< 0.039	< 0.039	< 0.039	< 0.039	< 0.039	< 0.039	< 0.039	< 0.039	< 0.039
Al_2O_3	< 0.038	0.08	< 0.038	0.08	< 0.038	0.12	0.08	0.10	< 0.038	0.07	< 0.038	< 0.038	0.05	< 0.038	0.05
Cr_2O_3	< 0.044	< 0.044	0.08	0.08	< 0.044	0.08	< 0.044	< 0.044	< 0.044	< 0.044	< 0.044	< 0.044	< 0.044	< 0.044	< 0.044
FeO	13.72	13.22	12.90	13.11	13.18	13.49	14.42	14.28	15.47	15.30	14.46	14.69	13.51	13.65	15.89
MnO	0.19	0.21	0.16	0.25	0.22	0.25	0.26	0.27	0.22	0.21	0.20	0.26	0.17	0.24	0.29
MgO	45.93	46.26	46.30	46.27	46.08	45.86	44.96	44.45	45.51	45.25	46.13	44.55	46.31	45.93	44.32
CaO	0.31	0.30	0.29	0.30	0.28	0.31	0.34	0.37	0.29	0.28	0.27	0.31	0.30	0.31	0.31
NiO	0.15	0.19	0.25	0.19	0.21	0.23	0.18	0.18	0.18	0.13	0.20	0.18	0.17	0.19	0.15
Total	99.87	100.55	100.15	100.29	99.95	100.59	99.88	99.60	100.84	100.48	100.47	99.77	100.01	99.83	100.11
Fo	85.35	85.83	86.12	85.89	85.79	85.41	84.36	84.33	83.64	83.76	84.70	84.00	85.63	85.33	82.87

Sample	10D-3	10D-9				11D-9		12D-1		12D-2		12D-3			
Size	micro	pheno	pheno	micro	micro	micro	micro	micro	micro	pheno	pheno	pheno	pheno	pheno	micro
Lat. (°S)	49.25	49.25	49.25	49.25	49.25	49.44	49.44	49.76	49.76	49.76	49.76	49.76	49.76	49.76	49.76
SiO_2	39.24	39.63	39.41	39.09	39.03	39.60	39.58	39.43	39.44	39.24	39.41	39.85	40.06	40.03	39.47
TiO_2	< 0.039	< 0.039	< 0.039	< 0.039	< 0.039	< 0.039	< 0.039	< 0.039	< 0.039	< 0.039	< 0.039	< 0.039	< 0.039	< 0.039	< 0.039
Al_2O_3	< 0.038	0.06	0.06	< 0.038	< 0.038	< 0.038	< 0.038	0.06	0.07	< 0.038	< 0.038	0.08	< 0.038	0.07	0.07
Cr_2O_3	< 0.044	< 0.044	< 0.044	< 0.044	0.08	< 0.044	< 0.044	< 0.044	< 0.044	< 0.044	< 0.044	< 0.044	< 0.044	0.11	< 0.044
FeO	15.46	14.49	14.57	16.24	15.96	14.09	14.30	13.34	13.75	14.14	13.93	13.17	11.56	12.02	14.17
MnO	0.22	0.20	0.20	0.25	0.27	0.23	0.24	0.26	0.23	0.22	0.18	0.20	0.19	0.18	0.26
MgO	44.58	45.88	45.51	44.54	44.59	44.72	44.50	45.97	45.69	45.34	45.52	45.52	47.01	46.32	45.54
CaO	0.28	0.28	0.32	0.30	0.29	0.30	0.35	0.29	0.28	0.31	0.31	0.29	0.28	0.27	0.30
NiO	0.17	0.22	0.23	0.15	0.16	0.26	0.22	0.25	0.24	0.20	0.20	0.23	0.23	0.24	0.24
Total	99.95	100.76	100.30	100.57	100.38	99.20	99.19	99.60	99.70	99.45	99.55	99.34	99.33	99.24	100.05
Fo	83.38	84.59	84.39	82.67	82.91	84.54	84.31	85.55	85.14	84.75	85.01	85.65	87.49	86.91	84.70

Fo: forsterite content as percentage

University of Cape Town

Table B.1 (cont.)

Sample	12D-3	13D-2			14D-1				15D-2		17D-1				19D-2
Size	micro	micro	micro	micro	micro	micro	micro	micro	micro	micro	micro	micro	micro	pheno	pheno
Lat. (°S)	49.76	49.99	49.99	49.99	50.27	50.27	50.27	50.27	50.58	50.58	50.76	50.76	50.76	50.76	51.06
SiO_2	39.59	39.87	40.03	40.65	39.57	39.56	39.67	39.90	39.24	39.47	39.87	39.27	39.54	41.92	39.08
TiO_2	< 0.039	< 0.039	< 0.039	< 0.039	< 0.039	< 0.039	< 0.039	< 0.039	< 0.039	< 0.039	< 0.039	< 0.039	< 0.039	0.42	< 0.039
Al_2O_3	< 0.038	0.07	< 0.038	0.07	< 0.038	< 0.038	< 0.038	< 0.038	0.08	< 0.038	< 0.038	< 0.038	< 0.038	2.36	< 0.038
Cr_2O_3	< 0.044	< 0.044	< 0.044	< 0.044	< 0.044	< 0.044	< 0.044	< 0.044	< 0.044	< 0.044	< 0.044	< 0.044	< 0.044	< 0.044	< 0.044
FeO	14.20	12.08	12.42	12.28	14.15	14.67	14.84	14.19	15.79	16.35	14.60	14.81	14.77	18.14	17.37
MnO	0.18	0.21	0.17	0.19	0.22	0.19	0.24	0.24	0.18	0.27	0.26	0.23	0.26	0.25	0.20
MgO	45.13	46.47	46.96	46.32	44.66	44.68	44.68	44.95	43.57	43.87	44.80	44.17	44.81	36.96	42.98
CaO	0.32	0.28	0.31	0.32	0.29	0.30	0.28	0.27	0.29	0.30	0.30	0.28	0.30	0.68	0.24
NiO	0.22	0.22	0.23	0.21	0.21	0.22	0.20	0.20	0.20	0.20	0.24	0.27	0.22	0.15	0.28
Total	99.64	99.20	100.12	100.04	99.10	99.62	99.91	99.75	99.35	100.46	100.07	99.03	99.90	100.88	100.15
Fo	84.64	86.88	86.72	86.70	84.52	84.09	83.91	84.56	82.76	82.30	84.11	83.72	83.97	78.04	81.10

Sample	19D-2				19D-7		19D-9				20D-3			21D-3	
Size	pheno	pheno	pheno	micro	pheno	pheno	pheno	micro	micro	micro	micro	micro	pheno	micro	micro
Lat. (°S)	51.06	51.06	51.06	51.06	51.06	51.06	51.06	51.06	51.06	51.06	51.43	51.43	51.43	51.82	51.82
SiO_2	39.40	39.45	39.33	38.60	38.67	39.13	39.85	39.55	39.97	39.55	39.58	39.31	38.80	40.04	39.32
TiO_2	< 0.039	< 0.039	< 0.039	< 0.039	< 0.039	< 0.039	< 0.039	< 0.039	< 0.039	< 0.039	< 0.039	< 0.039	< 0.039	< 0.039	< 0.039
Al_2O_3	< 0.038	< 0.038	< 0.038	< 0.038	0.07	0.07	< 0.038	< 0.038	< 0.038	< 0.038	< 0.038	< 0.038	< 0.038	< 0.038	< 0.038
Cr_2O_3	< 0.044	< 0.044	< 0.044	< 0.044	< 0.044	0.08	0.09	< 0.044	< 0.044	< 0.044	< 0.044	< 0.044	< 0.044	< 0.044	< 0.044
FeO	16.39	16.44	15.81	19.20	15.83	15.84	12.11	13.51	13.52	13.39	15.52	16.50	17.65	12.23	15.58
MnO	0.22	0.16	0.20	0.17	0.19	0.24	0.16	0.20	0.23	0.22	0.26	0.26	0.26	0.21	0.24
MgO	43.89	43.49	44.11	41.53	43.98	44.89	47.12	45.94	46.53	45.85	44.31	43.19	41.85	46.72	43.65
CaO	0.25	0.28	0.25	0.30	0.24	0.23	0.33	0.31	0.30	0.32	0.33	0.32	0.32	0.31	0.32
NiO	0.31	0.29	0.30	0.19	0.25	0.29	0.13	0.19	0.16	0.19	0.13	< 0.052	0.12	0.16	0.15
Total	100.46	100.11	100.00	99.99	99.23	100.77	99.79	99.70	100.71	99.52	100.13	99.58	99.00	99.67	99.26
Fo	82.23	82.12	82.83	79.10	82.82	83.02	87.13	85.49	85.64	85.56	83.23	82.12	80.53	86.86	82.97

Fo: forsterite content as percentage

University of Cape Town

Table B.1 (cont.)

Sample	21D-3		23D-1		22D-4			
Size	pheno	pheno	micro	micro	micro	micro	micro	micro
Lat. (°S)	51.82	51.82	52.16	52.16	52.46	52.46	52.46	52.46
SiO_2	39.74	38.80	38.36	39.04	37.63	37.42	37.63	37.88
TiO_2	< 0.039	< 0.039	< 0.039	< 0.039	< 0.039	< 0.039	< 0.039	< 0.039
Al_2O_3	< 0.038	< 0.038	< 0.038	0.07	< 0.038	< 0.038	< 0.038	< 0.038
Cr_2O_3	< 0.044	< 0.044	< 0.044	< 0.044	< 0.044	< 0.044	< 0.044	< 0.044
FeO	13.28	19.06	21.47	17.66	25.84	26.22	25.39	25.42
MnO	0.18	0.33	0.40	0.28	0.40	0.37	0.34	0.35
MgO	46.12	42.12	39.60	42.46	36.40	36.09	36.91	36.80
CaO	0.36	0.28	0.30	0.30	0.29	0.26	0.29	0.29
NiO	0.18	< 0.052	0.11	0.12	0.12	0.10	0.09	0.10
Total	99.86	100.59	100.24	99.93	100.68	100.46	100.65	100.84
Fo	85.77	79.47	76.25	80.73	71.11	70.68	71.81	71.71

Fo: forsterite content as percentage

University of Cape Town

Table B.2: Plagioclase phenocryst compositions (EMP) in oxide-weight percentages, with all iron reported as Fe^{2+}. The size of phenocrysts analysed varied between phenocrysts (pheno) and microphenocryst (micro).

Sample	45D-2				44D-3				43D-1			41D-2			
Size	pheno	pheno	pheno	micro	micro	pheno	micro	pheno	pheno	pheno	pheno	micro	micro	pheno	pheno
Lat. (°S)	40.59	40.59	40.59	40.59	40.86	40.86	40.86	40.86	42.19	42.19	42.19	44.02	44.02	44.02	44.02
SiO_2	46.57	48.29	46.88	48.25	47.91	47.49	51.14	52.11	48.63	47.85	49.46	52.40	51.31	51.68	52.01
Al_2O_3	33.38	32.45	33.30	31.93	31.97	32.42	29.95	29.63	31.92	32.27	31.95	29.97	30.18	30.09	29.53
FeO	0.29	0.33	0.22	0.27	0.32	0.31	0.44	0.48	0.41	0.33	0.45	0.40	0.49	0.56	0.45
MgO	0.17	0.23	0.16	0.24	0.18	0.18	0.24	0.29	0.20	0.19	0.23	0.27	0.22	0.28	0.26
CaO	18.00	17.03	18.05	16.64	16.79	17.12	14.43	14.16	16.59	17.01	16.36	14.17	14.50	14.40	13.92
NA_2O	1.19	1.85	1.07	1.87	1.86	1.69	3.24	3.52	1.98	1.73	2.26	3.55	3.22	3.35	3.57
K_2O	< 0.024	< 0.024	< 0.024	< 0.024	< 0.024	< 0.024	< 0.024	< 0.024	< 0.024	< 0.024	< 0.024	< 0.024	< 0.024	0.04	< 0.024
Total	99.60	100.18	99.68	99.20	99.03	99.21	99.44	100.19	99.73	99.38	100.71	100.76	99.92	100.40	99.74
An	89.30	83.59	90.30	83.09	83.29	84.85	71.13	68.98	82.25	84.48	79.97	68.80	71.33	70.22	68.31

Sample	40D-1				36D-5				32D-2				31D-1		30D-1
Size	pheno	pheno	pheno	pheno	pheno	pheno	micro	micro	pheno	micro	pheno	pheno	pheno	pheno	pheno
Lat. (°S)	44.41	44.41	44.41	44.41	44.68	44.68	44.68	44.68	46.23	46.23	46.23	46.23	46.39	46.39	46.59
SiO_2	49.64	50.25	48.98	51.61	48.65	49.10	50.77	51.19	47.86	51.90	49.47	48.09	47.58	48.32	48.91
Al_2O_3	31.01	30.64	31.66	30.21	31.81	31.82	30.74	30.35	32.55	29.80	31.62	32.83	32.79	32.40	31.05
FeO	0.36	0.37	0.38	0.36	0.38	0.45	0.39	0.45	0.23	0.45	0.40	0.35	0.29	0.37	0.38
MgO	0.22	0.23	0.21	0.25	0.21	0.21	0.21	0.21	0.19	0.23	0.27	0.20	0.16	0.16	0.24
CaO	15.73	15.19	16.12	14.71	16.47	16.30	15.28	14.67	17.29	14.29	16.37	17.26	17.42	17.04	15.99
NA_2O	2.52	2.92	2.31	3.15	2.15	2.26	3.00	3.16	1.82	3.58	2.37	1.77	1.63	1.96	2.48
K_2O	< 0.024	< 0.024	< 0.024	< 0.024	< 0.024	< 0.024	< 0.024	< 0.024	< 0.024	0.06	< 0.024	< 0.024	< 0.024	< 0.024	< 0.024
Total	99.48	99.60	99.66	100.29	99.67	100.14	100.39	100.03	99.94	100.31	100.50	100.50	99.87	100.25	99.05
An	77.52	74.17	79.40	72.04	80.89	79.96	73.78	71.97	84.02	68.53	79.26	84.33	85.54	82.79	78.09

An: anorthite content as percentage

University of Cape Town

Table B.2 (cont.)

Sample	30D-1			28D-2				28D-3						27D-1	
Size	pheno	pheno	pheno	pheno	pheno	micro	micro	pheno	pheno	pheno	pheno	micro	micro	pheno	pheno
Lat. (°S)	46.59	46.59	46.59	46.90	46.90	46.90	46.90	46.90	46.90	46.90	46.90	46.90	46.90	47.11	47.11
SiO_2	47.47	47.60	47.88	49.90	49.44	52.67	52.92	48.17	48.79	47.44	50.43	52.33	50.98	47.69	47.96
Al_2O_3	32.17	31.92	31.93	30.67	30.47	28.68	28.96	31.91	31.28	32.45	29.99	29.43	29.54	32.74	33.04
FeO	0.33	0.42	0.41	0.39	0.37	0.56	0.58	0.38	0.38	0.37	0.46	0.51	0.54	0.27	0.29
MgO	0.26	0.19	0.21	0.23	0.23	0.28	0.31	0.18	0.23	0.22	0.26	0.26	0.25	0.20	0.21
CaO	17.09	17.08	16.87	16.15	16.13	13.96	13.86	16.91	16.32	17.41	14.96	14.42	14.92	17.33	17.49
NA_2O	1.90	1.85	1.91	2.30	2.38	3.53	3.61	1.92	2.27	1.61	3.04	3.29	2.91	1.66	1.58
K_2O	< 0.024	< 0.024	< 0.024	< 0.024	< 0.024	< 0.024	< 0.024	< 0.024	< 0.024	< 0.024	< 0.024	< 0.024	< 0.024	< 0.024	< 0.024
Total	99.22	99.06	99.21	99.64	99.02	99.68	100.24	99.47	99.27	99.50	99.14	100.24	99.14	99.89	100.57
An	83.27	83.59	82.99	79.49	78.96	68.64	67.95	82.99	79.88	85.67	73.10	70.78	73.89	85.22	85.91

Sample	27D-1		26D-5			2D-3								3D-1	
Size	pheno	pheno	pheno	pheno	pheno	pheno	pheno	pheno	pheno	micro	micro	micro	micro	pheno	pheno
Lat. (°S)	47.11	47.11	47.35	47.35	47.35	47.55	47.55	47.55	47.55	47.55	47.55	47.55	47.55	47.80	47.80
SiO_2	47.79	49.51	52.29	53.51	53.62	51.00	51.11	52.62	52.22	51.81	52.64	52.04	52.68	47.33	49.00
Al_2O_3	33.18	31.91	30.32	29.31	29.27	30.49	30.35	28.94	29.52	29.73	29.27	29.56	29.33	32.52	31.78
FeO	0.34	0.32	0.39	0.54	0.48	0.34	0.38	0.48	0.43	0.48	0.48	0.50	0.56	0.36	0.37
MgO	0.21	0.22	0.23	0.21	0.21	0.21	0.21	0.25	0.23	0.23	0.24	0.25	0.24	0.21	0.24
CaO	17.49	16.45	14.20	13.17	13.20	14.62	14.41	13.29	14.08	14.05	13.45	13.91	13.49	17.17	15.92
NA_2O	1.54	2.08	3.32	3.82	4.07	3.24	3.33	4.01	3.69	3.57	3.95	3.64	3.85	1.48	2.05
K_2O	< 0.024	< 0.024	< 0.024	< 0.024	< 0.024	0.08	0.09	0.10	0.09	0.09	0.09	0.09	0.10	< 0.024	0.04
Total	100.55	100.49	100.75	100.56	100.85	99.98	99.88	99.69	100.26	99.96	100.12	99.99	100.25	99.07	99.40
An	86.26	81.40	70.26	65.55	64.18	71.05	70.13	64.33	67.48	68.17	65.00	67.53	65.59	86.49	80.86

An: anorthite content as percentage

University of Cape Town

Table B.2 (cont.)

Sample	3D-1		4D-7								6D-1				7D-1
Size	pheno	pheno	micro	micro	pheno	pheno	micro	micro	pheno	pheno	pheno	pheno	pheno	pheno	pheno
Lat. (°S)	47.80	47.80	47.97	47.97	47.97	47.97	47.97	47.97	47.97	47.97	48.55	48.55	48.55	48.55	48.76
SiO_2	48.38	48.61	48.90	50.27	48.74	48.14	49.60	49.56	48.24	48.65	49.88	51.12	52.63	49.59	50.80
Al_2O_3	32.32	32.08	32.38	31.35	32.34	32.27	31.71	31.43	32.58	32.35	31.77	30.90	29.89	32.20	30.21
FeO	0.35	0.33	0.35	0.42	0.27	0.31	0.34	0.44	0.36	0.31	0.41	0.42	0.49	0.36	0.37
MgO	0.23	0.25	0.21	0.25	0.19	0.21	0.27	0.25	0.20	0.18	0.24	0.25	0.18	0.20	0.25
CaO	16.49	16.36	16.79	15.94	16.71	16.85	16.25	16.01	16.91	16.50	15.52	14.54	13.52	15.78	14.97
NA_2O	1.91	1.92	1.75	2.18	1.76	1.77	1.99	2.04	1.58	1.70	2.32	2.81	3.56	2.14	2.78
K_2O	< 0.024	< 0.024	< 0.024	0.04	< 0.024	0.04	< 0.024	< 0.024	< 0.024	< 0.024	0.04	0.06	0.09	0.04	0.05
Total	99.68	99.55	100.38	100.45	100.01	99.59	100.16	99.73	99.87	99.69	100.18	100.10	100.36	100.31	99.43
An	82.67	82.46	84.15	79.97	84.03	83.83	81.85	81.28	85.57	84.30	78.50	73.81	67.37	80.06	74.62

Sample	7D-1	7D-2					7D-3				8D-1				9D-3
Size	pheno	pheno	pheno	pheno	pheno	pheno	pheno	pheno	micro	micro	pheno	pheno	pheno	pheno	pheno
Lat. (°S)	48.76	48.76	48.76	48.76	48.76	48.76	48.76	48.76	48.76	48.76	48.96	48.96	48.96	48.96	49.15
SiO_2	50.41	53.14	52.95	52.76	52.65	52.69	49.20	48.41	51.91	49.59	49.39	51.29	50.27	51.05	48.74
Al_2O_3	31.45	29.33	29.12	29.84	30.06	30.00	31.97	32.47	30.06	31.89	32.22	30.91	31.75	30.90	32.33
FeO	0.32	0.59	0.54	0.55	0.54	0.54	0.37	0.35	0.43	0.40	0.36	0.46	0.37	0.43	0.32
MgO	0.22	0.16	0.19	0.19	0.18	0.18	0.22	0.17	0.25	0.24	0.18	0.25	0.23	0.24	0.23
CaO	15.82	12.97	12.99	13.27	13.25	13.34	17.00	17.35	14.63	16.73	15.86	14.42	15.31	14.72	16.13
NA_2O	2.32	3.69	3.65	3.61	3.67	3.54	1.95	1.57	3.11	2.04	2.10	2.87	2.42	2.77	1.87
K_2O	< 0.024	0.10	0.12	0.09	0.11	0.09	< 0.024	< 0.024	0.06	< 0.024	0.04	0.06	< 0.024	0.05	0.04
Total	100.54	99.98	99.56	100.31	100.46	100.38	100.71	100.32	100.45	100.89	100.15	100.26	100.35	100.16	99.66
An	79.02	65.61	65.81	66.65	66.21	67.17	82.83	85.95	71.95	81.95	80.51	73.29	77.75	74.39	82.49

An: anorthite content as percentage

University of Cape Town

Table B.2 (cont.)

Sample	9D-3					10D-1			10D-2						10D-3
Size	pheno	pheno	pheno	micro	micro	micro	micro	pheno	pheno	pheno	pheno	pheno	micro	micro	pheno
Lat. (°S)	49.15	49.15	49.15	49.15	49.15	49.25	49.25	49.25	49.25	49.25	49.25	49.25	49.25	49.25	49.25
SiO_2	49.36	49.54	49.20	49.02	48.59	53.94	52.41	51.86	51.75	49.66	51.62	49.14	52.07	51.37	49.46
Al_2O_3	32.26	32.22	32.24	32.23	31.73	29.01	29.46	29.88	29.99	31.89	30.39	32.05	29.40	29.91	31.73
FeO	0.35	0.31	0.36	0.35	0.32	0.53	0.51	0.33	0.43	0.41	0.42	0.31	0.51	0.52	0.29
MgO	0.22	0.23	0.22	0.24	0.24	0.27	0.23	0.22	0.24	0.19	0.23	0.17	0.25	0.25	0.16
CaO	15.94	15.85	16.04	16.57	16.18	13.26	14.19	14.65	13.85	15.29	13.82	15.82	13.60	14.23	16.60
NA_2O	2.03	2.06	1.97	1.86	1.95	3.95	3.44	3.14	3.28	2.45	3.20	2.12	3.48	3.15	2.04
K_2O	0.04	< 0.024	< 0.024	0.04	< 0.024	< 0.024	< 0.024	0.04	< 0.024	< 0.024	< 0.024	< 0.024	< 0.024	< 0.024	< 0.024
Total	100.20	100.21	100.03	100.31	99.01	100.96	100.24	100.12	99.54	99.89	99.68	99.61	99.31	99.43	100.28
An	81.08	80.96	81.79	82.94	82.07	64.97	69.53	71.90	70.00	77.54	70.47	80.47	68.38	71.41	81.78

Sample	10D-3			10D-8			10D-9				11D-9		12D-1		12D-2
Size	pheno	micro	micro	pheno	micro	micro	pheno	pheno	micro	micro	pheno	pheno	pheno	micro	pheno
Lat. (°S)	49.25	49.25	49.25	49.25	49.25	49.25	49.25	49.25	49.25	49.25	49.44	49.44	49.76	49.76	49.76
SiO_2	49.10	53.14	53.41	49.04	53.26	53.51	49.32	50.91	53.03	52.73	49.74	49.39	48.48	49.20	49.66
Al_2O_3	31.94	29.05	28.85	32.22	29.06	28.93	31.63	30.46	29.02	28.96	31.43	31.49	31.33	29.73	31.27
FeO	0.28	0.57	0.49	0.28	0.59	0.57	0.38	0.41	0.47	0.67	0.44	0.36	0.37	1.25	0.39
MgO	0.18	0.25	0.25	0.18	0.27	0.24	0.15	0.21	0.22	0.26	0.15	0.19	0.20	0.94	0.25
CaO	16.74	13.64	13.25	16.72	13.64	13.42	16.23	15.13	13.58	13.73	15.66	15.54	16.94	15.86	16.37
NA_2O	1.94	3.83	3.97	1.78	3.60	3.73	2.12	2.86	3.75	3.60	2.19	2.40	1.84	2.16	2.15
K_2O	< 0.024	< 0.024	< 0.024	< 0.024	< 0.024	< 0.024	< 0.024	< 0.024	< 0.024	< 0.024	< 0.024	< 0.024	< 0.024	< 0.024	< 0.024
Total	100.18	100.48	100.22	100.22	100.42	100.40	99.83	99.98	100.07	99.95	99.61	99.37	99.16	99.14	100.09
An	82.64	66.30	64.85	83.86	67.70	66.53	80.87	74.52	66.65	67.82	79.78	78.16	83.54	80.20	80.77

An: anorthite content as percentage

University of Cape Town

Table B.2 (cont.)

Sample	12D-2	12D-3						13D-2				14D-1			
Size	pheno	pheno	pheno	pheno	pheno	micro	micro	micro	pheno	micro	micro	pheno	pheno	pheno	pheno
Lat. (°S)	49.76	49.76	49.76	49.76	49.76	49.76	49.76	49.99	49.99	49.99	49.99	50.27	50.27	50.27	50.27
SiO_2	49.99	49.10	49.00	49.06	51.19	50.60	49.41	48.90	48.25	49.05	50.02	48.86	47.58	47.87	47.74
Al_2O_3	31.13	31.49	31.50	31.69	30.37	30.75	31.70	31.73	32.03	31.57	30.65	31.60	32.73	32.82	32.45
FeO	0.41	0.34	0.33	0.30	0.33	0.37	0.48	0.33	0.43	0.31	0.38	0.33	0.39	0.36	0.40
MgO	0.20	0.24	0.24	0.23	0.27	0.23	0.23	0.22	0.23	0.24	0.28	0.21	0.18	0.18	0.21
CaO	15.97	15.89	16.05	15.76	14.42	15.05	15.72	16.17	16.50	16.04	15.22	16.11	17.08	16.92	16.72
NA_2O	2.37	2.21	2.15	2.19	3.06	3.00	2.69	2.12	1.84	2.10	2.64	2.02	1.45	1.42	1.59
K_2O	< 0.024	< 0.024	< 0.024	< 0.024	< 0.024	< 0.024	< 0.024	< 0.024	< 0.024	< 0.024	< 0.024	< 0.024	< 0.024	< 0.024	< 0.024
Total	100.07	99.27	99.27	99.23	99.64	100.00	100.23	99.47	99.28	99.31	99.19	99.13	99.41	99.57	99.11
An	78.81	79.88	80.46	79.89	72.28	73.51	76.32	80.85	83.20	80.88	76.10	81.48	86.68	86.78	85.28

Sample	15D-2			17D-1			18D-6				19D-2			19D-3	
Size	pheno	pheno	pheno	micro	micro	micro	pheno	pheno	pheno	pheno	micro	micro	micro	pheno	pheno
Lat. (°S)	50.58	50.58	50.58	50.76	50.76	50.76	51.05	51.05	51.05	51.05	51.06	51.06	51.06	51.06	51.06
SiO_2	46.85	46.69	47.29	51.63	52.08	51.21	47.65	48.81	48.32	48.84	52.90	52.17	53.02	47.64	49.65
Al_2O_3	33.29	33.41	32.87	30.22	30.11	30.08	32.66	31.92	32.07	32.20	28.85	29.78	29.53	31.99	31.73
FeO	0.36	0.36	0.40	0.45	0.62	0.44	0.32	0.39	0.42	0.27	0.54	0.51	0.48	0.34	0.39
MgO	0.17	0.18	0.22	0.24	0.24	0.23	0.19	0.25	0.22	0.24	0.19	0.18	0.17	0.16	0.21
CaO	17.77	17.81	17.31	14.31	14.11	14.24	17.36	16.58	16.54	16.58	12.89	13.70	13.35	17.58	16.62
NA_2O	1.03	0.99	1.24	3.13	3.23	3.00	1.32	1.72	1.70	1.67	3.78	3.31	3.64	1.35	2.01
K_2O	< 0.024	< 0.024	< 0.024	0.04	< 0.024	< 0.024	< 0.024	< 0.024	< 0.024	< 0.024	0.04	< 0.024	0.04	< 0.024	< 0.024
Total	99.47	99.44	99.33	100.02	100.39	99.20	99.50	99.67	99.27	99.80	99.19	99.65	100.23	99.06	100.61
An	90.54	90.86	88.53	71.47	70.70	72.40	87.89	84.19	84.34	84.62	65.17	69.57	66.78	87.76	82.05

An: anorthite content as percentage

University of Cape Town

Table B.2 (cont.)

Sample	19D-9	20D-3			21D-3				23D-1			22D-4			
Size	pheno	micro	pheno	pheno	pheno	pheno	pheno	pheno	micro	micro	micro	micro	micro	micro	micro
Lat. (°S)	51.06	51.43	51.43	51.43	51.82	51.82	51.82	51.82	52.16	52.16	52.16	52.46	52.46	52.46	52.46
SiO_2	47.81	50.59	52.69	52.24	49.14	48.75	49.50	48.85	51.38	51.00	52.01	54.84	53.99	54.17	54.72
Al_2O_3	32.50	31.02	29.33	29.66	31.92	32.23	31.35	32.10	30.69	31.19	30.46	28.32	28.56	28.59	28.22
FeO	0.41	0.38	0.57	0.58	0.38	0.34	0.41	0.39	0.39	0.43	0.41	0.60	0.75	0.65	0.66
MgO	0.18	0.23	0.16	0.22	0.23	0.22	0.24	0.22	0.24	0.22	0.24	0.17	0.14	0.13	0.17
CaO	16.91	15.20	13.56	13.72	16.35	16.71	15.98	16.46	14.93	15.22	14.50	12.13	12.45	12.62	12.23
NA_2O	1.53	2.72	3.61	3.53	2.01	1.83	2.33	2.06	3.00	2.80	3.27	4.55	4.49	4.31	4.45
K_2O	< 0.024	0.06	0.07	0.06	0.05	0.04	0.05	0.04	< 0.024	< 0.024	< 0.024	0.10	0.12	0.10	0.09
Total	99.34	100.20	99.99	100.01	100.08	100.12	99.86	100.12	100.63	100.86	100.89	100.71	100.50	100.57	100.54
An	85.96	75.25	67.23	68.01	81.54	83.27	78.90	81.31	73.35	75.04	71.04	59.20	60.07	61.47	59.96

An: anorthite content as percentage

University of Cape Town

Table B.3: Clinopyroxene phenocryst compositions (EMP) in oxide-weight percentages, with all iron reported as Fe^{2+}. The size of phenocrysts analysed varied between phenocrysts (pheno) and microphenocryst (micro).

Sample	2D-3		3D-1	6D-1	7D-3	20D-3
Size	micro	micro	micro	micro	pheno	micro
Lat. (°S)	47.55	47.55	47.80	48.55	48.76	51.43
SiO_2	50.76	52.90	52.56	51.92	52.37	52.45
TiO_2	0.96	0.53	0.31	0.42	0.30	0.53
Al_2O_3	4.29	1.98	2.93	3.60	3.30	1.95
Cr_2O_3	1.08	0.78	0.47	1.19	1.25	0.44
FeO	5.86	5.74	4.85	4.73	4.19	5.87
MnO	0.14	0.14	< 0.06	0.15	< 0.06	0.19
MgO	16.56	18.25	17.73	17.75	17.83	17.98
CaO	19.61	19.11	20.13	20.21	20.92	19.55
Na_2O	0.30	0.27	0.27	0.25	0.24	0.24
K_2O	< 0.023	< 0.023	< 0.023	< 0.023	< 0.023	< 0.023
Total	99.56	99.70	99.25	100.22	100.40	99.20
Wo	41.43	38.93	41.44	41.49	42.71	39.66
En	48.67	51.72	50.77	50.69	50.61	50.74
Fs	9.90	9.35	7.78	7.82	6.68	9.60

Wo, En, Fs: wollastonite, enstatite, and ferrosilite content as percentages

Table B.4: Spinel microphenocryst compositions (EMP) in oxide-weight percentages, with Fe_2O_3 calculated by stoichiometry (Droop, 1987). The phenocrysts analysed were all microphenocrysts (micro) in size.

Sample	34D-3		19D-7		
Size	micro	micro	micro	micro	micro
Lat. (°S)	45.85	45.85	51.06	51.06	51.06
SiO_2	< 0.038	< 0.038	< 0.038	0.09	2.01
TiO_2	0.38	0.37	0.74	0.68	1.38
Al_2O_3	40.01	39.74	32.84	32.82	26.88
Cr_2O_3	23.73	23.72	28.33	28.60	27.42
FeO	12.05	12.16	14.76	14.84	20.56
Fe_2O_3	4.94	5.06	7.80	7.16	7.64
MnO	0.14	< 0.078	0.19	0.20	0.23
MgO	16.92	16.96	14.96	14.84	12.18
CaO	0.06	0.07	< 0.027	< 0.027	0.28
Total	98.25	98.19	99.64	99.24	98.59
Mg#	0.71	0.71	0.64	0.64	0.51
Cr#	0.28	0.29	0.37	0.37	0.41

Mg#: atomic Mg^{2+}/(atomic Mg^{2+}+atomic Fe^{2+})
Cr#: atomic Cr^{3+}/(atomic Cr^{3+}+atomic Al^{3+})

University of Cape Town

Table B.5: Major- (EMP) and trace-element (LA-ICP-MS) compositional data for quenched igneous glasses. Major-element concentrations in oxide-weight percentages, with all iron reported as Fe^{2+}, and trace-element concentrations in ppm. MBSL: dredging depth in average metres below sea-level. Mg# (as %): atomic Mg^{2+}/(atomic Mg^{2+} + atomic Fe^{2+}), using $Fe_2O_3/FeO=0.15$.

Sample	45D-1	45D-2	45D-3	45D-4	44D-1	44D-2	44D-3	44D-4	44D-5	44D-6	44D-7	44D-8	44D-9	44D-10	44D-11
Lat. (°S)	40.59	40.59	40.59	40.59	40.86	40.86	40.86	40.86	40.86	40.86	40.86	40.86	40.86	40.86	40.86
Long. (°W)	16.77	16.77	16.77	16.77	16.79	16.79	16.79	16.79	16.79	16.79	16.79	16.79	16.79	16.79	16.79
MBSL	3203	3203	3203	3203	3067	3067	3067	3067	3067	3067	3067	3067	3067	3067	3067
SiO_2	49.30	50.06	50.20	49.81	51.38	51.34	51.11	50.30	50.06	50.11	49.93	50.02	49.85	50.21	50.10
TiO_2	0.92	1.03	0.96	1.02	1.45	1.38	1.33	1.39	1.43	1.38	1.40	1.41	1.38	1.41	1.38
Al_2O_3	16.77	16.71	16.73	16.85	15.05	15.18	14.99	15.28	15.30	15.31	15.17	15.20	15.17	15.18	15.09
FeO	8.80	8.95	8.91	8.76	9.95	9.89	9.80	9.84	9.75	9.73	9.63	9.90	9.65	9.55	10.16
MnO	0.16	0.13	0.13	0.15	0.13	0.15	0.16	0.14	0.20	0.17	0.18	0.18	0.16	0.19	0.15
MgO	9.47	9.05	9.25	9.35	8.02	8.00	7.94	8.11	8.00	8.21	7.98	8.05	8.11	8.10	8.04
CaO	12.32	12.05	12.17	12.18	11.84	11.92	12.20	11.98	12.09	12.11	11.95	11.90	12.02	12.06	11.97
Na_2O	2.35	2.41	2.43	2.41	2.72	2.72	2.77	2.68	2.70	2.70	2.76	2.65	2.64	2.64	2.74
K_2O	0.04	0.05	0.03	0.04	0.08	0.08	0.07	0.09	0.09	0.08	0.09	0.08	0.08	0.09	0.08
P_2O_5	0.08	0.13	0.06	0.06	0.14	0.12	0.11	0.15	0.14	0.14	0.11	0.17	0.12	0.10	0.12
Total	100.21	100.57	100.87	100.63	100.76	100.78	100.48	99.96	99.76	99.94	99.20	99.56	99.18	99.53	99.83
Mg#	68.5	67.2	67.7	68.4	62.0	62.1	62.1	62.5	62.4	63.1	62.6	62.2	63.0	63.2	61.6
Sc	39	38	41	40	47	47	49	46	47	49	47	48	47	47	46
Ni	156	133	131	139	80	85	88	90	91	86	90	84	85	88	89
Rb	0.47	0.36	0.40	0.40	1.06	0.85	0.92	1.03	0.96	1.02	0.83	0.93	0.85	1.08	0.87
Sr	96	96	95	94	96	97	100	95	97	101	97	98	100	98	97
Y	24	23	23	24	34	33	33	32	33	36	33	34	34	33	32
Zr	55	55	55	56	86	84	85	82	84	88	84	87	89	85	82
Nb	1.06	1.17	1.15	1.17	2.35	2.31	2.24	2.32	2.19	2.45	2.13	2.30	2.26	2.22	2.15
Ba	6.06	6.20	6.58	5.75	12.5	12.3	11.7	12.1	12.6	13.1	12.9	12.3	13.3	12.6	12.3
La	1.99	2.14	2.02	2.14	3.19	3.17	3.28	3.11	3.24	3.48	3.13	3.29	3.21	3.17	3.24
Ce	6.11	6.11	5.89	6.14	9.05	9.23	8.90	8.85	9.21	9.35	8.92	9.49	9.74	9.13	9.00
Nd	5.96	5.73	5.34	5.88	8.88	9.14	9.30	8.79	9.09	9.71	9.40	9.90	9.25	8.99	8.82
Sm	2.18	2.09	2.04	2.33	3.31	3.11	3.13	3.06	3.21	3.21	3.31	3.15	3.22	3.34	2.83
Eu	0.81	0.80	0.74	0.81	1.14	1.21	1.17	1.16	1.12	1.18	1.17	1.16	1.14	1.10	1.14
Gd	2.88	3.70	3.22	3.45	4.52	4.47	4.58	4.68	4.86	5.00	4.52	4.87	4.99	4.80	4.88
Dy	3.83	3.65	3.74	3.82	5.10	5.13	5.79	5.19	5.13	5.75	5.08	5.60	5.24	5.22	5.28
Er	2.30	2.28	2.53	2.44	3.07	3.23	3.57	3.34	3.46	3.40	3.30	3.44	3.45	3.34	3.38
Yb	2.42	2.31	2.33	2.46	3.49	3.23	3.14	3.04	3.39	3.37	3.31	3.39	3.57	3.19	3.19
Ta	0.11	0.12	0.10	0.10	0.23	0.16	0.17	0.15	0.17	0.17	0.13	0.20	0.20	0.12	0.14
Pb	< 0.18	< 0.18	< 0.18	< 0.18	< 0.18	< 0.18	< 0.18	< 0.18	< 0.18	< 0.18	< 0.18	< 0.18	< 0.18	< 0.18	< 0.18
Th	0.11	0.08	0.08	0.13	0.22	0.21	0.19	0.17	0.20	0.24	0.20	0.21	0.23	0.18	0.17
U	0.02	0.02	< 0.02	< 0.02	0.04	0.04	0.04	0.04	0.04	0.04	0.05	0.05	0.05	0.03	0.05

University of Cape Town

Table B.5 (cont.)

Sample	43D-1	43D-2	43D-3	42D-1	41D-1	41D-2	41D-3	41D-5	41D-6	41D-7	41D-9	41D-10	41D-11	41D-12	41D-13
Lat. (°S)	42.19	42.19	42.19	43.43	44.02	44.02	44.02	44.02	44.02	44.02	44.02	44.02	44.02	44.02	44.02
Long. (°W)	16.08	16.08	16.08	16.17	16.08	16.08	16.08	16.08	16.08	16.08	16.08	16.08	16.08	16.08	16.08
MBSL	2925	2925	2925	3449	3522	3522	3522	3522	3522	3522	3522	3522	3522	3522	3522
SiO_2	50.29	51.29	51.26	49.42	50.44	51.49	50.92	51.49	51.45	51.71	50.30	50.35	49.91	50.43	50.50
TiO_2	1.46	1.48	1.49	1.22	1.35	1.30	1.35	1.35	1.30	1.24	1.31	1.33	1.34	1.36	1.38
Al_2O_3	15.47	14.80	15.04	16.97	15.78	15.36	15.16	15.24	15.14	15.31	15.41	15.64	15.37	15.48	15.35
FeO	10.18	10.17	9.97	8.96	9.64	9.69	9.71	9.76	9.79	9.59	9.95	9.65	9.39	9.62	9.89
MnO	0.17	0.13	0.14	0.18	0.14	0.14	0.14	0.16	0.14	0.15	0.17	0.19	0.15	0.19	0.16
MgO	7.98	7.93	7.87	8.39	8.36	8.17	8.20	8.48	8.30	8.44	8.19	8.18	8.19	8.24	8.28
CaO	11.75	11.40	11.59	11.21	11.57	11.43	11.24	11.47	11.30	11.51	11.49	11.54	11.58	11.63	11.60
Na_2O	2.87	2.80	2.82	2.75	2.77	2.72	2.65	2.68	2.76	2.74	2.81	2.66	2.72	2.76	2.78
K_2O	0.11	0.10	0.10	0.36	0.10	0.10	0.09	0.09	0.09	0.09	0.11	0.11	0.12	0.11	0.10
P_2O_5	0.12	0.12	0.12	0.14	0.13	0.13	0.11	0.14	0.13	0.10	0.14	0.14	0.15	0.14	0.12
Total	100.40	100.22	100.40	99.58	100.29	100.53	99.57	100.86	100.40	100.88	99.88	99.79	98.92	99.96	100.16
Mg#	61.3	61.2	61.5	65.5	63.7	63.0	63.1	63.7	63.2	64.0	62.5	63.2	63.8	63.4	62.9
Sc	46	45	45	33	44	43	42	42	43	42	44	43	43	42	45
Ni	98	96	95	123	107	103	110	102	107	112	106	107	112	102	109
Rb	1.22	1.19	1.08	6.16	1.31	1.50	1.32	1.23	1.39	1.38	1.34	1.30	1.33	1.50	1.45
Sr	103	101	103	183	99	100	97	97	95	97	96	99	98	102	100
Y	35	34	34	23	33	33	32	33	32	33	32	33	33	34	33
Zr	89	87	87	73	82	84	80	81	81	83	82	85	83	83	85
Nb	2.16	2.25	2.44	7.60	2.44	2.34	2.26	2.15	2.21	2.12	2.20	2.50	2.18	2.27	2.27
Ba	14.9	14.2	13.9	79	15.9	16.0	15.1	14.3	14.7	15.3	15.9	15.8	14.2	16.7	15.1
La	3.44	3.30	3.35	6.07	3.27	3.35	3.15	3.27	3.05	3.24	3.18	3.31	3.26	3.44	3.36
Ce	9.64	9.15	9.29	13.4	9.25	9.16	8.86	8.86	8.84	8.83	8.80	9.18	9.04	9.42	8.94
Nd	8.92	9.37	9.45	9.16	8.80	8.35	8.42	8.48	8.59	9.10	9.06	8.96	8.59	9.52	8.68
Sm	3.10	3.32	3.45	2.62	3.36	3.25	2.98	3.13	2.84	3.05	3.03	3.19	3.04	3.30	3.32
Eu	1.21	1.15	1.08	1.14	1.15	1.13	1.12	1.16	1.04	1.08	1.18	1.18	1.17	1.19	1.19
Gd	4.54	5.15	4.81	3.57	4.61	4.46	4.36	4.76	4.16	4.74	4.56	4.31	4.96	4.97	4.44
Dy	5.39	5.44	5.17	3.73	4.83	5.38	5.27	4.91	5.23	5.16	5.36	5.33	5.06	5.33	5.36
Er	3.39	3.23	3.48	2.28	3.31	3.42	3.26	3.33	3.16	3.32	3.12	3.32	3.19	3.37	3.40
Yb	3.43	3.22	3.33	2.17	3.28	3.46	3.13	3.29	3.08	3.06	3.33	2.92	3.30	3.37	3.20
Ta	0.18	0.16	0.18	0.54	0.15	0.18	0.15	0.20	0.15	0.16	0.15	0.21	0.20	0.20	0.17
Pb	0.39	0.41	< 0.18	0.42	0.23	0.51	< 0.18	0.25	< 0.18	< 0.18	< 0.18	< 0.18	< 0.18	0.20	0.86
Th	0.22	0.17	0.20	0.65	0.22	0.21	0.19	0.20	0.18	0.19	0.20	0.20	0.18	0.20	0.21
U	0.04	0.04	0.04	0.14	0.05	0.05	0.03	< 0.02	0.05	0.03	0.04	0.03	0.03	0.05	0.04

University of Cape Town

Table B.5 (cont.)

Sample	40D-1	40D-2	40D-3	40D-4	40D-5	40D-7	40D-8	40D-9	40D-10	40D-11	39D-1	37D-1	37D-2	37D-3	37D-6
Lat. (°S)	44.41	44.41	44.41	44.41	44.41	44.41	44.41	44.41	44.41	44.41	44.68	45.23	45.23	45.23	45.23
Long. (°W)	15.91	15.91	15.91	15.91	15.91	15.91	15.91	15.91	15.91	15.91	15.39	15.08	15.08	15.08	15.08
MBSL	3488	3488	3488	3488	3488	3488	3488	3488	3488	3488	3603	3534	3534	3534	3534
SiO_2	51.06	51.64	51.77	50.36	51.54	50.68	50.79	50.69	50.38	50.48	50.09	49.39	51.11	51.26	51.02
TiO_2	1.27	1.28	1.56	1.52	1.54	1.29	1.33	1.55	1.52	1.58	1.64	1.66	1.76	1.75	1.71
Al_2O_3	15.07	15.61	14.92	15.09	14.72	15.67	15.49	15.24	15.07	15.12	15.49	15.69	15.50	15.68	15.59
FeO	9.33	9.16	9.78	9.85	10.19	9.01	9.21	10.17	10.14	10.38	10.27	9.89	10.05	9.82	9.68
MnO	0.15	0.14	0.16	0.15	0.16	0.19	0.14	0.24	0.19	0.21	0.15	0.15	0.13	0.14	0.15
MgO	8.30	8.27	7.99	8.16	8.22	8.47	8.41	8.14	8.37	8.24	8.25	8.11	7.62	7.73	7.90
CaO	11.47	11.28	11.13	11.04	11.12	11.57	11.55	11.13	11.24	11.18	10.58	10.69	10.54	10.50	10.52
Na_2O	2.85	2.88	2.94	2.95	2.76	2.86	2.79	2.83	2.82	2.83	2.97	3.16	3.24	3.33	3.31
K_2O	0.10	0.11	0.11	0.11	0.09	0.12	0.10	0.11	0.12	0.12	0.15	0.41	0.41	0.42	0.42
P_2O_5	0.11	0.13	0.13	0.14	0.14	0.13	0.14	0.16	0.15	0.15	0.17	0.19	0.20	0.21	0.23
Total	99.71	100.50	100.49	99.37	100.48	99.99	99.95	100.26	100.00	100.29	99.76	99.34	100.56	100.84	100.53
Mg#	64.3	64.6	62.3	62.6	62.0	65.5	64.9	61.8	62.6	61.6	61.9	62.4	60.5	61.4	62.3
Sc	42	42	44	44	43	41	42	42	43	44	41	40	39	40	39
Ni	122	121	119	123	113	128	128	112	119	114	148	139	127	129	116
Rb	1.71	1.49	1.58	1.51	1.52	1.63	1.62	1.35	1.53	1.55	2.15	6.60	6.82	7.11	7.01
Sr	104	103	98	95	97	105	107	96	99	99	123	178	181	184	180
Y	31	30	37	36	36	30	31	36	37	38	36	36	35	35	35
Zr	81	80	98	95	96	81	82	98	98	101	100	121	119	121	119
Nb	2.31	2.44	2.61	2.41	2.44	2.44	2.37	2.42	2.46	2.66	3.31	9.04	9.27	9.26	9.30
Ba	20	19.5	16.6	16.8	16.8	19.7	20	16.1	16.9	18.5	24	84	88	90	89
La	3.18	3.27	3.76	3.52	3.56	3.43	3.29	3.48	3.79	3.69	4.06	7.87	8.18	8.27	8.09
Ce	9.15	8.84	10.5	10.2	10.0	8.95	9.02	10.2	10.2	10.0	10.8	17.6	17.5	17.7	17.7
Nd	9.16	8.95	10.2	9.65	10.2	8.54	8.84	10.1	10.0	10.5	9.62	13.8	13.6	13.8	13.3
Sm	3.10	3.19	3.46	3.51	3.42	2.95	3.01	3.60	3.66	3.42	3.85	4.13	4.11	4.17	3.93
Eu	1.14	1.09	1.28	1.14	1.18	0.98	1.05	1.20	1.31	1.23	1.36	1.31	1.16	1.21	1.11
Gd	4.27	4.23	5.17	5.73	5.21	3.99	4.50	5.15	5.26	5.73	5.12	5.11	5.56	6.04	5.58
Dy	5.12	4.83	6.12	5.33	5.57	4.87	5.21	5.91	5.81	5.88	5.82	6.18	6.23	5.64	5.73
Er	2.61	2.91	3.59	3.46	3.34	2.77	2.97	3.90	3.57	3.73	3.33	3.50	3.30	3.42	3.38
Yb	2.83	3.09	3.83	3.69	3.65	2.95	3.05	3.52	3.58	3.72	3.85	3.41	3.34	3.24	3.50
Ta	0.17	0.17	0.18	0.18	0.19	0.17	0.21	0.24	0.17	0.20	0.24	0.62	0.64	0.64	0.58
Pb	0.92	0.71	0.81	0.82	0.71	0.55	0.70	0.60	0.72	0.56	0.79	0.71	0.66	0.80	0.79
Th	0.20	0.17	0.25	0.20	0.20	0.21	0.23	0.19	0.22	0.21	0.25	0.79	0.79	0.85	0.81
U	0.06	0.06	0.06	0.04	0.05	0.04	0.07	0.04	0.06	0.04	0.05	0.18	0.17	0.20	0.19

University of Cape Town

Table B.5 (cont.)

Sample	36D-1	34D-1	34D-2	34D-3	34D-5	34D-6	34D-7	34D-8	33D-1	33D-3	33D-4	33D-5	33D-6	33D-7	33D-8
Lat. (°S)	45.57	45.85	45.85	45.85	45.85	45.85	45.85	45.85	45.99	45.99	45.99	45.99	45.99	45.99	45.99
Long. (°W)	14.71	14.19	14.19	14.19	14.19	14.19	14.19	14.19	14.08	14.08	14.08	14.08	14.08	14.08	14.08
MBSL	3115	3443	3443	3443	3443	3443	3443	3443	3381	3381	3381	3381	3381	3381	3381
SiO_2	50.26	49.86	49.97	49.89	49.46	49.25	48.49	48.68	49.92	51.37	51.21	49.97	50.16	50.63	49.86
TiO_2	1.49	1.25	1.28	1.24	1.24	1.25	1.25	1.24	1.66	1.73	1.76	1.66	1.74	1.75	1.73
Al_2O_3	15.68	16.46	16.43	16.44	16.40	16.39	16.37	16.37	16.02	15.86	15.93	15.65	15.77	15.84	15.99
FeO	10.31	10.16	10.14	10.18	10.35	10.28	10.08	10.10	9.17	9.14	9.39	9.16	9.17	9.37	9.32
MnO	0.14	0.17	0.14	0.15	0.14	0.22	0.17	0.14	0.17	0.13	0.13	0.19	0.16	0.17	0.19
MgO	7.80	8.35	8.86	8.90	8.62	9.10	9.15	8.85	7.83	7.98	7.51	7.76	7.88	7.94	8.02
CaO	10.96	11.21	11.02	10.86	10.80	11.10	11.14	11.01	10.30	10.16	10.30	10.41	10.36	10.16	10.37
Na_2O	2.99	2.77	2.91	2.86	2.86	2.81	2.76	2.77	3.35	3.48	3.49	3.34	3.30	3.36	3.31
K_2O	0.10	0.06	0.11	0.07	0.06	0.08	0.08	0.07	0.74	0.72	0.73	0.70	0.71	0.74	0.71
P_2O_5	0.10	0.10	0.10	0.09	0.08	0.10	0.12	0.12	0.27	0.25	0.24	0.30	0.29	0.30	0.33
Total	99.83	100.39	100.96	100.68	100.01	100.58	99.61	99.35	99.43	100.82	100.69	99.14	99.54	100.26	99.83
Mg#	60.5	62.4	63.9	63.9	62.8	64.2	64.7	63.9	63.3	63.9	61.8	63.2	63.5	63.2	63.5
Sc	41	41	41	41	40	43	43	41	37	36	36	37	37	37	37
Ni	101	124	152	158	144	142	147	150	113	113	98	122	113	114	115
Rb	1.13	0.98	0.92	1.02	0.90	1.03	0.91	0.81	13.6	13.6	13.7	14.2	14.1	13.5	13.6
Sr	111	100	99	98	96	99	102	99	233	231	239	238	238	235	234
Y	34	32	31	30	31	31	33	31	31	29	30	30	31	30	30
Zr	93	72	71	71	70	73	75	72	129	127	128	129	131	130	127
Nb	2.34	1.57	1.55	1.56	1.57	1.79	1.76	1.71	15.8	15.3	15.8	16.1	16.1	15.6	15.7
Ba	14.3	11.5	10.7	11.5	11.0	11.9	11.6	10.9	154	153	159	157	160	152	158
La	3.30	2.79	2.63	2.66	2.56	2.65	2.84	2.69	11.8	11.6	11.7	11.9	12.1	11.7	11.8
Ce	9.58	7.62	7.48	7.60	7.43	7.70	7.82	7.55	23	23	23	24	23	23	23
Nd	9.83	7.17	7.94	7.75	7.51	7.86	7.68	7.19	15.3	15.1	15.1	15.5	15.3	14.8	15.3
Sm	3.37	2.61	2.66	2.70	2.54	2.87	2.87	2.89	4.31	4.05	4.11	4.35	4.39	4.33	4.37
Eu	1.04	0.75	0.74	0.76	0.56	0.57	0.80	0.53	1.51	1.44	1.46	1.40	1.49	1.60	1.44
Gd	4.71	4.22	4.34	3.75	3.83	3.94	4.49	4.37	4.73	4.82	4.70	5.13	5.46	4.60	4.78
Dy	5.43	5.31	4.69	4.62	4.80	4.74	5.06	4.67	5.11	5.14	5.20	5.07	5.53	5.44	5.19
Er	3.39	3.03	3.22	2.91	2.99	3.06	3.34	3.31	3.10	3.02	2.74	2.98	3.10	2.72	3.27
Yb	3.50	3.48	3.20	3.44	3.32	3.27	3.36	3.30	2.94	3.04	2.89	2.88	3.16	2.96	2.87
Ta	0.21	0.09	0.08	0.11	0.13	0.11	0.11	0.12	1.05	0.91	1.02	1.01	1.01	0.94	0.90
Pb	0.50	0.53	0.34	0.29	0.32	< 0.18	0.30	0.34	1.15	1.30	1.13	1.35	1.28	1.12	1.11
Th	0.20	0.16	0.16	0.12	0.15	0.13	0.15	0.13	1.48	1.34	1.42	1.39	1.48	1.51	1.36
U	0.05	0.03	< 0.02	0.04	0.03	< 0.02	0.04	0.04	0.33	0.33	0.34	0.33	0.33	0.35	0.30

University of Cape Town

Table B.5 (cont.)

Sample	33D-9	33D-10	33D-11	32D-1	32D-2	32D-3	32D-6	32D-7	32D-8	32D-9	31D-1	31D-2	30D-1	30D-2	28D-1
Lat. (°S)	45.99	45.99	45.99	46.23	46.23	46.23	46.23	46.23	46.23	46.23	46.39	46.39	46.59	46.59	46.90
Long. (°W)	14.08	14.08	14.08	13.56	13.56	13.56	13.56	13.56	13.56	13.56	13.46	13.46	13.39	13.39	13.45
MBSL	3381	3381	3381	3108	3108	3108	3108	3108	3108	3108	2822	2822	3153	3153	3417
SiO_2	50.08	50.22	49.75	49.94	51.09	51.33	49.82	49.79	50.03	50.07	49.61	50.73	50.08	51.50	51.04
TiO_2	1.77	1.70	1.72	1.38	1.49	1.51	1.42	1.47	1.50	1.44	1.40	1.40	1.31	1.73	1.24
Al_2O_3	15.73	15.86	15.87	15.27	15.45	15.49	15.42	15.73	15.21	15.70	16.56	15.84	15.85	14.97	14.88
FeO	9.18	9.54	9.12	10.03	9.39	9.70	9.83	9.88	10.10	9.62	8.89	8.88	9.51	10.34	8.99
MnO	0.18	0.20	0.14	0.16	0.14	0.14	0.22	0.14	0.22	0.22	0.15	0.14	0.15	0.14	0.14
MgO	7.82	7.97	7.90	8.08	7.41	7.55	7.98	7.73	7.84	7.78	8.19	8.19	8.36	7.62	8.22
CaO	10.44	10.30	10.46	11.61	10.95	11.19	11.76	11.34	11.70	11.67	11.25	11.11	11.55	11.13	11.89
Na_2O	3.34	3.38	3.31	2.73	3.04	3.05	2.81	2.98	2.80	3.01	2.94	3.02	2.89	2.91	2.87
K_2O	0.71	0.72	0.73	0.12	0.29	0.30	0.12	0.29	0.13	0.32	0.51	0.50	0.16	0.14	0.07
P_2O_5	0.33	0.30	0.33	0.13	0.15	0.18	0.19	0.16	0.13	0.17	0.16	0.18	0.11	0.15	0.12
Total	99.58	100.19	99.33	99.44	99.40	100.44	99.57	99.51	99.66	100.00	99.66	99.99	99.97	100.63	99.46
Mg#	63.3	62.8	63.7	62.0	61.5	61.2	62.2	61.3	61.1	62.1	65.1	65.1	64.0	59.9	64.9
Sc	37	37	38	50	41	44	49	42	48	44	37	36	43	44	44
Ni	115	116	114	86	84	85	83	90	85	81	113	113	97	95	95
Rb	13.7	13.7	13.4	1.50	4.60	4.57	1.78	4.72	1.83	5.41	8.32	8.08	2.10	2.03	0.70
Sr	239	234	236	99	142	146	106	149	105	159	195	190	119	109	108
Y	31	30	30	34	31	32	35	31	33	31	26	26	29	38	28
Zr	131	127	128	83	97	99	90	96	86	97	101	100	80	110	77
Nb	16.6	15.8	16.1	2.38	6.34	7.39	2.79	6.80	2.87	7.46	9.22	9.06	3.02	3.21	1.22
Ba	161	154	153	18.6	59	63	24	60	21	73	102	97	27	23	11.1
La	11.7	11.7	11.8	3.48	6.24	6.35	3.80	6.43	3.55	6.78	8.60	8.17	3.76	4.67	2.90
Ce	23	23	23	9.07	13.6	14.2	9.80	13.9	9.65	15.0	17.7	16.7	9.45	12.2	8.36
Nd	14.5	15.5	15.0	8.10	10.9	10.8	9.46	10.9	9.01	11.2	12.0	11.1	9.03	11.1	8.21
Sm	4.19	3.81	4.13	2.98	3.61	3.28	3.31	3.31	3.05	3.53	3.19	3.21	2.87	3.48	2.60
Eu	1.46	1.39	1.53	1.10	1.20	1.23	1.23	1.30	1.29	1.39	1.25	1.23	1.07	1.50	1.09
Gd	5.19	4.93	4.75	4.75	4.62	4.71	4.80	4.05	4.37	4.60	4.21	4.12	4.39	5.32	3.96
Dy	5.53	5.12	5.03	5.47	5.68	5.50	5.64	5.40	5.30	5.06	4.34	4.10	4.94	5.95	4.67
Er	3.20	2.92	2.78	3.60	3.15	3.05	3.23	3.08	3.44	2.99	2.44	2.49	2.93	3.78	2.78
Yb	3.00	2.82	2.77	3.52	3.01	3.06	3.22	2.82	3.27	3.01	2.41	2.38	2.75	3.62	2.86
Ta	1.02	1.00	1.08	0.15	0.41	0.32	0.18	0.44	0.17	0.45	0.63	0.67	0.19	0.22	0.11
Pb	1.04	0.95	1.20	0.52	0.91	0.79	0.55	0.82	0.75	0.60	1.01	1.03	0.53	0.69	< 0.18
Th	1.43	1.37	1.45	0.24	0.60	0.62	0.28	0.61	0.25	0.67	0.87	0.79	0.26	0.25	0.15
U	0.33	0.34	0.31	0.07	0.09	0.13	0.05	0.16	0.06	0.19	0.20	0.21	0.06	0.07	< 0.02

University of Cape Town

Table B.5 (cont.)

Sample	28D-2	28D-3	28D-5	28D-6	28D-7	28D-8	27D-1	27D-2	27D-3	27D-4	26D-1	26D-2	26D-3	25D-1	25D-4
Lat. (°S)	46.90	46.90	46.90	46.90	46.90	46.90	47.11	47.11	47.11	47.11	47.35	47.35	47.35	47.35	47.35
Long. (°W)	13.45	13.45	13.45	13.45	13.45	13.45	13.40	13.40	13.40	13.40	13.40	13.40	13.40	10.32	10.32
MBSL	3417	3417	3417	3417	3417	3417	3081	3081	3081	3081	3857	3857	3857	2032	2032
SiO_2	51.21	49.67	50.45	50.61	50.82	50.45	48.90	50.57	48.93	48.66	50.08	49.61	49.71	53.98	54.65
TiO_2	1.24	1.43	1.30	1.26	1.24	1.26	0.99	1.73	0.99	1.06	1.84	1.05	1.82	1.43	1.46
Al_2O_3	15.17	15.97	15.70	15.63	15.62	15.48	16.79	14.19	16.79	16.91	14.63	17.25	14.52	15.79	15.66
FeO	9.08	9.47	9.27	8.96	9.22	9.38	9.38	11.26	9.93	10.39	11.26	10.12	11.32	8.39	8.46
MnO	0.13	0.15	0.15	0.20	0.14	0.17	0.16	0.15	0.22	0.19	0.16	0.15	0.21	0.14	0.15
MgO	8.09	8.47	8.24	8.23	8.39	8.32	8.98	7.02	9.07	8.87	7.06	8.78	7.24	7.51	6.97
CaO	12.00	11.52	12.18	12.11	12.14	12.06	11.83	10.86	11.98	11.11	11.07	10.82	11.21	8.69	8.87
Na_2O	2.89	3.09	2.83	2.79	2.75	2.77	2.57	3.15	2.47	2.79	3.09	2.85	3.09	3.41	3.42
K_2O	0.07	0.14	0.08	0.07	0.07	0.07	0.05	0.11	0.05	0.06	0.12	0.05	0.09	0.28	0.28
P_2O_5	0.12	0.10	0.13	0.11	0.12	0.12	0.08	0.14	0.07	0.11	0.15	0.06	0.18	0.11	0.16
Total	100.00	100.01	100.33	99.97	100.51	100.08	99.73	99.18	100.50	100.15	99.46	100.71	99.39	99.73	100.04
Mg#	64.3	64.4	64.3	65.0	64.8	64.2	66.0	55.8	64.9	63.3	55.9	63.7	56.4	64.4	62.5
Sc	45	44	45	45	44	44	45	48	44	37	48	37	49	23	24
Ni	91	115	98	94	97	97	133	66	135	140	73	158	70	132	107
Rb	0.79	1.83	0.85	0.81	0.74	0.84	0.53	1.44	0.52	0.57	1.23	0.51	1.00	4.72	4.47
Sr	107	118	109	111	107	109	103	105	104	117	109	116	109	199	203
Y	28	32	28	28	28	27	26	42	26	26	43	25	43	18	19
Zr	77	92	79	79	77	75	65	123	64	67	125	62	123	79	80
Nb	1.34	2.96	1.43	1.25	1.42	1.44	1.08	2.66	1.09	1.12	2.50	0.98	1.79	5.45	5.67
Ba	11.4	24	12.0	12.5	11.4	11.5	7.29	15.9	7.28	8.11	17.4	7.78	14.8	60	65
La	2.83	4.21	2.82	3.00	2.85	2.87	2.51	4.57	2.48	2.42	4.74	2.31	4.36	5.53	5.69
Ce	8.11	11.2	8.45	8.33	8.36	8.58	7.38	13.3	7.23	7.36	13.4	6.91	12.9	11.4	11.7
Nd	8.37	10.0	8.80	8.45	8.15	8.72	7.55	13.4	7.30	6.96	13.2	6.48	13.6	9.77	10.8
Sm	3.12	3.42	2.98	2.78	3.13	2.74	2.56	4.23	2.55	2.30	4.80	2.42	4.73	3.57	3.71
Eu	1.06	1.20	1.05	1.04	1.07	1.02	0.97	1.38	1.03	0.91	1.30	1.05	1.57	1.36	1.51
Gd	4.45	5.40	4.30	3.92	4.32	4.29	4.21	6.01	3.77	4.07	6.02	3.84	7.04	4.28	4.63
Dy	4.67	5.17	4.93	4.82	4.70	4.57	4.46	7.15	4.10	4.11	7.86	4.20	7.29	3.48	3.76
Er	2.79	3.45	2.70	2.78	2.88	2.76	2.82	4.30	2.74	2.68	4.50	2.68	4.49	1.63	1.56
Yb	2.83	3.18	2.89	3.04	2.92	2.77	2.88	4.15	2.66	2.62	4.39	2.62	4.36	1.58	1.57
Ta	0.09	0.17	0.08	0.07	0.09	0.11	< 0.06	0.16	0.07	0.09	0.16	0.10	0.12	0.32	0.34
Pb	< 0.18	< 0.18	< 0.18	< 0.18	< 0.18	< 0.18	< 0.18	< 0.18	< 0.18	< 0.18	< 0.18	< 0.18	< 0.18	0.56	0.75
Th	0.10	0.28	0.12	0.15	0.13	0.12	0.12	0.21	0.12	0.10	0.27	0.09	0.18	0.52	0.53
U	< 0.02	0.06	0.03	0.03	0.04	0.02	< 0.02	0.05	0.02	< 0.02	0.02	< 0.02	0.02	0.09	0.09

University of Cape Town

Table B.5 (cont.)

Sample	25D-5	25D-6	25D-7	2D-1	2D-2	2D-3	2D-4	2D-5	2D-6	2D-7	2D-8	2D-9	3D-1	3D-2	3D-3
Lat. (°S)	47.35	47.35	47.35	47.55	47.55	47.55	47.55	47.55	47.55	47.55	47.55	47.55	47.80	47.80	47.80
Long. (°W)	10.32	10.32	10.32	10.19	10.19	10.19	10.19	10.19	10.19	10.19	10.19	10.19	10.15	10.15	10.15
MBSL	2032	2032	2032	2494	2494	2494	2494	2494	2494	2494	2494	2494	2549	2549	2549
SiO_2	54.08	54.59	54.52	51.66	51.73	51.76	51.74	51.51	51.02	51.51	51.36	51.52	50.95	51.34	51.21
TiO_2	1.43	1.44	1.45	2.14	2.03	1.70	1.66	1.66	1.68	1.66	1.64	1.72	1.80	1.77	1.53
Al_2O_3	15.12	15.42	15.61	14.92	14.13	14.26	14.85	14.73	14.68	14.77	14.84	14.78	15.50	14.32	14.26
FeO	8.39	8.35	8.32	9.86	9.76	9.56	9.13	9.06	8.98	9.05	9.11	9.05	9.17	9.80	9.68
MnO	0.15	0.13	0.15	0.16	0.14	0.14	0.16	0.16	0.17	0.13	0.15	0.16	0.15	0.14	0.12
MgO	7.50	7.47	7.12	6.24	6.29	7.06	7.19	7.15	7.07	7.21	7.21	7.05	7.21	7.53	7.46
CaO	8.61	8.73	8.73	10.42	10.41	11.18	11.00	10.91	10.81	10.85	10.80	10.94	11.09	10.48	11.35
Na_2O	3.43	3.30	3.50	3.35	3.52	3.37	3.19	3.19	3.09	3.10	3.14	3.14	3.01	3.08	2.93
K_2O	0.27	0.27	0.27	0.76	0.77	0.46	0.44	0.48	0.48	0.44	0.43	0.45	0.57	0.52	0.30
P_2O_5	0.16	0.16	0.15	0.25	0.30	0.20	0.21	0.18	0.18	0.19	0.21	0.18	0.24	0.22	0.15
Total	99.14	99.86	99.82	99.76	99.08	99.69	99.57	99.03	98.16	98.91	98.98	98.99	99.69	99.20	98.99
Mg#	64.4	64.4	63.4	56.2	56.6	59.9	61.4	61.5	61.4	61.7	61.6	61.2	61.4	60.9	60.9
Sc	23	22	23	38	38	39	40	39	40	38	39	40	38	38	44
Ni	134	145	112	43	41	52	50	51	46	52	49	52	80	86	74
Rb	4.27	4.60	4.53	13.7	13.0	6.85	6.66	6.74	6.48	7.17	6.99	7.85	10.6	8.86	5.67
Sr	196	204	201	263	259	197	195	193	192	201	193	198	213	172	122
Y	18	19	18	30	30	26	26	26	26	26	26	26	27	30	31
Zr	78	81	80	159	158	116	117	114	116	120	119	118	135	133	104
Nb	5.55	5.55	5.74	15.6	15.9	8.74	8.62	7.89	8.06	8.04	8.18	8.47	11.8	10.5	6.11
Ba	61	62	64	183	177	96	94	92	92	94	92	95	134	111	69
La	5.25	5.62	5.50	15.9	15.8	9.21	9.49	9.20	9.03	9.46	9.72	9.36	12.2	10.9	7.01
Ce	11.2	11.4	11.8	32	32	21	19.8	19.3	19.5	19.8	19.8	20	26	24	15.7
Nd	9.79	10.4	10.2	19.8	19.4	14.3	13.9	13.3	13.8	13.9	13.9	14.3	15.8	16.5	11.8
Sm	3.49	3.46	3.66	4.91	4.60	3.89	3.77	3.75	3.95	4.27	4.08	4.14	4.27	4.49	3.76
Eu	1.28	1.23	1.30	1.76	1.82	1.36	1.30	1.54	1.45	1.33	1.25	1.34	1.54	1.43	1.28
Gd	4.29	4.53	3.87	5.39	5.60	4.65	4.37	4.86	4.33	4.71	4.25	5.08	4.53	4.82	4.71
Dy	3.31	3.39	3.46	5.35	5.04	4.60	4.72	4.74	4.59	4.62	4.84	4.31	5.13	5.19	5.23
Er	1.67	1.82	1.55	2.73	2.83	2.43	2.53	2.39	2.57	2.61	2.66	2.66	2.60	3.09	3.20
Yb	1.37	1.50	1.44	2.67	2.70	2.20	2.24	2.48	2.63	2.37	2.54	2.57	2.60	2.95	3.08
Ta	0.32	0.36	0.37	1.03	0.95	0.48	0.57	0.50	0.57	0.58	0.60	0.58	0.71	0.62	0.42
Pb	0.48	0.65	0.61	1.68	1.64	1.22	0.88	0.76	0.93	1.20	1.04	1.19	1.41	1.09	0.98
Th	0.52	0.50	0.57	1.59	1.56	0.81	0.84	0.77	0.82	0.78	0.79	0.79	1.12	1.04	0.61
U	0.10	0.14	0.10	0.34	0.33	0.20	0.16	0.15	0.15	0.18	0.18	1.00	0.27	0.22	0.19

University of Cape Town

Table B.5 (cont.)

Sample	3D-4	3D-5	3D-6	3D-7	3D-8	3D-9	4D-1	4D-2	4D-3	4D-5	4D-6	4D-7	4D-8	4D-9	4D-10
Lat. (°S)	47.80	47.80	47.80	47.80	47.80	47.80	47.97	47.97	47.97	47.97	47.97	47.97	47.97	47.97	47.97
Long. (°W)	10.15	10.15	10.15	10.15	10.15	10.15	10.08	10.08	10.08	10.08	10.08	10.08	10.08	10.08	10.08
MBSL	2549	2549	2549	2549	2549	2549	2895	2895	2895	2895	2895	2895	2895	2895	2895
SiO_2	51.60	51.59	51.20	51.55	50.80	50.72	50.96	51.30	51.24	51.13	51.71	51.88	51.56	50.42	50.75
TiO_2	1.80	1.76	1.77	1.67	1.81	1.80	1.57	1.83	1.57	1.54	1.50	1.52	1.62	1.82	1.79
Al_2O_3	14.52	14.51	14.77	15.15	15.16	15.38	15.16	15.24	15.26	14.32	14.71	14.43	14.31	14.93	15.23
FeO	9.86	9.69	9.32	8.73	9.44	9.08	9.46	9.61	9.03	9.61	9.44	9.56	9.53	9.95	9.39
MnO	0.16	0.15	0.18	0.12	0.15	0.16	0.19	0.17	0.14	0.15	0.14	0.15	0.15	0.16	0.14
MgO	7.46	7.44	7.58	7.30	7.32	7.17	7.44	7.43	7.60	7.65	7.61	7.73	7.63	7.25	7.32
CaO	10.56	10.52	10.36	10.59	10.48	11.04	11.31	10.59	11.07	11.09	11.18	11.16	11.22	10.47	10.51
Na_2O	3.13	3.11	3.00	3.00	3.03	3.05	2.87	3.08	2.70	2.94	2.89	2.95	2.94	3.15	3.14
K_2O	0.52	0.50	0.50	0.56	0.52	0.56	0.39	0.53	0.40	0.40	0.39	0.41	0.41	0.53	0.53
P_2O_5	0.26	0.20	0.22	0.24	0.22	0.22	0.16	0.27	0.21	0.19	0.16	0.17	0.20	0.28	0.23
Total	99.87	99.47	98.90	98.91	98.93	99.18	99.51	100.03	99.22	99.02	99.73	99.96	99.57	98.96	99.03
Mg#	60.5	60.8	62.2	62.9	61.1	61.5	61.4	61.0	63.0	61.7	62.0	62.1	61.8	59.6	61.2
Sc	39	39	37	36	37	39	39	36	40	39	39	37	40	36	37
Ni	87	91	88	77	96	76	83	91	78	74	77	77	69	73	97
Rb	8.67	8.82	8.76	9.57	9.00	9.80	6.79	8.85	6.32	6.14	6.06	6.08	6.49	5.91	9.27
Sr	174	172	179	203	183	213	157	181	151	150	152	151	158	144	182
Y	31	31	29	26	29	28	26	29	26	26	25	25	26	23	31
Zr	138	135	132	127	131	136	101	134	99	102	100	97	102	92	135
Nb	10.6	10.5	10.4	11.1	10.9	11.9	8.30	11.2	8.36	8.01	8.02	8.24	8.16	7.66	11.3
Ba	115	116	117	128	117	131	96	123	90	89	91	91	96	86	123
La	11.4	11.2	11.0	11.8	11.4	12.3	8.71	11.5	8.19	8.24	8.47	8.12	8.89	7.94	11.9
Ce	24	24	24	24	24	25	19.3	26	18.5	18.5	18.4	18.2	19.5	17.6	26
Nd	15.6	15.7	15.6	15.2	15.5	15.9	13.1	17.1	12.4	12.6	12.6	12.1	13.3	11.4	16.5
Sm	4.40	4.26	4.08	3.93	4.28	4.39	3.60	4.38	3.47	3.45	3.47	3.43	3.54	3.34	4.59
Eu	1.36	1.53	1.49	1.29	1.36	1.46	1.24	1.54	1.30	1.22	1.12	1.18	1.29	1.10	1.53
Gd	5.16	4.72	5.33	4.09	4.82	4.75	4.06	5.26	4.04	4.14	4.32	4.09	4.02	3.62	5.43
Dy	5.34	5.17	5.01	4.59	5.24	4.99	4.30	5.24	4.40	4.32	4.25	4.45	4.47	3.99	5.06
Er	3.01	2.98	2.63	2.43	2.92	2.76	2.47	2.83	2.57	2.57	2.60	2.40	2.61	2.25	2.92
Yb	2.95	2.90	2.98	2.42	2.74	2.69	2.55	2.68	2.56	2.70	2.34	2.40	2.51	2.32	2.92
Ta	0.61	0.72	0.76	0.73	0.74	0.83	0.48	0.77	0.51	0.53	0.47	0.52	0.57	0.50	0.74
Pb	1.40	1.30	1.14	1.28	1.19	1.18	0.76	0.95	0.63	0.56	0.78	0.52	1.01	0.64	0.89
Th	1.12	1.03	1.06	1.07	1.04	1.12	0.76	1.07	0.73	0.78	0.77	0.77	0.81	0.76	1.20
U	0.24	0.24	0.27	0.24	0.22	0.25	0.17	0.28	0.16	0.16	0.17	0.17	0.18	0.17	0.24

University of Cape Town

Table B.5 (cont.)

Sample	4D-11	4D-12	4D-13	4D-14	4D-15	5D-1	5D-2	5D-3	5D-4	5D-5	5D-6	5D-7	5D-8	5D-9	6D-1
Lat. (°S)	47.97	47.97	47.97	47.97	47.97	48.24	48.24	48.24	48.24	48.24	48.24	48.24	48.24	48.24	48.55
Long. (°W)	10.08	10.08	10.08	10.08	10.08	10.00	10.00	10.00	10.00	10.00	10.00	10.00	10.00	10.00	10.17
MBSL	2895	2895	2895	2895	2895	3453	3453	3453	3453	3453	3453	3453	3453	3453	3267
SiO_2	51.49	50.81	50.77	50.86	50.84	51.69	52.01	51.76	51.46	51.09	51.31	50.93	51.00	51.14	51.85
TiO_2	1.84	1.82	1.81	1.84	1.81	1.81	1.82	1.73	1.86	1.86	1.94	1.80	1.90	1.84	1.52
Al_2O_3	15.08	15.17	15.10	15.10	15.08	14.90	14.94	14.61	14.92	15.55	15.50	15.52	15.59	15.49	15.51
FeO	9.42	9.46	9.61	9.60	9.64	9.26	9.24	9.33	9.10	9.21	9.09	9.21	9.11	9.16	8.38
MnO	0.20	0.17	0.21	0.14	0.15	0.15	0.14	0.14	0.14	0.15	0.15	0.16	0.18	0.15	0.15
MgO	7.25	7.35	7.28	7.24	7.36	7.14	7.29	7.26	7.29	7.08	6.59	6.97	7.27	7.28	7.46
CaO	10.51	10.53	10.41	10.47	10.68	10.40	10.57	10.47	10.45	10.52	10.72	10.46	10.75	10.59	11.31
Na_2O	3.04	3.17	3.09	3.08	3.09	3.24	3.33	3.23	3.30	3.14	3.16	3.24	3.15	3.15	2.75
K_2O	0.54	0.54	0.53	0.55	0.55	0.65	0.66	0.65	0.66	0.67	0.66	0.67	0.67	0.65	0.64
P_2O_5	0.26	0.27	0.27	0.25	0.26	0.25	0.25	0.26	0.28	0.24	0.25	0.25	0.29	0.24	0.17
Total	99.63	99.29	99.08	99.13	99.46	99.49	100.25	99.44	99.46	99.51	99.37	99.21	99.91	99.69	99.74
Mg#	60.9	61.1	60.5	60.4	60.7	60.9	61.5	61.2	61.8	60.9	59.5	60.5	61.8	61.7	64.3
Sc	37	37	37	36	36	33	34	34	34	33	35	34	34	35	35
Ni	92	83	90	91	91	77	87	84	82	86	92	84	91	96	83
Rb	8.96	8.57	8.66	9.20	8.82	10.6	10.1	10.1	10.0	10.5	10.3	10.1	10.8	10.4	9.88
Sr	181	182	178	178	180	224	229	226	224	227	230	228	233	229	228
Y	31	30	30	29	29	25	27	26	27	26	27	27	26	27	21
Zr	135	134	133	131	132	132	144	143	142	144	146	142	140	147	101
Nb	11.3	11.0	11.2	11.6	11.4	13.1	13.4	13.6	13.3	13.4	13.6	13.4	14.0	13.5	11.1
Ba	124	124	120	122	122	150	153	147	148	152	152	153	157	153	144
La	11.9	11.9	11.7	11.8	11.7	13.2	13.7	13.7	14.0	14.1	14.3	14.3	14.1	13.9	10.6
Ce	26	25	25	25	25	28	28	28	28	28	29	29	29	28	22
Nd	16.3	17.0	16.6	16.2	15.9	16.9	17.8	17.1	16.8	17.2	17.4	17.5	17.0	17.7	14.0
Sm	4.16	4.39	4.56	4.09	4.60	4.20	4.08	4.22	4.24	4.20	4.78	4.19	4.35	4.35	3.54
Eu	1.38	1.43	1.31	1.41	1.51	1.41	1.45	1.51	1.50	1.65	1.73	1.56	1.49	1.62	1.24
Gd	5.07	5.05	5.09	4.69	4.42	4.45	4.67	4.69	4.72	4.86	5.12	5.02	4.69	5.00	4.07
Dy	5.26	4.99	4.87	4.99	4.63	4.50	4.79	4.74	4.71	4.92	4.50	4.59	4.69	4.76	3.69
Er	3.06	3.01	2.97	2.91	2.83	2.47	2.70	2.76	2.76	2.54	2.97	2.54	2.52	2.73	2.18
Yb	2.93	2.94	2.99	2.79	2.71	2.52	2.54	2.37	2.56	2.54	2.43	2.73	2.39	2.47	2.06
Ta	0.69	0.73	0.78	0.75	0.71	0.87	0.94	0.91	0.78	0.88	0.93	0.87	0.86	0.92	0.74
Pb	1.04	0.75	1.07	0.71	0.92	1.00	1.44	1.31	1.28	1.45	1.46	1.35	1.43	1.35	0.92
Th	1.12	1.13	1.16	1.07	1.12	1.32	1.35	1.34	1.31	1.38	1.36	1.32	1.35	1.36	0.94
U	0.23	0.23	0.25	0.24	0.25	0.30	0.30	0.29	0.28	0.27	0.33	0.28	0.29	0.30	0.17

University of Cape Town

Table B.5 (cont.)

Sample	6D-2	6D-3	6D-4	7D-1	7D-2	7D-4	7D-5	7D-6	7D-7	7D-8	7D-9	7D-10	8D-1	8D-2	8D-3
Lat. (°S)	48.55	48.55	48.55	48.76	48.76	48.76	48.76	48.76	48.76	48.76	48.76	48.76	48.96	48.96	48.96
Long. (°W)	10.17	10.17	10.17	10.07	10.07	10.07	10.07	10.07	10.07	10.07	10.07	10.07	9.97	9.97	9.97
MBSL	3267	3267	3267	3218	3218	3218	3218	3218	3218	3218	3218	3218	3894	3894	3894
SiO_2	51.62	51.00	51.53	51.23	51.89	51.54	51.35	51.02	51.21	51.23	51.03	52.08	52.13	50.77	50.89
TiO_2	1.51	1.44	1.46	1.53	2.52	2.48	1.46	1.50	1.61	1.61	1.51	1.70	1.68	1.63	1.67
Al_2O_3	15.85	15.86	15.72	16.40	13.15	13.64	16.51	16.82	16.79	16.66	16.66	14.05	15.02	15.49	15.23
FeO	8.35	8.33	8.46	7.88	12.47	12.46	7.86	7.87	7.73	7.85	7.68	10.93	9.69	10.19	9.75
MnO	0.17	0.17	0.18	0.14	0.15	0.19	0.15	0.15	0.14	0.15	0.14	0.20	0.14	0.15	0.15
MgO	7.42	7.56	7.57	6.79	5.51	5.68	6.91	6.86	6.94	6.85	6.87	6.67	7.38	7.31	7.31
CaO	11.21	11.23	11.34	10.52	9.24	9.33	10.43	10.59	10.63	10.37	10.78	10.95	10.90	10.71	10.67
Na_2O	2.82	2.74	2.81	3.15	3.25	3.23	3.24	3.13	3.20	3.22	3.30	2.85	3.10	3.01	2.99
K_2O	0.61	0.61	0.61	1.22	0.64	0.62	1.21	1.16	1.18	1.19	1.17	0.45	0.37	0.38	0.39
P_2O_5	0.23	0.21	0.20	0.27	0.29	0.29	0.31	0.27	0.28	0.28	0.28	0.21	0.16	0.22	0.20
Total	99.79	99.15	99.88	99.13	99.11	99.46	99.43	99.37	99.71	99.37	99.42	100.09	100.57	99.86	99.25
Mg#	64.3	64.7	64.4	63.6	47.2	48.0	64.0	63.8	64.5	63.8	64.4	55.3	60.6	59.2	60.3
Sc	34	36	35	30	43	46	30	32	32	30	31	46	40	38	40
Ni	81	88	88	70	38	40	65	71	69	65	70	54	82	81	82
Rb	9.91	9.84	9.96	19.0	12.5	12.9	18.9	19.8	19.6	19.3	18.9	7.71	6.49	6.20	6.60
Sr	227	227	231	347	129	130	345	350	348	335	351	127	137	137	137
Y	21	21	22	19	47	48	19	20	19	19	19	32	32	32	32
Zr	100	101	102	126	174	182	127	135	130	127	128	109	118	120	120
Nb	11.0	11.1	11.3	21	13.8	13.5	19.4	20	21	19.8	21	8.05	7.49	7.53	7.51
Ba	143	148	150	305	156	154	289	303	298	295	304	108	91	90	89
La	10.3	10.7	10.9	17.8	13.4	13.9	17.5	18.0	18.0	17.8	17.9	8.60	8.51	8.72	8.61
Ce	21	21	22	34	30	29	33	34	34	33	35	19.1	18.9	18.5	18.7
Nd	12.5	13.6	13.3	18.2	21	21	17.7	18.5	18.1	17.9	18.6	13.1	13.5	13.8	13.8
Sm	3.59	3.56	3.42	4.16	5.42	5.90	3.85	4.13	4.12	4.02	4.33	3.58	4.05	4.36	3.99
Eu	1.27	1.25	1.24	1.56	1.92	1.90	1.37	1.50	1.53	1.36	1.45	1.48	1.37	1.36	1.38
Gd	3.89	4.23	3.82	3.85	7.37	6.84	4.33	4.33	3.84	3.84	3.94	4.83	4.61	4.80	4.99
Dy	3.50	3.94	3.88	3.74	7.77	8.26	3.51	3.79	3.56	3.31	3.66	5.65	5.34	5.09	5.40
Er	2.21	2.03	2.22	1.76	4.39	4.72	1.77	1.87	1.82	1.80	1.72	3.25	3.22	3.24	3.33
Yb	1.97	2.28	2.00	1.73	4.60	5.09	1.62	1.95	1.75	1.88	1.82	3.32	3.24	3.23	3.24
Ta	0.73	0.74	0.77	1.27	0.87	0.89	1.29	1.28	1.23	1.24	1.21	0.56	0.44	0.40	0.48
Pb	0.95	0.99	1.08	1.69	1.25	1.15	1.62	1.65	1.70	1.52	1.63	0.84	0.75	0.82	1.31
Th	0.88	0.96	0.95	1.90	1.08	1.05	1.71	1.88	1.88	1.75	1.81	0.61	0.65	0.56	0.61
U	0.21	0.22	0.21	0.42	0.27	0.28	0.43	0.42	0.41	0.39	0.47	0.16	0.17	0.14	0.16

University of Cape Town

Table B.5 (cont.)

Sample	8D-4	8D-5	9D-1	9D-2	9D-3	9D-4	9D-5	9D-6	9D-7	10D-1	10D-2	10D-3	10D-4	10D-5	10D-6
Lat. (°S)	48.96	48.96	49.15	49.15	49.15	49.15	49.15	49.15	49.15	49.25	49.25	49.25	49.25	49.25	49.25
Long. (°W)	9.97	9.97	9.91	9.91	9.91	9.91	9.91	9.91	9.91	8.14	8.14	8.14	8.14	8.14	8.14
MBSL	3894	3894	3892	3892	3892	3892	3892	3892	3892	3860	3860	3860	3860	3860	3860
SiO_2	51.28	51.13	52.14	51.99	49.27	50.86	50.77	51.36	51.15	51.51	51.47	50.69	50.67	50.84	50.46
TiO_2	1.71	1.61	1.76	1.75	0.99	1.78	1.77	1.74	1.74	1.47	1.46	1.50	1.51	1.53	1.48
Al_2O_3	15.37	15.29	15.34	15.00	15.22	15.45	15.73	15.57	15.63	14.78	15.50	15.34	15.58	15.32	15.35
FeO	9.89	9.96	9.60	9.71	10.13	9.57	9.94	9.59	9.61	9.79	9.60	9.68	9.80	9.81	10.06
MnO	0.18	0.18	0.14	0.14	0.15	0.16	0.14	0.15	0.14	0.16	0.15	0.15	0.17	0.15	0.20
MgO	7.18	7.27	7.16	7.34	8.67	7.06	7.15	7.12	7.24	7.99	7.79	7.89	7.94	8.16	8.14
CaO	10.79	10.79	10.38	10.08	11.86	10.17	10.21	10.03	10.14	11.20	11.07	11.12	11.17	11.15	11.17
Na_2O	3.08	3.07	3.15	3.20	2.58	3.24	3.25	3.18	3.21	3.16	3.04	2.96	3.01	2.90	2.96
K_2O	0.38	0.39	0.53	0.51	0.16	0.51	0.51	0.50	0.51	0.08	0.08	0.07	0.07	0.09	0.07
P_2O_5	0.19	0.19	0.26	0.28	0.08	0.25	0.24	0.22	0.27	0.12	0.12	0.11	0.13	0.14	0.13
Total	100.05	99.86	100.46	100.00	99.11	99.05	99.71	99.46	99.64	100.26	100.28	99.51	100.03	100.09	100.02
Mg#	59.5	59.6	60.1	60.5	63.4	59.9	59.3	60.0	60.4	62.3	62.1	62.3	62.1	62.7	62.1
Sc	40	40	38	36	45	36	35	35	36	41	41	42	43	42	42
Ni	82	80	101	101	84	94	100	95	96	88	92	106	97	106	111
Rb	6.34	6.51	8.94	9.21	2.29	8.79	8.83	8.35	8.76	0.63	0.72	0.69	0.62	0.82	0.78
Sr	138	139	174	165	112	164	167	165	166	101	100	104	104	107	104
Y	32	31	38	35	24	34	35	35	34	32	33	34	35	35	33
Zr	119	119	161	149	54	148	146	143	148	87	91	93	97	98	95
Nb	7.58	7.96	10.8	10.5	2.86	10.2	10.4	10.3	10.5	1.58	1.33	1.64	1.56	1.99	1.88
Ba	92	92	123	114	35	116	118	113	115	9.17	9.26	9.32	9.59	11.0	10.5
La	8.56	8.49	12.5	11.6	3.42	11.3	11.4	11.7	11.4	2.95	2.94	2.99	3.15	3.49	3.22
Ce	18.8	19.4	27	25	8.13	24	25	24	25	9.17	8.81	9.06	9.47	10.4	9.83
Nd	14.0	13.5	18.9	17.7	6.74	16.7	17.3	16.6	17.0	9.03	9.89	9.55	9.91	10.3	9.81
Sm	4.05	3.74	5.66	4.83	2.19	4.96	5.00	4.63	4.75	3.46	3.51	3.16	3.74	3.65	3.52
Eu	1.51	1.44	1.75	1.55	0.85	1.61	1.65	1.66	1.60	1.30	1.25	1.30	1.37	1.33	1.35
Gd	4.88	5.20	6.49	6.18	3.09	5.59	6.06	5.98	5.66	4.51	5.09	5.19	5.39	5.19	4.91
Dy	5.58	5.20	6.61	6.17	3.75	5.71	5.78	5.74	6.10	5.29	5.29	5.82	5.64	5.86	5.39
Er	3.21	3.23	3.71	3.69	2.55	3.38	3.45	3.47	3.52	3.30	3.41	3.54	3.47	3.44	3.25
Yb	3.21	3.05	3.80	3.38	2.66	3.52	3.43	3.39	3.35	3.39	3.55	3.75	3.55	3.45	3.48
Ta	0.45	0.43	0.70	0.65	0.19	0.65	0.63	0.68	0.68	0.13	0.12	0.15	0.14	0.15	0.16
Pb	0.65	0.78	1.06	1.10	0.31	1.24	0.95	0.97	1.00	0.34	0.40	0.32	0.31	0.40	0.30
Th	0.69	0.65	1.05	0.96	0.25	0.99	0.92	0.97	0.93	0.12	0.14	0.14	0.15	0.16	0.17
U	0.13	0.16	0.20	0.19	0.05	0.19	0.21	0.20	0.22	0.04	0.04	0.03	0.05	0.04	0.04

University of Cape Town

Table B.5 (cont.)

Sample	11D-1	11D-2	11D-3	11D-4	11D-5	11D-6	11D-7	11D-8	11D-9	12D-1	12D-2	12D-3	12D-6	12D-7	12D-8
Lat. (°S)	49.44	49.44	49.44	49.44	49.44	49.44	49.44	49.44	49.44	49.76	49.76	49.76	49.76	49.76	49.76
Long. (°W)	7.97	7.97	7.97	7.97	7.97	7.97	7.97	7.97	7.97	8.03	8.03	8.03	8.03	8.03	8.03
MBSL	3868	3868	3868	3868	3868	3868	3868	3868	3868	3874	3874	3874	3874	3874	3874
SiO_2	50.91	51.63	51.19	50.39	50.53	50.49	50.66	50.68	50.50	50.59	51.92	50.01	49.99	50.16	50.51
TiO_2	1.38	1.41	1.41	1.45	1.42	1.36	1.42	1.45	1.45	1.09	1.25	1.11	1.13	1.32	1.28
Al_2O_3	15.16	14.93	15.02	15.34	15.25	15.36	15.27	15.24	15.21	15.61	14.85	16.31	16.32	15.08	15.17
FeO	9.97	10.22	9.91	10.18	9.92	9.87	9.99	9.81	10.05	10.27	9.43	9.35	9.68	9.43	9.40
MnO	0.16	0.15	0.15	0.15	0.15	0.21	0.13	0.20	0.13	0.14	0.15	0.14	0.20	0.20	0.17
MgO	8.02	8.29	8.12	8.03	8.10	8.00	8.16	7.95	8.20	8.70	8.42	8.67	8.64	8.28	8.23
CaO	11.40	11.33	11.51	11.49	11.47	11.45	11.42	11.39	11.42	11.65	12.13	11.75	11.68	12.10	12.02
Na_2O	2.80	2.83	2.81	2.82	2.84	2.84	2.95	2.83	2.87	2.65	2.58	2.52	2.55	2.54	2.60
K_2O	0.05	0.06	0.06	0.06	0.07	0.06	0.06	0.06	0.06	0.04	0.04	0.05	0.04	0.05	0.05
P_2O_5	0.10	0.11	0.12	0.12	0.13	0.14	0.10	0.13	0.13	0.06	0.09	0.08	0.09	0.13	0.12
Total	99.95	100.96	100.30	100.03	99.88	99.78	100.16	99.74	100.02	100.80	100.86	99.99	100.32	99.29	99.55
Mg#	61.9	62.1	62.4	61.5	62.3	62.1	62.3	62.1	62.3	63.2	64.4	65.2	64.4	64.0	63.9
Sc	43	43	43	45	43	43	42	42	42	45	44	44	42	44	45
Ni	99	111	103	113	110	110	106	111	112	116	107	119	119	88	98
Rb	0.49	0.51	0.46	0.49	0.50	0.47	0.44	0.42	0.53	0.41	0.44	0.38	0.35	0.44	0.39
Sr	99	99	100	104	102	101	101	101	101	92	91	94	94	90	88
Y	31	30	32	35	32	30	31	31	30	26	29	25	24	28	28
Zr	82	83	88	91	85	82	83	82	82	59	73	57	57	72	72
Nb	1.40	1.25	1.43	1.36	1.43	1.30	1.32	1.38	1.37	1.13	1.22	1.07	1.09	1.38	1.15
Ba	6.61	6.64	7.51	6.69	7.22	7.24	6.83	7.75	6.91	5.98	6.94	6.11	5.76	6.89	6.64
La	2.63	2.79	2.72	2.79	2.73	2.74	2.55	2.65	2.80	2.04	2.51	1.88	1.85	2.30	2.43
Ce	8.34	8.35	8.52	8.99	8.62	8.61	8.53	8.70	8.43	6.12	7.37	5.99	6.13	7.34	7.36
Nd	8.25	8.15	9.27	9.25	8.96	8.85	8.76	8.34	9.18	6.54	8.03	6.07	6.07	7.62	7.91
Sm	3.05	3.21	3.05	3.34	3.15	2.96	3.21	2.97	3.12	2.19	2.97	2.22	2.20	2.66	2.87
Eu	1.23	1.16	1.12	1.26	1.25	1.18	1.20	1.18	1.29	0.96	1.02	0.90	0.97	1.16	1.13
Gd	4.36	4.19	4.81	5.09	4.51	4.33	4.48	4.72	4.16	3.39	4.05	3.50	3.27	4.17	3.99
Dy	4.98	4.99	5.24	5.27	4.92	5.02	4.68	4.69	4.88	4.25	4.52	4.46	4.13	4.36	4.11
Er	3.07	3.24	3.08	3.56	2.99	3.14	2.82	2.99	2.90	2.77	2.80	2.57	2.44	2.77	2.79
Yb	2.96	3.28	3.36	3.23	3.28	3.16	3.13	3.27	3.15	2.47	2.74	2.72	2.51	3.04	2.79
Ta	0.12	0.14	0.15	0.13	0.08	0.12	0.15	0.16	0.14	0.10	0.10	0.13	0.11	0.10	0.11
Pb	< 0.18	0.30	0.44	0.43	0.33	0.32	0.28	0.72	0.18	0.19	0.26	0.19	< 0.18	< 0.18	< 0.18
Th	0.11	0.12	0.13	0.13	0.12	0.11	0.09	0.11	0.12	0.09	0.10	0.09	0.09	0.09	0.09
U	0.03	< 0.02	0.04	0.04	0.03	0.03	0.03	0.03	0.02	< 0.02	0.02	0.03	< 0.02	0.03	0.03

University of Cape Town

University of Cape Town

Table B.5 (cont.)

Sample	13D-12	13D-13	13D-14	14D-1	14D-2	14D-3	14D-4	14D-5	14D-6	24D-3	15D-1	15D-2	15D-3	15D-4	15D-5
Lat. (°S)	49.99	49.99	49.99	50.27	50.27	50.27	50.27	50.27	50.27	50.46	50.58	50.58	50.58	50.58	50.58
Long. (°W)	7.88	7.88	7.88	7.06	7.06	7.06	7.06	7.06	7.06	6.53	6.43	6.43	6.43	6.43	6.43
MBSL	3555	3555	3555	3347	3347	3347	3347	3347	3347	3183	2980	2980	2980	2980	2980
SiO_2	50.48	50.14	50.45	51.04	51.14	51.02	50.81	51.68	49.75	50.58	50.10	51.36	51.01	51.43	49.88
TiO_2	1.13	1.11	1.08	1.62	1.61	1.56	1.59	1.66	1.56	1.82	1.64	1.46	1.59	1.38	1.61
Al_2O_3	15.58	15.48	15.33	14.33	14.93	14.89	15.04	13.99	15.71	14.82	14.64	14.10	13.96	14.56	14.60
FeO	8.83	8.72	8.61	10.83	9.98	10.00	9.68	10.98	9.92	10.92	10.80	10.64	10.53	9.93	10.73
MnO	0.16	0.17	0.16	0.15	0.15	0.15	0.14	0.14	0.14	0.15	0.17	0.15	0.15	0.14	0.20
MgO	8.88	8.77	8.78	7.41	8.31	8.36	8.33	7.55	8.05	7.37	7.81	8.23	8.03	8.27	8.03
CaO	12.32	12.64	12.38	11.52	11.23	11.19	11.27	11.36	11.33	11.22	11.45	11.75	11.51	11.99	11.35
Na_2O	2.49	2.43	2.45	2.58	2.75	2.75	2.83	2.67	2.73	2.75	2.49	2.46	2.50	2.50	2.48
K_2O	0.04	0.04	0.03	0.08	0.29	0.29	0.28	0.08	0.29	0.18	0.14	0.12	0.14	0.14	0.14
P_2O_5	0.09	0.10	0.08	0.12	0.16	0.16	0.16	0.12	0.15	0.19	0.13	0.10	0.14	0.13	0.14
Total	100.00	99.60	99.35	99.68	100.55	100.37	100.13	100.23	99.63	100.00	99.37	100.37	99.56	100.47	99.16
Mg#	67.1	67.1	67.4	58.1	62.8	62.8	63.5	58.2	62.2	57.7	59.4	61.0	60.7	62.8	60.2
Sc	44	45	45	49	40	40	40	48	41	45	44	44	46	44	43
Ni	148	107	102	79	113	118	116	77	121	84	89	94	89	90	97
Rb	0.33	0.32	0.32	1.17	4.28	4.38	4.38	1.02	4.21	2.70	2.28	1.84	2.04	2.08	2.18
Sr	89	91	86	88	122	123	127	86	123	98	92	85	93	96	94
Y	24	26	24	37	32	31	32	35	31	36	34	31	34	28	33
Zr	60	64	59	97	107	107	108	93	109	108	95	80	96	78	94
Nb	0.97	1.10	0.85	2.77	7.84	7.74	7.82	2.62	7.38	5.73	4.80	3.70	4.42	4.43	4.79
Ba	4.34	4.73	4.50	11.1	51	51	52	11.1	49	28	24	18.2	24	23	25
La	1.91	1.96	1.73	3.45	6.53	6.62	6.69	3.37	6.27	5.29	4.64	3.75	4.70	4.38	4.74
Ce	5.97	6.26	5.81	10.4	14.2	14.7	15.0	9.96	14.6	13.5	11.6	9.53	11.7	10.4	11.9
Nd	7.09	6.74	6.50	9.56	11.4	11.3	12.2	9.84	11.5	11.7	10.4	8.79	10.5	8.80	10.5
Sm	2.15	2.37	2.27	3.51	3.54	3.59	3.65	3.48	3.41	3.58	3.46	3.14	3.36	3.04	3.51
Eu	0.93	0.95	0.98	1.36	1.24	1.26	1.33	1.29	1.17	1.33	1.31	1.11	1.25	1.10	1.32
Gd	3.13	3.72	3.57	4.92	5.03	4.62	4.90	5.30	4.46	5.50	4.45	4.47	4.59	4.10	4.61
Dy	3.81	4.07	3.96	6.09	5.49	5.37	5.52	6.02	5.29	6.16	5.88	5.06	5.42	4.80	5.55
Er	2.35	2.47	2.46	3.60	2.95	2.89	3.25	3.65	3.07	3.56	3.52	3.04	3.27	2.89	3.27
Yb	2.25	2.40	2.34	3.96	3.09	3.19	3.13	3.80	2.96	3.83	3.50	3.26	3.59	2.90	3.60
Ta	< 0.06	< 0.06	< 0.06	0.19	0.53	0.45	0.52	0.17	0.46	0.38	0.31	0.24	0.30	0.25	0.30
Pb	0.26	0.36	0.25	0.57	0.88	0.63	0.67	0.60	0.79	0.73	0.58	0.44	0.63	0.38	0.39
Th	0.07	0.07	0.06	0.20	0.55	0.54	0.55	0.19	0.58	0.42	0.35	0.28	0.35	0.29	0.36
U	0.02	0.02	< 0.02	0.05	0.15	0.16	0.15	0.05	0.14	0.13	0.11	0.07	0.10	0.11	0.11

University of Cape Town

University of Cape Town

University of Cape Town

University of Cape Town

University of Cape Town

University of Cape Town

University of Cape Town

University of Cape Town

University of Cape Town

University of Cape Town

University of Cape Town

University of Cape Town

University of Cape Town

University of Cape Town

University of Cape Town

University of Cape Town

University of Cape Town

University of Cape Town

University of Cape Town

University of Cape Town

University of Cape Town

University of Cape Town